Vol. 283, No. 2, November 26, 1993 ISSN 0003-2670

ANALYTICA CHIMICA ACTA

An international journal devoted to all branches of analytical chemistry

ELSEVIER

ANALYTICA CHIMICA ACTA

Scope. *Analytica Chimica Acta* publishes original papers, preliminary communications and reviews dealing with every aspect of modern analytical chemistry. Reviews are normally written by invitation of the editors, who welcome suggestions for subjects. Preliminary communications of important urgent work can be printed within four months of submission, if the authors are prepared to forego proofs.

Submission of Papers

Americas

Prof. Harry L. Pardue
Department of Chemistry
1393 BRWN Bldg, Purdue University
West Lafayette, IN 47907–1393
USA

Tel:(+1-317) 494 5320
Fax:(+1-317) 496 1200

Computer Techniques

Prof. J.T. Clerc
Universität Bern
Pharmazeutisches Institut
Baltzerstrasse 5, CH-3012 Bern
Switzerland

Tel:(+41-31) 654171
Fax:(+41-31) 654198

Prof. Sarah C. Rutan
Department of Chemistry
Virginia Commonwealth University
P.O. Box 2006
Richmond, VA 23284-2006
USA
Tel:(+1-804) 367 1298
Fax:(+1-804) 367 8599

Other Papers

Prof. Alan Townshend
Department of Chemistry
The University
Hull HU6 7RX
Great Britain

Tel:(+44-482) 465027
Fax:(+44-482) 466410

Prof. Willem E. van der Linden
Laboratory for Chemical Analysis
Department of Chemical Technology
Twente University of Technology
P.O. Box 217, 7500 AE Enschede
The Netherlands
Tel:(+31-53) 892629
Fax:(+31-53) 356024

Prof. Paul Worsfold
Dept. of Environmental Sciences
University of Plymouth
Plymouth PL4 8AA
Great Britain

Tel:(+44-752) 233006
Fax:(+44-752) 233009

Submission of an article is understood to imply that the article is original and unpublished and is not being considered for publication elsewhere. *Anal. Chim. Acta* accepts papers in English only. There are no page charges. Manuscripts should conform in layout and style to the papers published in this issue. See inside back cover for "Information for Authors".

Publication. *Analytica Chimica Acta* appears in 16 volumes in 1994 (Vols. 281–296). *Vibrational Spectroscopy* appears in 2 volumes in 1994 (Vols. 6 and 7). Subscriptions are accepted on a prepaid basis only, unless different terms have been previously agreed upon. It is possible to order a combined subscription (*Anal. Chim. Acta* **and** *Vib. Spectrosc.*).
Our p.p.h. (postage, packing and handling) charge includes surface delivery of all issues, except to subscribers in the U.S.A., Canada, Australia, New Zealand, China, India, Israel, South Africa, Malaysia, Thailand, Singapore, South Korea, Taiwan, Pakistan, Hong Kong, Brazil, Argentina and Mexico, who receive all issues by air delivery (S.A.L.–Surface Air Lifted) at no extra cost. For Japan, air delivery requires 25% additional charge of the normal postage and handling charge; for all other countries airmail and S.A.L. charges are available upon request.

Subscription orders. Subscription prices are available upon request from the publisher. Subscription orders can be entered only by calendar year and should be sent to: Elsevier Science Publishers B.V., Journals Department, P.O. Box 211, 1000 AE Amsterdam, The Netherlands. Tel: (+31-20) 5803 642, Telex: 18582, Telefax: (+31-20) 5803598, to which requests for sample copies can also be sent. Claims for issues not received should be made within six months of publication of the issues. If not they cannot be honoured free of charge. Readers in the U.S.A. and Canada can contact the following address: Elsevier Science Publishing Co. Inc., Journal Information Center, 655 Avenue of the Americas, New York, NY 10010, U.S.A. Tel: (+1-212) 6333750, Telefax: (+1-212) 6333990, for further information, or a free sample copy of this or any other Elsevier Science Publishers journal.
Advertisements. Advertisement rates are available from the publisher on request.

US mailing notice – Analytica Chimica Acta (ISSN 0003-2670) is published biweekly by Elsevier Science Publishers (Molenwerf 1, Postbus 211, 1000 AE Amsterdam). Annual subscription price in the USA US$ 3035.75 (valid in North, Central and South America), including air speed delivery. Second class postage paid at Jamaica, NY 11431. *USA Postmasters*: Send address changes to Anal. Chim. Acta, Publications Expediting, Inc., 200 Meacham Av., Elmont, NY 11003. Airfreight and mailing in the USA by Publication Expediting.

ANALYTICA CHIMICA ACTA

An international journal devoted to all branches of analytical chemistry

(Full texts are incorporated in CJELSEVIER, a file in the Chemical Journals Online database available on STN International; Abstracted, indexed in: Aluminum Abstracts; Anal. Abstr.; Biol. Abstr.; BIOSIS; Chem. Abstr.; Curr. Contents Phys. Chem. Earth Sci.; Engineered Materials Abstracts; Excerpta Medica; Index Med.; Life Sci.; Mass Spectrom. Bull.; Material Business Alerts; Metals Abstracts; Sci. Citation Index)

VOL. 283 NO. 2 CONTENTS NOVEMBER 26, 1993

(Continued overleaf)

Analytica Chimica Acta, 283 (1993) 663–671
Elsevier Science Publishers B.V., Amsterdam

Amperometric internal enzyme gas-sensing probe for hydrogen peroxide

Shengtian Pan and Mark A. Arnold

Department of Chemistry, University of Iowa, Iowa City, IA 52242 (USA)

(Received 1st April 1993; revised manuscript received 28th June 1993)

Abstract

A novel sensor for the selective detection of hydrogen peroxide is described. This sensor is based on the internal enzyme concept configured in a gas-sensing arrangement. Hydrogen peroxide diffuses across a microporous PTFE membrane and enters the internal solution. The entering hydrogen peroxide is then electrochemically reduced by a horseradish peroxidase (HRP) catalyzed reaction with ferrocyanide as a mediator and the corresponding cathodic current is monitored. This sensing arrangement provides excellent selectivity over ionic species in solution that cannot penetrate the gas-permeable barrier. Critical design parameters include the pH and concentrations of electrolyte, HRP and ferrocyanide in the internal solution as well as the porosity and thickness of the gas-permeable membrane. The response properties are strongly influenced by temperature; where as, they are relatively insensitive to sample pH. The dynamic range for this sensor can be controlled by adjusting the composition of the internal solution, the physical properties of the membrane, and the temperature. The detection limit is 2 μM for sensors with an internal solution composed of 0.5 M potassium chloride, 0.05 M pH 7.4 phosphate buffer, 3 U ml^{-1} HRP and 0.5 mM ferrocyanide and a 0.45 μm microporous PTFE membrane. Sensors possess response times of 30 s and recovery times less than a minute.

Keywords: Sensors; Amperometry; Enzymatic methods; Enzyme gas-sensing probe; Hydrogen peroxide

The detection of hydrogen peroxide is commonly used in bioanalytical chemistry because of the wide availability of oxidase enzymes. These enzymes selectively catalyze the oxidization of a substrate, in the presence of oxygen, to form the reduced substrate and hydrogen peroxide. Oxidase enzymes coupled with direct amperometric detection of hydrogen peroxide have been used extensively to construct both biosensors and automated analyzers. Unfortunately, the direct oxidation of hydrogen peroxide requires a high overpotential (+0.6 V vs. SCE on platinum and +0.9 V vs. SCE on carbon) [1] which renders the measurement susceptible to interference by easily oxidizable compounds frequently present in biological matrices, such as ascorbic acid, uric acid and acetominophen. Size exclusion [2] and anionic [3] membranes have been used to enhance selectivity by physically restricting these interferences from reaching the electrode surface. Although these membranes increase the selectivity by several orders of magnitude, they do not provide absolute selectivity for hydrogen peroxide.

More recently, hydrogen peroxide has been measured by a horseradish peroxidase (HRP) catalyzed reduction reaction [4]. In this system, HRP catalyzes the reduction of hydrogen peroxide, thereby forming the oxidized form of HRP which is subsequently reduced by a suitable mediator such as ferrocene. The oxidized form of the mediator is then reduced electrochemically at an ap-

Correspondence to: M.A. Arnold, Department of Chemistry, University of Iowa, Iowa City, IA 52242 (USA).

plied potential close to 0 V. Selectivity over easily oxidizable compounds is greatly enhanced by this low potential. Unfortunately, compounds such as ascorbic acid are still oxidized, albeit only slightly, under these conditions which creates a negative interference when such compounds are present at high concentrations relative to the analyte. This approach requires either adding a mediator to the sample or constructing a mediating polymer network at the electrode surface [5].

We have recently demonstrated the feasibility of hydrogen peroxide measurements with a fiber-optic internal enzyme biosensor that uses a gas-permeable microporous PTFE membrane to differentiate hydrogen peroxide from potential interferences [6]. We have found that the vapor pressure of hydrogen peroxide allows a significant amount of hydrogen peroxide to cross the membrane and enter an internal solution composed of HRP and luminol. Upon entering this solution, the HRP catalyzed chemiluminescence reaction between hydrogen peroxide and luminol produces light that is monitored by a fiber-optic based detection system. The resulting intensity is directly proportional to the reaction rate which depends on the concentration of hydrogen peroxide in the sample.

Palleschi et al. [7] described a similar sensor for hydrogen peroxide based on an amperometric detection scheme. In this work a "hydrophobic blocking membrane" was used to prohibit interferences from entering an internal solution while freely passing hydrogen peroxide (the composition of their membrane was not provided in the paper). Upon entering the internal solution, the hydrogen peroxide was oxidized at a platinum electrode and the corresponding anodic current was monitored. We have found that the formation of protons and oxygen by this oxidation reaction can adversely affect sensor performance when a small volume of the internal solution is contained in a closed chamber. Under these conditions, pH changes can occur after limited operation. More importantly, the accumulation of oxygen in the chamber increases the internal pressure which ultimately forces the internal solution through the membrane, thereby emptying the chamber.

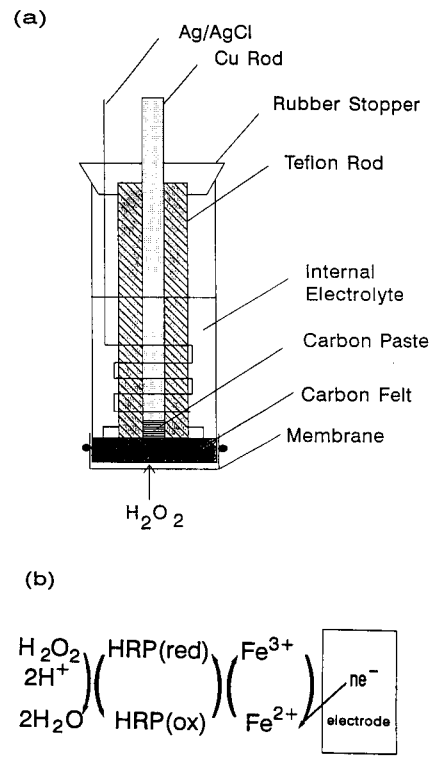

Fig. 1. Schematic diagram showing sensor configuration (a) and reaction steps (b) involved in hydrogen peroxide sensing.

This report details the analytical characteristics of an alternative amperometric gas sensor for hydrogen peroxide based on an internal enzyme configuration in conjunction with the reduction of hydrogen peroxide. A schematic of this electrode system and the reactions involved are presented in Fig. 1. As in the fiber-optic sensor, hydrogen peroxide vapor crosses a microporous PTFE membrane and enters the internal solution. This hydrogen peroxide is then reduced by HRP with ferrocyanide as the mediator between oxidized HRP and a carbon felt cathode. As before, the gas-permeable membrane provides absolute selectivity over ionic species such as ascorbate and urate which are not volatile and, therefore, cannot cross the membrane. A detection limit of 2 μM and response times of 30 s can be achieved by selecting the appropriate membrane and by adjusting the concentrations of components in the internal enzyme solution.

EXPERIMENTAL

Apparatus and reagents

All cyclic voltammograms (CVs) and amperometric measurements were made with a Model DCV-5 Voltammetry Controller from Bioanalytical Systems, (West Lafayette, IN): Voltammetric information was recorded on either a Soltex Model VP-6412S *X–Y* recorder or a Sargent-Welch Model XKR strip chart recorder. All pH measurements were made with a Ross-type combination pH electrode (Orion Model H4100-12) in conjunction with a Beckman Model ϕ72 meter.

Carbon paste electrodes and silver–silver chloride reference electrodes were purchased from Bioanalytical Systems. GF-S4 fine pressed carbon felt was obtained from Electrosynthesis (Lencaster, NY).

HRP (type I, 95 U mg^{-1}) was obtained from Sigma (St. Louis, MO). Concentrated hydrogen peroxide (30%) was purchased from Fisher (Chicago, IL) and was standardized periodically by titration with sodium thiosulfate. All other chemicals were obtained from common suppliers in reagent grade quality.

All solutions were prepared with distilled–deionized water by passing the house distilled water through a three-house Milli-Q water purification unit. Solution temperatures were controlled with a Fisher Model 80 bath coupled with glass jacketed cells.

Procedures

Gas-sensing probes were constructed according to the schematic diagram provided in Fig. 1a. The working electrode was a carbon felt disk with a diameter of 8.5 mm and a thickness of 0.3 mm. Carbon paste was used to connect this disk to a central copper rod. A silver–silver chloride electrode wrapped around a PTFE rod served as both reference and counter electrode. Individual sensors were built by securing a micro porous PTFE membrane to the tip of the sensor body with an O-ring. A 0.5-ml aliquot of the internal solution was then placed within the sensor body followed by insertion of the electrode assembly. The carbon felt electrode was pressed against the PTFE membrane to provide a thin layer of the internal solution between the membrane and the working electrode. A rubber stopper fixed the electrodes in place and sealed the inner chamber.

Probe responses were measured by recording cathodic currents as a function of time. The potential at the working electrode was maintained at 0 V vs. a silver–silver chloride reference electrode. Data for response curves were collected by first immersing the probe in a blank solution of working buffer to determine the background current. Microliter additions of a hydrogen peroxide standard were then added sequentially and the corresponding steady-state currents were measured. In most cases, the external solution was stirred continuously during the measurement with a magnetic stir bar. Stirring was stopped, however, to reduce noise when solutions with low hydrogen peroxide concentrations were measured. Response times were measured as the time required to achieve 95% of the final steady-state response after a step change in hydrogen peroxide concentration.

RESULTS AND DISCUSSION

The enzyme catalyzed reaction cycle illustrated in Fig. 1b was evaluated by cyclic voltammetry with a carbon paste working electrode. No reduction was detectable in solutions of phosphate buffer alone, phosphate buffer with hydrogen peroxide and phosphate buffer with both hydrogen peroxide and HRP. Curve A in Fig. 2 shows both the reduction and oxidation peaks observed for a solution composed of phosphate buffer with ferrocyanide. The addition of hydrogen peroxide had no influence on these currents in the absence of HRP. In the presence of both ferrocyanide and HRP, the anodic current decreased and, correspondingly, the cathodic current increased as a function of the concentration of hydrogen peroxide. Curves B and C in Fig. 2 show representative CVs for 0.2 and 0.5 mM hydrogen peroxide, respectively.

Internal solution composition

The nature of the amperometric response is influenced by the composition of the internal

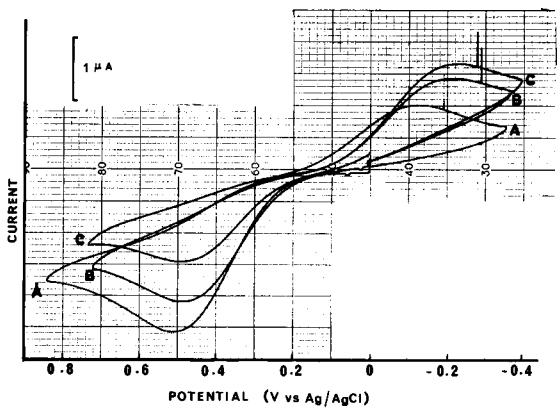

Fig. 2. Cyclic voltammograms for phosphate buffer, 0.5 M KCl, 3 U ml^{-1} HRP and 0.5 mM ferrocyanide with 0 mM (A), 0.2 mM (B) and 0.5 mM (C) hydrogen peroxide.

solution. Critical parameters investigated include pH and the concentrations of potassium chloride, HRP and ferrocyanide.

With potassium chloride as the supporting electrolyte, the cathodic and anodic peak positions can be adjusted somewhat by altering the potassium chloride concentration. The experimentally observed effect of the potassium chloride concentration on the peak positions is illustrated by the CVs presented in Fig. 3. These data were collected with a carbon felt working electrode in a 0.05 M, pH 7.4 phosphate buffer with 3 U ml^{-1} HRP, 0.5 mM ferrocyanide and a scan rate of 20 mV s^{-1}. Certainly, potassium chloride affects the peak potentials by altering the potential of the silver–silver chloride reference electrode. This effect shifts both the cathodic and anodic peaks in the same direction and has no effect on the difference between these peak potentials (ΔE_p). As can be seen in Fig. 3, however, higher concentrations of KCl shift the cathodic peak to more positive potentials while the anodic peak shifts to more negative potentials. Additionally, the peaks become more symmetrically at higher salt concentrations. Measured values for ΔE_p are 245, 215, 183, 140, 123, and 75 mV for potassium chloride concentrations of 0, 0.025, 0.05, 0.25, 0.5, and 1.0 M, respectively. Similar ΔE_p values were obtained under identical conditions but replacing the potassium chloride with potassium nitrate (ΔE_p = 360, 375, 255, and 280 mV for $[KNO_3]$ = 0.05, 0.1, 0.5, and 1.0 M, respectively). This salt effect has been described before for the ferricyanide/ferrocyanide redox couple and several explanations have been proposed [8–12].

The potassium chloride concentration selected for this particular sensor was 0.5 M which permitted an applied potential of 0 mV. This moderate potential provides high sensitivity for the cathodic reaction and this high salt concentration provides a low *IR*-drop which is critical for this two-electrode system.

The sensor response is independent of HRP concentration when saturating amounts of enzyme are added to the internal solution. Below this saturation point, however, the response is strongly affected by the amount of HRP. The effect of HRP concentration was determined by monitoring the response of individual sensors that were constructed with different HRP concentra-

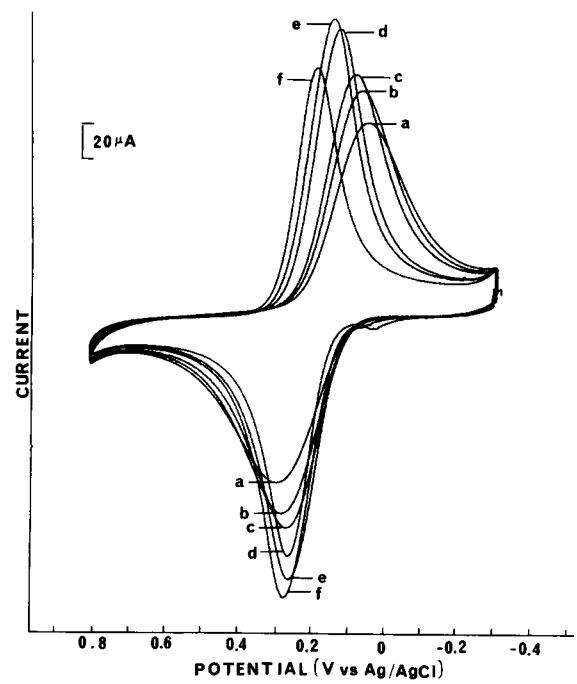

Fig. 3. Cyclic voltammograms for internal solutions with 0 M (a), 0.025 M (b), 0.05 M (c), 0.25 M (d), 0.5 M (e) and 1.0 M (f) potassium chloride.

tions in the internal solution. The remaining composition of this solution included 0.5 M potassium chloride, 0.05 M pH 7.5 phosphate buffer and 0.5 mM ferrocyanide. Both the magnitude of the steady-state current and the corresponding response time were measured for a step change in hydrogen peroxide concentration from zero to 0.678 mM. The results are plotted in Fig. 4 as a function of HRP concentration. The magnitude of response initially increases steeply with higher HRP concentrations until a saturating amount is reached. Shorter response times are obtained as the HRP level increases. A 3 U ml^{-1} HRP concentration was used in subsequent experiments.

Ferrocyanide concentrations ranging from 0.02 to 0.5 mM only slightly affect the sensor response. Plots of steady-state current versus hydrogen peroxide concentration, over the range from 0 to 6 mM, are linear for all tested ferrocyanide concentrations with slightly larger slopes with higher concentrations. Response times are affected only when responding to the highest hydrogen peroxide concentrations tested. At 2.43 mM hydrogen peroxide, response times range from 3.3 to 0.5 min over the tested range of ferrocyanide levels. The fastest sensor responses are obtained with a ferrocyanide concentration of 0.5 mM. Shorter response times were not observed at higher ferrocyanide concentrations.

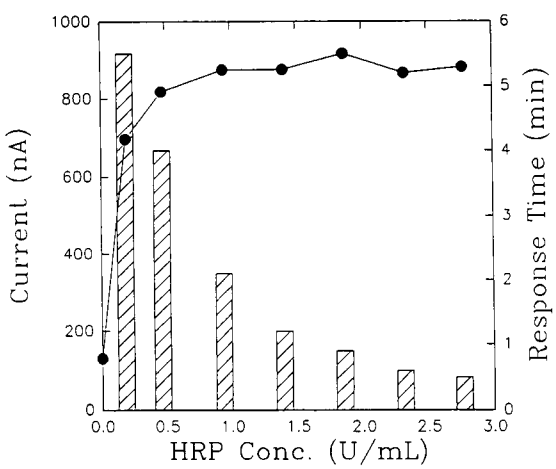

Fig. 4. Effect of HRP level on sensor response current (●) and response time (bar).

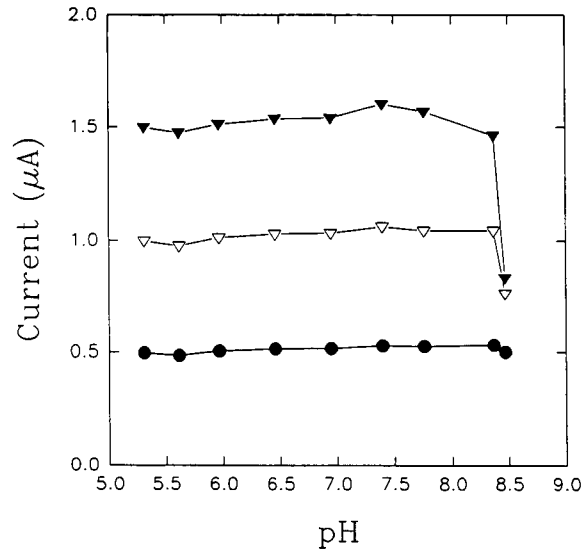

Fig. 5. Effect of internal solution pH on steady-state response for 0.346 mM (●), 0.678 mM (▽) and 0.988 mM (▼) hydrogen peroxide.

Both the steady-state and dynamic properties of the sensor are independent of the internal solution pH over the range from 5.3 to 7.8. Above pH 7.8, however, the magnitude of response decreases and response times increase with these effects being larger at higher hydrogen peroxide concentrations. The effect of pH on the measured steady-state response for three hydrogen peroxide concentrations is presented in Fig. 5. Response times are less than one minute for all hydrogen peroxide concentrations over the pH range from 5.3 to 7.8. Above 7.8, however, longer response times are obtained, particularly at higher concentrations of hydrogen peroxide. For example, response times of 2.5 and 3.5 min were measured for hydrogen peroxide concentrations of 0.678 and 0.998 mM, respectively, with an internal electrolyte pH of 8.4. The insensitivity of the response to pH is caused by using saturating amounts of HRP so that the overall reaction rate is not controlled by enzyme kinetics. At pH values above 7.8, the rate of the HRP catalyzed reaction rate decreases to a point of being rate limiting.

TABLE 1

Effect of membrane properties on sensor response

Membrane type	Pore size (μm)	Porosity (%)	Thickness (μm)	Slope (nA mM^{-1})
Plain [a]	0.02	50	76	135
Plain	0.45	84	76	1724
Laminated [b]	0.2	78	64	535
Laminated [b]	1.0	91	76	758
Laminated [c]	1.0	91	76	385

[a] Microporous PTFE. [b] Microporous PTFE with polyethylene lamination. [c] Microporous PTFE with polypropylene lamination.

Gas-permeable membrane

Five different microporous PTFE membranes were tested to identify the critical membrane parameters that affect sensor response. The effect of each membrane was ascertained by measuring the sensitivity of the corresponding sensor to hydrogen peroxide concentrations over a range from 0 to 600 μM. The pertinent information is summarized in Table 1.

Two membranes composed solely of microporous PTFE were tested first. These membranes had the same thickness, but different pore size and porosity. As indicated in Table 1, larger porosity resulted in higher sensitivity. Such an effect is characteristic of a gas-sensing configuration where the rate limiting step is mass transport across the membrane into the internal solution [13].

Three laminated membranes were also investigated, two with thin layers of polyethylene and one with polypropylene. In all cases, the additional layer decreased the sensor sensitivity considerably. Once again, higher sensitivity was obtained with greater porosity for the polyethylene laminated membranes, although the effect was not nearly as dramatic as with the unlaminated membranes. Higher sensitivity was obtained with polyethylene compared to polypropylene under the same conditions of porosity and thickness. Assuming the same thickness for the laminating polymer, these results indicate that the permeability rate for hydrogen peroxide is slower through polypropylene compared to polyethylene. Permeability is fastest through unlaminated membranes of microporous PTFE where the hydrogen peroxide can travel relatively unimpeded through the porous network of air pockets that traverse the membrane.

Response characteristics

The response characteristics of the resulting gas-sensing probe were examined in order to assess its analytical utility. The effects of temperature and sample pH were investigated. In addition, the selectivity of the response was evaluated and, finally, the calibration parameters were established.

Temperature strongly influences the sensor response as expected because of the effect of temperature on critical parameters such as gas solubility in liquids, membrane permeability, reaction kinetics, and enzyme stability. The effect of temperature can be minimized by controlling conditions so that mass transport across the membrane is rate limiting, thereby eliminating the influence of temperature on reaction kinetics.

The effect of temperature was evaluated by comparing sensor responses for a step in hydrogen peroxide concentration from zero to 260 μM at temperatures ranging from 25 to 55°C. A fresh internal solution was used for each temperature to account for potential thermal denaturation of HRP. The membrane used was pure microporous PTFE with an average pore size of 0.45 μm and 3 U ml^{-1} HRP was used for each sensor. Initially, the sensor tip was immersed into a fresh aliquot of blank buffer at the temperature in question. After reaching a steady-state background current, hydrogen peroxide was added and the current was monitored as a function of time. The resulting steady-state current was recorded and the sensor was left in this solution until the total time exposed to this temperature was 10 min. The sensor was then removed and placed in a new aliquot of buffer that had been preheated to the same temperature. Both the blank and hydrogen peroxide response measurements were repeated as before but the total time in this solution was fifteen minutes which resulting in a total time exposed to this temperature of 25 min. The sensor was immersed in a third and final aliquot of preheated buffer and the procedure was repeated

for another 15 min which resulted in a total time exposed of 40 min. The internal solution was then replaced and the next temperature was examined.

Temperature has a significant impact on the magnitude of the steady-state current. As expected for a diffusion controlled system, larger currents are obtained at higher temperatures. In addition, the stability of the sensor response depends on the temperature. At temperatures below 47°C, the steady-state currents were unchanged over the 40-min period of this experiment. At temperatures of 52.5 and 57.5°C, however, the magnitude of the sensor response decreased slightly over this period, presumably due to thermal degradation of HRP and a corresponding decrease in the reaction kinetics. Sensor responses at zero time (i_0) were calculated by extrapolating from a plot of sensor response versus time for each temperature. A plot of log i_0 versus 1000/absolute temperature reveals a linear relationship over the temperature range from 25 to 47°C. The linear portion of this plot includes six temperature values and is characterized by a slope of -2.78 ± 0.04, a y-intercept of 11.934 ± 0.008, and a correlation coefficient of 0.999. Above 47°C, the plot has a slight negative deviation from linearity which indicates a change in the rate limiting process. Thermal degradation of HRP likely causes a change from a diffusion limited condition to one in which reaction kinetics are involved.

Response times were affected only at higher temperatures. At temperatures between 25 and 47°C, response times were less than 1.5 min. As the temperature increased above 47°C, however, longer times were required to achieve the steady-state current. Response times increased as a function of the amount of time exposed to a particular temperature, thereby indicating that the degradation of HRP is responsible.

The magnitude of response and sensor response times are not affected by sample pH over the range from 4.6 to 8.5. This insensitivity to sample pH represents one of the key advantages of the internal enzyme design. Because the membrane isolates the enzyme from the external solution, sample pH has no affect on the chemical reactions involved. Sample pH could potentially affect sensor response, however, by altering speciation of the analyte. Speciation of hydrogen peroxide is not a concern at moderate pH values.

TABLE 2

Sensor response to tested potential interferences

Substance	Concentration (mM)	Response (nA)
Hydrogen peroxide	0.35	373
Ascorbic acid [a]	100	9.2 [c]
Ascorbic acid [b]	100	none
Uric acid	100	none
Methionine	10	none
Glutamine	10	none
Tyrosine	10	none
Glycine	10	none
Acetaminophen	2.5	none

[a] Ascorbic acid solution added in air saturated buffer. [b] Solid ascorbic acid added in N_2 saturated buffer. [c] Relative response is less than 0.01%.

The gas-sensing design provides excellent selectivity for hydrogen peroxide over compounds that interfere with conventional amperometric hydrogen peroxide detection schemes. Selectivity has been determined by measuring the magnitude of response to a series of potentially interfering compounds. Results are summarized in Table 2. Without the PTFE membrane, a small, but significant, anodic current (ca. 0.9 μA mM^{-1}) was measured in the presence of ascorbic acid at the carbon felt electrode at an applied potential of 0 V vs. the silver–silver chloride reference electrode. With the membrane in place, however, the sensor displayed absolutely no response to ascorbic acid at moderate concentrations. At 100 mM ascorbic acid, a small cathodic current was detected, but the relative response was less than 0.01% of that for hydrogen peroxide. This interfering current was not produced by a direct electrochemcial reaction with ascorbic acid, but by the formation of a small amount of hydrogen peroxide from the oxidation of ascorbic acid by endogenous oxygen. No response was observed for 100 mM ascorbate when solid ascorbic acid was added to N_2 saturated buffer. No responses were detected for any of the other potential interferences tested.

Properties of the calibration curve depend heavily on several construction and operation parameters. Critical parameters include thickness and porosity of the membrane, temperature, and concentrations of HRP and ferrocyanide. The linear dynamic range and limit of detection can be controlled by adjusting these parameters. Two unique sensor configurations have been designed to cover the micromolar and millimolar concentration ranges, respectively.

For responses to micromolar levels of hydrogen peroxide, a microporous PTFE membrane with an average pore size of 0.45 μm was used in combination with a temperature of 37°C. A typical response curve for this sensor has a slope of 3.610 ($\pm$0.015) μA mM^{-1}, a y-intercept of 0.002 ($\pm$0.002) μA and a correlation coefficient of 99.99%. The detection limit is 2.0 ($\pm$0.4) μM. Stability of an individual sensor was determined by comparing calibration lines generated from a single sensor with the same internal solution over a 5-day period. The sensor was stored in buffer at room temperature between calibrations. No significant differences were detected over this period. The following slopes were measured 3.59, 3.66, 3.68, 3.50, 3.52 and 3.50 μA mM^{-1}, producing an overall coefficient of variation of only 2.3%. Likewise, the y-intercept was essentially constant for each curve with a mean value ($\pm$standard deviation) of 0.0032 ($\pm$0.0030) μA. Although the sensor stability exceeds 5 days, sensors with fresh internal solution and a new membrane were typically prepared immediately before each experiment.

A seperate sensor was constructed to demonstrate the ability to measure mM concentrations by using a 0.02-μm membrane at 24°C. The resulting calibration curve has a slope of 2.278 ($\pm$0.001) μA mM^{-1}, a y-intercept of 0.002 ($\pm$0.002) μA and a correlation coefficient of 99.98%. The detection limit is 24 ($\pm$8) μM under these conditions and the sensor responds in a linear fashions to concentrations as high as 27.5 mM.

Sensor response times are approximately 30 s for both sensor configurations tested. A typical time dependent response profile is provided in Fig. 6 for the second sensor detailed above (mM

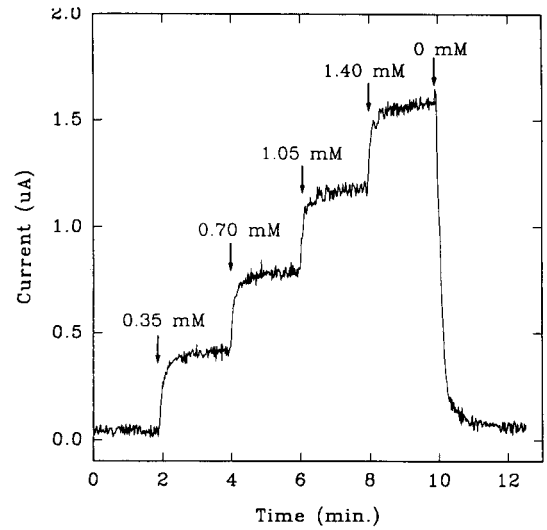

Fig. 6. Time dependent response to standard additions of hydrogen peroxide. Arrows indicate when the addition was made and the corresponding values indicate the final concentration of hydrogen peroxide in solution after this addition. The last arrow indicates when the sensor was removed from the solution, rinsed with water, and placed in a fresh aliquot of blank buffer.

responding sensor). Thirty second response times are observed for each of the concentrations shown. In fact, response time is essentially independent of the hydrogen peroxide concentration which differs considerably from dynamic response properties for gas-sensing probes based on an equilibrium measurement where shorter response times are typically observed at higher analyte concentrations. Concentration independent response times are consistent with a kinetic measurement where the steady-state signal is obtained when a constant rate is established. Another important point is that recovery times are very short. The recovery time indicated in Fig. 6 is only 40 s. The true sensor recovery time is somewhat shorter, however. The recovery curve illustrated in Fig. 6 represents more than just sensor recovery. The recovery curve in Fig. 6 was obtained by first removing the sensor tip from the hydrogen peroxide solution, then rinsing the sensor tip with water, and finally reimmersing the tip in a blank buffer solution. Nevertheless, the recovery time is short particularly compared to

equilibrium-based gas-sensing probes where 30–50 min are commonly required to reestablish the baseline condition [14]. Once again, the kinetic basis of this device provides rapid recovery times because analyte does not accumulate in the internal solution, therefore the baseline condition can be established faster.

Conclusions

The selectivity of this reagentless gas-sensing probe is excellent because the gas-permeable barrier effectively discriminates compounds that interfere with conventional sensors for hydrogen peroxide. A major finding is the ability to measure micromolar concentrations of hydrogen peroxide with a gas-sensing arrangement. Although the vapor pressure for hydrogen peroxide is relatively low compared to many other compounds, the vapor pressure is sufficient for detection of micromolar concentrations. The same sensor design could be used for other potential analytes with similar vapor pressures. Another important finding is the versatility of the sensor in terms of the dynamic range of operation. By controlling the composition of the internal solution, the physical parameters of the membrane and the solution temperature, sensors can be custom designed for a wide variety of applications.

The authors thank Professor Steve Weber for his insightful comments concerning the formation of hydrogen peroxide from ascorbic acid and oxygen. In addition, the financial support by the National Science Foundation (No. BNS-8716768) and the Office of Naval Research (No. N00014-91-J-1768) is greatly appreciated.

REFERENCES

1 G.G. Guilbault, Analytical Uses of Immobilized Enzymes, Marcel Dekker, New York, 1984.
2 R.J. Geise and A.M. Yachnych, in R.W. Murray, R.E. Dessy, W.R. Heineman, J. Janata and W.R. Seitz (Eds.), Chemical Sensors and Microinstrumentation, ACS Symposium Series, Vol. 403, Washington, DC, 1989, Chap. 4.
3 K. Hajizadeh, H.B. Halsall and W.R. Heineman, Talanta, 38 (1991) 37.
4 M.J. Green and H.A.O. Hill, J. Chem. Soc., Faraday Trans. 1, 82 (1986) 1237.
5 G. Jönsson, L. Gorton and L. Pettersson, Electroanalysis, 1 (1989) 49.
6 M.A. Arnold, X. Zhou and R.S. Petsch, Anal. Lett., submitted for publication.
7 G. Palleschi, M.H. Faridnia, G.J. Lubrano and G.G. Guilbault, Appl. Biochem. Biotechnol., 31 (1991) 21.
8 I.M. Kolthoff and W.J. Tomsicek, J. Phys. Chem., 39 (1935) 945.
9 M. Shporer, G. Ron, A. Loewenstein and G. Navon, Inorg. Chem., 4 (1965) 356.
10 P. Kukesza, T. Jedral and Z. Galus, J. Electroanal. Chem., 109 (1984) 141.
11 J. Kuta and E. Yeager, J. Electroanal. Chem., 59 (1975) 110.
12 L.M. Peter, W. Durr, P. Bindra and H. Gerischer, J. Electroanal. Chem., 71 (1976) 31.
13 M.L. Hitchman, P.J. Elving and J.D. Winefordner (Eds.), Measurement of Dissolved Oxygen, Chemical Analysis, Vol. 49, Wiley, New York, 1978, Chap. 4–5.
14 M.E. Collison and M.A. Arnold, Anal. Lett., 19 (1986) 1759.

Analytica Chimica Acta, 283 (1993) 673–682
Elsevier Science Publishers B.V., Amsterdam

Anion selective optical sensing with metalloporphyrin-doped polymeric films

Enju Wang and Mark E. Meyerhoff

Department of Chemistry, The University of Michigan, Ann Arbor, MI 48109 (USA)

(Received 27th April 1993; revised manuscript received 28th June 1993)

Abstract

Metalloporphyrins [Mn(III) and In(III)] are investigated as active polymer film components in the design of reversible anion-selective optical sensors. The optical measurements are made by casting thin plasticized polymer films (PVC, polyurethane, etc.) containing the given metalloporphyrins on glass plates. When bathed in aqueous test solutions, the optical response of such films is based upon the selective extraction of anions by metalloporphyrins into the organic membrane phase. Changes in optical absorbance occur via either of two mechanisms. For films based on Mn(III) tetraphenylporphyrins, the porphyrin itself can serve simultaneously as the ionophore and chromophore for the detection of iodide ions. In this instance, direct ligation of iodide as an axial ligand of the central Mn(III) results in a change in the molar absorptivity of the soret band of the porphyrin. In the case of In(III) octaethylporphyrin, the incorporation of an appropriate pH-indicator dye along with the metalloporphyrin is required to achieve films with optical selectivity toward nitrite and chloride. The analytical characteristics of these porphyrin-based films with respect to anion response time, dynamic measurement range, and reproducibility, are discussed.

Keywords: Sensors; Anion selectivity; Optical sensing; Polymeric films; Metalloporphyrins

The intrinsic properties of optical sensors has led to their suggested use in a wide range of analytical applications [1,2]. While many of the earliest optical sensors developed for detecting cations and neutral species (e.g., gases) were based on immobilizing chemically sensitive components on the surface of solid supports (e.g., glass fibers, silica particles, etc.,) [3–6], limitations of these systems including poor reversibility, selectivity and stability has prompted newer approaches. In recent years, a large number of ionophores used previously in the design of potentiometric ion-selective organic membrane electrodes have been adapted to design optical cation (M^+) sensing systems [7,8]. In these sensing schemes, the ionophores are doped, along with appropriate pH indicator dyes, into thin (< 10 μm) polymeric films. When bathed in a sample solution, simultaneous H^+/M^+ ion exchange equilibria occur between the two phases, resulting in a change in the optical absorbance of the film. Using this approach, highly selective optical sensing films for NH_4^+ [9], Ca^{2+} [10], K^+ [11], Na^+ [12] and Pb^{2+} [13] have been prepared.

Adopting this same ionophore/pH indicator approach to design optical anion sensors is, however, far more challenging. Indeed, there are relatively few anion selective ionophores that have been used successfully in previous polymer membrane type ion-selective electrodes. Recently, optical sensors for nitrate and chloride have been suggested based on polymer films doped with quaternary ammonium exchangers [14] and organic tin compounds [15], respectively. However,

Correspondence to: M.E. Meyerhoff, Department of Chemistry, The University of Michigan, Ann Arbor, MI 48109 (USA).

those based on quaternary ammonium exchangers always display Hofmeister type selectivity, with the largest response to lipophilic anions (e.g., perchlorate, thiocyanate, etc.). Behringer et al. [16] have used a chromophoric derivative of a known carbonate selective ionophore (based on reaction of carbonate with trifluoroacetophenone species) along with a lipophilic quaternary ammonium species within a thin polymeric film to devise a highly selective carbonate optical sensor. Alternate schemes for optical anion sensing have also been proposed, including sensors for halide ions based on direct quenching of fluorescence of acridinium or quinolinium immobilized on a glass surface via spacer groups [17,18], and cyanide/nitrite based on vitamin B_{12} derivatives dissolved in an organic solution trapped in contact with an optical fiber behind a gas permeable membrane [19,20]. Despite these early efforts, achieving novel anion selectivities in optical sensor technology remains a challenge.

We have previously demonstrated that when certain metalloporphyrins are used as carriers in polymeric membrane electrodes, the resulting sensors display unique anion responses [21–23]. Specifically, membranes formulated with Mn(III), Sn(IV), and In(III) porphyrins exhibit relatively high potentiometric selectivity toward thiocyanate [21], salicylate [22], and chloride [23], respectively. Such selectivity has been attributed to the preferred interaction of these anions as axial ligands with the metal center of the metalloporphyrin structure. As demonstrated earlier with cobalamin derivatives [20], these anion exchange ligation reactions can also influence the UV–visible absorption bands of the metal–ligand complexes which are potentially useful in designing optical anion sensors. Alternately, when the selective anion ligation reaction does not alter the absorption spectrum of the metalloporphyrins, incorporation of the porphyrin along with a pH indicator into an appropriate polymer film can be employed in devising anion selective sensors. In this report, both of these sensing schemes (see Figs. 1 and 2) are demonstrated by using Mn(III) porphyrins for the direct sensing of iodide and In(III) porphyrins in conjunction with a lipophilic pH indicator for the reversible detection of chloride and nitrite.

EXPERIMENTAL

Reagents

The structures of some representative metalloporphyrins and pH indicators used in this work are shown in Fig. 1. Octaethylporphyrin (OEP), chloro(5,10,15,20-tetraphenylporphyrinato) manganese(III) [Mn(TPP)Cl], chloro(5,10,15,20-tetraphenylporphyrinato) rhodium(III) [Rh(TPP)Cl] and dichloro(5,10,15,20-tetraphenylporphyrinato) tin(IV) [$Sn(TPP)Cl_2$] were obtained from Midcentury Chemicals (Posen, IL). Chloro(octaethylporphyrinato) indium(III) [In(OEP)Cl] was synthesized and purified according to the method described previously [24,25]. *Ortho*-nitrophenyl octyl ether (*o*-NPOE), bis(2-ethylhexyl)sebacate (DOS), 3-hydroxy-4-(4-nitrophenylazo)phenyl octadecanoate (ETH 2412), high molecule weight poly(vinyl chloride) (PVC), and tetrahydrofuran (THF) were obtained from Fluka (Ronkonkoma, NY). Tridodecylmethylammonium chloride (TDMAC or MTDDACl) was from Polyscience

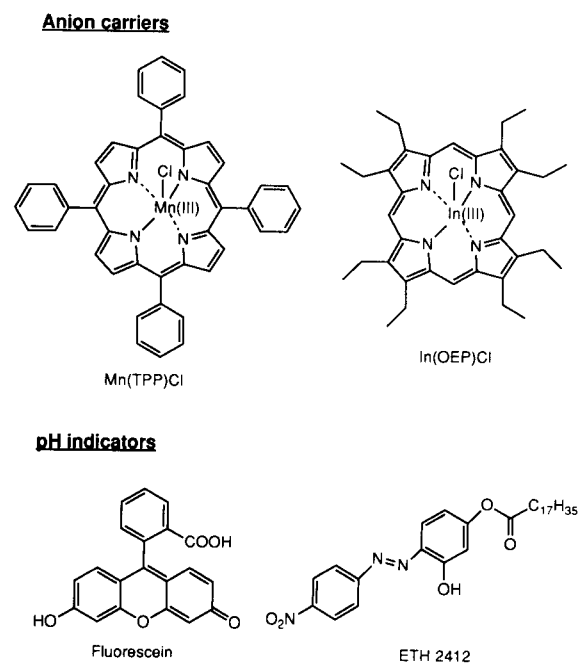

Fig. 1. Structures of some metalloporphyrins and pH indicators used to prepare anion sensing polymer films.

(Warrington, PA) and Tecoflex polyurethane (PU, SG-80A) from Thermedics (Woburn, MA). Fluorescein (Fl) was from Aldrich (Milwaukee, WI), while 2-(*N*-morpholino)ethanesulfonic acid (MES) and sodium salicylate were products of Sigma (St. Louis, MO). All other chemicals were commercial reagent grade products. Standard solutions and buffers were prepared with reverse osmosis-deionized water.

Film preparation

PVC film compositions were similar to that described for ion-selective electrode membranes [21–23] [30 wt.% of PVC, 1 wt.% of carrier (metalloporphyrins) and 69 wt.% of plasticizer (DOS or *o*-NPOE)]. The PVC/PU films were composed of 15 wt.% of PVC and 15 wt.% of PU, 1 wt.% of carrier and 69 wt.% of plasticizer. Films containing In(OEP)Cl and pH indicator (either Fl or ETH 2412) were formulated with 2 wt.% of In(OEP)Cl, 1 wt.% of indicator, 30 wt.% of polymer(s), and 67 wt.% of plasticizer. Blank films used as the reference had the same compositions but without the metalloporphyrin and/or the pH indicator [in the case of the In(III) porphyrin]. The solutions used to cast the optical anion sensing films were made by dissolving a total of 200 mg of membrane components in 2 ml THF. Final films were cast onto the glass slides (0.9×4 cm, 1 mm in thickness) manually with a pipette or by spin coating at 2000 rpm. The resulting films had thicknesses in the range of 3–10 μm.

Absorbance measurements

Optical measurements were made with a UV–visible double beam spectrophotometer (Lambda 3B, Perkin Elmer) with the polymer film coated glass plates placed in a conventional cuvette ($1 \times 1 \times 4$ cm^3) containing the test anion solution. The films were soaked in water or 0.05 M NaH_2PO_4 (pH 4.2) for 20 min before the first measurements were made. Test solutions were prepared by adding appropriate salts of the test anions to either water, a 0.05 M NaH_2PO_4 (pH 4.2) electrolyte solution, a 0.05 M tris(hydroxyamino)methanesulfuric acid (Tris-SO_4) buffer (pH 7.2), or a 0.05 M MES buffer (pH 5.5).

RESULTS AND DISCUSSION

Preliminary studies

Preliminary experiments involved casting polymer films containing several of the metalloporphyrins known to yield novel anion selectivities in previous potentiometric studies [21–23] [e.g., Mn(TPP)Cl, In(OEP)Cl, $Sn(TPP)Cl_2$] and observing changes in the absorption of the films when exposed to test anion solutions at various concentrations in water. Ion-exchange of the initial chloride ligand by other anions (including hydroxide from water) was expected to result in changes in the absorbances of the films. Indeed, upon exposing a PVC film containing Mn(TPP)Cl to 0.1 M of iodide or, perchlorate solution, a visual color change of the membrane is observed. Changes in absorbance also occurred when In(OEP)Cl in a PVC matrix was exposed to iodide, nitrite and

a) Metalloporphyrins serve as chromoionophore

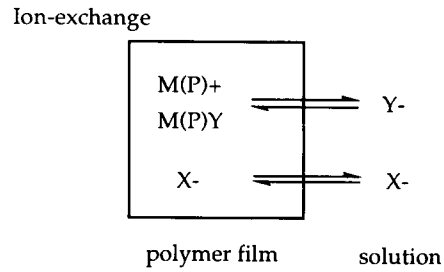

b) Metalloporphyrins serve as anion ionophore, pH indicators serve as chromophore.

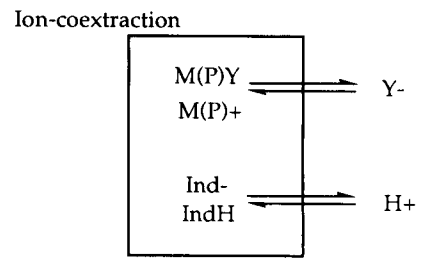

Fig. 2. Possible optical anion response mechanisms using metalloporphyrins as anion carriers in thin polymeric films; (a) porphyrin as chromophore; (b) added pH indicator as chromophore.

chloride, but the absorbance changes were generally much smaller. For $Sn(TPP)Cl_2$, and Rh(TPP)Cl doped membranes, iodide and salicylate (Sal^-) caused only slight changes in the intensity of the soret band (around 400 nm).

As indicated in Fig. 2a, the direct optical response of metalloporphyrin doped polymer films (without added pH indicator) may result from selective axial ligand exchange reactions. That is, if the extracted anion (Y^-) can coordinate directly to the metal center of the porphyrin, and this ligation concomitantly alters the electronic structure of the central metal ion, a change in the absorption spectrum will occur. The ligand exchange can either be between an initially ligated anion X^- (e.g., Cl^-, OH^-) or a neutral ligand such as water. In the latter case, the original anion in the film is not directly ligated to the porphyrin, but serves as a solvated counterion (X^-) to the positively charged porphyrin–H_2O complex. Thus, using Mn(III) tetraphenylporphyrin as an example, the two possible reactions that can yield direct optical anion response are as follows:

$$[Mn(TPP)X]_{(m)} + Y^-_{(aq)} \rightleftharpoons [Mn(TPP)Y^-]_{(m)} + X^-_{(aq)} \quad (1)$$

or

$$[Mn(TPP)(H_2O)]X_{(m)} + Y^-_{(aq)} \rightleftharpoons [Mn(TPP)Y]_{(m)} + H_2O_{(aq)} + X^-_{(aq)} \quad (2)$$

where Y^- is a strong axial ligand for the central Mn(III) ion of the porphyrin and (m) and (aq) refer to the organic membrane and aqueous sample phases, respectively.

When the original counter anion X^-, e.g., chloride, is a relatively weak inner sphere ligand that can readily be displaced by water, and the film is exposed to solutions containing anions that are also a relatively weak ligands (Z^-), then ion exchange can occur in accordance with following reaction:

$$[Mn(TPP)(H_2O)]Cl_{(m)} + Z^-_{(aq)} \rightleftharpoons [Mn(TPP)(H_2O)]X_{(m)} + Z^-_{(aq)} \quad (3)$$

In this case, since the exchange occurs without displacing the neutral water ligand, it is unlikely that significant changes in the absorption spectrum will occur. Indeed, without direct interaction with the metal center, the equilibrium constant for reaction 3 will be dictated by the relative free energies of hydration of X^- ions, and thus, when X^- is ClO_4^-, reaction 3 will be favored.

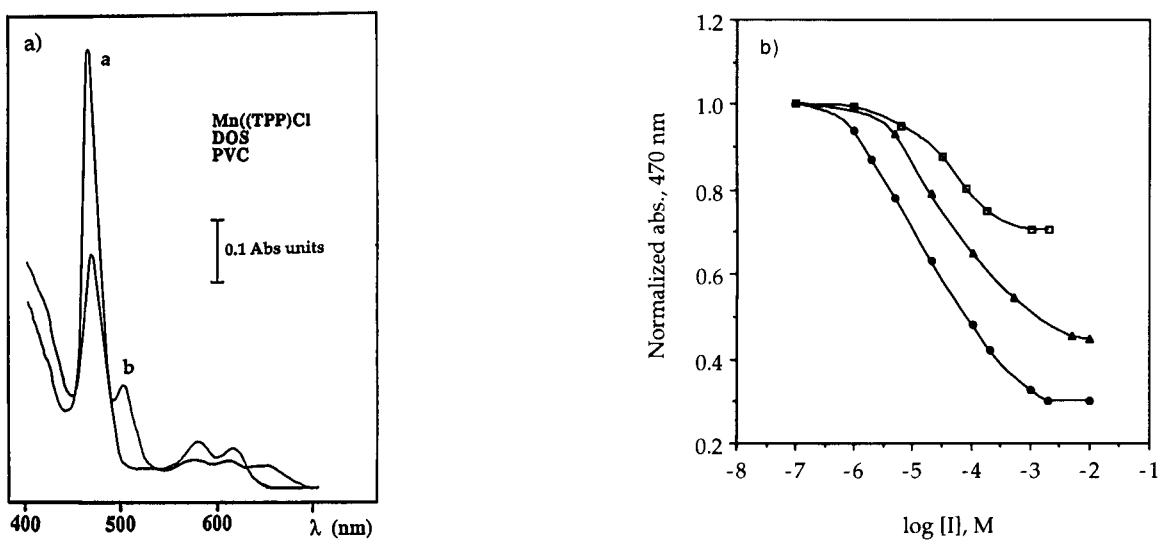

Fig. 3. (a) Absorbance spectra of Mn(TPP)Cl doped film (PVC/DOS) in solutions with (a) and without (b) iodide ions. (b) Calibration curves for iodide response at three different pH: (□) 7.2, (▲) 5.5, (●) 4.2.

Clearly, strong ligands (Y^-) that can replace coordinated water are most likely to yield direct changes in the optical properties of the film. Moreover, the ion exchange equilibrium constant for reactions 1–3 above will ultimately determine the anion selectivities of the membranes doped with the porphyrin structure.

Polymer films with Mn(TPP)Cl for iodide sensing

The polymer films doped with Mn(TPP)Cl yield the largest optical response towards changes in iodide ion levels in the sample. At 470 nm, the λ_{max} for the soret band of Mn(TPP)Cl, the changes in absorbance (decrease) toward various anions follow the order: $I^- > NO_2^- \gg ClO_4^- > Sal^- \sim Cl^- \sim H_2PO_4^-$. Figure 3a shows the change in the visible absorption spectrum of a PVC–Mn(TPP)Cl film when exposed to 1 mM pure iodide solution. As shown in Fig. 3b, the optical response of the membrane to iodide in aqueous solutions at different pH covers a wide range of concentrations, while relatively little change in absorbance is observed when the film is exposed to solutions of chloride, bromide, nitrate, or salicylate. (note: normalized optical response is the absorbance measured for given test solution divided by absorbance in background electrolyte)

The response and recovery times for the Mn(TPP)Cl doped PVC films toward iodide were examined in detail. For membranes $\sim 5\ \mu m$ thick, the response times range of 3–5 min ($t_{95\%}$), while the recovery time is ca. 10 min. These response and recovery times appear to be dictated by the slow on/off ligand exchange kinetics of the Mn(TPP) species, and the need to maintain charge neutrality in the polymer film. Indeed, when the film is first exposed to a solution of iodide ion followed by exposure to pure water, the latter solution does not have a high enough concentration of anions that can replace the ligated iodide to maintain charge neutrality within the polymer matrix. The recovery time can, however, be reduced to 2 min by adding salicylate ions to the wash solution; e.g., if the membrane is first exposed to a solution containing salicylate ion for 1 min, then exposed to pure water, the optical signal changes to its original value. It should be noted that the Mn(TPP)Cl doped PVC films maintain their reversible optical iodide response properties for at least 2 weeks, suggesting that Mn(TPP) is stable both optically and chemically in the PVC matrix. The two week limitation for the sensor life-time is due primarily to the partitioning of Mn(TPP)Cl from the very thin films to the aqueous test solution. Gradual loss of the carrier with time will cause a significant decrease in the absorbance signal necessitating frequent re-calibration. This problem may be minimized by using a more lipophilic Mn(III)–porphyrin structure to reduce the partitioning into the aqueous solution [26], thereby enhancing sensor life-time.

Films prepared with a PVC matrix alone exhibit relatively poor adhesion to the surface of glass slides used to test optical anion response of the films. This problem can be overcome by employing a mixture of polyurethane (PU) and PVC as the film matrix. Films composed of plasticized PVC/PU mixtures (15 wt.% each in film) have comparable life-times and optical properties to those prepared with pure PVC. Moreover, the PVC/PU matrix enables an easier, more reproducible fabrication of a thin, transparent and homogeneous film on the glass substrate, even without using a spin coating device.

The specific plasticizer used within the Mn(TPP)Cl films has relatively little affect on the optical anion response toward iodide; however, the solubility of Mn(TPP)Cl as well as other porphyrins in cast films was generally higher when *o*-NPOE rather than DOS was used as the plasticizer.

Although relatively little optical response is observed when the Mn(TPP)Cl films are exposed to anions other than iodide, some anions can in fact interfere with the optical iodide response by competing as counter anions for the $Mn(TPP)^+$ or $Mn(TPP)H_2O^+$ sites in the film (see reactions 1–3 above). As stated in Table 1, salicylate and perchlorate anions alone caused very small absorbance changes, but their interfering effects are rather large when present together with iodide. This suggests that these species have high extraction coefficients into the Mn(TPP)Cl doped film. Such anions can be extracted either as axial lig-

TABLE 1

Nomalized absorbance at 470 nm of the Mn(TPP)Cl film exposed to 1 mM solution of iodide and interfering anions in 1:1 mole ratio [a]

Anion	Background solution	
	NaH_2PO_4 [b]	H_2O
none	1.00	1.00
I^-	0.33	0.49
$I^- + Sal^-$	0.50	0.72
$I^- + SCN^-$	0.25	0.38
$I^- + NO_2^-$	0.45	0.60
$I^- + ClO_4^-$	0.42	0.56
$I^- + Br^-$	0.31	0.48
$I^- + NO_3^-$	0.34	0.52
$I^- + Cl^-$	0.35	0.52
$I^- + OAc^-$	0.36	0.53

[a] Film composition: Mn(TPP)Cl, DOS, PVC. [b] pH 4.2.

ands (reactions 1 and 2), or as counter anions to the solvent ligated $Mn(TPP)H_2O^+$ species (reaction 3). In either case, these reactions will compete with iodide as the preferred counter anion in the film. Since only the presence of thiocyanate yields positive errors, it is likely that thiocyanate coordinates directly and strongly to $Mn(TPP)^+$, also altering the electronic structure of the central Mn^{3+} ion. On the other hand, negative interferences from salicylate and perchlorate appear to be due to the large partition coefficients of these species into the polymer film as competing dissociated (non-ligated) counter anions to $Mn(TPP)H_2O^+$.

The optical response of the Mn(TPP)-doped films to iodide ion is also highly dependent on the concentration of the counter anion X^- in the sample (i.e., $X^-_{(aq)}$ in Eqns. 1–3). In practice this concentration should be fixed to define a conditional equilibrium constant for the ion-exchange reaction. In buffered sample solutions it appears that X^- is predominately hydroxide ion and hence, the pH of the sample will control the ion-exchange of I^- into the film. Indeed as shown in Fig. 3b, the sensitivity to iodide is decreased as the solution pH is increased. This is consistent with previous results obtained in the potentiometric measurement mode [21]. Both the potentiometric and optical data suggest that an increase in the pH of the sample solution causes deprotonation of the weakly coordinated water, yielding a very strong hydroxide ion ligand coordinated to the central Mn(III) [i.e., Mn(TPP)OH]. Thus, as with the potentiometric system, optical anion sensing based on Mn(III) porphyrins will require that the sample solution be buffered at a pH < 5.5.

Anion selectivities of polymer films doped with In(OEP)Cl and pH indicators

As mentioned above, the direct optical response of polymer films doped with In(OEP)Cl alone to various anions is very small. However, based on earlier membrane electrode potentiometric selectivity data, it appears that In(OEP) within polymeric films interacts quite strongly with chloride and nitrite [23,27]. To take advantage of this fact for optical sensing of these species, a pH indicator (IndH) was incorporated into the film to enhance the optical absorbance change. In this sensing mode (see Fig. 2b), selective extraction of anions (Y^-) by $In(OEP)^+$ will be accompanied by the co-extraction of a proton (to maintain charge neutrality in the film), and concomitant protonation of the added pH chromophore yielding a large change in the optical absorbance of the film. This process can be described by Eqns. 4 or 5 (depending on whether the anionic form of the indicator can actually ligate to the In(III) center of the porphyrin):

$$In(OEP)^+_{(m)} + Ind^-_{(m)} + HY_{(aq)} \rightleftharpoons In(OEP)Y_{(m)} + IndH_{(m)} \quad (4)$$

or

$$In(OEP)Ind_{(m)} + HY_{(aq)} \rightleftharpoons In(OEP)Y_{(m)} + IndH_{(m)} \quad (5)$$

where Y^- is the anion being sensed. By using α to represent the fraction of total indicator (Ind_T) in the deprotonated form ($[Ind^-]$), α can be related to the absorbance values at a given wavelength as follows:

$$\alpha = (A - A_0)/(A_1 - A_0) = [Ind^-]/[Ind_T] \quad (6)$$

where A_0 and A_1 correspond to the absorbance of the completely protonated and deprotonated pH indicator, respectively. In the case when the

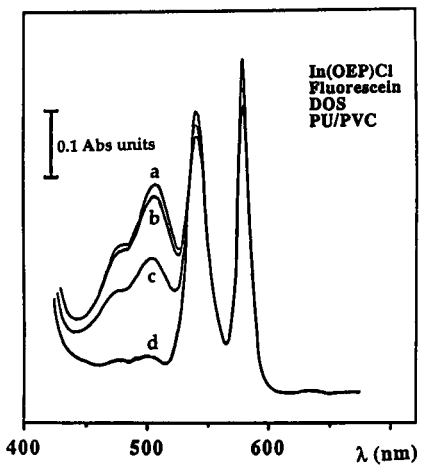

Fig. 4. Absorbance spectra of a In(OEP)Cl/Fl/PU/PVC/DOS film at varying chloride concentrations; (a) 0.0, (b) 1×10^{-5} M, (c) 1×10^{-4} M and (d) 10^{-3} M (at pH 4.2).

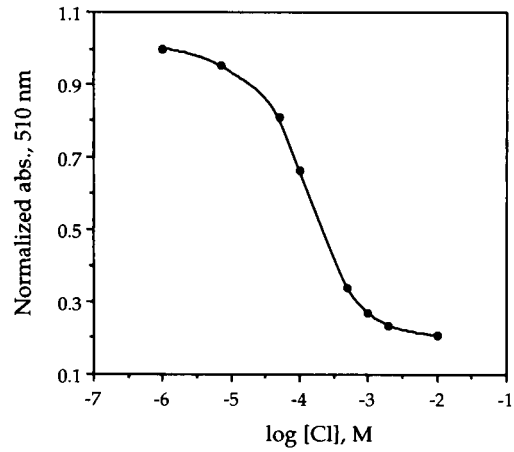

Fig. 5. Normalized absorbances of In(OEP)Cl/Fl doped film at 510 nm as a function of log [Cl]. Film composition is as in Fig. 4. (pH 4.2.)

porphyrin carrier and indicator are in a 1:1 ratio within the film, the relationship between relative absorbance (α), the equilibrium constant for reaction 4 or 5 (K_{eq}), the activities of protons and anions in the sample solution, and the optical selectivity coefficient $K_{i,j}^{opt}$ ($K_{i,j}^{opt}$ is defined by analogy to that for ion-selective electrodes [7,8,28]) can be expressed by Eqn. 7:

$$(1-\alpha^2)/\alpha^2 = K_{eq}a_{H^+}\left(a_{X^-} + K_{i,j}^{opt}a_j\right) \qquad (7)$$

Fluorescein was initially examined as the pH indicator within PVC and PVC/PU films. Polymer films containing fluorescein and In(OEP)Cl in a mole ratio of 1:1, change color from orange to red upon exposure to solutions containing chloride when the sample is at pH < 5. As shown in Fig. 4, there is a large absorption change in the range of 430–520 nm due to protonation of fluorescein, and a slight increase in the absorbance of the film at 540 and 576 nm owing to the binding (ligation) of chloride to the indium(III) of the porphyrin complex. Since the absorption λ_{max} for fluorescein does not change when the In(OEP)Cl ionophore is added to the film, it appears that the deprotonated fluorescein does not coordinate directly to indium (III), but rather serves as a dissociated counter anion (see Eqn. 4) to $In(OEP)^+$. This is in contrast to when ETH 2412 is used as the pH indicator within the film (see below).

The normalized optical response curve (absorbance at 510 nm) for chloride using fluorescein and In(OEP)Cl in a PU/PVC film at pH 4.20 is shown in Fig. 5. The dynamic range of response toward chloride is 10^{-5} to 10^{-3} M. The selectivity order follows: $Sal^- > I^- \sim Br^- \sim NO_2^- \sim Cl^- \gg SCN^- > ClO_4^- > NO_3^- > H_2PO_4^-$ (see Table 2). This selectivity sequence is consistent with that observed in potentiometric studies using In(OEP)Cl doped PVC membranes [23,27], and illustrates a much greater response to chloride

TABLE 2

Anion selectivity coefficients of various optical films [a,b]

Anions	log $K_{Cl,j}^{opt}$		
	In(OEP) fluorescein [c]	In(OEP)Cl ETH 2412 [c]	MTDDACl ETH 2412 [d]
Cl^-	0	0	0
Sal^-	0.6	0.7	2.6
I^-	0.3	0.2	2.8
Br^-	0.2	0.1	1.4
NO_2^-	0.3	0.2	0.5
SCN^-	−1.4	−1.8	2.9
ClO_4^-	−2.0	−2.2	3.4
NO_3^-	−2.9	−2.8	1.4
OAc^-	−2.0	−2.2	–
$H_2PO_4^{2-}$	< −3.5	< −3.5	< −1.0

[a] Film compositions: pH indicator, carrier in *o*-NPOE, PU/PVC matrix. [b] $K_{Cl,j}^{opt}$ is calculated at $\alpha = 0.5$. [c] measurement at pH 4.2. [d] measurement at pH 7.2.

than that which can be achieved using quaternary ammonium ion exchangers as membrane components (see Table 2 and Refs. 14, 15).

The response times for the fluorescein/In (OEP)Cl films were typically 2–3 min for 5 μm films (Fig. 6). By reducing the membrane thickness to 3 μm, response times of less than 2 min could be readily achieved. However, because of gradual leaching of fluorescein into the aqueous test solutions, the life-time of anion sensing films prepared with fluorescein are relatively short. This leach rate, and thus sensor lifetime, depends on the pH of the sample solution. At sample pH > 5.0, the leach rate was found to be fast, with optical anion response lasting for only 1–2 h; in contrast, at pH 4.2, optical anion response could be achieved for a period of one week.

To overcome this leaching problem, a more lipophilic pH chromophore, ETH 2412, was investigated. ETH 2412 has been used previously as an indicator for polymer film type anion optical sensors based on methyltridodecylammonium (MTDDA) sites [14]. In this earlier work, a large absorbance change at 540 nm was used for sensing purposes. Figure 7 illustrates the change in the absorption spectra of ETH 2412/In(OEP)Cl films when exposed to test solutions containing increasing levels of the chloride. Note, that the changes in the spectrum occur at 460–510 nm, not 540 nm as had been observed when this indicator was used with MTDDA [14]. The fact that the λ_{max} for ETH 2412 is shifted when

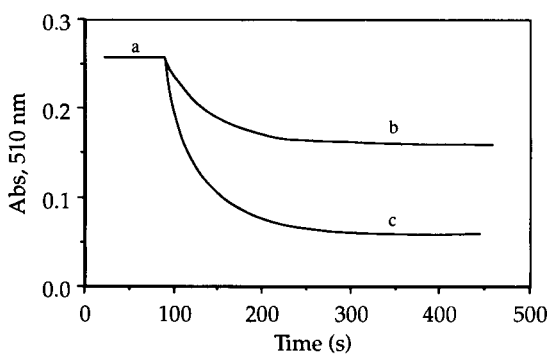

Fig. 6. Dynamic optical response of a In(OEP)Cl/Fl doped film at 510 nm to changes in chloride concentration at pH 4.2: (a) 1×1^{-5} M; (b) 1×10^{-4} M; and (c) 10^{-3} M. Film composition is as in Fig. 4.

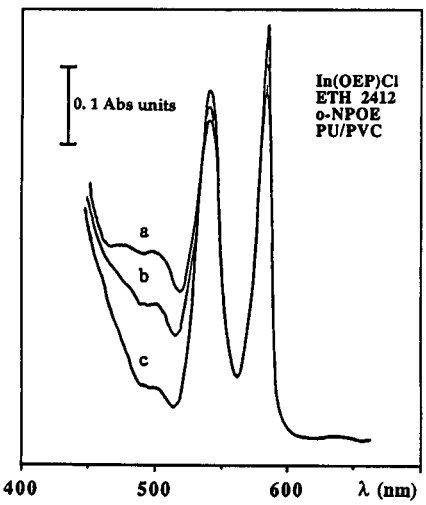

Fig. 7. Absorption spectra of In(OEP)Cl/ETH 2412/PU/PVC/*o*-NPOE film for chloride concentrations of (a) 0.0, (b) 1×10^{-4} M and (c) 10^{-3} M. (pH 4.2.)

In(OEP)Cl is present in the film suggests that, unlike fluorescein above, a direct ligation occurs between ETH 2412 and $In(OEP)^+$ (reaction 5 above). Considering the structure of ETH 2412 (see the structure below), this interaction likely involves the coordination of the nitro or hydroxy group of ETH 2412 to In(III). Despite this direct interaction, the presence of chloride and other anions in the test solution can compete effectively for the metal ion coordination site, yielding protonation of a non-coordinated indicator.

The normalized absorbance changes at 500 nm as a function of the logarithm of salicylate, chloride, nitrite, perchlorate and nitrate concentration for In(OEP)Cl/ETH 2412 in PU/PVC films are shown in Fig. 8. The resulting optical anion selectivity coefficients are summarized in Table 2. Again, this data shows clearly that In(OEP)Cl doped films respond in a non-Hofmeister pattern, with preference for Sal^-, I^-, Br^-, NO_2^-, and Cl^- over more lipophilic SCN^- and ClO_4^- anions. This is precisely the pattern observed with fluorescein (above) as the pH indicator within the film. This unique optical selectivity pattern for In(OEP)Cl doped films regardless of pH indicator used, is believed to be due to the specific interactions of given anions as axial ligands with the In(III) center. Thus, enchanced selectivity for

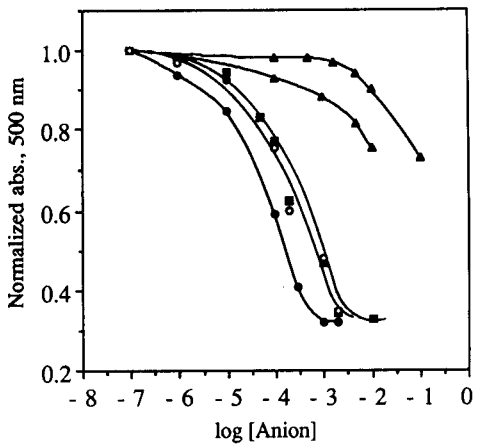

Fig. 8. Normalized absorbances of In(OEP)Cl/ETH 2412/PU/PVC/*o*-NPOE film at 500 nm for different anions. (▲) NO_3^-, (△) ClO_4^-, (■) Cl^-, (○) NO_2^-, (●) Sal^-. (pH 4.2.)

strongly ligated anions (e.g., Cl^-, NO_2^-, etc.) over some very lipophilic yet weakly coordinating anions (e.g., ClO_4^-, SCN^-) is observed.

Conclusions

This work demonstrates the concept of using metalloporphyrins as active film components in the design of reversible anion-selective optical sensors. As has been observed previously in potentiometric polymer membrane type ion-selective electrode configurations, the use of metalloporphyrins for optical anion sensing yields films with selectivities which differ substantially from the classical Hofmeister pattern. Two modes of transduction have been identified to achieve reversible optical anion response. As shown, Mn(TPP)Cl can be used alone within films as a chromoionophore for the detection of iodide, while In(OEP)Cl can be employed as an anion carrier in combination with a proton sensitive dye. Although the anion selectivities of the Mn(TPP)Cl and In(OEP)Cl based optical sensing films described here may not be adequate for many anion sensing applications, it is likely that the concept demonstrated here could be applied with other more selective metalloporphyrin or different metal–ligand complexes to yield optical anion sensors with selectivities more suitable for practical analytical applications. Indeed, based on previous potentiometric data, the use of a sterically hindered Mn(III) porphyrin [21], a Sn(IV) tetraphenylporphyrin, or a Hg(II)–diethyldithocarbamate complex along with suitable pH indicators within thin polymeric films, should yield highly selective optical sensors for thiocyanate, salicylate, and sulfite, respectively. Such studies are currently in progress.

We gratefully acknowledge the National Institutes of Health (GM 28882) for supporting this work.

REFERENCES

1 J. Janata, Anal. Chem., 62 (1990) 33R.
2 O.S. Wolfbeis, Fresenius' J. Anal. Chem., 337 (1990) 522.
3 L.A. Saari and W.R. Seitz, Anal. Chem., 55 (1983) 667.
4 Z. Zhujun and W.R. Seitz, Anal. Chim. Acta, 171 (1985) 251.
5 J.I. Peterson, S.R. Goldstein, R.V. Fitzgerald and D.K. Buckhold, Anal. Chem., 52 (1980) 864.
6 H.E. Posch, M.J.P. Leiner and O.S. Wolfbeis, Fresenius' J. Anal. Chem., 334 (1989) 162.
7 W.E. Morf, K. Seiler, B. Lehmann, Ch. Behringer, S.S.S. Tan, K. Hartman, P.R. Sorensen and W. Simon, in E. Pungor (Ed), Ion-Selective Electrodes, Vol. 5, Akademiai Kiado, Budapest, 1989, p. 115.
8 W.E. Morf, K. Seiler, P.R. Sorensen and W. Simon, in E. Pungor (Ed), Ion-Selective Electrodes, Vol. 5, Akademiai Kiado, Budapest, 1989, p. 141.
9 K. Seiler, W.E. Morf, B. Rusterholz and W. Simon, Anal. Sci., 5 (1989) 557.
10 W.E. Morf, K. Seiler, B. Rusterholz and W. Simon, Anal. Chem., 62 (1990) 738.
11 K. Wang, K. Seiler, W.E. Morf, U.E. Spichiger, W. Simon, E. Lindner and E. Pungor, Anal. Sci., 6 (1990) 715.
12 K. Seiler, K. Wang, E. Bakker, W.E. Morf, B. Rusterholz, U.E. Spichiger and W. Simon, Clin. Chem., 37 (1991) 1350.
13 M. Lerchi, E. Bakker, B. Rusterholz and W. Simon, Anal. Chem., 64 (1992) 1534.
14 S.S.S. Tan, P.C. Hauser, N.A. Chaniotakis, G. Suter and W. Simon, Chimia, 43 (1989) 257.
15 S.S.S. Tan, P.C. Hauser, K. Wang, K. Fluri, K. Seiler. B. Rusterholz, G. Suter, M. Kruettli, U.E. Spichiger and W. Simon, Anal. Chim. Acta, 225 (1991) 35.
16 Ch. Behringer, B. Lehman and W. Simon, Chimia, 41 (1987) 397.
17 E. Urbano, H. Offenbacher and O.S. Wolfbeis, Anal. Chem., 56 (1984) 427.
18 W.A. Wyatt, F.V. Bright and G.M. Hieftje, Anal. Chem., 59 (1987) 2272.

19 M.K. Freeman and L.G. Bachas, Anal. Chim. Acta, 241 (1990) 119.
20 M.K. Freeman and L.G. Bachas, Anal. Chim. Acta, 256 (1991) 269.
21 N.A. Chaniotakis, S.B. Park, A.M. Chasser, M.E. Meyerhoff and J.T. Groves, Anal. Chem., 60 (1988) 188.
22 N.A. Chaniotakis, S.B. Park and M.E. Meyerhoff, Anal. Chem., 60 (1989) 566.
23 S.B. Park, W. Matuszewski, M.E. Meyerhoff, Y.H. Liu and K.M. Kadish, Electroanalysis, 3 (1991) 909.
24 J. Buchler, in D. Dolphin (Ed.), The Porphyrins, Academic Press, New York, 1978, Chap. 6.
25 M. Bhatti, W. Bhatti and E. Mast, Inorg. Nucl. Chem. Lett., 8 (1972) 133.
26 O. Dinten, U.E. Spichiger, N. Chaniotakis, P. Gehrig, B. Rusterholz, W.E. Morf and W. Simon, Anal. Chem., 63 (1991) 596.
27 E. Wang, R. Schillar and M.E. Meyerhoff, unpublished results.
28 E. Bakker and W. Simon, Anal. Chem., 64 (1992) 1805.

Analytica Chimica Acta, 283 (1993) 683–688
Elsevier Science Publishers B.V., Amsterdam

Permselective lipid–poly(*o*-phenylenediamine) coatings for amperometric biosensing of glucose

Joseph Wang and Hui Wu

Department of Chemistry and Biochemistry, New Mexico State University, Las Cruces, NM 88003 (USA)

(Received 27th April 1993; revised manuscript received 6th July 1993)

Abstract

Highly selective biosensing of glucose is achieved by entrapping glucose oxidase into a composite poly(*o*-phenylenediamine)(PPD)–lipid layer. The composite layer, resulting from such immobilization scheme, combines the size-exclusion sieving of PPD films with the hydrophobicity of lipid coatings. While maintaining highly sensitive and fast response towards the target glucose substrate, it strongly influences the transport and response of potential electroactive interferents. A dramatic improvement in the discrimination against ascorbic and uric acids and acetaminophen is thus accomplished. Factors affecting the behavior of the PPD–lipid–enzyme layer are elucidated and the analytical advantages are illustrated under batch and flow conditions.

Keywords: Biosensors; Glucose; Surface coatings; Interferences

Enzyme immobilization technology has attracted much attention in connection with the design of amperometric biosensors [1–3]. Numerous recent studies have reported improved biosensor performance through a judicious choice of the enzyme immobilization conditions. One promising avenue involves the use of electropolymerization to entrap enzymes at electrodes surfaces [4–6]. Electrochemically polymerized films serve not only for immobilizing the biocomponent, but also provide some degree of selectivity against electroactive interferents and can protect the transducer against fouling species. The permselectivity of these coatings can be manipulated via control of the electropolymerization conditions [7]. In particular, the use of electropolymerized poly(*o*-phenylenediamine) (PPD) films has attracted a considerable recent attention because of its effective discrimination against common interferents (e.g. ascorbic and uric acids, cysteine). Yet, our work has indicated an incomplete rejection of such species at PPD-based enzyme electrodes. Further improvements in the permselectivity are thus highly desired.

The objective of the research described in this paper is to improve the selectivity of amperometric glucose sensors through the use of a mixed PPD–lipid layer. The coverage of amperometric transducers with two (or more) permselective films, based on different transport properties, has been shown to improve the discrimination against interfering species [8,9]. For example, composite or bilayer coatings of cellulose acetate–Nafion [8] or poly(vinylpyridine)–cellulose acetate [9] offer attractive size/charge exclusion characteristics. Lipid coatings are known to offer discriminative properties based on polarity [10–13]. The combination of such hydrophobic layers with the size-exclusion features of PPD films offers remarkable improvements in the selectivity of glucose biosen-

Correspondence to: J. Wang, Department of Chemistry and Biochemistry, New Mexico State University, Las Cruces, NM 88003 (USA).

sors. Even though the concept is presented here in the context of glucose measurements, it could be extended to the biosensing of many other important substrates. The behavior and advantages of the new PPD/lipid composite are elucidated in the following sections.

EXPERIMENTAL

Apparatus

All the electrochemical experiments were performed with EG&G PAR Model 264A polarographic analyzer coupled to a Houston Omniscribe strip-chart recorder. The platinum working electrode (1.6-mm diameter, Model MF2013 BAS), reference electrode (Ag/AgCl) (3 M NaCl) and the platinum wire auxiliary electrode joined the 10-ml electrochemical cell (Model VC-2 Bioanalytical System (BAS) through holes in its PTFE cover. The flow-injection system consisted of the carrier reservoir, a Rainin Model 5041 sample injection valve (20 μl loop), interconnecting PTFE tubings and a platinum thin-layer detector (Model TL-5, BAS). Flow of the carrier solution was maintained by gravity. All potentials were measured vs. the Ag/AgCl reference electrode (Model RE-1, Bioanalytical System (BAS)).

Reagents

All solutions were prepared from double-distilled water. Glucose, glucose oxidase (Type X-S, *Aspergillus Niger*, 135 000 U/g), *o*-phenylenediamine, L-α-phosphatidylcholine (Type XI-E, 100 mg/ml chloroform), acetaminophen, sodium acetate, ascorbic acid and uric acid (all reagent grade from Sigma) were used without further purification. All measurements were performed in a 0.05 M phosphate buffer (pH 7.0) solution.

Procedure

Prior to its modification, the platinum electrode was hand polished with a 0.05-μm alumina slurry and rinsed with doubly distilled water. The electrode was subsequently coated with 5 μl of the 1:10 diluted (in chloroform) lipid solution, placed to cover the active disk and its surrounding, and the solvent was then allowed to evaporate. The enzyme entrapment within the PPD was subsequently carried out in a quiescent solution of 0.2 M sodium acetate (pH 5.2) containing 5 mM *o*-phenylenediamine and 1000 U/ml glucose oxidase. The film was grown electrochemically on the platinum–lipid surface at a constant potential (+0.65 V) for 15 min. The modified surface was thoroughly washed with doubly distilled water prior to its analytical application.

Batch and flow amperometric experiments were performed at room temperature, by applying the desired potential (usually +0.70 V) and allowing the transient current to decay. All experiments were conducted at room temperature.

RESULTS AND DISCUSSION

The electropolymerization of *o*-phenylenediamine, in the presence of glucose oxidase (GOx), offers a convenient way to entrap the enzyme onto amperometric transducers [5,13]. Scanning or fixed potential conditions can be used to form the polymer–enzyme surface layer. Analogous experiments in the presence of a lipid have not been reported. Figure 1 assesses the effect of the phospholipid coating upon the growth of the PPD–GOx film. It shows repetitive cycling voltammograms obtained during the electropolymerization process, in the absence (A) and presence (B) of the lipid layer. The first cycle shows an irreversible oxidation peak (at 0.37 (A) and 0.42 (B) V). On subsequent potential cyclings the peak potential shifts towards more positive values and the peak current decreases significantly until practically no current flows. Note that while the first peak is larger and sharper at the bare platinum surface, no significant differences between the bare and lipid-coated electrodes are observed on successive scans. Overall, the data of Fig. 1 clearly demonstrate that the electropolymerization is proceeding through the lipid coating. The entrapment of glucose oxidase is also not compromised by the presence of the phospholipid layer, as evidenced from the following experiments.

Figure 2 compares current-time recordings for successive additions of 1×10^{-3} M glucose, as

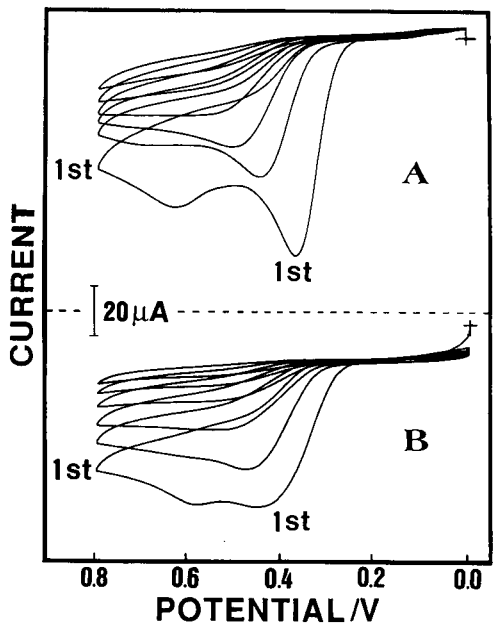

Fig. 1. Cyclic voltammograms for the electropolymerization of poly(*o*-phenylenediamine), in the absence (A) and presence (B) of the lipid layer. Scan rate, 50 mV/s. Solution, 0.2 M sodium acetate (pH 5.2) containing 5 mM *o*-phenylenediamine and 1000 U/ml GOx.

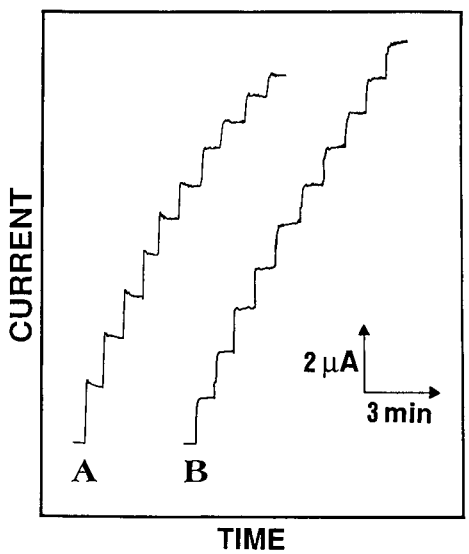

Fig. 2. Current–time recordings at the PPD (A) and PPD–lipid (B) enzyme electrodes upon increasing the glucose concentration in 1×10^{-3} M steps. Batch experiment with 400 rpm stirring and +0.70 V operating potential. Electrolyte, phosphate buffer (0.05 M, pH 7.0).

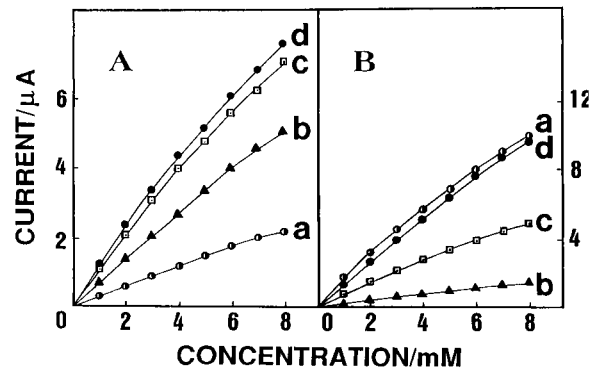

Fig. 3. Effect of preparation conditions, including levels of enzyme (A) and lipid (B) upon calibration plots for glucose. Enzyme activity (in deposition solution): 100 (A(a)), 500 (A(b)), 1000 (A(c), and B) and 1500 (A(d)) U/ml. Amount of casted lipid: 0 (B(a)), 5 (B(b)), 25 (B(c)) and 50 (B(d)) and (A) ng. Other conditions, as in Fig. 2.

obtained at the PPD (A) and PPD–lipid (B) enzyme electrodes. Both biosensors respond very rapidly to these additions of the substrate, producing steady-state signals within 8–10 s. The size of the glucose response, and the overall signal-to-noise characteristics, are also comparable. While maintaining the high speed and sensitivity inherent to PPD-coated enzyme electrodes, the PPD–lipid layer strongly influences the transport and response of potential electroactive interferents (see additional data below).

Various experimental parameters affecting the response of the PPD–lipid biosensor have been examined. Figure 3 shows the effect of the enzyme content (A) and lipid level (B) upon the glucose signal. As expected, higher surface loadings, and hence response to the substrate, are obtained upon increasing the biocatalytic activity (in the preparation solution). In addition, the response to glucose rapidly increases upon increasing the amount of the casted phospholipid between 5 to 50 ng (B (b–d)). The latter offers a response similar to that observed without the lipid layer (B (a)). Such coverage was used in all subsequent work. Note also that the linear range is extended from 2 to 7 mM glucose upon increasing the level of the enzyme or decreasing the amount of the lipid. The potential dependence was evaluated from hydrodynamic voltammo-

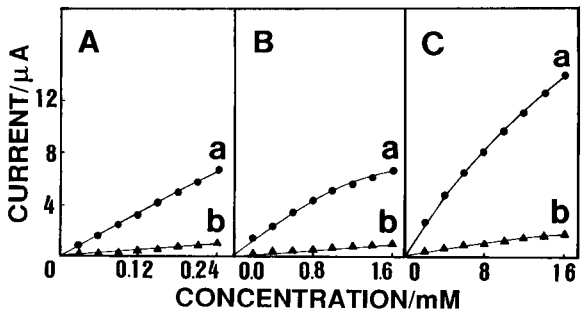

Fig. 4. Calibration plots for acetaminophen (A), uric acid (B) and ascorbic acid (C) at the PPD (a) and PPD–lipid (b) enzyme electrodes. Other conditions, as in Fig. 2.

grams for 1×10^{-3} M glucose (not shown). As expected for the detection of the liberated peroxide species at the platinum transducer, the response increased rapidly between +0.30 V and +0.65 V, and leveled off at higher values.

While offering a similar response towards the target substrate, the PPD–lipid surface structure offers substantially improved discrimination against otherwise interfering oxidizable compounds. Figure 4 compares calibration plots (at +0.70 V) for acetaminophen (A), uric acid (B) and ascorbic acid (C) at the PPD (a) and PPD–lipid (b) enzyme electrodes. Both electrodes exhibit some response towards these compounds. However, ca. eight-fold decrease in the sensitivity is observed upon adding the lipid layer. When compared to the response at the bare platinum surface (Table 1), the PPD–lipid coated enzyme electrode yielded peak ratios (coated/bare) of 0.04 (acetaminophen), 0.006 (uric acid) and 0.001 (ascorbic acid), as compared to ratios of 0.25, 0.05 and 0.01, respectively, using the PPD layer alone. Hence while the single-domain PPD film offers significant diminution of the response (vs. the bare surface), these are not sufficient for selective biosensing of glucose (see data below).

TABLE 1

Permeability of the PPD and PPD–lipid coatings toward common interfering species [a]

Solute	$i_{p,c}/i_{p,bare}$ [b]	
	PPD	PPD–lipid
Acetaminophen	0.250	0.040
Ascorbic acid	0.010	0.001
Uric acid	0.050	0.006

[a] Conditions as in Fig. 4. [b] $i_{p,c}/i_{p,bare}$ is the ratio between the peak current at the coated electrode over that at the bare one (for concentrations within the linear portions of Fig. 4).

While the exact morphology of the biosensor surface is not known, it appears that the PPD and the enzyme are deposited within the interstitial spaces of the precasted phospholipid layer. Simply, the lipid serves as a host layer to the growing PPD and the entrapped enzyme. Glucose can reach the active site of the enzyme, liberating the small peroxide species which can be transported and detected at the platinum surface. In contrast, the PPD–lipid composite serves as an effective barrier against common interferences (based on combined polarity and size effects), thus preventing them from reaching the surface. The fact that glucose can be conveniently detected implies that the enzyme is not completely covered by the composite layer. (One exception is use of a low lipid level which, surprisingly, appears to increase the coverage of the enzyme by the composite, e.g. Fig. 3B (b).)

The greatly improved exclusion of polar interferences by the additional lipid layer greatly enhances the selectivity of glucose biosensors. Figure 5 compares the amperometric response (at +0.8 V) to glucose (a), followed by additions of ascorbic acid (b), acetaminophen (c) and uric acid (d), at the PPD- (A) and PPD–lipid- (B) based biosensors. At the PPD-coated enzyme electrode the glucose signal is accompanied by relatively large contributions of the three oxidizable components. In contrast, these contributions are greatly diminished at the PPD–lipid coated sensor, thus resulting in higher selectivity towards the target substrate. Note again that the sensitivity and response time of the glucose signal are not compromised by the additional lipid layer. A similar selectivity advantage is illustrated in Fig. 6 from an experiment involving an addition of 2.5×10^{-3} M glucose, followed by five successive additions of 1.25×10^{-3} M ascorbic acid. Note again, the negligible contribution of ascorbic acid (up to 6.25×10^{-3}M) at the composite-based biosensor.

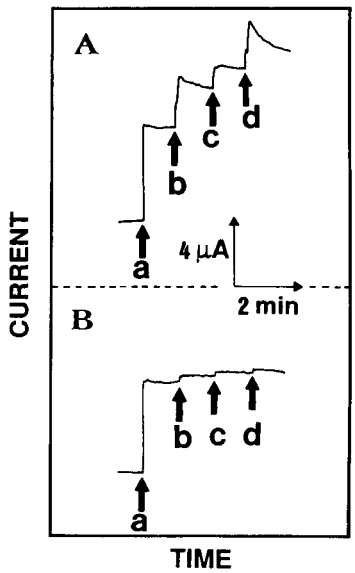

Fig. 5. Current–time recordings at the PPD (A) and PPD–lipid (B) enzyme electrodes upon adding 5×10^{-3} M glucose (a), 2.5×10^{-3} M ascorbic acid (b), 3×10^{-5} M acetaminophen (c) and 5×10^{-4} M uric acid (d). Other conditions, as in Fig. 2.

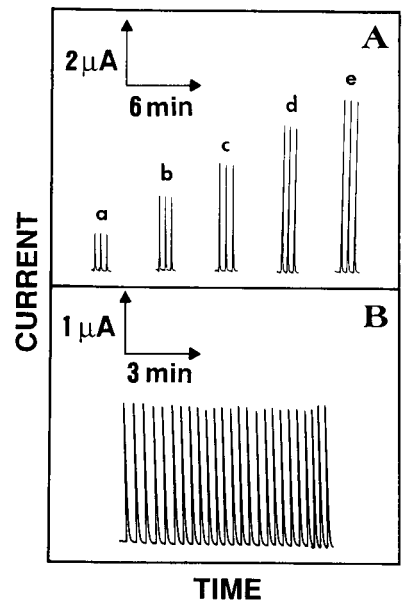

Fig. 7. Flow-injection calibration (A) and stability (B) data at the PPD–lipid–GOx detector. Glucose concentration, $(1–5)\times10^{-3}$ M (A) (a–e); 2×10^{-3} M (B). Flow-rate, 1.0 ml/min. Other conditions, as in Fig. 2.

The very fast response of the PPD–lipid–GOx electrode makes it suitable for use in dynamic flow systems. Figure 7A depicts typical flow injection response peaks at the PPD–lipid–GOx thin-layer detector for glucose solutions of increasing concentration, $(1–5)\times10^{-3}$ M (a–e). The detector exhibits a very short response time and a rapid return to the baseline, indicating a very facile transport of the substrate and removal of the product. The peak width is 15 s, allowing a high injection rate of 120 samples/h. A highly linear calibration plot resulted from these five concentration increments (slope, 1.08 μA/mM; correlation coefficient, 0.999; not shown). The flow-injection response is also very reproducible. The high precision is illustrated in Fig. 7B, using a prolonged series of 25 successive injections, for which a relative standard deviation of 2.2% was calculated. It appears that the incorporated PPD stabilizes (supports) the fragile lipid structure, and eliminates the need for adding modifying agents, e.g. steroids, to strengthen the phospholipid layer [10]. In addition, the phospholipid microenvironment may enhance the thermal and storage stabilities of the enzyme [14]. No apparent loss in the sensitivity was observed over a two-week period. The permselectivity was also maintained during this period.

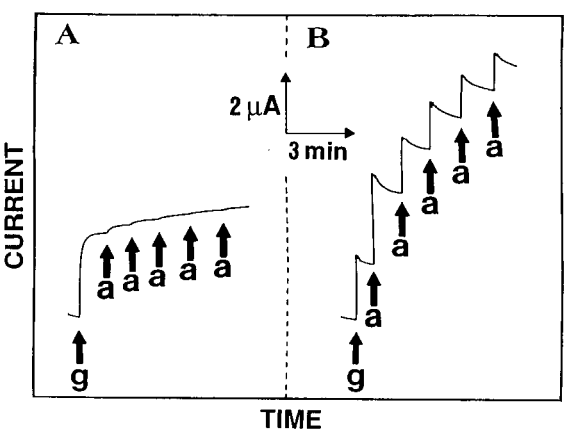

Fig. 6. Current–time recordings at the PPD–lipid (A) and PPD (B) enzyme electrodes upon adding 2.5×10^{-3} M glucose (g) and successive additions of 1.25×10^{-3} M ascorbic acid (a). Other conditions, as in Fig. 2.

In conclusion, the experiments described above indicate that significant selectivity advantage can be achieved by combining the discriminative properties of PPD and lipid films. The improved selectivity is achieved without compromising the sensitivity or speed inherent to PPD-based biosensors, or the enzyme entrapment capability of PPD. The entrapment of other enzymes within PPD–lipid layers should be valuable for the fabrication of other amperometric biosensors. Non-enzymatic sensors and detectors should also benefit from the improved permeability accrued from this multifunctional-film operation. it is clear that the versatility of multifunctional surface coatings can benefit electrochemical sensors in many practical situations. While the sensing utility of the PPD–lipid–enzyme layer has been clearly illustrated, additional fundamental work is desired to further elucidate the detailed structural features of this composite.

REFERENCES

1 O. Zaborsky, Immobilized Enzymes, CRC Press, Cleveland, OH 1973.
2 A. Turner, I. Karube and G. Wilson, Biosensors: Fundamentals and Applications, Oxford University Press, Oxford, 1987.
3 H. Weetall, Anal. Chem., 46 (1974) 602A.
4 M. Umana and J. Waller, Anal. Chem., 58 (1986) 2979.
5 S. Sasso, R. Pierce, R. Walla and A. Yacynych, Anal. Chem., 62 (1990) 1111.
6 P.N. Bartlett and D.J. Caruana, Analyst, 117 (1992) 1287.
7 J. Wang, S. Chen and M. Lin, J. Electroanal. Chem., 273 (1989) 231.
8 J. Wang and P. Tuzhi, Anal. Chem., 58 (1986) 3257.
9 J. Wang and P. Tuzhi, J. Electrochem. Soc., 134 (1987) 586.
10 J. Wang and Z. Lu, Anal. Chem., 62 (1990) 826.
11 J. de Gier, Bioelectrochem. Bioenerg., 27 (1992) 1.
12 A. Amine, J.M. Kauffmann, G.J. Patriarche and G.G. Guilbault, Anal. Lett., 22 (1989) 2403.
13 C. Malitesta, F. Palmisano, L. Torsi and P. Zambonin, Anal. Chem., 62 (1990) 2735.
14 K. Kallury, W. Lee and M. Thompson, Anal. Chem., 64 (1992) 1062.

Analytica Chimica Acta, 283 (1993) 689–694
Elsevier Science Publishers B.V., Amsterdam

Micro-optrode for urea using an ammonium ion-sensitive membrane covered with a urease-immobilized membrane

Yuji Kawabata, Hideyuki Sugamoto and Totaro Imasaka

Faculty of Engineering, Kyushu University, Hakozaki, Fukuoka 812 (Japan)

(Received 22nd April 1993; revised manuscript received 12th July 1993)

Abstract

A urea optrode was constructed using a polymer membrane optically sensitive to ammonium ions and a urease-immobilized membrane. A plasticized poly(vinyl chloride (PVC) membrane containing polynactin was prepared on the distal end of an optical fibre. The PVC membrane was covered with a polyacrylamide membrane, and a positively charged fluorescent dye of hexadecyl-acridine orange was immobilized on the PVC membrane through the polyacrylamide membrane to form an ammonium ion-sensitive membrane. The composite membrane was covered with another polyacrylamide membrane in which urease was immobilized. Urea in a sample solution was hydrolysed to ammonium ion by the immobilized urease and detected optically by the ammonium ion-sensitive membrane. The response of the optrode was reversible to urea concentration in the range 10^{-4}–0.1 M, the response time being 40 s. The selectivity coefficients for potassium and sodium ions were 0.3 and 5×10^{-4}, respectively. The optrode was applied to the determination of urea in blood serum. The observed concentration was corrected for the interference of potassium ion, and it agreed well with the specified urea concentration. The diameter of the optical fibre was 140 μm, so that the optrode could be easily applied to in vivo measurements.

Keywords: Biosensors; Fluorimetry; Ion-selective electrodes; Ammonium-sensitive membrane; Blood; Serum; Urea

An optrode with high sensitivity and selectivity to chemical species is an advanced chemical sensor especially for in vivo measurements [1]. Various optrodes for biosubstances have been developed [2], some of them being based on a biochemical reaction such as an enzymatic reaction [3]. The use of an enzyme such as penicillinase [4] or glucose oxidase [5] provides extremely high selectivity to the corresponding substrate in the optrode system.

In order to measure the substrate optically, the production [6] and consumption [7,8] of chemical species are usually monitored photometrically or fluorimetrically during the enzymatic reaction. Abdel-Latif et al. [9] reported a glucose optrode based on a colour change of a dye that occurs after the enzymatic reaction between glucose and glucose oxidase. Trettnak and Wolfbeis [10] developed a unique optrode in which the intrinsic fluorescence of glucose oxidase changes during the enzymatic reaction. For the optical measurement of urea there is a wide variety of analytical methods as ammonia and ammonium ion are produced in the urea–urease reaction. Urea optrodes have been constructed by using an ammonia gas-sensitive optrode and a urease-immobilized membrane [11,12]. As gaseous ammonia, which can permeate through the membrane, causes a pH change of the inner solution, their

Correspondence to: T. Imasaka, Faculty of Engineering, Kyushu University, Hakozaki, Fukuoka 812 (Japan).

optrodes are highly selective to ammonia derived from urea. However, the diffusion of gaseous ammonia through the membrane is slow, and it suffers from a long response time; a faster response of the optrode is desirably for clinical use. Luo and Walt [13] proposed avidin–biotin coupling to immobilize both an indicator and urease in order to shorten the response time. As the indicator is covalently attached adjacent to the enzyme, the response time for urea could be improved to less than 70 s. However, the procedure for the construction of the urea optrode is complicated. Wolfbeis and Li [14] developed a urea optrode using an ammonium ion-sensitive membrane consisting of a pH indicator and an ammonium ionophore. Their optrode is much easy to construct, and has a response time of 4 min because of the slow diffusion processes involved. Another approach to shorten the measurement time is to combine optrodes with a flow-injection system [15,16]. Urea concentrations can be determined with the sampling frequency of 20 h^{-1}. However, these systems are difficult to apply to the in vivo measurement of chemical species.

In this study, a urea optrode was developed by using an ammonium ion-sensitive membrane [17] covered with a urease-immobilized membrane. Ammonium ion is produced from urea by the immobilized urease, and is directly determined by the ammonium ion-sensitive membrane. The ammonium ion-sensitive membrane consists of an ammonium ionophore and a fluorescent probe, and the optrode response obtained by fluorimetry is selective to ammonium ion derived from urea. This composite membrane is attached to the distal end of a single optical fibre. As the composite membrane is very thin, the response time is substantially improved compared with that of the previous urea optrodes. The optical fibre, which connects the sensing membrane to a fluorescence detection system, allows great flexibility in the application of the optrode. Furthermore, miniaturization of the optrode can be achieved by using a thin optical fibre as the preparation of the sensing membrane is easy. It also allows the in vivo measurement of urea with the constructed optrode.

EXPERIMENTAL

Apparatus

The experimental apparatus of the optrode is similar to that described previously [17]. An argon ion laser (NEC, GLG3070, 488 nm, 3 mW) was used as an excitation source. The laser beam was square-wave modulated at 100 Hz by a mechanical chopper (Scitec Instruments, Hampshire, Model 300). The output power of the laser was then decreased to a certain value (see below) by neutral density filters (Fuji Photo Film, ND-2.0, ND-1.0 and ND-0.7) in order to avoid photodecomposition of the fluorescent probe. However, a sufficient fluorescence intensity was observed from the sensing membrane. The synchronized signal from the chopper was fed to a lock-in amplifier (NF Circuit Design Block, Model 5600) as a reference. The modulated beam was passed through a dichroic mirror, with a transmittance at 488 nm of 88% and a reflectance at 520 nm of 99% when the mirror was tilted at 45° to the laser beam. The transmitted beam was focused by a lens (focal length 50 mm) on to the front surface of an optical fibre. Two types of the quartz optical fibres were used in this study; the core and cladding diameters of fibre 1 (Fujikura, G100/140) were 100 and 140 μm, respectively, and those of fibre 2 (Showa Wire and Cable, NJ/SF-800/1000) were 800 and 1000 μm, respectively. The sensing membrane for urea was attached to the end surface of the optical fibre described below and was irradiated by the introduced laser beam. Fluorescence from the sensing membrane was collected by the same optical fibre and collimated by the lens. It was reflected by the dichroic mirror and focused by a lens (focal length 70 mm) on to the entrance slit of a monochromator (Jasco, CT-10, 520 nm) after passing through a bandpass filter (530 nm, bandwidth 60 nm). Fluorescence at 520 nm was detected by a photomultiplier tube (Hamamatsu Photonics, R3896) and the output signal from the photomultiplier tube was fed through the lock-in amplifier to a chart recorder.

Reagents

Urease from jack beans with an activity of 50–80 U mg^{-1} was obtained from Sigma (Type

IX). Acrylamide and blood serum (control serum I) were purchased from Wako. An aqueous solution of polyacrylamide (10%; average molecular weight 7×10^5), *N,N'*-methylenebis(acrylamide), ammonium peroxodisulphate and urea were supplied by Kishida. Riboflavin was obtained from Tokyo Kasei. All reagents were used as received. Other chemicals were the same as those used in a previous study [17]. A sample solution of urea was prepared by using phosphate buffer (pH 7.0) solvent.

Membrane preparation

First, sodium tetrakis[3,5-bis(trifluoromethyl)-phenyl]borate (Na^+TFPB^-, 0.9 mg), polynactin (2.5 mg) and bis(2-ethylhexyl) sebacate (0.5 g) were dissolved in tetrahydrofuran (15 ml). Poly(vinyl chloride) (PVC, 0.2 g) was added to the solution and the mixture was stirred for 1 h. The distal end of the optical fibre was dipped into the mixed solution and tetrahydrofuran was vaporized to form a plasticized PVC membrane [17].

Second, acrylamide (3.0 g), *N,N'*-methylenebis(acrylamide) (58 mg), riboflavin (2.7 mg) and ammonium peroxodisulphate (2.7 mg) were dissolved in phosphate buffer (pH 7, 25 ml) [18]. A 2.5-ml portion of this solution (solution 1) was mixed with the aqueous solution of polyacrylamide (0.3 g). The plasticized PVC membrane was then dipped into the solution containing the monomer and polymer of acrylamide. Acrylamide was photopolymerized by irradiation with light (tungsten lamp, 300 W). The polymerized membrane became very porous both on addition of polyacrylamide and with the use of a small amount of *N,N'*-methylenebis(acrylamide), and it would allow rapid diffusion of the ammonium ions, that were produced in the enzyme-immobilized membrane.

Third, the aqueous solution of the fluorescent probe hexadecyl-acridine orange (hexadecyl-AO^+, 1.6×10^{-5} M) was prepared, and the composite membrane was immersed in this aqueous solution. Hexadecyl-AO^+ was passed through the polyacrylamide membrane and immobilized on the PVC membrane by ion exchange with sodium ions in the PVC membrane.

Finally, a mixed solution with the same composition as solution 1 except for the amount of *N,N'*-methylenebis(acrylamide) (580 mg) was prepared, and urease (92 mg) was dissolved in a 0.5-ml portion of the acrylamide solution. The composite membrane was further dipped into the urease solution and photopolymerized by the procedure described above.

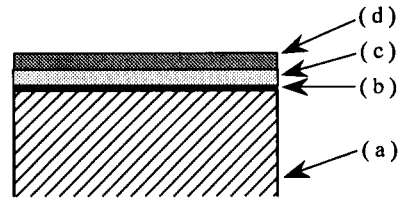

Fig. 1. Cross-section through sensing membrane of urea optrode. (a) Quartz optical fibre; (b) plasticized PVC membrane sensitive to ammonium ions; (c) polyacrylamide membrane which separates (b) and (d); (d) polyacrylamide membrane containing urease.

A cross-section through the sensing membrane of the urea optrode is shown in Fig. 1. The thickness of the membrane was measured with a low-vacuum scanning electron microscope (Topcon, ABT-32).

RESULTS AND DISCUSSION

Membrane preparation

At the beginning of this study, a sensing membrane for urea was prepared by two different procedures from that described under Experimental. However, the sensitivities of the optrodes obtained were poor. The first procedure was as follows. The plasticized PVC membrane was prepared on the distal end of the optical fibre and hexadecyl-AO^+ was immobilized on the PVC membrane in advance. This optrode was sensitive to ammonium ions. The plasticized PVC membrane was then covered with the polyacrylamide membrane in which urease was immobilized. However, the fluorescence from the membrane was significantly decrease by the polymerization of acrylamide. This was due to the decomposition of hexadecyl-AO^+ caused by the polymerization reaction. Therefore, hexadecyl-AO^+ should be immobilized on the PVC membrane after poly-

merization of acrylamide, which covered the PVC membrane.

The second procedure for preparing a sensing membrane was as follows. A plasticized PVC membrane without hexadecyl-AO^+ was prepared and was covered with the polyacrylamide membrane containing urease. Hexadecyl-AO^+ was then immobilized on the PVC membrane through the urease-immobilized membrane. However, high background fluorescence was observed from the sensing membrane and the sensitivity of the optrode was substantially degraded. Hexadecyl-AO^+ might be adsorbed on urease, causing the large background signal. Hence hexadecyl-AO^+ should be immobilized on the PVC membrane before immobilization of urease.

Considering these results, the polyacrylamide membrane was placed between the PVC and urease-immobilized membranes as described under Experimental. No decomposition of hexadecyl-AO^+ was observed during the polymerization of acrylamide. Further, adsorption of hexadecyl-AO^+ on urease could be avoided by this method.

Optrode response to ammonium ions and urea

The urea optrode was constructed by using fibre 1 and was first applied to the determination of ammonium ions in order to evaluate the optrode performance. The response of the optrode was inversely proportional to the ammonium ion concentration in the range 10^{-4}–0.1 M. The detection limit for ammonium ions was 1×10^{-4} M, the response time being 30 s. The response to ammonium ions was compared with that of an optrode constructed by using only the PVC membrane [17]. The sensitivity and response time to ammonium ions was almost the same for both optrodes. Hence no degradation of the sensitivity or lengthening of the response time were observed when the PVC membrane was covered with the polyacrylamide membrane.

This optrode was applied to the determination of urea, and the response curve obtained is shown in Fig. 2. The response of the optrode is inversely proportional to urea concentration in the range 10^{-4}–0.1 M, the response time being 40 s. The analytical range for urea is almost identical with that for ammonium ions. This implies that the

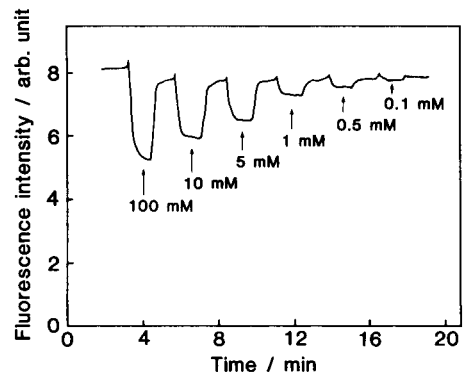

Fig. 2. Optrode response to various concentrations of urea.

sensitivity is not affected by the rate of hydrolysis of urea, as the activity of urease is fairly high. The analytical error in the urea concentration depends strongly on the concentration of the sample solution to be measured. It is roughly determined by the sensitivity and the fluctuation of the response, and is calculated to be $\pm 10\%$ for a urea concentration of 5×10^{-3} M. The optrode responses to potassium and sodium ions were also investigated; the selectivity coefficient were 0.3 and 5×10^{-4}, respectively. These values are comparable to those for the electrochemical [19] and optical [17] sensors using an ammonium ion-sensitive membrane and a urease-immobilized membrane.

The thickness of the sensing membrane was measured with a scanning electron microscope. In order to avoid shrinkage of the swollen membrane, the observation was effected under low vacuum. The thickness of the PVC membrane and the whole sensing membrane were < 1 μm and 6–8 μm, respectively. This thin sensing membrane may result in rapid response of the optrode to urea.

Several optrodes for urea were constructed by the same procedure, and the reproducibility of the response was evaluated. Unfortunately, the optrode responses differed so that calibration of each optrode is necessary at present. The sensitivity was not affected by the immobilized urease because of the high enzymatic activity. Hence a urea optrode with the same sensitivity can be obtained by the reproducible preparation of the

ammonium ion-sensitive membrane on the distal end of the optical fibre.

Determination of urea in serum

The optrode was developed for the direct measurement of urea in biological fluids, and urea in blood serum was determined to demonstrate the performance of the optrode. The concentrations of urea and potassium ions in the control serum were 2.6×10^{-3} and 3.8×10^{-3} M, respectively. As the selectivity of the optrode to urea against potassium ions was not high, potassium ions caused an interference in the measurement of urea. The calibration graph was first constructed by using various concentrations of urea and the optrode was then applied to the measurement of urea in blood serum. The concentration of urea observed was 3.7×10^{-3} M, which was higher than that specified. However, the interference response to potassium ions could be compensated, according to the unpublished results of Li et al. [16] when the concentration of potassium ion was independently determined. From the concentration of potassium ions (3.8×10^{-3} M) and the selectivity coefficient for potassium ions (0.3), the observed concentration of urea (3.7×10^{-3} M) was corrected to 2.6×10^{-3} M, which was in good agreement with the specified value. There might be other chemical species that interfered with the optrode response, but the interference caused by potassium ions was dominant for the measurement of urea in blood serum and only the deviation of the concentration due to potassium ions needs to be corrected for in practical measurements.

There are many chemical species present in a biological fluid, and some of them are strongly fluorescent. Further, biosubstances such as proteins are easily adsorbed on the sensing membrane and cause a serious interference in the measurements of urea. Therefore, the sample solution is usually diluted several-fold in order to decrease such interferences [20]. However, this pretreatment of the sample solution affects in vitro measurements even though the optrode is small enough to be applied to measurements in a living body. The response of the ammonium ion-sensitive membrane prepared in this study was also affected by components such as proteins in serum. However, surprisingly, the urea optrode showed no appreciable interference from such ingredients as the polyacrylamide membrane placed over the PVC membrane would have a filtration effect on serum. This implied that the direct measurement of urea in a biological fluid is possible, that is, dilution of the original sample solution is not necessary. Further, the optical fibre (fibre 1) used in this study is very thin, and the optrode was confirmed to work even when it was inserted into a needle for medical use. Therefore, the urea optrode could be readily applied to in vivo measurements.

Stability of optrode response and power density of light

Miniaturization of the optrode is desirable for clinical use. However, the power density of light significantly increases with miniaturization of the optrode, causing photodecomposition of a fluorescent probe. Hence the stability of the optrode response strongly depends on the power density of light introduced into the optical fibre. When the output power of the laser introduced into fibre 2 was adjusted to 8 μW, the response of the optrode was stable and no photodecomposition of hexadecyl-AO$^+$ was observed. The power density of light at the sensing membrane was calculated to be 16 W m^{-2}. When fibre 2 was replaced with fibre 1 and the power density of light at the sensing membrane was increased to 1.0×10^3 W m^{-2}, the fluorescence intensity from the optrode significantly decreased with time as photodecomposition of hexadecyl-AO$^+$ occurred. In order to avoid photodecomposition, the output power of the laser introduced into fibre 1 should be decreased. When the power density was adjusted to 16 W m^{-2}, no decrease in the fluorescence intensity from the optrode was observed. Therefore, the power density of light at the sensing membrane should be controlled to obtain a stable optrode response.

The measurement of the membrane thickness was made using the scanning electron microscope at the Centre of Advanced Instrumental Analysis, Kyushu University. This research was supported

by Grants-in-Aid for Scientific Research from the Ministry of Education, Science and Culture, Japan.

REFERENCES

1 M.E. Collison and M.E. Meyerhoff, Anal. Chem., 62 (1990) 425A.
2 J. Janata and A. Bezegh, Anal. Chem., 60 (1988) 62R.
3 J.I. Peterson and G.G. Vurek, Science, 224 (1984) 123.
4 T.J. Kulp, I. Camins, S.M. Angle, C. Munkholm and D.R. Walt, Anal. Chem., 59 (1987) 2849.
5 M.S. Abdel-Latif and G.G. Guilbault, Anal. Chem., 60 (1988) 2671.
6 R. Narayanaswamy and F. Sevilla, III, Anal. Lett., 21 (1988) 1165.
7 N. Uwira, N. Opitz and D.W. Lubbers, Adv. Exp. Med. Biol., 169 (1984) 913.
8 M.C. Moreno-Bondi, O.S. Wolfbeis, M.J.P. Leiner and B.P.H. Schaffar, Anal. Chem., 62 (1990) 2377.
9 M.S. Abdel-Latif, A.A. Suleiman and G.G. Guilbault, Anal. Lett., 21 (1988) 943.
10 W. Trettnak and O.S. Wolbeis, Anal. Chim. Acta, 221 (1989) 195.
11 T.D. Rhines and M.A. Arnold, Anal. Chim. Acta, 227 (1989) 387.
12 X. Xie, A.A. Suleiman and G.G. Guilbault, Talanta, 38 (1991) 1197.
13 S. Luo and D.R. Walt, Anal. Chem., 61 (1989) 1069.
14 O.S. Wolbeis and H. Li, Bisensors Bioelectron., 8 (1993) 161.
15 T.D. Yerian, G.D. Christian and J. Ruzicka, Anal. Chim. Acta, 204 (1988) 7.
16 H. Li, H. He, B. Kovacs, B. Weigl, W. Trettnak, W.W. Petek and O.S. Wolfbeis, unpublished results.
17 Y. Kawabata, T. Kamichika, T. Imasaka and N. Ishibashi, Anal. Chem., 62 (1990) 2054.
18 J. Montalvo, Jr., and G.G. Guilbault, Anal. Chem., 41 (1969) 1897.
19 G.G. Guilbault and J.G. Montalvo, J. Am. Chem. Soc., 92 (1970) 2533.
20 Y. Kawabata, T. Imasaka and N. Ishibashi, Anal. Chim. Acta, 255 (1991) 97.

Analytica Chimica Acta, 283 (1993) 695–701
Elsevier Science Publishers B.V., Amsterdam

Glucose-sensitive field-effect transistor with additional Nafion membrane

Reduction of influence of buffer capacity on the sensor response and extension of its dynamic range

A.P. Soldatkin and A.V. El'skaya

Institute of Molecular Biology and Genetics, Ukrainian Academy of Sciences, 150 Zabolotny Street, Kiev 252143 (Ukraine)

A.A. Shul'ga and L.I. Netchiporouk

Semiconductor Physics Department, Kiev State University, 64 Vladimirskaya Street, Kiev 252017 (Ukraine)

A.M. Nyamsi Hendji and N. Jaffrezic-Renault

LPCI, URA CNRS 404, Ecole Centrale de Lyon, BP 163, 69131 Ecully Cedex (France)

C. Martelet

LTDS, URA CNRS 855, Ecole Centrale de Lyon, BP 163, 69131 Ecully Cedex (France)

(Received 22nd April 1993; revised manuscript received 21st June 1993)

Abstract

Glucose-sensitive enzyme field-effect transistors (ENFETs) were prepared by cross-linking glucose oxidase with bovine serum albumin in saturated glutaraldehyde vapour on the gate area of the ISFETs. Nafion membranes were deposited on the top of the glucose ENFETs by a spin-coating procedure. Additional Nafion membranes resulted in a substantial reduction of the effect of the buffer concentration on the ENFET's response and in an extension of the dynamic range of the sensor up to concentrations of more than 10 mM glucose. The effects of pH, buffer concentration and ionic strength were examined for the glucose ENFETs with and without NAFION membranes.

Keywords: Biosensors; Enzymatic methods; Field-effect transistors; Glucose

Biosensors based on semiconductor structures have received considerable attention because it is expected that the innovative potential of the technology of microelectronics may result in the appearance of new biosensor technologies. These technologies are well adapted to the large-scale production of miniaturized devices. The final aim is the development of inexpensive, disposable, reliable devices suitable for rapid analytical tests made on-site [1]. The latter is of great interest in fields such as biomedicine, environmental monitoring and food quality control.

The semiconductor structures most frequently used as the transducers for biosensors are ion-sensitive field-effect transistors (ISFETs), introduced by Bergveld [2] in 1970 and used for the

Correspondence to: A.P. Soldatkin, Institute of Molecular Biology and Genetics, Ukrainian Academy of Sciences, 150 Zabolotny Street, Kiev 252143 (Ukraine).

first time in an enzyme biosensor [enzymatic field effect transistor (ENFET)] for penicillin detection by Caras and Janata [3] in 1980. However, in spite of the initial optimism, progress in this field was slower than expected [4].

Most papers published on ENFETs deal with the investigation of glucose-specific ENFETs (see references cited in [5]). In such biosensors, glucose oxidase (GOD) is immobilized on the gate insulator of the ISFET catalysing the oxidation of glucose according to the reaction

$$\text{D-glucose} + O_2 \xrightarrow{\text{glucose oxidase}} \text{D-glucono-}\delta\text{-lactone} + H_2O_2$$

The ISFET monitors the change of pH near the sensor surface induced by the hydrolysis of gluconolactone to gluconic acid.

Unfortunately, the analytical applications of glucose ENFETs are restricted by the dramatic decrease in the sensor response with increasing buffer capacity of a sample, a non-linear dependence of the enzyme kinetics and buffer capacity of a sample on pH, dependence of the response on ionic strength and co-substrate limitation of the enzymatic reaction rate [6].

The last factor in the particular case of amperometric enzyme biosensors can be overcome by using additional membranes that extend the dynamic range of the sensor [7]. Application of an additional albumin membrane giving the same effect in the case of glucose ENFETs was reported recently [8–10]. However, the determination of the glucose in undiluted serum or whole blood (concentration in the range 3–30 mM) with an ISFET-based biosensor is difficult, even if the dynamic range of this sensor is extended, owing to the high buffer capacity of the sample.

This paper presents results concerning the application of additional Nafion membranes to reduce the influence of buffer concentration on the glucose ENFET response and to extend its dynamic range.

EXPERIMENTAL

Materials

Glucose oxidase (EC 1.1.3.4) from *Penicillium vitale* having an activity of 168 U mg^{-1} was obtained from the Cosarsky alcohol plant (Cherkassy, Ukraine), bovine serum albumin (BSA) was purchased from Serva and a 25% aqueous solution of glutaraldehyde (GA) from Merck. Nafion perfluorinated ion-exchange powder [5% (w/v) in mixture of lower aliphatic alcohols and 10% water] was obtained from Aldrich. All other reagents were of analytical-reagent grade.

Enzyme immobilization

Glucose oxidase (GOD) was immobilized using a modified procedure described previously [6]. Solutions of 10% (w/w) GOD and BSA were prepared in 5 mM phosphate buffer (KH_2PO_4–NaOH) (pH 7.4). Prior to deposition on the gate area of the ISFETs, these solutions were mixed in defined proportions and glycerol was added. The mixture composition used was 5% GOD, 5% BSA and 10% glycerol. The use of glycerol prevents the loss of enzyme activity during the immobilization process and also allows better homogeneity of the membrane and better adhesion to the surface of the ISFETs. Because a differential experimental set-up was used, a drop of the enzyme-containing mixture was deposited on the measuring ISFET while only a mixture containing 10% BSA and 10% glycerol was deposited on the reference ISFET. The sensor chips were then placed for 30 min in saturated GA vapour. After exposure to GA, the membranes were dried at room temperature for 15 min. Before use, the membranes were soaked in 5 mM phosphate buffer (pH 7.5) for at least 30 min to equilibrate the membrane system.

Formation of additional membranes

Additional Nafion membranes were formed on the top of the glucose sensors by a spin-coating procedure using 1% or 5% Nafion solution (if necessary the stock solution was diluted with 96% ethanol). A 10-μl volume of Nafion solution was deposited on the ENFET, then the sample was rotated at 500 rpm for 1–2 min. After deposition, the membranes were dried at room temperature for 15 min. The membranes obtained with 1% and 5% Nafion solution were conventionally called 1% and 5% Nafion membranes, respectively.

Sensor design and measurements

n-Channel depletion-mode ISFETs were fabricated at the Research Institute of Microdevices (Kiev, Ukraine) on a p-Si wafer with orientation (100) and resistivity 7.5 Ω cm. After scribing, sensor chips (10 mm × 3 mm) containing two identical ISFETs were formed. A channel (250 μm × 7 μm) was made by ion implantation of phosphorus with a dose depending on the threshold voltage required. In the experiments ISFETs with a threshold voltage of about −3 V were employed.

Sensor chips were glued on a ceramic support made of fused alumina with dimensions 28 mm × 6 mm (thickness 0.5 or 1.0 mm). The sensor contact pads were electrically bonded by ultrasonic wiring to aluminium conducting paths photolithographically patterned on the ceramic support. After wiring, the contact pads and wires were encapsulated with epoxy resin. Detailed information about the construction and mode of operation of the ISFETs will be given elsewhere.

The sensor chip was immersed in the measurement cell filled with 2 ml of buffer solution and the sensors were soaked in 5 mM phosphate buffer (pH 7.4) for 30 min to equilibrate the membrane system. The differential output signal between the measuring and reference ISFETs was registered with a laboratory ISFET meter (Institute of Microelectronics, Neuchatel, Switzerland) and a Linear recorder (Linear Instruments, Reno, NY). All measurements were carried out at room temperature. Magnetic stirring was used during the operation to ensure homogeneity of the solution.

RESULTS AND DISCUSSION

One of the most serious problems arising in practical applications of glucose ENFETs is a dramatic decrease in the biosensor response with increase in the buffer concentration of the sample and their narrow dynamic range (usually up to about 2 mM concentration of glucose) [5–8].

Calibration graphs for glucose ENFETSs with and without additional Nafion membranes are presented in Fig. 1. Biosensors without an addi-

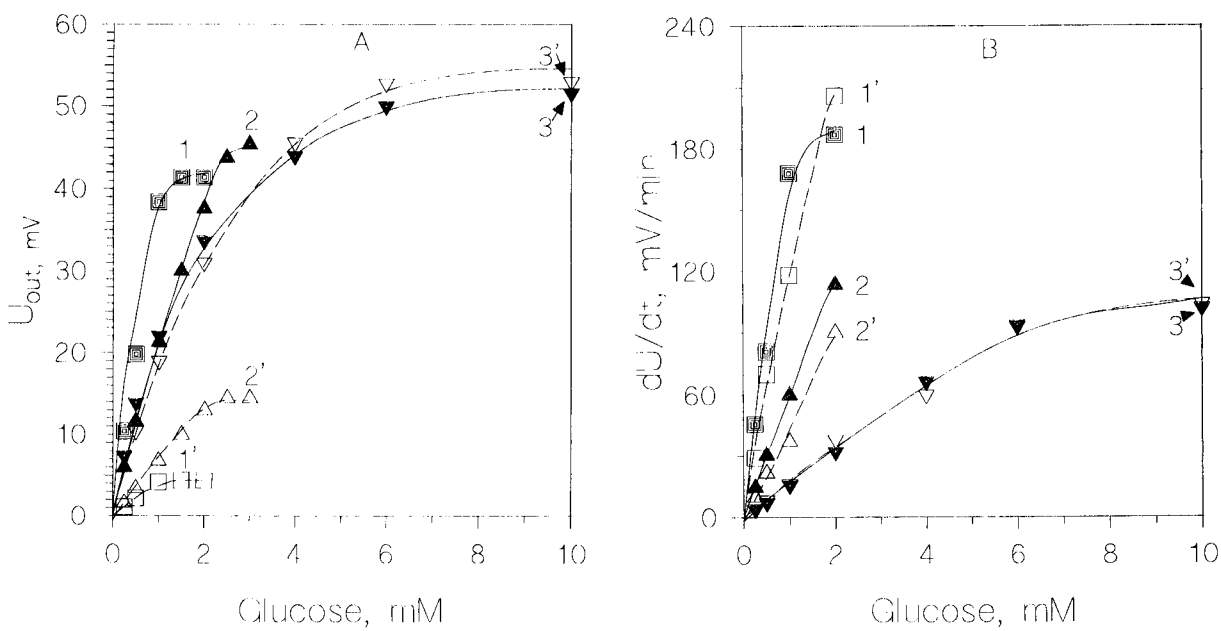

Fig. 1. Calibration graphs for (A) the steady-state and (B) kinetic response of the glucose ENFETs (1, 1′) without, (2, 2′) with 1% and (3, 3′) with 5% additional Nafion membranes in (1, 2, 3) 1 mM and (1′, 2′, 3′) 10 mM phosphate buffer (pH 7.4)–140 mM NaCl.

tional membrane demonstrated a rapid (about 30 s), reproducible response to the substrate addition. However, the dynamic range is very small (it extends only to about 1.5 mM) and the response amplitude is strongly dependent on the buffer concentration (the response value is decreased 20-fold when the concentration of buffer is changed from 1 to 10 mM). The reason for the limited dynamic range of the glucose ENFETs is the oxygen limitation of the biocatalytic glucose oxidation [6], and the dependence of the response amplitude on the buffer concentration is due to a kind of carrier-mediated transport of protons ("facilitated diffusion") out of the enzyme membrane in the presence of mobile buffer species [11].

The application of Nafion membranes strongly changes the characteristics of the biosensor, viz., dynamic range, dependence of the response on the buffer concentration and response time. As can be seen in Fig. 1, the use of the 1% Nafion membrane on top of the enzyme membrane extends the dynamic range of the ENFET up to 2 mM and slightly decreases its sensitivity to buffer concentration. Using 5% Nafion solution for the deposition of an additional membrane results in a 3–5-fold increase in the dynamic range of the sensor (especially when the kinetic response of the sensor is registered; see Fig. 1B) and makes the sensor response nearly insensitive to increases in buffer concentration from 1 to 10 mM. The response time for the ENFET with the 5% Nafion membrane is about 5–7 min in comparison with 30 s for the ENFET without an additional membrane. This indicates that the Nafion membrane forms a diffusional barrier.

In further experiments the sensors with 5% Nafion membranes and those without any additional membrane were employed.

The concentration of the low-molecular-weight components, mainly hydrogen carbonates, that define the pH and buffer capacity of blood, is about 25–30 mM [12]. Therefore, it was of interest to compare the response of the glucose ENFETs with and without additional membranes in 20 mM and more concentrated phosphate buffer solutions. The results are presented in Fig. 2. The response of the ENFET without an additional

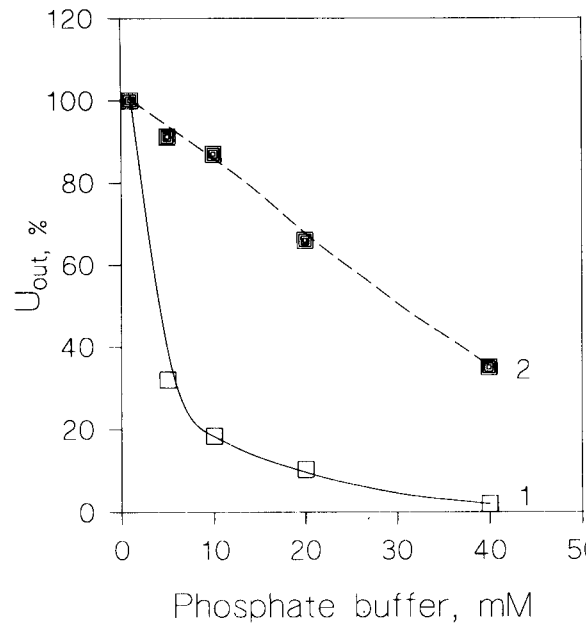

Fig. 2. Dependence of the steady-state sensor response [glucose ENFETs (1) without and (2) with additional Nafion membrane] on phosphate buffer concentration. Measuring conditions: phosphate buffer (pH 7.4)–140 mM NaCl; 2 mM glucose concentration.

membrane depends strongly on the buffer concentration and decreases about 50-fold when the buffer concentration is changed from 1 to 40 mM [the sensor response in 1 mM phosphate buffer (pH 7.4)–140 mM NaCl is taken as 100%]. In contrast, the ENFET with the Nafion membrane shows a much lower sensitivity of the response to the buffer concentration. Its response decreases linearly as the buffer concentration increases and in 40 mM phosphate buffer the differential output signal is about 35% of the value in 1 mM solution.

Such a reduction in the influence of the buffer capacity on the glucose ENFET response may be explained by taking into account the properties of Nafion as a cation-exchange membrane. It has been shown that, e.g., the diffusion coefficient across the Nafion membrane for Na^+ is almost 100 times greater than that for Cl^- [13]. Probably negatively charged sulphonate groups inside the Nafion membrane create a barrier for the diffusion of negatively charged ions. With the phos-

phate buffer used in this investigation, the buffer-mediated mechanism of the diffusion of protons out of the enzyme layer operates, owing to the movement of neutral and negatively charged buffer species across the membranes. The presence of the additional Nafion membrane effectively blocks the transfer of the charged buffer ions and thus drastically reduces the contribution of the "carrier-mediated" mechanism to the total diffusional flux of protons across the Nafion membrane.

Influence of ionic strength

Nafion is known as a specific ion-exchanging material, and it was therefore necessary to study the dependence of the ENFETs' response (with and without an additional membrane) on pH and ionic strength. The dependence of the glucose ENFET response on the NaCl concentration in the sample was measured (Fig. 3). In principle, an increase in ionic strength should result in a greater screening of the charges inside the Nafion membrane and in a decrease in its barrier properties [13]. In the range of salt concentrations tested no such effect was observed. The behaviour of the sensor with a Nafion membrane differs from that of the sensor without such a membrane and demonstrates not a decrease but an increase in the response with increasing NaCl concentration both for steady-state and kinetic responses. From a practical point of view it is important to note that in the range 100–200 mM NaCl, the responses of both biosensors are not dependent on the ionic strength.

Influence of pH

The detailed pH dependence of the glucose ENFET with and without an additional membrane in phosphate buffer is presented in Fig. 4. The data for the ENFETs without an additional Nafion membrane have a minimum at about pH 7.0, corresponding to the maximum of the buffer capacity (for phosphate buffer $pK = 7.2$). With the glucose ENFET with an additional membrane, variation of the pH from 6.2 to 8.2 leads to a nearly linear increase in response (Fig. 4). The exact origin of the pH dependence observed is not clear. Adding NaCl to the sample solution at

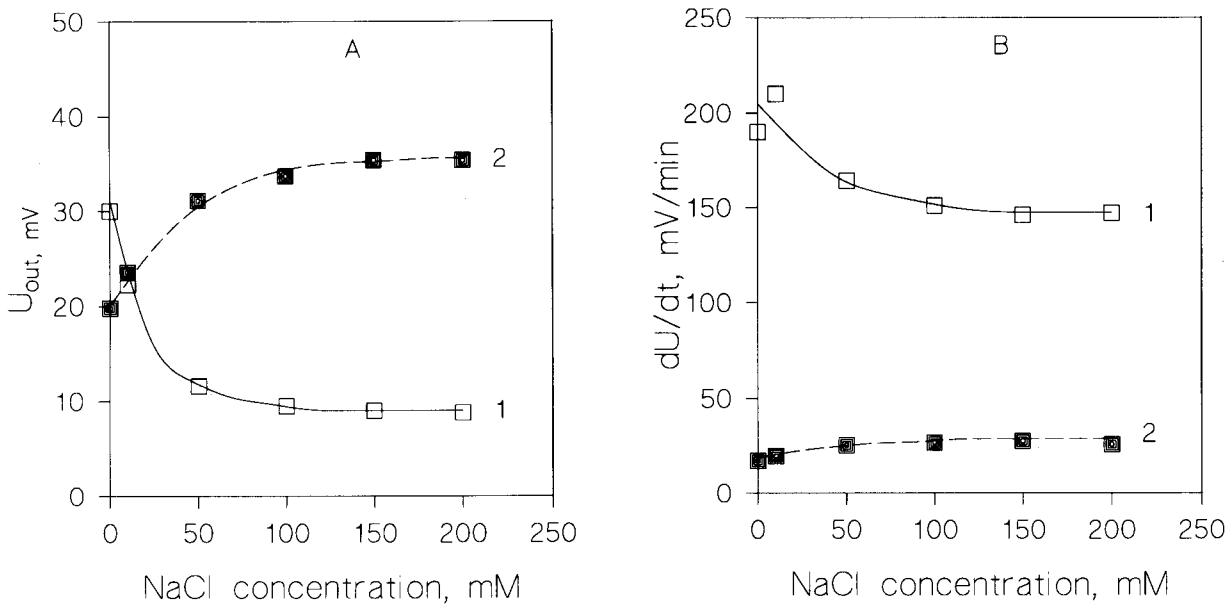

Fig. 3. Dependence of (A) the steady-state and (B) kinetic sensor response of the ENFETs (1) without and (2) with an additional Nafion membrane on NaCl concentration. Measuring conditions: 5 mM phosphate buffer (pH 7.4); glucose concentration for sensor (1) 1 mM and for sensor (2) 2 mM.

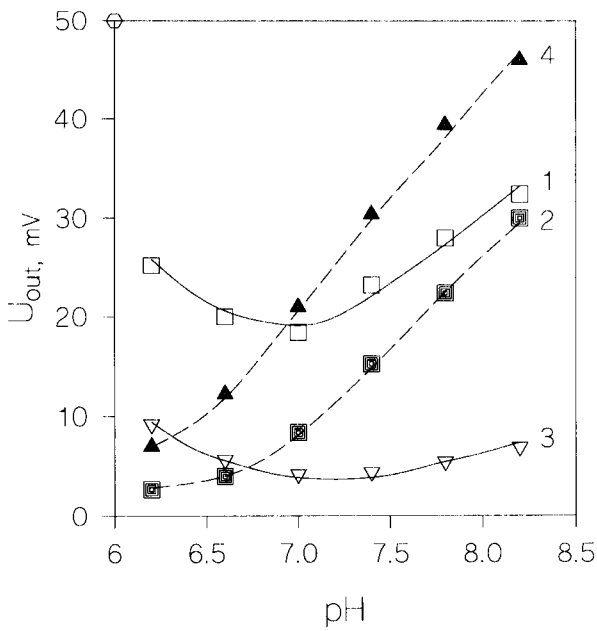

Fig. 4. pH dependence of the sensor response for the ENFETs (1, 3) without and (2, 4) with an additional Nafion membrane. Measuring conditions: (1, 2) 5 mM phosphate buffer; (3, 4) 10 mM phosphate buffer–140 mM NaCl; (1, 3) 1 mM glucose; (2, 4) 2 mM glucose.

a 140 mM concentration does not change the character of the curves for either type of ENFET (Fig. 4).

One of the major factors determining the appearance of the curves in Fig. 4 is the variation of the buffer capacity of the buffer solution when the pH is changed. To overcome the problem of changing buffer capacity with changing pH, in subsequent experimemts a multi-component buffer (polymix) was used with the composition. 2.5 mM Tris–2.5 mM KH_2PO_4–2.5 mM citric acid–2.5 mM sodium tetraborate–2.5 mM KCl–140 mM NaCl. The pH of this polymix buffer was adjusted by titration with NaOH. Polymix has a constant buffer capacity over a wide range of pH, at least between pH 5 and 9 [14]. NaCl (140 mM) was used as a background electrolyte to avoid the influence of the variation in ionic strength at different pH values on the ENFETs' response.

The dependence of the glucose ENFET response on the pH of the polymix buffer is shown in Fig. 5. The general form of these curves is similar for both types of sensors and differs strongly from the curves obtained with phosphate buffer. The curves in Fig. 5 are bell-shaped with a wide maximum between pH 6.0 and 7.0 for the sensor without an additional membrane and with a less wide maximum at pH 7.0–7.5 for the other sensor. Such a position of the pH maximum for the glucose ENFET without an additional membrane can be explained by the fact that immobilized GOD has the highest activity in this pH range [5]. The shift of the pH optimum and its narrowing for the glucose ENFET with an additional membrane is the result of the intrinsic properties of the Nafion membrane. Two possible explanations for this phenomenon can be presented. First, the presence of the additional membrane on the glucose sensor blocks the mechanism of carrier-mediated transport of protons out of the enzyme membrane, which leads to an increase in the response level up to about 30 mV and accordingly to a shift in the local pH of more than 0.5 units at the pH maximum. This

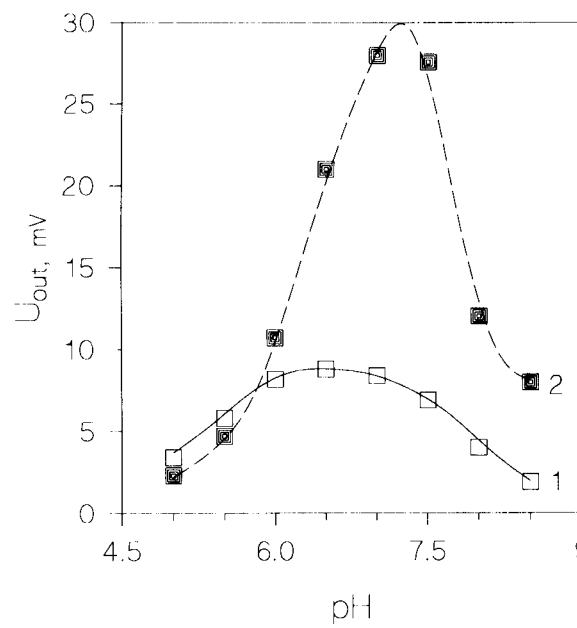

Fig. 5. pH dependence of the sensor response for the ENFETs (1) without and (2) with an additional Nafion membrane in polymix buffer. Measuring conditions: polymix (see text for details)–140 mM NaCl; glucose concentration (1) 1 mM and (2) 2 mM.

means that the enzyme actually works at a higher proton concentration and this is the reason for the pH shift with the ENFET with an additional membrane. Second the presence of a negatively charged additional membrane can lead to modification of the conformation of the immobilized enzyme that consequently can change the properties of the latter.

Comparison of the long-term stability and reproducibility of the sensor response was made for both types of ENFETs (with and without additional membranes) in 1 mM phosphate buffer (pH 7.4)–140 mM NaCl. The standard deviation of the sensor response to a 1 mM glucose concentration was less 2.5% for 40 successive measurements. The response of the sensors remained stable for at least 1 month when stored in a dry state at 4°C; the presence of glycerol in the enzyme layer avoids the formation of cracks in the membrane during storage.

Conclusion

Glucose-sensitive ENFETs without and with an additional Nafion membrane were prepared. It was shown that the formation of the additional Nafion membrane on top of the enzyme-containing membrane in a glucose ENFET results in a substantial decrease in the influence of buffer concentration on the sensor response and in an extension of the dynamic range of the sensor up to a glucose concentration of 10 mM. The results obtained are interpreted in terms of permselective properties of the additional membrane formed. The presence of negatively charged groups inside the Nafion membrane blocks the "carrier-mediated" transport of protons through the additional membrane in the presence of mobile buffer species, thus eliminating their effect on the output signal amplitude of the biosensor. The additional Nafion membrane also limits the diffusion of glucose more effectively than oxygen through the membrane, resulting in an extension of the dynamic range of the sensor.

Comparison of the properties of the glucose ENFETs developed demonstrates a better performance of the sensor with an additional Nafion membrane. The increase in the sensor response time due to the presence of the additional membrane can be overcome by measurements in the kinetic mode.

Part of this work was supported by a grant from CNRS (contract No. A69/766/92).

REFERENCES

1 A.A. Shul'ga and V.I. Strikha, in N.G. Ivanitskij (Ed.), Biotechnique—a New Way to Computerization, Nauka, Moscow, 1990, pp. 63–82.
2 P. Bergveld, IEEE Trans. Biomed. Eng., BME-17 (1970) 70.
3 S. Caras and J. Janata, Anal. Chem., 52 (1980) 1935.
4 G.G. Guilbaut, Chimia, 42 (1988) 267.
5 A.P. Soldatkin, A.K. Sandrovsky, A.A. Shul'ga, N.F. Starodub, V.I. Strikha and A.V. El'skaya, J. Anal. Chem. USSR, 45 (1990) 1405.
6 A.A. Shul'ga, A.K. Sandrovsky, V.I. Strikha, A.P. Soldatkin, N.F. Starodub and A.V. El'skaya, Sensors Actuators B, 10 (1992) 41.
7 M. Mascini and D. Moscone, in A.P.F. Turner (Ed.), Advances in Biosensors, Vol. 1, JAI Press, New York, 1991, p. 33.
8 A. Saito, K. Shionoya, J. Kimura and T. Kuriyama, in A.P.F. Turner (Ed.), Proceedings of the Second World Congress BIOSENSORS'92, Elsevier, Amsterdam, 1992, pp. 71–73.
9 A. Saito, S. Miyamoto, J. Kimura and T. Kuriyama, Sensors Actuators B, 5 (1991) 237.
10 A.A. Shul'ga, V.I. Strikha, A.P. Soldatkin, A.V. El'skaya, H. Maupas, C. Martelet and P. Clechet, Anal. Chim. Acta, 278 (1993) 233.
11 S. Varansi, S.O. Ogundizan and R. Ruckenstein, Biosensors, 3 (1988) 269.
12 Yu.V. Chmelevski and O.K. Usatenko, in R.A. Frol'kis (Ed.), The Main Human Biochemical Constants in a Norm and at a Pathology, Zdorov'e, Kiev, 1987, p. 160.
13 A. Varebska, S. Koter and W. Kujawski, Desalination, 51 (1984) 3.
14 D.D. Perrin and B. Dempsey, in Buffers for pH and Metal Ion Control, Kodansha, Tokyo, 1981, pp. 24–49.

Analytica Chimica Acta, 283 (1993) 703–717
Elsevier Science Publishers B.V., Amsterdam

The peroxidase–NADH biochemical oscillator: experimental system, control variables, and oxygen mass transport

Dean L. Olson and Alexander Scheeline

Department of Chemistry, University of Illinois at Urbana-Champaign, 600 S. Mathews Ave., Urbana, IL 61801 (USA)

(Received 17th May 1993; revised manuscript received 18th June 1993)

Abstract

Experimental control variables are defined and characterized to provide good reproducibility of oscillatory behavior, and allow other investigators to perform additional studies under consistently defined conditions. Fifteen variables are recognized and described. Oxygen mass transport has a large effect on the overall appearance of the oscillations, and is quantitatively related to stirring and several other variables. These conditions combine to yield a single, experimentally measurable oxygen mass-transport constant. Stirring is controlled with a precision motor which is used to explore the mass-transport constant and mixing time as a function of stirrer rotation rate. Oscillatory behavior is examined under identical conditions with and without the modifiers Methylene Blue and 2,4-dichlorophenol (DCP). Omission of DCP from the system does not appreciably change oscillatory behavior under the specified conditions. Slightly damped oscillations are maintained for six hours. The acidic degradation of NADH is significantly affected by illumination from the deuterium lamp used in UV–visible absorption measurements. The importance and value of an analytical approach to this complex system is emphasized throughout.

Keywords: Enzymatic methods; NADH; Oscillators; Peroxidase–NADH biochemical oscillator

The peroxidase–NADH biochemical oscillator has traditionally consisted [1] of an open system of initially five chemical species mixed in a semi-batch reactor. The oscillatory system is named after one of the dominant reactions catalyzed by horseradish peroxidase,

$$2NADH + O_2 + 2H^+ \rightarrow 2NAD^+ + 2H_2O \qquad (1)$$

where NADH is reduced β-nicotinamide adenine dinucleotide. The peroxidase enzyme in nature usually functions to catalyze a substrate using hydrogen peroxide as the cofactor. In reaction 1, however, oxygen serves as the enzyme cofactor. As a result, this reaction is termed the peroxidase/oxidase reaction to denote the involvement of oxygen in NADH oxidation.

The peroxidase–NADH oscillatory system studied here consists of a buffered, aqueous solution of horseradish peroxidase (HRP), Methylene Blue (MB), and 2,4-dichlorophenol (DCP) to which NADH and oxygen are added at constant rates. Under certain conditions, an unknown number of reactions occur which cause the concentrations of several species including oxygen, NADH, and at least two oxidation states of the enzyme, to oscillate in time. Though a significant number of papers have appeared over several years on a variety of topics, including bistability [2], mixed-mode and quasiperiodic oscillations

Correspondence to: A. Scheeline, Department of Chemistry, University of Illinois at Urbana-Champaign, 600 S. Mathews Ave., Urbana, IL 61801 (USA).

(using a chemically modified approach) [3], and period doubling and chaotic behavior [4–7], the experimental system itself has remained largely uncharacterized. Though reported observations are probably valid, knowledge is lacking about the particular conditions under which they were obtained, inhibiting corroborative efforts. The specific roles of DCP and MB remain to be elucidated, and a comprehensive, experimentally-based model still has not emerged. However, it was suggested recently that MB catalyzes the oxidation of NADH [8,9], and DCP is involved in the oxidation of NADH by hydrogen peroxide [10].

The main objective of this work has been to develop and characterize the analytical tools needed to study this particular complex chemical system. This paper identifies and describes previously unrecognized experimental control variables necessary to properly define oscillatory conditions. Consistently defined and controlled experimental parameters have provided good reproducibility (unreported in all previous work), and allow easier, more meaningful study and comparisons of the oscillator among investigators.

EXPERIMENTAL

Reagents

Disodium β-NADH was obtained as the lyophilized powder (No. N-8129, Sigma, St. Louis, MO). The enzyme immunoassay grade horseradish peroxidase was obtained as the salt-free lyophilized powder (90% isoenzyme C; No. 814393, Boehringer Mannheim, Indianapolis, IN). Both powders were stored at 4°C in a vacuum desiccator until just before use. Sodium acetate (NaAc) and acetic acid for buffers were obtained from Fisher, Chicago, IL; Methylene Blue came from Sigma (No. MB-1); 2,4-dichlorophenol was obtained from Aldrich, Milwaukee, WI (No.

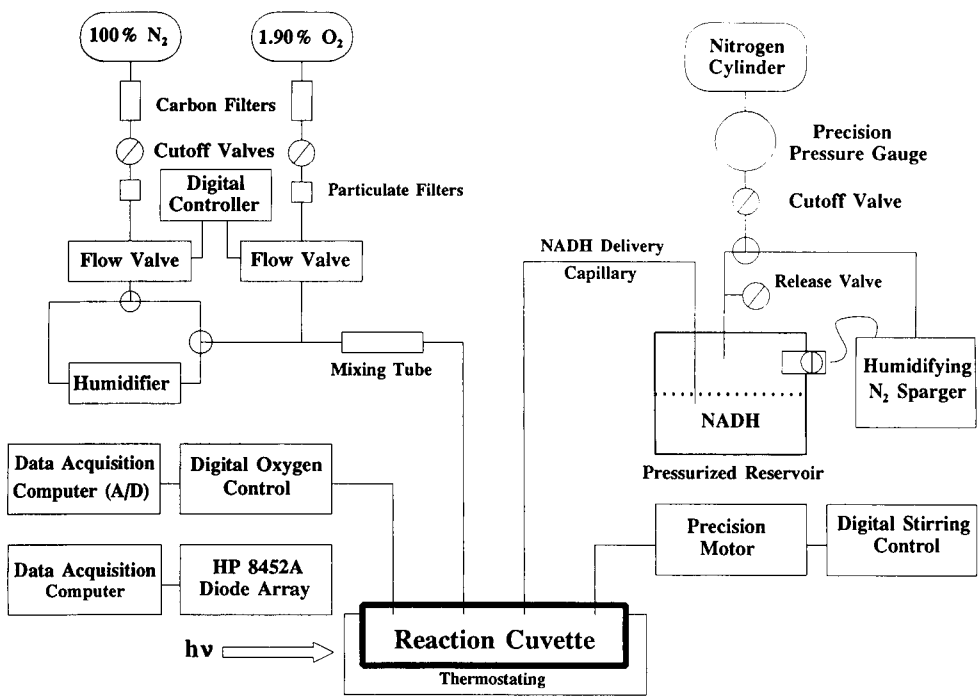

Fig. 1. Experimental layout of the oscillatory system. The six components shown here control the oscillatory system and simultaneously obtain dissolved oxygen and multiwavelength spectrophotometric data. Details are discussed in the text. Though already digitally controlled, computerized operation of the oxygen/nitrogen delivery system and stirrer could easily be added for future experiments. All tubing is 1/8 in. PTFE.

10,595-3); pyrogallol was ordered from Sigma (No. P-0381). All reagents were used as received. Deionized water was obtained from a Millipore (Bedford, MA) Ultrapure water system.

The experimental apparatus for studying oscillatory chemical behavior of the system includes pulseless delivery of the oxygen and NADH to a thermostated, cylindrical, quartz reactor, and the ability to collect simultaneous, multiwavelength spectrophotometric information and dissolved oxygen data from the reaction solution. All of these components affect the appearance of the oscillations, with the probable exception of monitoring dissolved oxygen. The experimental layout appears in Fig. 1 and is discussed below.

Reaction cuvette

The oscillatory reaction is conducted in a cylindrical quartz cuvette made from inexpensive, standard quartz tubing (outside diameter 23 mm, inside diameter 20 mm). A properly blanked spectrum taken in the cylindrical cuvette yields a spectrum identical to one taken in a square cuvette, after accounting for pathlength differences. The solution volume was always 5.00 ml as dispensed by a calibrated digital pipette, and fills about the bottom 1.5 cm of the cuvette. The head space above the solution is about 5 ml in volume and about 1.5 cm high. The cuvette is fitted with a PTFE cover which has holes for the oxygen electrode, gas inlet tube, NADH delivery capillary, and stirring rod (see Fig. 2). The spatial configuration of reagent delivery with respect to stirring has not been examined here, but its importance has been demonstrated in another oscillatory system [11]. Generally, mixing considerations are important in stirred reaction systems [12,13]. The cuvette was rinsed between uses with a solution of 36 g $(NH_4)_2S_2O_8$ per 2.5 l of H_2SO_4; then 10% HNO_3; then deionized water.

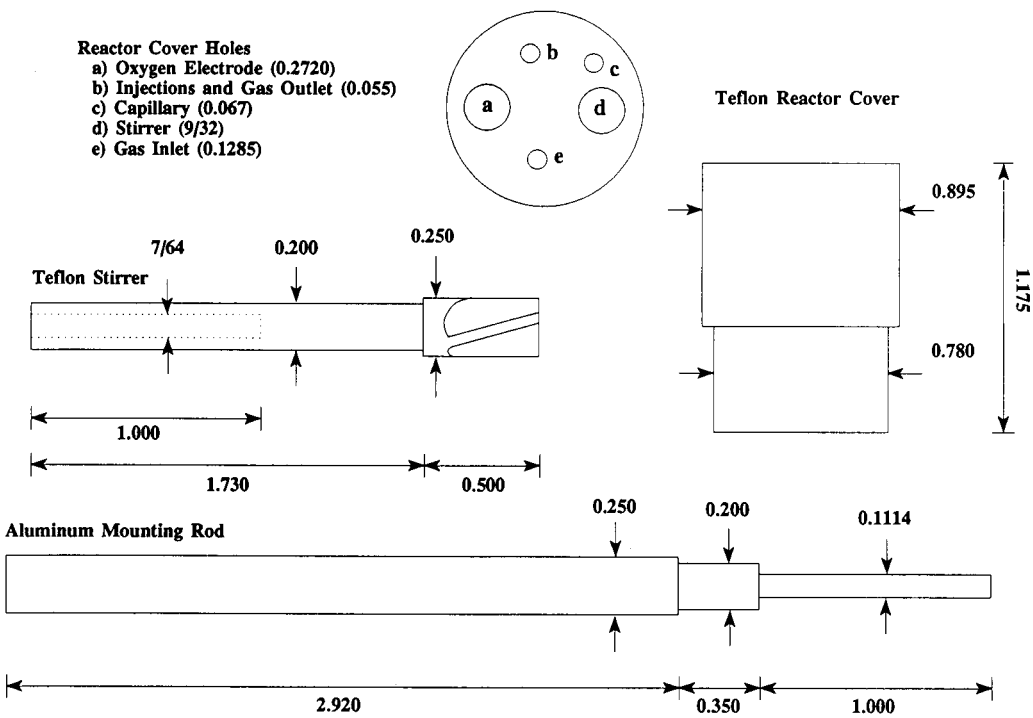

Fig. 2. Design of stirring impeller and reactor cover. The stirrer is constructed from a PTFE impeller mounted on an aluminum rod. The impeller has four flutes, 90 degrees apart, and 0.040 in. thick. Each flute was cut at 15° from the rotational axis, and 15° from the plane of the first angle. The cuts were begun 0.4 in. from the stirring tip. Viewed from above, the flutes are cut to the left to impart a downward motion to the fluid when rotated clockwise. Dimensions shown are in inches. The reactor cover is made of PTFE with holes as shown.

Thermostating and stirring

All experiments were thermostated at 25.00 ± 0.02°C using a circulating thermostater (Fisher Scientific) and a cylindrical jacket custom designed and built in-house. A fitting built into the jacket locks the cylindrical cuvette into place and allows unobstructed passage of the spectrophotometer light beam. Hydrodynamic considerations [14,15] were used to design the reaction container to insure good mixing. Efficient mixing was achieved by stirring off-center, and from above using a Servodyne motor and digital controller (Model 50000-40, Cole-Parmer, Chicago, IL) with an rpm precision of ±0.2%. The dissolved oxygen electrode (3 mm diameter) is also held off-center and serves as a baffle to enhance non-laminar fluid mixing. The motor was fitted with a flexible shaft (No. 4523A14, McMaster-Carr, Chicago, IL) to allow easy positioning of the stirring device over the spectrophotometer. Stirring was performed with a four-fluted PTFE rod machined in-house (see Fig. 2); the stirrer projects 10 mm into the solution. To provide stiffness for rapid rotation, the PTFE stirrer is mounted on a metal post which extends into the PTFE.

The impeller Reynolds number, Re_i, is a unitless expression of the turbulence imparted to a solution by stirring. It is defined as [14,15]:

$$Re_i = d_i^2 N\rho/\eta \qquad (2)$$

where d_i = impeller diameter = 0.635 cm; N = rotation rate (s^{-1}); ρ = solution density = 1 g/cm^3; η = solution viscosity = 0.01 poise (g cm^{-1} s^{-1}) for water at 25°C. Certain geometric reactor design criteria must be met for this equation to yield a good estimate of Re_i for a particular stirring vessel. The present reaction cuvette meets these criteria rather well. The cylindrical container includes a baffle (the dissolved oxygen electrode), and is stirred off-center from above; the solution depth is about the same as the cylinder diameter, and the stirrer diameter is about 1/3 the container diameter. Incorporation of the constants and conversion to RPM yields:

$$Re_i = 0.67 \times (\text{rpm}) \qquad (3)$$

Non-laminar conditions apply if $Re_i > 20$, corresponding to stirring rates of only 30 rpm. In all cases in these experiments, fluid dynamics are clearly non-laminar, since for stirring rates from 600–1600 rpm, Re_i = 400–1067. Use of a relatively high rotation rate yields a large impeller Reynolds number which, in turn, makes mixing artifacts unlikely. Consequently, in oscillatory experiments in this system, non-ideal reactor design is probably unimportant.

Gas delivery and measurement of dissolved oxygen

A tank of 1.90% oxygen (certified mixture, ±0.04% absolute accuracy; MG Industries, Valley Forge, PA) in nitrogen is used with a separate tank of pure nitrogen. The oxygen mixture and the nitrogen first flow through activated carbon prefilters (Airco, Model 126, Murray Hill, NJ), then 0.5-μm particulate, sintered stainless steel filters (Nupro, Willoughby, OH). The flow of each gas is regulated to an accuracy of ±1% and a precision of ±0.3 ml min^{-1} by a digitally set mass flow controller calibrated from 0–200 ml min^{-1} (Model 840 and Model 902C dual channel control unit; Sierra Instruments, Monterey, CA). The error in the accuracy of the total gas flow-rate used in this study (Table 1) is ±1.9 ml min^{-1}, and the precision is $(0.3^2 + 0.3^2)^{1/2} = 0.4$ ml min^{-1}. The mixing tube downstream from the two mass flow controllers consists of a stainless steel brush enclosed in a brass tube. FEP tubing and ferrules, brass fittings, and Swagelok (Solon, OH) connectors are used for all gas handling. The FEP gas delivery tube is snugly connected with the reactor cover using a plastic pipet tip. FEP tubing is oxygen permeable (permeability = 60×10^{-10} $mm_{thickness}$ cm^3_{gas} cm^{-2}_{area} s^{-1} (cm Hg)$^{-1}$; Nalge, Rochester, NY), however, no measurable oxygen leaks through the tubing at gas flow-rates used in these studies. This was demonstrated when a buffer solution purged with pure nitrogen showed no change in its dissolved oxygen reading when injected with excess sodium sulfite. The nitrogen stream is humidified and trace oxygen removed by sparging through an aqueous solution of sodium sulfite containing a trace of $CoCl_2$ [16]. A glass wool plug just downstream of the humidifier prevents any aerosol

TABLE 1

Control variables and conditions in the peroxidase–NADH oscillator

Controlled variable	Value
pH	5.10
Buffer	0.100 M sodium acetate
Horseradish peroxidase activity	100 pyrogallol units/ml (ca. 7.9 μM)
Oxygen mass-transport constant [a], k_m	0.148 ± 0.005 min^{-1}
Stirring rate	1300 rpm
% O_2	1.50%
O_2 flow-rate	150 ml min^{-1}
N_2 flow-rate	40 ml min^{-1}
Solution volume	5.00 ml
Solution surface area	3.1 cm^2
Temperature	25.00°C
Reservoir [NADH] and buffer	6.37 mM, pH 7.00, 0.010 M
NADH delivery rate	
Initial	0.59 mM h^{-1} (465 μl h^{-1}, 35 lb in.$^{-2}$)
Maintenance [b]	0.39 mM h^{-1} (309 μl h^{-1}, 23 lb in.$^{-2}$)
[2,4-Dichlorophenol]	10 μM
[Methylene Blue]	0.20 μM
Illumination	Continuous deuterium source

[a] Measured average and standard deviation of the first trial of Fig. 5, and all three trials of Fig. 6. Note that k_m is a composite of six experimental parameters. [b] NADH delivery rate changed from the initial to maintenance value at the 2nd spike in absorbance observed at 402 nm. See Fig. 3.

from reaching the reactor. Humidified nitrogen is used to purge the reaction solution of oxygen at the onset of an experiment. During an oscillatory run, however, neither gas is humidified, which causes water to evaporate from solution, but this loss is compensated by the NADH solution influx. The solution volume is routinely maintained to $\pm 1\%$.

Dissolved oxygen is monitored with a Clark-type oxygen electrode (Microelectrodes, Londonderry, NH). The platinum electrode has a cross-sectional diameter of 25 μm and is covered with a PTFE membrane 0.001 in. thick in a 3-mm acrylic housing. Based on product information which states that the electrode has a current response of 1700 pA in air (20.9% O_2), it can be computed using Henry's law and 1.50% O_2 equilibrated with water (see below), that the resultant current under experimental conditions is ≤ 4 pA. Current-to-voltage conversion is performed with a unit constructed in-house. Dissolved oxygen readings are recorded with a 12 bit, 100 kHz DASH-16F analog-to-digital converter card (MetraByte, Taunton, MA) installed in an IBM PC using a data acquisition program written in our laboratory. The electrode is calibrated such that 160 mV = 17.9 μM dissolved O_2 (the dissolved oxygen concentration imparted by equilibration with 1.50% O_2 gas, 25.0°C and 0.10 M ionic strength; [16]). Digital output yields 0.114 mV/bit resulting in a calibrated probe resolution of 0.013 μM dissolved O_2.

Determination and precision of the oxygen mass-transport constant

A first order growth process is governed by [17]

$$C_t = C_\infty(1 - e^{-kt}) \quad (4)$$

where C_t is the concentration of a species at time t, C_∞ is the concentration at infinite time, k is the first order rate constant, and t is time. This can be algebraically linearized to

$$\ln(C_\infty - C_t) = -kt + \ln(C_\infty) \quad (5)$$

It is helpful to more carefully define these variables to accommodate the way data are acquired and analyzed. Let

$$C_\infty = C'_\infty - C_o \quad (6)$$

and

$$C_t = C'_t - C_o \quad (7)$$

where the primed values are the A/D integers as acquired, uncorrected with respect to an initial baseline reading of C_o. The mean of the first 30 data points (taken at 1 s intervals) is defined as C_o. In using a spreadsheet program (in this case, SuperCalc 5.0, Computer Assoc., San Francisco, CA), it is convenient to rewrite Eqn. 5 as

$$\ln(C_\infty - C_t) = \ln(C'_{\infty(in)} - C'_t) = -k_m t + \ln(C'_{\infty(out)} - C_o) \quad (8)$$

where k_m is the mass-transport constant of oxygen from the gas phase to the liquid phase. Raw data can be plotted as $\ln(C'_{\infty(in)} - C'_t)$ vs. time and iteratively fitted to a line using linear regression

until the difference $C'_{\infty(in)} - C'_{\infty(out)}$ is as small as desired (0.01 was used); the resultant slope is $-k_m$. An initial value of $C'_\infty = C'_{t\,max} + 5$ was chosen. Only integers from the A/D converter were used for C'_t values. Transformation of digital output to dissolved oxygen concentration by a constant does not change the resultant k_m. In addition, it is unnecessary to correct the time axis to give an initial $t = 0$ to indicate when the oxygen is turned on. This merely shifts the plot along the x axis, but leaves the slope unchanged. In each run, 1500 data points were acquired, one per second, for 25 min (about five half-lives). Data acquired too close to C'_∞ result in a noisy linear plot at long times. The uncertainty in the slope was typically $\leq 0.05\%$ R.S.D. (relative standard deviation) with typical squared correlation coefficients, $r^2 \geq 0.999$. The first-order model is an excellent representation of mass transport of oxygen into solution from the gas phase in this system. Because the solution is stirred, oxygen influx is mass-transport limited and not diffusion limited. Oxygen mass transport is dependent on stirring rate, %oxygen, total gas flow-rate, solution volume and surface area, and temperature, all of which are held constant as specified in Table 1. The dependence of k_m on stirring rate is explored below.

At equilibrium, $k_m[O_2]_g = k_{-m}[O_2]_{aq}$, where k_{-m} is the mass-transport constant of oxygen from the aqueous solution into the gas phase [18]. Since $[O_2]_g = P_{O_2}/RT$ (ideal gas law), and $[O_2]_{aq} = k_H P_{O_2}$ (Henry's law), then $k_m/k_{-m} = k_H RT = 0.029$; ($k_H = 1.2 \times 10^{-3}$ M atm^{-1} at 25°C; computable from [16]). Consequently, due to mass transport alone, $d[O_2]_{aq}/dt = k_m[O_2]_g - k_{-m}[O_2]_{aq} = k_m\{[O_2]_g - ([O_2]_{aq}/0.029)\}$ and $[O_2]_g = 6.13 \times 10^{-4}$ M at 1.50% O_2.

NADH pulseless delivery

The NADH solution is delivered (see Fig. 1) through a capillary from a pressurized, 5 ml, thick-walled glass reactor vial (Kimax). The vial is sealed with a gasket modified from a funnel-shaped polyethylene insert taken from a culture tube. A stainless-steel fitting is held in place against the gasket to seal the unit. Before use, the NADH solution is purged with nitrogen through a sidearm in the vial to ensure that oxygen does not come from the NADH solution. To deliver NADH, the sidearm is closed, the vial is sealed and pressurized with nitrogen. Gas pressure is regulated using a 3-in. test gauge which reads from 0 to 100 lbs in.$^{-2}$ with an accuracy of ± 0.5 lbs in.$^{-2}$ (Ametek U.S. Gauge, Sellersville, PA). A fused-silica capillary with an outside coating of polyimide (inside diameter 63.5 μm; length 100.0 cm; Polymicro Technologies, Phoenix, AZ) is placed in the reservoir to allow NADH solution to pass from the pressurized vial to the reactor. The tube for nitrogen pressurization and the capillary for NADH delivery pass through separate holes in a PTFE plug sealed by a Swagelok fitting. Flow is regulated by the applied pressure, and since a mechanical pump is not used, delivery is pulseless. We consider this a prudent approach in the study of an oscillatory reaction since it prevents the possible excitation or entrainment of an excitable system by pulsed reagent influx [19,20].

NADH flow-rate calibration

The NADH solution flow-rate, F, through the capillary (or any tube under laminar flow conditions) is governed by the Hagen-Poiseuille equation [21]:

$$F = 2.48 \times 10^{-5}(Pr^4\pi/8\eta L) \quad (9)$$

where F = flow-rate (μl h^{-1}); 2.48×10^{-5} = conversion factor (μl g in.^{2} μm^{-4} s^{-1} h^{-1} lbs^{-1}); P = applied gauge pressure (lbs in.$^{-2}$); r = capillary inside radius (μm); η = solution viscosity = 0.01 poise for water at 25°C; L = capillary length (cm). Incorporation of the constants and the viscosity into a single conversion factor (with units of μl in.^{2} cm h^{-1} lbs^{-1} μm^{-4}) yields:

$$F = 9.70 \times 10^{-4}(Pr^4/L) \quad (10)$$

The condition for laminar flow through a tube [21] is that $Re_t < 2100$, where the unitless Reynolds number for tube flow is

$$Re_t = v\rho d_t/\eta \quad (11)$$

where, for the conditions in Table 1, v = the mean laminar flow velocity (cm s^{-1}) = F/A; F = flow-rate (1.29×10^{-4} cm^3 s^{-1} = 465 μl h^{-1});

A = tube cross-sectional area (3.17×10^{-5} cm^2); d_t = the inside tube diameter (6.35×10^{-3} cm), which yields $v = 4.1$ cm s^{-1} and $Re_t = 2.6 \ll 2100$. So, the capillary flow is laminar and Eqn. 10 does apply.

The solution flow-rate was estimated from Eqn. 10, then verified experimentally by spectrophotometric monitoring of the delivery of a solution of a dye from a reservoir to the reaction cuvette. If a dye solution of known absorption at a wavelength λ is delivered to a solution of known volume, V_o, and the absorbance monitored over time at λ, then the flow-rate, F, can be calculated from

$$F = 3.6 \times 10^6 (SV_o/A_R) \quad (12)$$

where F = flow-rate (μl h^{-1}); 3.6×10^6 = conversion factor (μl cm^{-3} h^{-1} s^{-1}); S = slope of absorbance vs. time (s); V_o = volume of fluid in the cuvette (ml = cm^3); A_R = initial absorbance at λ of reservoir solution. The slope of absorbance vs. time is nearly linear because V_o is almost constant due to the relatively slow flow-rate and brief time interval used to compute the slope. A calibration plot of flow-rate vs. gauge pressure of duplicates of five pressure values ranging from 10 to 50 lbs in.$^{-2}$ yielded $r^2 = 0.997$ and a relative standard error in the slope of $\pm 2\%$.

In an oscillatory experiment, suppose NADH is delivered to the oscillator at a constant flow-rate, F, from a reservoir of constant NADH concentration, $[NADH]_o$. The oscillator solution volume, V_o, is nearly unchanged during an oscillatory experiment and considered constant. This results in a first order rate constant for NADH delivery such that $d[NADH]/dt = k_{NADH}[NADH]_o$ where $k_{NADH} = F/V_o$ [18]. In Table 1, the NADH delivery rate is expressed as the resultant concentration change in the cuvette if the NADH did not react.

Spectrophotometry

A Hewlett-Packard UV–visible 8452A diode array spectrophotometer was used for all absorption measurements. Data were acquired by the HP 89531A software provided with the instrument. Spectrophotometer software was run on an 8 MHz IBM PC/AT computer. Data were collected at 10-s intervals, over an integration period of 10 s for each datum. The spectrophotometer as programmed provides constant (unpulsed) illumination at all wavelengths of light that originate from the deuterium lamp. This is accomplished by setting the data acquisition interval equal to the integration time so that the shutter is always open. The reaction cuvette is entirely enclosed in a darkbox so the only light reaching the sample is from the deuterium lamp.

The light from the spectrophotometer itself was seen to affect the degradation rate of NADH (see below). From information provided by the manufacturer, the mean intensity of the deuterium lamp from 190 to 820 nm was estimated at 14.5 mW impingent on the sample cuvette. An independent measurement with an uncalibrated power meter (Model 210, Coherent, Palo Alto, CA) gave a value of 15 mW. Wavelength-specific effects of instrumental light on the oscillator [22,23] will be the subject of future research.

Enzyme assay

Each shipment of enzyme is assayed to determine its activity before use. Activity expresses enzyme amount better than does concentration because specific activity refers to the ability of a mg of enzyme to catalyze a particular reaction. The specific activity takes into account the purity of a particular preparation. The activity unit is defined (Sigma) as the amount of enzyme that will form 1.0 mg of purpurogallin from pyrogallol in 20 s at pH 6.0 at 20°C. In practice, the spectrophotometer is blanked at 420 nm with 0.1 M phosphate buffer at pH 6.0. In a square, 1-cm cuvette, 2.42 ml of buffer is mixed with 0.16 ml of 0.147 M hydrogen peroxide (1.67 ml of 30% H_2O_2 diluted with water to 100.0 ml) and 0.32 ml of a pyrogallol solution (500 mg pyrogallol/10.00 ml water). To this is added 0.10 ml of horseradish peroxidase (about 1.8 mg HRP/l of buffer). Absorbance is monitored at 420 nm for 90 s. The specific activity is given by:

$$\text{U/mg} = \frac{[2500(\text{largest } \Delta A_{420} \text{ in 20 s})]}{\text{mg peroxidase/l}} \quad (13)$$

where ΔA is the increase in absorbance usually measured over the time interval of about 35–55 s;

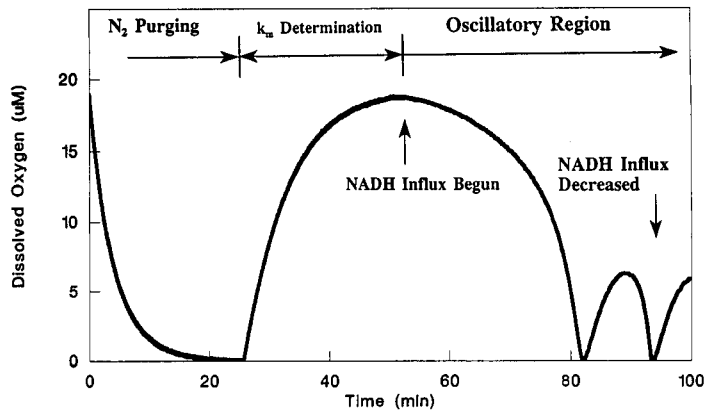

Fig. 3. Initialization of the oscillator. Typical appearance of data is shown from the initialization procedure used to begin an oscillatory run.

the conversion factor of 2500 takes into account the molar absorptivity of purpurogallol and dilution factors. This procedure is adapted from the literature included with horseradish peroxidase ordered from Sigma. The commercial horseradish enzyme preparation specified previously is commonly assayed at about 310 ± 3 U/mg; the range over several shipments has been from 290–315 U/mg.

Initialization of oscillatory reaction

The initialization procedure is depicted in Fig. 3. The solution in the cuvette initially contains the enzyme, MB, and DCP buffered at pH 5.10. It is placed into the spectrophotometer and purged of oxygen with humidified nitrogen at about 190 ml min^{-1}. Once a steady, oxygen lower baseline is achieved, dissolved oxygen data acquisition is begun, nitrogen and oxygen flow-rates are adjusted to the values in Table 1, the humidifier is taken off line, and both gases are allowed to flow to the cuvette. Data in this region are used later to compute k_m for a given run. A desired value of k_m is approximately specified in advance by choosing an rpm from the data in Fig. 4. Once a stable, dissolved oxygen maximum is reached, spectrophotometric data acquisition is begun, the NADH reservoir pressure is set, and the capillary is inserted through a guide tube into the cuvette. Almost immediately, a slow decrease

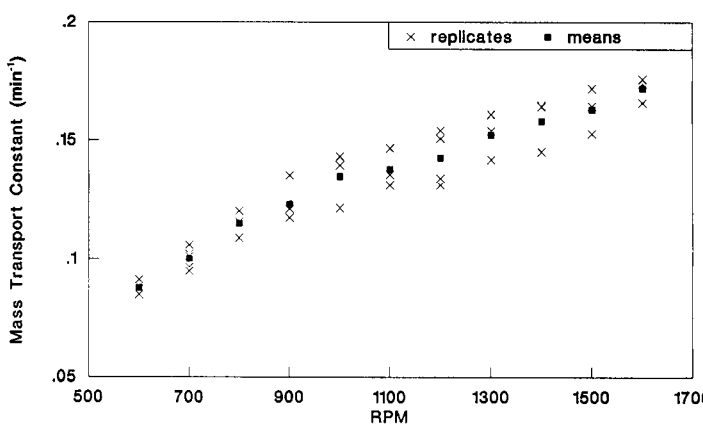

Fig. 4. Oxygen mass-transport constant vs. rpm. Values of k_m were determined using the buffer solution as explained in the text. Each set of data at a particular rpm were obtained from a single sample.

in $[O_2]_{aq}$ is observed, followed by a more rapid drop in $[O_2]_{aq}$, an increase in absorbance at 340 nm (λ_{max} for NADH), a decrease in absorbance at 402 nm (λ_{max} for the native enzyme, which is in the 3 + oxidation state) and an increase at 418 nm (λ_{max} for compound III, or Cp III, the designation for the enzyme in its 6 + oxidation state) [24]. In practice, NADH absorption is monitored at the less sensitive wavelength of 360 nm. The NADH reservoir solution is at pH 7.00, but has only $\frac{1}{10}$th the buffer concentration of the oscillatory mixture. Consequently, the oscillatory solution remains at pH 5.10.

To yield a long oscillatory train, a faster NADH influx rate is necessary initially, followed by a slower, maintenance rate. The pressure is changed (see Table 1) when the first distinct spike is observed in the absorbance at 402 nm immediately after the first minimum at that wavelength. This corresponds to the completion of the first full oxygen oscillation. After this single adjustment, the NADH influx remains constant for the remainder of the run.

RESULTS AND DISCUSSION

NADH stability

Under two differing conditions of UV–visible illumination of the reaction cuvette by the deuterium lamp of the spectrophotometer, a difference was observed in the second order degradation rate constant of NADH at pH values from 4.60 to 6.10 [25,26]. In the case of 100% illumination, the spectrophotometer is programmed such that the integration time = 1 s = data acquisition interval. This forces the shutter to remain open continously during data acquisition. To achieve conditions of 0.1% illumination, first the dead time of the spectrophotometer shutter was measured. The shutter opens longer than the value set for the integration time. Using a 125-MHz digital oscilloscope (LeCroy Model 9400, Chestnut Ridge, NY), and a photodiode detector with a 4.5-μs time constant (Model G1116, Hamamatsu, Middlesex, NJ), the shutter dead time was measured at 202 ms. For the case of 0.1% illumination, exposure time = integration time + dead time = 0.100 s + 0.202 s = 0.302 s = 0.001 × (data acquisition interval). As a result, an integration time of 0.1 s was used with a data acquisition time of 302 s to achieve 0.1% illumination.

An anoxic 0.100 mM NADH solution stirred at 1300 rpm was monitored at 340 nm, 25.00°C, under humidified nitrogen, at pH values of 4.60, 5.10, 5.60, and 6.10 under the two different illumination conditions. Buffers were made from appropriate mixtures of 0.100 M NaAc and 0.100 M acetic acid. The NADH decrease in absorbance was monitored for about one half-life, plotted as ln(absorbance) vs. time, and the pseudo first order rate constant was taken as $k'_D = -\text{slope}$. The mean error in the k'_D of eight trials (each illumination condition at each pH) was 0.59% R.S.D., demonstrating good linearity. Consequently, at each pH, a pseudo-first-order model was used where

$$-\mathrm{d}[\mathrm{NADH}]/\mathrm{d}t = k'_D[\mathrm{NADH}] \qquad (14)$$

From triplicate determinations for each illumination condition (% designated with a subscript on k_D), at pH 5.10, $k'_{D,100} = 8.30 \times 10^{-5}\ s^{-1} \pm 4.9\%$ R.S.D., and $k'_{D,0.1} = 5.56 \times 10^{-5}\ s^{-1} \pm 1.5\%$ R.S.D. A comparison of these results at the 99% confidence level indicates a statistically significant difference between the two k'_D values. The light from the deuterium lamp in the spectrophotometer increases the apparent NADH degradation rate constant nearly 50%. The corresponding half-life at pH 5.10 for constant illumination is about 2 h and 20 min, a time well within the length of typical oscillatory runs.

To explore the pH dependence of NADH degradation, Eq. 14 can be expanded to

$$-\mathrm{d}[\mathrm{NADH}]/\mathrm{d}t = k_D[\mathrm{H}^+]^m[\mathrm{NADH}] \qquad (15)$$

and since $k'_D = k_D[\mathrm{H}^+]^m$, then

$$\log k'_D = \log k_D + m \log[\mathrm{H}^+] \qquad (16)$$

A plot of $\log k'_D$ vs. $\log[\mathrm{H}^+]$ using the four pH values from 4.60 to 6.10 gives the order of the reaction in H^+ as m = slope. For 100% illumination, $m = 0.55 \pm 2.4\%$ R.S.D. and $r^2 = 0.999$, which indicates the reaction is not first order in H^+. For 0.1% illumination, under otherwise identical conditions, $m = 1.1 \pm 8.8\%$ R.S.D. and $r^2 =$

0.977, indicating that NADH degradation is first order in H^+ under conditions of virtually no illumination by the deuterium lamp. NADH degradation is clearly significant in experiments performed at pH 5.10, and is dependent on illumination in a manner which is the topic of current research. In oscillatory experiments, the NADH stock solution is buffered at pH 7.00 to prevent acidic degradation, which can be verified spectrophotometrically.

Mass-transport constant and stirring rate

Using just buffer solution, k_m was determined at a range of stirring rates (rotations per minute, rpm) from 600 to 1600 rpm in intervals of 100 rpm. Triplicate measurements were made at each rpm, and are shown with means in Fig. 4. The R.S.D. was 5–7% in the region of 1300 rpm, the stirring rate used in oscillatory experiments. Some of the error in reproducibility seems to result from a slight change in solution volume between runs. In addition, when the cuvette is emptied and refilled, some error results from inexact repositioning of the stirrer. The appearance of the data is somewhat linear, but no attempt was made to fit a curve to this data set. The plot still provides predictive capability for choosing an appropriate rpm to yield an approximate k_m. For an entirely unstirred system, but with the stirrer still in place, $k_m = 0.015\ min^{-1}$; so, most of the oxygen mass transport is due to stirring and not diffusion.

Effect of ethanol

In some recent studies [7,10,27,28], ethanol was used as a solvent to make a stock solution of DCP, so that the most concentrated species present in the oscillatory mixture (other than the buffer) was ethanol. In a report of a period doubling approach to chaotic oscillations [7], DCP in ethanol was added to the oscillatory mixture as a bifurcation parameter, but it is uncertain whether ethanol or DCP is responsible for the observed behavior. This study uses a 1.111 mM stock solution of DCP with no ethanol in the 0.1 M sodium acetate buffer at pH 5.10.

The effect of ethanol on the oxygen mass-transport constant was examined, since initial observations seemed to indicate that ethanol changed the k_m [28]. More careful investigation demonstrates that no statistically significant difference was seen in k_m due to the presence of ethanol. Three runs at 1300 rpm were performed in duplicate with and without ethanol in 5.00 ml of the buffer solution for a total of twelve k_m determinations. After purging by humidified nitrogen as previously described, and just before introduction of oxygen, 8.0 μl of ethanol was added using a micropipette tip (Research Products, Mount Prospect, IL). This imparted a concentration of 27 mM ethanol when added to the buffer. (This ethanol concentration was chosen because of the 32.2 μM DCP concentration derived from a 20 mM DCP in ethanol stock solution used in the period doubling study [7].) For duplicates, the solution cuvette was not refilled, and the stirrer was not repositioned. Between sets of duplicates, however, the cuvette was emptied and refilled with buffer to minimize the volume decrease through evaporative water loss, and the stirrer was repositioned. (Humidification of the gas stream during a run prevents water evaporation, but was not done because the bubbles cause irregular gas flow which results in noisy data.) The mass-transport constant was determined as described earlier. For a total of 12 runs, the mean k_m of the three duplicate runs without ethanol was $0.162\ min^{-1} \pm 8.8\%$ R.S.D., and the mean of the three duplicate runs with ethanol was $0.157\ min^{-1} \pm 8.7\%$ R.S.D. Note that the error is a combination of simple duplication of the measurement on a given buffer solution without the refill/reposition step, and triplicate replication including the refill/reposition step between duplicates. The computed t-test statistic for comparison of means [29] was 0.63, which is considerably less than 2.23, the two-sided t-test statistic at the 95% confidence level. The difference in mean k_m values is not statistically significant at the 95% confidence level. Indeed, only at the 40% confidence level is the difference statistically significant. It should be noted that the second trial of a duplicate pair of trials always yielded a k_m somewhat larger than the first, presumably due to a decrease in solution volume. As a result, a run to determine k_m without ethanol followed

by a run (without refilling or repositioning) with ethanol will yield an increase in k_m, but due to volume loss, not ethanol.

Though ethanol has no discernable effect on the oxygen mass-transport constant, the effect of ethanol on the chemistry of the oscillator remains unreported. Due to the ability of ethanol to act as a scavenger of the free radical HO· [30], and since free radicals are involved in the oscillatory mechanism [10,31–33], investigation of the effect of ethanol on oscillations is warranted. Since ethanol has been used as a solvent for DCP stock solutions in several previous studies, the possibility exists that effects attributed to DCP may be due to ethanol.

Mixing time and stirring rate

Mixing time, t_m, was determined by rapid injection of dye into the stirred cuvette solution through the same hole used for the delivery of NADH (c in Fig. 2). The spectrophotometer was programmed to acquire absorption data at 662 nm (λ_{max} for Methylene Blue) integrated over 0.1 s, at 0.1 s intervals. 50 μl of 0.22 mM Methylene Blue in buffer was manually injected through a tube using a gas tight syringe. The mixing time was taken as the time for absorbance to rise from its baseline value to 95% of its maximum. The mixing time decreases monotonically from 2.5 s to about 0.3 s as the rotation rate increases from 600 to 1600 rpm. Triplicates were done at each rpm, with a mean R.S.D. of 6.5%. The error is probably most attributable to the irreproducibility in manual injection and the limit of time resolution of the spectroscopic data. Several attempts were made to linearize the data, and a plot of $t_m^{-1/2}$ vs. rpm gave a least squares line of $t_m^{-1/2} = 9.5 \times 10^{-4} \times (\text{rpm}) - 0.08$ with 3.9% R.S.D. in the slope and $r^2 = 0.986$. This relationship between t_m and rpm is merely empirical, but nonetheless allows some predictive capability.

Mass-transport constant and mixing time

The oxygen mass-transport constant and mixing time are coupled, so that a particular stirring rate yields a unique k_m and t_m. As the mixing time increases, the mass-transport constant decreases monotonically. The fundamental interdependence of these two variables is characteristic of this particular system, and is dependent on the physical dimensions and spatial configuration of the impeller and reaction vessel. The mixing time for the target k_m used here, 0.150 min^{-1}, is about 0.5 s, much smaller than the period of oscillations.

Oscillatory reproducibility

Reported here for the first time is the reproducibility provided by well-controlled experimental parameters. Two typical trials performed un-

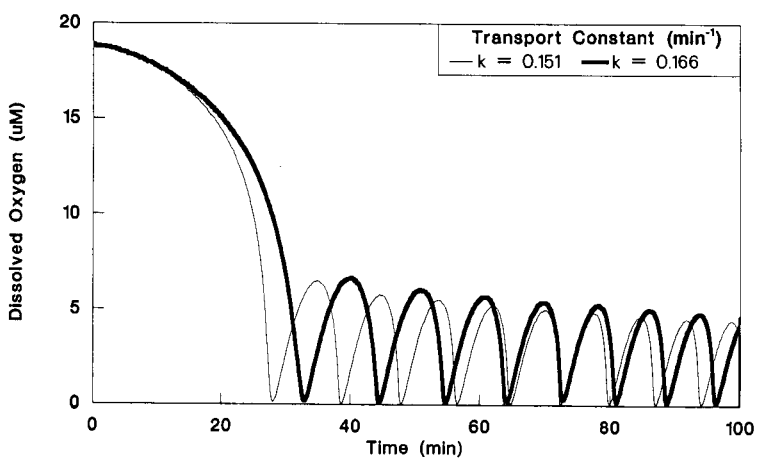

Fig. 5. Reproducibility of typical oscillatory runs. Two identical oscillatory runs were performed under the conditions specified in Table 1, and typical oxygen traces are presented. The three main chemical components (oxygen, peroxidase, and NADH), and both modifiers (Methylene Blue and 2,4-dichlorophenol) were present initially. NADH influx began at $t = 0$.

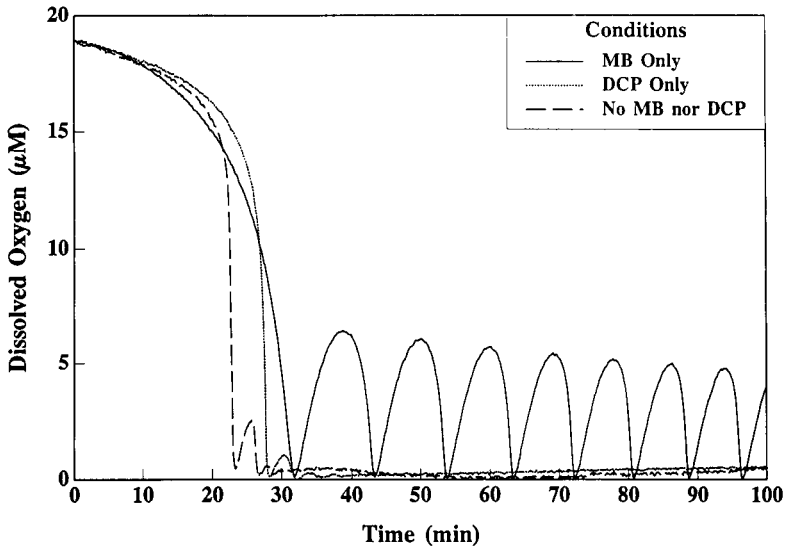

Fig. 6. Omission of modifiers. Under the conditions given in Table 1, the modifiers MB and DCP were omitted as indicated from oscillatory runs otherwise identical to those in Fig. 5.

der the conditions in Table 1 are shown in Fig. 5. Most of the difference in reproducibility is due to the difference in values of k_m. Both runs exhibited 54 oxygen oscillations in 20000 s (5 h 30 min), so the overall appearance of the two runs is virtually identical. The run with the larger oxygen mass transport constant has a longer induction time since it takes the [NADH] longer to reach a particular level due to the higher rate of oxygen influx. This same reasoning explains the longer period of oscillations in the run with the larger k_m. This verifies that the oxygen mass-transport constant is a major variable affecting the overall appearance of the oscillations. Analysis of the peak fronts similar to the analysis performed to compute k_m reveals that the rise in oxygen at the

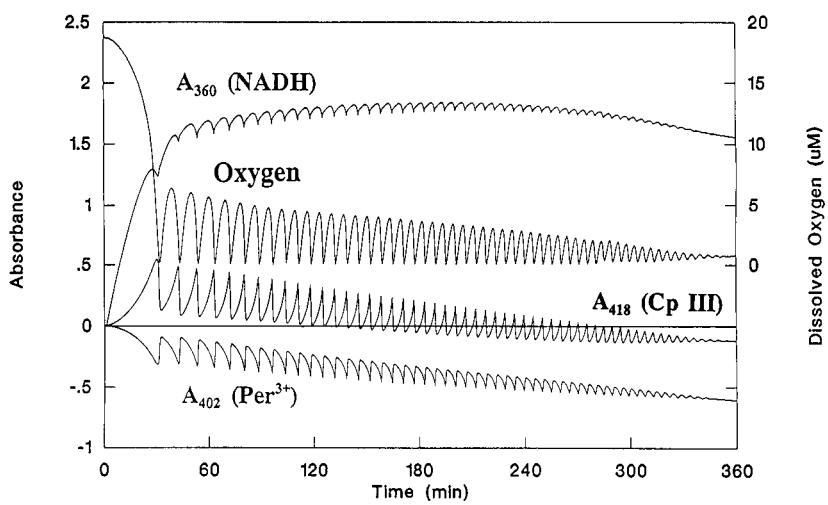

Fig. 7. Oxygen and spectrophotometric data for the omission of DCP. Absorbance at the three wavelengths corresponding to Per^{3+} (402 nm), Cp III (418 nm), and NADH (360 nm) are shown with the corresponding oxygen data.

beginning of each oscillation is not first order, and therefore involves more than oxygen diffusion into solution.

Role of Methylene Blue and 2,4-dichlorophenol

Figure 6 shows the results of oscillatory experiments identical to those in Fig. 5, except for omission of the modifiers MB or DCP, or both. MB alone is able to maintain oscillations without DCP under these conditions. Without MB, and without either modifier, only a small oscillation is observed followed by an approach to a steady state of very low oxygen concentration. Omission of DCP does not appreciably alter the oscillatory behavior under these conditions. MB and DCP have been included as standard ingredients of the peroxidase–NADH oscillator since 1973 [24]. They were originally introduced to eliminate oscillatory damping, and were initially described as having the ability to activate and sustain oscillations. MB has been implicated as a catalyst of NADH oxidation [8,9], and a role has been suggested for DCP in the oxidation of NADH by hydrogen peroxide [10]. Successive additions of DCP in ethanol drove an oscillating peroxidase–NADH system to chaotic behavior, so the ability of DCP to affect oscillations cannot be discounted. It was reported recently that conditions exist for oscillatory behavior that include DCP but not MB [10]. This raises the possibility that a set of conditions may exist at which sustained oscillations could be achieved with neither MB nor DCP. Pursuit of such conditions could lead to an understanding of the minimal chemical requirements for enzyme-mediated oscillations.

Oxygen and specrotrophotometric data

Data shown in Fig. 7 were acquired under the conditions specified in Table 1, but with the omission of DCP. Oscillations are maintained for nearly 6 h. Absorbance is monitored at three wavelengths simultaneously along with oxygen concentration. Absorbance is taken with respect to the initial mixture. Consequently, negative absorbance values represent net decreases in concentrations, and positive values represent net increases. A net decrease in absorbance is seen in both the native enzyme and Cp III. The system seems to cease oscillating when the enzyme concentration is low or depleted. A difference spectrum taken after oscillations ceased gave $A_{402} = -0.70$, compared to the initial A_{402} of 1.27. This leaves a residual A_{402} of 0.57, some of which may be absorbance of Cp III. Since these decreases in peak amplitude are nearly linear with time, they may represent a zero order deactivation reaction. Such a reaction suggests the photo-degradation of one or both forms of the enzyme by the spectrophotometer deuterium source. Another possibility is the inactivation of peroxidase by excess hydrogen peroxide [34], or by a surface-mediated reaction, perhaps involving the quartz cuvette. Oxygen concentrations are damped in a manner similar to the spectroscopic data, and after oscillations cease, a steady state of low oxygen concentration is maintained. In addition, despite continuous influx, NADH does not build up in solution, as evidenced by the NADH absorbance leveling off in Fig. 7 at about 1.5 (ca. 0.19 mM NADH, based on $\epsilon_{360} = 3900\ M^{-1}cm^{-1}$). The steady-state behavior of oxygen and NADH after oscillations cease is consistent with MB catalyzing the oxidation of NADH by oxygen [8,9].

Conclusions

The analytical approach used here to construct a well-characterized system to study the peroxidase–NADH oscillator has revealed several insights. A total of fifteen variables have been recognized and controlled. The oxygen mass-transport constant is difficult to control precisely since it is a convolution of six other variables. It seems to be very sensitive to the physical position of the stirring device. One way the mass-transport constant and mixing time can be controlled is by regulation of the stirring rate.

Reproducibility of oscillatory data was examined and best results are achieved when the oxygen mass-transport constants match closely between runs. Knowledge of the k_m is necessary to compare experimental results, since the k_m is a sensitive variable affecting the overall appearance of oscillations. Under the conditions of Table 1, DCP can be omitted from the oscillator with virtually no effect. Omission of MB from the initial mixture, however, resulted in short-lived

oscillations and rapid failure. Omission of both MB and DCP results in virtually no oscillations. Inclusion of ethanol, used in some previous studies as a DCP solvent, does not affect the mass-transport constant. The effect of ethanol on the chemistry of the oscillator has not been examined, but investigation is warranted. Spectrophotometric data acquisition conditions are important, because light from the spectrophotometer deuterium source increases the NADH acidic degradation, pseudo-first-order rate constant by nearly 50%. Several rate constants and differential terms have been defined. For oxygen under the conditions of Table 1,

$$d[O_2]_{aq}/dt = k_m\{[O_2]_g - ([O_2]_{aq}/0.029)\} \quad (17)$$

where k_m is determined using the procedure described in the text, $[O_2]_g = 6.13 \times 10^{-4}$ M, and $[O_2]_{aq}$ is found from the calibration method previously described. For NADH,

$$d[NADH]/dt = k_{NADH}[NADH]_o - k_{D,100}[H^+][NADH] \quad (18)$$

where k_{NADH} is the influx of NADH through the capillary ($= F/V_o$), which can be calibrated, and $k_{D,100}[H^+] = k'_{D,100} = 8.30 \times 10^{-5}$ s^{-1}, the pseudo-first-order NADH degradation rate constant at pH 5.10 and constant illumination. Equations 17 and 18 include the minimum number of terms for oxygen and NADH; a comprehensive model would include more terms for each species.

The systematic experimental strategy developed here has uncovered important fundamental aspects of the peroxidase–NADH oscillatory system. This work should allow easier corrobative efforts and eventually lead to an improved model which is more clearly related to experimentally controllable variables.

We thank J.S. Gwozdz for helpful initial work and S.R. Patel for assistance in NADH experiments. We are grateful to D.L. Miller for writing the software for acquisition of dissolved oxygen data. This work was supported in part by the Univeristy of Illinois Research Board.

REFERENCES

1 I. Yamazaki, K. Yokota and R. Nakajima, Biochem. Biophys. Res. Commun., 21 (1965) 582.
2 H. Degn, Nature, 217 (1969) 1047.
3 T. Hauck and F.W. Schneider, J. Phys. Chem., 97 (1993) 391.
4 L.F. Olsen and H. Degn, Nature, 267 (1977) 177.
5 L.F. Olsen, Z. Naturforsch., 34A (1979) 1544.
6 L.F. Olsen, Phys. Lett., 94A (1983) 454.
7 T. Geest, C.G. Steinmetz, R. Larter and L.F. Olsen, J. Phys. Chem., 96 (1992) 5678.
8 S. Alexandre and H.B. Dunford, Biophys. Chem., 40 (1991) 189.
9 P. Sevcik and H.B. Dunford, J. Phys. Chem., 95 (1991) 2411.
10 N. Watanabe and H. Inaba, Photochem. Photobiol., 57 (1993) 570.
11 M.J.B. Hauser, D. Lebender and F.W. Schneider, J. Phys. Chem., 96 (1992) 9332.
12 P. Rys, Chimia, 46 (1992) 469.
13 J. Villermaux, in N.P. Cheremisinoff (Ed.), Encyclopedia of Fluid Mechanics, Vol. 2, Dynamics of Single-Fluid Flows and Mixing, Gulf Publ. Co., Houston, TX, 1986, Chap. 27.
14 R.E. Treybal, Mass-Transfer Operations, McGraw-Hill, New York, 3rd edn., 1980, Chap. 6.
15 R.H. Perry and D.W. Green, Perry's Chemical Engineer's Handbook, McGraw Hill, New York, 6th edn., 1984, pp. 19-8 to 19-10.
16 L.S. Clesceri, A.E. Greenberg and R.R. Trussell (Eds.), Standard Methods for the Examination of Water and Wastewater, American Public Health Assoc., Washington, DC, 17th edn., 1989.
17 K.A. Connors, Chemical Kinetics: The Study of Reaction Rates in Solution, VCH, New York, 1990, Chap. 2.
18 D.L. Olson and A. Scheeline, Anal. Chim. Acta, 237 (1990) 381.
19 M.S. Samples, Y.F. Hung and J. Ross, J. Phys. Chem., 96 (1992) 7338.
20 J.G. Lazar and J. Ross, J. Chem. Phys., 92 (1990) 3579.
21 B.L. Karger, L.R. Snyder and C. Horvath, An Introduction to Separation Science, Wiley, New York, 1973, pp. 86–89.
22 V.R. Fed'kina, F.I. Ataullakhanov and T.V. Bronnikova, Theor. Exp. Chem., 24 (1988) 165.
23 B. Czochralska, W. Kawczynski, G. Bartosz and D. Shugar, Biochim. Biophys. Acta, 801 (1984) 403.
24 I. Yamazaki and K. Yokota, Mol. Cell. Biochem., 2 (1973) 39.
25 N.J. Oppenheimer, in D. Dolphin, O. Avramivic and R. Poulson (Eds.), Pyridine Nucleotide Coenzymes, Part A, Wiley-Interscience, New York, 1987, Chap. 10.
26 J.R. Miksic and P.R. Brown, Biochemistry, 17 (1978) 2234.
27 B.D. Aguda, L.H. Frisch and L.F. Olsen, J. Am. Chem. Soc., 112 (1990) 6652.
28 C.G. Steinmetz, T. Geest and R. Larter, J. Phys. Chem., 97 (1993) 5649.

29 G.K. Bhattacharyya and R.A. Johnson, Statistical Concepts and Methods, Wiley, New York, 1977.
30 G.V. Buxton, C.L. Greenstock, W.P. Helman and A.B. Ross, J. Phys. Chem. Ref. Data, 17 (1988) 513.
31 K. Yokota and I. Yamazaki, Biochemistry, 16 (1977) 1913.
32 B.D. Aguda and R. Larter, J. Am. Chem. Soc., 112 (1990) 2167.
33 B.D. Aguda and R. Larter, J. Am. Chem. Soc., 113 (1991) 7913.
34 M.B. Arnao, M. Acosta, J.A. del Rio, R. Varon and F. Garcia-Canovas, Biochim. Biophys. Acta, 1041 (1990) 43.

Analytica Chimica Acta, 283 (1993) 719–726
Elsevier Science Publishers B.V., Amsterdam

Electrochemical activation of human factor XII (Hageman factor) immobilized on carbon electrodes

Hyacinthe Randriamahazaka and Jean-Maxime Nigretto

Laboratoire d'Electrochimie et des Matériaux Appliqués, Université Cergy-Pontoise, B.P. 8428, 95806 Cergy-Pontoise Cedex (France)

(Received 12th March 1993; revised manuscript received 17th May 1993)

Abstract

Direct potential-mediated activation of purified human factor XII (FXII) immobilized on carbon electrodes has been evidenced. This required first to find a procedure for the immobilization of FXII on the electrode with good reproducibility. The adsorption isotherms of this zymogen and those of the enzymatic form, FXIIa, were characterized and discussed. The catalytic activities were estimated under stirring with a specific substrate (S-2302) provided with chromogenic properties and dissolved in the solution. Pretreatment of the electrode with negative square-wave potential pulses resulted in changes in the adsorption capacity of the carbon surface towards FXIIa. When the untreated electrode was covered with FXII at saturation, application of these pulses generated catalytic activities according to first-order kinetics.

Keywords: Enzymatic methods; UV-Visible spectrophotometry; Adsorption isotherms; Carbon electrodes; Electrochemical activation; Human factor XII; Immobilization

The contact system of human plasma consists of the zymogens factor XII (FXII; Hageman factor), prekallikrein (PK), factor XI and the non-enzymatic cofactor, high molecular weight kininogen (HMWK) [1,2]. Upon contact of plasma with negatively charged surfaces, a series of reactions takes place in which surface-assembled zymogens are converted into active proteases. These events initiate coagulation [3], kinin release [4] and fibrinolysis [5].

Surface-bound FXII plays a central role in these reactions. Recently, it has been shown that the binding of FXII to a negatively charged surface occurs via a 20-residue sequence in the heavy-chain portion of FXII. The binding induces self-generated conformational changes in the zymogen molecule which thereby exhibits catalytic properties attributed to the active form FXIIa [6].

Under physiological conditions, i.e. in human plasma, a kinetic loop of amplification then takes place. It begins with the FXIIa-catalyzed conversion of PK to kallikrein by cleavage of a single peptide bond [7]. The rate of this reaction is considerably increased by HMWK. In turn, kallikrein restrains the self-activation of the remaining surface-bound FXII by cleavage of a peptide bond in FXII via a second-order reaction.

Under artificial conditions, however, the mechanism of FXII activation is different. It proceeds via a second-ordered autoactivation reaction, in which the zymogen form plays the role of the substrate with respect to its own enzyme

Correspondence to: J.-M. Nigretto, Laboratoire d'Electrochimie et des Matériaux Appliqués, Université Cergy-Pontoise, B.P. 8428, 95806 Cergy Pontoise Cedex (France).

form. The role of the surface in the surface-assembly of the contact factors will receive considerable interest in the forthcoming literature. Conformational changes affecting the zymogen form are believed to coincide with an increased susceptibility to proteolytic cleavage of single-chain surface-bound FXII [8]. The extent of contact activation was examined in the presence of various negatively charged surfaces, a prerequisite to induce contact activation: urate crystals [9], kaolin, glass [10,11], ellagic acid [12,13], phospholipids [14,15], cholesterol sulphates [16], sulphatides (cerebrosides) [17] or polysaccharide sulphates (namely dextran sulphate) [18]. Thus, under artificial conditions, it is not surprising that heparin, a powerful anticoagulant, may also display a procoagulant behaviour due to the polyanionic structure [19].

An explicit model for the second-order autoactivation of FXII in the presence of dextran sulphate of MW 500 000 was developed by Tankersley and Finlayson [20] and recently discussed by Silverberg et al. [19]. Both the rate constant and the extent of the biological modification of FXIIa were found to depend on the MW of the activating material [22]. It should, however, be stressed that though the kinetics of the main autoactivation reaction seem by now almost completely elucidated, much controversy remains concerning the origin of the initial traces of FXIIa. To explain the presence of these first traces, most reports attributed the triggering of the autoactivation to the presence of contaminating proteins, such as residual serine proteases or zymogens (e.g. PK) due to incomplete purification of FXII [17].

Electrochemically modified carbon surfaces are known to promote irreversible binding of enzymes, generally with limited loss of activity. In this laboratory, we gained some experience in examining the catalytic behaviour of another blood serine protease, thrombin, which was also immobilized on the surface of the carbon-paste electrode. Catalytic activities could be characterized in the adsorbed state [23,24]. We shall show here that this technique can be successfully applied to characterize the early kinetic steps of FXII autoactivation.

EXPERIMENTAL

Chemicals and materials

For the buffer solutions (Tris buffer (50 mM, Carlo Erba); NaCl (125 mM), pH 8.5 (HCl)) Millipore Bioblock filtered ultra-pure water was used. Purified FXII was prepared according to a described procedure [25]. FXIIa was generated from FXII stock solutions after achieving full autoactivation with an excess of dextran sulphate in ca. 10 min [18]. Factor XII-deficient plasma as well as diagnostic kits for APTT (activated partial prothrombin time) measurements were purchased from Diagnostica Stago (France). Lyophilized kallikrein (0.1 unit/mg) was from Sigma (France). The chromogenic substrate used for the spectrophotometric assay of FXII or kallikrein (H-D-Pro–Phe–Arg–*p*-nitroaniline 2 HCl, denoted S-2302) was from Kabi-Vitrum AB (Sweden). T500 (MW 500 000 D) dextran sulphate (DS) used as the activator of FXII was from Pharmacia (Sweden). All other chemicals were analytical-grade reagents.

Graphite carbon powder (Ref. 9900 207-16594) was kindly provided by Société Le Carbone Lorraine, Gennevilliers, France. The carbon paste was made of 15 g of graphite mixed with 4,5 ml of nujol (Merck). The homogeneous paste was compacted in a Teflon® cavity and smoothened mechanically on a sheet of paper.

Electrochemical measurements

Electrochemical measurements were performed at 25°C using a potentio-dynamic set-up in a three-electrode configuration, including a PAR (Princeton Applied Research) galvanostat/potentiostat Model 173, driven by a PAR 175 wave generator. The one-compartment Teflon (to limit loss of enzyme through adsorption that would occur on glass) electrochemical cell supported the carbon-paste electrode (CPE), a saturated calomel electrode (SCE) and a platinum auxiliary electrode.

The electrochemical area of the CPE was measured in 0.51 M H_2SO_4 by chronoamperometric treatment (following the Cottrell equation) of the oxidation signal of a known redox system, *p*-aminophenol, which involves an exchange of two

electrons ($n = 2$) and a diffusion coefficient $D = 0.79 \cdot 10^{-5}$ cm^2 s^{-1} [26]. The time course of the current was followed at a potential of 1.0 V vs. SCE ($E_{1/2} = 0.53$ V). The electrochemical surface area was found to be 0.138 ± 0.005 cm^2 (geometric surface area = 0.07 cm^2).

Adsorption of FXII and FXIIa

On the CPE surface to be modified, one drop (ca. 10 μl) of a stock solution of either the enzyme or the zymogen was carefully deposited on the carbon surface so as to cover entirely the active part. After given lapses of time, the drop was discarded and the surface was vigorously rinsed with ultra-pure water in order to eliminate protein molecules weakly bound to the surface. The catalytic assay was then achieved as described in next section. The relative standard deviation was 8% ($n = 3$).

Spectrophotometric activity assays

Spectrophotometric assays of catalytic activities were carried out with a UVIKON 941 computerized photometer in thermostated (25°C) polystyrene cuvettes which contained the 0.4 mM S-2302 substrate solution in the buffer. In homogeneous solutions, FXIIa activities were measured by monitoring at 405 nm the release of *p*-nitroaniline (pNA) due to the amidolytic hydrolysis of the substrate. In a preliminary experiment, it was assessed that 1 nM of purified FXIIa produced a variation in absorbance of 16.44×10^{-3} min^{-1} at 37°C [25].

The amount of adsorbed FXIIa was determined as follows. The modified electrode surface was immersed in a cuvette containing 1 ml of the substrate solution and the amidolytic reaction was monitored at 405 nm under stirring. When adsorbed FXII had to be assessed, an indirect procedure was required since the protein was devoided from any catalytic activity. The amount in zymogen was always evaluated under homogeneous conditions after being subjected to total activation in the presence of an excess of DS (10 mg/ml). To estimate the amount of FXII being adsorbed on the CPE, an aliquot was directly taken from the drop covering the electrode surface. The loss in catalytic activity as compared to the activity before contact with the surface was attributed to the amount of FXII being irreversibly adsorbed.

Clotting times

Intrinsic clotting times were measured according to conventional procedures. APTTs were measured after recalcification of the plasma sample preactivated with cephalin and kaolin at 37°C [27].

RESULTS

Adsorption of preactivated FXII (FXIIa) on different CPE surfaces

The ability of the surface to adsorb the enzyme was first tested by depositing aliquots of the FXIIa stock solution onto the untreated CPE surface. After various equilibriation times, the superficial catalytic activity of the modified electrode was determined as described in Experimental. Linear increases in absorbance were then observed in stirred solutions for time ranges covering more than 20 min. These changes were attributed to the heterogeneous hydrolysis of the substrate occurring at the modified interface. The stirring was required in order to supply with forced convection the depletion in substrate concentration in front of the electrode surface, unless the absorbance changes rapidly levelled off.

When the treated surface was withdrawn from the substrate solution, the variation in absorbance stopped. This led us to conclude that FXIIa was irreversibly adsorbed on the CPE surface, since otherwise the release of some FXIIa molecules would still produce hydrolysis of the substrate and a subsequent increase in the concentration of pNA with time would be observed.

Experiments were repeated for increasing durations of the equilibriation time. Figure 1 shows the changes in adsorbance produced by the immobilized enzyme as a function of the contact time with the FXIIa stock solution. When the plateau was reached, the superficial density of FXIIa was maximum and equal to $2.0 \pm 0.1 \times 10^{-13}$ mol cm^{-2}. This amount was calculated with reference to the standardization of FXIIa in homogeneous substrate solutions and to the electrochemical surface area of the electrode.

Dextran sulphate was unavoidably present in the FXIIa stock solution. Accordingly, a possible interaction of this activating surface in the adsorption process could be suspected. To check this point, we enzymatically activated FXII with a low amount of the physiologic enzyme of FXII, i.e. kallikrein, instead of DS. The concentration was adjusted so as to prevent S-2302 from significant hydrolysis as compared to that due to FXIIa (the substrate is also sensitive to kallikrein). Moreover, the reaction time was lengthened enough to ensure total conversion of the initial amount of FXII to FXIIa. Under those conditions, results showed that the saturation plateau was enhanced up to about $3.5 \pm 0.2 \times 10^{-13}$ mol cm^{-2}.

In other experiments, the effect of the prepolarization of the CPE prior to the adsorption of FXIIa was studied in the presence of DS. Direct measurement of the rest potential (the equilibrium potential taken by the modified electrode dipped in the buffer solution in absence of any current) was first made to know the initial value of the potentials to be applied further. Thereafter, the procedure consisted of applying during 10 min one square-wave potential signal, from the rest potential potential (−0.27 V vs. SCE) of the modified electrode to values ranging up to −1.0 V (the cathodic discharge potential). Results presented in Fig. 2 indicate that negative polarization favored adsorption.

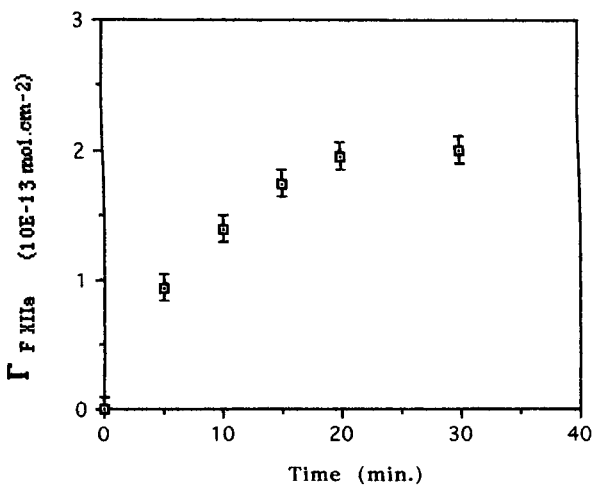

Fig. 1. Adsorption isotherm ($n = 3$) of preactivated FXIIa on the carbon paste electrode. FXIIa activities were determined by monitoring during 10 min the release in the solution of *p*-nitroaniline split by the immobilized enzyme from a specific substrate (see Experimental). Rates of the absorbance changes per minute were converted into FXIIa concentrations from the standardization of FXIIa in homogeneous solution.

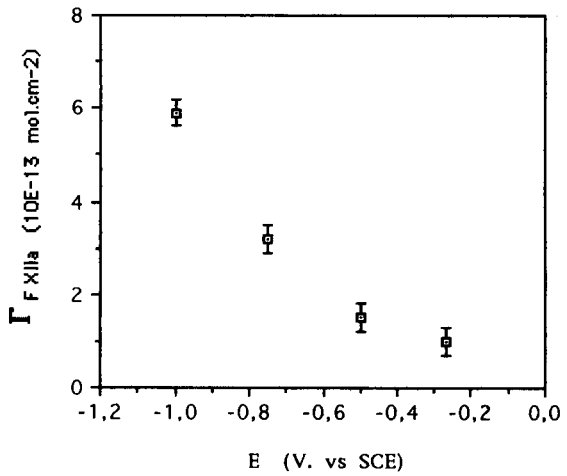

Fig. 2. Potential-mediated adsorption isotherm of FXIIa on the pretreated carbon paste electrode. The treatment consisted of square-wave pulses of increasing negative potentials (vs. SCE) applied during 10 min to the CPE and prior to adsorption.

Adsorption of FXII on different CPE electrode surfaces

Experiments conducted likewise with unactivated FXII led to an irreversible adsorbtion in 30 min of a maximum of $7.5 \pm 0.5 \times 10^{-13}$ mol cm^{-2} of zymogen on untreated or prepolarized surfaces. At this time, it was important to point out that in any case the immobilized FXII was totally exempted from residual catalytic activity. Heterogeneous activation of immobilized FXII could only be revealed with DS present in the solution.

Electrochemical activation of surface-bound FXII

We found that the application of potentials below −0.27 V vs. SCE (mean zero current potential) during 10 min to FXII-modified electrodes developed catalytic activities at the solution/modified electrode interface, as evidenced by the data given in Fig. 3. Maximum activity

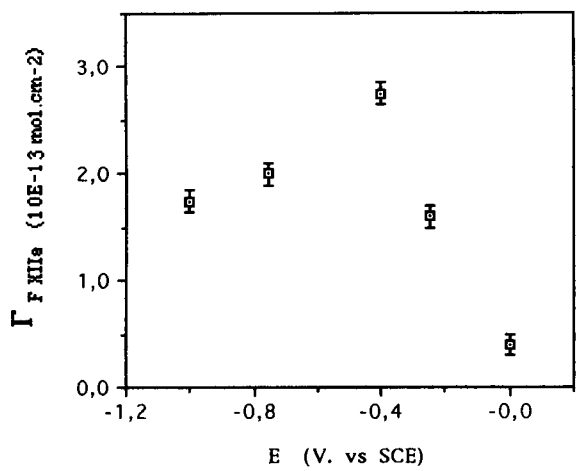

Fig. 3. Potential-mediated activation of FXII immobilized on the untreated CPE. The signals consisted of square-wave pulses of increasing amplitudes in the negative range.

occurred at ca. −0.5 V vs. SCE, before decreasing upon a cathodic shift of the potential. The effect of the polarization time is represented in Fig. 4. The maximum amount of electro-activatable FXII was attained after ca. 30 min of contact.

Separate experiments aimed at examining the possibility for Faradaic exchanges to occur between the electrode and the enzyme or zymogen layer were undertaken. Cyclic voltammograms, conducted with the FXII-modified electrode over the pertinent potential range, showed, as expected due to the modification of the surface, increases in the charging current but no apparent Faradaic current as compared to curves obtained with a bare surface [28]. Otherwise, we noted that the zero current potential remained unaffected whether the surface was modified or not.

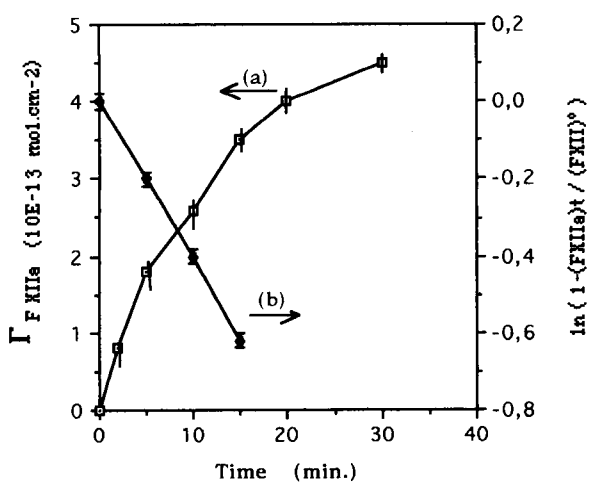

Fig. 4. Kinetics of the electrogeneration of FXIIa on the CPE. (a) Variation of the superficial density of FXIIa as a function of time. (b) Integration according to first order kinetics.

The shape of the time-dependent activation curve of FXII (Fig. 4, curve a) prompted us to analyze it according to a first-order formalism (Fig. 4, curve b). The resulting linear relationship led to calculate under these conditions an apparent heterogeneous rate constant of 0.04 min^{-1}. Under the condition of a heterogeneous first-order activation, there is no collision between the surface and the surface-bound zymogen since the process occurs locally. The dimension of the rate constant should therefore be expressed adequately without surface units. The data also showed that the maximal amount of FXIIa which was formed in 30 min under the appropriate conditions tended to be $5.0 \pm 0.1 \times 10^{-13}$ mol cm^{-2} since the maximal adsorption ability of the surface with respect to FXII was estimated to be $7.5 \pm 0.1 \times 10^{-13}$ mol cm^{-2}. The yield of the electrochemically-induced catalytic activity was accordingly estimated to be ca. 66%.

Biological functionality of electro-activated FXIIa

The existence of specific activity towards synthetic substrates does not unambiguously ascertain the biological integrity of the electrogenerated FXIIa since the distance from the catalytic site (in the α-FXIIa form) to the residues involved in adsorption is expectably long.

We therefore tested the functional integrity of this adsorbed enzyme with biological substrates, i.e. in the presence of human plasma. This was achieved by measurement of the APTT clotting time (see Experimental) produced by the surface-bound FXIIa in normal plasma samples. Since the amount of the electro-activated FXIIa on the electrode was rather low as compared to that involved in the conventional assay (ca. 0.3 μM), contact with plasma was prolonged up to 30

min. Past this duration, the normal clotting time value of 50 s was recovered. By using FXII-deficient instead of normal plasma, the same value was obtained, thus confirming the biological functionality of the electrogenerated enzyme.

DISCUSSION AND CONCLUSION

Adsorption of the proteins on carbon surfaces

The criteria for irreversible adsorption of a protein on a surface has been the subject of controversy in the literature. For some workers, an adsorption is considered to be irreversible if there is a change in protein conformation [28]. For others, adsorption is irreversible only when desorption is negligible or absent [29]. In the present instance, as desorption of either fixed FXIIa or FXII did not occur after adsorption and subsequent treatment of the modified electrode, it was concluded that these proteins were both irreversibly fixed to the carbon surfaces.

The fact that the catalytic behaviour remained unaltered following adsorption suggested that the active site of the enzyme does not exhibit too strong interactions with the carbon surface. This observation corroborated the pattern of FXII adsorption on negatively charged surfaces, which was known to occur preferentially via the histidine-rich region of the carboxylate end, thus keeping the catalytic end free. As a result, the affinity for the proteins to adsorb would be higher on the carbon particles dispersed on the surface than for the hydrophobic nujol phase, since otherwise the potential-induced modification of the surface would remain ineffective. This behaviour paralleled that of thrombin, another serine protease involved in coagulation [23].

With regard to the enhanced capacity of the surface to adsorb proteins in the presence of DS, it cannot be excluded that the polyelectrolyte also binds the carbon surface. In homogeneous solutions, dextran sulphate-mediated auto-activation of FXII requires the formation of DS–FXII and DS–FXIIa complexes [21]. The extent of activation is both enzyme- and polymer-dependent. In the latter event, it may even be limited by exceeding concentrations of polymer [30]. Inasmuch as these protein–polyelectrolyte assemblies are also effective on the surface by means of adsorption, there would be some propensity for the high molecular weight DS to develop locally electrostatic interactions and steric hindrance. This might explain why the mode of activation of the adsorbed FXII depended on the nature of the activator. When DS was used, it would be reasonable to assume that the negative charge density surrounding the FXIIa complexes was higher as compared to kallikrein. This hypothesis may account for the observed enhancement in the superficial density of protein, from 2.0×10^{-13} to 3.5×10^{-13} mol cm^{-2} whether the activation of FXII was carried out without kallikrein or with other DS-bound FXIIa molecules.

The finding that electrochemical modification of the carbon surface affects the adsorption capacity of the electrode was not surprising. In the current literature, a great deal of reports have evidenced the generation of negatively charged groups on carbon surfaces following cathodic polarization [31]. Since our treatment was applied in the presence of air, the formation of negatively charged or of hydrophilic surface groups was straightforward, particularly beyond -0.5 V vs. SCE, which corresponds with the reduction potential of dissolved oxygen. The gradual (Fig. 2) or bell-shaped (Fig. 3) variation of the plateau observed in the FXII and FXIIa adsorption isotherms should, at least partially, reflect such modifications. Indeed, attributing the isotherm variations solely to these effects seems questionable since changes in the hydrophilic/hydrophobic balance of the surface may also affect the surface properties of FXIIa.

Electrogeneration of FXIIa from surface-bound FXII

The most prominent finding in this study was that negative potentials to immobilized FXII generated appreciable catalytic activity via time-dependent and potential-controlled processes. The absence of any Faradaic current upon negative potential scanning suggested that hypothetical reduction of disulphide bonds was not of concern. The potential-induced catalytic activities should

rather account for other kinds of mechanisms. Being subjected to the high electric field prevailing at the electrode/solution interface, the immobilized FXII molecules might exhibit local conformational rearrangements or even rupture of electro-inactive hydrogen bonds [32]. Also, electrocatalytic breaks of peptide bonds were supposed to explain the biomimetic activation of prothrombin on platinum electrodes [33]. Kinetic studies carried out during the compression or the expansion of protein monolayers indicated that the intramolecular moves of the chemical bonds followed a first order mechanism [34].

The behaviour of FXII induced by negative potentials may also be explained on theses basis. Indeed, it is known that the biological mechanism accounting for FXII activation in the alpha-form proceeds via the break of arginin–valin peptide bonds [35,36], irrespective of the activator which is used, kallikrein or FXIIa [37,38]. These breaks do not require electrons and the amino acids are devoid of electrochemical properties. Therefore and as observed, changes should not affect the traces of the cyclic voltammograms run with the modified electrode.

We also noted a decrease in FXIIa catalytic activity when potentials less than -0.5 V vs. SCE were applied to the FXII-modified electrode. Since the optimal activity coincided with the reduction half-wave potential of oxygen as evoked above, the decrease may be attributed to the electrogeneration of oxygen radicals on the electrode surface, which would damage the catalytic sites.

Finally, we have shown that the electro-activation of FXII is a first-order reaction (Fig. 4), thus reinforcing the assumption of a heterogeneous mechanism of activation. To our knowledge, the description of the early stages of surface-bound FXII activation in the absence of an initiator had never been reported before. The reason for this might be that under homogeneous conditions the time lag during which the initial amounts of activated FXIIa have to be assayed is too short to afford precise determinations. However, under our conditions, the kinetics are considerably slowed down due to the heterogeneous state in which the proteins evolve.

This work was supported by Contrat Externe No. 89 9012 from INSERM and from MRT-GBM Pôle Grand Ouest.

REFERENCES

1 C.G. Cochrane and J.H. Griffin, Adv. Immunol., 33 (1982) 241.
2 A.P. Kaplan and M. Silverberg, Blood, 70 (1987) 1.
3 O.D. Ratnoff, Thromb. Haemost., 43 (1980) 95.
4 J. Margolis, J. Physiol., 144 (1958) 1.
5 S. Niewiarowski and O. Prou-Watelle, Thromb. Diath. Haemorrh., 3 (1959) 593.
6 R.A. Pixley, L.G. Stumpo, K. Birkmeyer, L. Silver and R.W. Colman, J. Biol. Chem., 262 (1987) 10140.
7 B.N. Bouma, L.A. Miles, G. Beretta and J.H. Griffin, Biochemistry, 19 (1980) 1151.
8 J.H. Griffin, Proc. Natl. Acad. Sci. USA, 75 (1978) 1998.
9 M.H. Ginsberg, B. Jaques, C.G. Cochrane and J.H. Griffin, J. Lab. Clin. Med., 93 (1980) 497.
10 A.P. Kaplan, Prog. Hemost. Thromb., 4 (1979) 127.
11 J.H. Griffin and C.G. Cochrane, Semin. Thromb. Hemost., 4 (1979) 254.
12 O.D. Ratnoff and J.D. Crum, J. Lab. Clin. Med., 63 (1964) 359.
13 P.E. Block, K.R. Srinivasan and J.D. Shore, Biochemistry, 20 (1981) 7258.
14 M.A. Griep, K. Fujukawa and G.L. Nelsestuen, Biochemistry, 25 (1986) 6688.
15 I. Schousboe, Int. J. Biochem., 20 (1988) 309.
16 T. Shimada, H. Kato, S. Iwanaga, M. Iwamori and Y. Nagai, Thromb. Res., 38 (1985) 21.
17 G. Tans, J. Rosing and J.H. Griffin, J. Biol. Chem., 258 (1983) 8215.
18 C. Kluft, J. Lab. Clin. Med., 91 (1978) 83.
19 M. Silverberg and S.V. Diehl, Biochem. J., 248 (1987) 715.
20 D.L. Tankersley and J.S. Finlayson, Biochemistry, 23 (1984) 273.
21 M. Samuel, R.A. Pixley, M.A. Villanueva, R.W. Colman and G.B. Villanueva, J. Biol. Chem., 267 (1992) 19691.
22 S. Tazi, G. Tans, H.C. Hemker and J.M. Nigretto, Thromb. Res., 67 (1992) 665
23 H. Randriamahazaka and J.M. Nigretto, Anal. Chim. Acta, 257 (1992) 247.
24 H. Randriamahazaka and J.M. Nigretto, Electroanalysis, 5 (1993) 231.
25 S. Tazi, PhD Thesis, University of Tours, 1989.
26 R.N. Adams, Electrochemistry at Solid Electrodes, Marcel Dekker, New York, 2nd edn., 1969, p. 220.
27 J. Caen, M.J. Larrieu and M. Samama, in L'Hémostase. Méthodes d'Exploitation et Diagnostique Pratique, 2nd edn., Expansion Scientifique Française, Paris, 1975, p. 339.
28 W. Norde, F. MacRitchie, G. Nowika and J. Lyklema, J. Colloid. Interface Sci., 112, (1986) 447.

29 B.M.C. Chan and J.L. Brash, J. Colloid Interface Sci., 82 (1981) 217.
30 C. Loiseau, H. Randriamahazaka and J.M. Nigretto, unpublished results.
31 K. Kinoshita, in Carbon. Electrochemical and Physicochemical Properties, Wiley Interscience, New York, 1987, p. 359.
32 F. Mac Ritchie, Adv. Protein Chem., 32 (1978) 283.
33 H. Durliat, C. Davet and M. Comtat, J. Electrochem. Soc., 132 (1985) 2310.
34 F. Mac Ritchie, J. Colloid Sci., 18 (1963) 555.
35 K. Fujikawa, K.A. Walsh and E.W. Davie, Biochemistry, 16 (1977) 2270.
36 K. Fujikawa, K. Kurachi and E.W. Davie, Biochemistry, 16 (1977) 4182
37 K. Fujikawa, R.L. Heinmark, K. Kurachi and E.W. Davie, Biochemistry, 19 (1980) 1322.
38 G. Tans and J. Rosing, Semin. Thromb. Haemost., 13 (1987) 1.

Analytica Chimica Acta, 283 (1993) 727–737
Elsevier Science Publishers B.V., Amsterdam

D-Lactic acid in pork as a freshness indicator monitored by immobilized D-lactate dehydrogenase using sequential injection analysis

Hun-Chi Shu, Håkan Håkanson and Bo Mattiasson

Department of Biotechnology, Chemical Center, Lund University, P.O. Box 124, S-221 00 Lund (Sweden)

(Received 21st January 1993; revised manuscript received 9th June 1993)

Abstract

A sequential injection analysis system was set up to quantify D-lactic acid in pork. D-Lactic acid seems to be a useful indicator of metabolism of spoilage organisms. The analytical system is fully computerized and is able to monitor the concentration of the acid in an assay cycle of 160 s including 90 s incubation time when the flow is stopped. The enzyme used in the analysis is D-lactate dehydrogenase that is co-immobilized with L-alanine aminotransferase on porous glass. The experimental set-up gave good reproducibility down to 0.1 mM D-lactate and the assay could be repeated at least 500 times with the response maintained.

Keywords: Enzymatic methods; Sequential injection analysis; Lactic acid; Vacuum-packed meat

Biosensors or analytical systems involving immobilized enzyme reactors together with a suitable detector system have been predicted to have wide areas of applications in food science and processing. Analyses of individual compounds like vitamins [1,2] and amino acids [3,4] have been presented earlier. More complex matters like freshness have been addressed both concerning fish and meat [5,6]. These latter examples are based on the use of indicator enzymes to monitor metabolites that function as indicators of the degree of deterioration. Assaying the level of nucleosides gives valuable information with regard to degradation of the raw material.

The quality of meat products is often determined by counts of bacteria. However, the traditional shelf-life determination by quantification of bacteria is not so easy to use with regard to vacuum-packed meat. In such preparations the maximum number of viable cells on a meat surface is typically below 10^8 cm^{-2} and may remain at this level for several weeks. The flavor of meat remains acceptable also after the total count of aerobic microorganisms reaches the maximum level [7]. Instead, the odoriferous end-products of bacterial metabolism progressively accumulate and yield the typical off-flavor of vacuum-packed meat. Thus, the number of bacteria is not always related to the quality of the meat but the end-products of bacteria may be more useful indicators of spoilage and meat sensory quality. D-Lactic acid produced by lactic acid bacteria has been proven as a good indicator of reduced freshness in vacuum-packed chilled raw pork [8]. Furthermore, in several kinds of vacuum-packed meat products a better correlation has been reported between sensory quality and levels of D-lactate than between bacteriological counts and sensory quality [9]. Obviously, the determination of D-lactate has the potential to become more impor-

Correspondence to: B. Mattiasson, Department of Biotechnology, Chemical Center, Lund University, P.O. Box 124, S-221 00 Lund (Sweden).

tant and time-saving than bacterial count as a tool to determine freshness in vacuum-packed meat and meat products.

For the determination of D-lactate, several enzymatic methods have been reported using batch or flow systems [10,11,12]. However, all the methods related to flow systems are flow-injection systems, which usually need several pumps and a complicated flow system design. When cofactor dependent enzymes are used, relatively large amounts of cofactor are necessary and the waste of the expensive material is unavoidable. Although, sequential injection of buffer, sample, and cofactor has been done by a complicated flow-injection system, in order to reduce the consumption of cofactor [13], the whole system is still complicated from the practical point of view. A less complicated process has been demonstrated [14]. However, a more simple process configuration is offered by the use of sequential injection analysis (SIA) which has the additional benefits of easy handling and flexibility in stopped flow operations. By the possibility to inject small volumes of each reagent in a predetermined order it is realistic that comsumption of reagents will be reduced. So far, there is no application reported on SIA with an immobilized enzyme. In the work presented here, the concentration of D-lactate in pork was determined by combining the stopped-flow SIA and the immobilized two-enzyme system. An enzyme sequence of a specific D-lactate dehydrogenase (D-LDH) and L-alanine aminotransferase (ALT) was used since the D-LDH alone turned out to have a less favourable equilibrium with respect to the process to be analyzed.

EXPERIMENTAL

Chemicals

D-Lactate dehydrogenase (E.C. 1.1.1.28) from *Leuconostoc mesenteroides subsp. cremoris* (specific activity, 284 U mg^{-1}) was prepared by affinity precipitation with Eudragit-Cibacron blue complex and DEAE cellulose ion exchange chromatography [15]; L-alanine aminotransferase (glutamic-pyruvate transaminase, E.C. 2.6.1.2.; 76 U mg^{-1} protein) from porcine heart, D-lactic acid, NAD^+, glutamic acid and glycylglycine were purchased from Sigma (St. Louis, MO). The L-lactic acid and UV-enzymic kits for D-lactate and L-lactate were obtained from Boehringer (Mannheim). The silica beads were supplied by EKA Nobel AB (Surte, Sweden). The average diameter of the beads was 41 μm with a mean pore diameter of 20 nm and the specific surface area was 300 m^2 g^{-1}, according to the specifications given by the supplier. All other chemicals were of analytical grade.

Instrument and procedures

The sequential injection manifold as shown in Fig. 1 was constructed from the following components: a dual-piston, sinusoidal flow pump (Alitea AB, Stockholm); a six-port rotary valve (Cheminert 4162510, Valco instruments, Houston, TX); a three-way slider valve with pneumatic actuator (Rheodyne, 5300 and 5301, Cotati, CA); and a spectrophotometer (Shimadzu, UV-120-02, Japan) equipped with a 30-μl dead volume and 10-mm light path flow-through cuvette (Hellma, Model 178.711, Germany) for absorbance measurements. NADH was monitored by measuring the absorbance at 340 nm. All the tubings connecting the different units were made of PTFE (0.8 mm i.d.). The holding coil, having a volume of 2 ml, served as a buffering volume to prevent the sample from entering the syringe pump. The principle of SIA was first presented by Ruzicka et al. [16] and has been reviewed recently [17]. The principle involves the aspiration of small liquid segments of the different reactants into the tubing. When the reagents are arranged in the desired order, a valve is switched, the flow is reversed and the liquid is pumped through the enzyme column prior to passage through the flow cuvette. The time lapse of the measuring cycle and the response curve is shown in Fig. 2. The total time for one analysis is 165 s including 90 s incubation time when the flow is stopped. The measuring cycle is described as follows (see Figs. 1 and 2); (1) Turn of the 3-way valve, and aspiration of wash/carrier buffer from rotary valve position a and b, while the piston makes a large and a small reverse step, respectively; (2) aspira-

tion of NAD^+ solution from position c using small piston reverse step; (3) aspiration of sample solution with valve in position d with a small reverse piston move; (4) aspiration of NAD^+ in valve position e with the same reverse move as above; (5) aspiration of carrier buffer in position f with a small piston reverse step; (6) turn the 3-way valve, while forwarding the piston with the stroke length adjusted such that the carrier buffer, NAD^+, and sample zone is transported to the enzyme column; (7) stopped-flow period for enzyme catalysis; (8) forward large piston stroke that expels all reagents and products through detector and washes the enzyme column to baseline for next cycle. The aspirated volume of wash/carrier buffer, NAD^+, sample, NAD^+, carrier buffer are 1.21, 0.21, 0.20, 0.19, and 0.19 ml, respectively. A schematic representation of the train of liquid segements is shown in Fig. 2. During the whole study, the rate of pump setting was 20 rpm. Because the sinusoidal flow pump is a cam-driven piston pump, the flow-rate is variable in different rotation angles [16]. In this study, the arc of cam was driven from 50 to 130 degree, corresponding to the syringe setting from 2.1 to 4.1 ml. The average flow-rate was 3.2 ml min^{-1}. It is to be noted that the pump was stopped whenever the valve was being turned, in order to prevent the pressure from building up which would otherwise effect the reproducibility. Furthermore, for better reproducibility, computer control is inevitable. The software used to control the pump and valve movements in the measuring cycle allowed synchronization to be made, by programming all events on a time basis given by the computer clock [18]. However, each analysis cycle was terminated individually by a microswitch inside the pump (i.e., the starting position of every cycle is the same), to prevent from any time errors accumulated during a long series of measurement.

The automated SIA is based on the use of a personal computer (UPC-386, Taiwan) working at 33 MHz, and equipped with 57-Mb hard disk, 2-Mb RAM and VGA graphics. A four-channel digital input/output board (MetraByte, DAS-8PGA, Townton, MA) was used to expand the communication between the computer and the external devices. The valves and the pump are digitally monitored by computer via a driver circuit (Epipactis AB, Lund). Pneumatic valves were selected to obtain short and reproducible switching time and low dead volume. These valves are activated by an electromagnetic valve (Festo, MZH-5/2-1.5-L-K, Esslingen). The pneumatic pressure was kept at about 7 bar. The analog output signals from the spectrophotometer were fed via a dc-amplifier to the computer by which peak width, peak height are calculated and baseline can be adjusted automatically.

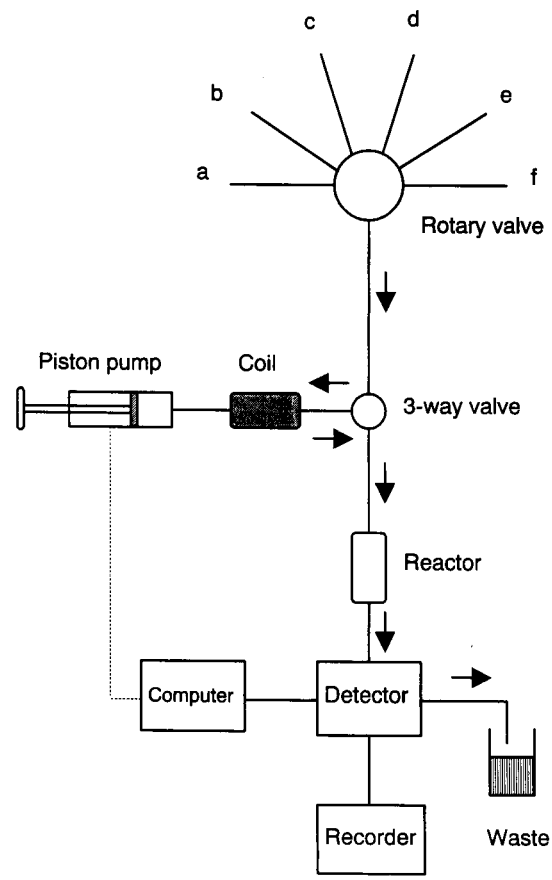

Fig. 1. Schematic presentation of the sequential injection system including syringe pump, holding coil, three-way valve, six-ways rotary valve, enzyme column, recorder, spectrophotometer and computer. Positions a–f of the six-way rotary valve: (a, b) wash/carrier buffer; (c) cofactor; (d) sample; (e) cofactor; (f) carrier buffer.

Immobilization of enzyme

Silica was modified with γ-aminopropyltrieth-oxysilane and later with glutaraldehyde following procedures described by Weetall [19]. D-LDH (550 U) dissolved in 400 μl of 50 mM sodium phosphate buffer pH 7.0 was added to 0.5 g of aldehyde functionalized silica. The mixture was left on a blood mixer at room temperature for coupling to take place. After 3 h, 110 U of ALT solution was added and coupling continued for another 2 h. Finally, 20 mg of sodium cyanoboro-hydride ($NaBH_3CN$) was added to reduce the Schiffs-base bonds between aldehyde and enzymes in order to stabilize the coupling. The mixture was left for 1 h at room temperature and then overnight in a refrigerator. The preparation was then washed on a glass filter with 0.1 M phosphate buffer pH 7.0 and was packed in a column (30 × 4 mm i.d.) with porous vyon discs at each end. The column was supplied with adapters for connection to the flow system to be used for analysis. The column, when not used, was stored in 0.1 M phosphate buffer pH 7.0 containing 0.02% sodium azide at 4°C.

Solution preparation

Standard solutions of D-lactic acid (0.1, 0.2, 0.5, 0.75, 1, 2, 5, 7.5, and 10 mM) were prepared in water from a Milli-Q system (Millipore, bedford, MA). Various buffers as well as different concentrations and pH values of the NAD^+ solution were tested. Glutamate (70 mM), serving as the substrate for ALT, was added to the buffer solution when evaluating the effect of using a mixed enzyme reactor (D-LDH + ALT) over a reactor containing solely D-LDH. Since NAD^+ is unstable in alkaline media, the NAD^+ solution was prepared fresh for daily use.

Sample treatment

Freshly ground pork was purchased from a local market. Some portions of the pork were frozen immediately and used as controls. The other part, around 400 g, was placed in a glass container over a layer of some sterile water in order to keep humidity constant. The meat and the water were kept separated. The vessel was degassed by vacuum for 10 min. The whole container was covered with aluminum foil and then kept at 4°C. Fifty grams of pork were taken every week for 3 weeks and the container was degassed and stored as described above. D-Lactic acid in the pork was extracted as follows: 5 g of meat sample was homogenized with 20 ml of 1 M perchloric acid in a Waring blender for 10 min and then transferred to a beaker with approx. 40 ml of water. The mixture was adjusted to pH 10–11 by 2 M potassium hydroxide and the volume was adjusted to 100 ml with water. The whole procedure followed the method described

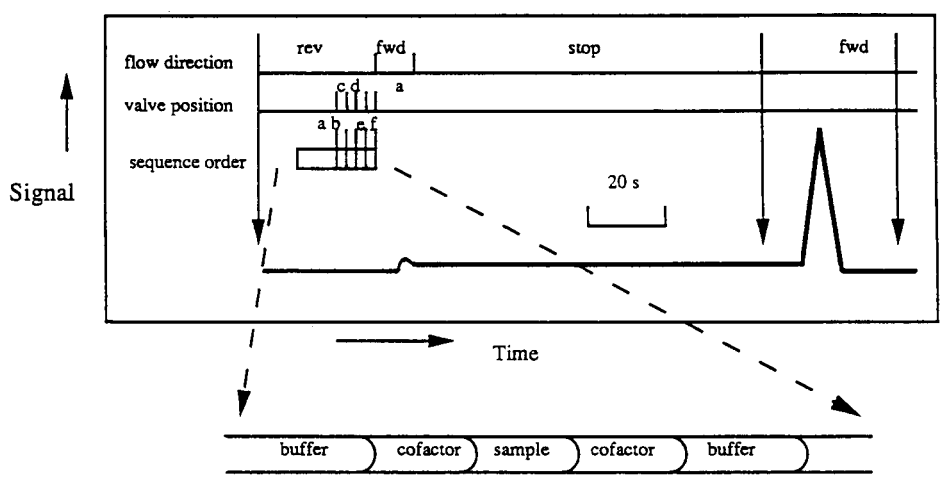

Fig. 2. Time lapse and response curve of SIA (details in the text).

in the Boehringer test kit [10] and the concentration determined by SIA and also with a commercial test kit separately. The pork sample serving as blank was used in studies of the lactic acid recovery. Defined amounts of D-lactic acid were added and the samples were then extracted by the same method as above. The solutions were analyzed by the two methods to determine the content of D-lactic acid and then to calculate the recovery.

Stability of enzyme column

In order to check the stability of the enzyme column and the reliability of the SIA system for longer time operation, a 1 mM D-lactic acid solution was analyzed repeatedly for 24 h (ca. 520 assay cycles) under the conditions of 0.1 M glycylglycine + 70 mM glutamate as carrier buffer at pH 10 using 4 mM NAD^+ as cofactor and 90 s stop time in the enzyme column.

RESULTS AND DISCUSSION

The analytical system that was set up was studied concerning its performance, e.g., reliability and reproducibility. It was found that a well defined analytical protocol helped to keep variations down and to make the performance fully acceptable with regard to flow of buffer, switching of valves etc. The computerized procedure simplified the assays substantially.

Choice of carrier buffer

The effect of buffer composition, tested with 0.1, 0.5, 1 and 2 mM of D-lactic acid under the condition of 4 mM NAD^+ as cofactor, incubation time 90 s, and pH 10 on the SIA response is shown in Fig. 3. The highest response and the best linearity ($r = 0.999$, $n = 5$) was obtained in 0.1 M glycylglycine buffer containing 70 mM glutamic acid. The linearity of the calibration graph for 0.1 M pyrophosphate buffer containing 70 mM glutamate was not so good ($r = 0.893$, $n = 5$). The highest response was obtained in 0.25 M glutamate. However, the background signal was too high and unstable to be used in routine analysis.

Effect of pH

When dealing with sequential enzyme reactions one has to consider the effect of pH on the activity of both enzymes [20]. Furthermore, when dealing with coenzyme dependent reactions, stability issue of the cofactor becomes important. The calibration graph obtained with the SIA system based on the use of the enzyme sequence at different pH values of glycylglycine buffer (0.1 M, 70 mM glutamate) in the presence of 4 mM NAD^+ solution having same pH as the buffer and 90 s incubation time is shown in Fig. 4. Because the enzyme reaction for D-lactic acid determination was favoured in alkaline condition, the response of the D-LDH + ALT column was increased with rise in pH. However, when pH of the buffer solution was increased to 11, the response of the enzyme column was decreased probably because of denaturation of the enzyme.

It is important to compare the difference in sample and cofactor handling between the FIA and the SIA systems. In the former, the mixing between carrier buffer and sample or cofactor may be much better, because of use of larger reaction volumes and continuous dispersion of the buffer. In the latter, the mixing of the different reagents only happens in the boundary be-

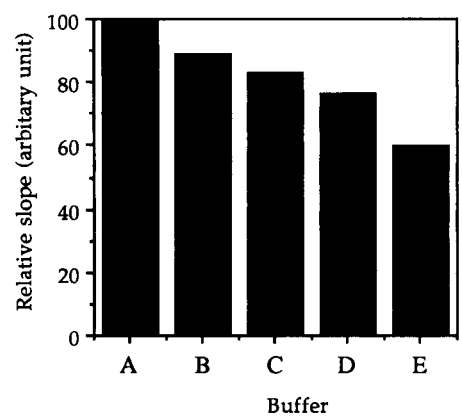

Fig. 3. Influence on the analytical response in the SIA of D-lactate using different buffers containing 2 mM D-lactate and 4 mM NAD^+, respectively. (A) 0.1 M glycylglycine + 0.07 M glutamate; (B) 0.1 M HEPES + 0.07 M glutamate; (C) 0.1 M glutamate; (D) 0.1 M pyrophosphate + 0.07 glutamate; (E) 0.25 M glutamate. The experimental details are given in the text.

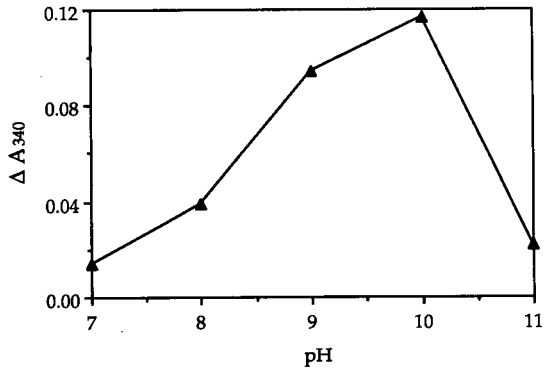

Fig. 4. Influence of pH on the analytical response of SIA after injection of 2 mM D-lactate and 4 mM NAD^+ into the system. Buffer was 0.1 M glycylglycine containing 70 mM glutamine with the pH as shown in the figure.

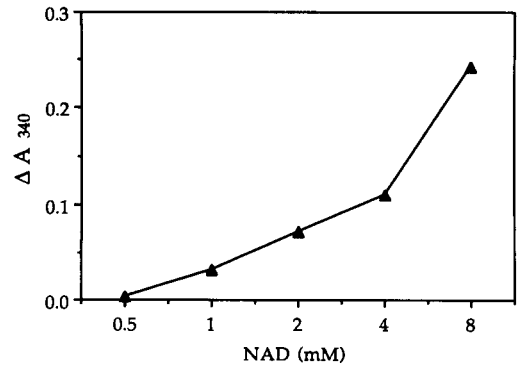

Fig. 5. Influence of varying concentrations of NAD^+ on the analytical outcome when injecting 2 mM D-lactate and varying concentrations of NAD in glycylglycine buffer, pH 10.0. Experimental details are given in the text.

tween two adjacent sections and usually the volume of this mixed zone is rather small. Since NAD^+ is more stable on the acidic side (pH around 4 or 5) aqueous solutions of NAD^+ with low pH were tried in SIA system. However, the response of the enzyme column at lower concentrations of D-lactic acid was very weak. When the pH of the NAD^+ solution was adjusted to pH 10, the response became much better and the analysis more sensitive than that at pH 5. In spite of the stability problems with the cofactor, pH of the NAD^+ solution was kept at 10 during the whole study.

Effect of NAD^+ concentration

The cost of cofactor is one of the hampering factors for a wider application of coenzyme-dependent enzymes in analysis. The use of SIA offers a possibility to operate with only small volumes of coenzyme, thus making the use of such enzyme reactions perhaps more attractive.

The concentration dependence with regard to NAD^+ for the coupled enzyme sequence is shown in Fig. 5. As a working compromise between the concentration behaviour and the need to keep the amounts of cofactor low, 4 mM was chosen as a suitable concentration for the cofactor stock solution.

Effect of varying the stopping time

It is important to keep control of the mixing processes in SIA. Since mixing is a prerequisite for reaction to take place, the analytical result will very much depend on the efficiency of mixing and the time elapsed between mixing and reading the outcome of the analytical reaction. In order to improve the degree of conversion, the segment of liquid containing the cofactor and the sample was stopped in the enzyme reactor for varying time periods.

The effect of stopping time is shown in Fig. 6 under the same experimental conditions as in Fig. 4, except that the pH was kept at 10. When reagents flow through the column without stopping, the response of D-LDH + ALT for D-lactic acid is almost undetectable. Increase in the hold-

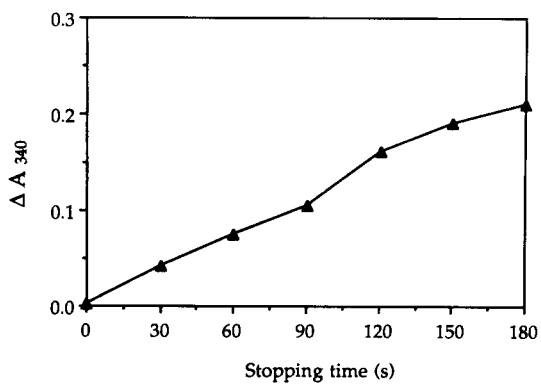

Fig. 6. Effect of stopping the reagent flow for various time durations in the enzyme column. Incubation mixture consisted of 2 mM D-lactate and 4 mM NAD^+. Buffer used was 0.1 M glycylglycine pH 10.0.

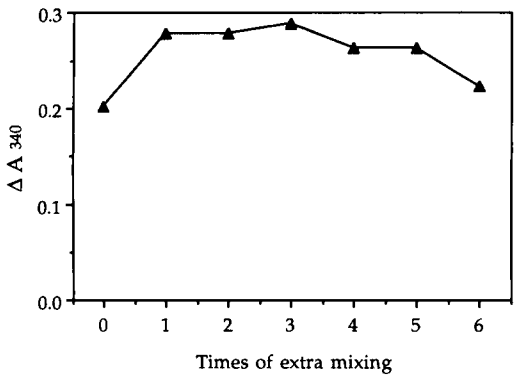

Fig. 7. Effect on assay response of reversing the flow of pulses of 2 mM D-lactate and 4 mM NAD^+ back and forth in the enzyme column. Each reversal took 2 s.

ing time of the reaction mixture within the enzyme column improves the sensitivity of the reaction but at the expense of sample throughput. A realistic compromise under the conditions studied was found to be 90 s.

In order to test if the mixing of the sequentially injected liquid segments could be improved in the enzyme reactor, the flow direction was reversed a few times so that the substrate pulse and the surrounding cofactor segments were pumped back and forth within the enzyme reactor during the stopping time. It was regarded essential to keep the reactants within the enzyme reactor in order to keep control over the reaction time when the enzyme was in contact with substrate. In Fig. 7 is shown the outcome of these flow manipulations. The first cycle of reversed flow improved the response from the analysis substantially, whereas on the subsequent steps very small effects were achieved. This indicates that mixing is not perfect when the substrate pulse enters the enzyme column and that already after one reversal cycle, the situation seems to come to equilibrium.

From the results obtained, the experimental conditions chosen for analysis of D-lactic acid using a column of immobilized D-LDH–ALT was 0.1 M glycylglycine (pH 10), containing 0.07 M glutamate as carrier buffer solution, 4 mM NAD^+ at pH 10 as cofactor and 90 s stopping time. The comsumption of NAD^+ for the SIA system was approximately 0.16 μmol per sample.

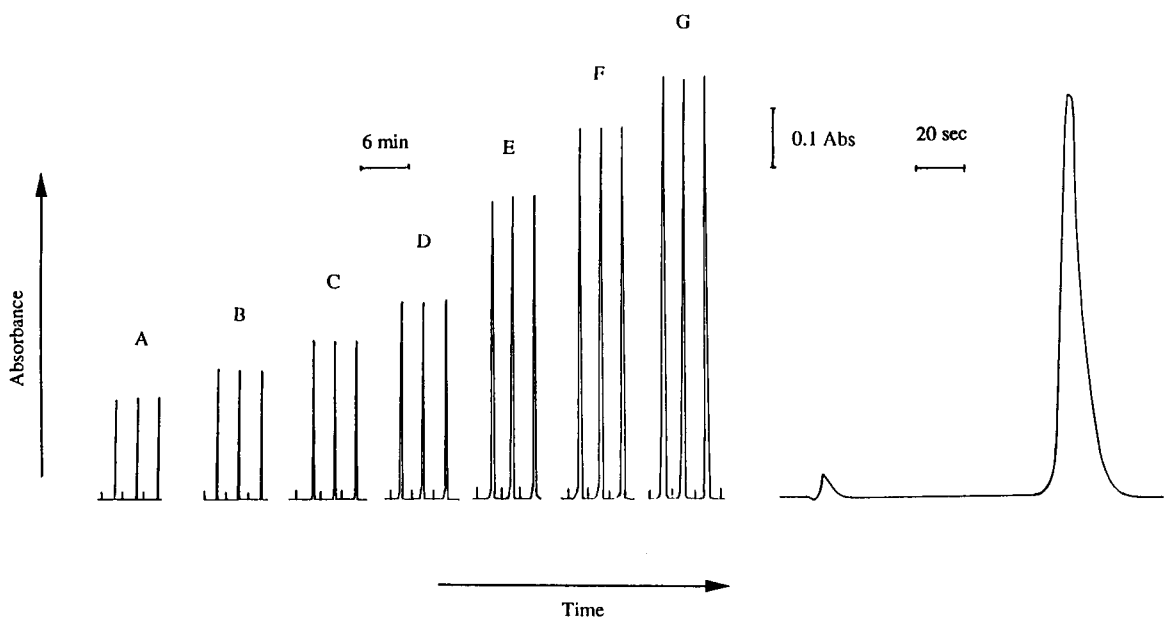

Fig. 8. Typical peaks recorded after injecting calibration solutions of D-lactate of the following concentrations: (A) 0; (B) 0.5; (C) 1.0; (D) 2.0; (E) 5.0; (F) 7.5; (G) 10.0 mM in water solution. A solution of 4 mM NAD^+ was used. The buffer used was 0.1 M glycylglycine with 0.07 M glutamate, pH 10. The flow was stopped for 90 s according to the procedure described in the text.

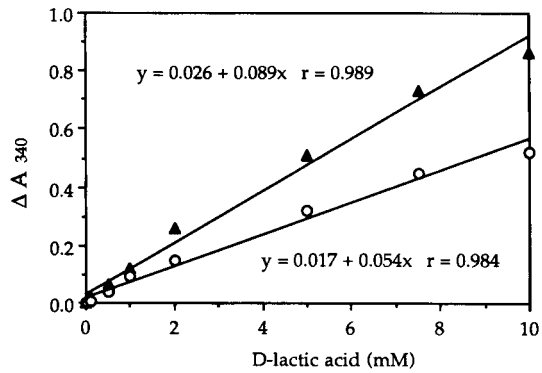

Fig. 9. Calibration graphs for D-lactic acid obtained by the use of co-immobilized D-LDH + ALT. (▲) with 0.07 M glutamate in glycylglycine buffer; (○) in glycylglycine buffer.

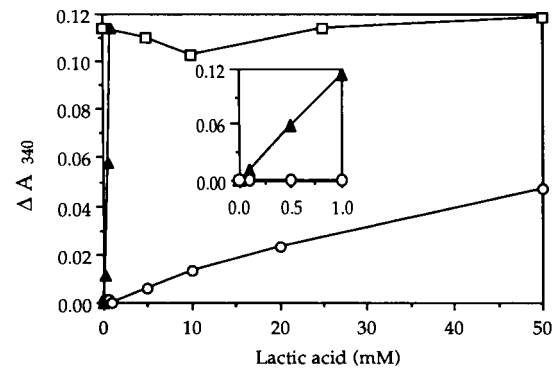

Fig. 10. Calibration graphs obtained using the immobilized D-LDH–ALT and varying concentrations of D-lactate (▲), L-lactate (○) and 1 mM D-lactate in the presence of increasing concentrations of L-lactate (□). Incubation conditions are otherwise the same as described in legend to Fig. 8. Inserted is shown the response for the two isomers up to 1.0 mM.

Determination of D-lactic acid

A series of standard solutions of D-lactic acid were analyzed using the conditions given above. Some typical peaks registered are shown in Fig. 8. The initial small peak was caused by the mixture of leading NAD^+ solution and the carrier buffer passing to the detector during the first forward aspiration. When comparing the results from a column with co-immobilized D-LDH and ALT with these from a column with D-LDH alone, it was seen that the former showed approx. 60% higher response than the latter (Fig. 9). The method is useful in the concentration range down to 0.1 mM.

The relative standard deviation (R.S.D) of the method in the analytical range of D-lactic acid solution was below 3% ($n = 5$).

Specificity of the analysis

In order to check for interference of L-lactic acid and other acids 1, 5, 10, 20, 50, 100 mM L-lactic acid and 1 and 10 mM of the other acids were used in a SIA system. All the samples were adjusted to pH 5–7 (the same pH as D-lactic acid). The calibration graphs for D- and L-lactic acid, and the response from 1 mM D-lactic acid in various concentrations of L-lactic acid are shown in Fig. 10, and the slopes of the calibration graphs given in Table 1. The interference of L-lactic acid in analysis using D-LDH + ALT is very small. The residue of L-lactic acid in vacuum-packed raw pork is normally in the range 5.6–7.8 mmol/100 g according to [8]. L-Lactic acid in these concentrations showed very small interference with the determination of D-lactate using the enzyme sequence mentioned above.

TABLE 1

Specificity of D-LDH–ALT in SIA method

Compound	Slope (%) of "calibration" graph
D-Lactic acid	100
L-Lactic acid	0.86
Citric acid	0.59
L-Malic acid	0.39
Oxalic acid	0.00
Pyruvic acid	4.81
Succinic acid	0.00

In the model studies where even higher concentrations of L-lactic acid were used, the interference was lower than 1%. The other acids have even less interference except for pyruvic acid. In situations when D-lactic acid is determined, pyruvic acid will not constitute a problem. Thus, the assay is specific from a practical point of view and it is selective between the two isomers of lactate.

Some considerations with regard to a comparison of SIA and FIA

The comparison of the methods for D-lactate analysis is shown in Table 2 SIA as well as FIA have much higher sample throughout than batch

TABLE 2

Comparison of different methods for determination of D-lactate

Method	Time for extracting sample (min)	Time needed per sample (min)	Consumption of reagents per sample			Note	Ref.
			buffer [a] (ml)	NAD (μmol)	D-LDH (U)		
Boehringer	≈ 40	≈ 25	1	≈ 10.6	109	Batch	10
SIA	≈ 40 [b]	2.75	1.4	0.16	1.1 [c]	–	this work
FIA	– [d]	≈ 3 [e]	≈ 1.5 [e]	≈ 0.15 [e]	– [f]	Bioluminiscence	11
LC	> 65 [g]	> 300	–	0.5	5	Sensitive nmol mol^{-1}	12

[a] Various kinds of buffers: Boehringer and SIA (0.1 M glycylglycine); FIA (0.05 M pyrophosphate). [b] The same extraction method as the Boehringer method. [c] Immobilized enzyme (550 U) stable for ≥ 500 cycles. [d] No meat sample analyzed by this method. [e] No direct information given (3 min was estimated from the flow-rate and the flow system). Consumption of reagents was calculated from the flow-rate and the duration of the reagent pulse. [f] Immobilized enzyme. [g] Extraction time for rat liver sample.

analysis and liquid chromatographic methods have. The consumption of reagents, especially enzyme and cofactor, is also much less for the continuous flow systems than the batch method. Theoretically, SIA and split loop FIA have the similar function for the immobilized enzyme preparation, but the higher flexibility of SIA in stopped flow operations and the savings in capital investment for injection valves and flow system design are also important. SIA is based on the use of one piston pump which never comes in direct contact with the reagents. This gives the basis for a reproducible and reliable operation. Peristaltic pumps are often used in FIA systems. The aging of the pump tubing is a major problem to keep under observation since this process results in changing flow-rates and even system breakdown. However, it is worth noticing that SIA instruments require more sophisticated computer control than FIA equipment. SIA is still a technique under development and SIA instruments are not yet commercially available.

Change in D-lactic acid concentration during the vacuum storage of minced pork

The concentrations of D-lactic acid and L-lactic acid in pork change during vacuum- and chilled-storage, as shown in Table 3. The concentration of D-lactic acid was increased in the first two weeks and decreased in the third week. The concentration of D-lactic acid accumulated in ground pork is much higher than that in beef [20] probably because of the higher initial load of bacteria in ground pork. In the first week, the D-lactic acid was high enough to show the deterioration of the pork and actually, a slight acidic smell could be identified in this period. When the storage time was prolonged to 2 weeks, the amount of D-lactic acid as well as the acidic smell increased significantly. The pork was unacceptable to the consumer. The quicker spoilage in this study as compared to what is reported from a previous study of vacuum-packed pork [8] is reasonable. D-Lactic acid-producing bacteria will start to grow when the oxygen tension in the atmosphere is decreased and carbon dioxide is increased. Therefore, in this study with a holding container that is larger than flexible package film it will take longer time to consume all residual

TABLE 3

Changes in D-lactic acid and L-lactic acid levels during storage of ground pork at 4°C under vacuum

Item	Conc. (mmol/100 g) on day				
	0	7	14	18	21
D-Lactic acid (SIA)	0.00	0.97	2.13	1.89	1.68
D-Lactic acid (Boehringer)	0.01	0.75	1.90	1.88	1.50
L-Lactic acid (Boehringer)	4.88	4.40	3.10	2.55	1.79

oxygen and to create the efficient carbon dioxide concentration that prevents the growth of the aerobic microorganisms. Furthermore, as mentioned earlier, the higher initial load is another important factor to speed up the spoiling of the meat. The similar profile of D-lactic acid produced in uninoculated beef has been found recently [21]. In contrast, the amount of L-lactic acid decreased constantly during the storage. The same profile has been found in the sliced beef inoculated with *Lactobacillus* [21].

Comparison of the SIA and Boehringer methods

The pork samples stored after external D-lactic acid addition were analyzed for the acid content over the range 0–2.5 mM by the two different methods. There was a linear correlation which could be described by [D-lactic](Boeh.) = 0.916[D-lactic](SIA) − 0.026($r = 0.991$, $n = 10$, concs. in mM). The concentration of D-lactic acid appears slightly higher (ca. 10%) when using the SIA method, but a good agreement between the results can be seen for these two methods. The recoveries of D-lactic acid were between 95 and 105% when 0.2–2 mM D-lactic acid solutions were added to the pork of known lactic acid concentration. It is important to note that the samples extracted from pork have a slightly yellowish colour that influences the absorbance at 340 nm. Thus, a column packed with blank silica beads (the same activation procedure as enzyme reactor but without any enzyme) was used to check the blank absorbance and the blank values were used to correct for the interference of the extra pigment extracted from pork.

Stability of the enzyme column

In general, after prolonged use of the enzyme, denaturation or inhibition of enzyme may affect the response. The enzyme column was tested and found to have a good response after more than 500 assays (24 h) operational time (data not shown). It is clear that the reliability of the SIA system and enzyme column makes it fully possible for process monitoring. However, when real samples are to be used, the complex components of the biological samples will most probably interfere with the stability of the enzyme column.

Conclusion

Sequential injection systems have proven suitable in combination with immobilized enzymes. The ability to introduce a range of reagents together with the sample by means of one single pump and suitable valves makes this technology very attractive as a complement to, or substitute for FIA. It is yet too early to make fair comparisons between the different technologies since SIA needs to be tried both on more model systems but also under realistic conditions.

The present study clearly shows that spoilage of pork can be monitored by registering the concentration of D-lactic acid [8,9,21] using the SIA technology.

Part of this work was supported by The National Swedish Board for Technical and Industrial Development (NUTEK). H-C.S. was supported by The Educational Ministry of Taiwan.

REFERENCES

1 T. Matsunaga, I. Karube and S. Suzuki, Anal. Chim. Acta, 99 (1978) 233.
2 B. Mattiasson, P.-O. Larsson, L. Lindahl and P. Sahlin, Enzyme Microb. Technol., 4 (1982) 153.
3 M. Hikuma, H. Ooana, T. Yasuda, I. Karube and S. Suzuki, Anal. Chim. Acta, 116 (1980) 61.
4 W.C. White and G.G. Guilbault, Anal. Chem., 50 (1978) 1481.
5 E. Watanabe, K. Toyama, I. Karube, H. Matsuoka and S. Suzuki, Appl. Microbiol. Biotechnol., 19 (1984) 18.
6 A. Mulchandani, K.B. Male and J.H.T. Luong, Biotechnol. Bioeng., 35 (1990) 739.
7 R.H. Dainty, B.G. Shaw and T.A. Roberts, in T.A. Roberts and F.A. Skinner (Eds.), Microbial and Chemical Changes in Chill-Stored Red Meats (Food Microbiology), Academic Press, London, 1983, p. 151 (cited in Ref. 8).
8 B.D. Pablo, M.A. Asensio, B. Sanz and J.A. Ordonez, J. Appl. Bacteriol., 66 (1989) 185.
9 W. Schneider, G. Hildebrandt and H.J. Sinell, Fleischwirtschaft, 63 (1983) 1198 (abstract).
10 K. Gawehn, in H.U. Bergmeyer (Ed.), Methods of Enzymatic Analysis, Vol. VI, Verlag Chemie, Weinheim, 3rd edn., 1984, pp. 588–592.
11 S. Girotti and S. Ghini, Anal. Chim. Acta, 255 (1991) 259.
12 S. Ohmori and T. Iwamoto, J. Chromatogr., 431 (1988) 239.

13 W. Schuhmann, T. Becker, R. Betken, H.-L. Schmidt, M.B. Leible and A. Albrecht, Abstracts of Biosensor and Flow-Injection Analysis in Bioprocess Control, 1992, Freising, April 6–9, 1992.
14 A.M. AlMuaibed and A. Townshend, Anal. Chim. Acta, 214 (1988) 161.
15 H.-C. Shu, G. Dong, R. Kaul and B. Mattiasson, submitted for publication.
16 J. Ruzicka, G.D. Marshall and G.D. Christian, Anal. Chem., 62 (1990) 1861.
17 J. Ruzicka and G.D. Marshall, Anal. Chim. Acta, 237 (1990) 329.
18 M. Nilsson, H. Håkanson and B. Mattiasson Process Contr. Qual., 4 (1992) 37.
19 H.H. Weetall, Methods Enzymol., 44 (1976) 134.
20 S. Gestrelius, B. Mattiasson and K. Mosbach, Biochim. Biophys. Acta, 276 (1972) 339.
21 E. Borch and H. Agerhem, Int. J. Food Microbiol., 15 (1992) 99.

Analytica Chimica Acta, 283 (1993) 739–745
Elsevier Science Publishers B.V., Amsterdam

Electroosmotically pumped capillary flow-injection analysis

Valve-based injection systems and sample throughput

Shaorong Liu and Purnendu K. Dasgupta

Department of Chemistry and Biochemistry, Texas Tech University, Lubbock, TX 79409-1061 (USA)

(Received 18th May 1993; revised manuscript received 1st July 1993)

Abstract

In flow-injection analysis (FIA) systems with electroosmotic flow (EOF), the maximum permissible sample throughput is a function of the electric field strength, capillary length and injection volume. The relation between the various parameters is theoretically and experimentally discussed. Experimental results are in reasonable agreement with theoretical expectations. The potential of EOF pumped FIA using very short capillaries and relatively low applied voltages is discussed.

Keywords: Flow injection; Electroosmotic pumping; Valve injection; Sample throughput

Miniaturization results in many benefits, one aspect is the minimization of waste generation. This is a particularly important issue when many samples are to be analyzed or a chemical process must be monitored in a virtually continuous manner. An electroosmotic pump has no moving parts and is thus ideally suited for a miniaturized FIA system. Such a system was introduced in our previous paper [1].

To date, capillary electroosmosis has been largely studied in the context of capillary electrophoresis, specifically capillary zone electrophoresis (CZE). In CZE, a very small sample volume (typ. $\leqslant 20$ nl) is introduced, most commonly by a pressure difference (hydrostatic or pneumatic) or by the electric field itself (electrokinetic injection). Both methods are susceptible to changes in sample viscosity, temperature, etc. In addition, the second technique results in different amounts of the different constituents of the sample being introduced into the capillary because of their differences in electrical mobility [2]. In our first utilization of EOF pumped FIA, we utilized the hydrostatic sample introduction technique.

In terms of implementation, this injection approach is similar to that in segmented flow analysis (SFA) where the sample probe travels to a sample container and the sample is aspirated in, the volume introduced being dependent on time. Although there is no real barrier to utilizing loop injection valves in SFA [3], they are not commonly used. Practitioners who are familiar with both SFA and valve-based FIA generally recognize the considerable advantages of valve-based fixed volume injection. Attempts have been made to devise small volume injection valves for use in CZE. Tsuda et al. [4] have described a rotary injection valve for CZE. However, this valve has an injection volume of 350 nl which is larger than that desired. We have developed a valve capable of smaller injection volumes that will be de-

Correspondence to: P.K. Dasgupta, Department of Chemistry and Biochemistry, Texas Tech University, Lubbock, TX 79409-1061 (USA).

scribed in a later publication. Meanwhile an internal loop injection valve with nonmetallic contact parts with an injection loop volume of $\geqslant 60$ nl has become commercially available. Since extremely narrow bands are neither necessary nor desirable in FIA (some dispersion is necessary in a single line system for the analytical reaction to occur), this injection volume is adequate.

The present paper describes theoretical considerations on sample throughput in valve-based electroosmotic flow (EOF) pumped FIA and its experimental implementation.

PRINCIPLES

In hydrostatic injection as carried out previously [1], sample throughput is limited by the necessity to lift the inlet end of the capillary from various sample vials to the running electrolyte reservoir back and forth. During the transfer and sample introduction steps no high voltage (HV) is applied and there is no EOF.

Consider the EOF pumped FIA manifold in Fig. 1. The running electrolyte is contained in vials A and B respectively. With a typical electrolyte in the capillary (pH > 2, no cationic surfactants), the surface of a fused silica capillary (C1 + C2) is negatively charged and EOF proceeds from the positive high voltage end to the other side (A → B) and thus sample S injected by valve V is detected by detector D.

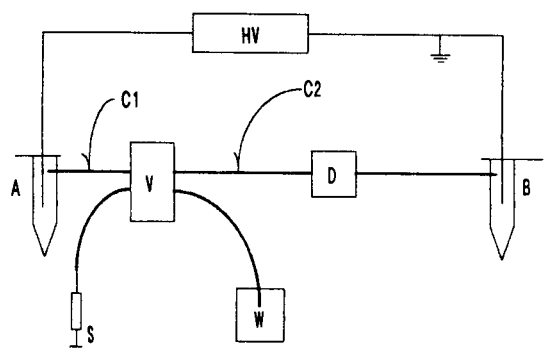

Fig. 1. Valve-based EOF-pumped single line FIA manifold. (A) source vial; (C1) connecting capillary to internal loop nonmetallic injector V; (C2) reaction conduit (of active length L) to detector D; (B) terminating vial; (HV) high voltage power supply; (S) sample; (W) waste.

We are concerned here with a single line FIA system where the analyte reacts with a reagent in the carrier electrolyte to form a detectable colored product. Because flow-induced dispersion during EOF is minimal, situations in which both the reagent and the analyte are uncharged species are not conducive to product formation and are not considered. In most situations, EOF is significantly higher than the electrophoretic movement of sample or reagent ions, whether these are concurrent or countercurrent to the EOF. Consequently, in any situation other than when both the sample and reagent are neutral, the injected sample zone will be contacted by the reagent species either from behind or from ahead, regardless of the direction and relative magnitudes of their electrophoretic movement. The resulting colored product, regardless of the sign or magnitude of its charge, is then swept by the EOF to the detector.

If a sample contains more than one component that reacts with the reagent, these may be separated electrophoretically before they reach the detector. Even in the simplest case where only the analyte of interest reacts with the reagent to form a product detectable under the given conditions (this is the typical FIA application, requiring no separations), in a single-line system the fate of the sample matrix must be considered. While other sample constituents are typically largely invisible to the detector either because they do not react with the reagent or their products are not detectable, the sample matrix itself is typically visible to the detector either as a refractive index artifact or as a negative peak because the carrier reagent typically displays some finite background absorbance. In conventionally pumped FIA, no separation takes place between the matrix, the analyte and other sample constituents. In EOF pumped FIA, the sample matrix, typically uncharged water molecules, will be separated from charged analyte ions (or a charged colored product). With the polarity of the applied voltage as shown in Fig. 1, the sample matrix will lag behind a positively charged product zone or proceed in advance of a negatively charged product zone. This separation from the matrix constitutes an interesting and potentially beneficial as-

pect of EOF-pumped FIA, namely removal of matrix interferences.

The requirement for the maximum sample throughput condition is that the product zone from successively injected samples are just at the edge of the matrix zone from the neighboring sample. To assess the situation quantitatively, we need also to consider the following.

(a) Referring to Fig. 1, the voltage drop across capillary C1, which serves merely to connect the valve to the source vial, is not germane. In practice, this capillary is of much larger bore than the reaction conduit C2 and the voltage drop across C1 is therefore much smaller. We shall assume that this can be neglected in comparison to the voltage drop across C2, the latter is assumed to be equal to the total applied voltage V.

(b) Since the internal channel inside the valve is short and wide, we assume that there is very little voltage drop across this as well. Movement of the sample matrix and sample constituents through this channel thus occurs primarily by electroosmotic flow generated exterior to the valve that acts as a pump. We assume that because of the low electric field, any electrophoretic movement is small and can be neglected.

Various scenarios can be constructed as to the sign of the charge of the analyte and the product. The following two examples are illustrative, others can be evaluated in a similar manner.

If we consider the case of a positively charged analyte species reacting with an uncharged reagent to form a positively charged product (e.g., Fe^{2+} reacting with 1,10-phenanthroline to form orange Fe(o-phen)$_3^{2+}$), electroosmotic and electrophoretic flows are concurrent. The leading edge of the sample zone in the valve contacts the reagent zone ahead and forms the product; the leading edge of the analyte does not therefore travel through the injection loop. The velocity ν is given by

$$\nu = (\mu_{eo} + \mu_{ep})E \tag{1}$$

where μ_{eo} is the electroosmotic mobility, μ_{ep} is the electrophoretic mobility of the product and E is the applied field strengths:

$$E = V/L \tag{2}$$

where V is the total applied voltage and L is the length of capillary C2 from the valve to the point of detection. The time t taken for the leading edge of the product zone to reach the detector is therefore

$$t = L/\nu \tag{3}$$

In the present situation, the product zone precedes the sample matrix. The rear edge of the matrix zone moves through the entire valve channel and thus the time t' for this rear edge to reach the detector is

$$t' = (L + L_s)/\nu_{eo} \tag{4}$$

where L_s is the length the sample matrix occupies in the capillary:

$$L_s = 4V_{inj}/\pi d^2 \tag{5}$$

where V_{inj} is the injection volume and d is the diameter of the capillary and ν_{eo} is the electroosmotic flow velocity

$$\nu_{eo} = \mu_{eo} \cdot E \tag{6}$$

The temporal width w of the entire product and the matrix zone is therefore

$$w = t' - t \tag{7}$$

and the maximum sampling frequency f is given by

$$f = 1/w \tag{8}$$

or in expanded form:

$$f = \mu_{eo}(\mu_{eo} + \mu_{ep})E/\left(L_s(\mu_{eo} + \mu_{ep}) + L\mu_{eo}\right) \tag{9}$$

For a negatively charged product (e.g., the determination of Bi^{3+} as yellow BiI_4^- upon reaction with I^-), the product zone will trail behind the sample matrix. The product zone moves in the capillary with a net velocity ν_{net} that is governed by the difference of the electroosmotic and electrophoretic mobilities:

$$\nu_{net} = (\mu_{eo} - \mu_{ep})E \tag{10}$$

within the valve channel electrophoretic movement is small, the liquid moves by electroosmotic pumping exerted by the capillary ahead. The total time t'' taken by the rear of the product zone to reach the detector is

$$t'' = L_s/\nu_{eo} + L/\nu_{net} \quad (11)$$

The front edge of the sample matrix zone reaches the detector in a time t''':

$$t''' = L/\nu_{eo} \quad (12)$$

and the sampling frequency f_a in the case of an anionic product is given by

$$f_a = 1/(t'' - t''') = (\mu_{eo} - \mu_{ep})\mu_{ep}E / \left(L_s(\mu_{eo} - \mu_{ep}) + L\mu_{ep}\right) \quad (13)$$

From Eqn. 9 or 13 the following conclusions can be drawn:

(1) The maximum permissible sample frequency is directly related to the electric field strength.
(2) The denominator contains both L_s and L terms. Depending on whichever one is the major contributor, a reduction of L_s or L can increase sample throughput. (However, a reduction in L is only practical if reaction time is not a consideration.)
(3) If L_s was the dominant term, for any fixed value of V_{inj}, the sample throughput can be increased by increasing the diameter of the capillary since this decreases the width of the product zone.
(4) If for a positively charged product

$$(\mu_{eo} + \mu_{ep})L_s \simeq \mu_{ep}L \quad (14a)$$

or for a negatively charged product

$$(\mu_{eo} - \mu_{ep})L_s \simeq \mu_{ep}L \quad (14b)$$

either Eqn. 9 or 13 approximate to a common form:

$$f_{max} = \mu_{eo}E/2L_s \quad (15)$$

Note that if the product is neutral (the reagent cannot be neutral under such a condition, there will be no reaction), there will essentially be no separation between the product and the sample matrix and the maximum sample throughput in this case is twice that given by Eqn. 15.

EXPERIMENTAL

Equipment and reagents

The experimental system has been previously described [1,5]. The notable exception is valve V in Fig. 1. This type of internal loop valves has previously been available in a metallic version. The manufacturer has made available for us an electropneumatically actuated nonmetallic version (Kel-F body, PTFE rotor, ACI4WTFKF.01, Valco Instruments, Houston, TX) with a 100-nl injection volume. (Smaller loop versions with 60-nl injection volumes or a choice of both 60 nl/100 nl injection volumes on the same rotor have since become available).

The Fe^{2+}–*o*-phenanthroline reaction was chosen as a test case. Ferrous sulfate (0.5 mM), with 0.1 mM hydrazine sulfate as a preservative, was used as the sample. The carrier electrolyte was 10 mM NBu_4ClO_4, 25 mM 1,10-phenanthroline and 5 mM 2-[bis-(2-hydroxyethyl)aminoethane sulfonic acid], adjusted to pH 7.3 with strong acid/base.

The inlet of capillary C1 (8 cm × 250 μm i.d., 375 μm o.d.) is connected to the vial containing the running electrolyte and the other end connects to the valve. Capillary C2, constituting the reaction conduit, was 75 μm in i.d. and 375 μm in o.d. The optical window in the capillary was created in the conventional fashion, by removing ~ 10 mm of the polyimide coating with hot conc. H_2SO_4. Physical dimensions of the valve and the detector constrain the minimum length of capillary C2 (from valve V to the point of detection) to be 6 cm. Experiments were conducted with C2 lengths in the range 6–25 cm. The length of the capillary between the detection point and vial B is irrelevant except for the voltage drop it represents and varied in different experiments. To avoid the issue of differing voltage drops in this segment, results are presented in terms of the field strength E on C2.

The exact injection volume was determined by repeated injection of a 1.0 mM bromthymol blue solution into a 5-ml volumetric flask, dilution and absorbance measurement. The measured injection volume, 101 ± 5.5 nl, corresponds well to the nominal value stated by the manufacturer and

corresponds to an L_s value of 22.6 mm for a 75-μm capillary.

RESULTS AND DISCUSSION

Characteristic of system output

Typical system output is shown in Fig. 2. The typical reproducibility of peak heights in successive injection is ~ 1.5% in relative standard deviation – this is a significant improvement over automated hydrostatic or electrokinetic injection methods, testifying to the benefits of valve injection. In Fig. 2, the small peaks correspond to the sample matrix. If the sample is prepared in the carrier electrolyte, these peaks disappear but this does not constitute a realistic application.

Maximum attainable sampling frequency in any analytical system is a figure that is largely defined on arbitrarily chosen criteria. In most of the FIA literature, the throughput is typically computed based on a 1% carryover from sample to sample, as suggested by Ruzicka and Hansen [6]. In the present case, there is a more direct means to judge the maximum permissible sampling rate. Because of minor differences in EOF from run to run, when the analyte peak and the adjacent matrix peak just begin to overlap, there is a marked increase in the observed standard deviation of the analyte signal. This is illustrated in Fig. 3. In the present experiments we decreased sample injection intervals in 10 s steps until the abrupt increase in standard deviation was observed. The sampling frequency just prior to this was taken as the maximum permissible sample throughput.

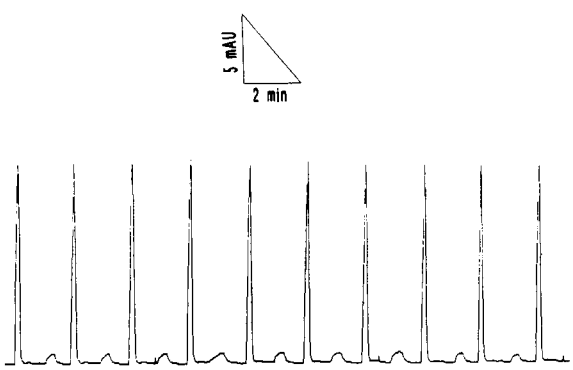

Fig. 2. Typical system output. Fe^{2+}–1,10-phenathraline reaction sytem, $\lambda = 508$ nm, $L = 600$ mm, $E = 28.5$ V/mm.

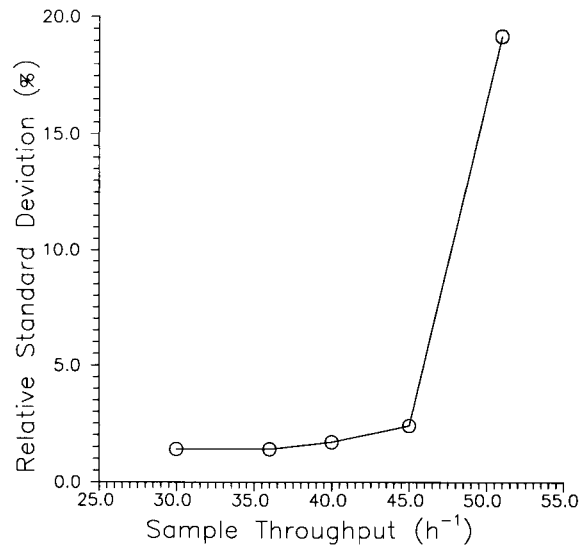

Fig. 3. Relative standard deviation of analyte signal as a function of sampling frequency; experimental conditions as in Fig. 2.

Maximum sample throughput measured in this fashion is depicted in Fig. 4, as a function of the electric field strength. The solid line is computed

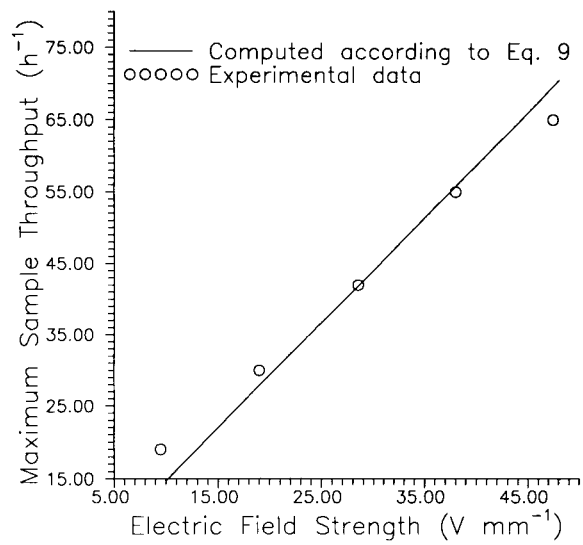

Fig. 4. Maximum sample throughput as a function of applied field strength, $L = 60$ mm.

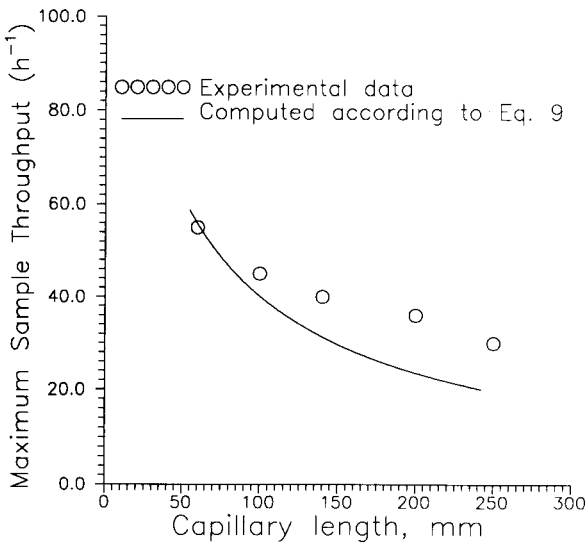

Fig. 5. Maximum sample throughput as a function of reaction capillary length, $E = 38$ V/mm.

from Eqn. 9 ($L = 60$ mm; $L_s = 22.6$ mm; $\mu_{eo} = 1.34$ mm^2 min^{-1} V^{-1}, computed from the migration time of the neutral matrix peak; $\mu_{ep} = 1.16$ mm^2 min^{-1} V^{-1}, computed from the migration time of the analyte peak). The agreement with the experimental points is considered good. The observed deviation, i.e., greater than predicted throughput at low applied field strengths and lower than predicted throughput at high applied field strengths can be rationalized as follows.

The theoretical treatment assumes for simplicity that the analyte moves evenly inside and outside the sample zone. The uncomplexed Fe^{2+} has a much greater electrophoretic mobility than the complexed cation. Further, the sample is much more dilute than the carrier and consequently the electric field strength across the sample zone is significantly higher, resulting in stacking of the analyte at the front edge of the sample zone [7].

At low applied field strengths, the migration time is longer and the diffusion of the carrier reagent into the matrix zone perceptibly reduces the effective value of L_s, the "non-reagent zone". Since the maximum sampling frequency is inversely related to L_s, the use of the nominal value underpredicts maximum throughput. Conversely, the finite zone width of the analyte signal becomes a significant factor at high applied field strengths to reduce sample throughput.

Figure 5 shows the maximum sample throughput at constant field strength (38 V/mm) as a function of the capillary length L. The results are qualitatively in accord with the expectations – the quantitative departure at higher field strengths is due to the finite zone width.

The theoretically predicted relationship of the maximum attainable sampling frequency directly to the field strength and inversely to the capillary

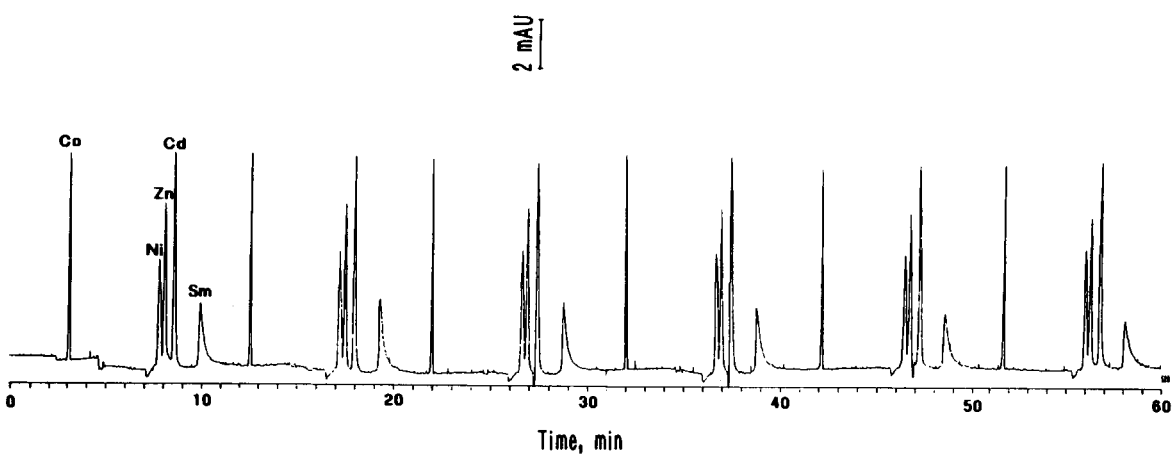

Fig. 6. Multiple analyte determination in a FIA electrophoresis system. Six repeated injections, $\lambda = 520$ nm. 50 μm × 800 mm capillary, hydrostatic injection (10 s at $\Delta h = 10.5$ cm). Concentrations Sm: 2 mM, all other metals: 1 mM.

length is thus experimentally confirmed. Changing the diameter of the capillary did afford an increase in sampling throughput. However, this was relatively minor since the sampling volume was not the dominant term. An increased diameter of the capillary conduit degraded reproducibility as well.

To match L_s and L (Eqn. 14a), a length of 49 mm would have been required for L – this was precluded by the physical dimensions of our valve and detector. The point of note, however, is that the use of the shortest permissible capillary length (both from the standpoints of physical limitations and necessary reaction time) is beneficial not only for increasing sample throughput but also for minimizing the magnitude of the applied voltage necessary. Figure 4 shows that if a sampling frequency of 20 h^{-1} is acceptable, the use of $L = 60$ mm and allowing for small lengths of capillaries before the valve and after the detector will require a total applied voltage substantially less than 1000 V. It should also be borne in mind that the choice of the present chemical scheme, specifically the near-neutral pH, leads to relative low μ_{eo} values and thus limits sampling frequency. Relative to the value of 1.34 $mm^2\ V^{-1}\ min^{-1}$, if μ_{eo} was, e.g., 5.77 $mm^2\ V^{-1}\ min^{-1}$ (as obtained with a 2 mM borate electrolyte, μ_{eo} computed from the data cited in Ref. 5), Eqn. 14a predicts a maximum sample throughput in excess of 225 samples h^{-1} relative to $\sim 70\ h^{-1}$ observed under the present conditions.

Finally, the considerations in the present paper are only germane to situations where a multitude of temporally separated responses is not generated from the single injection of a multiconstituent sample. In a case such as that shown in Fig. 6, where flow-injection is accompanied by an electrophoretic separation, the attainable sample throughput is clearly controlled by the migration time of the last peak to elute. These systems may obviously be beneficial in some applications. However, arrangements where separation is deliberately not carried out and EOF is still used for pumping are also attractive in their own right and will be presented in a future publication.

REFERENCES

1 S. Liu and P.K. Dasgupta, Anal. Chim. Acta, 268 (1992) 1.
2 S.F.Y. Li, Capillary Electrophoresis, Elsevier, New York, 1992.
3 W.S. Gardner and J.M. Malczyk, Anal. Chem., 55 (1983) 465.
4 T. Tsuda, T. Mizuno and J. Akiyama, Anal. Chem., 59 (1987) 799.
5 S. Liu and P.K. Dasgupta, Anal. Chim. Acta, 283 (1993) 747.
6 J. Ruzicka and E.H. Hansen, Flow Injection Analysis, Wiley, New York, 2nd edn., 1988, p. 93.
7 R.-L. Chien and D.S. Burgi, Anal. Chem., 64 (1992) 489A.

Analytica Chimica Acta, 283 (1993) 747–753
Elsevier Science Publishers B.V., Amsterdam

A simple means to increase absorbance detection sensitivity in capillary zone electrophoresis

Shaorong Liu and Purnendu K. Dasgupta

Department of Chemistry and Biochemistry, Texas Tech University, Lubbock, TX 79409-1061 (USA)

(Received 18th May 1993; revised manuscript received 18th June 1993)

Abstract

Up to a threefold gain in sensitivity without loss of separation efficiency can be achieved by the simple expedient of connecting a larger diameter capillary at the measurement point. This is unique to electroosmotically pumped systems. Theoretical considerations are outlined and experimental verification is presented. With measurement performed by presently available commercial absorbance detectors designed for on-column detection, the gain in detectabilities can be very substantial when capillaries smaller than 75 μm in bore are used for separation.

Keywords: Electrophoresis; Capillary analysis; Capillary electrophoresis

The interest in capillary format analysis techniques has been on a steady rise for some time now. In particular, capillary zone electrophoresis (CZE) has emerged as a powerful separation technique for the analysis of a wide variety of complex mixtures [1–3]. Most CZE separations are performed in fused-silica capillaries with internal diameters of less than 100 μm. To achieve sensitive optical detection, laser-based fluorescence or thermooptical absorbance measurements are widely used in research laboratories [4]. However, to become routine, these approaches require the advent of affordable lasers tunable into the UV. With UV–visible absorbance measurement across the radial path using noncoherent light sources, the most common detection technique in routine use, small diameter capillaries also mean limited detection sensitivity because of the short optical path length available.

Correspondence to: P.K. Dasgupta, Department of Chemistry and Biochemistry, Texas Tech University, Lubbock, TX 79409-1061 (USA).

Z-path capillary cells with light path lengths ranging from 3 to 20 mm have become commercially available and are typically available integrally connected to the separation capillary. Although large sensitivity gains can be realized [5], the cells are difficult to fabricate and are expensive. There can also be a significant loss of the number of theoretical plates. In another approach, Tsuda et al. [6] demonstrated the feasibility of using rectangular glass capillaries. Using the longer dimension of the rectangular cross section as the optical path length, detection sensitivity could be markedly increased. In our laboratory, we have also used these capillaries successfully in a similar manner. However, they are very fragile and are consequently difficult to use. Moreover, they are generally available only in glass and wavelengths less than 300 nm cannot be utilized. When and if polyimide coated silica capillaries of this type become easily available, it would be attractive to use them in for situations where enhanced detection sensitivity is desired.

Multiple reflections to increase the optical path length [7] is practical only with laser-based sources

because of the need to focus the probe beam to very small dimensions. In macroscale systems, Dasgupta and Rhee [8] showed that a nonlinear absorbance gain is possible if the absorbance measurement cell is placed between two partially reflecting mirrors (i.e., the cell is within an etalon). We attempted to adapt this concept to capillary systems where one (radial) half of a capillary was provided with a full mirror and the other half with a partially reflecting mirror. Light from a conventional source was introduced into the capillary through a pinhole on the full-mirror side. Although some absorbance gain was realized, this cell was also difficult to fabricate and use. The poor light throughput increased detector noise and thus resulted in only limited gain in detection limits [9].

It is interesting that potentially the most obvious approach to increase the optical pathlength, namely to increase the bore of the conduit at the point of measurement, has not been much pursued, likely due to concerns with flow streamlining, leading to development of stagnant zones and consequent loss of separation efficiency. During the progress of this work, one instrument manufacturer has introduced capillaries with a bubble blown at the measurement point that increase the optical pathlength by a factor of three, without measurable loss of system efficiency [10]. In the present communication, we show that the simple expedient of connecting a larger bore capillary at the measurement point can also be used to achieve a modest gain in measurement sensitivity without significant loss of system efficiency. Because of the nature of electroosmotic flow, flow streamlining at the junction is inhibited.

PRINCIPLES

If capillaries of two different inner diameters are subjected to the same electrical field strength, the electroosmotic flow rate in the larger capillary is greater. However, when two capillaries of different inner diameters filled with the same solution are serially connected and a voltage is impressed across the ensemble, the electric field strengths in the two segments differ. The field is lower in the larger diameter capillary due to the smaller electrical resistance per unit length. It is easily shown that

$$E_i = V_i/L_i = V_{tot}/(A_iC) \quad (1)$$

where E_i is the electric field strength on segment i resulting from a voltage V_i being impressed across a length L_i and A_i is the cross sectional area of the segment;

$$V_{tot} = \Sigma V_i \quad (2)$$

and

$$C = \Sigma L_i/A_i \quad (3)$$

The electroosmotic mobility, μ_{eo}, is given by [11]

$$\mu_{eo} = \xi/(4\pi\eta) \quad (4)$$

where ξ is the zeta potential and η is the viscosity constant. With capillaries of commonly used inner diameters (25–75 μm), the change in radius of curvature should not have a marked effect on the zeta potential. Since the serially connected capillaries are composed of the same material and contains the same solution, electroosmotic mobilities should be the same. The intrinsic electroosmotic volumetric flow rate of each segment, F_i, is thence

$$F_i = \mu_{eo}E_iA_i \quad (5)$$

Using the expression of E_i from Eqn. 1,

$$F_i = \mu_{eo}V_{tot}/C \quad (6)$$

This indicates that the intrinsic electroosmotic flow (EOF) in the connected components of the systems are the same. Of course in a serially connected system, in reality there can be only one flow rate. The important point of note is that a true plug flow, as vital to CZE, can be maintained only if the intrinsic EOF in the different components are the same. Minor differences in the surfaces of the connected capillaries as well as any difference in temperature between them can affect the constancy of the EOF in the connected components. However, our experience indicates that it is not a major problem – the intrinsic EOF values can also be experimentally verified.

With plug flow maintained, as an analyte zone passes from a narrower to a wider capillary, the length of the zone decreases in direct relationship to the cross sectional area and the flow velocity decreases in the same proportion. As long as the detector aperture is relatively small compared to the zone length (which is typically the case), the transit time of the analyte zone through the detector and thus the peak width remains unchanged. Meanwhile the optical pathlength increases by a factor given by the ratio of the radial dimensions of the two capillaries resulting in a proportional sensitivity increase.

EXPERIMENTAL

Equipment and reagents

The capillary electrophoresis apparatus was homemade but fully automated, consisting of a CZE 1000 power supply (Spellman High Voltage, Plainview, NY), a pneumatically actuated lift/lower/transport system that allows the capillary to be lifted from a buffer station, transported to a rotatable sample turret (of adjustable height), dipped in an individual sample vial for any preset period of time and then transferred back to the buffer station, also on a rotatable turret containing individual buffer vials. In some experiments, a SRS PS350 high voltage power supply (Stanford Research Systems, Sunnyvale, CA), capable of more accurate voltage regulation at lower voltages than the Spellman unit, was used. All instrument functions were controlled by a programmable microcontroller (LS-100, Minarik Electric, Denver, CO). The detector used was a Model 206 PHD (Linear Instruments/Spectra-Physics) equipped with a ball lens for use with capillaries. This type of focusing optics is preferred for small radial path capillary detection systems [12]. Nevertheless, stray light rejection is poor, especially for very small bore capillaries, unless further measures are taken to reduce the optical aperture. The detector aperture was covered with two layers of (adhesive-backed) aluminum tape. The first layer consists of two pieces of tape separated by ~ 250 μm with the aperture perpendicular to the long axis of the capillary – this defines the width of the zone monitored. The second layer, put atop the first, consists of two pieces of tape separated by ~ 75 μm with the aperture parallel to the long axis of the capillary – this slit reduces excess stray light. Vendor supplied software and a 80386 class personal computer were used for data acquisition.

Except as stated, hydrostatic injection (10 s, $\Delta h = 10.5$ cm) was used. The sample solution consisted of 40 μM bromthymol blue (BTB), 50 μM bromcresol green (BCG) and 150 μM thymol blue (TB), singly or in combination in ~ 0.4 mM $Na_2B_4O_7$. The stock dye solution was made in ethanol and the final sample contained $\sim 2\%$ ethanol. The running electrolyte was 4 mM $Na_2B_4O_7$ + 5 mM sodium anthraquinone-2-sulfonate; the latter large anion is incorporated in the electrolyte to improve peak symmetry [13,14].

Capillary connections

All capillaries used were polyimide coated fused silica (Polymicro Technologies, Phoenix, AZ). Typically a 50-cm separation capillary was connected to a 15-cm long capillary of larger diameter. In all cases, the outer diameter of the two capillaries were approximately equal (375 μm). A butt joint was made using a 5-mm length of a hand-drawn glass capillary (~ 380 μm i.d. $\times$ 600 μm o.d.) as a sleeve and securing with epoxy adhesive. The arrangement is shown in Fig. 1. A conventional ceramic capillary scoring device is sufficient to cut the capillaries without further need for finishing the surface. No special effort was made to align the capillaries beyond that

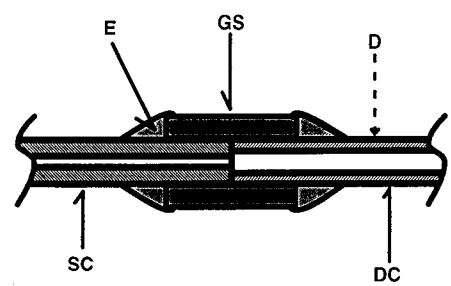

Fig. 1. Connection of capillaries: (SC) separation capillary; (GS) glass sleeve; (E) epoxy adhesive; (DC) detection capillary; (D) detector location.

automatically provided by the sleeve of the butt joint. It may be noted that because the electric field extends only along the lumen of the joint, flow should largely be self-aligning [15].

In all cases, a total voltage of 15 kV was impressed across the capillary ensemble. The detector was positioned immediately before and after the joint to determine the increase in sensitivity. Plate numbers were calculated according to the literature [1].

RESULTS AND DISCUSSION

Constancy of intrinsic electroosmotic flow in a serially connected system

If a 75 μm i.d., 50 cm long capillary is connected to a 150 μm i.d., 15 cm long capillary and 10.75 kV is impressed across the assembly, Eqn. 1 suggests that 10 kV will appear across the first capillary and 0.75 kV across the second. The gravimetrically measured flow rate for such a system with a 2 mM $Na_2B_4O_7$ electrolyte was 510 ± 4.5 nl/min ($n = 3$). When 10.0 and 0.75 kV were respectively impressed directly across the first and second capillary on an individual basis with the same 2 mM borate electrolyte the respective flow rates were measured to be 510 ± 5.1 and 507 ± 4.2 nl/min, proving the hypothesis of constant intrinsic EOF in this serially connected system.

Detector behavior with capillaries of different dimensions

Making absorbance measurements through a small diameter capillary requires a compromise between two different objectives – minimizing detector noise by maximizing light throughput, and minimizing stray light (light transmitted around the lumen of the capillary and the capillary itself). To achieve a small enough illuminated zone with a conventional light source, the more successful commercial detector designs typically use a ball lens or a fiber optic or both to couple the incident light to the capillary. In general, presently available commercial detectors are designed to work with a 75 μm i.d. $\times$ 375 μm o.d. capillary, stray light rejection and consequently sensitivity is degraded when these dimensions are smaller. An illustrative Beer's law plot is shown in Fig. 2 for the fiber optic/ball lens based detector used in this study – similar results have been observed with a fiber-optic based detector from another vendor. Note that without further reduction of the slits incorporated into the commercial detector, there is no discernible signal at all from the 25 μm i.d. capillary.

It should be further obvious from the data in Fig. 2 that because of the stray light effects, the gain in sensitivity in going from a capillary of $\leqslant 75$ μm bore to a larger capillary is actually more than that predicted by a simple ratio of the radial dimensions. Perhaps more importantly, the

TABLE 1

Senstivity gain and separation efficiency [a]

Capillary system [b]:	75/150		50/150		25/150 [c]	
Measurement position [d]:	S	L	S	L	S	L
Migration time (s)	389 ± 2	416 ± 2	371 ± 2	431 ± 2	e	580 ± 4
Half peak width (s)	3.03 ± 0.07	3.23 ± 0.08	2.81 ± 0.7	3.2 ± 0.5	e	5.57 ± 0.06
Number of plates (thousands)	92 ± 4	92 ± 5	97 ± 5	100 ± 4	e	60 ± 2
Absorbance, mAU [f]	10.4 ± 0.3	28.8 ± 1.3	1.2 ± 0.2	7.3 ± 0.3	e	0.22 ± 0.03

[a] Presented data ($n = 3$–6) are for BCG, as test sample measured at 620 nm with one standard deviation indicated as the uncertainty. [b] Internal diameters given in μm, outer diameters are 375 μm. Sensitivity gain with 150 μm o.d. capillaries are comparable but there are difficulties in rigidly positioning such capillaries in a detector, leading to greater measurement uncertainties. [c] Test sample is 80 μM BTB. [d] S = Signal measured on small capillary. L = signal measured on large capillary. [e] Signal is not detectable. [f] Note that with identical hydrostatic injection conditions, introduced sample volume decreases with capillary diameter.

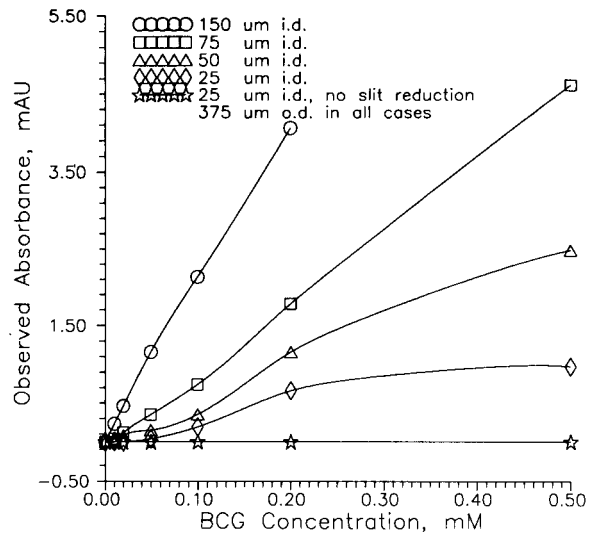

Fig. 2. Observed absorbance at 600 nm for different concentrations of bromcresol green on a ball-lens equipped commercial detector with reduced slit. Note that no response at all is observed for the 25 μm capillary without slit reduction.

improvement can be particularly marked for low concentration analytes in very small bore capillaries which show a significantly nonlinear response. In going from 25 μm bore capillaries to larger capillaries, typically there is also a modest decrease in noise and drift because of better light throughput; this further improves detectability.

Sensitivity gain and separation efficiency

Data are presented in Table 1 that show that when 75 or 50 μm i.d. capillaries are coupled to 150 μm i.d. capillaries, significant sensitivity gains are attained without measurable loss of efficiency. We have chosen not to present any fixed number for the gain in sensitivity – as previously stated, due to stray light effects, this value can be dependent on the absorbance level measured. Figure 3 shows the situation for a serially connected 75/150 μm capillary system. Note that although the base width of the peaks measured in larger capillary are slightly wider, these appear at longer migration times with essentially the same half-width. Figure 4 shows the results for a 25/150 μm coupled serially connected capillary system. In the latter situation, plate numbers are degraded relative to the other cases, but using the

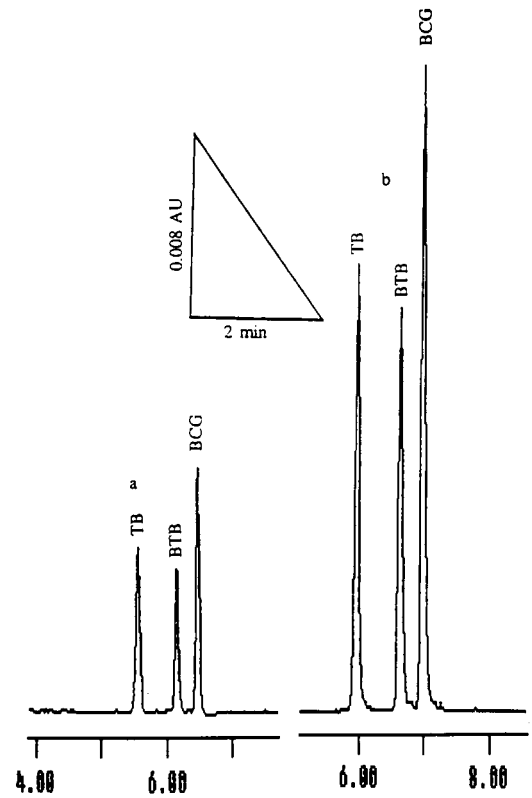

Fig. 3. Gain in sensitivity without loss of plates: (a) detection at 75 μm capillary, (b) detection at 150 μm capillary. The sample is a mixture of thymol blue, bromthymol blue and bromcresol green, see text for details.

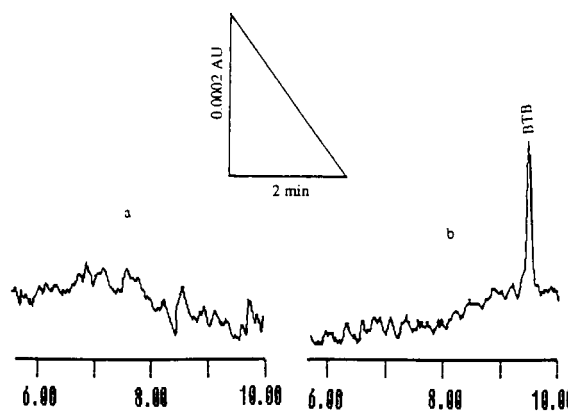

Fig. 4. Gain in detection limits with the present approach with very small diameter capillaries: (a) detection at 25 μm capillary, (b) detection at 150 μm capillary. Sample is 40 μm bromthymol blue ($\Delta h = 10.5$ cm, 10 s).

25 μm capillary as such, no detection was possible. When a substantially larger sample amount was introduced using electrokinetic injection (5 s at 15 kV), it was possible to detect the analyte on the 25 μm capillary (0.5 mAU) but the peak shape was obviously distorted (61 000 ± 7000 plates) and in this case detection on the larger capillary showed a large and very distorted peak (5.9 mAU, ~ 30 000 plates).

Plate loss with the present approach apparently becomes significant when the increase in bore exceeds ~ 3. We observe a 50% plate loss in going from a 75 μm to a 250 μm i.d. capillary as well. In this case, the observed sensitivity gain (3.39) was identical within experimental uncertainty to the diameter ratio (3.33). Part of this broadening can be attributed to the fact that the detector slitwidth may be insufficiently narrow to accurately follow a very narrow band in the larger capillary. The data in the second column of Table 1 indicates a half width of 3.9 mm in the 75 μm capillary. In a 250 μm capillary, in the absence of additional dispersion this half width would decrease to 350 μm. However, the observed loss is not due to an inadequate slitwidth alone. The peak asymmetry (at 10% peak height) increases by a factor of ~ 1.8 between detection at 75 μm and that at 250 μm. This type of peak tailing is strongly indicative of some other source of dispersion. We believe that this arises primarily from the distortion of the electric field at the joint where the lumen abruptly changes. Note that neither plate loss nor any increase in band asymmetry was measurable in going from a 75 μm to a 150 μm capillary. The use of detection capillaries more than three times in diameter than the principal conduit does not appear to be very practical for CZE. However, for capillary analysis systems where the above degree of plate loss is tolerable, such as capillary format EOF pumped flow injection systems [14,16], this approach may still be attractive for improving detection sensitivity.

Plate loss in systems without electroosmotic flow

The central theme herein is that dispersion in a EOF governed serially connected system is inhibited because of the constancy of intrinsic EOF in the components of the system. It behooves us then to prove that in a system where flow does not occur by electroosmotic means, large plate losses would be observed. As the data in Table 1 shows, there is no discernible plate loss in going from a 75 μm to a 150 μm bore capillary in an EOF system. Of course, it is impossible to obtain bands as narrow as those in an EOF system in any conventionally pumped systems and therefore "plate counts" are going to be much lower even in the narrower capillary to begin with. We designed an experiment in which a 75 μm × 6 cm capillary was connected to a 150 μm × 9 cm capillary and the detector was positioned on either side of the joint in turn. The free terminus of the 75 μm × 6 cm capillary was dipped in either a vial containing BCG or 2 mM $Na_2B_4O_7$, the carrier. The other end of the 150 μm capillary was connected to a 75 μm × 60 cm capillary, the latter was lowered for sample introduction (Δh = 2.5 cm, 10 s) or fluid flow in general. Even with the small volume of sample introduced (~ 4 × smaller than the other experiments described in this paper) and the relatively small distance allowed for migration, the number of plates observed in the small capillary was quite low, 1420 ± 160. There was more than a factor of three loss in plate counts of this already broad band at the large capillary (plate count 450 ± 70).

Finally, in what we believe to be a conclusive experiment, with a 75/150 μm serially connected capillary system, the injected dye was moved by EOF pumping to the joint end of the smaller capillary. The expected relatively large plate counts, 80 000 ± 5000 were observed. Now the band was pumped only a few mm further by conventional hydrostatic means. The plate count, immediately after it entered the larger capillary, was observed to be only 13 700 ± 580 (peak widths and travel times were both converted to volume units for consistency). Therefore, the present approach is uniquely suited for electroosmotically driven systems.

In summary, approximately a threefold gain in sensitivity can be achieved in most CZE absorbance detection applications through the simple expedient of connecting a large capillary at the measurement point, without significant plate loss. Note that a length of capillary is obligatorily

needed to project past the detection point (to dip in a destination vial for electrode connections) and the field dissipated on this segment contributes nothing to separation. The arrangement proposed herein may be superior to a blown-in bubble in this respect because less voltage is dissipated past the detection point with a larger capillary. For a large increase in bore, it would appear that an ideal situation may be where a small capillary ends in a larger bore through a taper, to minimize distortion of the electric field at the joint.

REFERENCES

1 J.W. Jorgenson and K.D. Lukacs, Anal. Chem., 53 (1981) 1298.
2 J.W. Jorgenson and K.D. Lukacs, Science, 222 (1983) 266.
3 A.G. Ewing, X. Huang, S.L. Pentony and R.N. Zare, Science, 242 (1988) 224.
4 W.G. Kuhr and C.A. Monnig, Anal. Chem., 64 (1992) 389R.
5 J.P. Chervet, M. Ursem, J.P. Salzmann and R.W. Vannoort, J. High Resolut. Chromatogr. Chromatogr. Commun., 12 (1989) 278.
6 T. Tsuda, J.V. Sweedler and R.N. Zare, Anal. Chem., 62 (1990) 2149.
7 T. Wang, J.H. Aiken, C.W. Huie and R.A. Hartwick, Anal. Chem., 63 (1991) 1372.
8 P.K. Dasgupta and J.S. Rhee, Anal. Chem., 59 (1987) 783.
9 H.J. Zheng and P.K. Dasgupta, unpublished work, Texas Tech University, 1992.
10 Hewlett Packard Company, Peak, 2 (1993) 11.
11 A.W. Adamson, Physical Chemistry of Surfaces, Wiley, New York, 1982, pp. 198–203.
12 G.J.M. Bruin, G. Slegmann, A.C. Van Asten, X. Xu, J.C. Kraak and H. Poppe, J. Chromatogr., 559 (1991) 163.
13 F.E.P. Mikkers, F.M. Everaers and Th.P.E.M. Verheggen, J. Chromatogr., 169 (1979) 11.
14 S. Liu and P.K. Dasgupta, Anal. Chim. Acta, 268 (1992) 1.
15 M. Albin, R. Weinberger, E. Sapp and S. Moring, Anal. Chem., 63 (1991) 417.
16 S. Liu and P.K. Dasgupta, Anal. Chim. Acta, 283 (1993) 739.

Analytica Chimica Acta, 283 (1993) 755–761
Elsevier Science Publishers B.V., Amsterdam

Comparative studies of the determination of cyanide at low concentration levels in waste waters

P.C. do Nascimento [1] and G. Schwedt

Institut für Anorganische und Analytische Chemie, Technische Universität Clausthal, Paul-Ernst-Str. 4, 38678 Clausthal-Zellerfeld (Germany)

(Received 13th January 1993; revised manuscript received 29th June 1993)

Abstract

Different methods for the determination of cyanide in waste waters were compared. After formation of the stable tetracyanonickelate(II) anion complex spectrophotometric, polarographic and atomic absorption spectrometric methods were used as off-line systems. Potentiometric determination with a flow-injection system was used on-line. Criteria for the comparison of methods were the limit of detection, linear range, precision, recovery and analysis time. The on-line analysis provided the simplest and most rapid method with a limit of detection of 60 $\mu g\, l^{-1}$. All the methods used showed a cyanide recovery in waste waters in the range 90–104%. The influence of some interfering ions was also tested.

Keywords: Atomic absorption spectrometry; Flow injection; Polarography; Potentiometry; UV–Visible spectrophotometry; Cyanide; Waters

The high toxicity of cyanide and its widespread industrial applications make it necessary to determine it at very low concentration levels [1]. A number of methods for the determination of cyanide ions have been proposed for various applications, but comparative studies are relatively rare. After a distillation step, cyanide can be determined by spectrophotometry [2–6], fluorimetry [7–9] or electrochemical methods [10–15]. The highest allowed cyanide concentrations in waste waters internationally accepted [16] are in the sub-mg l^{-1} range. The aim of this work was to develop and to compare methods for cyanide determination in water, suitable for routine measurements.

Correspondence to: G. Schwedt, Institut für Anorganische und Analytische Chemie, Technische Universität Clausthal, Paul-Ernst-Str. 4, 38678 Clausthal-Zellerfeld (Germany).
[1] Present address: UFSM (Campus), Caixa Postal 5051, Santa Maria 97119 911, RS-Brazil.

Different methods were used for cyanide determination. For off-line methods the rapid formation of a stable nickel–cyano complex [tetracyanonickelate(II) anion] in ammoniacal solution was used. This anion has a characteristic ultraviolet spectrum [16] and therefore cyanide could be determined spectrophotometrically. Polarographic determination was based on the fact that the nickel–cyano complex is active in aqueous solution at −1350 mV (vs. Ag/AgCl). After its extraction into an organic phase, indirect atomic absorption spectrometric (AAS) determination of cyanide was possible. As an on-line system, flow-injection analysis (FIA) with potentiometric detection without complex formation was used.

EXPERIMENTAL

Analytical-reagent grade chemicals were used without further purification. Working standard

cyanide solution was prepared from a potassium cyanide stock standard solution (100 mg l^{-1} CN^- in 0.1 mol l^{-1} NaOH), standardized by argentimetric titration with dithizone as indicator [17]. Solutions of 2×10^{-3} mol l^{-1} $NiCl_2$ (pH 9) and 0.2 mol l^{-1} NH_3/NH_4Cl were required for cyanide complex formation. For extraction of the nickel–cyano complex, a solution of 20 g l^{-1} tetrabutylammonium bromide (TBAB) in butanol was required.

Absorbance measurements were made with a Perkin–Elmer Lambda 5 spectrophotometer using 1-cm quartz cells. A PU 9200 atomic absorption spectrometer (Pye Unicam) was used at 232.0 nm (nickel lamp; lamp current 5.0 mA) in an air–acetylene flame (0.9 l min^{-1}) with a spectral bandpass of 0.2 nm and deuterium compensation.

Electrochemical measurements were performed with a Polarographie-Stand VA 663 and Polarecord E 506 (Metrohm) with a three-electrode arrangement (mercury dropping electrode, saturated silver/silver chloride electrode and glassy carbon electrode). The polarographic parameters used were drop size = 2, drop time = 0.8 s per drop, scan rate = 20 mV s^{-1}, current range = 2.5×10^{-10} A mm^{-1}, pulse amplitude = 50 mV, purge time = 2 min, equilibrium time = 15 s and sample volume for differential-pulse polarography (DPP) = 15 ml. On-line measurements were made with a FIAstar 5020 analyser coupled with a FIAstar 5025 ISE-meter and a FIAstar 5032 detector controller (Perstorp Analytical). A cyanide-sensitive electrode (Perstorp Analytical) and a saturated silver/silver chloride electrode were used. The flow-rates of the reagents for the on-line measurements were 1.2 ml min^{-1} for the carrier and electrolyte and 0.6 ml min^{-1} for the reference electrode.

RESULTS AND DISCUSSION

Quantitative extraction of the nickel–cyano complex into the butanolic phase was observed in the presence of TBAB, which forms an ion pair with the nickel–cyano complex at the required pH to ensure stability of the complex (pH > 4). For extraction of the complex, a shaking time of 40 s was sufficient. Extraction with apolar solvents such as chloroform, toluene, benzene, tetrachloromethane and hexane was not possible.

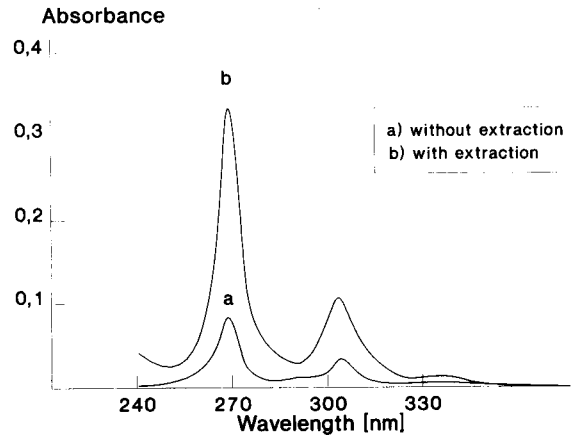

Fig. 1. Ultraviolet spectrum of $[Ni(CN)_4]^{2-}$ in (a) water and (b) butanol–TBAB solution recorded against the respective reagent blanks.

Absorption spectra

Fig. 1 shows the absorption spectra of the nickel–cyano complex in water and butanol–TBAB phases, recorded against the respective reagent blanks. The wavelength of maximum absorbance for both systems is 267 nm.

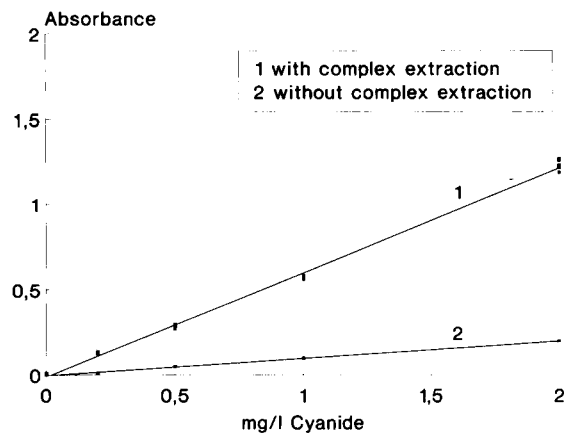

Fig. 2. Calibration graphs for the spectrophotometric determination of the nickel–cyano complex in (1) the organic and (2) the aqueous phase.

Beer's law for determinations in the aqueous and organic phases (Fig. 2) was obeyed over a wide range. Plot 1 (Fig. 2) shows the results obtained after the extraction procedure (butanolic phase) and represents replicate measurements ($n = 5$), whereas plot 2 shows the results obtained for the aqueous phase and represents single data points. The molar absorptivity of the nickel–cyano complex in the butanolic phase was about 16 000 whereas Scoggins [16] obtained 11 000 in aqueous phase.

AAS determinations

After the extraction of the nickel–cyano complex the nickel excess remained in the aqueous phase. Hence the nickel concentration in the organic phase was proportional to the total cyanide concentration and so an indirect determination of cyanide ions by means of AAS was feasible.

For indirect determination by means of flame AAS, aqueous nickel solutions (without cyanide) were submitted to the extraction procedure and the butanolic phase obtained was used as a blank solution to avoid transport interferences due to the different nebulizer efficiencies in the aqueous and organic phases. The standard and blank solutions were atomized directly in the spray chamber of the spectrometer.

Table 1 shows the absorbance of the cyanide solutions after extraction. The original cyanide concentration in the aqueous phase is given in the first column. The low absorbance of the blank solution [$c(CN^-) = 0.0$ mg l^{-1}] confirms the slight extraction of free nickel species.

TABLE 1

Cyanide determination by AAS after nickel–cyano-complex extraction

CN^- concentration (mg l^{-1})	Absorbance (mean, $n = 10$)
0.0	0.003 ± 0.002
0.2	0.044 ± 0.003
0.5	0.092 ± 0.002
1.0	0.177 ± 0.002
2.0	0.338 ± 0.002
4.0	0.618 ± 0.003

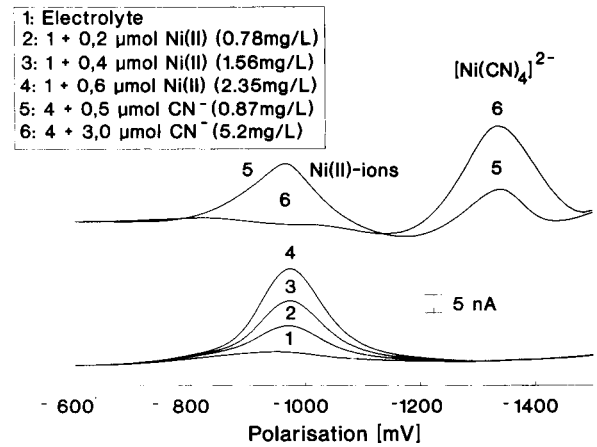

Fig. 3. Pulse polarographic waves (1–4) before and (5,6) after nickel–cyano complex formation.

Polarographic determinations

For the polarographic determination of cyanide ions, the behaviour of the nickel–ammonia complex in the presence of cyanide ions was investigated. In the absence of cyanide the reduction of nickel in ammoniacal solution occurs at −0.98 V (plots 1–4, Fig. 3), whereas in the presence of cyanide this signal decreases and a polarographic wave arises at −1.35 V (plots 5 and 6, Fig. 3). The height of this signal is proportional to the cyanide concentration and permits the determination of small amounts of cyanide in the range 100–2000 μg l^{-1} where the calibration graph is linear (Fig. 4).

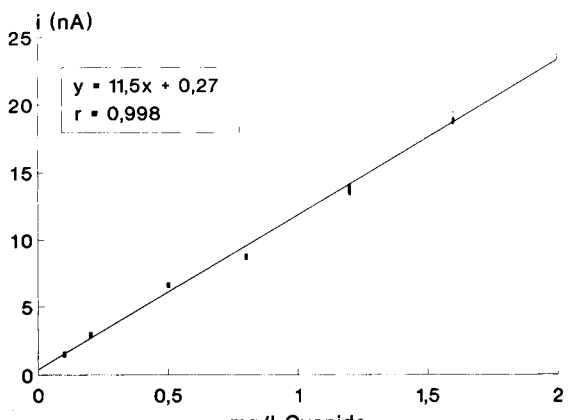

Fig. 4. Calibration graphs for the polarographic determination of cyanide after nickel–cyano complex formation.

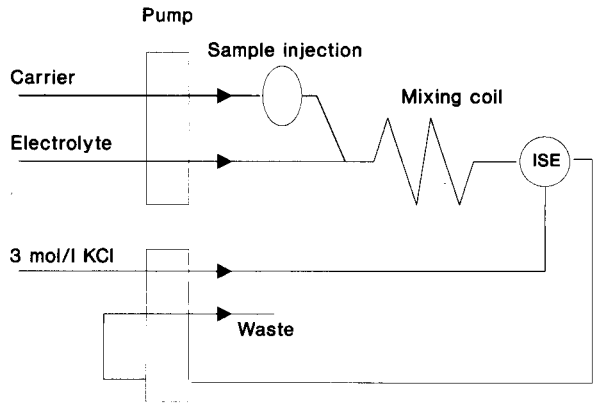

Fig. 5. Flow scheme for the on-line determination of cyanide.

In Fig. 3, range 0.01 mg l^{-1}, an excess of cyanide (relative to the nickel content) was added and so this peak height does not correspond to a linear calibration behaviour.

After extraction of the nickel–cyano complex into the butanolic phase, the the DPP determination of cyanide was not feasible.

On-line determinations

The arrangement in Fig. 5 was used for the on-line determination of cyanide with potentiometric detection. The electrolyte (0.01 mol l^{-1} NaOH–0.1 mol l^{-1} KNO_3, pH 11) ensures a suitable ionic strength and also the pH to keep the cyanide in the CN^- form. The reference electrode was in contact with a 3 mol l^{-1} KCl solution, which was pumped directly onto it (wall-jet configuration). The ion-selective electrode in this wall-jet configuration was also continuously in contact with a narrow jet, from which the sample streams to the sensitive surface.

Calibrations for the on-line determination of cyanide are shown in Fig. 6. The graphs are not linear in the concentration range studied but calibration is possible either in the linear interval or by means of a non-linear calibration procedure in the total concentration interval. The right-hand plot (Fig. 6) shows an approximately linear interval but with a preliminary addition of cyanide to the electrolyte to reduce the memory effect of the sensitive electrode. In this test 100 $\mu g\ l^{-1}$ cyanide was used as the original concentration in the electrolyte.

Although these electrodes respond to changes in concentration until a statistical limit of detection is reached [18], the measurements are usually limited to the linear region of response. The limit

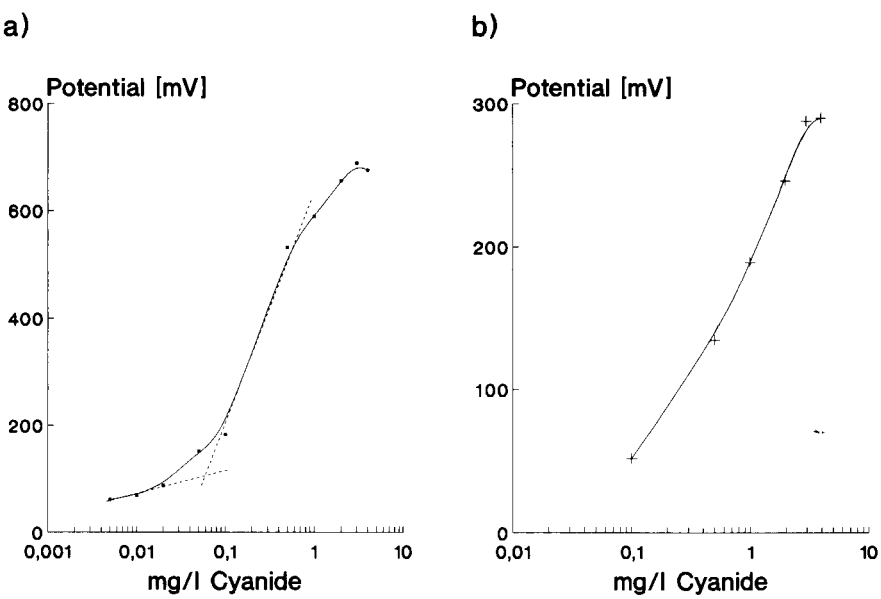

Fig. 6. Calibration of the cyanide determination by means of the FIA system with potentiometric detection. (a) Total concentration range; (b) linear range.

of detection depends on different factors for different electrodes. Midgley [18] pointed out that the detection limits for most electrodes extend to far lower concentrations than those of the linear or Nernstian response limit. Nevertheless, in this work, for the sake of practical convenience, a simple practical limit of detection may be considered. This practical limit of detection may be taken as the measured species concentration at the intersection point of the extrapolated linear segments of the calibration graphs [19]. The left-hand plot in Fig. 6 shows the calibration procedure used to calculate the practical limit of detection. The extrapolated intercept of the rough linear segments indicates the practical limit of detection on the abscissa.

Comparison of the methods

The different methods of cyanide determination were compared by means of the usual criteria of detection limit, relative standard deviation, linear correlation coefficient in calibration, analytical range of analysis, recovery of cyanide and duration of analysis, as shown in Tables 2 and 3.

The detection limits for the spectrophotometric and AAS determinations were calculated from the standard deviations of the blanks [20] for five determinations. For the polarographic measurements [21] the detection limit was calculated from the noise of the equipment at the maximum sensitivity (1.5×10^{-11} A mm^{-1}) during 3 min at -1.35 V and, for the flow-injection measurements, by graphical calculations [19].

The range of analysis was determined relative to the lowest concentration by means of the determination limit, L_q [20], taking into account that this limit can be determined with a fixed maximum relative standard deviation. For practical purpose it was considered that

$$L_q = \mu_{bl} + 10\sigma_{bl}$$

where μ_{bl} is the mean signal of the blank and σ_{bl} is the relative standard deviation, for the spectrophotometric, AAS and polarographic determinations. For the flow-injection determinations the determination limit was considered as the lowest concentration close to the graphically calculated limit of detection. The upper limit of concentration was not critical and it was taken approximately as the end of the linear calibration range.

The recovery of cyanide was tested for each method of analysis with waste water samples [22] after filtration with a microporous membrane (0.45 μm). Cyanide ions were determined by means of the various methods in waste water samples without cyanide addition. No signal was found and the samples, for practical purposes, were considered to be free from uncombined cyanide ions. The waste water samples were subsequently spiked with cyanide ions at levels ranging from 0.5 and 1.0 mg l^{-1} in the final samples.

TABLE 2

Statistical criteria for comparing different methods of cyanide determination [a]
(R.S.D. = relative standard deviation (n = 5–10); r = regression coefficient)

Method	L_d ($\mu g\ l^{-1}$)	R.S.D. (%)	r
Spectrophotometry	40	4.3–0.4	0.999
AAS	50	6.0–0.5	0.998
Polarography	50	6.0–0.8	0.998
FIA-ISE	60	8.4–2.4	0.995 [b]

[a] L_d = limit of detection. [b] See Fig. 6.

TABLE 3

Analytical criteria for comparing different methods of cyanide determination [a]

Method	A_r (mg l^{-1})	R (%)	A_d (min)
Spectrophotometry	0.1 –2.0	104	2.5
AAS	0.2 –4.0	98	1.0
Polarography	0.1 –2.0	95	2.0
FIA–ISE	0.05–4.0	90	0.5

[a] A_r = Analytical range of analysis; R = recovery of cyanide; A_d = analysis duration.

Interferences

Although the determination of cyanide in waste water samples often requires a previous separation step in order to remove interfering ions that are commonly present in such samples, here the proposed methods were studied without distilation steps to establish the direct effect of some ions on the recovery of cyanide. The results ob-

TABLE 4

Effect of diverse ions on the determination of cyanide as the nickel complex

Method	Foreign ion	Foreign ion concentration (mg l^{-1})	Cyanide concentration (mg l^{-1})	Recovery Mean (%)
Spectrophotometry	S^{2-}	10	1.0	> 150
	$S_2O_3^{2-}$	10	1.0	93
	SO_3^{2-}	10	1.0	90
	$H_2PO_4^-$	100	1.0	105
	NO_3^-	10	1.0	97
Polarography	S^{2-}	10	0.5	82
	SO_3^{2-}	25	0.5	92
	I^-	10	0.5	96
	Br^-	10	0.5	98
	SCN^-	10	0.5	95
	CO_3^{2-}	10	0.5	90
	$H_2PO_4^-$	4	0.5	106
AAS	S^{2-}	10	0.5	92
	$S_2O_3^{2-}$	10	0.5	100
	SO_3^{2-}	10	0.5	90
	$H_2PO_4^-$	100	0.5	92
	NO_3^-	10	0.5	92

tained for cyanide determination in presence of these ions are given in Table 4. Among the tested ions only sulphide gives a serious interference. However, cyanide and sulphide do not often occur in the same samples [23].

The interference of sulphide in the determination of cyanide in waste water was tested by means of the flow-injection system with regard to the effect of sulphide on the potentiometric cyanide signal. The electrode is equally sensitive to sulphide and cyanide ions and therefore the elimination of sulphide ions before the analysis is necessary.

Conclusions

This investigation has shown that the flow-injection system provides a very simple, rapid and sensitive method for direct cyanide determination. The indirect analysis after stabilization of cyanide as the nickel–cyano complex also showed advantages owing to the possibility of using particular analytical methods.

The criteria used for the comparison of the different methods indicated a similar sensitivity and cyanide recovery for the off-line and on-line methods, but the shorter analysis duration is an advantage of the on-line determination. Among the interfering ions tested only sulphide could not be tolerated at low levels.

REFERENCES

1 International Standards for Drinking Water, World Health Organization, Geneva, 1958.
2 N.P. Kelada, J. Water Pollut. Control. Fed., 61 (1989) 350.
3 S. Nagashima, Anal. Chem., 56 (1984) 1944.
4 G. Schöndorf and H. Engelhardt, Fresenius' Z. Anal. Chem., 333 (1989) 719.
5 E. Figuerola, A. Florido, M. Aguilar and J. de Pablo, Fresenius' Z. Anal. Chem., 331 (1988) 620.
6 S. Nagashima, Anal. Chim. Acta, 91 (1977) 303.
7 D. Chen, M.D. Luque de Castro and M. Valcárcel, Talanta, 37 (1990) 1049.
8 A. Sano, M. Takezawa and S. Takitani, Anal. Sci., 2 (1984) 491.
9 T. Toida, S. Tanabe and T. Imanari, Chem. Pharm. Bull., 29 (1981) 3763.
10 A.G. Fogg and R.M. Alonso, Analyst, 112 (1987) 1071.
11 U. Spohn, G. Nagy and E. Pungor, Anal. Sci., 2 (1985) 431.
12 P.W. Alexander, P.R. Haddad and M. Trajanovicz, Anal. Chem., 56 (1984) 2417.
13 R.A. Durst, Anal. Lett., 10 (1977) 961.

14 B. Philar, L. Kosta and B. Hristowski, Talanta, 26 (1979) 805.
15 F. Opekar, Anal. Chim. Acta, 183 (1986) 293.
16 M.W. Scoggins, Anal. Chem., 44 (1972) 1294.
17 E.E. Archer, Analyst, 83 (1958) 571.
18 D. Midgley, Ion-Sel. Electrode Rev., 3 (1981) 43.
19 IUPAC Analytical Chemistry Division, Pure Appl. Chem., 48 (1976) 129.
20 D.L. Massart, B.G.M. Vandeginste, S.N. Deming, Y. Mochotte and L. Kaufman, Chemometrics: a Textbook, Elsevier, Amsterdam, 1988.
21 M. Geissler, Polarographische Analyse, 1. Aufl., Verlag Chemie, Weinheim, 1981.
22 P.C. Nascimento, Dissertation, Technische Universität Clausthal, Clausthal-Zellerfeld, 1991.
23 G. Schwedt, Labor Praxis, (1990) 596.

Analytica Chimica Acta, 283 (1993) 763–771
Elsevier Science Publishers B.V., Amsterdam

Flow-injection analysis–wall-jet electrode system for monitoring glucose and lactate in fermentation broths

Yu Liang Huang

Bioprocessing Technology Unit, National University of Singapore, 10 Kent Ridge Crescent, Singapore 0511 (Singapore)

Soo Beng Khoo

Department of Chemistry, National University of Singapore, 10 Kent Ridge Crescent, Singapore 0511 (Singapore)

Miranda G.S. Yap

Bioprocessing Technology Unit and Department of Chemical Engineering, National University of Singapore, 10 Kent Ridge Crescent, Singapore 0511 (Singapore)

(Received 2nd December 1992; revised manuscript received 24th June 1993)

Abstract

A novel and straightforward approach for the monitoring of glucose and lactate in fermentation broths based on flow-injection analysis (FIA) coupled with a wall-jet electrode (WJE) is described. Glucose or lactate present in the fermentation broths was converted to hydrogen peroxide by immobilised glucose oxidase or lactate oxidase respectively. The hydrogen peroxide was then detected anodically by a platinum wall-jet electrode at +0.65 V (vs. Ag/AgCl, saturated KCl). For the FIA–WJE, a linear response was obtained for hydrogen peroxide ranging from 1.00×10^{-7} M to 1.00×10^{-3} M, with a detection limit of 1.00×10^{-8} M for hydrogen peroxide based on a signal-to-noise ratio of 3. The range of glucose which can be measured by this FIA–WJE system was 5.67×10^{-5} M to 2.78×10^{-3} M, while the range for lactate was 2.22×10^{-5} M to 5.56×10^{-4} M. Interferences from the fermentation media were observed but could be eliminated by pretreatment of the electrode with Fe^{2+}. The electrode response showed good stability and reproducibility after pretreatment. The system was used to monitor the glucose and lactate concentrations in different fermentation broths both for bacteria cell lines cultivation and for mammalian cell lines cultivation. The results showed good agreement with those determined by a commercial glucose–lactate analyzer.

Keywords: Flow injection; Glucose; Lactate; Fermentation broths

With the development of modern genetic engineering, numerous therapeutical recombinant proteins, diagnostical monoclonal antibodies (MAb) and many kinds of vaccines can be produced efficiently through industrial or laboratory scale cultivation of recombinant bacteria [1,2], insect cells [3,4] and hybridoma cells [5–7]. Glucose is known to be essential for the growth of different kinds of cells and it has been shown experimentally to be a precursor for the synthesis of the nutritionally nonessential amino acids, pyrimidines, purines, carbohydrates and lipids of the cell [8]. Moreover, glucose consumption is also an indicator of cellular metabolic activity. Undesirable consequences of excess glucose concentration, such as catabolite repression [9], might

Correspondence to: S.B. Khoo, Department of Chemistry, National University of Singapore, 10 Kent Ridge Crescent, Singapore 0511 (Singapore).

be avoided by controlled feeding. The fermentation of *E. coli* K12 HB101 for recombinant human tumour necrosis factor beta (rhTNF-β) production, for example, requires careful monitoring of the glucose level for both cell growth and protein expression [10]. Lactate, which is the end product of glycolysis, must be monitored to trace the metabolic pathways of glucose and glutamine [11–13], especially during hybridoma cell culture. Also, excessive lactate is an inhibition factor, for cell growth as well as for MAb formation, arising due to a pH effect and/or to the lactate itself [14,15].

At present, there is a need for fast, efficient and reliable means to determine physiological parameters such as glucose and lactate, not only off-line for routine monitoring, but also on-line monitoring for intelligent control [16]. Other than the traditional method for glucose or lactate determination based on their reducing properties, two major methods have been developed to enhance the accuracy of analysis. First, liquid chromatography can quantify both substrates [17]. However, this technique requires expensive instrumentation and sometimes also requires time consuming sample derivatization, depending on the method of detection. Second, enzymatic assays for both compounds have been developed, using either glucose oxidase (GOD) [18], glucose dehydrogenase (GDH) [19] or glucose-6-phosphate dehydrogenase (G-6-PDH) [20] for glucose determination, and either lactate oxidase (LOD) [21] or lactate dehydrogenase (LDH) [22] for lactate determination. Various methods based on enzymes employ the technique of flow-injection analysis (FIA) coupled with spectroscopic [23–26] or electrochemical [27–29] methods of detection.

Hydrogen peroxide is produced stoichiometrically from the enzymatic reactions of both glucose and lactate:

$$\text{D-glucose} + O_2 + H_2O \xrightarrow{\text{GOD}} \text{D-gluconic acid} + H_2O_2 \quad (1)$$

$$\text{L-lactic acid} + O_2 + H_2O \xrightarrow{\text{LOD}} \text{acetate} + CO_2 + H_2O_2 \quad (2)$$

Oxidation of the hydrogen peroxide at a suitable anode yields a current which can be used to quantify glucose and lactate:

$$H_2O_2 \rightarrow 2e + 2H^+ + O_2 \quad (3)$$

The major difficulty in fermentation monitoring using electrochemical detectors in the amperometric mode is the complexity of the fermentation broths. Interferences due to electrolysis of background species are common. One method which has been used to alleviate this problem is to modify the electrode so that a mediating reaction occurs at a lower potential [30]. The electrocatalytic effect has also been employed to shift the potential for analyte detection to a lower value [31]. At lower applied potentials, interferences from electrolysis of background substances could be prevented. Another problem is the fouling of the electrode arising from the electrolysis and/or adsorption of background materials. In fermentation media, the presence of high concentration of proteins may be a factor. Protective membranes have been used on the surfaces of electrodes to prevent interfering substances from reaching them [29,32]. However, the introduction of a film at the electrode surface must be carefully controlled. Otherwise, sensitivity, precision or response time of the electrode could be adversely affected.

The wall-jet electrode (WJE), first described by Yamada and Matsuda [33], is useful as an electrochemical detector in many flow applications [30,34,35]. It offers many useful features such as well-defined hydrodynamic properties, low dead volume, good sensitivity, fast response, ease of operation and it is inexpensive. For the FIA–WJE, we have derived an equation relating peak current response to the relevant hydrodynamic parameters and shown the suitability of this system for bioprocess monitoring in an earlier work [36]. The main objective of this paper is to demonstrate the applicability of the FIA–WJE system together with an immobilized enzyme reactor (GOD or LOD) for monitoring of glucose or lactate in fermentation broths. For this purpose, in view of the complex matrix of the fermentation broth, particular attention is given to elimination of interferences, optimization of electrode response and stability of the electrode.

EXPERIMENTAL

Chemicals and reagents

Glucose oxidase (GOD grade I, EC 1.1.3.4, from *Aspergillus niger*, 250 U mg^{-1}) and lactate oxidase (LOD, EC 1.13.12.4, from *Mycobacterium smegmatis*, 50 U mg^{-1}) were purchased from Boehringer (Mannheim). D-Glucose, L-lactic acid and hydrogen peroxide (30%) were obtained from Sigma (St. Louis, CA). Aminopropyl derivatised controlled-pore glass (AMP-CPG-550 Å, 120–200 mesh) was from Fluka (Neu-Ulm). Glutaraldehyde (25%) and potassium phosphate were supplied by Merck (Darmstadt). All chemicals were of analytical reagent grade and used as received. Milli-Q water was used for all experiments.

Aqueous solutions of hydrogen peroxide ranging from 1.00×10^{-7} M to 1.00×10^{-1} M were prepared just prior to use by dilution of 30% stock solution. Glucose and lactate standards were prepared by sequential dilution of the stock solution, which was stored at 4°C for at least 24 h before use to ensure attainment of mutarotational equilibrium.

Enzyme immobilization by means of glutaraldehyde

The optimized enzyme immobilization procedure [37] can be described briefly as follows: 20 mg GOD or LOD were dissolved in 5 ml 0.10 M potassium phosphate buffer, pH 7.0, and then mixed with 100 mg of AMP–CPG pre-activated with 2.5% glutaraldehyde (30°C, 3 h). After 24 h incubation at 4°C, the enzyme, either GOD or LOD immobilized on CPG, was packed by sucking with a peristaltic pump into an enzyme reactor (homemade polycarbonate tube of appropriate dimensions). Nylon nets (400 mesh) were attached to both ends of the reactor to retain the glass beads containing the immobilized enzyme.

Instrumentation and procedures

The set-up is shown schematically in Fig. 1. The detector was a home-made large volume wall-jet cell with a 0.5-mm inlet nozzle diameter [38] including a platinum disk working electrode (3 mm diameter) placed vertically upwards, a saturated silver/silver chloride reference electrode and a glassy carbon (5 mm diameter) counter electrode. The flow-injection analyzer consisted of two highly accurate peristaltic pumps, an injection valve with a 20-μl sample loop and PTFE tube (260 mm × 0.5 mm i.d.) (Tecator). The potential was controlled by a potentiostat (EG&G Polarographic Analyzer, Model 264A, Princeton Applied Research Co.) and FIA peaks were recorded by a chart recorder (BD41, Kipp and Zonen).

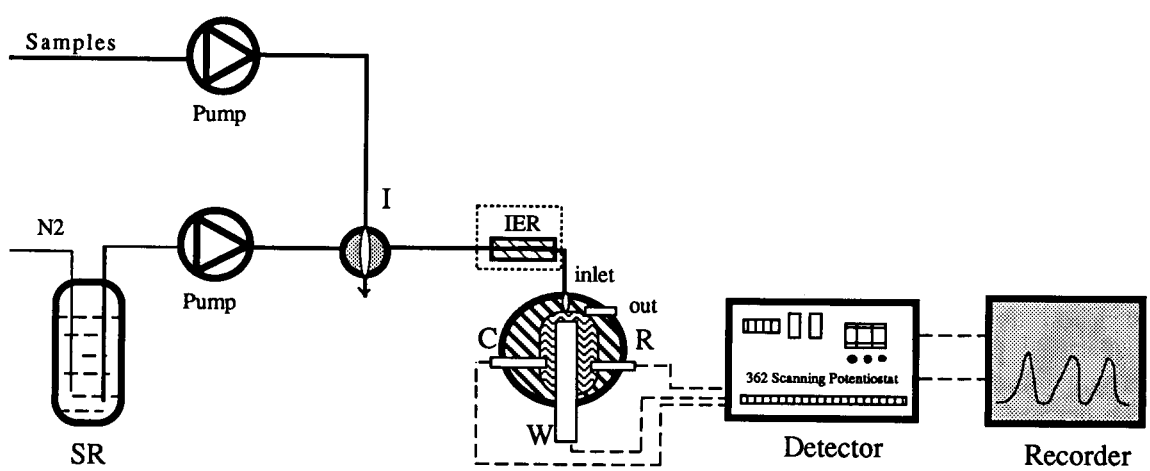

Fig. 1. Schematic diagram of FIA–WJE system coupled with an immobilized enzyme reactor. B = buffer (0.1 potassium phosphate buffer, pH 7.0), I = injection valve, C = counter electrode, W = working electrode, R = reference electrode, IER = immobilized enzyme reactor.

Prior to use, the platinum working electrode was polished with an aqueous slurry of 0.3 μm alumina (Fluka) on polishing cloth and then sonicated in Milli-Q water for 10 min. The carrier was 0.10 M potassium phosphate buffer, pH 7.0 and the working electrode was controlled at +0.65 V, in the diffusion controlled region for oxidation of hydrogen peroxide. The distance between the electrode surface and the inlet nozzle was adjusted from 2 mm to 3 mm [35]. The pump was calibrated by timing the delivery of a fixed volume of solution. All experiments were carried out at an ambient temperature of 25°C (±1°C). The Fe^{2+} modified electrode was prepared by a single injection of a given concentration of $FeCl_2$ solution. Samples drawn from fermenters were centrifuged and the supernatants were diluted manually to fall into the range of the calibration curves for glucose and lactate (dilution factor was normally from 25 to 50, depending on concentrations of the samples). In all cases the average of four determinations was reported (R.S.D. less than 3%).

Reference method

Both glucose and lactate concentrations of the samples as well as the standard stock solutions were determined by the commercial YSI-glucose and lactate analyzer, Model 2000 (Yellow Springs Co.) for the purpose of comparison.

RESULTS AND DISCUSSION

Hydrogen peroxide calibration

Linear dependence of the peak current (I_p) of the WJE on the injected sample concentration (C^b) was verified experimentally by injection and oxidation of hydrogen peroxide, which was the electroactive analyte during applications. For H_2O_2 concentrations from 10^{-7} M to 10^{-3} M, a linear calibration plot was obtained with the regression equation of: $I_p = 0.948C^b + 6.601$ (correlation coefficient 0.9986). The detection limit was estimated at 1.00×10^{-8} M based on a signal-to-noise ratio of 3. Flow-rate studies also showed that peak height depended on the volume flow-rate to the power of 1.22 (average value) [36].

Elimination of background interferences

In complex media, electrodes are susceptible to fouling leading to reduced response signal and sometimes complete passivation. This fouling usually arises from the electrolysis of extraneous substances present in the media and is especially serious at high potentials. For the media in this work, at +0.65 V applied to the platinum working electrode, a very high background current was observed on injection of the sample which completely swamped the peak signal from the oxidation of H_2O_2. After several injections of the samples, very much reduced signals were obtained even when solutions of H_2O_2 dissolved in buffer (in the absence of interfering substances) were injected. The main sources of interference were organic complexes (casein hydrolysate, tryptose, yeast extract, etc., as listed in Table 1). To eliminate the interference, the following procedure was found to be effective: After the working electrode was polished and cleaned, 20 μl of Fe^{2+} ion solution ($FeCl_2$ in 0.1 M potassium phosphate buffer, pH 7) was injected once into the WJE when a potential of +0.65 V was applied. As shown by Fig. 2, the concentration of

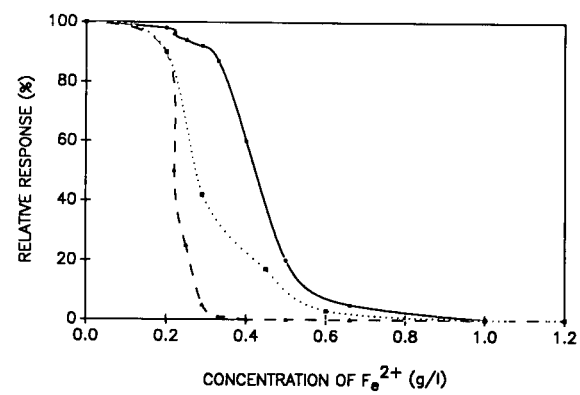

Fig. 2. Plot of relative responses vs. concentration of Fe^{2+} used for film formation. H_2O_2 (●———●): peak current for injected H_2O_2 at given concentration of Fe^{2+} used for film formation divided by peak current for injected H_2O_2 at bare electrode. Media (▲— —▲): peak current for injected sample at given concentration of Fe^{2+} used for film formation divided by peak current for injected sample at bare electrode. Ascorbate (■···■): peak current for injected ascorbate at given concentration of Fe^{2+} used for film formation divided by peak current for injected ascorbate at bare electrode.

TABLE 1

Summary for the background of samples [a]

Sample	A	B	C	D	E
Cell-line	*E. coli* K12HB101	*Pasteurella anatipestifer* serotype I	*Helicobacter pylori*	2HG-11	B10
Product	rhTNF-β [a]	Vaccine [b]	Antigen [c]	IgG	IgM
Medium	M_9 medium with 20 g l^{-1} of casein hydrolysate	Glucose and 20 g l^{-1} of tryptose	Brain–heart infusion, with yeast extract and horse serum	DMEM/F12 and 10% serum	RPM1 and 10% serum

[a] rhTNF-β = recombinant human tumour necrosis factor-beta. [b] Vaccine = duck vaccine. [c] Antigen = antigen used for ELISA kits.

Fe^{2+} at 0.33 g l^{-1} was critical, where the interferences from media practically disappeared on subsequent application of samples, but response to H_2O_2 was almost unchanged. The mechanism for this procedure can probably be illustrated as follows [39]:

$$Fe^{2+} \xrightarrow{+0.65\ V\ vs.\ Ag/AgCl} Fe^{3+} \quad (4)$$

$$Fe^{3+} + H_2O \xrightarrow{pH>2} Fe(OH)_3 \downarrow \quad (5)$$

Fe^{2+} is oxidized at the applied potential of +0.65 V and the precipitated Fe^{3+} at pH 7 in the phosphate buffer (Fe^{3+} hydrolysis occurred) formed a thin film of hydroxide and/or other oxyferric species on the surface of the electrode. For a 20-μl injection of Fe^{2+} at 0.33 g l^{-1} under the experimental conditions employed, the film formed at the electrode surface was probably thin enough to allow H_2O_2 to rapidly diffuse through but not the larger molecules present in the sample. However, when the concentration of Fe^{2+} was too low (< 0.25 g l^{-1}) the coverage of electrode was not effective enough to exclude interfering substances (see Fig. 2). For Fe^{2+} concentration greater than 0.35 g l^{-1}, the signal of the analyte (H_2O_2) decreased and reached zero at concentrations of Fe^{2+} greater than 1.15 g l^{-1}. The probable reason for this was the increasing thickness of the surface film which blocked even the smaller H_2O_2 molecule from reaching the electrode surface. Our preliminary studies also indicated that the formation of the surface film at higher pH values tended to shift the oxidation of H_2O_2 to lower potentials, thus providing another possible route to elimination of interferences. Detailed investigations on this phenomenon is in progress and will be published later. Taha and Wang [31] had observed a similar behaviour when a glassy carbon was coated with a layer of oxy-manganese species. At this modified electrode,

TABLE 2

Performance characteristics of different dimensions of enzyme reactors for glucose

Reactors	R_1	R_2	R_3	R_4	R_5	R_6	R_7	R_8	R_9	R_{10}	R_{11}
Reactor dimension [diameter(mm) × length(mm)]	1 × 10	1 × 20	1 × 30	1 × 40	2 × 10	2 × 20	2 × 30	3 × 20	3 × 45	5 × 10	5 × 60
Linear range (g l^{-1})	0–0.40	0–0.40	0–0.40	0–0.40	0–0.40	0–0.40	0–0.40	0–0.50	0–0.80	0–0.50	0–1.80
Response sensitivity (μA/g l^{-1})	5.05	5.71	7.24	6.52	7.27	6.87	6.28	3.61	1.49	5.30	1.17
Detection limit (mg l^{-1})	5.0	5.0	5.0	5.0	5.0	5.0	5.0	10.0	25.0	5.0	40.0
Response time (s)	30	30	40	60	45	50	60	70	90	60	150
Precision (%) [a]	2.23	1.89	2.50	1.36	2.02	1.16	1.72	2.44	2.21	3.54	3.28

[a] Relative standard deviation, for eight determinations.

they found that smaller molecules like H_2O_2 and hydrazine were oxidised at lower potentials which they attributed to electrocatalytic effect. However, larger molecules such as ascorbic acid, ferrocyanide, oxalic acid and aniline did not show this behaviour from which they interpreted that their modified electrode coupled electrocatalytic behaviour with molecular size selectivity. In our case, a larger molecule such as ascorbic acid showed a penetration (response) level intermediate between H_2O_2 and the interferences from the media (assumed to be larger molecules) (see Fig. 2).

The influence of the dimension of immobilized enzyme reactor on detector response

In this work, it was necessary to introduce immobilized enzyme reactors for quantitation of glucose and lactate via their conversions to hydrogen peroxide. The electrode response is expected to be highly dependent on the performance characteristics of the reactor. Factors affecting performance include activity of immobilized enzyme, packing, size of reactor, etc. After optimization of enzyme immobilization (see earlier section) [37] and ensuring a consistent reactor packing procedure, the effects of reactor dimension were studied. The results are given in Table 2 for reactors loaded with glucose oxidase. From Table 2, it can be seen that at constant reactor diameter of 1 mm, increasing the reactor length from 10 to 40 mm (R_1 to R_4) did not increase the linear range of 0–0.40 g l^{-1} for glucose detection. The same linear range was observed for reactors of 2 mm diameter but varying lengths of 10 to 30 mm (R_5 to R_7). For larger reactors, the linear range increased and a range of 0–1.80 g l^{-1} was obtained for the largest reactor (R_{11}). These observations indicate that the conversion efficiency for the smaller reactors (R_1 to R_7) was not the dominating factor controlling the linear range but rather the dispersion, otherwise we would expect an increase in linear range. However, further increases in size of reactors (R_8 to R_{11}) resulted in increases in linear range. This can be attributed to the increasing contribution of substrate conversion. The response sensitivity generally decreased with increase in length as well as inner diameter of the reactors. This is due to the increase of convective mixing. In the case of the reactors with small inner diameters (1 mm i.d.) a maximum in sensitivity (R_3) can be observed from R_1 to R_4. The detection limit, response time as well as precision of the peak responses generally increased with increase in either length or inner diameter of the reactors. It can be seen from Table 2 that for R_{11}, the signal in terms of sensitivity ($1.17/7.24 = 16\%$ of maximum value), detection limit (40 mg l^{-1} compared to 5 mg l^{-1}), response time ($150/30 = 5$ times as high) as well as precision (more than 3% of R.S.D.) are much poorer compared to the small reactors. This is because dispersion increased with increase in either length or inner diameter of the reactor. Another aspect that should be considered for a packed-bed reactor is the pressure drop (ΔP), which can be defined by the Darcy equation [40] (Eqn. 6),

$$\Delta P = \mu \eta L / k_0 d_p^2 \qquad (6)$$

where μ represents the linear velocity of flow, η is viscosity, L is the length of the reactor, k_0 is the permeability of the packed material and d_p represents diameter of particles. Obviously ΔP is proportional to the L, so L should be chosen as small as possible for FIA application. In our experiments, ΔP increased drastically with increasing length of reactor. Therefore, for subsequent work R_1 was used. This was justified because it led to lower pressure drop and also lower residence time which resulted in higher assay rate. Although R_2 has equal or better performance characteristics in terms of sensitivity, detection limit, response time and precision, it was not chosen because of difficulties arising from higher ΔP. While the larger reactors gave a wider linear range, (0–1.80 g l^{-1} for R_{11}), this still did not cover the complete variability of glucose concentration in the fermentation broths during cell cultivation, so that dilution was still necessary whichever reactor was used.

For lactate (data not shown), the results were generally similar to those for glucose. Therefore, R_1 was also chosen for lactate determination, which has a linear range of 0–0.06 g l^{-1} and the detection limit of 2 mg l^{-1}.

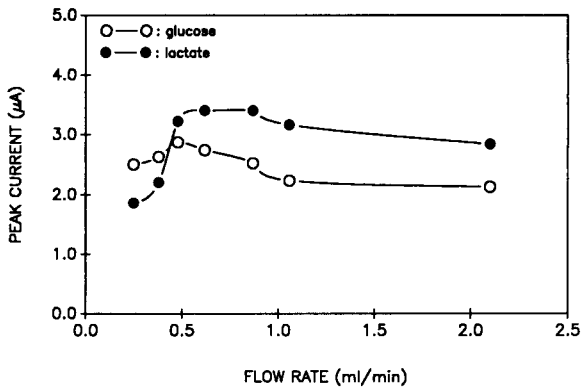

Fig. 3. Plot of peak current vs. flow-rate. Enzyme reactor: 10 mm × 1 mm i.d.

The influence of the flow-rate on the response

Principally, flow-rate should have two opposite effects on the response of the FIA–WJE with an enzyme reactor. One is the dependence of the FIA–WJE response on volume flow-rate to the power of 1.25 [36]. The other is the residence time of substrate in the reactor, which decreases with the increase of flow-rate and thus will reduce substrate conversion. As shown by Fig. 3, obviously the intrinsic characteristics of the WJE dependence on the flow-rate was affected because of the decrease in substrate conversion with the increase of flow-rate. At low values of flow-rate, the relatively larger residence time allowed the substrate conversion efficiency maintained at a certain level, but less than 100%, therefore peak response still showed an increasing trend and the power of flow-rate dependence dropped to around 0.50. At moderate values of flow-rate, the two opposing effects of flow-rate on the FIA–WJE and the substrate conversion by the enzyme reactor neutralised each other and a rather flat region in the response was observed with increasing flow-rate. At higher flow-rate, the response decreased with increasing flow-rate, evidence that the reduction in substrate conversion overwhelmed the increase in peak response with flow-rate. The optimum flow-rate chosen for further experiments was 0.5 ml min^{-1}.

Stability and reproducibility of the system

Both stability and reproducibility of the FIA–WJE (modified with Fe^{2+}) coupled with immobi-

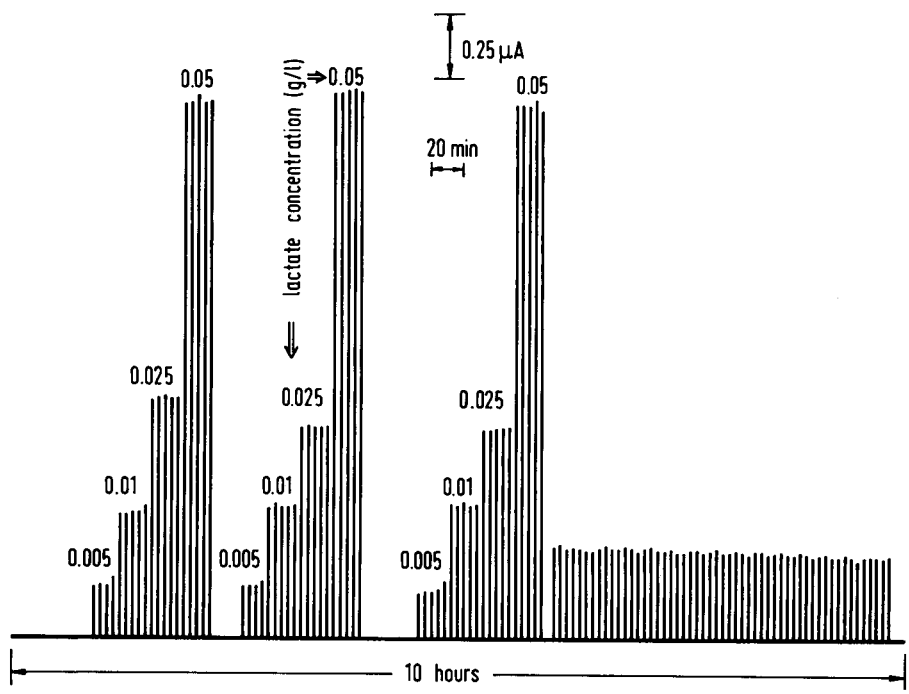

Fig. 4. The response stability and reproducibility of FIA–WJE coupled with immobilized LOD.

TABLE 3

Summary for the glucose testing

Samples	A_1	A_2	A_3	A_4	B	C
Results from FIA–WJE (g l^{-1})	21.47	18.91	8.98	0.10	2.05	1.22
Results from YSI (g l^{-1})	21.2	19.6	8.59	n.d. [a]	2.02	1.18
Sample volume (ml)	7	7	7	7	7	7
Calibration by 1 point standard addition						
Concentration of added standard (g l^{-1})	19.12	19.12	19.12	19.12	19.12	19.12
Volume of standard added (ml)	3	3	3	3	3	3
Total volume (ml)	10	10	10	10	10	10
Expected result (g l^{-1})	20.76	18.93	12.02	5.8	7.17	6.59
Determined value (g l^{-1})	19.46	18.84	12.05	5.3	7.19	6.62
Recovery (%)	93.7	99.5	100.2	95.5	100.3	100.4

[a] n.d. = Undetectable sample by YSI glucose and lactate analyzer.

TABLE 4

Summary for the lactate testing

Samples	D_1	D_2	E_1	E_2
Results from FIA–WJE (g l^{-1})	1.448	0.219	1.699	0.617
Results from YSI (g l^{-1})	1.44	0.22	1.76	0.60
Sample volume (ml)	5	5	5	5
Calibration with one point standard addition				
Concentration of added standard (g l^{-1})	0.25	0.25	0.25	0.25
Volume of standard added (ml)	5	5	5	5
Total volume (ml)	10	10	10	10
Expected result (g l^{-1})	0.849	0.235	0.975	0.434
Determined value (g l^{-1})	0.826	0.238	0.990	0.456
Recovery (%)	97.3	101.3	101.5	105.2

lized enzyme reactor were also investigated. Figure 4 shows the results obtained from the system with immobilized LOD. These confirmed that the system was reliable for both stability (R.S.D. $\leq$ 3%, $n = 54$) and reproducibility for at least 10 h (three sets of calibration are shown). It should be noted that the response had a decreasing trend during the application, mainly because of the decrease of enzyme activity, which is inevitable for the immobilized enzyme. This implies that regular calibration of the system is necessary.

Similar results were also obtained from the system with immobilized GOD (data not shown).

Calibration with glucose and lactate and the results for the samples determination

Based on the conditions mentioned above, the calibration curves both for glucose (ranging from 0 to 0.50 g l^{-1}) and for lactate (ranging from 0 to 0.040 g l^{-1}) were obtained with equations of $I_p = 3.61C_{glucose} + 0.015$ (correlation coefficient 0.9993) and $I_p = 39.82C_{lactate} + 0.0069$ (correlation coefficient 0.9996) respectively. Subsequently, several samples from different sources were tested and the results are summarized in Table 3 (glucose) and Table 4 (lactate). The data show good agreement between the results from the FIA–WJE system and those determined by the commercial analyzer.

Conclusions

It can be concluded that the FIA–WJE system employed here is suitable for monitoring glucose and lactate concentrations in fermentation broths. Interferences from media can be eliminated by forming a thin film of oxyferric species during

application. The typical response time, long term stability and reproducibility indicate that the FIA–WJE system is applicable to on-line monitoring of fermentation.

Thanks are due to Mr Cai Qiantao for useful discussions.

REFERENCES

1 H.F. Seow, C.R. Goh, L. Krishnan and A.G. Porter, Biotechnology, 7 (1989) 363.
2 E. Wingender, G. Bercz, H. Blöcker, R. Frank and H. Mayer, J. Biol. Chem., 264 (1989) 4367.
3 L.K. Miller, Ann. Rev. Microbiol., 42 (1988) 177.
4 V.A. Lucknow and M.D. Summers, Biotechnology, 6 (1988) 47.
5 S.R. Adamson, S.C. Fitzpatrick, L.A. Behie, G.M. Gancher and B.H. Lesser, Biotechnol. Lets., 5 (1983) 573.
6 G.M. Lee, T.K. Huard and B.O. Palsson, Science, 178 (1972) 65.
7 K. James and G.H. Bell, J. Immunol. Methods, 100 (1987) 5.
8 H. Eagle, S. Barban, M. Levy and H.O. Schulze, J. Biol. Chem., 233 (1958) 551.
9 A.L. Demain, J. Appl. Chem. Biotechnol., 22 (1972) 345.
10 K.W.Y. Mak, M.G.S. Yap, Y.L. Huang and W.K. Teo, in S. Furusaki, I. Endo and R. Matsuno (Eds.), Biochemical Engineering for 2001, Springer, Tokyo, 1992, p. 189.
11 W.H. Munyon and D.J. Merchant, Exp. Cell Res., 17 (1959) 490.
12 H.R. Zielke, C.M. Sumbilla, D.A. Sevdalian, R.L. Hawkins and P.T. Ozand, J. Cell. Physiol., 104 (1980) 433.
13 Y.T. Luan, R. Mutharasan and W.E. Magee, Biotechnol. Lett., 9 (1987) 751.
14 M.W. Glacken, R.J. Fleischaker and A.J. Sinskey, Biotechnol. Bioeng., 28 (1986) 1376.
15 J.M. Strand, J.M. Quarles and S. McConnell, Biotechnol. Bioeng., 26 (1983) 503.
16 B. Danielsson, Current Opinion in Biotechnology, 2 (1991) 17.
17 U.A. Th. Brinkmann, Chromatographia, 24 (1987) 190.
18 E.J. D'Costa, I.J. Higgins and A.P.F. Turner, Biosensors, 2 (1986) 71.
19 B. Persson, L. Gorton, G. Johansson and A. Torstensson, Enzyme Microbiol. Technol., 7 (1985) 549.
20 A. Kunst, B. Draeger and J. Ziegenhorn, in U. Bergmeyer and J. Bergmeyer (Eds.), Methods of Enzymatic Analysis, Vol. 6, Verlag Chemie, Weinheim, 3rd edn., 1984, p. 163.
21 R. Renneberg, G. Trott-Kriegeskorte, M. Lietz, V. Jäger, M. Pawlowa, G. Kaiser, U. Wollenberger, F. Schubert, R. Wagner, R.D. Schmid and F.W. Scheller, J. Biotechnol., 21 (1991) 173.
22 F. Holl, in H.V. Bergmeyer (Ed.), Methods of Enzymatic Analysis, Vol. 3, Academic Press, New York, 1974, p. 1475.
23 M. Wolff and M. Mottola, Anal. Chem., 50 (1978) 94.
24 Y.L. Huang, S.Y. Li, B.A.A. Dremel, U. Bilitewki and R.D. Schmid, J. Biotechnol., 18 (1991) 161.
25 J.I. Peterson and G.G. Vurek, Science, 224 (1984) 123.
26 G. Moody, G. Sanghera and J. Thomas, Analyst, 111 (1986) 605.
27 J. Ruzicka and E.H. Hansen, Anal. Chim. Acta, 106 (1979) 207.
28 B. Persson, L. Gorton, G. Johansson and A. Torstensson, Enzyme Microbiol. Technol., 7 (1985) 549.
29 J. Bradley, P.A. Anderson, A.M. Dear, R.E. Ashby and A.P.F. Turner, in N.M. Fish, R.I. Fox and N.T. Tuomhid (Eds.), Computer Applications in Fermentation Technology, Elsevier, Amsterdam, 1989, p. 47.
30 H. Gunasingham and C.H. Tan, Anal. Chim. Acta, 229 (1990) 83.
31 Z. Taha and J. Wang, Electroanalysis, 3 (1991) 215.
32 W. Künnecke and R.D. Schmid, Anal. Chim. Acta, 234 (1990) 213.
33 J. Yamada and H. Matsuda, J. Electroanal. Chem., 44 (1973) 189.
34 M. Varadi, Zs. Feher and E. Pungor, J. Chromatogr., 20 (1974) 747.
35 B. Fleet and C.J. Little, J. Chromatogr. Sci., 12 (1974) 747.
36 Y.L. Huang, S.B. Khoo and M.G.S. Yap, Electroanalysis, in press.
37 Y.L. Huang and M. Pfeiffer, The optimum immobilization procedure to attach the enzymes covalently on the controlled-pore glass (CPG), unpublished data.
38 H. Gunasingham and C.H. Tan, Anal. Chim. Acta, 234 (1990) 321.
39 F. Vydra, K. Stulik and E. Julakova, Electrochemical Stripping Analysis, Ellis Horwood and Wiley, New York, 1976, pp. 255–257.
40 R.S. Deelder, M.G.F. Kroll and A.J.B. Beeren, J. Chromatogr., 149 (1978) 669.

Analytica Chimica Acta, 283 (1993) 773–783
Elsevier Science Publishers B.V., Amsterdam

Application of thermal lens spectrometry to kinetic speciation studies of metal ions in natural water models with colloidal ligands

Donald W. Gutzman and Cooper H. Langford

Department of Chemistry and Biochemistry, Concordia University, 1455 deMaisonneuve West, Montreal, Quebec H3G 1M8 (Canada)

(Received 22nd February 1993; revised manuscript received 28th June 1993)

Abstract

Thermal lensing spectrometry (TLS) has been applied to measurement of kinetics with the aim of extending kinetic speciation methods to the low concentrations of metal ions in the presence of colloidal ligands which are important in many natural systems. Using bromination of acetone as a test reaction, it is shown that 2–3 significant figure rate constants can be obtained from runs with a total absorbance change of < 0.003. Results are presented on TLS kinetic analysis of hydrous ferric oxide colloids hydrolyzing in the presence of sulfosalicylic acid (SSA) to give FeSSA and on the kinetic analysis of Cu(II) bound to hydrous ferric oxides. In both cases, it is seen that lability is increased at the lower concentrations accessed by TLS as compared to behaviour previously reported at concentrations required for analysis by conventional spectrophotometry. That this is a change of the colloids and not a disagreement between TLS and conventional methods is confirmed by demonstrating agreement between the two methods at different concentrations of samples of Cu(II) ion exchanged into zeolite particles of defined size. Noise levels were higher than in bromination of acetone. Studies using colloidal latex particles of known size show that light scattering by nonabsorbing particles causes no interference in TLS absorbance measurements but homodisperse hematite colloids which absorb at the pump laser wavelength cause a significant noise increase.

Keywords: Spectrophotometry; Kinetic methods; Thermometric methods; Metal speciation; Thermal lens spectrometry; Waters; Colloids

The technique of laser thermal lensing spectrometry (TLS) enjoys both the selectivity and the sensitivity of fluorescence. A beam from a laser having a radial Gaussian intensity profile ($TEM_{0,0}$ mode) is focused into a cell containing the absorbing analyte. Nonradiative relaxation of the electronically excited complex leads to heating of the solvent in the path of the pump beam. Since the refractive index of the solvent is a function of density, local heating results in the formation of a transverse refractive index gradient. This gradient reflects the Gaussian character of the incident beam and is, in effect, a thermal lens [1,2]. A second beam (probe) tuned to a wavelength not absorbed by the analyte is directed through the sample coaxially to the pump beam. After passing through the sample, the pump beam is filtered and the intensity at the centre of the probe is monitored with a pinhole/photodiode combination. The change in peak intensity is a sensitive indicator of *absorbed energy*, hence of the analyte concentration. This affords two advantages. First, sensitivity may be increased by use of higher pump beam power. Second, since the signal is directly dependent on energy absorbed and converted to heat it is theoretically less sensitive to scattering by small particles in the sample. This offers a potential advantage in terms of pretreat-

Correspondence to: C.H. Langford, Department of Chemistry, University of Calgary, 2500 University Dr. N.W., Calgary, AB T2N 1N4 (Canada).

ment of environmental samples over normal spectrophotometric analysis which measures energy transmitted (where absorbance and scattering both contribute). Larger particles which may block a significant fraction of the focused laser beam present some problem.

The impetus for this work has been ongoing study of methods of speciation of trace metals associated with naturally occurring complexants. Speciation has been performed by spectrophotometrically monitoring the rate of reaction of the complexed metals with a preferentially complexing chromophore leading to a common product. The resulting absorbance–time curves may be analyzed to provide information of complex concentration and relative kinetic lability. This method has been applied to the study of several metal–complexant systems including Ni(II)–fulvic acid, Cu(II)–humic acid, and Cu(II)–hydrous ferric oxide [3] and the hydrous ferric oxide–fulvic acid system. The extension to concentrations more consistent with those found in natural systems is possible using thermal lensing. Of course the implications for use of the technique in kinetics are not limited to the objectives of the program on speciation.

Several kinetic studies have exploited TLS for "relaxation kinetics" where the pump beam perturbs the concentration distribution to initiate [4–7]. One study has used TLS to monitor kinetics of a chemical change initiated by an external light source [8]. It appears that *no previous studies have reported the TLS monitoring of conventional kinetics with reaction initiated by the mixing of reagents*. Consequently, the first effort of this study is to demonstrate the power of thermal lensing for kinetics.

It is important at this point to discuss some of the factors affecting the TLS signal and how the signal may provide quantitative information. Of greatest importance for analytical studies is the relationship:

$$\frac{I_0 - I_\infty}{I_\infty} = \frac{\Delta I}{I_\infty} = \frac{2.303P(\mathrm{d}n/\mathrm{d}t)}{\lambda k} A = 2.303EA \qquad (1)$$

I_0 is the intensity of the centre of the probe beam at the detector in the absence of a pump source. Upon irradiation by the pump beam the lens begins to form. Steady state is obtained when the rate of energy input is equal to the rate of its loss by thermal diffusion. The intensity of the probe at the detector after passing through this steady state lens is I_∞. The magnitude of the thermal lens effect is dependent on the power of the pump beam at the cell (P), the absorbance (A) of the sample at the pump wavelength (λ), thermal conductivity of the sample solvent (k) and the change in refractive index of the solvent with temperature ($\mathrm{d}n/\mathrm{d}t$). As shown in Eqn. 1, several of these parameters are combined into an enhancement factor (E) which expresses the gain in signal intensity of TLS over conventional spectrophotometry (CS).

Other things held constant, $\Delta I/I_\infty$ is linearly related to absorbance and hence solute concentration in the lower range of the variable. Linearity is maintained up to a value of $\Delta I/I_\infty$ of about 0.15. There are many parameters related to the optical configuration affecting the intensity of the TLS signal. As such, its application is most safely and easily handled by calibration versus a purely absorbing standard.

It is clear from the terms in Eqn. 1 that while the absorbing solute is responsible for energy input to the solution, the magnitude of the signal is also very dependent on the solvent. Several studies have considered the effect of solvents [9,10] on TLS signal intensity and the thermo-optical constants for various gases, liquids and solids have been summarized [11]. Unfortunate for the studies of aquatic systems is the fact that water is one of the poorest solvents having both a high thermal conductivity (5.95 mW cm^{-1} $°C^{-1}$ at 20°C) which prevents build up of a large thermal gradient and a small $\mathrm{d}n/\mathrm{d}T$ ($-8.1 \times 10^{-5}°C^{-1}$ at 20°C) [11]. In spite of this, enhancement factors of 10 or greater are frequently observed for water. Less polar solvents (such as CCl_4) offer significantly greater enhancement.

EXPERIMENTAL

Reagents

Colloidal hydrous ferric oxide (Fehox) solutions were prepared by slow base hydrolysis. The

weak base "Tris" [tris(hydroxymethyl) aminomethane; Sigma] was added dropwise over 4–6 h to an acidified solution of Fe(III) until the desired pH was obtained. Solutions were at room temperature and continuously stirred. Colloids were prepared at pH 4.5, 5.5, 6.0, 6.7 and 7.0. Copper(II) was associated with the colloids by either being added prior to Tris addition or by being added to the already formed colloids ("post addition"). Acidified stock solutions of Fe(III) and Cu(II) were prepared at approximate concentrations from $FeCl_3$ (Fisher) and $CuSO_4 \cdot H_2O$ (Fisher; recrystallized from water before use), respectively and standardized using flame atomic absorption. Colloids were aged for 24 h before analysis.

Homodisperse colloidal hematite samples (α-Fe_2O_3) were generously provided by Prof. L.K. Koopal, Wageningen Agricultural University, Netherlands [12]. Particles having mean diameters of 107, 212 and 404 nm were used.

The final colloidal substances used were spherical polystyrene latex particles (Marivac, Halifax) These particles are homodisperse having mean diameters of 176 ± 2, 481 ± 3 and 1090 ± 8 nm. As received, their concentrations were 3.35×10^{11}, 1.64×10^{10} and 1.36×10^{9} particles ml^{-1}, respectively, corresponding to ca. 0.1% (w/v).

For thermal lensing scattering studies, hematite and latex solutions were repeptized prior to dilution by sonicating small volumes for 5–7 min (Sonic 3000 dismembrator, Artek systems, Farmingdale, NY). Samples were diluted with water as required to obtain an absorbance of 0.050 at 458 nm. Solutions were then diluted a further 10-fold with water for thermal lensing analysis.

Binding of Cu(II) to the 212-nm hematite particles was studied by adjusting a solution containing aliquots of hematite and Cu(II) to pH 6.00 with Tris. The solution was left to equilibrate for 24 h before analysis.

Copper in hydrous ferric oxide was determined using the chromophore PHTTT [3-propyl-5-hydroxy-5-(D-arabino-tetrahydroybutyl)-thiazolidine-2-thione] [13,14]. This analytical method is described in detail in a separate publication [15].

The acid hydrolysis of the hydrous ferric oxides themselves was studied as follows. Colloids were prepared at pH 5.5, 6.0 and 6.7 by the base hydrolysis method described earlier. No copper was present. Iron concentration of all colloidal solutions was 1.56×10^{-4} M. Colloids were used at this concentration for kinetic analysis by conventional spectrophotometry. For TLS analysis, hydrous ferric oxide samples were diluted to 1.25 or 1.56×10^{-5} M. The chromophore solution for CS analysis contained 0.0150 M SSA (sulphosalicylic acid, Fisher) and 0.100 M HCl. The SSA concentration was reduced 10-fold for measurements by TLS. Kinetics were followed at both 455 nm (a pump laser wavelength) and 502 nm (the FeSSA absorption maximum) by CS. Kinetic curves obtained by TLS showed significantly higher noise levels than are generally observed in non-scattering media. Therefore data was smoothed by frequency domain filtering. CS data were analyzed without smoothing.

Experiments for the bromination of acetone employed spectral grade acetone (Baker) and dilutions of bromine (Anachemia) prepared from a saturated solution. Sulphuric acid (Baker) was used as the catalyst. The concentration of stock H_2SO_4 was determined by titration with NaOH previously standardized from Anachemia "Acculute" acid.

A number of factors of importance to thermal lensing analysis were considered in determining optimal reagent conditions to be used. Both H_2SO_4 and acetone alter the thermo-optical properties of the solvent. Two approaches may be used to prevent problems resulting from this. Concentrations may be maintained sufficiently low so as to have negligible contribution to the solvent properties. Alternatively, higher concentrations may be used provided they remain constant through the course of the kinetic run. The former approach was necessary for the acetone as calibration standards must be prepared in a matrix having the same thermo-optical properties as those of the kinetic runs. An acetone containing matrix was unfeasible for preparation of the standards. This required the use of a somewhat higher concentration of H_2SO_4 to allow reactions to proceed at convenient rates. Sulphuric acid concentrations were 0.0516 M (0.0602 M H^+) in the kinetic mixtures and in the standards. This con-

centration has only a limited effect on the solvent matrix.

For kinetic study bromine was added at time zero to a solution containing acetone and H_2SO_4. The reaction was followed by conventional spectrophotometry at both 394 nm (absorption maximum of Br_2) and 458 nm (TLS pump beam wavelength). Sulphuric acid was maintained at 0.0516 M in kinetic mixtures and standards for both CS and TLS analyses. The change in reaction rate with variation of acetone concentration was monitored over the range 0.200 to 1.00 M acetone by CS. Concentrations of acetone and Br_2 were reduced by two orders of magnitude for TLS study. Exact concentrations of bromine were calculated based on molar absorptivities determined by Pink [16].

Spectrophotometric analysis

Visible absorbance was measured with a Hewlett-Packard Model 8452A photodiode array UV/VIS spectrophotometer. Kinetics were initiated by mixing 1.00 ml of chromophore containing solution with 1.00 ml of colloid containing solution in a 1.00-cm pathlength cell. Solutions were pre-equilibrated and the reaction maintained at 25.0°C with a variation of ±0.01°C by a thermostated circulating water bath.

Thermal lensing analysis

A schematic of the thermal lensing apparatus employed is shown in Fig. 1. Sample excitation (pumping) is by means of an argon ion laser (Ar^+). The laser used was a Spectra-Physics Model 165 chassis with a Model 265 exciter. The chassis was fitted with a Coherent Innova ionpure metal-ceramic tube (SPICE upgrade). On/off cycling of the pump beam was effected by the use of a shutter (Ledex) connected to a transducer allowing automated control. The pump beam is then focused by a lens (L), through an optical flat (OF; 9.0 mm thick optical glass) to the position of sample cell. A cylindrical sample cell of 10.0 mm path length and 18 mm diameter was used. A clamped piece of tubing connected to a nipple at the bottom of the cell allowed drainage without movement of the cell. The pump beam was focused to the center of the cell (along the axis of beam propagation). The beam was directed through the center of the circular cell faces. Cell positioning was optimized dynamically to maximize signal-to-noise ratio for an absorbing standard. After exciting the sample, the pump beam is removed by a colour filter (CF; Oriel 630 nm cut-off).

A He–Ne laser (Siemens LGK 7623) is used as a probe beam. It is "mixed" with the pump beam

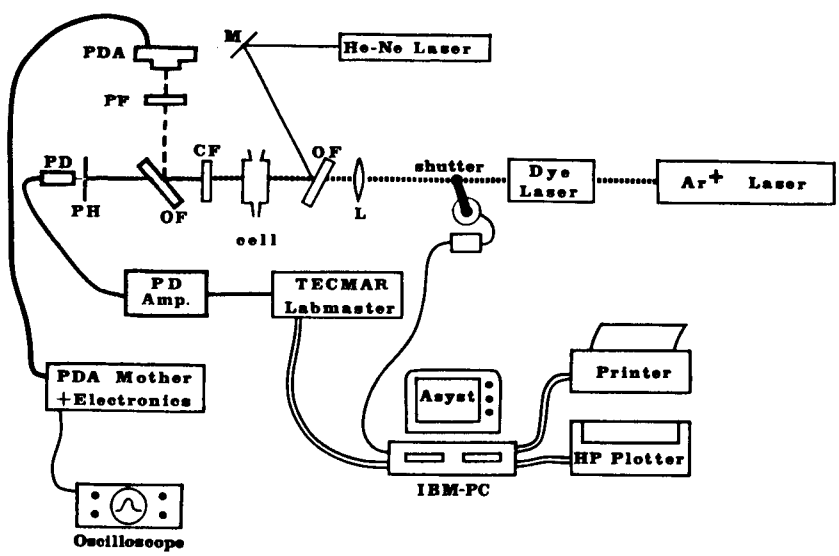

Fig. 1. Diagram of the dual-beam mode mismatched laser thermal lensing apparatus used in this work. See text for description of terms.

by reflection off the front face of the optical flat. The flat also acts as a simple probe beam attenuator as only about 5% is reflected. About 90% of the pump beam passes through the flat. The probe beam then passes through the sample and the colour filter to the detector system. The focus of the probe beam is prior to encounter with the sample cell resulting in a mode-mismatched configuration.

Optical alignment is facilitated by use of a 256 element linear photodiode array (PDA; Reticon RL256G with an RC301 current amplifier) to image a cross section of the probe beam. The profile is viewed on an oscilloscope. A polarized filter (PF) allows attenuation of the light reaching the PDA. The detector is comprised of a pinhole/photodiode (PH/PD) combination. The pinhole has a diameter of 100 μm allowing only the centre of the probe beam to reach the photodiode (Silonex NSL-810). The detector and shutter are interfaced to an IBM-PC using an A/D/A (Tecmar Labmaster; Scientific Solutions).

Data acquisition and control of the thermal lensing apparatus signal was performed using programs written in the Asyst language (ASYST: A Scientific System V 1.02; Asyst Software Technologies). The program has a number of user adjustable parameters which allow control of timing. Some of the parameters are interdependent and were chosen on the basis of an optimization study [17].

The thermal lensing signal is extremely sensitive to turbulence in the sample cell. Such a disturbance disrupts the thermal gradient induced by irradiating the sample with the pump beam. Efficient mixing of reagents requires the introduction of turbulent action. To limit this conflict, reagents for kinetic analysis were mixed in a separate vessel with stirring at time zero. This mixture was then slowly transferred to the cell using a pasteur pipette. Passage through the narrow tip of the pasteur leads to a laminar flow which significantly reduces the turbulence. The solution was then left for a further period of time to become tranquil before commencing TLS analysis. For non-kinetic samples, where signal is time independent, a long period was allowed to minimize noise levels. The minimum time was 1–2 min.

Noise levels for TLS spectroscopy of several types of samples are summarized in Table 1. They are discussed below and in the Appendix.

"Peculiarity" of TLS analysis: aperiodic signal oscillation

On numerous occasions I_0 and I_∞ signals monitored over a period of time have been observed to oscillate. When the two oscillate in phase,

TABLE 1

Noise levels observed in the laser thermal lensing analysis of colloidal suspensions of polystyrene latex and hematite

	Concentration	Sonicated	A_{458}	$\Delta I/I_\infty$		% scattered
				Mean	Mean σ_{n-1}	
Latex: – 176 nm	4.6×10^8 n ml^{-1}	yes	0.0048	0.011	0.002	100 ± 10
– 481 nm	3.7×10^6 n ml^{-1}	yes	0.0049	0.013	0.002	98 ± 5
– 1090 nm	2.8×10^5 n ml^{-1}	yes	0.0050	0.012	0.002	99 ± 8
Water				0.010	0.002	–
$Cu(PHTTT)_3$	3.8×10^{-8} M		0.0050	0.117	0.002	0
Hematite – 107 nm	2.0×10^{-6} M Fe	yes	0.0049	0.088	0.005	26 ± 2
– 212 nm	8.4×10^{-5} M Fe	yes	0.0049	0.073	0.010	40 ± 3
– 404 nm	8.0×10^{-6} M Fe	yes	0.0050	0.091	0.008	23 ± 7
Water				– 0.010	0.001	–
$Cu(PHTTT)_3$	~ 3.4×10^{-7} M		~ 0.0004	0.095	0.002	0
Hematite – 107 nm	2.5×10^{-6} M Fe	no	0.0049	0.071	0.007	30 ± 2
– 212 nm	1.2×10^{-4} M Fe	no	0.0048	0.061	0.021	37 ± 3
– 404 nm	8.5×10^{-6} M Fe	no	0.0051	0.085	0.009	21 ± 16

$\Delta I/I_\infty$ is unaffected. On occasion I_∞ was found to oscillate more slowly than I_0. This leads to oscillation in the analytical signal, $\Delta I/I_\infty$. Oscillation, whether in or out of phase, has been observed over a wide range of concentrations (including pure water) and both in the presence and absence of light scattering particles. The dependence of the effect on these parameters has not been quantified.

The time scale of these oscillations indicate a phenomenon related to convection. In several instances thermally induced oscillations observed during TLS analysis have been discussed in the literature [18–20]. In all of the cases referenced oscillations were periodic. Those observed here are clearly aperiodic. The damping of both amplitude and frequency indicates that something occurs before or near the start of analysis which requires a long period of time to diminish. Removal of the oscillation "noise" by frequency domain filtering would be very difficult as kinetic changes under study also occur at low frequency.

RESULTS AND DISCUSSION

A step-wise progression is used to demonstrate the potential and limitations for application of thermal lensing to kinetic analysis.

Kinetics in non-scattering media

Among the most thoroughly kinetically studied reactions is the halogenation of ketones. The rate of bromination of acetone was measured by both conventional spectrophotometry and thermal lensing. The decrease in bromine concentration was monitored at 458 nm by both methods as well as at 394 nm (the Br_2 absorption maximum) by CS. Reactions monitored by TLS were carried out using bromine and acetone at concentrations two orders of magnitude lower than those measured by CS.

To allow a more rigorous comparison of the two techniques, the concentration of acetone was varied allowing determination of the reaction order. Variation in initial concentrations of Br_2 occurred in solutions analyzed by both techniques as a result of the volatility of Br_2. However, the zero order $[Br_2]$ dependence leaves the rates measured for the disappearance of bromine unaffected.

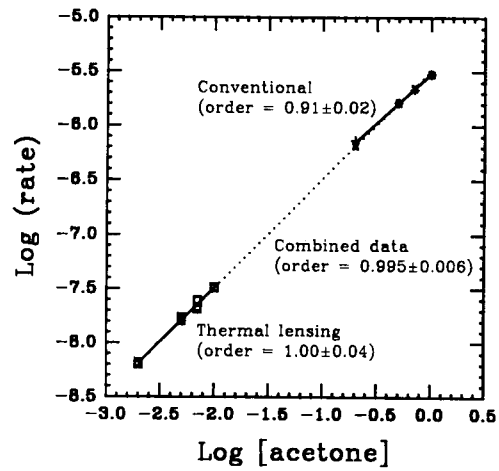

Fig. 2. Effect of acetone variation on the rate of its bromination. The reaction was monitored at high concentrations by conventional absorbance measurement and at concentrations two orders of magnitude lower by thermal lensing. Measurements by CS were made at both 394 nm (×) and 458 nm (+).

Average rate constants of $5.3(\pm 0.3)\times 10^{-5}$ M^{-1} s^{-1} and $5.4(\pm 0.2)\times 10^{-5}$ M^{-1} s^{-1} found by CS and TLS analyses, respectively are in very good agreement. This is demonstrated in Fig. 2 which shows the reaction order for acetone determined over nearly three orders of magnitude. In both cases internal consistency is confirmed by correlation coefficients of > 0.999 in CS and > 0.995 in TLS.

It is impressive that continuity is observed in results obtained over such a wide range of concentration. Total absorbance change for most of the reactions measured by TLS was less than 0.003. Indeed, with the use of a slightly higher pump beam power the concentration range covered could have been extended by another order of magnitude. *We remark that, to our knowledge, a two to three significant figure rate constant has not previously been obtained from a total absorbance change of 0.003!*

Iron(III) hydrous oxide in an acid medium

The monitoring of kinetics using the thermal lens effect was next applied to the study of acid

hydrolysis of Fe(III) hydrous oxides, a reaction important to kinetic speciation of iron in natural water. The liberated Fe(III) species were reacted with the chromophore SSA. Conventional spectrophotometric study of this chemical system [21] revealed three components in the initial solution. Monomeric Fe(III) had a rate constant (k_1) of 0.89 s^{-1}. A second component had $k_2 = 7.0 \times 10^{-4}$ s^{-1}. A final more slowly reacting component was related to larger (possibly crystalline) particles.

Of the three components expected in this system from earlier work, only the middle one should be observed within the timescale of these experiments. The fastest component is readily monitored only by stop flow techniques. The third is extremely slow to react and therefore makes negligible contribution. Trial analysis of several TLS data sets gave no evidence of more than one component. Consequently, the kinetic data were treated as a single first-order process.

Data obtained for this system by TLS monitoring were fairly noisy (as will be discussed below) and required smoothing. This involved manual removal of "spikes", frequency domain filtering, and polynomial fitting. Results were fit as first-order both with and without polynomial fitting.

Rate constants from both TLS and CS analyses are summarized in table 2. Internal consistency of TLS and CS results is reasonable. The difference between the CS and TLS results appears to be significant and possibly indicates a change in the colloid characteristics on dilution to the TLS concentration domain. Further concrete evidence for this interpretation appears below. This is an important point. It illustrates the danger in model studies at concentration levels significantly higher than occur in nature.

TABLE 2

Rate constants determined from conventional absorbance and thermal lensing data for the reaction of Fehox with SSA in an acid medium. The concentration of hydrous ferric oxide was 10 times lower in solutions analyzed by TLS

	Average rate constant ($\times 10^4$ s^{-1})		
	pH 5.5	pH 6.0	pH 6.7
Conventional: −502 nm	4.3±0.1	6.4±0.4	5.4±0.3
Thermal lens (458 nm):			
Blackman	3.6±0.6	4.0±1.1	3.5±1.2
+polynomial fit	3.5±0.4	3.8±0.3	3.1±0.8

TLS analysis of copper–hydrous ferric oxide

Some efforts were directed to the kinetic speciation of copper(II) bound to iron hydrous oxides using TLS monitoring. This is an attempt to extend CS studies using higher Cu(II) concentrations which were reported in Ref. 15. The cop-

TABLE 3

Comparison of results obtained by CS and TLS for determination of the labile "X" component of copper(II) in iron(III) hydrous oxide colloid

Fe to Cu mol ratio	Conventional spectrophotometry (%component)		Thermal lens spectrometry %Cu recovered		
	Highly labile	Not Recovered	Time since dilution (min)	Measured	Calculated [a]
Fehox prepared with Cu(II) present:					
6.5	55 ± 5	18 ± 2	2	89 ± 4	75
			6	86 ± 4	72
			90	86 ± 4	72
			400	105 ± 5	91
12.9	36 ± 5	31 ± 2	2	74 ± 7	56
19.3	30 ± 5	30 ± 5	2	72 ± 9	52
Cu(II) addded to Fehox ("post addition"):					
6.5	ca. 80	ca. 5	2	98 ± 4	> 84

[a] This is the quantity predicted on the basis of the CS determined rate constants.

per-containing colloids at pH 6.0 were diluted 50-fold with a matrix matched solution and mixed with the (50-fold diluted) chromophore–buffer at kinetic time zero. A delay of 120 s was used to allow the solutions to calm in the cell. The $\Delta I/I_\infty$ values were rather noisy but did have one striking feature. They showed no sign of a change for up to 60 min. Further, the signal indicated that almost all of the copper had already reacted before data acquisition began! This contrasts with results obtained by CS which showed observable change in reaction product concentration for up to about one hour.

These observations are quantified in Table 3. The column on the right was calculated from the rate constants k_2 and k_3 determined for speciation of copper in Fehox by CS. (Rate constant k_1 is related to those highly labile components which react on a time scale shorter than may be observed by the apparatus and therefore contribute to the observed background.) These values account for reaction which may have occurred during the 120 s delay and represent the %Cu recovered which should have been observed if speciation was the same in both cases. The values measured by TLS clearly exceed those determined by CS. The implication is that far more copper was in highly labile components in the system analyzed by thermal lensing. The only difference between the two systems was the concentrations of Fehox and Cu(II). Fifty-fold dilution of the colloidal solution has resulted in a prompt change in speciation. Species of intermediate kinetic lability have broken down into a more labile state. The results show that only a percentage of copper similar to the "not recovered" fraction in CS work is not reacted although even this component seems to become available at long times after dilution (result measured at 400 minutes in Table 3). In view of these results it is not unexpected that analysis of a dilute post-addition colloid (where little Cu(II) is in the "not recovered" fraction) showed complete recovery of copper.

The significance of the above observations are confirmed by kinetics measured for the release of copper which was ion exchanged into a sodium-A zeolite. This zeolite has an effective pore size of 4 Å. The formation of $Cu(PHTTT)_3$ was measured by both conventional and thermal lensing spectrometries. A first-order rate constant of 0.0026 s^{-1} was determined from CS data and 0.0025 s^{-1} from TLS data. The similarity of rate constants is significant. Since the zeolite is a crystalline structure its properties are concentration independent. Exactly the same processes are being monitored in both concentration regions. The similarity of results confirms that both CS and TLS are reliable monitoring techniques and the concentration dependence in the colloidal systems arises from changes in the colloids.

All results, those on Fehox alone, Fehox reacting with SSA and Cu-Fehox reacting with PHTTT, confirm the importance of modelling colloidal hydrous oxide ligands at "realistic" concentration. The nature of the colloidal ligand systems seems quite sensitive to total Fe concentration. That this is not an artifact of use of TLS is clearly shown by the result on zeolite particles where the ligand cannot be altered by dilution since it is a crystalline phase.

Conclusion

Several kinetic experiments compared thermal lensing detection to conventional spectrophotometry. In both the bromination of acetone and Cu exchanged zeolite studies agreement between CS and TLS results was very good. In studies involving hydrous oxide colloids of Fe, CS and TLS results differed reflecting variation in the chemistry of Fehox with total iron concentration. This variation points out the need to conduct model studies at concentrations of direct environmental relevance.

APPENDIX: NOISE SOURCES

Effect of light scattering material on thermal lensing analysis

Since the thermal lensing process depends on the energy transformed and not too much on the net energy loss from the beam, scattering should be a minor factor. This had been previously supported by a test using silica [22,23]. The study using polystyrene latex particles confirmed the

expectation. A serious limitation was found with absorbing particles since they have a non-homogeneous distribution of light absorbing centres in this solution. This adds greatly to noise in TLS. This limits precision in the attempt to study several systems monitored earlier and at higher concentrations by conventional spectrophotometry. The finding does not rule out the study of binding, for example, by organic fractions. A colorimetric analysis system which uses a pump laser line outside the spectral range of the particles would, of course evade the difficulty but appropriate color forming ligands are not easily found.

Among metal complexants present in the natural environment there are many based on colloidal suspensions such as dissolved organic matter and hydrous oxides. It is of utmost importance in speciation studies that natural samples be minimally perturbed prior to analysis. Pre-analysis filtration both removes the species associated with the colloids and may displace other equilibria. Problems associated with filtration itself are another factor. The results of speciation analyses after filtration may no longer reflect the initial sample condition.

The presence of these light scattering materials presents some problem for sample analysis by conventional spectrophotometry. In CS the analytical signal is derived from the amount of light not transmitted through the sample. Any factor (such as scattering) which contributes to the loss of transmitted light will affect measured absorbance values. In TLS the analytical signal results from the amount of energy absorbed and redeposited into the solvent as heat. In this case the signal is due solely to the absorption of light energy by electronic excitation of the analyte. In first approximation the scatter of light does not contribute to the TLS signal. In dual beam TLS the probe beam is equally affected by light scattering matter both in the presence and in the absence of excitation. The attenuation of the pump beam power due to scattering results in a loss of sensitivity proportional to the amount of light scattered. Provided there is a minimal change in pump beam power as it traverses the sample, the scatter of light should not effect the TLS signal.

The following sections identify some effects of scattering material on thermal lensing measurements which illustrate that the first approximation is too simple. This discussion follows a progression from materials which are pure scatterers to those which both scatter and absorb light at the analytical wavelength. The term "pure" will be employed in the following discussion to describe two extremes. Materials which scatter light but do not absorb at the wavelength of the pump beam are termed "pure" scatterers. Those which absorb light but do not scatter it are "pure" absorbers. It is important for kinetic speciation by TLS that noise levels be minimized as elevated noise can prevent the resolution of minor components. Noise levels for all types are summarized in Table 1.

Silica particles. The effect of one type of scattering material on the thermal lensing analysis of some natural organic matter has been evaluated [22,23]. Solutions of Armadale fulvic acid were analyzed by TLS in the absence and presence of 0.01–0.025% SiO_2 (w/w solution). The resulting curves were evaluated for linearity, detection limit and uniformity of response. It was observed that the signals remained unaffected by the presence of the SiO_2. It was concluded that TLS is insensitive to the presence of light scattering material in this region of particle concentration and that the pump beam was not measurably attenuated.

Polystyrene latex particles. To verify the silica results and to determine if particle size plays a role in the effect of pure scatterers on the thermal lensing signal, spherical polystyrene latex particles were examined. Homodisperse particles having mean diameters of 176, 481 and 1090 nm were dispersed, absorbance matched at 458 nm and further diluted. TLS analysis revealed that signal magnitude and noise levels appear similar for the 3 sizes of latex particles and a background solution (water). The pure absorber, a homogeneous solution of $Cu(PHTTT)_3$ was measured for comparison. Although the signal for this analyte was fairly large, the noise level is comparable to those of the blank and the purely scattering particles. Values of mean $\Delta I/I_\infty$ were compared to those measured for the pure absorber. This allowed determination of the fraction of "ab-

sorbance" as measured by conventional means which is due to scattering rather than electronic excitation.

From these results it is clear that latex particles having a significant range of sizes do not contribute to a TLS signal nor do they increase noise levels beyond those observed for non-scattering samples.

Homodisperse hematite. The results obtained in the previous sections for pure scatterers may be easily contrasted to those observed for a material which both scatters and absorbs in the analytical wavelength region. Approximately spherical homodisperse hematite particles having mean diameters of 107, 212 and 404 nm were again absorbance matched at 458 nm, further diluted and analyzed by TLS.

Noise levels were significantly higher than those observed for water, a pure absorber or the purely scattering latex particles which, it is pointed out, are of similar particle diameter. The source of the noise is large fluctuations in the I_∞ intensities. The major difference between the colloidal hematite and the other materials discussed here is that it is neither a pure absorber nor a pure scatterer. As seen in Table 1, 20–40% of the absorbance measured by CS is a result of light scatter.

Other chemical systems. With the guidance provided by the well defined silica and hematite systems, data derived from a number of experiments performed on other systems were evaluated with respect to noise level and scattering properties. These data were collected on different occasions over a long period of time. Some day-to-day variations in sensitivity and noise levels occur. Further, most of these experiments were not designed and conducted specifically for the study of noise levels. As a result there are some gaps in the data. Where possible these missing pieces of information were estimated by extrapolation or interpolation.

Some general observations may be made concerning these results. The noise levels of the background (water) were relatively low and consistent, ranging from 0.001 to 0.003. Noise levels for pure absorbers tended to be slightly higher than background but did not exceed 0.004. Further, where analyses were performed over a range of concentrations (and hence of $\Delta I/I_\infty$) for a purely absorbing analyte, noise levels are observed to be only slightly higher for the larger signals.

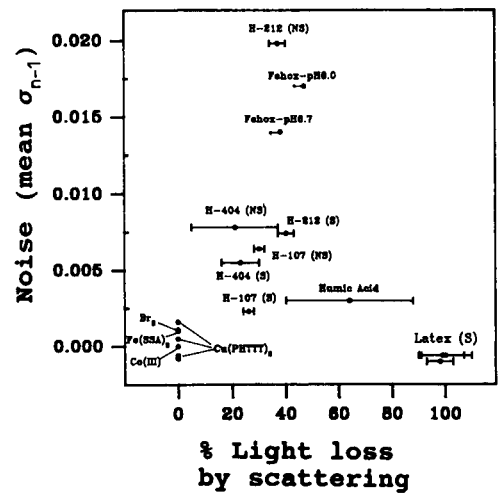

Fig. 3. Average TLS noise levels observed for materials having a range of scattering properties. At one extreme are pure scatterers such as latex particles. At the other end are purely absorbing compounds. Intermediate are particles whose absorbance measured by CS is a combination of scattering and "true" absorbance (electronic excitation of the chromophore). Note that noise levels are significantly higher for this latter group. All values refer to measurement at 457.9 nm. Abbreviations used: H = hematite; Fehox = ferric hydrous oxide; Co(III) = *cis*-$[Co(en)_2Cl_2]^+$; (S) = sonicated; (NS) = not sonicated.

Since hydrous iron oxide is of considerable importance to the speciation study it is worth commenting on TLS noise levels associated with its presence. Noise levels for all solutions containing hydrous ferric oxide were considerably higher than those containing pure absorbers only. The average noise level for Fehox containing solutions was 0.020 with values ranging from 0.007 to 0.041.

One light scattering material worthy of note is humic acid. Noise levels measured for humic acid containing solutions were unusually low. This may indicate that scattering behaviour of humic acid actually approaches that of a pure absorber.

Figure 3 compares measured noise levels to the calculated values of % scattered light. To account for day-to-day variations in system noise, Fig. 3 shows noise levels above a background

level, defined to be that measured with water in the sample cell, which was measured daily. Noise is clearly lowest for the extreme cases of pure scatterers (latex particles) and pure absorbers. Noise level seems to rise fairly quickly with increasing scattering properties of the light absorbing colloidal matter. This identifies the limits which will arise in efforts to use TLS for kinetic studies on natural waters.

REFERENCES

1 D.S. Kliger, Acc. Chem. Res., 13 (1980) 129.
2 K. Miyaishi, T. Imaska and N. Ishibashi, Anal. Chem., 54 (1982) 2039.
3 C.H. Langford and D.W. Gutzman, Anal. Chim. Acta, 256 (1992) 183.
4 K. Fuke, A. Hasegawa, M. Ueda and M. Itoh, Chem. Phys. Lett., 84 (1981) 176.
5 K. Fuke, M. Ueda and M. Itoh, J. Am. Chem. Soc., 105 (1983) 1091.
6 R.T. Bailey, F.R. Cruickshank, D. Pugh and K.M. Middleton, J. Chem. Soc., Faraday Trans. 2, 81 (1985) 255.
7 S.J. Isak, S.J. Komorowski, C.N. Merrow, P.E. Poston and E.M. Eyring, Appl. Spectrosc., 43 (1989) 419.
8 M. Franko and C.D. Tran, Rev. Sci. Instrum., 62 (1991) 2438.
9 J.R. Whinnery, Acc. Chem. Res., 7 (1974) 225.
10 K. Miyaishi, T. Imasaka and N. Ishibashi, Anal. Chim. Acta, 124 (1981) 381.
11 N.J. Dovichi, Crit. Rev. Anal. Chem., 17 (1987) 357.
12 N.H.G. Penners, Ph.D. Thesis, Wageningen Agricultural University, Netherlands, 1985.
13 Y.M. Chow, K.S. Mak and O.W. Lau, Analyst, 102 (1977) 139.
14 M.J. Stiff, Analyst, 97 (1972) 146.
15 D.W. Gutzman and C.H. Langford, Environ. Sci. Technol., (1993) in press.
16 J.M. Pink, Can. J. Chem., 48 (1970) 1169.
17 D.W. Gutzman,, Ph.D. Thesis, Concordia University, Montreal, 1992.
18 R. Anthore, P. Flament, G. Gouesbet, M. Rhazi and M.E. Weill, Appl. Opt., 21 (1982) 2.
19 C.E. Buffett and M.D. Morris, Appl. Spectrosc., 37 (1983) 455.
20 E.F.S. Alfonso, M.A.R. Revert, M.C.G. Alvarez-Coque and G.R. Ramos, Appl. Spectrosc., 44 (1990) 1501.
21 C.H. Langford, R. Kay, G.W. Quance and T.R. Khan, Anal. Lett., 10 (1977) 1249.
22 J.F. Power and C.H. Langford, Anal. Chem., 60 (1988) 842.
23 J.F. Power,, Ph.D. Thesis, Concordia University, Montreal, 1986.

Analytica Chimica Acta, 283 (1993) 785–793
Elsevier Science Publishers B.V., Amsterdam

Comparative studies on data collection and data treatment in kinetic-based determinations with two rotating bioreactor/amperometric detection systems

J.J. Baeza Baeza [1], Kiyoshi Matsumoto [2] and Horacio A. Mottola

Department of Chemistry, Oklahoma State University, Stillwater, OK 74078-0447 (USA)

(Received 1st April 1993; revised manuscript received 6th July 1993)

Abstract

Two cell configurations involving a rotating bioreactor and a stationary platinum-ring amperometric detector are compared with regard to data produced by continuous-flow and continuous-flow/stopped-flow/continuous-flow operations. In addition to data collection, six kinetic-based approaches to data treatment are also compared. The approaches to data treatment considered here are: (1) the initial rate measurement, (2) integration of the signal time profile, (3) a linear steady-state predictive approach, (4) a nonlinear steady-state predictive approach, (5) a single measurement fixed-time mode, and (6) a multimeasurement fixed-time mode.

Keywords: Amperometry; Kinetic methods; Bioreactors; Data collection and treatment; Rotating bioreactor

The basic design and performance of an integrated reactor/detection system for use with continuous-flow sample/reagent(s) processing, comprising a rotating bioreactor and an amperometric ring electrode, has been reported recently [1]. The approach minimizes diffusional limitations that slow down reactions in low-dimensional spaces, a situation common to the use of immobilized reagents. The practical result is the possibility of using smaller amounts of immobilized reagents than in other conventional ways (e.g., packed column reactors). This, in turn, results in a better utilization of relatively expensive reagents and materials. The reactor/detector arrangement proposed in Ref. 1 also facilitates rate measurements and kinetic-based measurements.

A commonly employed method of data treatment is based on initial-rate measurements when a continuous-/stopped-flow operation is applied, or the measurement of peak height when an uninterrupted continuous-flow mode is used. Other avenues of data manipulation are, however, available and open for consideration. This paper presents data and critically compares two different geometrical arrangements of the reactor/detector system for sample/reagent(s) processing and six methods of data treatment. The two approaches of data collection compared here are: (1) a continuous-, uninterrupted-flow operation, and (2) a continuous-/stopped-/continuous-flow mode. A simple change in the detector location and in the overall size of the cell, as described here, results in: (a) the reduction and

Correspondence to: H.A. Mottola, Department of Chemistry, Oklahoma State University, Stillwater, OK 74078-0447 (USA)

[1] Permanent address: Department of Analytical Chemistry, Faculty of Chemistry, University of Valencia, 46100-Burjassot (Valencia) (Spain).

[2] Permanent address: Department of Food Science and Technology, Faculty of Agriculture, Kyushu University 46-09, Fukuoka 812 (Japan).

stabilization of the background current since the electrochemical area is reduced, and (b) an increase of the rate coefficients and better pseudo-first-order behavior because the cell volume is decreased with a concomitant increase in the relative reaction area of the reactor. The six methods of data treatment discussed here are: (1) initial-rate measurement, (2) integration of the signal vs. time profile, (3) a linear steady-state predictive approach, (4) a nonlinear steady-state predictive approach, (5) a single-measurement fixed-time mode, and (6) a multi-measurement fixed-time mode.

EXPERIMENTAL

Apparatus

The bioreactor/amperometric detector basic design and overall experimental set-up have been described elsewhere [1]. In the work described here the platinum disk electrode was used in two different configurations. One configuration was exactly as described in Ref. 1; the second one, aimed at reducing the volume of solution in contact with the bioreactor, had the ring electrode located above the bioreactor instead of concentric to it. This is shown in Fig. 1. All other pieces of apparatus utilized in this work have also been described previously [1]. The potential applied to the Pt-ring electrode for H_2O_2 measurement was +0.60 V vs. Ag/AgCl, 3 M NaCl reference.

Reagents and solutions

All chemicals used, except as noted, were of analytical reagent grade. The water used for solution preparation was deionized and further purified by distillation in an all-borosilicate-glass still with a quartz immersion heater. The enzymes, immobilized as described in Ref. 1 were tyrosinase [EC 1.14.18.1] from mushroom (Sigma, St. Louis, MO), alcohol oxidase [EC 1.1.3.13] from *Pichea Pastoris* (ICN Biochemicals, Cleveland, OH), and glucose oxidase [EC 1.1.3.4] from *Aspergillus niger* (Type VII, from Sigma). The β-D-glucose was from Sigma, the catechol (pyrocatechol; 1,2-benzenediol) from Eastman Kodak (Rochester, NY), and the ethanol (absolute) from AAPER Alcohol and Chemicals Co. (Shelbyville, KY).

RESULTS AND DISCUSSION

Sample / reagent processing

As illustrated in Fig. 5 of Ref. 1, concentric location of the ring electrode with respect to the rotating reactor does not provide a convenient configuration for uninterrupted flow operation. The arrangement is, however, satisfactory for rate-based measurements by application of a continuous-/ stopped-/ continuous-flow operation. To improve the kinetic characteristics of the device, the ring was moved from the concentric location to just above the rotating reactor (Fig. 1). The modification reduces the volume of the chamber in which the reactor and the detector are located, as well as the gap separating the electrode and the rotating reactor. Consequently, there is an increase of the reacting area with respect to the total cell volume. This increases the apparent rate of reactions. On the other

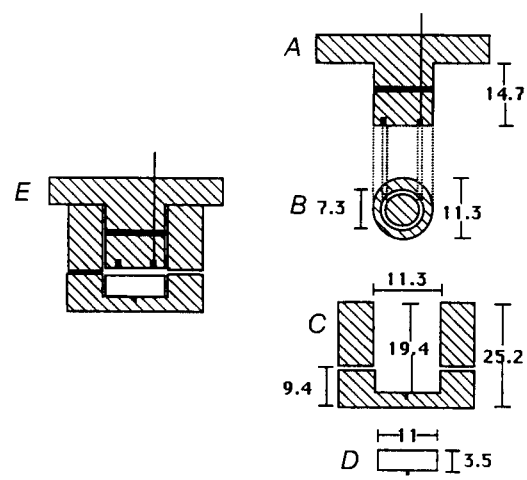

Fig. 1. Schematic representation of the flow-through cell containing the platinum ring electrode just above the rotating reactor. (A) Upper cell body showing the concentric Pt-ring electrode. (B) Bottom view of the upper cell body. (C) Lower cell body defining the flow-through reaction/detection chamber and showing the well for the rotating reactor. (D) Rotating reactor showing the positioning needle point. (E) Cell assembled. The upper cell body is inserted by pressure on the lower cell body for cell assembling.

hand, the area of the electrode is decreased considerably. This leads to a decrease and stabilization of the background signal and to lower consumption of electroactive species, facilitating the study of the kinetics of enzymatic reactions. Applying rotation to the enzyme reactor (at relatively high velocities) propels the products of the reaction taking place on the surface of the reactor away from the surface. Depending on the size of the chamber above the reactor, the coefficients of mass transfer may be considerably larger than the conventional unidirectional, molecular diffusion coefficient that typically operates in unstirred environments [2]. Mass transport at the surface is controlled by convection of the active species caused by rotation. If D_{turb} is defined as a diffusion coefficient characterizing mass transfer in a turbulent moving fluid and differing form D (the molecular diffusion coefficient assumed to be independent of concentration), three characteristic regions can be distinguished in the vicinity of the rotating reacting surface: (1) a turbulent diffusion layer in which transfer by turbulent pulsations predominates ($D_{turb} \gg D$), (2) a viscous laminar sublayer in which both D_{turb} and D contribute to mass transfer, and (3) a laminar diffusion sublayer in which D_{turb} is unimportant and mass transfer is determined by molecular diffusion. Decreasing the gap between the detector and the reactor helps to bypass the molecular diffusion region and enter the intermediate, or even the turbulent region. The situation is similar to the one in a thin-layer electrochemical cell [3] in which, as long as the cell thickness is smaller than that of the diffusion layer and for a given experimental time, molecular diffusion within the cell can be neglected.

Figure 2 shows typical transient signals recorded with the arrangement illustrated in Fig. 1 and acquired under continuous-flow operations. The transient signals shown in this figure have the typical characteristics of signals observed in uninterrupted, unsegmented, continuous-flow sample/reagents (s) processing (e.g., in flow-injection analysis). As expected, the change in electrode location with the concomitant decrease in the cell volume provides satisfactory conditions for circumventing the use of stopped flow. Table 1 provides comparative information of analytical figures of merit with the two cell geometries.

In Fig. 3 is shown the variation of the values of the first-order rate coefficients evaluated with an increasing number of points. This shows an improvement in the pseudo- first-order behavior when the new design is used instead of the one reported previously [1]. This can be explained by the increase in the value of the apparent rate coefficient and the decrease in electrode area; both tend to reduce the relative amount of electroactive species consumed at the electrode.

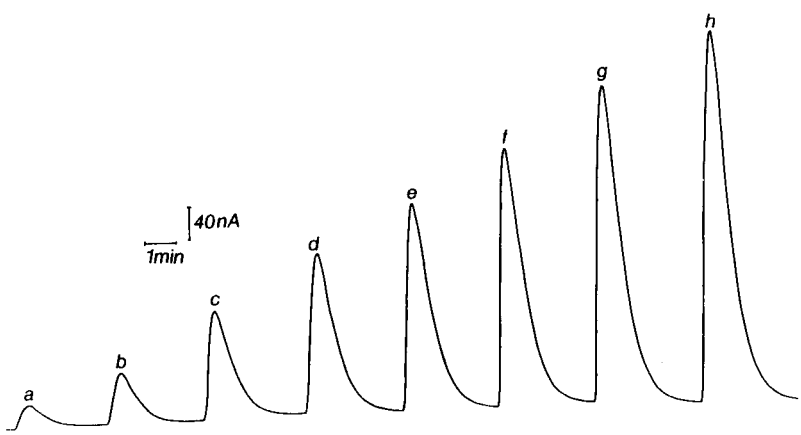

Fig. 2. Typical signals obtained at different glucose concentrations. Flow: 1.36 ml min^{-1}. Sample size: 0.34 ml. Glucose concentrations (mM): (a) 0.050; (b) 0.100; (c) 0.200; (d) 0.300; (e) 0.400; (f) 0.500; (g) 0.600; (h) 0.700. Reactor rotation velocity: 847 rpm.

Comparison of different approaches to data treatment

The signal at any time t, S_t, can be described by:

$$S_t = (S_{inf} - S_0)[1 - e^{-kt}] + S_0 \quad (1)$$

in which S_{inf} is the signal when the system is allowed to reach a steady-state situation, S_0 is the initial signal at $t = 0$, and k is the rate coefficient for the overall rate. S_{inf} must not be confused with the maximum initial rate, which should depend on experimental conditions and the actual enzymatic activity at the surface of the rotating enzyme reactor. Pseudo-first-order kinetic data can be treated in several ways, but rate-based determinations commonly employ initial rate (IR) measurements. This method evolves from a first-order approximation of a Taylor expansion:

$$e^{-kt} = 1 - kt + (kt)^2 - (kt)^3 + \ldots = 1 - kt \quad (2)$$

for small values of kt.

From this:

$$S_t = (S_{inf} - S_0)[1 - e^{-kt}] + S_0 = (S_{inf} - S_0)kt + S_0 \quad (3)$$

then, for small values of kt, the initial rate is proportional to $(S_{inf} - S_0)\,k$ and initial-rate measurements can be used for quantification. The maximum time useful for a given maximum relative error in percentage (e) can be determined by the equation:

$$t_{max} = (2e^{1/2})/[k(20 + e^{1/2})] \quad (4)$$

and for a 4% maximum error $t_{max} = 0.2/k$.

Another approach [4] is a predictive kinetic method (PR) based on extrapolation of a fitted kinetic profile to predict the signal at infinite time. The advantage of this approach, when a single chemical reaction is in operation, is the bypassing of errors due to experimental changes in k that go with changes in temperature, reagent concentration, or rotation velocity of the disk reactor. The predictive kinetic treatment is complicated here by a situation illustrated by the following series process: (1) at the reactor surface, the enzyme-catalyzed reaction: A → P, (2) at the electrode surface, the detection reaction: P ± e^- → P′. This complication requires the use of a method to evaluate $(S_{inf} - S_0)$ based on data obtained at the early times of signal formation. Two

TABLE 1

Comparative values of relevant analytical parameters for reactor/detector units with different locations of the amperometric ring electrode [a]

	Pt-ring concentric to the rotating reactor	Pt-ring above the rotating reactor	
	Stopped flow	Stopped flow	Continuous flow
Concentration range amenable to determination (mM)	0.0050–1	0.0025–1	0.0050–3
Sensitivity (slope of the calibration curve) (nA min^{-1})	417	1391	734
Limit of detection ($3s$) [b] (mM)	2.4	1.3	1.5
Number of determinations per hour	20	32	53
Relative rate coefficient for glucose oxidase reactor.	1	5.4	–
Average relative error [c]	3.5	2.0	2.1

[a] Determination of glucose as described in Ref. 1. Rotation velocity: 870 rpm. As indicated in Ref. 1 these values (except the number of determinations per hour) are dependent on reactor rotation velocity. [b] The standard deviation was evaluated for a sample of 0.0050 mM. [c] This error is the average of the relative error in percentage of a four-sample determination with glucose concentrations of 0.10, 0.20, 0.30 and 0.40 mM.

approaches can be used, the consecutive linear determination of k and $(S_{inf} - S_0)$ or the simultaneous nonlinear determination of k, $(S_{inf} - S_0)$ and S_0 based on Eqn. 1.

The fixed-time method (FT)is based on the use as an analytical parameter of the variation of the signal between two fixed times. The sample concentration is determined by:

$$C_s = [(S_t - S_0) - n_t]/m_t \quad (5)$$

where m_t and n_t are the slope and the intercept of the calibration line.

A variation of the above method is the multiple-constant-time method (MT) in which several increments of the signal at different constant times are used. Now the final concentration is obtained from the weighted mean of the different concentrations:

$$C_s = \sum_{i=1}^{n} \frac{m_i^2 \dfrac{(S_i - S_0) - n_i}{m_i}}{\sum_{i=1}^{n} m_i^2} \quad (6)$$

where n is the number of chosen constant times, S_i is the sample signal at the ith time, and m_i and n_i are the slope and intercept of the calibration line at the ith time.

Finally, it is also possible to integrate the area under the signal-time profile between two times (SI). In electrochemical detection of the product of the reaction a side effect, due to the consumption of the product at the electrode surface, slightly distorts the kinetic signal from the first-order behavior. This is significant in the last part of the signal and makes less accurate the predictive kinetic approach for enzymes with low rates of reaction because only a small portion of the signal can be used, with consequent loss of information.

Study of different linear methods to determine the rate coefficient. Application of the linear predictive kinetic method requires counting with a reliable method to determine the rate coefficients. Several linear methods to evaluate rate coefficients of first-order reactions without knowledge of the signal at infinite time have been proposed. Among these, the most useful have been the Guggenheim method [5] and the KMS method [6].

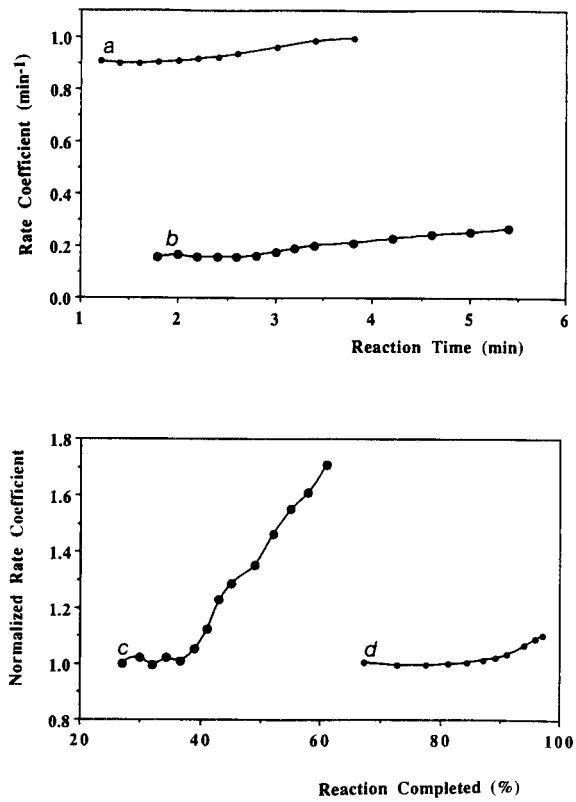

Fig. 3. Variation of evaluated kinetic coefficients with increasing number of points (time and %reaction completed) used. Glucose concentration = 0.50 mM. Reactor rotation velocity: 847 rpm. (a and d) Cell with detector located just above the rotating reactor; (b and c) cell with detector concentric to the rotating reactor. [reference values: first points in curves a and b (i.e., 0.159 s^{-1} and 0.913 s^{-1} for c and d, respectively)].

The Guggenheim method is based on the equation:

$$\ln(S_{t+jh} - S_t) = -kt + \ln(S_{inf} - S_0)(e^{-kjh} - 1) \quad (7)$$

where j is an integer and h is the time interval between two consecutive points. This equation was found to give better results if a weight, $w_t = (S_{t+jh} - S_t)^2$ was used in accordance with Ref. 7.

The KMS method is based on the equation

$$S_{t+jh} = S_t\, e^{-kjh} - S_{inf}(e^{-kjh} - 1) \quad (8)$$

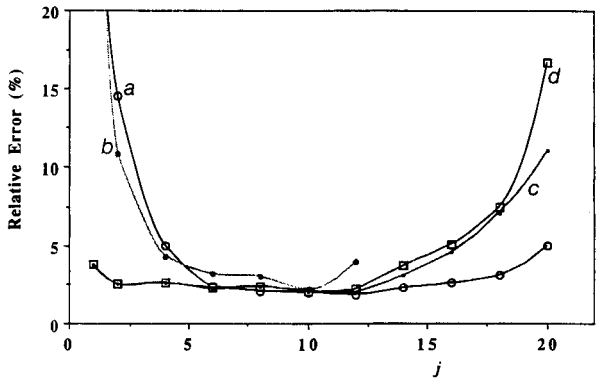

Fig. 4. Average relative error in percentage in the evaluation of a first-order rate coefficient ($k = 1$) using different mathematical methods and different values of j (see text). Each experiment has 25 points taken into account corresponding to 95% degree of progress of the reaction. The $S_{inf} = 1$. The results are the average of 24 simulated experiments with a Gaussian random error of $s = 0.02$ added. (a) Guggenheim method; (b) Eqn. 10 (see text); (c) Eqn. 9 (see text); (d) KMS method.

Together with these methods, two new approaches based on the following equations:

$$(S_{t1+jh} - S_{t2+jh}) = (S_{t1} - S_{t2})\, e^{-kjh} \quad (9)$$

$$(S_{t2+jh} - S_{t+jh}) = (S_{t+jh} - S_t)\, e^{-kjh} \quad (10)$$

have been evaluated here.

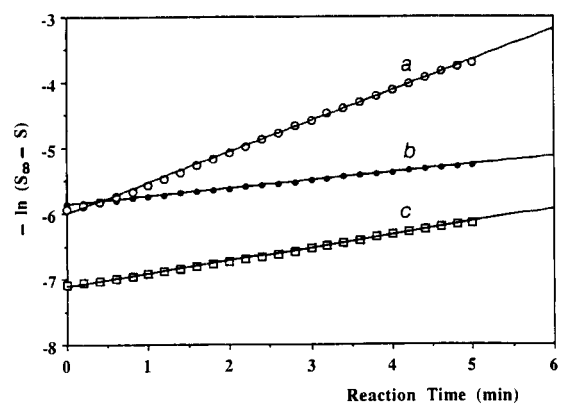

Fig. 5. First-order behavior of the enzymatic reactions under study. In all cases the substrate concentration was 0.20 mM and the reaction was recorded between 0 and 5 min. The degree of advance was: ≈ 50%, ≈ 75% and ≈ 90% for glucose, ethanol, and pyrocatechol, respectively. Reactor rotation velocity: 847 rpm. (a) pyrocatechol determination with immobilized tyrosinase; (b) glucose determination with immobilized glucose oxidase; (c) ethanol determination with immobilized alcohol oxidase.

TABLE 2

Comparison of percent error determined for simulated data by several mathematical methods [a]

Degree of progress (%)	Relative error (%)			
	GU [b]	KMS	Eqn. 9	Eqn. 10
50	11.5	11.3	11.1	15.1
70	4.9	5.2	5.1	6.0
90	2.5	2.6	2.6	2.9
95	2.0	2.1	2.0	2.1

[a] The error is the average of 144 simulated experiments divided into six groups of 24 each and simulated using different random number generators. Gaussian errors with $s = 2\%$ of S_{inf} were used to generate the simulated curves [8]. [b] GU = Guggemheim method.

A comparison and optimization of conditions for the use of these methods were performed in order to improve the determination of rate coefficients. The selection of the best value of j is critical, as can be seen in Fig. 4. This figure shows that for the Guggenheim, KMS and Eqn. 9 methods there is an interval of better performance between $j = (3N/12)$ and $j = (7N/12)$ where N is the total number of points in the data set. With regard to Eqn. 10 the optimal interval appears between $j = (3N/12)$ and $j = [N - 1)/2]$.

Table 2 shows the difference in results obtained by these methods in the valuation of the percent error using data sets of different degrees of advance (%reaction completion). The errors are based on coefficients which are the weighted average, k_{av}, of those values obtained with j values in the region of minimum error in Fig. 4:

$$k_{av} = \frac{\sum_{j=j_i}^{j=j_f} j^2 k_j}{\sum_{j=j_i}^{j=j_f} j^2} \quad (11)$$

With j_i equal to initial $j = |3N/12|$, j_f equal to final $j = |7N/12|$, $[(N - 1)/2]$ for Eqn. 10; with N equal to the number of data points, k_j is the rate-evaluated coefficient. It can be noted that although the methods are quite similar, the Guggenheim method is computationally faster, and this is why it was chosen to perform linear predictive kinetic calculations.

TABLE 3

Relative errors for the determination of substrate concentration using several strategies with simulated data [a]

Substrate concentration	Relative error (%)						
	IR	SI	PKL	PKN	PKC	FT	MT
0.1	3.2	3.1	2.9	2.7	0.45	3.8	2.4
0.2	5.0	2.9	0.7	1.0	0.21	1.1	0.2
0.3	0.7	0.4	0.2	0.3	0.06	0.2	0.1
0.4	1.2	0.3	1.7	1.4	0.07	0.6	0.8
0.6	2.1	1.2	0.4	0.3	0.06	0.2	0.3
Average error	2.4	1.6	1.18	1.14	0.17	1.2	0.8

[a] The data sets were 26 points between $t = 0$ and $t = 5$ (extent of reaction 63%); $k = 0.20$; $S_{inf} = 2000$; $S_0 = 0$. Gaussian errors added with $s = 0.50$. Symbols: IR = initial rate obtained by using the first 5 points (1 min of reaction). PKL = linear predictive kinetics, derived by using the Guggenheim method. PKN = nonlinear predictive kinetics derived by using Powell and pit-mapping optimization methods [9]. PKC = linear predictive kinetics derived by using the average weighted constant of all the points in the calibration ($k = 0.2001 \pm 0.0074$). FT = fixed-time method. MT = multiple fixed-time method.

EXPERIMENTAL APPLICATIONS

The different methods discussed above have been evaluated by using simulated and experimental data. Table 3 shows relative errors in percentage for concentrations when a simulated data set of 26 points was used. The experimental evaluation was performed by the determination

TABLE 4

Relative errors in the determination of glucose, ethanol and pyrocatechol obtained using different mathematical methods [a]

Substrate concentration	Relative error (%) [b]						
	IR	SI	PKL	PKN	PKC	FT	MT
Glucose							
0.100	9.8	7.2	7.4	10.1	2.4	3.6	4.5
0.200	2.3	0.7	14.1	11.1	0.1	1.9	2.1
0.300	1.5	2.7	4.6	2.9	1.7	1.1	1.7
0.400	2.7	3.4	2.1	4.6	1.4	2.8	1.9
Average error	4.1	3.5	7.1	7.2	1.4	2.4	2.6
Ethanol							
0.100	5.3	4.4	0.1	0.6	1.9	0.7	1.4
0.128	4.2	4.3	5.5	4.7	0.3	1.5	0.9
0.152	3.2	2.4	6.7	6.1	1.0	2.1	0.8
0.180	4.8	4.2	1.2	1.5	3.7	4.1	4.5
Average error	4.4	3.8	3.4	3.2	1.7	2.1	1.9
Pyrocatechol							
0.075	0.3	0.9	0.2	0.1	2.2	1.6	4.7
0.100	5.1	5.2	1.8	1.8	1.6	1.2	1.7
0.150	3.6	2.4	3.3	3.2	0.7	4.1	2.6
0.200	1.2	0.3	1.3	1.4	0.8	2.4	1.5
Average error	2.6	2.2	1.7	1.6	1.3	2.3	2.6

[a] Symbols: see Table 3. [b] The average rate coefficient used in PKC was the weighted average of the individual ones: 0.143 ± 0.011, 0.197 ± 0.016 and 0.503 ± 0.037 for glucose, ethanol, and pyrocathecol, respectively. The average extent of reaction was 50, 70 and 85%, respectively with 22, 25 and 21 points used, respectively.

of glucose (glucose oxidase as immobilized enzyme), ethanol (alcohol oxidase as immobilized enzyme), and pyrocatechol (tyrosinase as immobilized enzyme). The comparison is based on signals measured at different substrate concentrations and during a 5-min interval. Figure 5 illustrates the linear relationship expected for first-order or pseudo-first-order behavior. The H_2O_2 was monitored at +0.600 V vs. Ag/AgCl, 3 M NaCl (for glucose and ethanol determination) and the quinone in pyrocatechol determination at −0.200 V vs. the same reference. Substrate concentrations tested were as follows: (a) glucose: 0.050, 0.10, 0.20, 0.30, 0.40 and 0.80 mM; (b) ethanol: 0.075, 0.10, 0.13, 0.15, 0.18 and 0.20 mM; and (c) pyrocatechol: 0.050, 0.075, 0.10, 0.15, 0.20 and 0.25 mM. For each concentration a calibration curve was fitted with the analytical variable of the other five concentrations and from this line the concentration was estimated and compared with the known value. Table 4 shows relative errors in percent for the intermediate concentrations. As can be seen, the method that gave results with least error was the PKC. This seems to indicate that the change in the value of the rate coefficient within a given calibration curve is mainly due to random errors within each run. As to be expected, the calculation of the rate coefficients is most in error when the concentration of substrate is low, and this can make the PKL or PKN methods useless at low concentrations. It is then necessary to use the PKC, with coefficients obtained at relatively high concentrations to estimate the $(S_{inf} - S_0)$ at low concentrations. This, however, does not take advantage of predictive kinetic methods which are able to deal with changes in values of rate coefficients during the calibration process.

The predictive kinetic methods (PKL and PKN) show an improvement in error value when determining ethanol instead of glucose, and the error decreases even more in the pyrocatechol determinations (7.2% for glucose, 3.2% for ethanol, and 1.6% for pyrocatechol). This behavior can be explained by the increase in the final degree of progess of the reaction (≈ 50, ≈ 70, $\approx 90\%$ respectively), which improves the accuracy in the calculation of rate coefficients and the value of the signal at infinite time.

Predictive kinetics requires a relatively long time of measurement, and in the case of the rotating disk reactor, the more time passes, errors in measurements are more likely to occur owing to the consumption of the electroactive species at the electrode surface. The PKC shows very similar results with the three substrates, and this may mean that if the rate coefficients could be determined with lower errors, data obtained at a low extent of reaction could be used. In the PKC method, the average coefficient represents a more accurate value. On the other hand, the PKL and PKN methods give similar results, and consequently, it is not worthwhile to use a nonlinear method to obtain the parameter for a first-order process since the increase in computation time and mathematical complexity did not improve the accuracy of the results, at least in this case. Moreover, the use of a non-linear method requires the use of a linear method to evaluate the initial value of the parameters.

Finally, methods FT and MT give similar results, indicating that there are systematic errors that cannot be accounted for in the model for each determination. Such errors affect all points of the profile, and as a result, the use of the average value for the rate coefficient (obtained using the MT method) does not improve individual values obtained with the FT method.

One of the authors (JJBB) gratefully acknowledges a FPI grant from the Conselleria de Cultura, Educación y Ciencia de la Generalitat Valenciana. This work was partially supported by the Water Research Center (Oklahoma State University).

REFERENCES

1 K. Matsumoto, J.J. Baeza Baeza and H.A. Mottola, Anal. Chem., 65 (1993) 636.
2 F. Opekar and P. Beran, J. Electroanal. Chem., 69 (1976) 1.
3 A.J. Bard and L.R. Faulkner, Electrochemical Methods: Fundamentals and Applications, Wiley, New York, 1980, pp. 406–407.
4 G.E. Mieling and H.L. Pardue, Anal. Chem., 50 (1978) 1611.

5 E.A. Guggenheim, Philos. Mag., 2 (1926) 538.
6 (a) P.C. Mandelsdord, Jr., J. Appl. Phys., 30 (1959) 442; (b) E.S. Swinbourne, J. Chem., Soc., (1960) 2731; (c) G.H. McKinnon, C.J. Backhouse and A.H. Kalantar, Int. J. Chem. Kinet., 16 (1984) 1427.
7 R. de Levie, J. Chem. Educ., 63 (1986) 10.
8 J.J. Baeza Baeza, G. Ramis Ramos and C. Mongay Fernandez, Anal. Chim. Acta, 223 (1989) 419.
9 (a) M.J.D. Powell, Comput. J., 7 (1964) 155; (b) S.S. Rao, Optimization: Theory and Applications, Wiley, New York, 1984, pp. 274–283; (c) L.G. Sillen, Acta Chem. Scand., 18 (1964) 1086.

Analytica Chimica Acta, 283 (1993) 795–802
Elsevier Science Publishers B.V., Amsterdam

Amperometric air gap cell for the measurement of free cyanide

Anita Nagy and Géza Nagy

Institute for General and Analytical Chemistry, Technical University of Budapest, Technical Analytical Research Group of the Hungarian Academy of Sciences, Gellért tér 4, 1111 Budapest (Hungary)

(Received 27th February 1993; revised manuscript received 5th July 1993)

Abstract

A simple air gap cell is described for the determination of the free cyanide content of sample solutions. The cell contains a micro-sized silver disc working electrode. It employs amperometric detection of the cyanide at 0.0 V vs. a 0.1 M silver/silver chloride reference electrode. The three-electrode assembly necessary for detection is located on the flat surface of a probe that is coated by a basic measuring film. The cyanide content of the sample is liberated by the addition of tartaric acid. The hydrogen cyanide gas diffusing through the air gap is accumulated in the measuring film. Owing to the working principle, cyanide concentrations as low as a few $\mu g\ l^{-1}$ can be measured. The effect of interfering species was also studied.

Keywords: Amperometry; Cyanide

The strongly poisonous character of hydrogen cyanide gas is well known. On the other hand, cyanide salts are used in large quantities in industry. Cyanide plays an important role in the synthetic fibre industry, in extraction processes, in galvanic techniques and in different areas of synthetic organic chemistry.

Determinations of cyanide are carried out for the control of the above processes and also in different environmental, food and forensic samples for the safety monitoring. Usually in the latter instances very low concentrations of cyanide (sometimes lower than 0.1 $\mu g\ l^{-1}$ have to be measured in complex matrices.

Several reviews have appeared on the analytical chemistry of cyanide (e.g., [1–3]). Various methods for cyanide measurements employ electroanalytical detection. The cyanide-sensing character of silver halide precipitate-based ion-selective electrodes is widely used and numerous papers have dealt with their application in cyanide measurements [4–9]. The cyanide concentration in the samples is often lower than the measuring range of potentiometric ion-selective cyanide electrodes, in which event a preconcentration is usually carried out using distillation and/or gas purging or Conway cell diffusion.

Frant et al. [10] achieved a lower potentiometric cyanide determination range by using a multiple standard addition method. This employs a silver measuring electrode and addition of an indicating solution containing silver dicyanide ions ($Ag[CN]_2^-$). The silver electrode detects the silver ion activity in the solution, which is influenced by the cyanide concentration of the sample through the dissociation equilibrium of the complex. A simple potentiometric air gap cell for the measurement of free cyanide was described by Fligier and co-workers [11–13]. Its function is also based

Correspondence to: G. Nagy, Institute for General and Analytical Chemistry, Technical University of Budapest, Technical Analytical Research Group of the Hungarian Academy of Sciences, Gellért tér 4, 1111 Budapest (Hungary).

on the dissociation equilibrium of the silver dicyano complex. In the air gap cell a separation and preconcentration step precedes the detection.

Amperometric methods have also been successfully used for the determination of cyanide. With the combination of amperometric detection and appropriate flow conditions, a favourable low measuring range could be achieved. Easty et al. [14] used a tubular gold electrode for the amperometric determination of cyanide. Pihlar and coworkers [15,16] developed a silver wire-based flow-through amperometric cell that could be used for cyanide determination. Recently Nikolic et al. [17] reported the successful application of a lipid membrane-coated amperometric silver electrode in flow-injection cyanide measurements. The lipid coating provided good selectivity for the detection.

Opekar and Bruckenstein [18] reported a pneumato-amperometric measuring technique for the sequential determination of cyanide and sulphide using a porous gold electrode. In the measuring apparatus a stream of nitrogen bubbling through the cell carries the hydrogen cyanide in to the surface of the working electrode.

Owing to the enhanced spherical diffusion, microelectrodes can also produce quasi-steady-state amperometric signals in quiescent solutions. For example, Pletcher and Valdes [19] observed this experimentally with gold micro band electrodes. Accordingly, it was expected that using a micro-sized working electrode, an amperometric air gap probe could be prepared for measuring free cyanide; the probe is similar to that used in potentiometric air gap cells in the surface layer of which separation and preconcentration of the volatile species take place before detection. In this paper results obtained in investigations with an amperometric air gap cell and a laboratory measuring procedure for cyanide determination are reported.

EXPERIMENTAL

Apparatus and chemicals

All current–time and current–electrode potential measurements were carried out with a PAR Model 174A polarographic analyser connected to an Omniscribe strip-chart recorder or a PAR Model 9002A X–Y recorder. For recording dynamic voltammograms a flow-injection manifold containing a peristaltic pump (Labor MIM Type OL-602) and injector (Rheodyne Model 7125) with a 150-μl loop, a dispersion coil (made of 100 mm × 0.8 mm i.d. PTFE tubing coiled on a 12 mm o.d. glass rod) and a laboratory-made wall-jet cell were used. A silver disc working electrode (diameter 1.0 mm), a double-junction silver/silver chloride reference (Radelkis Type OP-0821P) and a platinum wire (diameter 0.2 mm) auxiliary electrode were employed in the flow cell.

All chemicals used were of analytical-reagent grade.

Working principle of the amperometric air gap cell

The silver metal undergoes electrochemical oxidation at a relatively low positive potential, which limits the potential range accessible by silver electrode amperometry. However, in solutions containing species such as cyanide ions which form a stable complex or precipitate with the silver ions, the electrochemical dissolution of the silver starts at a lower potential. Under given conditions a well defined prewave appears, the height of which depends on the concentration of the mentioned species.

The amperometric measurement of cyanide concentration can be done by keeping the potential of the silver electrode in the range of the prewave. This works well in streaming solutions or with a rotating disc electrode.

The air gap cell is a closed vessel in which the sample solution is separated by the air gap from the electrode assembly. The surface of the latter is coated with a thin basic aqueous solution film (measurement film). As long as the sample solution in the cell is basic the cyanide is dissolved in ionized form. After acidification, the free cyanide present becomes protonated, forming volatile HCN gas, which, diffusing through the air gap, is accumulated in the basic measuring film on the probe surface.

If a conventional-sized (diameter 1–5 mm) sil-

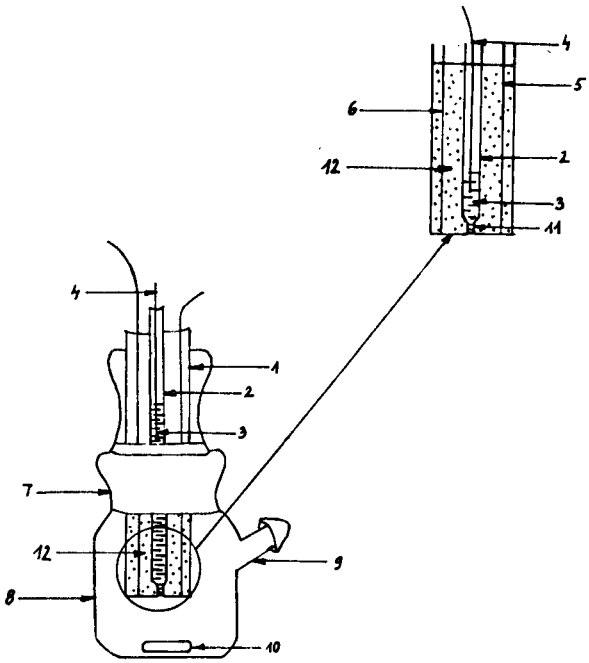

Fig. 1. Schematic diagram of the amperometric air gap cell. 1 = Glass body of the probe; 2 = reference electrode body; 3 = internal filling solution of the reference electrode; 4 = internal electrode (silver chloride-coated silver wire); 5 = platinum wire serving as auxiliary electrode; 6 = silver wire for micro-sized disc working electrode; 7 = glass stopper; 8 = measuring cell; 9 = side-tube for reagent addition; 10 = magnetic stirring bar; 11 = current bridge of reference electrode; 12 = dental cement.

ver disc working electrode were used for amperometric detection, no quasi-steady-state amperometric signal could be obtained with the air gap cell because of the depletion of the film around the electrode due to the electrode process. However, with a small electrode and an appropriate film thickness, a quasi-steady state of the electrolysis and the diffusion can be expected.

Description of the cell

Based on previous experiments, an amperometric air gap cell was prepared. A schematic diagram of the cell is shown in Fig. 1. The cell (8) is a 50 mm high cylindrical glass vessel of diameter 30 mm. A small magnetic stirring bar (10) is placed inside it. To the side of the cell a glass tube (9), through which the acidifying reagent can be introduced, is attached slantwise. The top of the cell and the side tube are closed by appropriate glass stoppers (7). A flat-end cylindrical probe, holding the electrode assembly, reaches down in the lumen of the cell through the top closing stopper.

To prepare the probe (1), a 60-mm section of a glass tube of 6 mm i.d. was selected. One of its ends was closed by a flat end-plate prepared by a standard glass-blowing technique. A sintered-glass plug was cemented in the end of another glass tube (4 mm o.d.). This tube served as the reference electrode body (2). It was placed in the centre of the other tube. The end of a silver wire (diameter 0.1 mm) (6) and that of a platinum wire (diameter 1 mm) (5) were soldered to copper wire leads. With the platinum and the silver wire reaching down to the bottom, the two wires were inserted into the wider glass tube by the two sides of the centre tube symmetrically, avoiding electric contact. Dental cement (12) was poured inside the tube. After hardening, the glass end-plate was machined off. In this way the silver and the platinum electrode discs and the current bridge (11) of the reference electrode embedded in dental cement were exposed. Finally, the end-plate was polished and the internal filling solution (0.1 M potassium chloride) (3) of the reference electrode and a silver chloride-coated silver wire as internal electrode (4) were introduced.

Procedure

Cyanide measurements were carried out with the cell in the following way: 2.0 ml of the basic sample or standard solution were introduced into the cell. The surface of the probe was coated with a measuring film consisting of 0.1 M sodium hydroxide solution. After preparation of the measurement film (see later) the probe-holding stopper was plugged in and the electrodes were connected to the potentiostat. Stirring was started and the amperometric current was followed applying 0.0 V as the working electrode potential. When a steady-current had been obtained, 1 ml of tartaric acid solution (30%) was introduced with a syringe through the side-tube of the cell. When the liberated hydrogen cyanide gas reached the measurement film, the amperometric current

sharply increased. The change in current was taken as the cyanide signal.

Preparation of measurement film

Two different procedures were used for preparation of the measurement film. In certain instances a given volume of the film-forming solution (0.1 M NaOH containing 1% methylcellulose; see later) was added and spread on the surface of the probe using a Hamilton syringe. In other instances the probe was inserted in an auxiliary cell containing the film-forming solution (see later) and a sponge soaked in it. On lifting up the electrode, the excess of the liquid was soaked off by the expanding sponge.

RESULTS AND DISCUSSION

For the amperometric detection of the cyanide the proper selection of the working electrode potential is very critical. To obtain experimental data for this selection voltammetric measurements were made with a silver disc working electrode in 0.1 M sodium hydroxide background electrolyte. Voltammograms measured in 1.3 mM cyanide solutions were compared with the voltammograms taken in the background electrolyte. Dynamic voltammograms were also recorded under flow-injection conditions. In those measurements 0.1 mM potassium cyanide solution was injected and the current peak heights

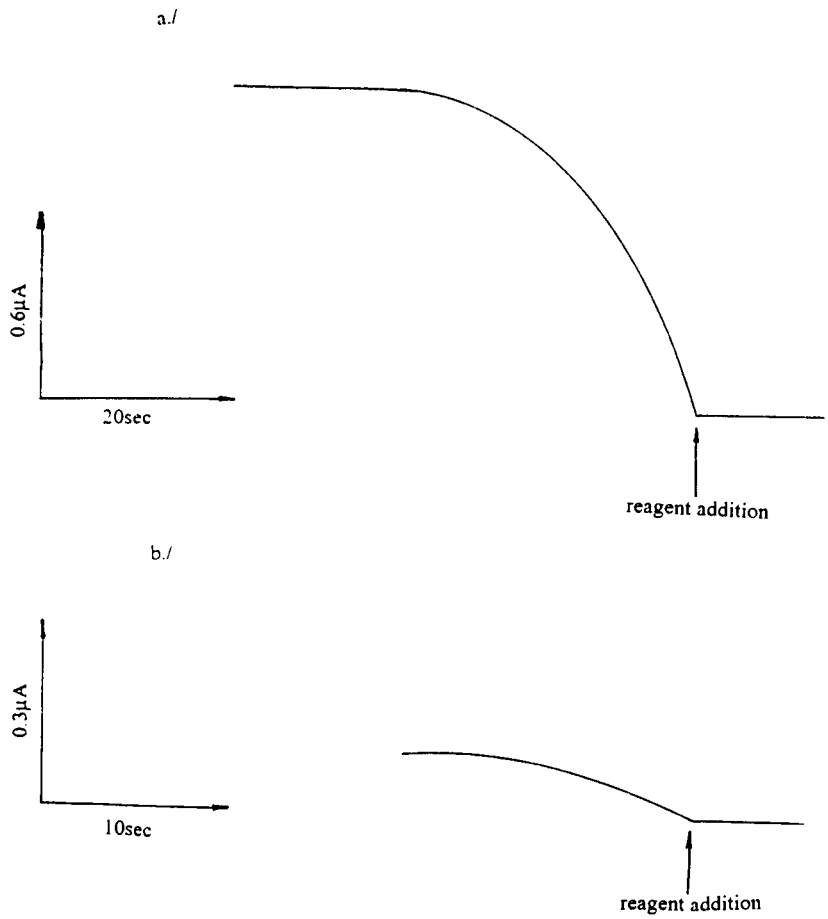

Fig. 2. Current–time recordings obtained during cyanide measurements. Cyanide concentration: (a) 0.1 mM and (b) 1 μM.

obtained were plotted against the preset working electrode potential. Based on the shapes of the voltammograms, a working electrode potential of 0.0 V (vs. 0.1 M silver/silver chloride) was selected for the amperometric measurements. This potential value is in the early section of the cyanide plateau and at this potential no electrochemical oxidation of silver in an indifferent background solution was observed. Nikolic et al. [17] employed a similar potential in their flow-injection studies.

To investigate the cyanide response of the cell, the amperometric current was recorded at 0.0 V working electrode potential. Following the procedure described above the sample was introduced into the cell. After the current had reached a steady value, the pH of the sample was decreased by addition of 1 ml tartaric acid solution (30%). As the liberated hydrogen cyanide gas accumulated in the measuring film, the current increased and eventually reached a steady value that was maintained for a long period; a decrease in the current could be observed only after relatively long times at higher cyanide concentrations (e.g., 15 min at 1 μM cyanide concentration). This behaviour supports the assumption that a 0.1 mm diameter silver disc behaves as a microelectrode in the measuring film. The preconcentration, diffusion and electrode processes achieve a quasi-steady state during the cyanide measurements. Figure 2 shows time-based recordings of the current obtained during cyanide measurements with the cell. The cyanide concentration was (a) 0.1 mM and (b) 1 μM. The difference between the steady-state currents measured before and after acid addition was taken as the cyanide signal (Δi).

As indicated above, the operation of the measurement cell is based on a separation step in which the cyanide content of the acidified sample solution is concentrated in a basic measuring film on the surface of the amperometric electrode assembly. The electrode process producing the amperometric signal takes place at the measurement film–working electrode interface. Therefore, the composition of this film can critically influence the cyanide measuring function. It was found that 0.1 M sodium hydroxide solution can be used as a film-forming solution. However, this sodium hydroxide solution often resulted in an irregular film thickness and the solution readily formed droplets on the polished probe surface. Therefore, based on previous studies [13], 1% methylcellulose was dissolved in the film-forming liquid; it decreases the surface tension and increases the viscosity, making the film preparation easy and reproducible. Using this film-forming liquid, stable measuring films were obtained.

Because of the preconcentration–separation working principle of the cell, it is expected that the thickness of the measuring film and the total volume of the film-forming liquid on the probe will influence the cyanide response. Controlled volumes (v) of the film-forming solution were employed and spread on the probe surface using a Hamilton syringe. Cyanide determinations were performed using 2 ml of 1 μM potassium cyanide solution as the sample. The electrolyte film volume–Δi dependence obtained shows that in the range studied (2–5 μl) a thicker measuring film provides a higher cyanide signal and a higher slope of the calibration graph: $\Delta i(\mu A) = 0.2971v(\mu l) - 0.2242(\mu A)$, $r = 0.9962$. This contradicts the preliminary expectations as it can be assumed that the higher film volume results in a lower cyanide concentration in the film, which would give a smaller cyanide signal. The unexpected behaviour is probably caused by the enhanced mass transport of cyanide to the microelectrode in the case of a thicker film. This may mean that in thicker measurement films spherical diffusion is more dominant.

The other property that the measuring film thickness can influence is the response time of the cell. The response time was characterized by the time period between the addition of the acid reagent and achievement of 90% of the total amperometric current change, t_{90}. A thicker measuring film resulted in a substantial increase in t_{90}: $t_{90}(s) = 9.53v(\mu l) - 12.8095(s)$, $r = 0.9981$.

From the film thickness study it is concluded that a thicker film may result in higher sensitivity, but at the same time it can cause longer response times of the cell. Therefore, the use of a thin measurement film seems a better choice. Thin measurement films can easily be prepared on the

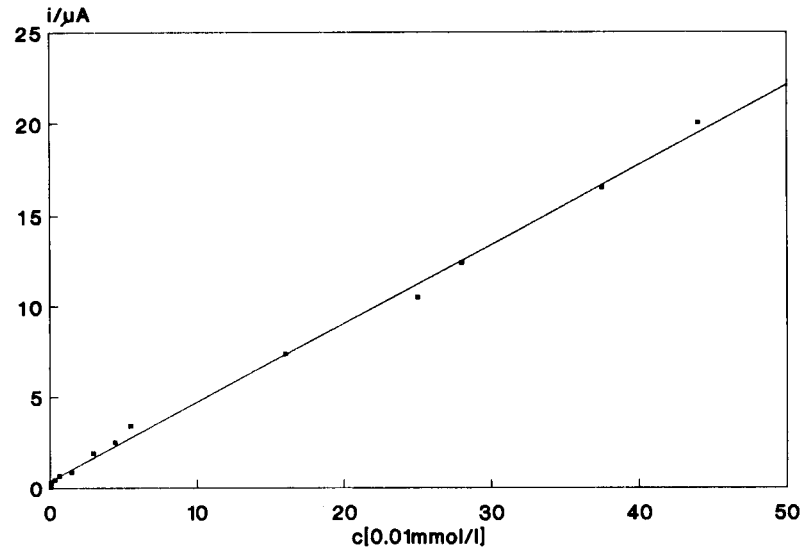

Fig. 3. Cyanide calibration graph measured with the amperometric air gap cell.

probe by simply dipping it into an auxiliary cell that contains a few mm deep layer of the film-forming liquid and a sponge soaked in it. The sponge extending above the solution removes the excess of liquid when the probe is lifted up after inserting it in the sponge.

To study the dependence of this signal on cyanide concentration, measurements were made with 2.0-ml portions of freshly prepared potassium cyanide solutions of known concentrations. The calibration graph obtained is shown in Fig. 3. As can be seen, the response is linear over a broad range. The relative standard deviation of the measured current difference values ($n = 5$) was 10% for a 0.66 μM solution and 2.0% for a 0.16 mM solution.

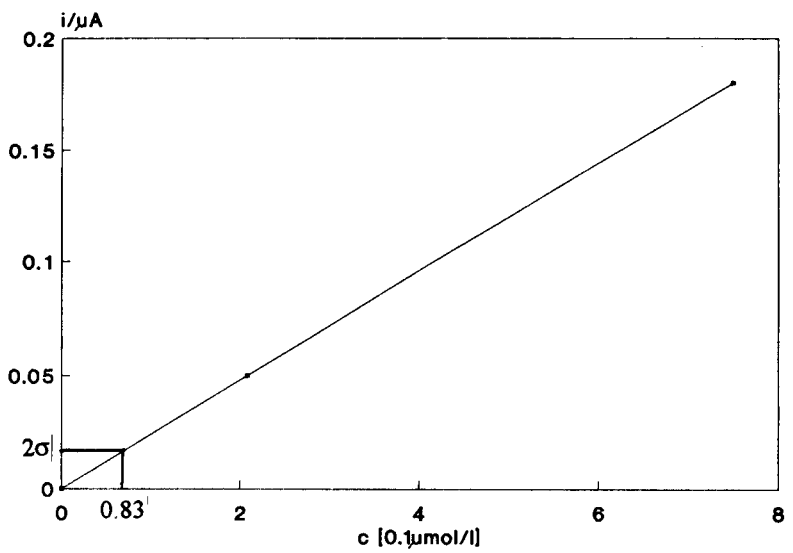

Fig. 4. Working graph for determination of the lower concentration limit of cyanide measurement.

To establish the lower limit of cyanide determinations with the amperometric air gap cell, the standard deviation of the Δi values was calculated using the results of five consecutive measurements with 0.66 μM cyanide solution. Twice this standard deviation value (2σ) of Δi was projected on the extrapolated calibration graph. The working graph prepared in this way is shown in Fig. 4. As can be seen, the lower concentration limit of measurements in the given circumstances is about 0.083 μM, i.e., 0.0021 mg l^{-1}.

The effect of the sample volume on the cyanide signal was also investigated. Different volumes of 10 μM potassium cyanide solution were introduced into the cell and the amperometric cyanide signal was recorded after the addition of the acid reagent. According to expectation, the larger the sample volume (v_s) the higher was the amperometric cyanide signal. The dependence is linear in the range studied (1–1.5 ml): $\Delta i(\mu A) = 6.37 v_s(\text{ml}) - 4.262(\mu A)$, $r = 0.9959$. This means that the cyanide signal of the amperometric air gap cell depends on the total amount of the cyanide in the sample rather than on the free cyanide concentration. This property, although easy to understand, is unusual in amperometry.

It is important to know what kind of species can interfere with the free cyanide measurements and how to avoid interferences or separate interfering sample components. It is easy to predict that any species electroactive at the potential of the working electrode would interfere after entering the measuring film. Hence the primary interferents are volatile electroactive molecules (e.g., hydrogen sulphide). It can also be expected that to some extent volatile acids, such as acetic acid, will also affect the amperometric cyanide signal by inducing pH changes in the measuring film.

To investigate the extent of interferences, cyanide measurements were made with 0.1 M sodium hydroxide solutions containing cyanide at the same concentration (0.1 mM) and the interfering component at different concentrations. The results obtained for sulphide interferences are shown in Fig. 5, which is a plot of the amperometric signal against sulphide concentration. It is obvious that with a 0.1 mM cyanide concentration the presence of 6 μM sulphide seriously disturbs the amperometric cyanide determination. The hydrogen sulphide gas formed after addition of acid enter the measuring film and produces an increase in the amperometric current at the silver disc microelectrode similar to that due to cyanide.

Sample pretreatment with lead nitrate reagent was found to be effective in eliminating the sulphide interference. Sample solutions (25 ml) containing sodium sulphide at different concentrations (0.6 μM–6.6 mM) were treated with lead

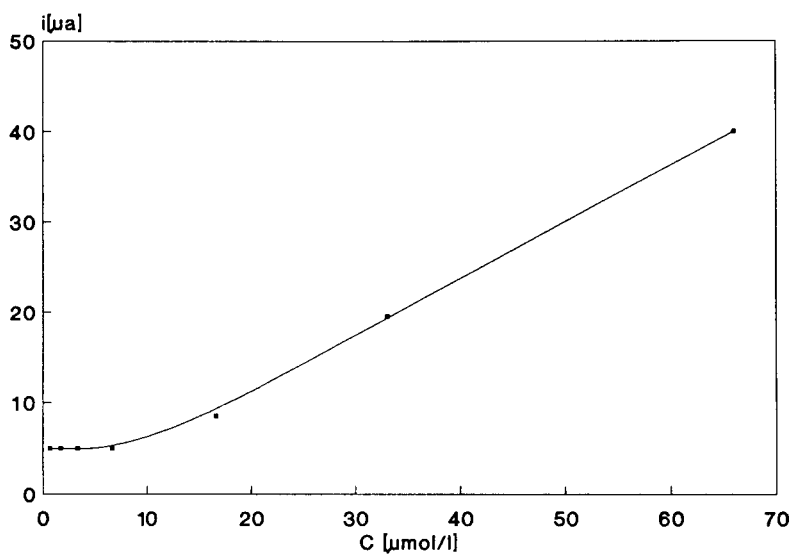

Fig. 5. Interfering effect of sulphide on the cyanide response.

nitrate (total concentration in the sample 1 mM). After a reaction time of about 10 min the solutions were filtered and 2-ml portions of the filtrate were introduced into the measurement cell. The amperometric signal was recorded after addition of acid. The current change obtained after pretreatment reflected well the free cyanide concentration regardless the original sulphide concentration. The interfering effect of acetate as a model species for volatile acids was also studied in a similar way, but no noticeable interference was obtained in the range investigated (0.66 μM–0.5 mM).

The cell could be successfully used to analyse directly environmental air samples collected by a sample collector impinger containing 0.1 M sodium hydroxide solution.

The results presented show that the amperometric air gap cell containing a micro-sized silver disc working electrode can be used for the determination of the free cyanide content of sample solutions down to very low cyanide concentrations. It is expected that other volatile electroactive species also can be determined based on the same principle and using a similar air gap cell.

The financial support of OTKA 5346 is greatly appreciated.

REFERENCES

1 W.J. Williams, Handbook of Anion Determination, Butterworths, London, 1979.
2 G.L. Roberts, in F.D. Snell and L.S. Ettre (Eds.), Encyclopedia of Industrial Chemical Analysis, Vol. 14, Interscience, New York, 1971, p. 403.
3 L.S. Bark and H.G. Higson, Analyst, 88 (1963) 753.
4 E. Pungor, Anal. Chem., 39 (1967) 28A.
5 E. Pungor and K. Tóth, Anal. Chim. Acta, 47 (1969) 291.
6 E. Pungor and K. Tóth, Analyst, 92 (1970) 625.
7 B. Fleet and H. von Storp, Anal. Chem., 43 (1971) 1575.
8 M. Mascini, Anal. Chem., 45 (1972) 614.
9 C. Harzdorf, Anal. Chim. Acta, 86 (1976) 103.
10 M.S. Frant, Jr., J.W. Ross and J.H. Riseman, Anal. Chem., 44 (1972) 2227.
11 J. Fligier, P. Czichon and Z. Gregorowicz, Anal. Chim. Acta, 118 (1980) 145.
12 P. Czichon, J. Fligier and Z. Gregorowicz, Anal. Chim. Acta, 126 (1981) 221.
13 J. Fligier, M. Gratzl, G. Nagy and E. Pungor, Anal. Chim. Acta, 134 (1982) 263.
14 D.B. Easty, W.J. Blaedel and L. Anderson, Anal. Chem., 43 (1971) 509.
15 B. Pihlar and L. Kosta, Anal. Chim. Acta, 114 (1980) 275.
16 B. Pihlar, L. Kosta and B. Hristovski, Talanta, 26 (1979) 805.
17 S.D. Nikolic, E.B. Milosavljevic, J.L. Hendrix and J.H. Nelson, Analyst, 117 (1992) 47.
18 F. Opekar and S. Bruckenstein, Anal. Chim. Acta, 169 (1985) 407.
19 D. Pletcher and E.M. Valdes, Anal. Chim. Acta, 248 (1991) 173.

Analytica Chimica Acta, 283 (1993) 803–810
Elsevier Science Publishers B.V., Amsterdam

Evaluation of neglecting electrostatic interactions on the determination and characterization of the ionizable sites in humic substances

Jorge C. Masini

Instituto de Química, Universidade de São Paulo, CP 20780, CEP 01498-970, São Paulo, SP (Brazil)

(Received 25th February 1993; revised manuscript received 7th July 1993)

Abstract

The stoichiometry and pK_a of the ionizable sites in humic acids has been determined by means of potentiometric titrations. The analytical implications of neglecting the free electrostatic energy that accompanies the proton dissociation in polyelectrolytes or humic acids is presented. Simulated titration curves of polyelectrolytes with known composition were generated according to an electrostatic model. The data of these titrations were treated by a linear calculation method developed for determination and characterization of weak monoprotic acids in mixtures. The influence of the polyelectrolyte molar mass was also studied. Besides, experimental titration curves of humic acids at ionic strength 0.010, 0.10 and 1.0 were performed and the titration data were treated by the same calculation method. The results showed that the indication of the existence of two or three kinds of carboxylic groups in high-molar-mass polyelectrolytes may have been affected by a mathematical fit as consequence of ignoring electrostatic interactions. However, the experimental titrations data treatment have characterized five kinds of titratable groups which have concentration and pK_as few affected by changes in the ionic strength. These results indicate that the chemical heterogeneity among groups with the same chemical nature is the major factor governing acid–base properties of humic acids having low charge accumulation.

Keywords: Potentiometry; Titrimetry; Humic substances; Electrostatic model

Humic substances are the major constituents of the natural organic matter in waters, soils and sediments. The humic substances have a large number of ionizable sites with acid–base properties. Thus, they play an important role in the proton buffering of the aforementioned environmental compartments [1]. The bioavailability of toxic metals and the metal complexation capacity are pH-dependent, so that the determination of the stoichiometry and pK_as of the ionizable sites is a first step in speciation studies. The determination of these parameters has been made by potentiometric titration [2,3].

However, the interpretation of the titration curves of humic acids is complicated by the presence of carboxylic, phenolic and amine groups – a mixture of acidic species with different acid strengths. In addition, the humic acids have polyelectrolytic characteristics, so that a large number of electrical charges (pH-dependent) affect the dissociation constants of the titratable groups. Another problem is that the intensity of these electrostatic interactions is dependent on the molar mass of the macromolecule [4–6] and, if no

Correspondence to: J.C. Masini, Instituto de Química, Universidade de São Paulo, CP 20780, CEP 01498-970, São Paulo, SP (Brazil).

further separations are made, a humic acid sample may contain molecules with a wide range of molar masses.

Several authors [7,8] have interpreted the acid–base titration curves of humic acids based on the electrostatic theory developed by Tanford for macromolecules [9]. In this model all carboxylic groups would be identical in their affinity for H^+. The proton dissociation would be described by an intrinsic pK_a which depends only on the chemical identity of the group and by an apparent pK_a. The latter is dependent on the electrostatic interactions resulting from the charge accumulation on the macromolecule surface. However, the chemical heterogeneity among the carboxylic groups, or among the phenolic groups, has been neglected. Some authors have assumed a model in which the binding sites behave as a continuum and have varying pK_a values [10,11].

Other authors [2,3] have assumed the ionizable groups in humic acids behaving as a mixture of weak monoprotic acids. The dissociation constants would be only dependent on the chemical identity of the ionizable group, as well as on the local interactions due to chemical and physical ambient in which the group is located on the macromolecule. Here, the effects of the charge accumulation on dissociation constants are neglected. Marinsky and Ephraim [12] and Tipping et al. [13] proposed a combination of the chemical heterogeneity and electrostatic interaction to describe the acid–base properties of humic acids.

A linearization method for potentiometric titration data treatment was applied to humic acid by Aleixo et al. [3]. This method uses the modified Gran functions [14] – a collection of linear equations based on a rigorous charge–mass balance describing the equilibria involved in a titration of mixtures of weak monoprotic acids in the presence of a strong acid. When these equations have been applied to polyelectrolytes the electrostatic free energy needed to produce the proton dissociation has been neglected [15]. Aleixo et al. [3] have characterized six kinds of titratable groups in humic acid. The same methodology has already been applied to proteins [15,16] and, in this case, the carboxylic and amine groups have been divided in sub-groups with different pK_as. Godinho et al. [17] have shown that this division may be a consequence of ignoring the electrostatic effects on dissociation constants, so that the characterization of two or three kinds of carboxylic groups in polyelectrolytes could be a mathematical fit.

The purpose of the research described herein was to evaluate the effects of neglecting the electrostatic interactions on the stoichiometry and pK_as of the titratable groups in humic acids. To attain this goal, simulated titration curves of hypothetical polyelectrolytes with known composition and different molar masses were generated according to the electrostatic model proposed by Tanford [9]. In addition, according to Debye–Hückel theory the electrostatic free energy of a molecule is inversely proportional to the square root of the ionic strength [9]. Thus, an experimental approach in order to evaluate the effects of ignoring electrostatic interactions was carried out by titrations of humic acids at ionic strength 0.01, 0.10 and 1.0. The simulated and experimental titration data were treated by the modified Gran functions.

EXPERIMENTAL

Apparatus and reagents

A Metrohm 654 potentiometer and a Metrohm 6.0203.100 combined glass electrode were used in the pH measurements. The outer chamber of the combined electrode was filled with saturated potassium chloride solution. The calibration of the electrode in solutions of 0.01, 0.10 and 1.0 M sodium chloride was done with solutions of known hydrogen ion concentration and at the same ionic media. The values of $E^{0\prime}$, junction potential and K_w, were calculated as earlier described [3].

A Radelkis OP931 automatic burette with capacity of 10 ml and precision of 2 μl was used for titrant increments.

The analytical grade reagents sodium chloride, sodium hydroxide and hydrochloric acid were obtained from Merck.

The solutions of 0.1 M sodium hydroxide were prepared free of carbon dioxide in the presence of 0.010, 0.10 or 1.0 M sodium chloride, stocked

in polyethylene flasks protected from carbon dioxide contamination by an ascarite tube and handled without contact with atmosphere. These solutions were standardized with potassium hydrogenphtlalate, dried at 110°C, and using phenolphtlalein as indicator.

The sodium salt of humic acid from Aldrich (catalog H1-675-2 lot No. 01816HH) was used.

Procedure

Suspensions containing 1.0 g l^{-1} of sodium salt of humic acid were prepared in the presence of 0.010, 0.10 or 1.0 M sodium chloride. A volume of 50.00 ml of these suspensions was transferred to a titration flask. A 0.10 M hydrochloric acid (with the same concentration of sodium chloride as the humic acid suspension) was added until the pH was adjusted to about 2. The carbon dioxide interference was removed by passing N_2 above the solution for 15 min before the titration was started and during the titration. Water at 25.0 ± 0.1°C was circulated through the external jacket of the titration flask and the solution was stirred with a magnetic stirrer during the titration. The suspensions of humic acid were titrated with the standard sodium hydroxide containing the same concentration of sodium chloride as the titrated suspension. The potential was read after the addition of each aliquot of titrant only when its variation was smaller than 0.555 mV min^{-1} (0.009 pH units min^{-1}). These measurements were made using the drift control of the Metrohm 654 pH meter.

The titrations were performed until pH reached c.a. −250 mV (pH 11.5) and about 150 points were taken. The conversion of potential in hydrogen ion concentration was made as has been described earlier [3,18].

TABLE 1

Composition of the hypothetical polyelectrolyte used to simulate titration curves according to the electrostatic model (Assumed values for $w = 0.01$, 0.03 or 0.1. Molar mass = 1000, 5000 or 10000)

Group (i)	Concentration (C_i) (mmol g^{-1})	pK^i_{int}
$COOH_I$	2.00	4.00
$COOH_{II}$	0.500	7.00
Phenolic	1.00	9.00

CALCULATIONS

Simulation of titration curves of fully protonated polyelectrolytes according to the electrostatic model

Potentiometric titration curves of polyelectrolytes are described by:

$$pH = pK^i_{int} + \log\frac{x_i}{1-x_i} + 0.434\frac{e\psi}{KT} \quad (1)$$

where K^i_{int} is the intrinsic dissociation constant for titratable group of type i. It is the dissociation constant in the absence of electrostatic interactions. x_i is the average degree of dissociation of type i group, e is the proton charge, K is the Boltzmann constant, T is the absolute temperature and ψ is the potential at the polymer surface. The term $0.434\ e\psi/KT$ is related to the work of removing a proton from its ionized site against electrostatic forces of other charged groups on the macromolecule.

The potential ψ cannot be directly determined, but it can be related to the overall charge, on the macromolecule, Q, which depends on the number of ionized sites per mole of the macromolecule, according to the following equation

$$\psi = \left(\frac{RT}{F}\right) 2WM(Q_{max} \cdot x_i) \quad (2)$$

where R and F are respectively the gas and Faraday constants, M is the molar mass of the polyelectrolyte and Q_{max} is the charge on the macromolecule when all ionizable groups are protonated or deprotonated. W is an electrostatic function which depends on the ionic strength of solution [9] as well as on the conformation, geometry and molar mass of the polyelectrolyte [4].

In this work, the calculation of the simulated titration curves of polyelectrolytes were based on the following semi-empirical equation

$$pH - \log\frac{x_i}{1-x_i} = pK^i_{int} - 0.868w_iZ \quad (3)$$

which was extensively used in the interpretation of titration curves of globular proteins [9]. In this equation, Z is the net charge on the macromolecule and w_i is the electrostatic interaction parameter for type i of titratable groups.

A hypothetical polyelectrolyte with two kinds of carboxylic groups ($COOH_I$ and $COOH_{II}$) and one kind of phenolic group was considered to simulate the titration curves. The stoichiometry and pK_{int} of these groups are given in Table 1. The molar mass was considered in the range of 1000 to 10000 g mol^{-1} The net charge, Z, on the polyelectrolyte was calculated as a function of pH by Eq. 4:

$$Z = T - \frac{1}{C_p}\left[\sum_{i=1}^{I}\left(\frac{C_i K^i_{int} 10^{0.868 w_i Z}}{|H^+| + K^i_{int} 10^{0.868 w_i Z}}\right)\right] \quad (4)$$

where T is the charge when the polyelectrolyte is fully protonated, C_p is the polyelectrolyte concentration, C_i is the analytical concentration of the group i and I is the number of different kinds of titratable groups.

The volumes of titrant, V, with concentration C_B needed to attain the predetermined pH were calculated using the Eqn. 5.

$$V = \frac{V_0\left(|H^+| - |OH^-| - \sum_{i=1}^{I} C_i D_i\right)}{\sum_{i=1}^{I} C_i D_i - |H^+| + |OH^-| - C_B} \quad (5)$$

where

$$D_i = \frac{K^i_{int} \cdot 10^{0.868 w_i Z}}{|H^+| + K^i_{int} 10^{0.868 w_i Z}} \quad (6)$$

and V_0 is the initial volume in the titration flask.

The values of the electrostatic interaction parameter, w, have been assumed in the range of 0.01 to 0.1. These values are in the same range shown by Tanford [9] for proteins with molar mass and hydrodynamic diameter similar to that found for the maximum distribution in Aldrich humic acid [19] (95.9% with distribution maximum at molecular weight 8000 and hydrodynamic diameter 32.5 nm).

Simulated and experimental data treatment

The simulated and experimental titration data were treated by the modified Gran functions. In application of this method the ionizable groups have been treated as a mixture of weak monoprotic acids, so that the term 0.868 wZ has not been included in derivation of the equations. The modified Gran functions and the procedure for their application have already been described [3,15]. In this work the computational program was compilated in quick-Basic language using a PC-AT 286 microcomputer for data processing.

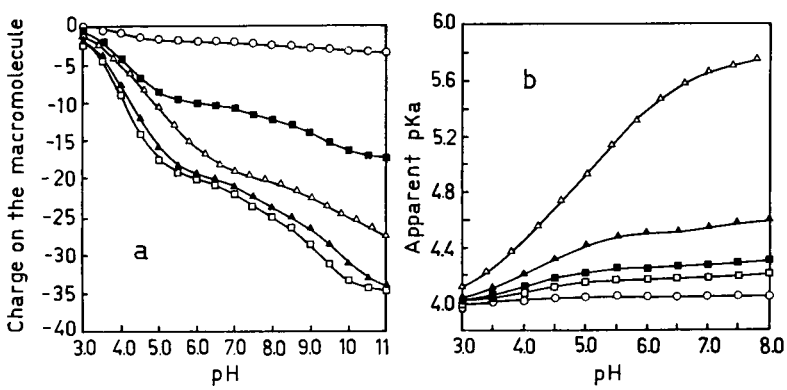

Fig. 1. Charge accumulation (a) and apparent pK_a for $COOH_I$ groups (b) as a function of pH according to the electrostatic model for the hypothetical polyelectrolyte given in Table 1. (△) mol.wt. 10000, and $w = 0.1$; (▲) mol.wt. 10000, $w = 0.03$; (□) mol.wt. 10000, $w = 0.01$; (■) mol.wt. 5000, $w = 0.03$; (○) mol.wt. 1000, $w = 0.03$.

TABLE 2

Results obtained from the data for simulated titration curves of hypothethical polyelectrolyte given in Table 1 (concentrations, C_{HA_i} in mmol g^{-1})

w [a]	M [b]	C_{HA_1}	pK_1	C_{HA_2}	pK_2	C_{HA_3}	pK_3	$\sum_{i=1}^{3} C_{HA_i}$	C_{HA_4}	pK_4	C_{HA_5}	pK_5	C_{HA_6}	pK_6	$\sum_{i=5}^{6} C_{HA_i}$	$\sum_{i=1}^{6} C_{HA_i}$
0.01	1000	2.00	4.00					2.00	0.500	7.00	1.00	9.00			1.00	3.50
	5000	1.59	3.95	0.411	3.85			2.00	0.501	7.11	0.985	9.12			0.985	3.49
	10000	1.15	3.85	0.854	4.41			2.00	0.493	7.19	0.453	9.03	0.552	9.44	1.01	3.50
0.03	1000	2.00	4.00					2.00	0.500	7.00	1.00	9.00			1.00	3.50
	5000	1.12	3.84	0.878	4.52			2.00	0.486	7.27	0.300	8.98	0.709	9.54	1.01	3.50
	10000	1.04	3.80	0.954	4.78			1.99	0.478	7.54	0.295	9.20	0.707	9.94	1.00	3.47
0.10	1000	1.31	3.89	0.697	4.48			2.00	0.502	7.22	0.975	9.25			0.975	3.48
	5000	1.02	3.83	0.970	5.09			1.99	0.446	7.88	0.167	9.12	0.783	10.28	0.950	3.38
	10000	0.825	3.83	0.857	5.33	0.330	6.49	2.01	0.410	8.83	0.401	10.48			0.401	2.82

[a] Electrostatic interaction parameter. [b] Molar mass.

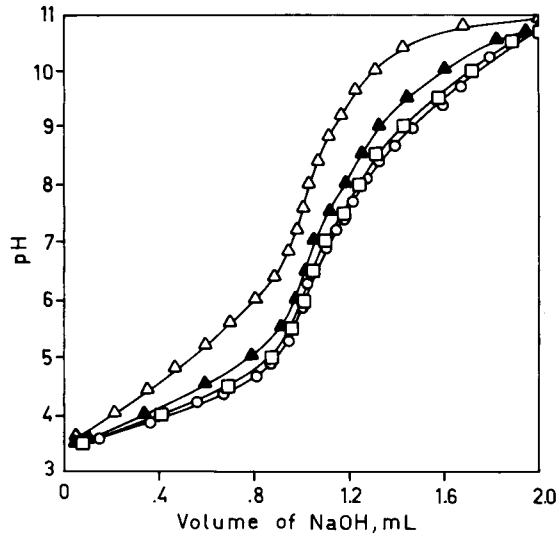

Fig. 2. Simulated titration curves according to the electrostatic model for the hypothetical polyelectrolyte given in Table 1. (△) mol.wt. 10000, $w = 0.1$; (▲) mol.wt. 10000, $w = 0.03$; (□) mol.wt. 10000, $w = 0.01$; (○) mol.wt. 1000, $w = 0.03$.

RESULTS AND DISCUSSION

Simulated titration curves

The charge accumulation on the hypothetical polyelectrolytes was calculated by Eqn. 4 and it is shown as a function of the pH in Fig. 1a. The variation of the apparent pK_a was calculated for $COOH_I$, $COOH_{II}$ and phenolic groups using Eqn. 7. The variation of apparent pK_a for the $COOH_I$ group is shown in Fig. 1b.

$$pK^i_{apparent} = pK^i_{int} - 0.868 w_i Z \qquad (7)$$

Figure 2 shows the simulated titration curves obtained acording to Eqn. 5. Table 2 shows the results obtained from the application of the modified Gran functions to the simulated titration curves of hypothetical polyelectrolytes with composition given in Table 1. The stoichiometry of the $COOH_I$ groups has been determined as the sum of groups present in the sub-classes HA_1, HA_2 and HA_3. A larger number of sub-classes was characterized for $COOH_I$ group as large were the assumed values of w and molar mass. However, when the molar mass is assumed as 1000 g mol^{-1} (typical for fulvic acids) the division of the $COOH_I$ groups in sub-classes was not observed ($w = 0.03$ or 0.01) or it was not so pronounced ($w = 0.1$) as for higher molar masses. It may be explained by the lower charge accumulation on polyelectrolytes with lower molar mass as shown in Fig. 1a. A consequence of a small charge is that the electrostatic interaction effects on the dissociation constants (Fig. 1b) could be neglected as proposed by Paxéus and Wedborg [2] for fulvic acid. These authors have characterized six kinds of titratable groups in an aquatic fulvic acid (molar mass 1000–2500). These results have indicated that chemical heterogeneity is the major factor governing the titration curves of low-molar-mass polyelectrolytes, i.e., fulvic acids.

On the other hand, for hypothetical polyelectrolytes with molar mass 5000 and 10000, the negative charge accumulation is large enough to make the titratable groups behave as weaker acids as a function of the increasing pH. Thus, the determination of the 2.00 mmol g^{-1} of $COOH_I$ groups as a sum of two or three classes of subgroups (HA_1 HA_2 and HA_3) may be a mathematical fit caused by the increasing apparent pK_a values (Fig. 1b). So, it is necessary to be cautious when attributing the characterization of two or three kinds of carboxylic groups in polyelectrolytes to the chemical heterogeneity among these groups.

In addition the charge accumulation can explain the high pK_a values determined for $COOH_{II}$ groups ($pK_{int} = 7.00$), characterized as HA_4 in Table 2.

The phenolic groups have been characterized as HA_5 and HA_6 classes in Table 2. However, the sum of groups in each class tends to be less than the total number of mmoles of phenolic groups admitted to be present. It may be explained by the high electrostatic effects making a part of these groups behave as very weak acids so that they cannot be determined by the studied methodology.

Experimental titration curves

An experimental titration curve linearized by the modified Gran functions is shown in Fig. 3. Table 3 shows the results obtained from the linearization of the titration curves of humic acid suspensions in the presence of 0.010, 0.10 and 1.0

M sodium chloride. The three more acidic species HA_1, HA_2 and HA_3 may be assigned to carboxylic groups. It is interesting to note that these three classes were characterized in each different experimental condition. In addition their concentrations were not significantly altered by changes in ionic strength. These results suggest the existence of a real chemical heterogeneity among carboxylic groups.

The effects of ignoring electrostatic interactions on titration curves of humic acid have been less pronounced than for proteins [17] and hypothetical polyelectrolytes. This fact suggests that the chemical heterogeneity is a more important factor than electrostatic interactions to explain titration curves of Aldrich humic acids.

The classes HA_4 and HA_5 in Table 3 may be assigned to secondary amines and phenolic groups respectively. The stoichiometry of these groups has not been significantly affected by the ionic strength. Phenolic groups with pK_a higher than 10 have not been determined. However it is possible that a few of these groups exist behaving as such weak acids that they have not been determined by the studied methodology.

The influence of electrostatic interactions on experimental results appears as a systematic increase of pK_a values with decrease of the ionic strength. This is shown in Table 3 as a ΔpK_a value between the values determined in 0.010 M and 1.0 M NaCl. The larger ΔpK_as were observed for groups titrated at higher pH. It may be

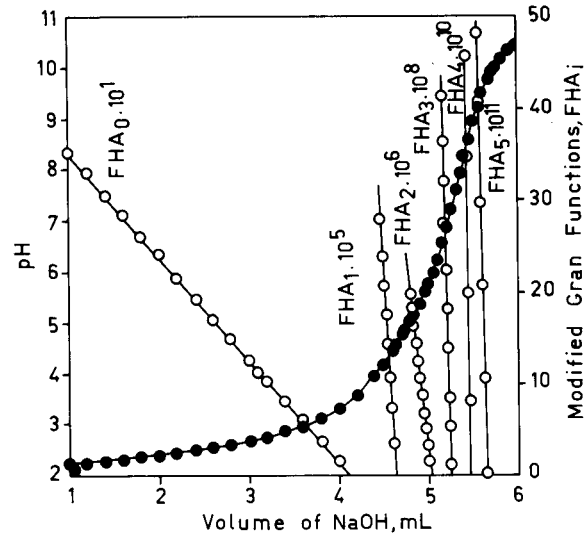

Fig. 3. Titration curve (•) and modified Gran functions (○) FHA_i, for the titration of 55.85 ml of 0.91087 g l^{-1} humic acid in the presence of excess of HCl with 0.1138 M NaOH at ionic strenght 0.10 and temperature 25.0°C.

TABLE 3

Results [a] obtained from experimental titrations of humic acid (Aldrich) for stoichiometry and equilibrium constants of each acid group at ionic strength 0.010, 0.10 and 1.0 and a temperature of 25.0 ± 0.1°C

Titratable group	0.010 M NaCl		0.10 M NaCl		1.0 M NaCl		ΔpK_a [b]
	C_{HA_i} (mmol g^{-1})	pK_{a_i}	C_{HA_i} (mmol g^{-1})	pK_{a_i}	C_{HA_i} (mmol g^{-1})	pK_{a_i}	
HA_1	1.03 ± 0.03	3.92 ± 0.02	1.25 ± 0.09	3.82 ± 0.05	1.32 ± 0.09	3.72 ± 0.08	0.20
HA_2	0.97 ± 0.03	5.27 ± 0.07	0.88 ± 0.05	5.17 ± 0.11	0.90 ± 0.11	4.94 ± 0.06	0.33
HA_3	0.59 ± 0.06	6.82 ± 0.14	0.48 ± 0.02	6.55 ± 0.02	0.46 ± 0.04	6.34 ± 0.14	0.48
$\sum_{i=1}^{3} HA_i$	2.59 ± 0.12		2.61 ± 0.16		2.68 ± 0.24		
HA_4	0.52 ± 0.02	8.47 ± 0.08	0.48 ± 0.01	8.09 ± 0.15	0.49 ± 0.03	7.89 ± 0.13	0.58
HA_5	0.41 ± 0.04	10.01 ± 0.10	0.45 ± 0.04	9.55 ± 0.20	0.51 ± 0.02	9.49 ± 0.13	0.52
$\sum_{i=4}^{5} HA_i$	0.93 ± 0.04		0.93 ± 0.05		1.00 ± 0.05		
$\sum_{i=1}^{5} HA_i$	3.52 ± 0.18		3.54 ± 0.21		3.68 ± 0.29		

[a] These results correspond to an average of four titrations in each ionic strength. [b] These values are the difference between pK_{a_i} values at ionic strength 0.01 and 1.0.

a consequence of the higher negative charge accumulation and electrostatic interactions more intense at elevated pH.

The electrostatic interaction theory, as well as a minor humic fraction with high molar mass, may explain the systematic variations in the stoichiometry of HA_1, HA_3 and HA_5 classes observed in Table 3. However, these variations are not far from experimental errors.

Conclusion

The results obtained from experimental titrations show the presence of approximately 3.5 mmol g^{-1} of ionizable sites in the Aldrich humic acid, so that the molar mass of one chargeable group is approximately 286. By admitting that the average molar mass of this Aldrich humic acid is 8000 g mol^{-1} [19] an accumulation of approximately 28 negative charges could result at the end of the titration (if all titratable groups were supposed to be carboxylic and phenolic). On the other hand, if one considers only the purely electrostatic model, a charge accumulation of this order of magnitude should be enough to promote significant differences in the results obtained from suspensions at different ionic strengths, as shown in Table 2. One could speculate that the free energy needed for the proton dissociation and the related electrostatic parameter, w, would be negligible in comparison to that observed for globular proteins [9]. Thus, it could be concluded that the heterogeneity among the titratable groups is the major factor governing the acid–base properties of this Aldrich humic acid. Thus, the potentiometric titrations data could be treated as the working solutions were a mixture of monoprotic acids. This would be a reliable method for determining the stoichiometry and pK_a of the ionizable groups in humic substances with low charge accumulation (fulvic acids).

On the other hand, humic acids can differ in their charge density properties, so that the charge accumulation behavior should be carefully studied before admitting the ionizable sites as a mixture of monoprotic acids. This feature was observed by Tipping et al. [6] Studying humic acids from different origins as well as fractions with different molar masses from a same humic acid.

The author is grateful to FAPESP, Fundação de Amparo à Pesquisa do Estado de São Paulo, for financial assistance (Project 90/1696-5) and to Prof. Dr. Paschoal E.A. Senise for reviewing this article.

REFERENCES

1. J. Buffle, Anal. Chim. Acta, 232 (1990) 1.
2 N. Paxéus and N. Wedborg, Anal. Chim. Acta, 169 (1985) 87.
3 L.M. Aleixo, O.E.S. Godinho and W.F. da Costa, Anal. Chim. Acta, 257 (1992) 35.
4 J.C.M. de Wit, W.H. van Riemsdijk, M.M. Nederlof, D.G. Kinniburgh and L.K. Koopal, Anal. Chim. Acta, 232 (1990) 189.
5 D.E. Wilson and P. Kinney, Limnol. Oceanogr., 22 (1977) 281.
6 E. Tipping, C.A. Backes and M.A. Hurley, Wat. Res., 22 (1988) 597.
7 G.R. Choppin and L. Kullberg, J. Inorg. Nucl. Chem., 40 (1978) 651.
8 T. Takamatsu and T. Yoshida, Soil Sci., 125 (1978) 377.
9 C. Tanford, Adv. Protein Chem., 17 (1962) 70.
10 E.M. Perdue and C.R. Lytle, Environ. Sci. Technol., 17 (1983) 654.
11 E.M. Perdue, J.H. Reuter and R.S. Parish, Geochim. Cosmochim. Acta, 48 (1984) 1257.
12 J.A. Marinsky and J. Ephraim, Environ. Sci. Technol., 20 (1986) 349.
13 E. Tipping, M.M. Reddy and M.A. Hurley, Environ. Sci. Technol., 24 (1990) 1700.
14 M.D. Seymour, J.N. Clayton and Q. Fernando, Anal. Chem., 49 (1977) 1429.
15 O.E.S. Godinho and L.M. Aleixo, Anal. Biochem., 112 (1981) 323.
16 O.E.S. Godinho, L.M. Aleixo and J.P. Hora Alves, Anal. Biochem., 123 (1982) 244.
17 O.E.S. Godinho, J.C. Masini and L.M. Aleixo, Bioelectrochem. Bioenerg., 29 (1992) 135.
18 L. Pehrsson, F. Ingman and A. Johansson, Talanta, 23 (1976) 769.
19 J.I. Kim, G. Bukau, G.H. Li, H. Duschner and N. Psarros, Fresenius' J. Anal. Chem., 338 (1990) 245.

Analytica Chimica Acta, 283 (1993) 811–829
Elsevier Science Publishers B.V., Amsterdam

Automatic polarographic elucidation of electrode mechanisms by means of a knowledge-based system

Part 3. Mechanisms ECE, EE and mechanisms involving adsorption

M.J. Pałys [1], M. Bos and W.E. van der Linden

Laboratory for Chemical Analysis, Department of Chemical Technology, Twente University of Technology, P.O. Box 217, 7500 AE Enschede (Netherlands)

(Received 8th February 1993; revised manuscript received 19th March 1993)

Abstract

The previously described expert system has been extended: rules allowing the elucidation of a larger number of mechanisms have been added and automatic control of additional experimental parameters such as concentration and composition of the solution in the cell and the electrode size has been made possible. The new rules cover a number of mechanisms consisting of two electron transfer steps (ECE, EE, "square" and "triangle" schemes) and simple mechanisms in which either the reactant or the product undergoes a fast, reversible adsorption. Previously used criteria for the detection of a net reaction in the system and for the determination of the type of the electron transfer were made more robust by combining results obtained with cyclic voltammetry and convolution voltammetry. With the present set of rules, the expert system is capable to evaluate 39 mechanisms and their variants. To validate this set, the system was run with a number of compounds for which reaction mechanisms have already been studied. In all cases, the mechanism found as the most probable was the correct one. The time of the elucidation depended on the number of experiments that had to be done and varied from 4 up to 6 h. During this time, the system worked practically without human supervision.

Keywords: Polarography; Voltammetry; Electrode mechanisms; Knowledge-based systems

In two previously published papers [1,2] a knowledge-based (expert) system, capable to elucidate simple electrode reaction mechanisms in a fully automatic manner, has been described. The set of rules for the elucidation in that system covered a number of mechanisms where a single electron transfer step (ETS), possibly coupled to a homogeneous chemical reaction, occurred. Currently, this set has been extended and improved: more complicated mechanisms, where two electron transfer steps take place (EE and ECE mechanisms) and a number of instances of "triangle" and "square schemes", mechanisms often encountered among electrochemical processes of complexes (see below), have been included

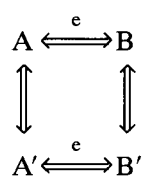

or

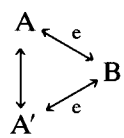

[1] On leave from the Department of Chemistry, University of Warsaw and author for correspondence.

Additionally, rules have been provided for the elucidation of simple mechanisms involving either strong or weak adsorption of the substrate or the product of the charge transfer.

Generally, the method of reasoning, the representation of knowledge and the principal structures of the expert system remained identical to those described previously [2]. The main change was the addition of new experimental parameters that can be controlled by the expert system and the improvement of the user interface. At present, the expert system can control two (or more) burettes and a pump, which allows to vary the concentration of the electroactive compound, as well as to replace the solution to start a new series of experiments without the need of human intervention. The size of the mercury drop used as the electrode can be varied, too, giving on one hand a tool to study spherical diffusion effects and on the other hand, to eliminate them. All these changes significantly improved the degree of automation of the whole system.

Changes in the user interface resulted in a capability to generate extensive reports on the elucidation as well as to produce semi-graphic representation of decision trees, showing how the system has reached the final conclusion about the reaction mechanism.

EXTENSIONS AND IMPROVEMENTS OF THE EXISTING RULE SET

Substantial improvements of old rules defining the determination of factors controlling the transport to the electrode and the detection of a net chemical reaction in the system have been carried out. The new versions of rules are either based on more complete experimental evidence or they are better theoretically supported.

Net reaction

Irreversible steps (of electrochemical or chemical character) in cyclic voltammetry cause consumption of the substrate(s) during the measurement leading to the presence of a net reaction in the system. A criterion for the detection can be based on the restoration of the initial state at the electrode surface after a cyclic change of the potential: if a net reaction does not occur, the surface concentration of all species after the experiment should be exactly the same as before. If there is a net reaction, concentrations will differ.

In the previous version of the expert system, the rule for the detection of a net reaction was based on an arbitrary criterion: if the charge passed during the voltammetric backward scan was less than 50% of the charge passed during the forward scan, the hypothesis that there is a net effect was accepted. Currently, the surface concentrations are explored as primary quantities and a combination of criteria based on convolution voltammetry and cyclic voltammetry is used.

Because the charge is only indirectly related to the surface concentrations, the direct application of the latter quantities is the better approach. The value proportional to the surface concentration of the product of an electrode reaction during the experiment can be obtained by convolution [3–5] of the voltammetric current with a $(\pi t)^{-1/2}$ function (semi-integration) [6,7]

$$i(t) * g(t) = nFAD^{1/2}c^{s}(t) \qquad (1)$$

where n, F, A and D having their usual electrochemical meaning, $i(t)$ being current, $c^{s}(t)$ the surface concentration and $g(t)$ the convolution function, equal to $(\pi t)^{-1/2}$. Equation 1 is valid under the assumption, that the transport to and from the electrode can be described by semi-infinite linear diffusion. In practice, however, the assumption about the linearity of the diffusion is rarely valid and therefore it is better to use so-called spherical convolution [7], delivering the surface concentration of the product under mixed (linear and spherical) diffusion conditions that are much more frequently encountered. A method presented in a paper by Engblom and Oldham [8] is even better, because it takes into account that datapoints could be acquired using staircase voltammetry rather than the linear sweep method. The disadvantage is that it requires the value of the diffusion coefficient, which is often unknown or not exactly known.

The semi-integral criterion for the presence of a net reaction can then be formulated as follows: if the initial concentration of the compound is

restored, the convolute value should return exactly to its initial value (usually zero) after the cycle is completed, which means that the product of the reaction has been converted back to the substrate [7,9]. If it does not return to its original value, consumption of the initially present substance is suggested.

The convolution criterion alone is insufficient, because the substrate or the product of the reaction can be accumulated on (or in) the electrode by adsorption, deposition or amalgamation. In this case, the initial value of the surface concentration is not restored after the completion of the voltammetric cycle and convoluted voltammograms will not deliver proper results. However, if the accumulation effect becomes dominant, an alternative approach is possible: because there is no loss of the compound by its diffusing away, the total charge passed during the voltammetric cycle should approach zero.

Because the possible reaction consuming the reagent can be either slow or fast compared to the time scale of the experiment, both criteria should be evaluated for a number of different scan rates. Deviations from zero can then be checked using statistical tests; consequently, the probability that a net reaction occurs is a conjunction of probabilities that both normalized charge and normalized convolute (semi-integral) differ from zero.

Characteristics of separate signals

Suggestion of the mechanism of observed signals. The philosophy of rules characterizing the separate signals has not been changed, but the rules have been given broader theoretical foundations and multiple techniques have been employed to obtain experimental information.

Suggestions for mechanisms, previously exclusively based on the Nicholson and Shain criteria involving variation of voltammetric peak potential with scan rate [10], have been extended to semidifferential voltammetry for cases of uncomplicated, fast and slow electron transfers. According to Goto and Ishii [11], the semiderivative peak obtained in the case of a fast, uncomplicated electron transfer step can be described using the equation

$$d^{1/2}i/dt^{1/2} = (n^2F^2AvCD^{1/2}/4RT) \times \cosh^{-2}[(nF/2RT)(E - E_{1/2})] \quad (2)$$

where, c, R, T and E have their usual meaning, v is a scan rate and $E_{1/2}$ is a polarographic halfwave potential of the reacting redox couple. It is found, that the peak appears at a potential value equal to $E_{1/2}$ irrespective of the scan rate used; the peak height is represented by the expression $n^2F^2AvCD^{1/2}/4RT$ and it increases linearly with the scan rate.

In case of a slow, uncomplicated electron transfer, the semiderivative peak can be described with the following equation [12]:

$$d^{1/2}i/dt^{1/2} = (n^2\alpha F^2AvCD^{1/2}/RT) \times \sum_{j=1}^{\infty} (-1)^j \exp(jz)(j!)^{-1/2} \quad (3)$$

where $z = (n\alpha F/RT)(E^{0'} - E) + \frac{1}{2} \ln(RTk_s/n\alpha FvD)$, k_s being the standard heterogeneous rate constant. The maximum value of the sum,

TABLE 1

Diagnostic criteria for suggestion of mechanism of the ETS, based on semiderivative staircase voltammetry (Acronyms as in the Table 4 in Ref. 2)

Suggestion of the mechanism of electron transfer step (ETS)	Trend of semiderivative		Value of semiderivative	
	dE_p/dv vs. v	$dE_p/d \ln v$ vs. v	dE_p/dv vs. v	$dE_p/d \ln v$ vs. v
E	Constant		0	
Es (cathodic branch)		Constant		$< -RT/2nF$
Es (anodic branch)		Constant		$> RT/2nF$

0.2970, occurs at $z = -0.055$ and the potential of the semiderivative peak can be expressed as

$$E_p = \left[E^{0'} + 0.055RT/\alpha nF + (RT/2\alpha nF)\ \ln(RTk_s/\alpha nFD)\right] - (RT/2\alpha nF)\ \ln v \quad (4)$$

showing a linear dependence on the logarithm of the scan rate. The peak height equals

$$0.2970n^2\alpha F^2AvCD^{1/2}/RT$$

On the basis of these equations, the diagnostic criteria collected in Table 1 can be established.

Control of the transport to the electrode. As far as factors controlling the transport of electroactive substance to the electrode are concerned, a larger number of different situations is considered than before and more techniques are employed. The main line of reasoning, i.e., description of different types of transport as deviations from the semi-infinite linear diffusion, is preserved. The transport can be larger than in semi-infinite linear diffusion, for example if spherical diffusion or kinetic effects (chemical or catalytic reaction) take place; in this latter case it can even lead to a steady state. Lower intensity of the transport can be observed in cases of limited diffusion and reactions from the adsorbed state. In the latter case, the whole amount of substance adsorbed reacts within a very short time and the current drops sharply to zero after exhaustion of the component.

In the current set of rules, criteria based on cyclic chronocoulometry, staircase voltammetry and convolution voltammetry are employed. In chronocoulometry, according to Anson [13], the quantity of charge in cyclic chronocoulometry can be described using the equation

$$Q = 2nFAD^{1/2}C\pi^{-1/2}t^{1/2} \quad (5)$$

and

$$Q(t > \tau) = 2nFAD^{1/2}C\pi^{-1/2}\left[t^{1/2} - (t-\tau)^{1/2}\right] \quad (6)$$

if, after the time τ, the potential is changed to a value at which the concentration of the product of the reaction is zero (semi-infinite linear diffusion assumed). One can find, that the charge passed in each half-cycle should vary linearly with the square root of the time elapsed from the beginning of the half-cycle. If additional contributions enhance the transport, the charge is greater than predicted from the purely linear model. The inverse effect appears when the transport is slower than for linear diffusion (limited diffusion, strong adsorption of product or substrate on the electrode): the observed charge increases slower and for adsorbed species it can even reach a constant value almost instantaneously.

A unique effect can be observed in the case of weak adsorption of the reactant: effects of the reaction of diffusing species (visible in long times) and adsorbed ones (observable in short times) are combined, the plot Q vs. $t^{-1/2}$ is linear, but shifted along the charge axis with an amount corresponding to the charge consumed in the reaction of the substance present at the electrode surface.

In staircase voltammetry (SCV), information about the transport of the reactant to the electrode surface is primarily included in the height of the voltammetric peak and in its shape, particularly in the form of the descending branch of the peak. As before, different types of transport can be treated as distortions of the semi-infinite linear diffusion caused by, e.g., chemical processes, depletion of the bulk of the solution, etc. All these effects, except adsorption, have one common feature: they become more important with time and their influence is better visible at slow scan rates.

To derive appropriate criteria, a classic analysis of Nicholson and Shain [10] can be employed: the measured current follows the equation

$$i = c_0 v^{1/2}\chi(c_1 t) \quad (7)$$

where c_0 represents a general proportionality constant, c_1 is the constant relating the time scale of the experiment to the time scale of the phenomena involved, v is the scan rate and $\chi(c_1 t)$ is a function defining the peak shape. The constant c_1 is different for various mechanisms, but independent of the scan rate if the flux of the substance at the electrode surface is governed by semi-infinite linear diffusion. In such cases, the

variation of the height of the voltammetric peak should be linear with the square root of the scan rate.

For mixed spherical and linear diffusion the situation is different: the increased flux of the electroactive substance leads to an increase of the recorded currents. The quantitative description of the effect is difficult, but it can be intuitively expected that the peak height will no longer be linearly dependent on $v^{1/2}$, particularly in the slow scan rate region. The current in the descending branch of the peak will also deviate from a $t^{-1/2}$ decay with an increasing distance from the top of the peak and with a decrease of the scan rate. A qualitatively very similar effect can be observed when an extra amount of substance is delivered in a chemical way. In the extreme case, the production rate of the reactant in the solution becomes equal to the consumption rate at the electrode and a steady state is obtained: the current is entirely controlled by the rate of the chemical reaction. In the voltammogram, after reaching the maximum value, the current becomes constant and a wave instead of a peak appears.

In some cases, electrolysis can cause a decrease of the bulk concentration of the reagent (limited diffusion). It can be expected, that the main effect is a more rapid decay of the current after reaching the top of the peak (faster than the usual $t^{-1/2}$ relationship). Also, a decrease of the scan rate leads to a faster decrease of the peak current, again resulting in deviations from the linear $i - v^{1/2}$ dependence. In the extreme situation when the reagent is completely consumed, the equivalent amount of charge passes through the electrode: in such a case, the peak height becomes linearly dependent on the scan rate. In situations when mixed linear and limited diffusion occurs, transition from a proportionality to v to a proportionality to $v^{1/2}$ could be observed.

If the reactant is strongly adsorbed on the electrode forming a mono- or a submonolayer on its surface and the adsorption equilibrium is rapidly reached, the situation resembles the extreme form of limited diffusion. The amount of substance is limited and it is available directly in the place where the electron transfer occurs, so no transport is necessary. The charge consumed in the reaction is constant, dependent only on the amount of substance and independent of scan rate. The result is a symmetric, sharp voltammetric peak, whose height is proportional to the scan rate; the width of the peak can be very small, because it is related to the variation of the adsorption energy with the electrode potential [7]. Theoretical studies of adsorption in voltammetry were done by several authors (see for example [7,14,15]).

Also useful is the dependence of the peak current and peak shape on the concentration. In principle, when the electron transfer is preceded by a first-order (or pseudo-first order) homogeneous process with respect to the electron transfer substrate or if there is no preceding step, the peak height should change linearly with the concentration. The situation differs, when the reaction is of higher order, but that case is not considered here. When adsorption occurs, the limited capacity of the monolayer causes a characteristic "saturation" effect: above a certain value of the bulk concentration, the peak height stabilizes and becomes independent of the concentration.

Convolution voltammetry facilitates the interpretation of SCV curves, particularly the information included in the peak shape. In the simplest case of semi-infinite linear diffusion and fast electron transfer, the convolution of the voltammetric current with a $t^{-1/2}$ decay results in an S-shaped wave [16–18]. Other mechanisms have been discussed in a number of papers [19–23].

When the transport to the electrode is enhanced or diminished compared to semi-infinite linear diffusion, the plateau of this wave has positive or negative slope, respectively. In this latter case, a "badly formed" peak is obtained. This method was applied in the detection of adsorption [24]. In this manner the problem of the detection of decreased flux can be reduced to finding peaks in semi-integral voltammograms.

To extend this test to processes in which the transport is larger than semi-infinite linear diffusion, a mathematical trick can be made: instead of semi-integration, integration to slightly lower order (e.g., 0.45-integration) can be used. In such a transformation, all voltammetric peaks for which

the transport is as fast as or slower than linear diffusion, are converted to "badly formed" peaks or waves, while others are only partially broadened. Comparing peaks visible on the original, the 0.45-integrated and the semi-integrated voltammogram it is possible to classify them with respect to the type of the transport.

The criteria described above are very simple, but they have an important limitation: all waves obtained in convoluted voltammograms overlap, i.e., every subsequent one rises from the plateau of the previous wave. The bias of one plateau is taken over by all following waves, making them difficult to interpret. Due to this feature, simple classification gives reasonable results for the first peak in the forward branch of the voltammogram only.

To reduce the risk of an error in the determination of factors controlling the transport, a combination of criteria employing all three techniques (chronocoulometry, staircase voltammetry and convolution voltammetry) is used. The validity of the obtained results is subject to different restrictions. The general one is that different types of transport are always treated as different types of deviations from the semi-infinite linear diffusion model, but in order to detect them the magnitude of the deviation has to be significant. This implies, that the hypothesis about the linear diffusion model is the default one and, to some extent, preferred: if there is no *significant* reason to reject it, it is accepted. Another limitation concerns overlapping signals: when more than one electrode process takes place at the given potential with a comparable rate, criteria for the determination of the transport type may deliver results for an averaged effect.

In Table 2, the diagnostic criteria used for the determination of factors controlling the flux of the electroactive substance are collected.

NEW RULES

A common feature of rules for all new mechanisms is that they are largely based on the correlation of the measured currents with the variation of experimental parameters, as well as on the changes in the current ratios with the time scale of the experiment. The new rules cover mechanisms collected in Table 3.

ECE mechanisms

This group consists of 18 variants of ECE mechanisms, differing in the reversibility of electrochemical and chemical steps. Criteria used are

TABLE 2

Diagnostic criteria for the determination of the type of transport to the electrode (Criteria within one set of columns, separated by vertical lines, are joined by the AND operator; between separated columns OR operator is used. Acronyms of dependences: $IV = i_p/v^{1/2}$ vs. v, $IC = i_p/C$ vs. C, $DIV = (d^{1/2}i/dt^{1/2})/v$ vs. v, $DIC = (d^{1/2}i/dt^{1/2})/C$ vs. C; $(d^{1/2}i/dt^{1/2})$ is a current semiderivative)

Transport type	Q vs. $t^{1/2}$	$dQ/d(t^{-1/2})$	Peak in convolution voltammetry [a]				Trend in the absolute value of			
			0.5	0	−0.45	−0.5	IV	IC	DIV	DIC
From adsorbed state (ADS)	Nonlinear	Decrease	yes	yes	yes	yes	Incr.	Decr.		
Mixed limited-linear diffusion (LIM-LIN)	Nonlinear	Decrease	yes	yes	yes	yes	Decr.	Const.		
Mixed adsorption-linear diffusion (ADS-LIN)	Linear	Constant	yes	yes	yes	yes	Incr.	Not incr.		
Semi-infinite linear diffusion (LIN)	Linear	Constant	yes	yes	yes	no	Const.	Const.	Const.	Const.
Mixed linear and kinetic effect (LIN-KIN)	Nonlinear	Increase	yes	yes	no	no	Decr.	Const.		
Totally kinetic (KIN)	Nonlinear	Increase	yes	no	no	no	Decr.	Const.		

[a] Numbers describe instances of so-called differintegration (generalized differentiation and integration operation): 0.5 = semiderivative, 0 = original voltammogram, −0.45 = 0.45-integration, −0.5 = semi-integration.

the number of signals observed under various circumstances, their interrelation, the presence of a net reaction, characteristics of the separate reduction and oxidation signals and the ratio of heights of semiderivative peaks (see Table 4). Taking into account that there are at least four compounds involved in the entire reaction scheme

$$A_1 \overset{e}{\Leftrightarrow} B_1 \Leftrightarrow A_2 \overset{e}{\Leftrightarrow} B_2$$

it can be generally expected, that signals of the four processes: $A_1 \rightarrow B_1$, $B_1 \rightarrow A_1$, $A_2 \rightarrow B_2$ and $B_2 \rightarrow A_2$ should be observed. The actual number of observable signals is, however, influenced by the characteristics (e.g., irreversibility) of reactions taking place. In principle, the process $A_1 \rightarrow B_1$ is of EC type, whereas $A_2 \rightarrow B_2$ should exhibit some similarities with CE reaction.

A useful criterion in the elucidation of ECE mechanisms is the appearance of an additional peak (secondary peak) in the third branch of the voltammogram. Such peaks can be observed if the standard potential of the reversible second electron transfer step is less extreme than that of the first charge transfer; they originate from the A_2 intermediate produced during the second half-cycle.

In the elucidation of ECE mechanisms, the relative heights of voltammetric peaks play an important role [24]. However, the determination of these parameters in the case of an ECE process is likely to be difficult, or even impossible, due to the overlap of SCV peak tails. To avoid this problem, rules in this expert system make use of semiderivative voltammetry: with its narrower peaks with easily measurable heights this technique is advantageous. The chance of overlap is significantly reduced and results for peak heights are much more reliable.

Table 4 collects criteria for the elucidation of ECE mechanisms.

There is a number of restrictions for the applicability of the above criteria: generally, if the chemical step is very fast, an ECE mechanism is indistinguishable from EE. Additionally, the possibility of cross-reaction (disproportionation) has been neglected in the present rules.

Mechanisms with adsorption

Four simple cases of uncomplicated electron transfer are considered here, where adsorption (either strong or weak) of substrate or product takes place. Rules are based on the paper by Wopschall and Shain [25]. In the case of strong adsorption, two peaks in each branch can be observed; if the adsorption is weak, only one peak with a characteristic shape can be found in each branch.

Elucidation criteria (see Table 5) are primarily based on the determination of factors controlling the transport to the electrode, among others on the characteristic dependence of adsorptive peak height on the scan rate in voltammetry. This latter feature is also exploited in criteria involving peak height ratios.

It should be emphasized, that above criteria are valid under the assumption, that no complications accompany the electron transfer step and the rate of adsorption is very high compared to the time scale of the experiment. It is also assumed, that no competitive adsorption (for instance of the substrate *and* the product of the electrode reaction) takes place.

EE Mechanisms

This group covers four combinations of two electron transfer steps, where each step can be either fast or irreversible (ErEr, ErEi, EiEr and EiEi) and one special case of ErEs mechanism with $E_2^{0'} \ll E_1^{0'}$. There is no coupled homogeneous chemical process and no adsorption takes place.

The variation of potentials of both processes with scan rate should follow patterns predicted for electron transfers with an uncomplicated character.

The most crucial step in proving the EE mechanisms is the exclusion of the chemical reaction intervening the electron transfer steps. If the substrate of the second step is produced in a chemical step, the relative height of peak 2 with respect to peak 1 in the forward branch of the semiderivative voltammogram increases with a decrease of the scan rate. If there is no intermediate chemical reaction, such an effect does not occur and the ratio of peak heights is constant.

The difference between the ECE and EE mechanism is also manifest in a different type of transport for the first and the second signal in the ECE mechanism, while in the EE mechanism the type of transport is the same. It is, however, impossible to exclude the presence of a very fast chemical reaction between steps 1 and 2. Such a reaction has no visible effects in the time scale of the experiment and, as already mentioned in the part concerning the ECE mechanism, ECE and EE mechanisms would not be distinguishable under such circumstances.

Table 6 lists criteria used to elucidate EE mechanisms.

TABLE 3

List of additional mechanisms, that can be elucidated by the expert system (Symbols: E = electron transfer step, C = chemical step, A = adsorption, "$\leftrightharpoons$" and "$\overset{e}{\rightarrow}$" = reversible and irreversible electr. transfer, "$\Leftrightarrow$" and "$\rightarrow$" = reversible and irreversible chemical reaction)

Symbol	Reaction	Description
ErCrEr	A $\leftrightharpoons$ B $\Leftrightarrow$ C $\leftrightharpoons$ D	ECE reaction with both electron transfers fast and reversible chemical step; three cases: $E_2^{0'} \ll E_1^{0'}$, $E_2^{0'} \approx E_1^{0'}$ and $E_2^{0'} \gg E_1^{0'}$
ErCiEr	A $\leftrightharpoons$ B $\rightarrow$ C $\leftrightharpoons$ D	ECE reaction with both electron transfers fast and irreversible chemical step; three cases: $E_2^{0'} \ll E_1^{0'}$, $E_2^{0'} \approx E_1^{0'}$ and $E_2^{0'} \gg E_1^{0'}$
ErCrEi	A $\leftrightharpoons$ B $\Leftrightarrow$ C $\overset{e}{\rightarrow}$ D	ECE reaction with the first E step fast, the second one, irreversible and reversible C step. Three cases: $E_2^{0'} \ll E_1^{0'}$, $E_2^{0'} \approx E_1^{0'}$ and $E_2^{0'} \gg E_1^{0'}$
ErCiEi	A $\leftrightharpoons$ B $\rightarrow$ C $\overset{e}{\rightarrow}$ D	ECE reaction with the first E step fast, the second one, irreversible and irreversible chemical reaction. Three cases: $E_2^{0'} \ll E_1^{0'}$, $E_2^{0'} \approx E_1^{0'}$ and $E_2^{0'} \gg E_1^{0'}$
EiCEr	A $\overset{e}{\rightarrow}$ B $\Leftrightarrow$ C $\leftrightharpoons$ D or A $\overset{e}{\rightarrow}$ B $\rightarrow$ C $\leftrightharpoons$ D	ECE reaction with the first electron transfer irreversible and the second one, fast, three cases: $E_2^{0'} \ll E_1^{0'}$, $E_2^{0'} \approx E_1^{0'}$ and $E_2^{0'} \gg E_1^{0'}$
EiCEi	A $\overset{e}{\rightarrow}$ B $\Leftrightarrow$ C $\overset{e}{\rightarrow}$ D or A $\overset{e}{\rightarrow}$ B $\rightarrow$ C $\overset{e}{\rightarrow}$ D	ECE reaction with both electron transfers irreversible, three cases: $E_2^{0'} \ll E_1^{0'}$, $E_2^{0'} \approx E_1^{0'}$ and $E_2^{0'} \gg E_1^{0'}$
EAs	A $\leftrightharpoons$ B*	Fast electron transfer with a fast, strong adsorption of the product
EAw	A $\leftrightharpoons$ B*	Fast electron transfer with a fast, weak adsorption of the product
AsE	A* $\leftrightharpoons$ B	Fast electron transfer with a fast, strong adsorption of the substrate
AwE	A* $\leftrightharpoons$ B	Fast electron transfer with a fast, weak adsorption of the substrate
ErEr	A $\leftrightharpoons$ B $\leftrightharpoons$ C	Uncomplicated double-step electron transfer, both steps fast, $E_2^{0'} \ll E_1^{0'}$
ErEs	A $\leftrightharpoons$ B $\leftrightharpoons$ C	Uncomplicated double-step electron transfer, the first step fast, the second one slow, $E_2^{0'} \ll E_1^{0'}$
ErEi	A $\leftrightharpoons$ B $\overset{e}{\rightarrow}$ C	Uncomplicated double-step electron transfer, the first step fast, the second one irreversible, $E_2^{0'} \ll E_1^{0'}$
EiEr	A $\overset{e}{\rightarrow}$ B $\leftrightharpoons$ C	Uncomplicated double-step electron transfer, the first step irreversible, the second one fast, $E_2^{0'} \ll E_1^{0'}$
EiEi	A $\overset{e}{\rightarrow}$ B $\overset{e}{\rightarrow}$ C	Uncomplicated double-step electron transfer, both step irreversible, $E_2^{0'} \ll E_1^{0'}$
E $\Leftrightarrow$ E	A $\leftrightharpoons$ B $\leftrightharpoons$ A' $\Leftrightarrow$ A	"Triangle scheme": electron transfers fast, chemical reaction reversible, large difference in formal potentials
E $\rightleftarrows$ E	A $\leftrightharpoons$ B $\Leftrightarrow$ B' $\leftrightharpoons$ A' $\Leftrightarrow$ A	"Square scheme": electron transfers fast, chemical reaction reversible, large difference in formal potentials

"Square" and "triangle" scheme mechanisms

In this case two different forms of the electroactive compound, remaining in a chemical equilibrium, can react giving either two different products or only one product. It is taken for granted that electron transfer steps (ETS) are not irreversible, that the differences of potentials at which electron transfer steps occur are significant and that all signals can be observed separately. The overall scheme of reaction can be written as

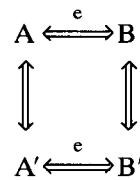

TABLE 4

Diagnostic criteria for ECE mechanisms (Acronyms: F = signal in the forward branch, B = signal in the backward branch of the voltammogram, HS = hidden signals (see [2]), SS = secondary signals, NR = net reaction, SMS = suggestion of mechanism of the electron transfer, RSDH = ratio of semiderivative peak heights)

Mechanism	Relation $E_2^{0'}/E_1^{0'}$	Number of F, B	HS	SS	Signal assignment	NR	Type of the transport (see Table 2)	SMS	Absolute trend in RSDH
ErCrEr	$E_2^{0'} \ll E_1^{0'}$	2, 2	no	no	B1 → F1 B2 → F2	no	F1: LIN F2: LIN-KIN	F1: ECr	B1/F1 const F2/F1: decr B2/B1: decr
ErCrEr	$E_2^{0'} \approx E_1^{0'}$	1, 1	no	no		no	F1: LIN-KIN F2: LIN-KIN		B1/F1: const
ErCrEr	$E_2^{0'} \gg E_1^{0'}$	1, 2	no	yes		no	F1: LIN-KIN	B1: E or CEr	B2/F2: incr B2/F1 incr
ErCiEr	$E_2^{0'} \ll E_1^{0'}$	2, 2	no	no	B1 → F1 B2 → F2	yes	F1: LIN F2: LIN-KIN	F1: ECi	B1/F1: incr B2/B1: decr B1/F1: const
ErCiEr	$E_2^{0'} \approx E_1^{0'}$	1, 1	no	no		yes	F1: LIN-KIN F2: LIN-KIN		B1/F1: incr
ErCiEr	$E_2^{0'} \gg E_1^{0'}$	1, 2	no	no		yes	F1: LIN-KIN	B1: E or CEr	B2/F2: incr B2/F1 incr
ErCrEi	$E_2^{0'} \ll E_1^{0'}$	2, 1	no	no	B1 → F1	yes	F1: LIN F2: LIN-KIN	F1: ECr	F2/F1: decr B1/F1: incr
ErCrEi	$E_2^{0'} \approx E_1^{0'}$	1, 1	no	no		yes	F1: LIN-KIN B1: LIM-LIN		B2/F1: incr
ErCrEi	$E_2^{0'} \gg E_1^{0'}$	1, 1	no	no		yes	F1: LIN-KIN B1: LIM-LIN		B2/F1: incr
ErCiEi	$E_2^{0'} \ll E_1^{0'}$	2, 1	no	no	B1 → F1	yes	F1: LIN F2: LIN-KIN	F1: ECi	F2/F1: decr B1/F1: incr
ErCiEi	$E_2^{0'} \approx E_1^{0'}$	1, 1	no	no		yes	F1: LIN-KIN B1: LIM-LIN		B2/F1: incr
ErCiEi	$E_2^{0'} \gg E_1^{0'}$	1, 1	no	no		yes	F1: LIN-KIN B1: LIM-LIN		B2/F1: incr
EiCEr	$E_2^{0'} \ll E_1^{0'}$	2, 1	no	no		yes	F1: LIN F2: LIN-KIN		F2/F1: decr B2/F1: decr
EiCEr	$E_2^{0'} \approx E_1^{0'}$	1, 1	no	no		yes	F1: LIN-KIN F2: LIN-KIN		B1/F1: decr
EiCEr	$E_2^{0'} \gg E_1^{0'}$	1, 1	no	yes		yes	F1: LIN-KIN		
EiCEi	$E_2^{0'} \ll E_1^{0'}$	2, 0	no	no			F1: LIN F2: LIN-KIN		B1/F1: decr
EiCEi	$E_2^{0'} \approx E_1^{0'}$	1, 0	no	no			F1: LIN-KIN		
EiCEi	$E_2^{0'} \gg E_1^{0'}$	1, 0	no	no			F1: LIN-KIN		

TABLE 5

Diagnostic criteria for single mechanisms with adsorption (F = Signal in the forward branch, B = signal in the backward branch of the voltammogram, HS = hidden signals (see [2]), SS = secondary signals, DDPH = difference of semiderivative peak height vs. scan rate)

Mechanism	Number of F, B	HS	SS	Type of the transport	Trend in DDPH
EAs	2, 2	no	no	F1: ADS	F1–F2 decrease [a]
	1, 1	yes		B1: ADS	B1–B2 increase [a]
EAw	1, 1	no	no	F1: LIN	
				B1: ADS-LIN	
AsE	2, 2	no	no	F1: LIN	F1–F2 increase [a]
	1, 1	yes		B1: LIN or LIN-KIN	B1–B2 decrease [a]
AwE	1, 1	no	no	F1: ADS-LIN	
				B1: LIN or LIN-KIN	

[a] For reduction in forward branch and oxidation in backward one; otherwise trends should be reversed.

TABLE 6

Diagnostic criteria for double-step mechanisms (Acronyms: F = signal in the forward branch, B = signal in the backward branch of the voltammogram, HS = hidden signals (see [2]), SS = secondary signals, NR = net reaction, SMS = suggestion of mechanism of the electron transfer, RDPH = ratio of semiderivative peak heights, DDPP = difference of semiderivative peak potentials)

Mechanism	Number of F, B	HS	SS	Peak assignment	NR	Type of transport	SMS	Trend in RDPH	Trend in DDPP
ErEr	2, 2	no	no	F1 → B1, F2 → B2	no	F1: LIN F2: LIN	all E	F2/F1: const.	F1–B1: const. F2–B2: const.
ErEs	2, 2	no	no	F1 → B1	no	F1: LIN F2: LIN	F1: E B1: E	F2/F1: const.	F1–B1: const. F2–B2: not const.
ErEi	2, 1	no	no	F1 → B1	yes	all LIN	F1: E F2: Es B1: E	F2/F1: const.	F1–B1: const.
EiEr	2, 1	no	no	F2 → B1	yes	all LIN	F1: Es F2: E B1: E	F2/F1: const.	F2–B1: const.
EiEi	2, 0	no	no			all LIN	all E	F2/F1: const.	

TABLE 7

Diagnostic criteria for triangle and square scheme mechanisms (F = Signal in the forward branch, B = signal in the backward branch of the voltammogram, HS = hidden signals (see [2]), SS = secondary signals, RDPH = ratio of semiderivative peak heights, SPH = semiderivative peak height, i_p = SCV peak height)

Mechanism	Number of F, B	HS	SS	type of transport	Trend in		d(i_p/C) dC value
					RDPH	d(SPH/C) dC Value	
E ⇔ E	2,1	no	no	F1: LIN-KIN	F2/F1 incr [a]	F1: const.	F1: 0.0
				B1: LIN-KIN		F2: const.	F2: 0.0
E ⇄ E	2,2	no	no	F1: LIN-KIN	F2/F1 incr [a]	F1: const.	F1: 0.0
				B1: LIN-KIN		F2: const.	F2: 0.0

[a] For the reduction in forward and the oxidation in the backward branch; otherwise trend is reverse.

or

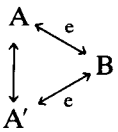

A general discussion of this type of reaction has been presented by Ashley and Reilley [26]. It is assumed, that the chemical steps proceed according to first-order kinetics and are reversible; additionally it is assumed, that the electron transfer steps are very fast.

The diagnostic criteria (Table 7) take advantage of the fact, that depletion of the diffusion zone for one substrate, say A, induces its production from A′ in the chemical reaction thus enhancing the transport to the electrode. However, the consumption of A′ causes a reduction of the corresponding A′ → B$^{(')}$ signal (lower peak in SCV and semiderivative voltammetry), this effect being more pronounced for slower scan rates. This results in an increase of the height ratio of the second to the first peak of the forward branch with the scan rate.

The criteria from Table 7 will not apply if the chemical reactions are irreversible, if they have other than first-order kinetics and if their rates are very high or very low compared to the time scale of the experiment.

VALIDATION

To validate the modified and the newly added rules, a number of compounds for which reaction mechanisms are already established have been studied. The selected electrochemical systems were mixture of Zn^{2+} and Cd^{2+} ions, 2-nitrophenol, 4-nitrosophenol and Methylene Blue. The mixture of zinc and cadmium ions was used to validate ErEs mechanism; for the expert system it is indistinguishable from a substance undergoing a double-step reduction.

For each system, validation results are collected in two tables: the first one presents support for separate features used as criteria to elucidate the pertaining mechanism, on the basis of Tables 4–7, and the list of possible mechanisms, ordered according to decreasing support. In the second table, for each mechanism the feature that had the strongest influence on the support is given. Because rules for the elucidation of mechanisms involve mainly conjunctions of features, the most influential feature is the one with the lowest supporting pair.

Experimental

Autolab-100 General Purpose Electrochemical System (Eco Chemie, Utrecht) coupled to an Olivetti M24 personal computer (IBM PC-compatible, 8086 cpu and 8087 numerical coprocessor) were used to carry out experiments and to run the expert system. All measurements were made on the static mercury electrode (Metrohm VA-663), composition of the solution in the cell was controlled using two Dosimat 665 burettes (Metrohm) and a Metrohm 661 pump unit.

In all experiments, solutions were prepared with deionized water (Millipore Q2). Oxygen was expelled with polarographic grade nitrogen (Hoekloos, Netherlands). Mercury for the filling of the electrode (commercial grade), has been successively purified by shaking with ethanol, 2 M sodium hydroxide and 2 M nitric acid and finally doubly distilled at low pressure.

0.05 M + 0.05 M solutions of cadmium chloride (Merck, Suprapur) and of zinc sulphate (Fluka, p.a.) were prepared by the dissolution of respective salts in 1 M KCl (Suprapur). Methylene Blue (for electrophoresis, Merck) was dissolved in 80% 0.1 M boric acid–KCl–NaOH buffer (pH 10.0, Merck) mixed with 20 vol.% ethanol (Merck). The solution of *p*-nitrosophenol (Aldrich) was prepared in 0.1 M KNO_3 containing 0.067 M acetate buffer (pH 4.66, Merck) and 20% ethanol. The stock solution of *o*-nitrophenol (p.a., Fluka) was obtained by the dissolution of the compound in 0.1 M CH_3COOH + 0.1 M CH_3COONa buffer mixed with ethanol (50 vol.%).

All potentials were measured in respect to Ag/ AgCl (3 M KCl) reference electrode (Metrohm). As auxiliary electrode a glassy carbon rod was used.

During the experiments with the Cd^{2+} and Zn^{2+} ions mixture, the concentration in the electrochemical cell was varied from 0.8×10^{-4} to 2.6×10^{-4} mol dm^{-3} and the range of scan rates used in voltammetric measurements was from 0.25 V s^{-1} up to 10.0 V s^{-1}. The potential was scanned in the range −0.3 to −1.45 V. In chronocoulometric experiments, the conditioning period of 1 s at −0.3 V was followed by two potential steps, respectively −0.8 and −0.3 V, with a duration of 0.4 s each.

In cyclic voltammetry of Methylene Blue, the range of potentials of −0.1 V to −0.8 V was scanned with a rate that varied between 0.3 and 1.6 V s^{-1}. The concentration range investigated was 8.0×10^{-5} to 2.6×10^{-4} mol dm^{-3}. Chronocoulometric experiments were carried out in exactly the same time regime as for the cadmium + zinc mixture.

p-Nitrosophenol was investigated in the range of potentials from +0.35 V to −0.4 V using scan rates varying from 0.05 V s^{-1} to 2.15 V s^{-1}. The concentration was changed from 2.0×10^{-4} to 2.0×10^{-3} mol dm^{-3}. In the chronocoulometric experiment, the duration of the steps was 1 s (preconditioning), 0.4 s and 0.4 s (potentials +0.35 V, −0.4 V and +0.35 V, respectively).

Voltammograms of *o*-nitrophenol were re-

TABLE 8

Features and their support obtained during the elucidation of the ErEs mechanism imitated by the reduction of a mixture of Zn^{2+} and Cd^{2+} ions in KCl solution (Acronyms: F = signal in the forward branch, B = signal in the backward branch)

F = 2, B = 2	**[1.000, 1.000]**	*Assignment of peaks*	
Net reaction present	[0.000, 1.1E-16]	B1 → F1, B2 → F2	[1.000, 1.000]
Suggestion for the type of the ETS (Table 4 in Ref. 2)			
F1: E	**[0.469, 0.613]**	B1: E	**[0.487, 0.594]**
F1: ECr	[0.007, 0.054]	B1: CEr	[0.018, 0.159]
F1: Es	[0.006, 0.855]	B1: Es	[0.013, 0.785]
F1: EiCat	[1.1E-5, 6.7E-5]	B1: EiCat	[0.012, 0.079]
F1: ECi, CEi	[8.5E-6, 6.2E-5]	B1: ECi, CEi	[3.009, 0.077]
F1: ErCat	[2.2E-6, 5.7E-5]	B1: CEr	[0.006, 0.147]
F1: CEr	[2.1E-6, 5.5E-5]	B1: ECr	[0.000, 0.000]
F2: Es	**[0.418, 0.706]**	B2: CEr	**[0.536, 0.666]**
F2: ECi, CEi	[0.398, 0.636163]	B2: Es	[0.446, 0.705]
F2: EiCat	[0.1848, 0.294]	B2: ErCat	[9.303, 0.377]
F2: E	[8.5E-7, 0.265]	B2: EiCat	[0.303, 0.377]
F2: CEr	[0.000, 0.238]	B2: E	[0.002, 0.486]
F2: ErCat	[0.000, 0.110]	B2: ECi, CEi	[0.000, 0.130]
F2: ECr	[0.000, 0.000]	B2: ECr	[0.000, 0.000]
Transport to the electrode		B1: LIM-LIN	**[0.995, 0.995]**
F1: LIN	**[0.890, 0.890]**	B1: ADS	[0.333, 0.333]
F1: LIN-KIN	[0.750, 0.750]	B1: LIN	[0.227, 0.227]
F1: ADS-LIN	[0.001, 0.001]	B1: LIN-KIN	[0.201, 0.201]
F1: other	[0.000, 0.000]	B1: ADS-LIN	[0.001, 0.001]
		B1: KIN	[0.000, 0.000]
F2: LIM-LIN	**[1.000, 1.000]**		
F2: LIN	**[1.000, 1.000]**	B2: LIM-LIN	**[1.000, 1.000]**
F2: LIN-KIN	**[1.000, 1.000]**	B2: LIN	**[1.000, 1.000]**
F2: other	[0.000, 0.000]	B2: LIN-KIN	**[1.000, 1.000]**
		B2: other	[0.000, 0.000]

System mechanism:	
ErEs	**[0.116, 0.257]**
ErCrEr, E2 ≪ 1	[4.0E-4, 0.004]
E ⇄ E	[1.5E-25, 0.000]
other	[0.000, 0.000]

corded in the range +0.1 V to −0.9 V, with scan rate varying from 0.3 to 10.0 V s^{-1} and the concentration in the range 10^{-4} up to 10^{-3} mol dm^{-3}. In chronocoulometric experiments, the potential was changed from +0.1 V to −0.9 V for 0.4 and 0.4 s, respectively; the preconditioning pulse at +0.1 V took 1 s.

ErEs mechanism, reduction of Cd^{2+} and Zn^{2+} mixture in KCl

A mixture of zinc and cadmium ions can imitate a substance that is reduced according to the ErEs mechanism. The difference can be detected by comparison of the products $nFAD^{1/2}C$ for the first and second steps (obtained either by chronocoulometry or SCV technique): their ratios should equal n_1/n_2 (n_1 and n_2 are the numbers of electrons involved in each electron transfer step). In the case of a mixture of two substances, the chance that the ratio of $nFAD^{1/2}C$ terms equals exactly 0.5, 1.0, 1.5 or 2.0 is extremely small due to differences in concentrations and in diffusion coefficients. Nevertheless, because the expert system does not use the value of the $nFAD^{1/2}C$ ratio as a criterion, a mixture of two compounds cannot be distinguished from a substance reducible in two subsequent steps.

Table 8 presents features evaluated by the expert system and the support for different hypotheses about the electrode reaction mechanism.

It can be seen, that the hypothesis about the absence of the net reaction is strongly supported. Inspection of the results for the type of transport to the electrode shows, that in the cases of the second electron transfer in the forward and in the backward branch, the support has gotten value either 1.0 or 0.0: this results from the use of a restricted set of conditions if parallel reactions take place on the electrode (signals other than the first one). The conditions are then based exclusively on the number of peaks appearing in voltammograms differintegrated to various instances and because this is a Boolean feature, the final results for the transport type also acquire a Boolean character. These restrictions have a limited significance for the determination of the mechanism of the reaction, because conditions employing the type of the transport for signals other than the first one occur very seldom in the rules.

The semi-infinite linear diffusion has been found to be the most probable type of the transport for the first signals in the forward and in the

TABLE 9

Features with the strongest influence on the support pair for hypotheses about the reaction mechanism for the reduction of the mixture of Cd^{2+} and Zn^{2+} ions (F, B = Number of peaks in forward and backward branches of the SCV voltammogram)

Er, Es, Ei, CEr, CEs, CEi, ECr, ECi, ErCat, EiCat	F, B
ErCrEr ($E_2^{0'} \ll E_1^{0'}$)	Sugg. for the type of the ETS
ErCrEr ($E_2^{0'} \approx E_1^{0'}$, $E_2^{0'} \gg E_1^{0'}$)	F, B
ErCiEr ($E_2^{0'} \ll E_1^{0'}$)	Type of transport
ErCiEr ($E_2^{0'} \approx E_1^{0'}$, $E_2^{0'} \gg E_1^{0'}$), ErCrEi ($E_2^{0'} \ll E_1^{0'}$, $E_2^{0'} \approx E_1^{0'}$, $E_2^{0'} \gg E_1^{0'}$), ErCiEi ($E_2^{0'} \ll E_1^{0'}$, $E_2^{0'} \approx E_1^{0'}$, $E_2^{0'} \gg E_1^{0'}$), EiCEi ($E_2^{0'} \ll E_1^{0'}$, $E_2^{0'} \approx E_1^{0'}$, $E_2^{0'} \gg E_1^{0'}$)	F,B
EAs	Type of transport
AsE	Trend in semidiff. peak height difference
AwE, EAw	F, B
ErEr	Trend in semidiff. peak potential difference
ErEs	Sugg. for the type of the ETS
ErEi, EiEr, EiEi	Trend in normalized semidiff. peak height
E ⇔ E	F, B
E ⇄ E	Trend in normalized semidiff. peak height

backward branch. For the second signals in both branches, the types of transport: LIM-LIN, LIN and LIN-KIN were equally possible. The first signal in the backward branch is suggested to be controlled by mixed linear and limited diffusion.

For the first and the second signal in each branch, E and Es mechanisms are suggested, respectively. The only exception is the reoxidation of zinc, where the CEr mechanism has been found to be more probable. This can be explained by the accumulation effect (criteria for suggestions for ETS mechanisms assume semi-infinite linear diffusion) and possible complexation/decomplexation phenomena.

In Table 9 the most influential features in the determination of the mechanism of the reaction are collected.

EAs mechanism, reduction of Methylene Blue in buffered water–ethanol solution

Methylene Blue is a compound well known to be reduced according to the EAs mechanism: the

TABLE 10

Support for features obtained during the elucidation of the mechanism of the electrode reaction of Methylene Blue in buffered water–ethanol solution (Acronyms: F = signal in the forward branch, B = signal in the backward branch)

F = 2, B = 2	**[1.000, 1.000]**	*Hidden and secondary signals:*	
Net reaction present	**[0.000, 4.5E-4]**	Hidden signals	**[0.000, 0.000]**
		Secondary signals	**[0.000, 0.000]**
Suggestion for the type of the ETS		B1: E	**[0.216, 0.462]**
F1: E	**[0.241, 0.604]**	B1: Es	[0.179, 0.75]
F1: ECr	[0.008, 0.442]	B1: CEr	[1.5E-16, 0.667]
F1: EiCat	[0.001, 0.04]	B1: EiCat	[1.3E-16, 0.333]
F1: ErCat	[3.3EA, 0.039]	B1: ECi, CEi	[1.2E-16, 0.667]
F1: Es	[4.1E-5, 0.936]	B1: ErCat	[7.4E-17, 0.333]
F1: other	[0.000, 0.000]	B1: ECr	[0.000 0.000]
F2: E	**[0.177, 0.440]**	B2: E	**[0.118, 0.348]**
F2: Es	[0.063, 0.699]	B2: Es	[0.106, 0.750]
F2: ECi, CEi	[0.000, 0.667]	B2: EiCat	[4.6E-17, 0.333]
F2: CEr	[0.000, 0.667]	B2: ECr	[4.6E-17, 0.333]
F2: ErCat	[0.000, 0.333]	B2: ECi, CEi	[4.6E-17, 0.333]
F2: EiCat	[0.000, 0.333]	B2: ErCat	[0.000, 0.333]
F2: ECr	[0.000, 0.000]	B2: CEr	[0.000, 0.333]
Transport to the electrode:			
F1: LIM-LIN	**[1.000, 1.000]**	B1: LIM-LIN	**[0.929, 0.929]**
F1: ADS	**[1.000, 1.000]**	B1: ADS	[0.929, 0.929]
F1: LIN-KIN	[0.750, 0.750]	B1: LIN	[0.071, 0.071]
F1: LIN	[2.5E-5, 2.5E-5]	B1: other	[0.000, 0.000]
F1: KIN	[0.000, 0.000]		
F1: ADS-LIN	[0.000, 0.000]	B2: LIM-LIN	**[1.000, 1.000]**
		B2: LIN	**[1.000, 1.000]**
F2: LIM-LIN	**[1.000, 1.000]**	B2: LIN-KIN	**[1.000, 1.000]**
F2: LIN	**[1.000, 1.000]**	B2: ADS	**[1.000, 1.000]**
F2: LIN-KIN	**[1.000, 1.000]**	B2: KIN	[0.000, 0.000]
F2: ADS	**[1.000, 1.000]**	B2: ADS-LIN	[0.000, 0.000]
F2: KIN	[0.000, 0.000]		
F2: ADS-LIN	[0.000, 0.000]		
System mechanism:			
EAs	**[0.413, 0.413]**		
ErEs	[2.6E-7, 7.2E-6]		
ErCrEr, E2 ≪ E1	[4.6E-8, 2.5E-6]		
other	[0.000, 0.000]		

TABLE 11

Features with the strongest influence on the support pair for hypotheses about the reaction mechanism for the reduction of Methylene Blue (F, B = Number of peaks in forward and backward branches of the SCV voltammogram)

Er, Es, Ei, CEr, CEs, CEi, ECr, ECi, ErCat, EiCat	F, B
ErCrEr ($E_2^{0'} \ll E_1^{0'}$)	Type of transport
ErCrEr ($E_2^{0'} \approx E_1^{0'}$), $E_2^{0'} \ll E_1^{0'}$)	F, B
ErCiEr ($E_2^{0'} \ll E_1^{0'}$)	Sugg. for the type of the ETS
ErCiEr ($E_2^{0'} \approx E_1^{0'}$, $E_2^{0'} \gg E_1^{0'}$), ErCrEi ($E_2^{0'} \ll E_1^{0'}$, $E_2^{0'} \approx E_1^{0'}$, $E_2^{0'} \gg E_1^{0'}$), ErCiEi ($E_2^{0'} \ll E_1^{0'}$, $E_1^{0'} \approx E_1^{0'}$, $E_2^{0'} \gg E_2^{0'}$), EiCEr ($E_2^{0'} \ll E_1^{0'}$, $E_2^{0'} \approx E_1^{0'}$, $E_2^{0'} \gg E_1^{0'}$), EiCEi ($E_2^{0'} \ll E_1^{0'}$, $E_2^{0'} \approx E_1^{0'}$, $E_2^{0'} \gg E_1^{0'}$)	F, B
EAs	Trend in i_p/v
AsE	Trend in semidiff. peak height difference
AwE, EAw	F, B
ErEr	Trend in semidiff. peak potential difference
ErEs, ErEi, EiEr, EiEi	Type of transport
E ⇔ E	F, B
E ⇄ E	Type of transport

product of the electron transfer, the leuco form of the substance, is strongly adsorbed on the electrode surface [25,27,28]. The substrate, Methylene Blue itself, is also adsorbed but this effect is much weaker than the adsorption of the product, so it can be neglected.

The results of the elucidation (determined features as well as the list of supports for different mechanisms) are presented in the Table 10.

Results for the type of transport generally allow to exclude certain types: for the signal for which in reality the transport is governed by

TABLE 12

Support for features obtained during the elucidation of the mechanism of reaction of *p*-nitrosophenol in buffered KNO_3–ethanol solution (Acronyms: F = signal in the forward branch, B = signal in the backward branch)

F = 1, B = 2	**[1.000, 1.000]**	Net reaction	**[0.868, 1.000]**
Hidden and secondary signals:		*Sugg. for the type of the ETS:*	
Hidden signals	**[0.000, 0.000]**	F1: E	**[0.009, 0.444]**
Secondary signals	**[1.000 1.000]**	F1: ECr	[1.5EA,0.34]
		F1: EiCat	[1.5EA, 0.322]
Type of the transport:		F1: ECi, CEi	[1.5E-4, 0.321]
F1: LIN	**[0.995, 0.995]**	F1: Es	[5.9E-13, 0.496]
F1: LIN-KIN	[0.750, 0.750]	F1: ErCat	[1.2E-13, 0.325]
F1: other	[0.000, 0.000]	F1: CEr	[1.2E-13, 0.321]
B1: LIM-LIN	**[0.978, 0.978]**	B1: E	**[0.258, 0.548]**
B1: LIN-KIN	[0.778, 0.778]	B1: CEr	[0.011, 1.000]
B1: LIN	[0.444, 0.444]	B1: ErCat	[0.003, 0.281]
B1: ADS	[0.111, 0.111]	B1: EiCat	[0.003, 0.281]
B1: ADS-LIN	[0.000, 0.000]	B1: Es	[8.3E-5, 0.733]
B1: KIN	[0.000, 0.000]	B1: ECi, CEi	[2.4E-9, 0.989]
		B1: ECr	[0.000, 0.000]
System mechanism:			
ErCiEr, E2 ≫ E1	**[0.116, 0.500]**		
ErCrEr, E2 ≫ E1	[0.018, 0.000]		
other	[0.000, 0.000]		

adsorption, this feature is ADS or LIM-LIN, while for signals associated with diffusional transport of the compound, the only conclusion is that two possibilities (KIN and ADS-LIN) are excluded.

Results for the mechanism of the electron transfer steps suggest, that all these reaction steps are fast and proceed without complications. From the data from Table 10 it can be found, that the result of the elucidation is mainly influenced by the analysis of the changes of heights of the voltammetric peaks with the variation of the scan rate.

The most influential features for the determination of the final support for the mechanisms are collected in Table 11.

ErCiEr mechanism, reduction of p-nitrosophenol

p-Nitrosophenol has been used as a model compound for the experimental confirmation of the theoretical description of LSV curves for the ECE mechanism [3]. The mechanism of the reduction of this compound is known to include a relatively slow, irreversible chemical step between two fast electron transfers; the formal potential of the reduction of the intermediate is much more positive compared to the original substrate and therefore reduction signals totally overlap. The results of the expert system run are presented in the table below (Table 12).

During the investigations, two important features of the system have been found: the presence of a net reaction and the appearance of a secondary signal in the third voltammetric half-cycle. The most supported type of transport for the forward peak is the linear diffusion and the LIN-KIN one. This suggests, that the influence of the chemical reaction on the flux of the electroactive substance is limited; indeed, the time-scale of the experiment is relatively short in comparison with the rate of the chemical reaction.

The support for the mechanism of the single electron transfer step in the forward branch is actually very low and on this basis no hypothesis can be considered as reasonably true. This is correct, because each signal does not belong to any of the listed classes.

The list of features that had the most important influence on the determination of the support is collected in Table 13.

EiCEr mechanism, reduction of o-nitrophenol

Nitrophenols have been extensively investigated and a number of papers devoted to the mechanism of their electrode reactions appeared [29–35]. The *o*-nitrophenol undergoes a complicated reaction, most probable consisting of the formation of a radical followed by its fast dismutation and protonation. The rate-determining step is the protonation [32], therefore the overall mechanism is EiCiEr (irreversible electron transfer, then an irreversible chemical step followed by a fast electron transfer step). The reported existence of a chemical step (protonation) prior to the first electron transfer, which is relatively fast,

TABLE 13

Features with the strongest influence on the support pair for hypotheses about the reaction mechanism for the reduction of *p*-nitrosophenol (F, B = number of peaks in forward and backward branches of the SCV voltammogram)

Er, Es, Ei, CEr, CEs, CEi, ECr, ECi, ErCat, EiCat, ErCrEr ($E_2^{0'} \ll E_1^{0'}$, $E_2^{0'} \approx E_1^{0'}$, $E_2^{0'} \gg E_1^{0'}$), ErCiEr ($E_2^{0'} \ll E_1^{0'}$, $E_2^{0'} \approx E_1^{0'}$)	F, B
ErCiEr ($E_2^{0'} \gg E_1^{0'}$)	Sugg. for the type of the ETS
ErCrEi ($E_2^{0'} \ll E_1^{0'}$, $E_2^{0'} \approx E_1^{0'}$, $E_2^{0'} \gg E_1^{0'}$), ErCiEi ($E_2^{0'} \ll E_1^{0'}$, $E_2^{0'} \approx E_1^{0'}$, $E_2^{0'} \gg E_1^{0'}$), EiCEr ($E_2^{0'} \ll E_1^{0'}$, $E_2^{0'} \approx E_1^{0'}$, $E_2^{0'} \gg E_1^{0'}$), EiCEi ($E_2^{0'} \ll E_1^{0'}$, $E_2^{0'} \approx E_1^{0'}$, $E_2^{0'} \gg E_1^{0'}$), EAs, AsE, AwE, EAw, ErEr, ErEs, ErEi, EiEr, EiEi, E ⇔ E, E ⇄ E	F, B

TABLE 14

Support for features obtained during the determination of the mechanism of *o*-nitrophenol reduction in mixed aqueous-ethanol solution (Acronyms: F = signal in the forward branch, B = signal in the backward branch)

F = 1, B = 1	**[1.000, 1.000]**	Hidden signals	**[0.000, 0.000]**
Net reaction	**[1.000, 1.000]**	Secondary signals	**[1.000, 1.000]**
Type of the transport:		B1: LIN-KIN	**[0.750, 0.750]**
F1: LIN	**[0.859, 0.859]**	B1: LIN	[0.555, 0.555]
F1: LIN-KIN	[0.333, 0.333]	B1: LIM-LIN	[0.501, 0.501]
F1: other	[0.000, 0.000]	B1: other	[0.000, 0.000]
Sugg. for the type of the ETS:			
F1: Es	**[0.577, 0.821]**	B1: CEr	**[0.358, 0.673]**
F1: ECr	[0.319, 0.412]	B1: ErCat	[0.171, 0.322]
F1: EiCat	[0.185, 0.239]	B1: EiCat	[0.171, 0.322]
F1: ECi, CEi	[0.168, 0.216]	B1: Es	[0.016, 0.703]
F1: E	[2.8E-5, 0.361]	B1: E	[0.007, 0.438]
F1: ErCat	[0.000, 0.054]	B1: ECi, CEi	[0.000, 0.315]
F1: CEr	[0.000 0.049]	B1: ECr	[0.000, 0.000]

System mechanism	
EiCEr, E2 ≫ E1	**[0.121, 0.272]**
other	[0.000, 0.000]

has no visible effect on the results in the time scale of experiments carried out by the expert system [34].

Results of the expert system run-are presented in Table 14.

The most characteristic features of this system

TABLE 15

Features with the strongest influence on the support pair for hypotheses about the reaction mechanism for the reduction of *o*-nitrophenol (F, B = Number of peaks in forward and backward branches of the SCV voltammogram)

Er, Es	Hidden and secondary signals
Ei	F, B
CEr, CEs	Hidden and secondary signals
CEi, ECr, ECi	F, B
ErCat	Hidden and secondary signals
EiCat, ErCrEr ($E_2^{0'} \ll E_1^{0'}$)	F, B
ErCrEr ($E_2^{0'} \approx E_1^{0'}$)	Hidden and secondary signals
ErCrEr ($E_2^{0'} \gg E_1^{0'}$)	Net reaction
ErCiEr ($E_2^{0'} \ll E_1^{0'}$)	F, B
ErCiEr ($E_2^{0'} \approx E_1^{0'}$)	Hidden and secondary signals
ErCiEr ($E_2^{0'} \gg E_1^{0'}$), ErCrEi ($E_2^{0'} \ll E_1^{0'}$)	F, B
ErCrEi ($E_2^{0'} \approx E_1^{0'}$, $E_2^{0'} \gg E_1^{0'}$)	Hidden and secondary signals
ErCiEi ($E_2^{0'} \ll E_1^{0'}$)	F, B
ErCiEi ($E_2^{0'} \approx E_1^{0'}$, $E_2^{0'} \gg E_1^{0'}$)	F, B
EiCEr ($E_2^{0'} \ll E_1^{0'}$)	F, B
EiCEr ($E_2^{0'} \approx E_1^{0'}$)	Hidden and secondary signals
EiCEr ($E_2^{0'} \gg E_1^{0'}$)	Type of transport
EiCEi ($E_2^{0'} \ll E_1^{0'}$, $E_2^{0'} \approx E_1^{0'}$, $E_2^{0'} \gg E_1^{0'}$)	F, B
EAs, AsE	Secondary signals
AwE, EAw	Hidden and secondary signals
ErEr, ErEs, ErEi, EiEr, EiEi, E ⇔ E, E ⇄ E	F, B

are the appearance of the secondary signal (the signal in the third branch of the voltammogram) and the detection of the net reaction caused by the irreversibility of the chemical step. The type of the transport m the case of the first reduction signal has been found to be linear diffusion (LIN, most probably) and mixed kinetic effect and linear diffusion (LIN-KIN, less probably). The order of these features on the ranking list should be, actually, reverse; this discrepancy can be explained by a probably relatively small contribution of the chemical reaction the transport of the electroactive compound to the electrode.

Table 15 presents the most influence features for the support for each hypothesis about the mechanism of the reaction.

DISCUSSION

For all compounds, the expert system assigned the highest support to the correct mechanism of the electrode reaction. There is also a very clear difference in support between the first and next hypotheses on the list of electrode reactions, which facilitates the easy distinction between alternative hypotheses.

The values of numbers composing the supporting pairs should not be considered as probabilities: support is quite closely related to the probability, but the use of relative calculations in some of the statistical tests and the intermixing of Boolean and fuzzy facts makes this relation not straightforward. In these terms, support [0.1, 0.1] does not mean, that the probability that the considered mechanism is false is 90%: instead, the support should be compared to supports obtained for other mechanisms. From experience, supports above approx. 0.01 can be interpreted as acceptation of the hypothesis and below this limit, as rejection.

The time necessary for a complete elucidation is quite short: the fill cycle of work, including all experiments, takes approx. 4–6 h. It could be slightly shortened if a more powerful computer is used, however, most of the time is spent on experiments. All experimental results are available in such a form, that they can be processed by other application programs. The report facility delivers the full list of suggested mechanisms and features determined during the ES run in a form similar to the tables presented in the preceding sections of this chapter.

The inspection of partial results leads to the conclusion, that Boolean features like the number of visible electron transfer steps, the presence of hidden peaks etc. are determined properly; the same applies to the detection of a net chemical reaction in the system. Results are less informative for suggestions for the type of electron transfer step and in the determination of the type of transport of the electroactive substance for separate signals.

Problems with the first of these features stem from the fact, that the group of mechanisms of single electron transfer steps for which rules are implemented is quite limited; additionally, rules have been designed under the assumption, that the transport of electroactive substance proceeds according to the semi-infinite linear diffusion scheme. It is important to notice, that rules for some mechanisms are more strict (e.g., $dE_p/d \ln v = 0$ for Er), while for others they are more general ($dE_p/d \ln v$ not constant for ErCat): one can expect that the support obtained in the first case will be less than the support for the second case.

The result for the type of transport to the electrode suffers from the lack of corrections for the effect of parallel reactions proceeding on the electrode. As a consequence, all available tests are only applied to the investigation of the first reduction and oxidation signals. For other signals, only a reduced set of criteria is used, increasing the chance for misinterpretation of the experimental data. In possible future extensions of the expert system, particular attention should be paid to the improvement of this part of the set of rules. Partial improvement of the results could be obtained by the application of statistical tests more sophisticated than those currently used to investigate the trend and the values of the data.

The fact, that the right mechanism is obtained even in situations, where the relative support for one or two simple features does not reflect the truth means that there is a redundancy in the

structure of rules. This redundancy decreases the chance for making mistakes in the determination of the support for hypotheses about the mechanism and thanks to it the final results are more reliable.

The operation of the expert system requires only a small number of interactions with the operator. Almost all information necessary for the expert system is provided at the beginning of the ES run and thereafter the system can work independently until the result is obtained.

REFERENCES

1 M. Pałys, M. Bos and W.E. Van der Linden, Anal. Chim. Acta, 231 (1990) 59.
2 M. Pałys, M. Bos and W.E. Van der Linden, Anal. Chim. Acta, 248 (1991) 429.
3 R.S. Nicholson and I. Shain, Anal. Chem., 37 (1965) 178.
4 A.M. Bond, Modern Polarographic Methods in Analytical Chemistry, Dekker, New York, 1980.
5 R. Guidelli, in A.J. Bard (Ed.), Chemical Reactions in Polarography, Electroanalytical Chemistry, Vol. 5, Dekker, New York, 1971, p. 149.
6 K.B. Oldham, Anal. Chem., 58 (1986) 2296.
7 J.C. Myland, K.B. Oldham and C.G. Zoski, J. Electroanal. Chem., 193 (1985) 3.
8 S.O. Engblom and K.B. Oldham, Anal. Chem., 62 (1990) 625.
9 I.D. Dobson, N. Taylor and L.R.H. Tipping, in M.R. Smyth, J.G. Vos (Eds.), Electrochemistry, Sensors and Analysis, Elsevier, Amsterdam, 1986, p. 61.
10 R.S. Nicholson and I. Shain, Anal. Chem., 36 (1964) 706.
11 M. Goto and D. Ishii, J. Electroanal. Chem., 61 (1975) 361.
12 P. Dalrymple-Alford, M. Goto and K.B. Oldham, J. Electroanal. Chem., 85 (1977) 1.
13 F.C. Anson, Anal. Chem., 38 (1966) 54.
14 M.H. Hulbert and I. Shain, Anal. Chem., 42 (1970) 162.
15 S.W. Feldberg, in J.S. Matson, H.B. Mark and H.C. MacDonald (Eds.), Electrochemistry. Calculation Simulation, Instrumentation, Vol. 2, Dekker, New York, 1972, p. 185.
16 M.G. Grenness and K.B. Oldham, Anal. Chem., 44 (1972) 1121.
17 M. Goto and K.B. Oldham, Anal. Chem., 45 (1973) 2043.
18 M. Goto and K.B. Oldham, Anal. Chem., 48 (1976) 1671.
19 J.C. Imbeaux and J.M. Saveant, J. Electroanal. Chem., 44 (1973) 169.
20 F. Ammar and J.M. Saveant, J. Electroanal. Chem., 47 (1973) 215.
21 J.M. Saveant and D. Tessier, J. Electroanal. Chem., 61 (1975) 251.
22 C.P. Andrieux, J.M. Saveant and D. Tessier, J. Electroanal. Chem., 63 (1975) 429.
23 J.M. Saveant and D. Tessier, J. Electroanal. Chem., 65 (1975) 57.
24 R. Bowling and R.L. McCreery, Anal. Chem., 60 (1988) 605.
25 R.H. Wopschall and I. Shain, Anal. Chem., 39 (1967) 1514.
26 J.W. Ashley jr., and Reilley, J. Electroanal. Chem., 7 (1964) 253.
27 R. Brdicka, Coll. Czech. Chem. Commun., 12 (1947) 522.
28 W. Kemula, Z. Kublik and A. Axt, Roczniki Chem., 35 (1961) 1009.
29 A.C. Testa and W.H. Reinmuth, J. Am. Chem. Soc., 83 (1961) 784.
30 C. Corvaja, G. Farnia and E. Vianello, Electrochim. Acta, 11 (1966) 919.
31 G. Farnia, G. Mengoli and E. Vianello, J. Electroanal. Chem., 50 (1974) 73.
32 G. Farnia, A. Roque da Silva and E. Vianello, J. Electroanal. Chem., 57 (1974) 191.
33 L. Camacho, A. Heras, J.L. Avila and F. Garcia Blanco, J. Electroanal. Chem., 172 (1984) 161.
34 A.M. Heras, E. Munoz, J.L. Avila and L. Camacho, Electrochim. Acta, 32 (1987) 1495.
35 A.M. Heras, E. Munoz, J.L. Avila, L. Camacho and J.L. Cruz, J. Electroanal. Chem., 243 (1988) 293.

Analytica Chimica Acta, 283 (1993) 831–844
Elsevier Science Publishers B.V., Amsterdam

Development of the H-point standard additions method for analyte determinations in unknown matrix

Location of linear matrix spectral interval

F. Bosch-Reig, P. Campíns-Falcó and J. Verdú-Andrés

Departament de Química Analítica, Facultat de Química, Universitat de València, c / Dr. Moliner 50, 46100-Burjassot, València (Spain)

(Received 17th March 1993; revised manuscript received 29th June 1993)

Abstract

The development of the H-point standard additions method is proposed in order to obtain the unbiased analyte concentration when the matrix of the sample is completely unknown. A spectral region where the interferent behaviour can be considered linear at three wavelengths must be chosen. The method uses the analytical signal data at these three wavelengths, usually situated in the maxima region of the analyte. Two procedures are proposed in order to know and to locate this behaviour for the unknown interferent. Several binary and ternary mixtures of phenol, 4-chlorophenol and 4-chloro-3-methylphenol as representative examples have been assayed, with accurate (less than 3% relative error) and precise (less than 3% R.S.D. for $n = 6$) results for the analyte concentration, obtaining for the binary mixtures also the interferent one.

Keywords: Linear matrix spectral interval; H-Point standard additions method

A number of methods aimed at increasing analytical selectivity by using mathematical algorithms taking due account of the potential interferences of the different species involved have been reported. Many of these developments have emerged from the spectroscopic field.

Derivative spectroscopy [1] is one of these methods; it is able to eliminate those interferents that present a broad spectrum which overlaps the interest band of the analyte. Wahbi et al. [2] proposed this technique for detecting and, if possible, correcting for interferents, especially when the irrelevant absorption originally present in the substance sought is of an indefinite nature. They used ratios of first-derivative maxima and compensated derivative absorption curves.

Correspondence to: P. Campíns-Falcó, Departament de Química Analítica, Facultat de Química, Universitat de València, c/Dr. Moliner 50, 46100-Burjassot, València (Spain).

Another method developed is the compensation method for the spectrophotometric determination of a single substance in the presence of interferents, but the unwanted absorption curve must possess the simplest possible shape and none of the characteristics of the pure compound [3]. The accuracy of this method for the determination of the analyte concentration depends on correct evaluation of the balanced-point [4].

When extensively overlapping exists between the analyte and the interferent spectra, other types of methods have been proposed, as multivariate calibration [5,6]. A variety of this has been developed recently. Usually, these methods require the knowledge of the interferents which can perturb the analytical signals of the analyte or analytes.

A great number of them are based in the multiple linear regression methods (MLR), and lead to a series of equations of the different

parameters, which are resolved by the matricial calculus.

Other linear algorithms employed in this kind of calibration are extensions of pattern-recognition methods of a more qualitative nature, such as regression on latent variables (principal components, partial least-squares solutions).

Multi-wavelength linear regression analysis (MLRA) [7,8], is a graphic method of linear regression that allows comparable results to those obtained by the multivariate calibration or the multicomponent analysis.

Salinas et al. [9] and Berzas Nevado et al. [10,11] have proposed a new spectrophotometric method for the multicomponent analysis, resolving binary [9,10] and ternary [11] mixtures, based on use of the first derivative of the ratios of spectra of the species involved.

We have suggested a modification of the standard addition method, called H-point standard addition method (HPSAM), where the error resulting from the presence of a direct interferent in the determination of an analyte is transformed into a systematic constant error that can be evaluated and permits the determination of the analyte concentration free from bias error, also in the presence of a direct interferent and/or total Youden blank, TYB [12]. The basis of the method was established in [13,14], and it needs the knowledge of the absorption spectrum of the interferent, in order to choose two wavelengths where it presents the same absorbance. HPSAM has been applied to the determination of two species with extensively or even coincident overlapping spectra [15]. In cases in which only the analyte concentration was required, a variant of the method was developed, where the absorbance increment (ΔA) is used as the analytical signal [16]. This variant can be adapted to the calibration method with a unique standard and, in addition, it allows eliminating the blank bias error due to the use of absorbent blanks [17]. It has been applied to kinetic data too, with an additional variable, the time [18] and it was adapted to liquid chromatography [19].

In spite of these advances in the study of different kinds of mixtures, the determination of the analyte concentration when the interferent is not known is, at present, an unresolved problem in the chemical analysis field. In this way this paper is presented, where an HPSAM variant is developed in order to permit the calculation of the analyte concentration in a completely unknown sample, starting with only the spectral record of the sample and the successive standard additions. The only condition needed to apply the method is the linear behaviour of the interferent at three previously selected wavelengths, according with the basis of the method. At the same time, two procedures are developed to allow knowing when the interferent shows this linear behaviour, without any previously knowledge about the sample composition, neither the spectral behaviour of the interferent or interferents.

With the purpose to check the validity of the proposed method, several binary and ternary mixtures of phenol (the analyte), 4-chlorophenol and 4-chloro-3-methylphenol were studied. Starting from these prepared samples where the linearity of the interferent is known, we will demonstrate how the proposed method is able to obtain the analyte concentration free from bias error. These results can become general for all the samples where the interferent behaviour can be considered linear, or almost linear, at the selected wavelengths.

BACKGROUND

HPSAM develops a procedure to quantify an X analyte in the presence of a Y direct interferent, by the construction of two standard addition plots, with $M(\lambda_1)$ and $M(\lambda_2)$ slopes, at two previously selected wavelengths, λ_1 and λ_2, which intersect at the H-point, with $(-C_{H'}\ A_H)$ coordinates. H-Point is a function of the analyte concentration (C_X) by means of this expression [13–15]:

$$-C_H = \frac{(A_0 - b_0) + (A' - b)}{M(\lambda_1) - M(\lambda_2)}$$

$$= -C_X + \frac{A' - b}{M(\lambda_1) - M(\lambda_2)} \qquad (1)$$

where b_0 and A_0 are the absorbance values for the analyte and b and A' the interferent ones at λ_1 and λ_2 in the sample problem.

If λ_1 and λ_2 are selected in such a way that the interferent absorbance values are equals ($A' = b$), abscise of the H-point will be the analyte concentration, $-C_H$:

$$-C_H = \frac{A_0 - b_0}{M(\lambda_1) - M(\lambda_2)} = -C_X \qquad (2)$$

according to the HPSAM proposed bases. The interferent must be previously known in order to choose adequately λ_1 and λ_2 to fulfil the established condition ($A' = b$).

This HPSAM restriction is resolved in this paper by the development of a compensation method for the parameter $A' - b/M(\lambda_1) - M(\lambda_2)$ in Eqn. 1, that allows the direct calculation of C_X.

In this work, three wavelengths, λ_1, λ_m and λ_2, are selected, lying in the maximum region of the analyte. This is a big difference with the established HPSAM basis [13–15], where the selected region was the interferent maximum.

Fundamentals of the method

Let us consider X the analyte to be determined and Y the interferent, or mixture of interferents; their spectrum is shown in Fig. 1, where is included an analyte maximum and an interferent of which the $\Delta A/\Delta\lambda$ variation is constant in this zone.

If two wavelengths, λ_1 and λ_2 lying on both sides of the absorption maximum of the analyte X are selected in such a way that their absorbances for this component are the same, it will be true the next expression:

$$b_i = A_i \quad i = 0, 1, 2, \ldots, n \qquad (3)$$

where b_i is the absorbance value for the analyte at λ_1 and A_i at λ_2. The subscript i denotes the different solutions for 0 to n additions of known amounts of analyte X, according to the method of standard additions (MOSA); $i = 0$ corresponds with the solution where only sample exists.

For this proposed variant of the HPSAM, a third wavelength, λ_m, must be selected. In order to simplify the calculations, it will be selected as

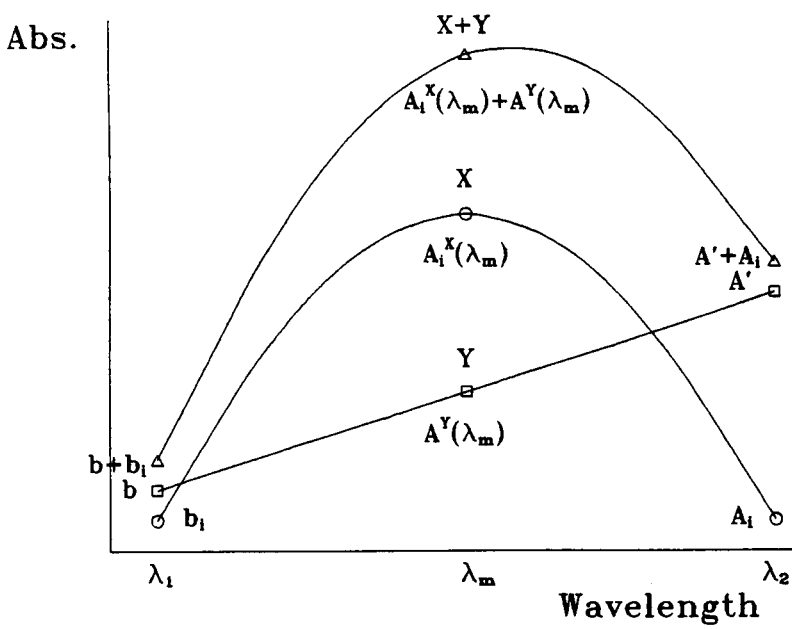

Fig. 1. Spectral features for the X analyte, Y interferent and the addition of both in the wavelength interval λ_1–λ_2.

the average wavelength of λ_1 and λ_2, applying the following expression:

$$\lambda_m = \frac{\lambda_1 + \lambda_2}{2} \quad (4)$$

The absorbance values for the analyte and the interferent (or interferents) at this wavelength, λ_m, will be $A_i^X(\lambda_m)$ $(i = 0, 1, 2, \ldots, n)$ and $A^Y(\lambda_m)$, respectively. $A^Y(\lambda_m)$ remains constant for all the additions carried out, because the sample amount added is constant for all the solutions.

If HPSAM is applied at two wavelengths, λ_m and one of the other two (λ_1 or λ_2), expression 1 transforms to:

$$-C_H = \frac{[A_0^X(\lambda_m) - b_0] + [A^Y(\lambda_m) - b]}{M(\lambda_1) - M(\lambda_m)}$$

$$= -C_X + \frac{A^Y(\lambda_m) - b}{M(\lambda_1) - M(\lambda_m)} \quad (5)$$

b is the absorbance of the interferent Y at λ_1, and $C_H \neq C_X$, because $A^Y(\lambda_m) \neq b$. So, H-point calculated abscissa, $-C_H$, do not correspond with the analyte concentration in the sample, $-C_X$.

The same conclusions are reached if the selected wavelengths are λ_m and λ_2, because in this case the absorbances for the interferent at λ_m and λ_2 are not equals $[A^Y(\lambda_m) \neq A']$, where A' is the absorbance of the interferent at λ_2.

In order to eliminate this problem, we have developed a "compensation procedure" for the interferent absorbances at λ_1, λ_m and λ_2. Its justification is the next.

If we apply the method of standard additions at the three previously selected wavelengths (λ_1, λ_m and λ_2), we will obtain three lines (R_1, R_m and R_2) (Fig. 2), where the absorbance values (A_i) are related with the added analyte concentration (C_i), and their equations will be:

for λ_1, R_1:

$$A(\lambda_1) = b_0 + b + M(\lambda_1) \cdot C_i \quad (6)$$

for λ_m, R_m:

$$A(\lambda_m) = A_0^X(\lambda_m) + A^Y(\lambda_m) + M(\lambda_m) \cdot C_i \quad (7)$$

for λ_2, R_2:

$$A(\lambda_2) = A_0 + A' + M(\lambda_2) \cdot C_i \quad (8)$$

where $A(\lambda_1)$, $A(\lambda_m)$ and $A(\lambda_2)$ are the measured absorbance values at the three selected wavelengths; $M(\lambda_1)$, $M(\lambda_m)$ and $M(\lambda_2)$ are the

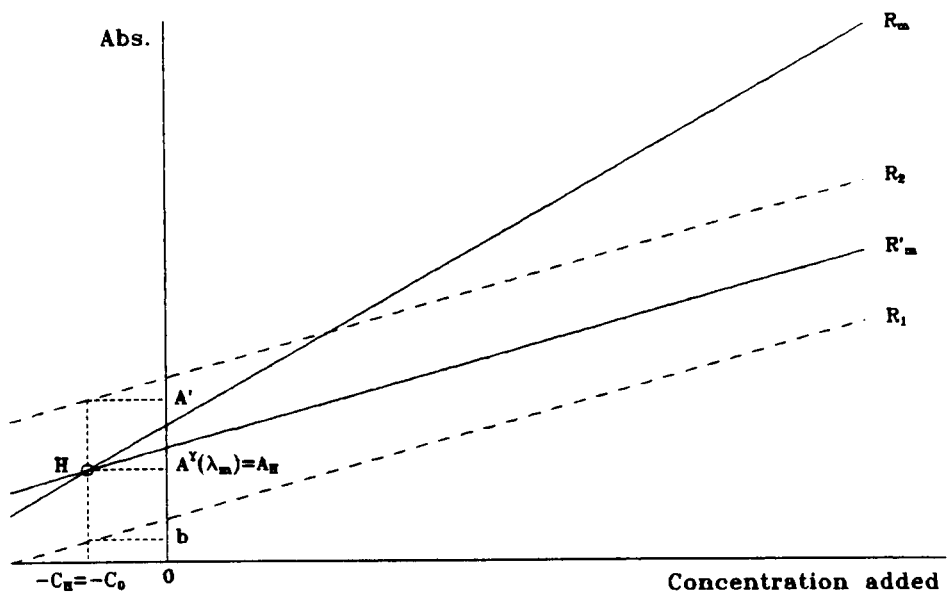

Fig. 2. Graphic representation of the lines R_1, R_2, R_m and R'_m.

slopes of the HPSAM lines at these wavelengths and C_i is the added analyte concentration.

Starting from R_1 and R_2 we can obtain a new line, called R'_m; it will be the average line of these two, and it allows us to locate correctly the H-point. The equation for R'_m will be:
for λ_m, R'_m:

$$A'(\lambda_m) = \frac{A(\lambda_1) + A(\lambda_2)}{2} = \{(b_0 + A_0) + (b + A') + [(M(\lambda_1) + M(\lambda_2)] \cdot C_i\}/2 \quad (9)$$

$M(\lambda_1) = M(\lambda_2)$, because analyte shows the same absorbance at λ_1 and λ_2. In the same way, $b_0 = A_0$, so R'_m can be rewritten as:

$$A'(\lambda_m) = b_0 + \frac{(b + A')}{2} + M(\lambda_1) \cdot C_i = A_0 + \frac{(b + A')}{2} + M(\lambda_2) \cdot C_i \quad (10)$$

R_m and R'_m will intersect at the H-point; its value is obtained resolving the system of the Eqns. 7 and 10:

$$-C_H = \frac{\left[A_0^X(\lambda_m) - b_0 + \left\{A^Y(\lambda_m) - \frac{b + A'}{2}\right\}\right]}{M(\lambda_1) - M(\lambda_m)} \quad (11)$$

as

$$A^Y(\lambda_m) = \frac{A' + b}{2} \quad (12)$$

because λ_m is equidistant from λ_1 and λ_2, and $A^Y(\lambda_m)$, b and A' are linearly related as can be seen in Fig. 1, it results:

$$-C_H = \frac{A_0^X(\lambda_m) - b_0}{M(\lambda_1) - M(\lambda_m)} \quad (13)$$

equivalent to Eqn. 2 previously enunciated. It corresponds to the correct solution of the problem ($C_H = C_X$), because C_H only depends of variables related exclusively to the analyte, so this expression justifies that the spectral record for the interferent has been transformed into a horizontal one in the $[\lambda_1, \lambda_2]$ wavelength interval, or for the λ_1, λ_m and λ_2 points, because R'_m is equivalent to R_1 displaced $(A' - b)/2$ or R_2 displaced $-(A' - b)/2$.

On the analogues of Eqn. 13, we can obtain another one with constants corresponding with λ_m and λ_2.

The calculated concentration ($-C_H$) is equivalent to the real analyte one,

$$-C_X = \frac{-b_0}{M(\lambda_1)} = \frac{-A_0^X(\lambda_m)}{M(\lambda_m)} = \frac{-A_0}{M(\lambda_2)}$$

as the HPSAM basis shows, because the incorrigible error resulting from the presence of a direct interferent is transformed into a systematic constant error.

If we are working with binary mixtures, and so the interferent is a pure compound, we can calculate the Y concentration in the sample with a calibration plot of Y species, or by applying the calibration method with a unique standard, because $A^Y(\lambda_m) = A_H$ is known by the resolution of the system of equations.

Replacing Eqn. 13 in R_m:

$$A_H = \frac{A^Y(\lambda_m) \cdot [M(\lambda_1) - M(\lambda_m)]}{M(\lambda_1) - M(\lambda_m)} = A^Y(\lambda_m) \quad (14)$$

This expression shows that the A_H obtained corresponds with the analytical signal at λ_m for the interferent if it is a pure compound, and the addition of all the interferents if they are a mixture. If only one interferent is present, it permits to estimate its concentration. In Fig. 2 all the lines mentioned are represented.

Selection of the spectral zone of measurement

The only required condition to apply this variant of the HPSAM is the linearity of the interferent absorbances (b, $A^Y(\lambda_m)$ and A') at the three selected wavelengths (λ_1, λ_m, λ_2). So, it is necessary to adequately select the measurement region, or the verification of the fulfilment of this condition, in order to obtain an optimum application of the method.

Two methods are proposed to corroborate the linearity of the interferent in the interesting region of the analyte: (1) study of the global linear-

ity of the interferent and (2) study of the first derivative value at the analyte absorption maximum. Below the theoretical backgrounds are explained.

Study of the global linearity of the interferent. If the interferent is linear in the wavelength interval $[\lambda_1, \lambda_2]$, or it is linear at λ_1, λ_m, λ_2, every pair of selected wavelengths lying on both sides of the absorption maximum of the analyte will be according to the described equations in the theoretical basis. If we select two pairs of wavelengths λ_1–λ_2 and λ'_1–λ'_2, we will have two pairs of lines, whose averages lines (Fig. 3, R'_m and $R'_{m'}$) will intersect with the line which describes the absorbance at $\lambda_m(R_m)$ in the same point, as can be seen in the Fig. 3. Such figure shows the absorbance of the analyte, the interferent, the addition of both, and the lines obtained by applying the HPSAM at the selected wavelengths. For each pair of wavelengths included in the $[\lambda_1, \lambda_2]$ interval with the same absorbance for the analyte, the average line intersects with R_m in the H-point.

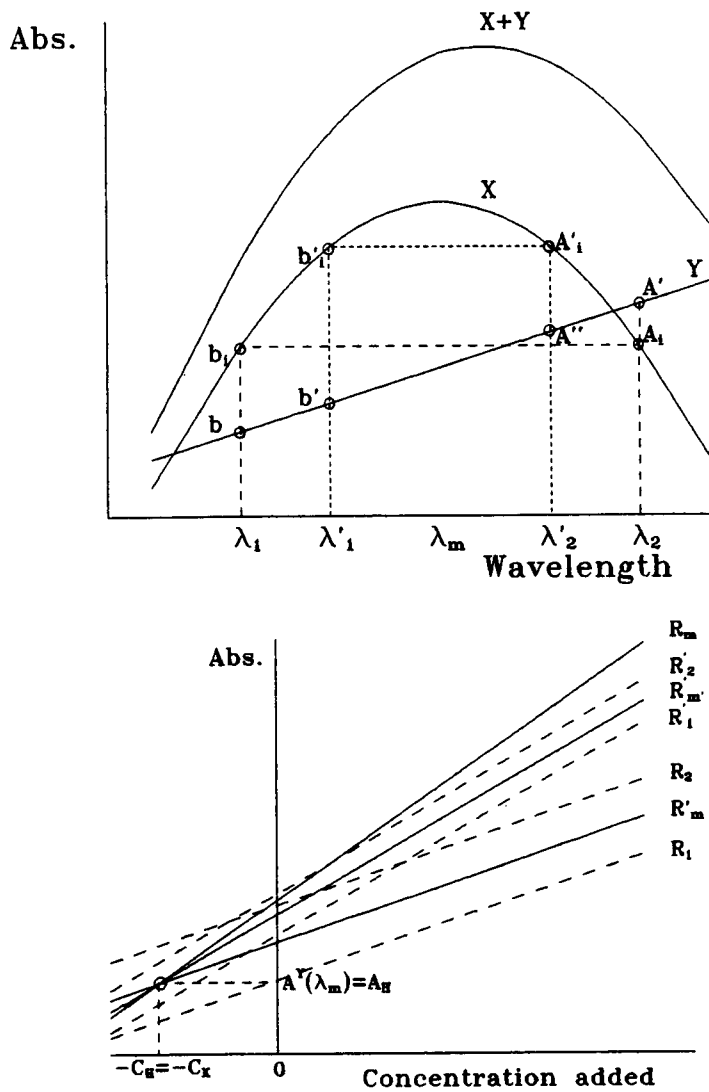

Fig. 3. Absorption spectra and standard additions lines obtained for two pairs of wavelengths λ_1–λ_2.

For another different spectral behaviour of the interferent, the average lines intersect with R_m at different points, but not at the H-point. This graphic will be different, as will be shown later.

Study of the first derivative value at the analyte absorption maximum. It will be always true that the first derivative value of the problem at the maximum of the analyte, λ_M, is equal to the first derivative value of the interferent at λ_M. So, for $\lambda = \lambda_M$:

$$\left(\frac{dA}{d\lambda}\right)^{X+Y}_{\lambda_M} = \left(\frac{dA}{d\lambda}\right)^{Y}_{\lambda_M} \quad (15)$$

We also know that the absorbance values of the problem at λ_1 and λ_2 are the additions of the corresponding ones of the analyte and interferent

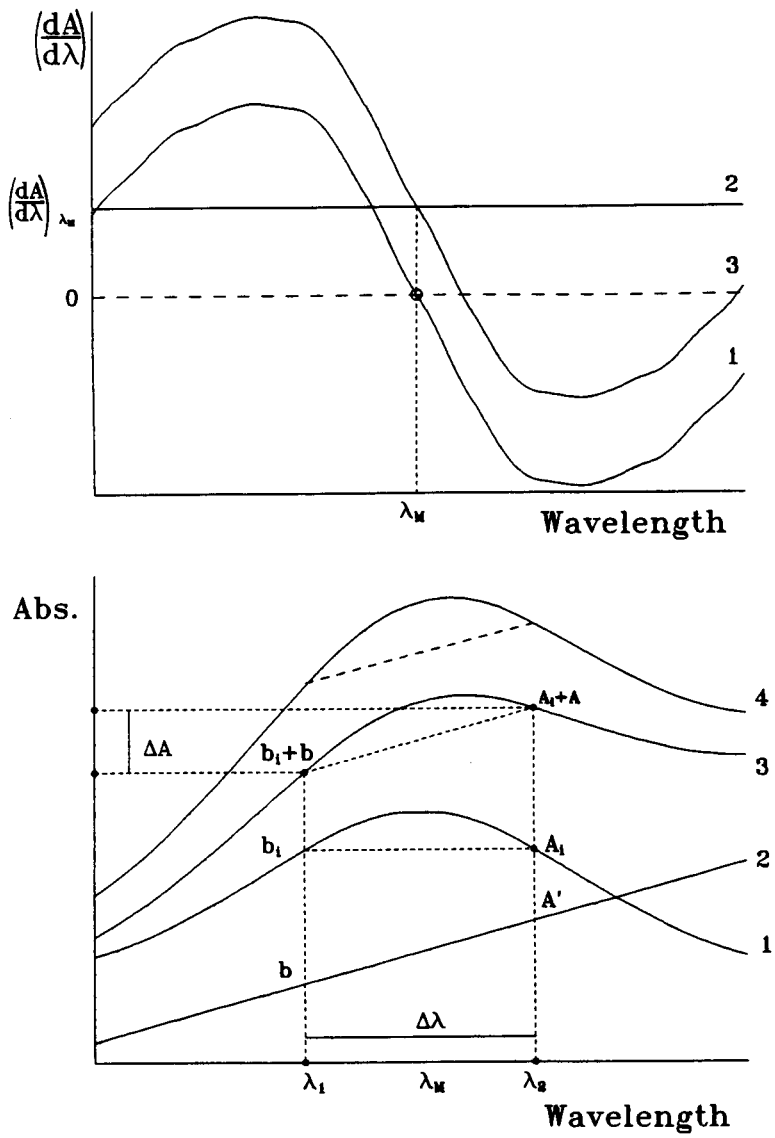

Fig. 4. Absorption spectra and derivative spectra for: (1) analyte; (2) linear interferent; (3) addition of both; and (4) first standard addition.

(Fig. 4). The difference between both absorbances, $\Delta A_{1,2}$, is described by the next expression:

$$\Delta A_{1,2} = A(\lambda_2) - A(\lambda_1)$$
$$= A_i + A' - b_i - b = A' - b \quad (16)$$

because λ_1 and λ_2 has been selected to obey the condition $A_i = b_i$.

If $\Delta A_{1,2}$ is divided by the corresponding $\Delta\lambda$, we will obtain a value, which will be equivalent with the first derivative value of the problem at λ_M, $(dA/d\lambda)^{X+Y}_{\lambda_M}$, if the interferent is linear:

$$\frac{\Delta A_{1,2}}{\Delta\lambda} = \frac{A' - b}{\lambda_2 - \lambda_1} = \left(\frac{dA}{d\lambda}\right)^{X+Y}_{\lambda_M} \quad (17)$$

The variation of the value of $\Delta A/\Delta\lambda$ for different wavelength intervals has been studied experimentally. If this values are included inside the interval $(dA/d\lambda)^{X+Y}_{\lambda_M} \pm 3 \cdot S_{(dA/d\lambda)^{X+Y}_{\lambda_M}}$ [20], the interferent can be considered linear.

Another kind of behaviour of the interferent will produce $\Delta A/\Delta\lambda$ values completely different for each wavelength interval selected.

EXPERIMENTAL

Apparatus

A Shimadzu UV-240 double-beam spectrophotometer and the OPI-2 data print program, which prints out absorbance values at selected wavelengths, equipped with 1-cm quartz cuvettes, were used, together with an Epson EL2 personal computer connected to Epson LQ-500 printer.

Reagents

Stock solutions were sodium hydroxide (Panreac) 0.5 M, daily prepared; stock solutions of the different phenols were prepared by weighing the appropriate amount of the substance and dissolving in 250 ml of water: phenol (Merck), 1.704×10^{-3} M; 4-chlorophenol (Aldrich), 1.565×10^{-3} M; 4-chloro-3-methylphenol (Aldrich), 2.202×10^{-3} M.

They were stored in borosilicated glass and in a refrigerator. Working solutions were prepared daily by appropriate dilution of the stock solutions.

Procedure

First of all, the absorption spectra of phenol, 4-chlorophenol and 4-chloro-3-methylphenol solutions (prepared in 0.1 M NaOH immediately before the measurements in order to prevent alterations in the solution composition) was registered. The wavelength interval selected was 190–320 nm. The baseline correction was made with 0.1 M NaOH immediately before each replicate measurement.

In order to apply the H-point standard additions method mixtures were prepared with a phenol concentration of 2.73×10^{-5} M, and making additions of analyte in the interval 6.82×10^{-6} to 3.41×10^{-5} M. The sample compositions assayed are shown in Table 1. All the solutions were prepared in 0.1 M NaOH, and spectra were registered in the wavelength interval 212–265 nm. Six replicates of each sample were made.

RESULTS AND DISCUSSION

Figure 5 shows the spectra of the synthetic mixtures prepared according to Table 1 data, where the linearity of the interferents in the maximum region of the analyte is remarkable. As it can be observed, there are wavelength intervals where the interferent is completely linear, but there are, in addition, spectral zones where this behaviour is true for the points λ_1, λ_m and λ_2. In Table 2 the linearity *t*-test [20] for the wavelength interval where the interferent can be considered linear is shown.

TABLE 1

Composition of the three samples assayed

Sample	Phenol concentration (M)	4-Chlorophenol concentration (M)	4-Chloro-3-methylphenol concentration (M)
A	$2.73 \cdot 10^{-5}$	$2.50 \cdot 10^{-5}$	–
B	$2.73 \cdot 10^{-5}$	–	$3.52 \cdot 10^{-5}$
C	$2.73 \cdot 10^{-5}$	$1.25 \cdot 10^{-5}$	$1.76 \cdot 10^{-5}$

As it has been demonstrated in the fundamentals of the method, in order to apply the HPSAM in the determination of an analyte in a completely unknown sample, we have to confirm that the interferent, or interferents, present(s) a linear behaviour.

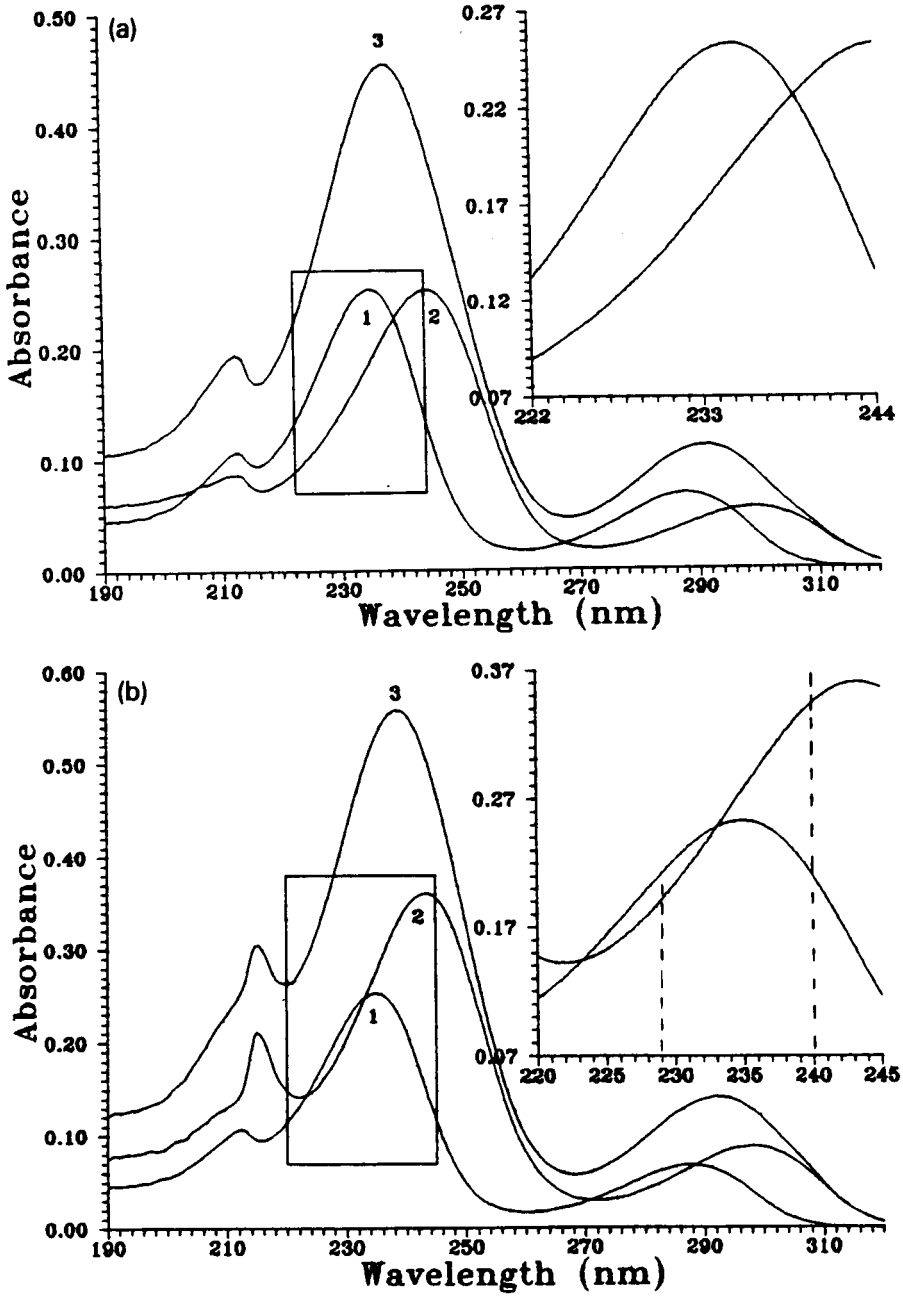

Fig. 5. (a) Absorption spectra for sample A (1 = phenol; 2 = 4-chlorophenol; 3 = addition of both). Region, between 222 and 244 nm. (b) Absorption spectra for sample B (1 = phenol; 2 = 4-chloro-3-methylphenol; 3 = addition of both). Region, between 220 and 245 nm. (c) Absorption spectra for sample C (1 = phenol; 2 = 4-chlorophenol; 3-4-chloro-3-methylphenol; 4 = addition of all of them). Region, between 218 and 246 nm (with the dashed line indicating the addition of both interferents).

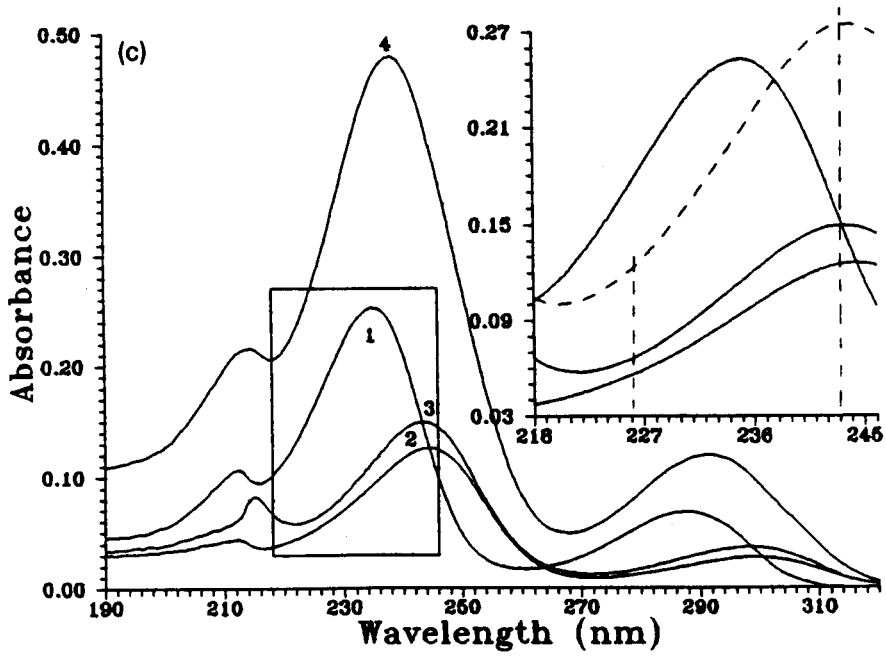

Fig. 5 (continued).

If we suppose the completely unknown nature of the species present in the synthetic samples (A, B and C), we will utilize the two previously described procedures to demonstrate the linear behaviour of the interferents, with the next results.

Study of the global linearity of the interferent

In the three selected examples, phenol has always been the analyte. Therefore, the spectral zone to study is the corresponding zone with its maximum $\lambda_M = 235$ nm. The A vs. C_{added} calibration lines at all wavelengths included in the selected wavelength interval ($\Delta\lambda = 220$–250 nm) were obtained for each replicate. Then pairs of wavelengths in both sides of the maximum of the analyte were selected in order to fulfil the Eqn. 3 of the theoretical background. Here this compound shows the same absorbance, and so, the same slope of the calibration plot. The statistical test used was the analysis of homogeneity of the variance with the Snedecor and Bartlett tests [20,21]. If positive, the analysis of parallelism with the Student and Snedecor tests [20,21]. The pairs of wavelength selected are similar among replicates, but not equals because of the random error. That is why the statistical treatment must be done for each replicate.

TABLE 2

Global linearity of the interferent in the wavelength interval $[\lambda_1, \lambda_2]$ in the three samples assayed (the linearity conditions is fulfilled when $t_{calc} > t_{tab}$)

Wavelength interval	Number of points	$a \pm s_a$	$b \pm s_b$	r	t_{calc}	t_{tab} ($P = 95\%$)
222–244	23	-1.74 ± 0.04	$(8.19 \pm 0.15) \cdot 10^{-3}$	0.99669	56.209	2.080 [a]
229–240	12	-3.11 ± 0.03	$(14.41 \pm 0.14) \cdot 10^{-3}$	0.99954	103.982	2.228 [b]
226–242	17	-2.39 ± 0.04	$(11.14 \pm 0.17) \cdot 10^{-3}$	0.99834	67.147	2.131 [c]

[a] Degrees of freedom (v) = 21. [b] $v = 10$. [c] $v = 15$.

When λ_1 and λ_2 pairs have been selected, from the absorbance values at λ_1, λ_m and λ_2, and following the procedure explained in the background, the calculated values for the analyte concentration in the different wavelength intervals assayed are shown in Table 3, where the statistically aberrant values were removed by use of the Dixon's Q or ts assay test [20] and marked with an asterisk. The greater number of removed values belongs to the shorter wavelength intervals, because of the little difference between the slopes of R_m and R'_m. This little difference produces a great error in the determination of the intersection point, as can be easily deduced from Eqn. 13. There is a great concordance among the calculated values and the real ones, in spite of the great value of the interferent absorbance in the analyte maximum (75% in sample A, 110% in

TABLE 3

Calculated values for the analyte concentration in the different wavelength intervals assayed for the samples A, B and C. The outlier results appear marked with an asterisk, and calculated values for the interferent concentration in the different wavelength intervals assayed for the samples A and B (for the added concentrations, see Table 1)

Replicate	Analyte conc. in different wavelength intervals, samples A, B and C										$C \pm$ R.S.D.
1	$\lambda_1\lambda_2$	225,243	228,241	229,240	232,238	233,237					
	$C_{found} \cdot 10^5$ (M)	2.80	2.79	2.71	2.74	2.43*					2.76 ± 0.04
2	λ_1, λ_2	226,242	229,240	230,239	231,238	232,238	233,236	233,237			
	$C_{found} \cdot 10^5$ (M)	2.77	2.79	2.70	3.02*	2.85	2.76	2.65			2.75 ± 0.07
3	λ_1, λ_2	224,243	226,242	227,241	229,240	230,239	231,238	232,237	233,236		
	$C_{found} \cdot 10^5$ (M)	2.62	2.60	2.62	2.64	2.59	2.46*	2.67	2.59		2.62 ± 0.03
4	λ_1, λ_2	226,242	229,240	231,238	232,238	233,236	233,237				
	$C_{found} \cdot 10^5$ (M)	2.69	2.68	2.52	2.76	3.00	2.91				2.76 ± 0.17
5	λ_1, λ_2	222,244	227,241	231,238	232,237	233,236					
	$C_{found} \cdot 10^5$ (M)	2.80	2.73	2.82	2.89	3.14*					2.81 ± 0.07
6	λ_1, λ_2	224,243	227,241	229,240	230,239	231,238	232,237	232,238	233,236	233,237	
	$C_{found} \cdot 10^5$ (M)	2.72	2.70	2.66	2.73	2.49	2.38*	2.51	2.94*	2.58	2.63 ± 0.10
1	λ_1, λ_2	224,243	226,242	229,240	230,239	232,238	233,237				
	$C_{found} \cdot 10^5$ (M)	2.75	2.84	2.86	2.80	3.04*	3.14*				2.81 ± 0.05
2	λ_1, λ_2	220,245	222,244	224,243	226,242	229,240	230,239	232,238	232,237	233.237	
	$C_{found} \cdot 10^5$ (M)	2.61	2.75	2.87	2.98*	2.99*	2.90	2.79	2.65	2.42	2.76 ± 0.12
3	λ_1, λ_2	226,242	229,240	231,239	232,238	233,237					
	$C_{found} \cdot 10^5$ (M)	2.86	2.79	2.73	2.54	2.42*					2.73 ± 0.14
4	$\lambda_1\lambda_1$	226,242	230,239	232,238	233,237						
	$C_{found} \cdot 10^5$ (M)	2.84	2.86	2.87	2.48*						2.86 ± 0.02
5	$\lambda_1\lambda_2$	221,245	224,243	229,240	230,239	231,238	232,237	233,237			
	$C_{found} \cdot 10^5$ (M)	2.75	2.81	3.08*	2.99	2.83	3.13*	3.49*			2.85 ± 0.10
6	λ_1, λ_2	223,244	225,243	228,241	230,240	231,239	232,238	233,237			
	$C_{found} \cdot 10^5$ (M)	2.66	2.67	2.59	2.64	2.68	2.57	2.68			2.64 ± 0.08
1	λ_1, λ_2	222,244	224,243	226,242	229,240	230,239	232,238	233,237			
	$C_{found} \cdot 10^5$ (M)	2.77	2.82	2.79	2.79	2.93	2.54*	2.20 *			2.82 ± 0.06
2	λ_1, λ_2	224,243	226,242	229,240	230,239	232,238	233,236	233,237			
	$C_{found} \cdot 10^5$ (M)	2.75	2.75	2.84	2.85	3.05*	2.68	3.12*			2.77 ± 0.07
3	λ_1, λ_2	226,242	229,240	230,239	231,238	232,238	233,236	233,237			
	$C_{found} \cdot 10^5$ (M)	2.78	2.77	2.73	3.02*	2.93	3.98*	3.48*			2.80 ± 0.09
4	λ_1, λ_2	221,245	223,244	229,240	231,239	232,238	233,237				
	$C_{found} \cdot 10^5$ (M)	2.81	2.81	2.86	2.82	2.80	2.65*				2.82 ± 0.02
5	λ_1, λ_2	226,242	229,240	232,238	233,237						
	$C_{found} \cdot 10^5$ (M)	2.81	2.60	2.81	2.75						2.74 ± 0.10
6	λ_1, λ_2	226,242	229,240	231,238	232,238	233,236	233,237				
	$C_{found} \cdot 10^5$ (M)	2.84	2.88	2.98	2.96	5.09*	2.82				2.90 ± 0.07

TABLE 3 (continued)

Replicate	Interferent conc. in different wavelength intervals, samples A and B								$C \pm$ R.S.D.
1	λ_1, λ_2	225.243	228,241	229,240	232,238				
	$C_{found} \cdot 10^5$ (M)	2.60	2.61	2.71	2.66				2.64 ± 0.05
2	λ_1, λ_2	226,242	229,240	230,239	232,238	233,236	233,237		
	$C_{found} \cdot 10^5$ (M)	2.62	2.61	2.72	2.53	2.64	2.77		2.65 ± 0.08
3	λ_1, λ_2	224,243	226,242	227,241	229,240	230,239	232,237	233,236	
	$C_{found} \cdot 10^5$ (M)	2.75	2.77	2.75	2.73	2.79	2.69	2.79	2.75 ± 0.03
4	λ_1, λ_2	226,242	229,240	231,238	232,238	233,236	233,237		
	$C_{found} \cdot 10^5$ (M)	2.59	2.63	2.83	2.54	2.23	2.36		2.53 ± 0.21
5	λ_1, λ_2	222,244	227,241	231,238	232,237				
	$C_{found} \cdot 10^5$ (M)	2.49	2.58	2.49	2.40				2.49 ± 0.07
6	λ_1, λ_2	224,243	227,241	229,240	230,239	231,238	232,238	233,237	
	$C_{found} \cdot 10^5$ (M)	2.65	2.68	2.73	2.64	2.94	2.90	2.82	2.77 ± 0.11
1	λ_1, λ_2	224,243	226,242	229,240	230,239				
	$C_{found} \cdot 10^5$ (M)	3.63	3.53	3.50	3.58				3.56 ± 0.06
2	λ_1, λ_2	220,245	222,244	224,243	230,239	232,238	232,237		
	$C_{found} \cdot 10^5$ (M)	3.69	3.52	3.38	3.35	3.43	3.65		3.50 ± 0.14
3	λ_1, λ_2	226,242	229,240	231,239	232,238				
	$C_{found} \cdot 10^5$ (M)	3.38	3.45	3.50	3.73				3.52 ± 0.15
4	λ_1, λ_2	226,242	230,239	232,238					
	$C_{found} \cdot 10^5$ (M)	3.21	3.21	3.22					3.21 ± 0.01
5	λ_1, λ_2	221,245	224,243	230,239	231,238				
	$C_{found} \cdot 10^5$ (M)	3.65	3.57	3.34	3.56				3.53 ± 0.13
6	λ_1, λ_2	223,244	225,243	228,241	230,240	231,239	232,238	233,237	
	$C_{found} \cdot 10^5$ (M)	3.63	3.60	3.72	3.66	3.60	3.75	3.60	3.65 ± 0.06

sample B and 80% in sample C, referred to the analyte absorbance at 235 nm).

As all the R'_m intersects with R_m at the same point (the H-point), the linearity of the interferent is confirmed.

Table 4 shows the concentration mean values obtained for the six replicates of the three mixtures. These values are consistent with the added analyte concentration. All of this is evidence for the agreement between the theoretical basis and experimental results obtained with the method.

In addition, mixtures A and B are binary, so, applying Eqn. 14 of the theoretical background, we can obtain the interferent concentration starting from the respective calibration lines and the A_H value (Table 4). The mean calculated results

TABLE 4

Final results obtained for the analyte and interferent in the three samples assayed

Sample	C_{added}	C_{found}	Error (%)	%R.S.D. ($n = 6$)
Analyte				
A	$2.73 \cdot 10^{-5}$ M	$(2.72 \pm 0.08) \cdot 10^{-5}$ M	−0.37	2.94
B	$2.73 \cdot 10^{-5}$ M	$(2.78 \pm 0.08) \cdot 10^{-5}$ M	1.83	2.88
C	$2.73 \cdot 10^{-5}$ M	$(2.81 \pm 0.05) \cdot 10^{-5}$ M	2.93	1.78
Interferent				
A	$2.50 \cdot 10^{-5}$ M	$(2.64 \pm 0.11) \cdot 10^{-5}$ M	5.60	4.17
B	$3.52 \cdot 10^{-5}$ M	$(3.50 \pm 0.15) \cdot 10^{-5}$ M	−0.57	4.29

are also shown in Table 5, where a great agreement is shown among the calculated values and the added ones.

Study of the first derivative value at the analyte absorption maximum

In order to apply this procedure, the wavelength pairs lying on both sides of the analyte maximum, with the same absorbance for the analyte checked as it has been mentioned before, are used. The difference between the ordinate of the straight lines at λ_1 and λ_2 will be $\Delta A_{1,2}$ and then, it is possible calculate the $(\Delta A/\Delta\lambda)_{\lambda_2-\lambda_1}$ values.

In Table 5 the estimated mean values for $(\Delta A/\Delta\lambda)_{\lambda_2-\lambda_1}$ in the three samples studied are shown and the value for $(dA/d\lambda)^{X+Y}_{\lambda_M}$ at the maximum of the analyte calculated from the first derivative spectra. We have estimated that the $(\Delta A/\Delta\lambda)_{\lambda_2-\lambda_1}$ values are statistically similar when those are included in the interval $(dA/d\lambda)^{X+Y}_{\lambda_M} \pm 3 \cdot s_{(dA/d\lambda)^{X+Y}_{\lambda_M}}$ [20], for $s_{(dA/d\lambda)^{X+Y}_{\lambda_M}} = 0.0005$ (experimental value). The intervals found by this procedure (Table 5) are enclosed in those found for standards of the interferent. Then, the proposed procedure is satisfactory. This is a quick and easy method to validate the global linearity of the interferent in the maximum region of the analyte.

Conclusions

Starting from the obtained results, we can conclude that, applying HPSAM, it is possible to calculate the analyte concentration in a com-

TABLE 5

Estimated mean values for the parameter $(\Delta A/\Delta\lambda)_{\lambda_2-\lambda_1}$ in the three samples assayed, the corresponding value for $(dA/d\lambda)^{X+Y}_{\lambda_M}$ and the wavelength interval where the interferent can be considered linear from those data

	Replicate					
	1	2	3	4	5	6
Sample A	*n*					
	3	6	5	6	4	7
$(\Delta A/\Delta\lambda) \pm s_{(\Delta A/\Delta\lambda)}$ mean value	0.0102 ± 0.0004	0.0104 ± 0.0008	0.0098 ± 0.0007	0.0106 ± 0.0009	0.0101 ± 0.0012	0.0095 ± 0.0005
$(dA/d\lambda)^{X+Y}_{235}$ $\pm 3 \cdot s_{(dA/d\lambda)^{X+Y}_{235}}$	0.0092–0.0122	0.0088–0.0118	0.0082–0.0112	0.0093–0.0123	0.0082–0.0112	0.0077–0.0107
Maximum linear wavelength interval	228,241	226,242	224,243	226,242	222,244	224,243
Sample B	*n*					
	2	3	3	2	2	2
$(\Delta A/\Delta\lambda) \pm s_{(\Delta A/\Delta\lambda)}$ mean value	0.0149 ± 0.0006	0.0156 ± 0.0009	0.0141 ± 0.0003	0.0136 ± 0.0005	0.0136 ± 0.0005	0.0132 ± 0.0001
$(dA/d\lambda)^{X+Y}_{235}$ $\pm 3 \cdot s_{(dA/d\lambda)^{X+Y}_{235}}$	0.0141–0.0171	0.0138–0.0168	0.0135–0.0165	0.0125–0.0155	0.0118–0.0148	0.0126–0.0156
Maximum linear wavelength interval	229,240	230,239	229,240	230,239	230,239	232,238
Sample C	*n*					
	2	3	4	3	3	5
$(\Delta A/\Delta\lambda) \pm s_{(\Delta A/\Delta\lambda)}$ mean value	0.0124 ± 0.0006	0.0116 ± 0.0010	0.0113 ± 0.0007	0.0125 ± 0.0004	0.0118 ± 0.0003	0.0118 ± 0.0009
$(dA/d\lambda)^{X+Y}_{235}$ $\pm 3 \cdot s_{(dA/d\lambda)^{X+Y}_{235}}$	0.0115–0.0145	0.0106–0.0136	0.0101–0.0131	0.0118–0.0148	0.0110–0.0140	0.0105–0.0135
Maximum linear wavelength interval	229,240	226,242	226,242	229,240	229,240	226,242

pletely unknown sample, free from bias error, from the abscissa of the H-point (analytical difficulty not resolved in the bibliography).

For the correct application of the method, it is necessary to select the spectral zone where the interferent matrix was linear. This behaviour can be checked with the two proposed methods in the present paper.

If the interferents are known, independently of their complexity, it is easy to locate the specific spectral zone in order to apply the HPSAM, and therefore, to determine the analyte concentration.

If the mixture is binary, it is possible too to calculate the interferent concentration starting from the ordinate of the H-point, with a calibration line of the interferent or the analytical signal of a stock solution, by applying the calibration method with a unique standard.

The authors are grateful to the DGICYT for financial support (Project No. PB91-0651). J.V.A. acknowledges a grant from the Conselleria de Cultura, Educació i Ciència of the Generalitat Valenciana for carrying out PhD studies.

REFERENCES

1 T.C. O'Haver and G.L. Green, Anal. Chem., 48 (1976) 312.
2 A.-A.M. Wahbi, M.A. Abounassif and H.M.G. Al-Kahtani, Analyst, 111 (1986) 777.
3 A.-A.M. Wahbi, H. Mahgoub and M. Barary, Analyst, 114 (1989) 505.
4 C.F. Hiskey, Anal. Chem., 33 (1961) 927.
5 H. Martens and T. Naes, Trends Anal. Chem., 3 (1984) 204.
6 T. Naes and H. Martens, Trends Anal. Chem., 3 (1984) 266.
7 M. Blanco, H. Iturriaga, S. Maspoch and P. Tarín, J. Chem. Educ., 66 (1989) 178.
8 M. Blanco, J. Gene, H. Iturriaga, S. Maspoch and J. Riba, Talanta, 12 (1987) 987.
9 F. Salinas, J.J. Berzas Nevado and A. Espinosa Mansilla, Talanta, 37 (1990) 347.
10 J.J. Berzas Nevado, J.M. Lemus Gallego and C. Castañeda Peñalvo, Fresenius' J. Anal. Chem., 342 (1992) 723.
11 J.J. Berzas Nevado, C. Guiberteau Cabanillas and F. Salinas, Talanta, 39 (1992) 547.
12 W.J. Youden, Anal. Chem., 19 (1947) 946.
13 F. Bosch Reig and P. Campíns Falcó, Analyst, 113 (1988) 1011.
13 F. Bosch Reig and P. Campíns Falcó, Analyst, 115 (1990) 111.
15 P. Campíns Falcó, F. Bosch Reig and A. Molina Benet, Fresenius' J. Anal. Chem., 338 (1990) 16.
16 P. Campíns Falcó, F. Bosch Reig and J. Verdú Andrés, Talanta, 39 (1992) 1.
17 P. Campíns Falcó, F. Bosch Reig and J. Verdú Andrés, Anal. Chim. Acta, 270 (1992) 253.
18 F. Bosch Reig, P. Campíns Falcó, A. Sevillano Cabeza, R. Herráez Hernández and C. Molíns Legua, Anal. Chem., 63 (1991) 2424.
19 P. Campíns Falcó, F. Bosch Reig, R. Herráez Hernández and A. Sevillano Cabeza, Anal. Chim. Acta, 257 (1992) 89.
20 Commissariat à l'Énergie Atomique, Statistique Apliquée à l'Exploitation des Mesures, Masson, Paris, 1978.
21 M.A. Sharaf, D.L. Illman and B.R. Kowalski, Chemometrics, Wiley-Interscience, New York, 1986.

Analytica Chimica Acta, 283 (1993) 845–853
Elsevier Science Publishers B.V., Amsterdam

Effects of resolution, peak ratio and sampling frequency in diode-array fluorescence detection in liquid chromatography

Russell B. Poe and Sarah C. Rutan

Department of Chemistry, Virginia Commonwealth University, Richmond, VA 23284–2006 (USA)

(Received 13th April 1993)

Abstract

In this work, different methods of quantification that use both fluorescence spectral and retention time data were evaluated for accuracy and precision in diode-array fluorescence detection in liquid chromatography. The methods evaluated include the peak height and peak area methods of quantification, an adaptive Kalman filter and the generalized rank annihilation method. All of these methods were used to estimate the concentration of a model led component in the presence of other partially resolved unmodelled components. The peak area and peak height methods of quantification gave the largest errors as the chromatographic resolution was decreased. The generalized rank annihilation method gave the most reliable results when the chromatographic resolution was greater than 0.3. However, this method was affected by retention time shifts between the calibration and unknown samples and the rate at which the spectra were acquired.

Keywords: Liquid chromatography; Accuracy; Chemometrics; Diode-array fluorescence detection

Over the past several years, recent advances in instrumentation have brought about changes in the way chromatography is performed and the way the resulting data are analyzed. With new detectors emerging, hyphenated methods such as GC–MS, GC–FTIR, LC–MS, LC–UV are becoming commonplace. However, with these new detectors comes an ever increasing amount of data. Traditional ways of analyzing data from these hyphenated methods do not fully utilize the additional information obtained from these instruments. Therefore, new data analysis methods must take into consideration the complexity and vast amount of data from these new methods.

There are several multivariate analysis methods that are suited for the analysis of chromatographic data from these hyphenated methods. Methods such as multiple linear regression [1], the adaptive Kalman filter [2], factor analysis [3] and generalized rank annihilation (GRAM) [4–6] are some of the available methods for quantification. Each of these methods has its own set of advantages and limitations.

This paper addresses different methods of quantification that can be used in conjunction with these hyphenated chromatographic approaches. Specifically, we have evaluated these methods in terms of their ability to accurately estimate sample concentrations when unmodelled, interfering components are present. The effects of chromatographic resolution and peak ratio between unmodelled and modelled components were systematically studied in order to determine the robustness of each quantitative

Correspondence to: S.C. Rutan, Department of Chemistry, Virginia Commonwealth University, Richmond, VA 23284–2006 (USA).

method mentioned above. These studies are based on data obtained from the separation of polycyclic aromatic hydrocarbons using reversed phased liquid chromatography coupled with fluorescence spectral detection using a diode-array detector.

EXPERIMENTAL

The experimental setup has been previously described in detail [7]. To summarize, the liquid chromatographic system consisted of Rainin liquid chromatography pumps fitted with 5–ml pump heads. The column was a 10-cm Spherisorb ODS-2 (Alltech) column containing 3-μm particles. The effluent entered a 8-μl flow cell, and a modified Farrand Mark I spectrofluorometer was used as the fluorescence detector. The photomultiplier tube was replaced with a Tracor Northern 1024 element intensified diode-array detector.

The stock solutions of benzo[*a*]pyrene and perylene were 100 μM solutions in acetonitrile. These stock solutions were used to make standards ranging in concentration from 50 μM to 0.781 μM dissolved in 1:1 mixtures of acetonitrile and water.

Chromatography was performed using isocratic conditions with a mobile phase of acetonitrile–water (80:20). The mobile phase flow-rate was 2 ml min^{-1} and the column was maintained at 35°C. The excitation wavelength was 300 nm and an emission spectrum from 350–550 nm was collected every second. The original spectra contained 1024 data points; however, the spectral data were reduced to 256 data points by taking every fourth point. For every sample analyzed, 90 spectra were taken across the elution profile. The data were further reduced by averaging two sequential spectra together.

The original data contained contributions due to the elution of benzo[*a*]pyrene or perylene and an emission background. Chromatographic resolution and peak ratio were varied by adding together perylene and benzo[*a*]pyrene data sets at different concentrations, where the perylene data set was shifted in time relative to the benzo[*a*]-pyrene peak position [8]. This technique provided a means of easily changing the resolution and peak ratio of the mixture. Another reason why this type of simulation was used is that experimental non-idealities such as non-zero or sloping baseline, the diode-array detector scan rate, and heteroscedasticity are included in the simulation thus resulting in a simulation that mimics actual experimental conditions [9,10].

Additional simulations were performed to evaluate the performance of two different GRAM algorithms that have been previously reported [4,5]. A model composed of 7 Gaussian peaks was fit to the chromatographic peak shape for a 25 μM benzo[*a*]pyrene sample using simplex optimization. The Gaussian peaks were used to replicate the tailing peak shape and allowed the retention time between the calibration and unknown data sets to be shifted. The Gaussian peaks model fit the experimental peak with a standard error of 0.3% of the maximum peak height. This peak shape was then used to create the concentration profiles for benzo[*a*]pyrene and perylene for the bilinear data matrices used in GRAM.

The spectral models were the background subtracted spectra of benzo[*a*]pyrene and perylene obtained under the same isocratic conditions. Retention time reproducibility was estimated by finding the standard deviation of the retention time for six replicate injections. The retention time for the target compound was shifted between the standard and unknown spectrochromatographic matrices, with a standard deviation as determined by the replicate injections. Heteroscadastic noise was added to each spectrochromatogram by fitting the standard deviation of the noise (s_{noise}) from previous isocratic experiments to the equation

$$s_{noise}(i, j) = ar(i, j)^b$$

where $r(i, j)$ is the detector response at time i and wavelength j and a and b are the fitting parameters. For the experimental conditions used here, a and b were determined to be 0.15 and 0.58, respectively. All simulations were performed using 386-Matlab (version 3.5L) with a MS-DOS 386 or 486 computer.

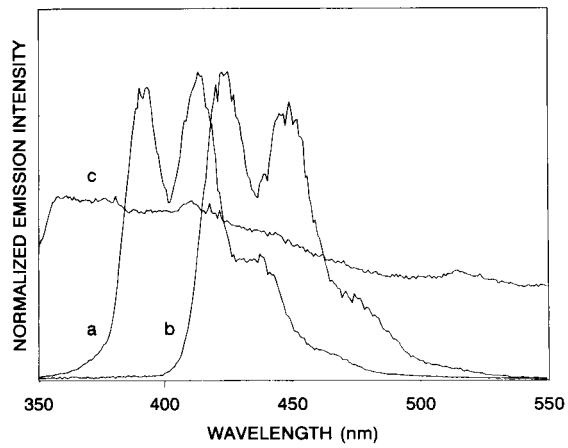

Fig. 1. Spectral models for multiple linear regression and the adaptive Kalman filter. Excitation wavelength 300 nm. (a) Benzo[*a*]pyrene, (b) perylene, and (c) background.

Multiple linear regression (MLR)

Multiple linear regression is a matrix technique that gives the least-squares estimates for the concentrations of all the components present in a mixture when all the mixture components are properly modelled [1]. In this work, this technique was used as a reference method, and all components present (benzo[*a*]pyrene, perylene, and the background contribution) were included in the model. The model for multiple linear regression can be expressed as

$$\mathbf{m} = \mathbf{Rc}$$

where **m** (256×1) is the sum of all the spectra in the spectrochromatographic matrix **M** (256×45) after data reduction, **R** (256×3) is a matrix that contains the spectral models for benzo[*a*]pyrene, perylene, and the emission background (Fig. 1), and **c** (3×1) contains the concentration estimates for each of the spectral components. The concentrations are estimated from

$$\mathbf{c} = (\mathbf{R}^T\mathbf{R})^{-1}\mathbf{R}^T\mathbf{m}$$

Note that for all the other methods described below, one of the components was assumed to be an interferant and was not accounted for in the quantification.

Peak height method

Each spectrochromatogram forms a matrix (**M**), where the rows of the matrix are chromatograms and the columns are spectra. A total chromatogram is obtained by summing the 256 elements comprising each spectrum; therefore, each point in the chromatogram is the summed fluorescence emission intensity of the spectrum at that time in the elution profile. The background is estimated from the signal preceding the peak and is subtracted from the peak height. The background subtracted peak height and retention time are calculated for a standard sample and compared to the peak height of the unknown chromatogram at the same retention time as the standard.

Peak area method

To estimate the component concentrations using the peak area, the chromatogram is generated using the same method described in the peak height section. The area of the standard chromatogram is calculated and compared to the area for the mixture peak. The perpendicular drop method of integration is used when a valley is present in the chromatogram due to the overlapped unmodelled component.

Generalized rank annihilation (GRAM)

GRAM is a matrix method that allows quantification of a modelled component when other unmodelled components are present in the sample being analyzed. Currently there are several algorithms for GRAM [4–6]. In this research, two GRAM algorithms were studied. The first method was described by Sanchez and Kowalski (SK) [4], and the other is a modification that was described by Wilson et al. (WSK) [5].

The calibration sample data matrix **N** must have a known contribution from the component or components to be quantified. The spectrochromatographic matrix to be analyzed, **M**, may contain unmodelled components not present in the calibration matrix. A summary of the SK algorithm is given below [4].

Step 1.

$$\mathbf{W} = \mathbf{M} + \mathbf{N}$$

Step 2. Perform singular value decomposition of **W**,

$$\mathbf{W} = \mathbf{USV}^T$$

where **U** and **V** are unitary matrices that contain the eigenvectors of **W**, and **S** is a square matrix that contains the square roots of the eigenvalues along the diagonal.

Step 3. Estimate the number of components present in **W** based on the eigenvalues obtained in Step 2. This can be accomplished by a number of methods such as the *F*-test [11], the IND function [12], and the residual standard deviation [13]. Once the number of components, n, has been estimated, the matrices **U**, **S**, and **V** are truncated to contain the first n columns. The new matrices are denoted by $\overline{\mathbf{U}}$, $\overline{\mathbf{S}}$, and $\overline{\mathbf{V}}$.

Step 4. The concentrations of the components can be estimated by obtaining the eigenvalues, λ, of the matrix $\overline{\mathbf{U}}^{\mathrm{T}}\mathbf{M}\overline{\mathbf{V}}\overline{\mathbf{S}}^{-1}$, where the concentration of the k^{th} component, c_k, is

$$c_k = \lambda_k/(1-\lambda_k)$$

The WSK algorithm is implemented as shown below [5].

Step 1. Create two concatenated matrices

$$(\mathbf{M}\,|\,\mathbf{N}) \quad \text{and} \quad \left(\frac{\mathbf{M}}{\mathbf{N}}\right)$$

Step 2. Determine a set of orthonormal vectors, that forms a basis set for the joint column and row spaces, using singular value decomposition (SVD) or partial least squares-type decomposition. The row vectors are denoted as **P** and the column vectors are denoted as **Q**.

Step 3. Estimate the number of components present in the concatenated matrices. Once the number of components, n, has been estimated, the matrices **P** and **Q** are truncated to contain the first n columns. The new matrices are denoted by $\overline{\mathbf{P}}$ and $\overline{\mathbf{Q}}$.

Step 4. Project **M** and **N** into square matrices using **P** and **Q** where

$$\mathbf{M}_{PQ} = \overline{\mathbf{P}}^{\mathrm{T}}\mathbf{M}\overline{\mathbf{Q}}$$

$$\mathbf{N}_{PQ} = \overline{\mathbf{P}}^{\mathrm{T}}\mathbf{N}\overline{\mathbf{Q}}$$

Step 5. Solve the generalized eigenvalue problem

$$\mathbf{M}_{PQ}\mathbf{Z} = (\mathbf{M}_{PQ} + \mathbf{N}_{PQ})\mathbf{Z}\boldsymbol{\Lambda}$$

where **Z** are the generalized eigenvectors and $\boldsymbol{\Lambda}$ is a diagonal matrix containing the generalized eigenvalues, λ_k. The concentration of the k^{th} component, c_k, is

$$c_k = \lambda_k/(1-\lambda_k)$$

Adaptive Kalman filter (AKF)

The adaptive Kalman filter is a recursive digital filter that can reliably fit data in cases where only a partial model of the chemical system is available [2,14–16]. The adaptive Kalman filter has an advantage over the regular Kalman filter and multiple linear regression in that the filter has the ability to predict the concentration of known components when unmodelled components are present. This is accomplished by fitting only the modelled portion of the data and not fitting the portion of the data where the unmodelled components contribute to the overall signal. Therefore, the limitation of the adaptive Kalman filter is that there must be a portion of the data where only the modelled components contribute to the overall signal within the limits of the experimental variance. When using a single pass algorithm, the filter must first fit the modelled section of the data before passing over the portion of the data with the unmodelled response [17]. The spectral models for the adaptive Kalman filter are shown in Fig. 1. These spectra are fit to the sum of all the spectra (**m**) in the spectrochromatographic matrix, so the results from this method do not depend on the chromatographic resolution.

RESULTS AND DISCUSSION

Effects of peak ratio and chromatographic resolution

In Figs. 2–5, we show the effects of chromatographic resolution and peak ratio on the accuracy of the SK GRAM algorithm [4], the adaptive Kalman filter, peak height, and peak area relative to multiple linear regression. These different methods, except for multiple linear regression, have the ability to predict the concentration of a modelled component even though an unmodelled component may be partially overlapped with the

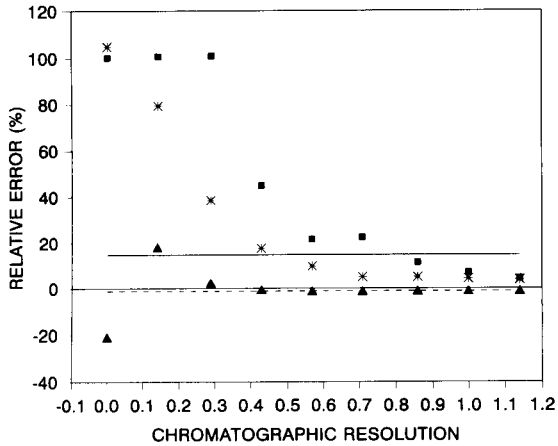

Fig. 2. Estimation error for perylene, present in a 1:1 peak ratio of perylene to benzo[*a*]pyrene (unmodelled component). (▲) SK GRAM algorithm [4], (———) adaptive Kalman filter, (*) peak height, (■) peak area, and (— — —) multiple linear regression.

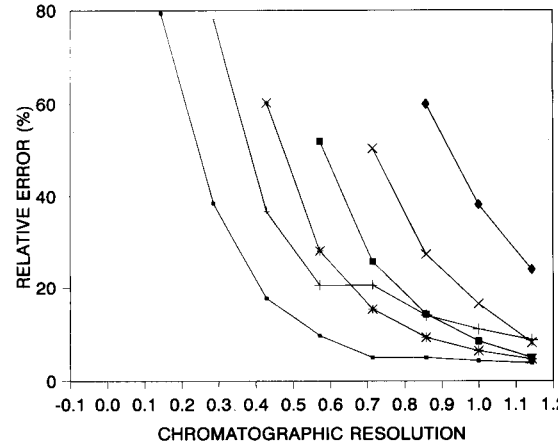

Fig. 4. The effects of chromatographic resolution and peak ratio on the accuracy of the results obtained using the peak height method. Lines connect the experimental points for clarity. (■) 1:1, (+) 1:2, (*) 1:4, (■) 1:8, (×) 1:16, and (◆) 1:32 peak ratio between perylene and the unmodelled component, benzo[*a*]pyrene.

target component. Multiple linear regression results are also shown for comparison, however, all components are included in the model to give the best results. The errors that will affect all the methods include dilution errors, injection errors, modelling errors and errors caused by lamp fluctuations.

Perylene and the background were the modelled components while benzo[*a*]pyrene was the unmodelled component. The peak ratio is the ratio of the overall summed emission intensity of the perylene compared to the overall summed emission intensity of the benzo[*a*]pyrene.

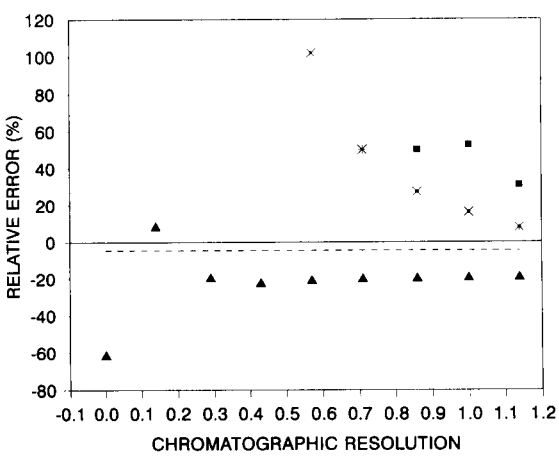

Fig. 3. Estimation error for perylene, present in a 1:16 peak ratio of perylene to benzo[*a*]pyrene (unmodelled component). (▲) SK GRAM algorithm [4], (*) peak height, (■) peak area, and (— — —) multiple linear regression.

Figures 2 and 3 give the errors for the different methods as a function of chromatographic resolution, for peak ratios of 1:1 and 1:16 perylene to benzo[*a*]pyrene, respectively. These figures illustrate that the peak area method is the quantification method most susceptible to errors when an unmodelled component is present. Also, as the resolution decreases or as the relative peak intensity of the known component decreases, there is an increase in the relative error. The method that is next most prone to errors is the peak height method. The most accurate method when overlapping unmodelled components are present is GRAM. The basic trends in the relative errors as a function of resolution and peak ratio are useful in evaluating the minimum resolution required for a particular method. In addition, the trends in Figs. 2 and 3 indicate that the peak height method, peak area method and the adaptive Kalman filter overestimate the actual concentration, and GRAM underestimates the concentration for chromatographic resolutions of 0.3 or greater.

In previous work, it was found that the different quantitative methods under investigation performed comparably with respect to accuracy and precision for well resolved mixtures [18]. However, when the chromatographic peaks begin to overlap, the accuracy of the different quantitative methods varies.

Figures 4 and 5 illustrate how both chromatographic resolution and peak ratio affect the accuracy of the results obtained using the peak height method (Fig. 4) and SK GRAM algorithm (Fig. 5). The peak height method is more susceptible to the presence of an overlapped, unmodelled component than GRAM. As the concentration of the modelled component, perylene, is decreased relative to the unmodelled component, benzo[*a*]pyrene, the relative error for the prediction of perylene dramatically increases. Also, as the resolution between perylene and the unmodelled component decreases, the relative error for the prediction of perylene dramatically increases.

GRAM is the most accurate method for predicting the perylene concentration when an unmodelled component is present. In addition, this method is less sensitive to peak ratio than the peak height or peak area methods. However, this method is affected by the chromatographic resolution between the unmodelled component and perylene. When the chromatographic resolution is less than 0.3, large relative errors resulted for all the peak ratios studied. However, these large errors in concentration were far less than those obtained using the peak height or peak area methods. For the 1:1 peak ratio, the relative error never exceeded 20%.

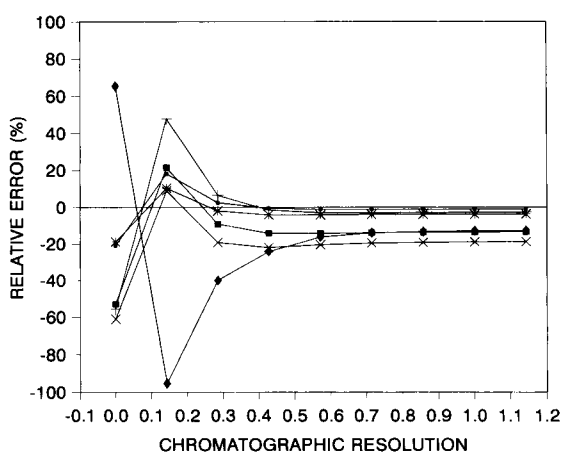

Fig. 5. The effects of chromatographic resolution and peak ratio on the accuracy of the results obtained using the SK GRAM algorithm [4]. Lines connect the experimental points for clarity. (■) 1:1, (+) 1:2, (*) 1:4, (■) 1:8, (×) 1:16, and (◆) 1:32 peak ratio between perylene and the unmodelled component, benzo[*a*]pyrene.

TABLE 1

Adaptive Kalman filter results

B[*a*]P [a]:Per [b] peak ratio	Relative error (%)	
	B[*a*]P	PER
1:1	2.0	19
1:2	4.8	10
1:4	1.1	5.6
1:8	4.5	3.4

[a] Benzo[*a*]pyrene. [b] Perylene.

The adaptive Kalman filter method used here is independent of chromatographic resolution, since the spectra comprising the chromatographic elution profile are summed before fitting the data. However, the requirement that the spectra of the modelled components are interference-free for at least some portion of the spectrum is not met in this case (see Fig. 1), resulting in a 15% error for the 1:1 peak ratio case shown in Fig. 2 and an error of 270% for the 1:16 peak ratio, which is out of the range of Fig. 3. These errors can be further clarified by examination of the results shown in Table 1, where two different situations are given. The first case is when benzo[*a*]pyrene and the background are the components that are modelled and the other is when perylene and the background are the two components included in the model. The relative error for the mixture with a 1:1 peak ratio of benzo[*a*]pyrene to perylene when perylene is the unmodelled component is 2.0%. The relative error for the 1:1 peak ratio of benzo[*a*]pyrene and perylene when benzo[*a*]pyrene is the unmodelled component is 19%. The difference is due to the fact that the benzo[*a*]pyrene spectrum has a spectral region where the intensities are significantly different from zero where the perylene spectrum shows no emission (see the region from 360–400 nm in Fig. 1). However, in the other case, pery-

lene is determined and benzo[*a*]pyrene is the unmodelled component. In this case, there is only a very limited region in the perylene spectrum where the benzo[*a*]pyrene emission intensity is zero. In addition, the relative intensity of the perylene signal in this spectral region is quite small (see the spectral region from 510–530 nm in Fig. 1). Thus the adaptive Kalman filter is less accurate for the prediction of perylene than for benzo[*a*]pyrene, since the condition that there must be a portion of the spectrum that is free of interference from unmodelled components is not met. When the benzo[*a*]pyrene signal is smaller than the perylene signal, the predictions for perylene increased in accuracy. However, no significant changes in the accuracy of predictions resulted when benzo[*a*]pyrene is the target component.

Effect of retention time variability

In previous studies, it was determined that GRAM has a tendency to underestimate the concentration [18]. This in part was due to slight variations in the retention time between the calibration standard and the sample mixture being analyzed. Here, the performance of the two GRAM algorithms were evaluated using realistic spectrochromatographic conditions [4,5]. One difference between these two GRAM algorithms is that SVD performed on a concatenated matrix constructed from the unknown and calibration data sets [5] while the other algorithm is based on the SVD of the sum of the unknown and calibration matrices [4]. The other major difference between the two algorithms is that the WSK algorithm is based on the generalized eigenvector and eigenvalue solution.

The results for 250 simulations for each set of experimental conditions are shown in Table 2. The calibration data set contained benzo[*a*]pyrene and a background component and the unknown data set contained benzo[*a*]pyrene and a different background component. These results indicate that the original SK GRAM algorithm is more accurate and precise when compared to the WSK GRAM algorithm, when chromatographic peak shifts affect the data. The simulation also shows that both algorithms underestimate the actual concentrations. The differences in the results are due to the WSK algorithm being more

TABLE 2

Effect of variability of retention time [a]

	Sanchez and Kowalski GRAM algorithm [4] (μM B[*a*]P)				
	Expt. 1 [b]	Expt. 2 [c]	Expt. 3 [d]	Expt. 4 [e]	Expt. 5 [f]
Mean	19.76	19.71	19.78	1.977	1.950
S.D.	0.29	0.36	0.94	0.029	0.062
Min.	18.33	17.93	16.33	1.839	1.660
Max.	20.02	20.02	21.05	2.008	2.005
	Wilson et al. GRAM algorithm [5] (μM B[*a*]P)				
	Expt. 1 [b]	Expt 2 [c]	Expt. 3 [d]	Expt. 4 [e]	Expt. 5 [f]
Mean	18.8	17.2	19.2	1.944	1.940
S.D.	1.8	4.1	1.5	0.070	0.073
Min.	8.4	0.0	11.2	1.607	1.596
Max.	20.0	20.0	20.5	2.007	2.005

[a] All results for 250 replicate simulations with a standard deviation of the retention time shifts of 0.7 s. [b] Experimental conditions: calibration standard concentration 50 μM, actual unknown concentration 20 μM, 1 spectrum per second before averaging. [c] Experimental conditions: calibration standard concentration 50 μM, actual unknown concentration 20 μM, 2 spectra per second before averaging. [d] Experimental conditions: calibration standard concentration 50 μM, actual unknown concentration 20 μM, 1/2 spectrum per second before averaging. [e] Experimental conditions: calibration standard concentration 5 μM, actual unknown concentration 2 μM, 1 spectrum per second before averaging. [f] Experimental conditions: calibration concentration 50 μM actual unknown concentration 2 μM, 1 spectrum per second before averaging.

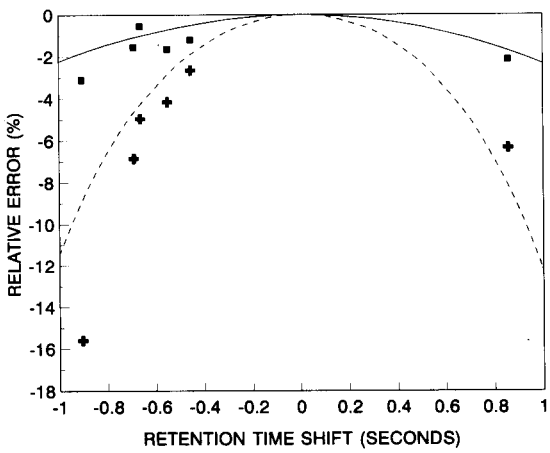

Fig. 6. The effect of retention time reproducibility on the SK GRAM algorithm [4] and the WSK GRAM algorithm [5]. The peak width used was 14 s and a sampling frequency of 1 spectrum per second before the averaging process described in the experimental section. (■) Experimentally determined SK GRAM results, (———) simulated SK GRAM results, (+) experimentally determined WSK GRAM results, and (— — —) simulated WSK GRAM results.

sensitive to retention time shifts between the calibration and unknown data sets and to the sampling frequency (number of spectra acquired per second). The sensitivity to retention time reproducibility can be seen in Fig. 6, where the relative error is plotted as a function of the peak shift between the standard and the unknown. The simulated and experimental results agree, which supports the validity of our simulation conditions. A 10% error for SK GRAM algorithm occurs for a 2-s peak shift, and the same error occurs for a 0.9-s peak shift for the WSK GRAM algorithm. The reason that the latter algorithm is more sensitive to retention time shifts is due to the use of the concatenated matrices. This method incorporates the retention time shift into the eigenvectors; this can be seen visually by examining the eigenvectors obtained from the two different methods. When the eigenvectors from the SK method were used in the WSK method, both algorithms provided the same results.

Table 2 indicates that when the sampling frequency was increased to 2 Hz, the accuracy and precision were degraded relative to the 1-Hz sampling rate. This was probably due the increased number of points better describing the peak shape, but also better describing peak shifts to which the WSK method is particularly sensitive. However, when the sampling frequency was changed to 0.5 Hz, the SK algorithm gave poorer accuracy and precision, while the WSK algorithm gave improved accuracy and precision, compared to 1-Hz sampling rate. The decrease in precision caused by the lower sampling rates was because there were not enough spectra to describe the elution of B[*a*]P, especially in the case of the SK algorithm. Although the SK GRAM still outperformed the WSK GRAM, the difference was not as great in this case. Therefore, there must be an optimal sampling frequency which allows the peak to be adequately described without enhancing peak shift errors. Table 2 also indicates that the best calibration model was the one most similar in concentration to the unknown.

In an attempt to compensate for chromatographic peak shifts observed experimentally between the unknown and calibration data sets, we examined the possibility of using the retention time of an internal standard added to both samples to determine the peak shift between the unknown and calibration data set. To test this idea, 20 μM benzo[*a*]anthracene was used as an internal standard and perylene was used as the compound to be quantified using the same isocratic conditions described in the experimental section. The retention time shifts of benzo[*a*]anthracene and perylene were correlated. However, when the unknown data set was shifted using a 3-point parabolic interpolation, to match the retention times of benzo[*a*]anthracene for the two samples, no improvement in accuracy was observed. However, when the retention time of perylene was used to adjust the peak position, there was a slight improvement in the accuracy of both GRAM algorithms, but this approach is not feasible if overlapped interferents are present. These results indicate that errors caused by retention time shifts cannot be corrected by using an internal standard, at least for the relatively small retention time shifts (0.7 s) found for these data.

Conclusions

In this study, we focused on determining the accuracy of quantification methods used for liquid chromatography coupled with fluorescence diode-array detection when unmodelled components overlap with the component of interest. The trends show that quantification using peak area was the method that was most sensitive to the degree of chromatographic overlap and the peak ratio between the target compound and the unmodelled component. The next method most prone to errors caused by unmodelled components was the peak height method. The most accurate quantification method was GRAM. However, when chromatographic resolution between the unmodelled component fell below 0.3, significant errors also affected the results from the GRAM algorithm. These errors suggest that an alternative method should be used when the resolution is very low. In these situations, the adaptive Kalman filter may be advantageous to use if the spectral resolution requirements of the filter are met.

This work was supported by the U.S. Department of Energy. The authors would like to acknowledge P.J. Gemperline and K. Booksh for helpful suggestions during the course of this work.

REFERENCES

1 K.R. Beebe and B.R. Kowalski, Anal. Chem., 59 (1987) 1007A.
2 S.C. Rutan, Anal. Chem., 63 (1991) 1103A.
3 E.R. Malinowski, Factor Analysis in Chemistry, Wiley, New York, 2nd edn., 1991.
4 E. Sanchez and B.R. Kowalski, Anal. Chem., 58 (1986) 496.
5 B.E. Wilson, E. Sanchez and B.R. Kowalski, J. Chemometr., 3 (1989) 493.
6 S. Li, J.C. Hamilton and P.J. Gemperline, Anal. Chem., 64 (1992) 599.
7 T.L. Cecil and S.C. Rutan, J. Chromatogr., 556 (1991) 495.
8 M.J.P. Gerritsen, N.M. Faber, M. van Rijn, B.G.M. Vandeginste and G. Kateman, Chemom. Intell. Lab. Syst., 12 (1992) 257.
9 H.R. Keller and D.L. Massart, Anal. Chim. Acta, 263 (1992) 21.
10 H.R. Keller, D.L. Massart, Y.Z. Liang and O.M. Kvalheim, Anal. Chim. Acta, 263 (1992) 29.
11 E.R. Malinowski, J. Chemometr., 3 (1988) 49.
12 E.R. Malinowski, Anal. Chem., 49 (1977) 612.
13 E.R. Malinowski, Anal. Chem., 49 (1977) 606.
14 S.C. Rutan and S.D. Brown, Anal. Chim. Acta., 160 (1984) 99.
15 S.C. Rutan and S.D. Brown, Anal. Chim. Acta., 167 (1985) 39.
16 H.R. Wilk and S.D. Brown, Anal. Chim. Acta., 225 (1989) 37.
17 Y. Hayashi and S.C. Rutan, Anal. Chim. Acta., 271 (1993) 91.
18 T.L. Cecil, R.B. Poe and S.C. Rutan, Anal. Chim. Acta., 250 (1991) 37.

Analytica Chimica Acta, 283 (1993) 855–867
Elsevier Science Publishers B.V., Amsterdam

Analytical study of salt migration and efflorescence in a mediaeval cathedral

L. Backbier and J. Rousseau

DSM Research, P.O. Box 18, 6160 MD Geleen (Netherlands)

J.C.J. Bart

Dipartimento di Chimica Industriale, Università di Messina, 98010 Sant'Agata di Messina (Italy)

(Received 21st October 1992; revised manuscript received 5th July 1993)

Abstract

Ion chromatography was used to examine stone damp and the concentration profiles of leachable salts (mainly nitrates, sulphates and chlorides) in the limestone building blocks of the interior of a mediaeval basilica in The Netherlands before and after desalination with the aid of the paper pulp poulticing technique. Autochthonous sulphates contained in the marl and periodical variations in humidity are held to be primarily responsible for the observed weathering effects. After the marl substrate had been cleaned the inner walls run a much smaller risk of damage due to moisture in the future with more confidence as to conservation.

Keywords: Chromatography; Salt migration; Mediaeval cathedral

The originally Romanesque Saint Servatius cathedral of Maastricht, which is one of the oldest in the southern Netherlands, has undergone several changes since its erection (between 1000 and 1039). Gothic and baroque elements were incorporated first and subsequently the interior of the basilica was decorated in the neo-classical style. Around 1860 both the inside and the outside of the building were given a neo-Gothic appearance in two restoration campaigns. Restoration was badly needed again between 1983 and 1990. At this time it was apparent that humidity constitutes a serious threat to the cathedral built of locally mined friable limestone. Although at first condensation was thought to be the sole cause of the damage suffered by the inner walls and frescoes [1], the effects of percolation and upward migration of water through the stone often appeared to be more serious. In many places the plaster covering the building blocks was found to be humid or even saturated with water. Much of the damage suffered by the frescoes on the plaster could originate from migration of nitrates (from bird droppings under the roof) and salts from the sedimentary stone. Thorough repair work done to the roof did not solve the problem of moisture in the cathedral; in particular, the stone walls of the chapels on the south-western side of the building were in a very poor state of preservation. Evidently, large patches of the walls were affected by humidity flow from the soil and subsequent crystallization of salts at the surface of the walls. In many places the plaster adhered poorly to the marl substrate or was even totally detached; the neo-Gothic pictural coatings were covered with salt encrustations and large areas

Correspondence to: J.C.J. Bart, Dipartimento di Chimica Industriale, Università di Messina, 98010 Sant'Agata di Messina (Italy).

were affected by efflorescence (bloom). It was decided to investigate the chemical and physical structure of the marl building blocks and of the blooming so as to be able to contribute to the determination of the most effective restoration measures.

EXPERIMENTAL

Sampling procedures

In cooperation with the restorer, samples were taken from the inner walls of the cathedral, in particular on the rain exposed south-western side of the building where the Baptistry, the Pietà Chapel and the chapels of St. Joseph and Mary Magdalene and of St. Barbara are situated and of St. Anthony's at the north-eastern side. The samples were obtained from several wall stretches (the overall church wall thickness is about 1 m with a 30-cm central cushion of debris), just above ground level up to about 5 m (above the limits of the rising humidity zone), and differed in the degree of decay, blackening, softness, exfoliation, humidity, etc. Apart from samples taken at the surface all samples were taken by mechanical splitting. In most instances, it proved very easy to remove mechanically the layers of plaster from the limestone substrate, indicating little adhesion. In total, 23 samples (some measuring up to 25 × 25 × 35 cm) were sawn from badly affected inside walls of the cathedral constructed without the use of mortar joints. The blocks were then sliced parallel to the surface of the wall into 1-cm thick layers, which were ground in an agate mortar. Of the homogenized powder thus obtained 100-mg portions were leached in 250-ml portions of demineralized water at 90°C for 2 h with constant stirring (a fresh portion of water did not lead to further ion extraction). The acqueous suspensions obtained were filtered through Millipore membrane filters (pore size 0.2 μm) and the filtrates were analysed, where necessary after further dilution, using ion chromatography.

Apparatus

Mercury porosimetry measurements were performed with a Micromeritics Autopore 9200 porosimeter after drying of the samples at 120°C for 48 h. Particle size analysis was carried out with a Micromeritics Sedigraph 5000 ET apparatus. The helium density was determined with a Micromeritics Autopycnometer 1320. Water-vapour adsorption isotherms for the humidity range 0–95% were determined gravimetrically at 20°C with the use of a Sartorius vacuum microbalance. The water-accessible surface area of the samples was determined from the isotherms using the linear BET two-parameter equation. X-ray powder diffraction patterns were obtained with a Philips PW 1050 diffractometer using Cu Kα radiation.

In view of its high selectivity and wide measuring range and the possibility of the (almost) simultaneous analysis of several components in one sample, ion exclusion chromatography was considered to be a suitable method for rapidly determining the leachable salt contents of the samples. This method has been used before in research on weathered historic buildings [2–7]. Use was made of a Dionex Model 4000i ion chromatograph fitted with automatic injection and data elaboration systems. Under the conditions of the experiment [anion separation column, Bio-Gel TSK IC-anion PW column (Bio-Rad); eluent, hydrogencarbonate buffer solution; conductivity detector], chloride, nitrate, sulphate and phosphate ions could easily be separated within a retention time of $t_R = 8$ min (the detection limit in water is ca. 20 μg l^{-1}). The anion contents were determined by comparison with standards of known composition.

RESULTS AND DISCUSSION

Building material

Maastricht stone (tufeau de Maestricht, locally called marl) is a ferruginous limestone obtained from alluvial deposits formed in a shallow sea (Upper Cretaceous and Lower Tertiary era). The limestone used for the cathedral was quarried in South Limburg, apparently at Kanne or at the St. Petersberg quarries near Maastricht, at an elevation of ca. 50 m, for the inner walls, and at Zichen for the outer walls (enhanced frost resis-

tance) [8,9]. For restoration purposes marl from the Sibbe area (ca. 10 km east of Maastricht) is now being used. The tannish coloured marine sedimentary rock of South Limburg is a soft, high-quality, high-calcium limestone, comparable to Indiana high-calcium stone [10]. The fairly homogeneous Maastricht stone consists of about 98% $CaCO_3$ intermixed with about 2% of other constituents: 1.3% $MgCO_3$, 0.2–0.4% Fe_2O_3, 0.3–0.4% SiO_2 (sand, quartz and silex), < 0.1% Al_2O_3, < 0.2–0.3% SO_4^{2-}, < 0.1% PO_4^{3-}. Typical salt concentrations are 30–50 mg l^{-1} chloride, 20–60 mg l^{-1} nitrate and 120–750 mg l^{-1} sulphate in fresh (unweathered) Sibbe stone. Occasionally, however, high salt concentrations (Cl^- 250, NO_3^- 4400, SO_4^{2-} 2500 mg l^{-1}) were visibly present as strata.

Table 1 gives some physical properties of the soft stone, which indicate its highly porous structure favouring the migration of soluble salts. Table 2 gives the intrusion volumes of four typical samples as a function of the pore size. The mercury porosimetry results can be divided into two pore size ranges, namely 150–0.1 μm (intergranular external porosity) and 0.1 μm–1.5 nm (internal porosity). The skeletal density, calculated from the bulk density (1.23–1.33 g cm^{-3} for powder samples, 1.70–1.79 g cm^{-3} for blocks) and the total intrusion volume of mercury penetrated at a pressure of 60 000 p.s.i., according to

$$V(\mathrm{p}) = \frac{1}{d(\mathrm{bulk})} - \frac{1}{d(\mathrm{skeleton})}$$

approaches the true density of matter. The results correspond closely to the helium density, which can be interpreted as indicating that the material does not contain any pores with radii < 1.8 nm. For the marl blocks and plaster the calculated skeletal density (2.73–3.10 g cm^{-3}) exceeds the helium density (2.61–2.70 g cm^{-3}), possibly owing to cracking of pores. The measured internal pore volume is 0.5–0.6 cm^3 g^{-1} for pores in the range 0.1 μm–1.5 nm. The porosity of the limestone (internal porosity 6.6–8.7%) is mainly due to the presence of macropores, i.e. pores of diameter > 0.05 μm. Powder samples of Maastricht stone are mainly composed of angular particles in the range 100–200 μm (medium-grained limestone [10]) with an external porosity of about 46%. In marl blocks and plaster the measured external porosity is about 30%. The low density and high hygroscopicity of Maastricht stone indicate a low flow resistance to water. Indeed, samples are saturated with water in a very short time (t < 5 min). The total open-pore volume of the limestone that can be filled through capillary action is about twice (or more) that of brick, tufa, mortar or sandstone [11]. The porosity of the stone is an important property with respect to salt penetration, freeze–thaw cycles and crystallization pressures. The diffusion resistance number (μ) of marl is 7.7(9) (as compared with values of 10, 25, 35 and > 10^6 for natural stone, brick, dense gravel concrete and water vapour-proof granite or basalt, respectively).

Kozłowski et al. [12] have shown that coarse-grained texture, high crystallinity and lack of quartz give good weathering resistance to lime-

TABLE 1

Properties of Maastricht limestone [a]

Air porosity	45–60%
Maximum water content, ψ_{max} (wt.%)	27.4 (n.d.) [e]
Capillary water content, ψ_{cap} (wt.%)	23.1 (2)
ψ_{cap}/ψ_{max} [b]	0.84
Water-absorption coefficient, S (kg m^{-2} $s^{-1/2}$)	5.24 (n.d.)
Water-penetration coefficient, $T \times 10$ (m $s^{-1/2}$)	125 (n.d.)
Diffusion equivalent air layer thickness, S_d (m) [c]	0.17 (2)
Drying index, Δ [d]	0.11–0.13
Transition point water content (wt.%)	1.6–2.2
Salt content (fresh marl), $[SO_4^{2-}]$, $[NO_3^-]$, $[Cl^-]$ (mg kg^{-1})	120–750, 20–60, 30–50
Compression resistance (kg cm^{-2})	29–58

[a] See ref. 11 for test methods. [b] Corresponds to the proportion of the total open-pore volume that can be filled through capillary action. [c] Measures resistance to transport of water vapour through diffusion (μ). [d] $[\int_{0h}^{240h}\psi(t)\mathrm{d}t]/\psi_0 \times 240$ or the ratio of the area under the curve of the moisture content against drying time from $t = 0$ to $t = 240$ h and the area under the line $y = \psi_0$ measured between $t = 0$ and $t = 240$ h. [e] Values in parentheses are standard deviations, n.d. = not determined.

stone. Quartz possibly leads to lack of cohesion between the components of the stone. For fine-grained varieties the degree of recrystallization of the matrix correlates with weathering resistance. In crystallization tests [13] marl has been found to disintegrate after 6–8 cycles. Gypsum formation deep within the stone fabric is the dominant deterioration factor [12]. Sedimentation rocks with high soluble salt contents are generally considered inferior building materials. Marl is easily workable owing to its friability. This property would make it less desirable as a building material, yet Maastricht stone is sufficiently weather resistant owing to the spontaneous formation of a "calcin" layer, a thin, superficial hard layer composed of recrystallized calcite. This protective solid crust is permeable to water and gases. In fact, a study of the external weathering of the O.L.V. Basilica in Tongeren [5] indicates either that such an outer layer does not form a protection for the inner stone as far as air pollution is concerned or can be taken as "breathing" of the stone. In the interior of the St. Servatius basilica the protective layer of "free" wall sections is very thin in comparison with that of the external walls.

Deterioration of limestone fabric

Several corrosion effects were observed in the interior of the church, such as salt crusts formed on the limestone, exfoliation, efflorescence, structural decay (powdering, blistering) and loss of adhesion between marl and plasterwork (scaling). The frescoes on the (rather porous) plaster were also damaged. The damage rate is dependent on a variety of very local micro-climatic and environmental conditions ranging from chemical reactivity with sulphur dioxide to susceptibility to physical damage by ice or salt crystallization. This in turn is again dependent on textural features (particle size distribution, surface area, nature of cation/anion distribution, nature of intergranular cement, ratio of micro/macropores). In the present case the principle cause of physical damage seems to be migration of water through the walls. Long-lasting humidity in the stone in the cathedral's interior is considerably more harmful than rain at the exterior, which rapidly washes out potential harmful agents [5]. Migration of water is obviously mainly affected by variations in the relative humidity and to a lesser extent by the temperature of the surroundings. Soluble salts

TABLE 2

Intrusion volumes of Maastricht stone as a function of pore size [$r(p)$ = pore radius; $\bar{r}(p)$ = average pore radius]

Sample	$r(p)$ (μm)	V(intrusion) ($cm^3\ g^{-1}$)	$\bar{r}(p)$
Fresh Sibbe stone (powder)	(1) 150–4.86	0.30	
	4.86–0.1	0.08	
		0.38 (total)	2.27 μm
	(2) 0.1–0.0018	0.06	3.90 nm
Aged Maastricht stone (powder)	(1) 150–1.1	0.26	
	1.1–0.1	0.08	
		0.34 (total)	1.20 μm
	(2) 0.1–0.0018	0.05	4.15 nm
Maastricht stone (block)	(1) 150–2.21	0.12	
	2.21–0.1	0.06	
		0.18 (total)	0.94 μm
	(2) 0.1–0.0018	0.05	5.14 nm
Plaster	(1) 150–0.539	0.12	
	0.539–0.1	0.05	
		0.17 (total)	0.60 μm
	(2) 0.1–0.0018	0.05	4.44 nm

originally present in the marl or subsequently absorbed into it become mobile when water vapour (from any source) penetrates the pores and dissolves the salts [14]. Movement of salt-bearing moisture to the surface of the stone does not require an exceptionally high degree of humidity (50–60% is probably sufficient [14,15], a value which is usually exceeded in the local wet climate). A combination of a decrease in the amount of water vapour and a change in temperature causes salt-bearing moisture to move towards the surface of the wall; dissolved salts are then deposited at or close to the surface [14–17]. According to Everett [18] crystal growth of salts in smaller pores starts only after the larger pores are filled. The deposited minerals were found to consist mainly of sulphates, in particular gypsum. Gypsum crystals are very fragile (Moh's scale 2); size and habit are influenced by the environment (nature and concentration of cationic and anionic impurities, pH, hydrodynamic conditions, etc. [19,20]) and are difficult to predict, especially in the inherently unsteady-state conditions of a wall, i.e. with time-varying conditions.

The water-soluble salts causing discolorations due to crystallization at the surface (efflorescence) consisted mainly of nitrates and sulphates originating either from the marl itself or from other sources (chemical weathering). It is well known than when such salts crystallize as hydrates within or behind the stone blocks, they literally shatter them [14]. In fact, the pressures exerted by hydrate crystals formed in the pores cause microcracks in the stone, which lead to powdering and flaking, particularly in areas already affected by long-term exposure to water [14]. In areas where the wall was coated with plaster, crystals (again mainly sulphates) had been formed between the stone wall and the plaster coating due to differences in the capillarity of the

TABLE 3

Depth profiling (concentrations in mg kg^{-1})

St. Anthony's chapel (m = 0.25 m)			
Sampling depth (cm)	Cl^-	NO_3^-	SO_4^{2-}
0– 1	n.d.	7200	12000
1– 2	39	191	110
2– 3	30	101	108
3– 4	22	36	127
4– 5	15	7	81
5– 7	19	22	64

St. Anthony's chapel (m = 1.7 m)			
Sampling depth (cm)	Cl^-	NO_3^-	SO_4^{2-}
0– 1	n.d.	4000	12000
1– 2	40	94	128
2– 3	20	33	99
3– 4	10	22	146
4– 5	15	21	226
5– 6	10	16	181
6– 7	25	12	181
9–11	< 5	8	105
11–13	< 5	8	113
> 13	< 5	4	121

Mary Magdalene and St. Barbara chapel (m = 0.25 m)			
Sampling depth (cm)	Cl^-	NO_3^-	SO_4^{2-}
0– 1	600	2400	2100
1– 2	90	270	140
2– 3	50	190	180
3– 4	40	110	70
4– 5	35	60	80
5– 6	40	40	60
6– 7	40	30	100
7– 9	30	20	90
9–11	25	10	60
11–14	20	30	80

Mary Magdalene and St. Barbara chapel (m = 1.6 m)			
Sampling depth (cm)	Cl^-	NO_3^-	SO_4^{2-}
0– 1	n.d.	8000	1600
1– 2	590	3000	240
2– 3	610	3000	190
3– 4	560	2800	200
4– 5	560	2800	190
5– 7	560	2600	140
7– 8	530	2400	140
8–10	540	2300	140
10–12	550	2200	120
12–14	520	2000	120

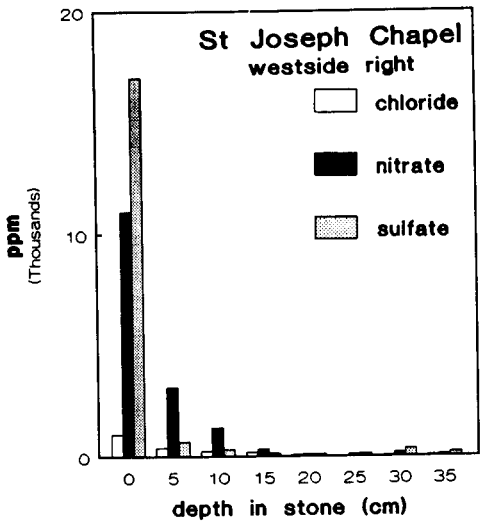

Fig. 1. Quantitative depth profile of salt concentrations in mg kg^{-1} (ppm) in inner wall (perpendicular to surface) of St. Joseph chapel (westside right). Analyses refer to a 1-cm thick slice.

two fabrics. These crystals had affected the adhesion of the plaster to the marl substrate. The damage suffered by the frescoes (efflorescence) is also attributable to the presence of soluble salts.

Depth profiles. Table 3 and Fig. 1 show a selection of the results of the analyses of the samples taken in the variously exposed chapels. As the results vary considerably, even when samples were collected only a short distance apart, no standard deviation (S.D.) values are given; trends are more important than exact figures. It is emphasized that S.D. values in ion chromatographic analysis itself are much smaller than the natural spread of ion concentrations in the wall; sample size is here an asset in this respect. All of the data (referring to 23 sampling points) obtained show salt concentration profiles reaching extremely high values at the 1 cm top layer of the wall (up to 5.7% sulphate) and decreasing to values of the autochthonous stone at variable depth. For a correct evaluation of the results it is of interest to consider observations in similar projects. However, these all relate to outdoor situations. At variance with our results it is of interest to note the absence of any variable CaO and SO_3 (electron microprobe) depth profiles (perpendicular to the surface) in the limestone outer wall of St. Stephan's Cathedral in Vienna, which was protected by a hard weathering crust [21]. This was interpreted as absence of diffusion. Without a weathering crust $CaSO_4$ is found inside the stone (ascribed to migration of SO_3 containing H_2O) [21]. At the external wall surface of the O.L.V. Basilica in Tongeren, where a thin outer coherent layer of gypsum is present (the mean values of SO_4^{2-}, NO_3^- and Cl^- in a <1 mm surface layer are 12.1, 0.21 and 0.031% respectively), nearly unaltered stone material is found at a depth of about 100 μm [5]. Results collected inside the various St. Servatius chapels point to different situations. Salt migrations towards the surfaces are considerable, ranging from 6 to 11 g SO_4^{2-} kg^{-1} and from 2.2 to 1.2 g NO_3^- kg^{-1} in the Mary Magdalene and St. Joseph chapels, respectively; chloride surface concentra-

TABLE 4

Solubility in water

Compound	Solubility (g per 100 ml)	Temperature (°C)	Compound	Solubility (g per 100 ml)	Temperature (°C)
$CaCO_3$	0.016	25	$BaCO_3$	0.002	20
$CaCl_2$	75	20	$BaCl_2$	38	26
$CaCl_2 \cdot 2H_2O$	98	0	$Ba(OH)_2$	6	15
$CaCl_2 \cdot 6H_2O$	279	0	$Ba(NO_3)_2$	9	20
$Ca(OH)_2$	0.2	0	$BaSO_4$	0.0002	25
$Ca(NO_3)_2$	121	18	$(NH_4)_2CO_3 \cdot H_2O$	100	15
$Ca(NO_3)_2 \cdot 4H_2O$	266	0	$(NH_4)_2CO_3$	12	0
$CaSO_4$	0.63	25	NH_4Cl	30	0
$Ca(SO_4)_2 \cdot 2H_2O$	0.24	20	NH_4NO_3	118	0
$Ca(SO_4)_2 \cdot 0.5H_2O$	0.71	25	$(NH_4)_2SO_4$	71	0

tions were of the order of 2500 mg kg^{-1}. Salt enrichment (as compared with the bulk) in the 1-cm thick top layers varies considerably from sampling point to sampling point but present very high values for NO_3^- (100–500 ×), high values for SO_4^{2-} (10–125 ×) and moderate values for Cl^- (25 ×). This order cannot be explained only on the basis of solubility in water (Table 4), but is also site and height dependent [22]. In the St. Joseph's chapel (on the south-western side of the cathedral), whose inside walls were badly worn and ornamental frescoes were seriously damaged, "normal" salt concentration values are reached gradually only at considerable depth inside the wall (at about 16 cm for Cl^-, 30 cm for NO_3^- and 10 cm for SO_4^{2-}). In the soft stone of the Mary Magdalene and St. Barbara chapel normal sulphate levels are attained immediately under the 1 cm top layer, but nitrate and chloride levels stay very high (100 ×) on the sampling site at 1.6 m; at ground level the stone is very fragile. In a different position in this chapel, at 0.4 m from the ground level the extracted tannish coloured stone contained a hard white stratum (Cl^- 250, NO_3^- 4400, SO_4^{2-} 2500 mg kg^{-1}). To a large extent the depth profile in this position (Fig. 2) reflects the presence of such strata of high salt concentration. In the St. Anthony's chapel with good-quality stone average levels are also reached quickly behind the top level; no significant effect of sampling height is observed in this chapel. The results point to locally very different salt diffusion schemes, probably connected to the coverage of the wall with more or less impenetrable layers or (vertical) water migration.

Nature and effects of salt migration. The results of the analyses reflect the local nature of the effects of the salt migration: samples obtained from the same wall, at a relatively short distance from one another, were found to vary considerably. In some instances more salts were found in the marl than in the plaster. (It could be argued that some of the gypsum found in the marl could have originated from the layer of plaster. However, gypsum depth profiles were also encountered in samples taken from wall sections that were not plastered.) In all of the samples the absolute amount of chlorides was much smaller

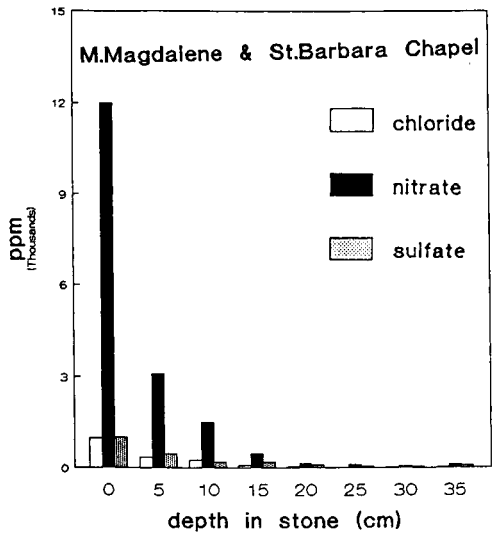

Fig. 2. Quantitative depth profile of salt concentrations in mg kg^{-1} (ppm) in inner wall (perpendicular to surface) of Mary Magdalene and St. Barbara chapel ($h = 0.4$ m). Analyses refer to a 1-cm thick slice.

than the amount of sulphates and nitrates. In comparison with other studies on similar objects [4,23,24], the high nitrate concentrations are striking. In accordance with findings elsewhere [22,23], the soluble salt content was found to vary with the sampling height. A good example is the St. Joseph's chapel with its groundwater problems, where one observes a more pronounced decrease with height in $[SO_4^{2-}]$ (14560, 2050, 610 and 760 mg l^{-1} at 1, 2, 3 and 5 m from ground level, respectively; concentrations in the top 3 mm averaged over three different positions, determined by ion chromatographic analysis) than in $[NO_3^-]$ (3000, 3000, 1090 and 710 mg kg^{-1}, respectively). On the whole the chloride problem (330 mg kg^{-1} at 1 m height) is the least relevant, partly owing to the absence of salt layers at small depths in the Limburg area. The nitrate levels at 5 m exceed significantly the values for fresh Maastricht stone (salt strata or damp); the less soluble sulphates approach normal values. The results clearly point to migration of salts through the highly porous limestone in correspondence with drainage water (vertical profile) and day/night and seasonal vari-

ations in humidity (horizontal profile); the salts are deposited at the surface on (partial) evaporation of the solvent.

Salts involved in weathering of building stones are the same as those found in natural occurrences of evaporites [22]. The effect of the migration of water through porous fabrics is well known: a portion of the binding constituents of sedimentary stone, mortar and plaster is hereby dissolved. In this process, the pores at the surface are filled, thus forming an upper layer of a corrosion structure. Salts deposited as the solvent evaporates (mainly gypsum) cause efflorescence and whisker growth on the surface of the wall and damage the friable wall texture [14,22]. Scaling is a further development of surface encrustations: a scale is separated as a result of crystallization at the surface following up evaporation and hydration pressure.

Chlorides are very hygroscopic; water condensing from the atmosphere will first dissolve chloride salts. In fact, chlorides are hardly ever found in efflorescences; their weathering activity is related to damage to the alveolar cell structure of porous stone [25]. As to nitrates, allowance should be made for the possible effect of nitrifying bacteria, which may be present in building materials in high concentrations and to great depths [26]. These may transform nitrogen and traffic exhaust nitrogen oxides into nitric acid. The observed, greatly different, nitrate concentration levels at various wall sections call for a different source. High nitrate build-up in wall stretches connected to water migration paths from the roof could result from bird droppings or NO_3^--rich strata. As nitrates and chlorides are highly hygroscopic and soluble they are transported highest up and damp (hygroscopic humidity) is based on these salts [22]. The composition of efflorescences varies according to the prevailing relative humidity. Sulphates (in particular gypsum and bassanite, $CaSO_4 \cdot 0.5H_2O$) are considered to be the most active corrosive weathering agents affecting building materials. Badly weathered stone invariably contains large amounts of gypsum in its pores. As a consequence, gypsum content must be identified as the main factor in deterioration.

Role of water. Apart from acting as a transport vehicle for salts, water also acts physically. Crystallization of hydrates is accompanied by the build-up of pressure [cf. volume expansions on the basis of reduced unit cell dimensions (Å^3): $CaSO_4$ 88.60 and $CaSO_4 \cdot 2H_2O$ 123.93; $CaCl_2$ 83.86 and $CaCl_2 \cdot 6H_2O$ 212.46; $Ca(NO_3)_2$ 109.74 and $Ca(NO_3)_2 \cdot 4H_2O$ 206.12]. Expansion stresses, often up to hundreds of atmospheres, can cause damage if the resistance of the porous stone of the wall is exceeded. Very low pressures are found when coarser pores prevail and high pressures in the case of fine pores (e.g., in bricks with small pore size, cf. ref. 27 as a classical example; extensive damage to marble surface due to embedded gypsum [3]). Solutions containing more than 0.1% sulphate are assumed to constitute a risk for porous fabrics [28]. This situation was found to be present in the walls of the St. Joseph's chapel (4-cm thick endangered layer). The damage caused by the very high concentrations of sulphates and the smaller amounts of chlorides, which lead to the formation of $CaSO_4 \cdot 2H_2O$ and $CaCl_2 \cdot 6H_2O$, respectively, is assumed to exceed the damage caused by $Ca(NO_3)_2$.

Chemical and biological damage. Where damage arising from physical phenomena is ascertained, effects of chemical origin could play an additional role. In limestone and sandstone buildings, both of which are very susceptible to disintegration, various external chemical sources of damage are conceivable, such as gaseous sulphur dioxide, the slight acidity of 'clean' rain (pH 5.6) and acid rain [29]. A polluted atmosphere is an important source of soluble salts [2,30]. Comparison with other reported situations and careful consideration of the role of sulphur may give a clue for the importance of chemical effects in the present case. Air pollution-induced chemical decay has been observed at the exterior of a sandy limestone cathedral in Belgium [31]. However, it appears that the concentration of pollutants is much lower in the interior than outside [32]. Further, a direct correlation has been established between the pore volume of the stone (high in case of Maastricht stone) and the amount of SO_2 absorbed [26]. As to the possible role of SO_2, Riederer [33] claimed that catalytic conversion of SO_2 into SO_3 only takes place at 400–600°C. In a

study of in situ weathered calcitic sandstone from St. Stephan's Cathedral (Vienna), Weber et al. [2] emphasized the role of sulphurous gases and traces or iron. Cheng et al. [3] suggested the catalytic action of fly ash and its effect on the formation of gypsum. In the case of marble (a hard, relatively non-porous stone), the rate of $CaSO_4$ formation depends on the surface area of the carbonaceous particles present and not on the SO_2 concentration [34]. No sulphates are formed on dry walls without carbon deposits. Wet $CaCO_3$ surfaces absorb gaseous SO_2 but the deposition rates diminish as surfaces become saturated with gypsum. Gaseous SO_2 usually leads to the formation of a hard surface layer (consisting mainly of sulphates), which eventualy flakes off owing to insufficient adhesion to the substrate [4–6]. Being much more soluble in water than calcite, gypsum does not accumulate on very wet stone surfaces. Key factors explaining the difference in the chemical weathering of buildings in Venice and Milan are the relative humidity and soot (from oil residues) adsorbed on the stone. However, on the whole, the specific roles of HNO_3, organic acids and atmospheric particles, such as soot in creating SO_4^{2-} crusts, with respect to atmospheric damage are still major unknowns. As Maastricht, like near-by Tongeren [35], both in a rural environment with some industry, does not suffer greatly from atmospheric pollution, SO_2-induced sulphate formation is not considered to be the main cause of the ageing phenomena observed in the interior of the church {As shown by Mohenjo-daro, in a rural Sind (Pakistan) area, disintegration processes due to salt migration are highly destructive and efficient also in the absence of SO_2 contamination [27]}.

If we therefore exclude the effect of sulphuric acid aerosols on the inside walls of the cathedral [2], in addition to the (still heavily debated [3,4,36]) effects of other aggressive solutions containing sulphuric acid (acid rain) and the cleansing action of run-off water, we must accept that the observed efflorescence and ion concentration profiles are mainly due to the migration of salts contained in the sedimentary building material itself. Indeed, the profiles obtained for the three ions investigated, i.e., SO_4^{2-}, NO_3^- and Cl^-, are similar (Fig. 1, St. Joseph), which suggests a common source, namely migration of water and breathing through the intonaco. Water filling the pore system remains even on dry days and its partial evaporation from the near-surface region results in an increase in $[SO_4^{2-}]$ deeper in the mass. At relative humidities exceeding 60%, typical of most days in The Netherlands, condensation of water takes place, so that the stone stays continuously saturated with water.

Some wall sections of St. Joseph's chapel were black, indicating organic material. Organisms living at the surface of a stone build a barrier against water vapour diffusion between the stone and the atmosphere. By action of the products of acid metabolism, such organisms may attack the mineral substance. Growth of organisms and crystal formation may lead to removal of the top layer [37], as indeed is observed.

Conservation

In some places where samples were taken (e.g., in the St. Joseph's chapel), a dry, brownish black tarry layer was observed between the plaster and the marl. This layer, which was found to consist of rosin, was probably applied during Cuyper's restoration campaign; it suggests that the wall stretches in question were already affected by moisture in the 19th century. The St. Joseph's chapel showed the overall greatest humidity problems (something different from just preferential condensation). Shielding of the wall (which was apparently breathing anyway or was made to breath through the build-up of crystallization pressure) was not the correct remedy here as groundwater problems turned out to be most severe.

Before the damaged pictorial layers could be restored, the substrate had to be effectively preserved. As already discussed above (and elsewhere [23,38,39]), one of the main causes of exfoliation of the pictorial layer and poor adhesion of the plaster is the presence of water-soluble salts in the walls. The measures to be taken in restoring and preserving ancient buildings depend on whether the damage is caused by the infiltration of moisture, capillary action or condensation. Rising damp contains both soluble ions and CO_2

from microorganisms, which favour the dissolution of minerals.

A first requirement in the restoration of the Maastricht cathedral was drainage of all stagnant or percolating water. As the work was carried out in a very dry season, marl blocks of the bottom sections of the walls that remained humid in the dry atmosphere were replaced by fresh blocks after a damp-proof course had been installed beneath the wall to prevent an upsurge of moisture from the groundwater, which would otherwise soon have led to the rapid accumulation of new salts at the surface of the walls. Similar precautions have been taken elsewhere [27]. As pointed out by Arnold and Zehnder [22], such insulation measures initially lead to increased damage due to crystallization phenomena at decreased wall humidity, but subsequently to an improvement. However, the continuous presence of salts in the wall does not cure the presence of damp zones.

Salt migration can be effectively prevented by creating a stable, dry environment (relative humidity $\leqslant 40\%$; even at relatively low relative humidities of 50–60% movement of salts to the surface of the stone occurs). Obviously, however, it is difficult to achieve and maintain such a microclimate in a Dutch cathedral (the mean relative humidity in Maastricht is about 75%).

Desalination. Other ways of preventing the problems described above are immobilization of the salts and (partial) desalination. Immobilizing salts by reducing the porosity and transforming $CaCO_3$ into the less soluble $BaSO_4$ presents considerable drawbacks, such as visible damage [40]. Desalination of the walls through extraction seemed a more suitable option. This is usually effected by either (repeated) soaking or poulticing [15]. The effectiveness of the process depends on the distribution of the salts throughout the stone and the depth to which the moisture has penetrated the stone, which, in turn, depends on the porosity of the stone. Desalination was expected to lead to good and quick results in the case of porous marl, as suggested by the data in Tables 1 and 2. In the past, poulticing has been reported to lead to a decrease in the salt content of the first 5 cm of stone [15]. Thorough desalination of the stone is very important as it not only removes the salts disrupting the stone structure but also reduces considerably condensation phenomena and moisture content and therefore the presence of damp zones.

Problematic wall sections of the aforementioned chapels at the south-western side of the church (up to 3 m in height) with high concentrations of gypsum and other salts were treated according to the paper pulp method [24,40], which consists in applying directly to the wall a 1-cm thick poultice of cellulose pulp (KNP Botnia pine K 11075) previously impregnated with ammonium carbonate solution (80 g l^{-1}) in demineralized

TABLE 5

Salt concentrations (mg kg^{-1}) in St. Joseph's chapel (western side) before and after poulticing

Sample [b]		Concentration [a]							
		1 m		1.5 m		2 m		2.5 m	
		−	+	−	+	−	+	−	+
$[SO_4^{2-}]$	0–1 cm	2300	680	770	190	440	360	170	220
	3–5 cm	330	160	280	80	270	140	270	150
$[NO_3^-]$	0–1 cm	3100	400	6400	40	7500	80	5900	10
	3–5 cm	80	20	3500	270	5500	60	6000	110
$[Cl^-]$	0–1 cm	330	70	560	100	810	60	770	80
	3–5 cm	260	60	450	40	680	60	790	70

[a] Depth profile (ion chromatographic analysis). [b] Samples before (−) and after (+) desalination were extracted from closely separated wall sections at various heights from ground level.

water. This results in the following reactions:

$$Ca(NO_3)_2 \downarrow + (NH_4)_2CO_3 \longrightarrow CaCO_3 \downarrow + 2NH_4NO_3 \quad (1)$$

$$CaSO_4 \downarrow + (NH_4)_2CO_3 \longrightarrow CaCO_3 \downarrow + (NH_4)_2SO_4 \quad (2)$$

The highly porous stone of the cathedral was easily wetted and the nitrates and sulphates present in the wall were rapidly dissolved; the dissolution process was further favoured by differences in the solubility of the components of Eqns. 1 and 2 (cf., Table 4), which resulted in the formation of calcium carbonate and the conversion of gypsum into ammonium sulphate. Any other salts present were simultaneously extracted. After about 2 h a barium hydroxide solution [50 g l^{-1} of $Ba(OH)_2 \cdot 8H_2O$] was sprayed on to the poultice in order to bring about the following reactions:

$$Ba(OH)_2 + 2NH_4NO_3 \longrightarrow Ba(NO_3)_2 \downarrow + 2NH_3 \uparrow + 2H_2O \quad (3)$$

$$Ba(OH)_2 + (NH_4)_2SO_4 \longrightarrow BaSO_4 \downarrow + 2NH_3 \uparrow + 2H_2O \quad (4)$$

During the contact time the chemical equilibria were shifted towards the formation of insoluble barium salts and the evaporation of ammonia and the solvent. When the cellulose mat had dried (after 48 h) it was removed from the wall. Table 5 shows the analytical results obtained before and after poulticing at closely spaced positions. Before treatment the sulphate levels decrease with height from ground level, in particular in the 1-cm thick top layer; at 3–5 cm depth inside the wall differences in $[SO_4^{2-}]$ with height are less pronounced. In contrast, at the same sampling points $[NO_3^-]$ increases with height, especially in the subsurface layers (3–5 cm; greater depths were not examined). We attribute this phenomenon to damp. The same trend, although less pronounced, was found for chlorides. After desalination $[SO_4^{2-}]$ settles at values from 700 to 100 mg kg^{-1} (with decreases of 4 to 2 times). In most instances the nitrate levels decrease to values of 20–100 mg kg^{-1}, almost independently of the starting values (100–7500 mg kg^{-1}), improving by 5–100 times. Chloride levels decrease to 40–80 mg kg^{-1} from concentrations of 100–900 mg kg^{-1} before desalination. In almost all instances salt concentrations of "fresh" marl were attained, indicating that the desalination process was effective to a sufficient depth. One poultice treatment is apparently sufficient for porous marl. Leysen et al. [4] consider a 0.03 wt.% sulphate content to be acceptable for cleaned stone. Similar results were observed at other sampling points in the very humid St. Joseph's chapel.

Very high nitrate and sulphate concentrations (11 000 and 57 000 mg kg^{-1}, respectively) in the Mary Magdalene and St. Barbara chapel (1.5 m height, top 3 mm) decreased to 320 and 570 mg kg^{-1} after desalination. In this and in the Pietà chapel soluble ammonium salts at 5 cm depth amounted to < 5 mg kg^{-1}, indicating the absence of NH_4NO_3 and $(NH_4)_2SO_4$ in the wall. On average (22 samples) $[NO_3^-]$ and $[SO_4^{2-}]$ decreased by 20 and 30 times, respectively, as a result of desalination according to Eqns. 1–4.

Durability. It is difficult to guarantee the long-term effects of the actions undertaken, as water will remain a constant source of trouble. However, in addition to the actions described above, a few more precautions were taken to control the moisture level in the church whenever possible. The presence of sulphate in natural marl makes it extremely important to minimize the amount of water used in construction work involving this particular kind of building material. The use of water-repellent agents was not considered because they are known to lose their effectiveness at a penetration depth of more than 10 mm when used for marl building material [11]. Water-repellent treatments are particularly necessary for fine-grained limestones, as they will considerably lower the damage rate [12] (the aim of the aforementioned rosin layer applied in the last century was to repel water).

As already indicated by Keuller et al. [8] and explained by Arnold and Zehnder [14,22], the use of modern alkali-containing materials, such as Portland cement, containing 0.5–2.5% soluble alkali ions and a maximum of 1–3% SO_4^{2-} [41,42], instead of slaked lime as a binder for mortar,

water glass, alkaline tightening and cleaning materials, should be avoided in restoration and conservation. The alkali metal carbonates interact with the original alkaline earth metal salts of the old stone, leading to less soluble alkaline earth metal carbonates with increased blooming. Consequently, the repair work was carried out using mortars with the lowest possible salt contents (Andernach tufa: 120 mg kg^{-1} Cl^-, <20 mg kg^{-1} NO_3^-, 0.5% SO_4^{2-}).

Finally, in order to mitigate the risk of damage due to cyclic variations in temperature and related changes in relative humidity, it was advised to make moderate use of the (newly installed) heating facilities in the cathedral [43] and to control condensation through sufficient ventilation. Obviously, microclimatization at relative humidity ca. 55% would be the optimum treatment, but was not considered to be economically feasible in the present instance.

Conclusions

Analytical methods were used to evaluate the deterioration phenomena observed in the cathedral of Maastricht. The damage was found to be largely attributable to the moisture-induced migration and subsequent crystallization of autochthonous salts, particularly sulphates. On the basis of the analytical results the most effective measures were chosen for preserving and restoring the cathedral.

Thanks are due to the restorer, Mr. E.J. Tjebbes, for his expert cooperation and for suggesting the subject to us. The authors are indebted to Dr. M.J. Luys for porosimetric measurements and to KNP for kindly supplying cellulose.

REFERENCES

1 C.J.M. v.d. Veken, Sint-Servaaskerk te Maastricht, Studierapport, Maastricht, 1975.
2 J. Weber, A. Vendl, H. Paschinger and H. Richard, Wiener Ber. Naturwiss. Kunst, 2/3 (1985–86) 239.
3 R.J. Cheng, J.R. Hwu, J.T. Kim and S.-M. Leu, Anal. Chem., 59 (1987) 104A.
4 L. Leysen, E. Roekens, Z. Komy and R. v. Grieken, Anal. Chim. Acta, 195 (1987) 247.
5 E. Roekens, L. Leysen, E. Stulens, J. Philippaerts, R. v. Grieken and G. de Geyter, in J. Ciabach (Ed.) Proceedings of the VIth International Congress on the Determination and Conservation of Stone, Torún, Nicolas Copernicus University Press Department, Torún 1988, pp. 45–55.
6 L.A. Leysen, E.J. Roekens, R.E. v. Grieken and G. de Geyter, Sci. Total Environ., 90 (1990) 117.
7 C. Saiz-Jimenez, J. Garcia-Rowe, M.A. Garcia del Cura, J.J. Ortega-Calvo, E. Roekens and R. v. Grieken, Sci. Total Environ., 94 (1990) 209.
8 L. Keuller, E. Lahaye and W. Sprenger, Publ. Soc. Hist. Archéol. Limbourg, 46 (1910) 307.
9 J. Diederen, Grondboor Hamer, 43 (1989) 173.
10 R.S. Boynton, Chemistry and Technology of Lime and Limestone, Wiley, New York, 1980.
11 Characterization of Types of Stone. Comparative Assessment of Water-Repelling and Stone-Reinforcing Agents, NATO CCMS Pilot Study on the Conservation and Restoration of Monuments, Rijksdienst voor de Monumentenzorg, Zeist, 1985.
12 R. Kozłowski, J. Magiera, J. Weber and J. Haber, Stud. Conserv., 35 (1990) 205.
13 Crystallization Test with Sodium Sulphate, DIN 52111, German Standards Institute, Berlin, 1976.
14 A. Arnold, Schweiz. Miner. Petrogr. Mitt., 61 (1981) 147.
15 S.M. Bradley and S.B. Hanna, in N.S. Brommelle and P. Smith (Eds.), Case Studies on the Conservation of Stone and Wall Paintings, International Institute for the Conservation of Historic and Artistic Works, London, 1986, pp. 57–61.
16 K.L. Gauri, Sci. Am., 238, No. 6 (1978) 104.
17 C.A. Price, Chem. Br. 11 (1975) 350.
18 D.H. Everett, Trans. Faraday Soc., 57 (1961) 1541.
19 S. Sarig and J.W. Mullin, J. Chem. Technol. Biotechnol., 32 (1982) 525.
20 J. Budz, A.G. Jones and J.W. Mullin, J. Chem. Technol. Biotechnol., 36 (1986) 153.
21 Ch. Koeberl and H.H. Weinke, Wiener Ber. Naturwiss. Kunst, 2/3 (1985–86) 200.
22 A. Arnold and K. Zehnder, Eclogae Geol. Helv., 77 (1984) 287.
23 M. Dupas and E. de Witte, M&L (Monumenten en Landschappen), 7, No. 2 (1988) 49.
24 J. Twilley and J.C. Podany, in N.S. Brommelle and P. Smith (Eds.) Case Studies on the Conservation of Stone and Wall Paintings, International Institute for the Conservation of Historic and Artistic Works, London, 1986, pp. 174–179.
25 J.P. Pauly, in 2éme Colloque International sur la Detérioration des Pierres en Œuvre, Athens, 1976, pp. 79–91.
26 H. Vieser, Bild Wiss., No. 12 (1986–87) 42.
27 M. Jansen, in Civilisations Anciennes du Pakistan, Musées Royaux d' Art et d'Histoire, Brussels, 1989, pp. 224–236.

28 B. Butterworth, in Transactions of the VIIth International Ceramic Congress, London, 1960, pp. 275–285.
29 F. Lipfert, Atmos. Environ., 23 (1989) 415.
30 R.J. Schäfer, J. R. Soc. Arts, C111 (1954–55) 843.
31 L. Leysen, E. Roekens and R.E. v. Grieken, Sci. Total Environ., 78 (1989) 263.
32 V. Furlan and F. Girardet, Materials Science and Restoration, Techn. Akad., Esslingen, 1983, pp. 285–290.
33 J. Riederer, Staub-Reinhalt. Luft, 33 (1973) 15.
34 M. Del Monte and O. Vittori, Natuur Tech., 54 (1986) 764.
35 L.A. Leysen, E.J. Roekens and R.E. v. Grieken, Eur. Cult. Heritage Newsl. Res., (1990) 15.
36 F. Pearce, New Sci., Sept. 26 (1985) 26.
37 A. Mentler, H.W. Müller and B. Schwaighofer, Wiener Ber. Naturwiss. Kunst, 2/3 (1985–86) 212.
38 H. Weber, in E. Wippler (Ed.), Fassadenschutz und Bausanierung, Expert Verlag, Grafenau, 1983, pp. 306–321.
39 J. Pühringer, Werkstoffenwissenschaften und Bausanierung, Internationale Kolloquium, Techn. Akad. Esslingen, 1983, pp. 361–366.
40 P. Mora, L. Mora and P. Phillipot, Conservation of Wall Paintings, Butterworths, London, 1984, p. 229.
41 P. Barnes (Ed.). Structure and Performance of Cements, Applied Science, London, 1983.
42 B. Marchese, Tecnologia dei Materiali e Chimica Applicata, Liquori, Naples, 1978.
43 A. Arnold, K. Zehnder, A. Küng and O. Emmenegger, Z. Kunsttech. Konserv., 2 (1991) 171.

Analytica Chimica Acta, 283 (1993) 869–880
Elsevier Science Publishers B.V., Amsterdam

Prediction of gas chromatographic retention index data by neural networks [1]

A. Bruchmann and P. Zinn

Ruhr-Universität Bochum, Universitätsstr. 150, D-44780 Bochum (Germany)

Chr. M. Haffer

Hahn-Meitner-Institut Berlin GmbH, Glienickerstr. 100, D-14109 Berlin (Germany)

(Received 26th November 1992; revised manuscript received 23rd March 1993)

Abstract

Neural networks using the backpropagation algorithm can be applied to quantitative structure–physical property relationship studies. Neural networks can be trained with electrotopological indexes of monofunctional compounds to predict the corresponding retention index data. These networks can also be applied to the prediction of retention index data of acyclic and cyclic monoterpenes and a mixed set of monosubstituted and terpene compounds. Predictions by neural networks are generally in good agreement with predictions done by multilinear regression techniques. In the case of predicting retention index data of compounds from a class not represented in the training data, neural networks show strong deficiencies in comparison with multilinear regression methods.

Keywords: Gas chromatography; Back propagation; Multilinear regression; Neural networks; Retention index

Quantitative structure–property relationship (QSPR) research often involves a two-stage procedure. In a first step molecular descriptors are found that represent structural features of the molecule. In a second step these descriptors are correlated with molecular properties to find a quantitative relationship between the structure and its property. A representation of structural features is often done by using topological, geometric, electrotopological or quantum-chemical descriptors [1]. Special software systems to derive such descriptors have been discussed in the past. For example Stuper et al. [2] describe the ADAPT system that incorporates both steps of QSPR research. Gautzsch and Zinn [3,4] have introduced a system for the construction of molecular descriptors based on list processing done in LISP. The statistical analysis for the correlation between descriptors and molecular properties is then done with commercial statistical software. Among these methods, multilinear regression is the predominant technique [5–10]. Other statistical correlation methods involve partial least squares [11], principle component analysis [12] and target factor analysis [13].

Finding a suitable model when applying these statistical methods is often a problem [14]. A possibility to overcome this problem is the use of a neural network. Instead of developing a model as proposed by the classical QSPR approach, neural networks are trained with a representative data set containing the structural descriptors and the corresponding molecular properties in a coded

Correspondence to: P. Zinn, Ruhr-Universität Bochum, Universitätsstr. 150, D-44780 Bochum (Germany).

[1] Dedicated to Prof. Dr. Gerhard Bergmann on the occasion of his 70th birthday.

form. Anker and Jurs [15] describe this technique for the prediction of ^{13}C nuclear magnetic resonance (NMR) shifts. Reviews of the application of neural networks in chemistry have been published in the past years [16,17]. Although a manifold of neural network types have emerged in the last years, the most widespread type of neural network is the backpropagation type network. Besides for the prediction of ^{13}C NMR shifts, backpropagation networks are used in many different chemical applications. Among these are the prediction of secondary and tertiary protein structures [18], process fault diagnosis [19], interpretation of measurement results obtained by ion-sensitive electrodes [20], peak recognition in systems of overlapping infrared (IR) bands [21], interpretation of IR spectra [22] and calibration of UV–Vis spectra [23].

The aim of our work was the prediction of gas chromatographic retention index data with the help of neural networks. Experiences with such predictions using multilinear regression methods have been discussed in [24,25]. The data sets used therein served as training data for the neural networks in this paper. The results obtained hereby can therefore be compared to those achieved by multilinear regression techniques. Generalization, a key feature of neural networks mentioned by Janson [16], will be investigated. This is of interest, especially when examining cases of extrapolative prediction of retention index data. The training set consisted of retention index data for monofunctional compounds (Table 1). After training, the networks were used to predict retention index data given for a collection of acyclic and cyclic monoterpenes (Table 2).

METHODOLOGY

The scope of this paper will cover the prediction of retention index values by backpropagation networks of different topologies submitted to different training procedures. The backpropagation algorithm, used for training these prediction net-

TABLE 1

Compounds used for training neural networks and corresponding experimental retention index data I

Compound	I (Lit.) [27]
2,2-Dimethylpropane	412.3
2-Methylbutane	475.3
2,2-Dimethylbutane	536.8
2,3-Dimethylbutane	567.3
2-Methylpentane	569.7
3-Methylpentane	584.2
2,2-Dimethylpentane	625.6
2,4-Dimethylpentane	629.8
2,2,3-Trimethylbutane	639.7
3,3-Dimethylpentane	658.9
2-Methylhexane	666.6
2,3-Dimethylpentane	671.7
3-Ethylpentane	686.0
2,2,4-Trimethylpentane	689.9
2,2-Dimethylhexane	719.4
2,5-Dimethylhexane	728.4
2,4-Dimethylhexane	731.9
2,2,3-Trimethylpentane	737.1
3,3-Dimethylhexane	743.5
2,3,4-Trimethylpentane	752.4
2,3,3-Trimethylpentane	759.4
2-Methylheptane	764.9
4-Methylheptane	767.2
3,4-Dimethylhexane	770.6
3-Methylheptane	772.3
2,2,4,4-Tetramethylpentane	772.7
3-Methyl-3-ethylpentane	774.0
2,2,5-Trimethylhexane	776.3
2,2,4-Trimethylhexane	789.1
2,4,4-Trimethylhexane	807.7
2,3,5-Trimethylhexane	812.0
2,2-Dimethylheptane	815.4
2,2,3,4-Tetramethylpentane	819.6
2,2,3-Trimethylhexane	821.6
2,2-Dimethyl-3-ethylpentane	822.2
3,3-Dimethylheptane	835.8
2,4-Dimethyl-3-ethylpentane	836.5
2,3,4-Trimethylhexane	849.1
2,3,3,4-Tetramethylpentane	858.0
3-Methyloctane	870.2
3,3-Diethylpentane	877.2
n-Butane	400
n-Pentane	500
n-Hexane	600
n-Heptane	700
n-Octane	800
n-Nonane	900
n-Decane	1000

TABLE 1 (continued)

Compound	*I* (Lit.) [27]
Ethylcyclopropane	510.2
Cyclopentane	565.7
Ethylcyclobutane	621.1
Methylcyclopentane	627.9
Cyclohexane	662.7
1,1,2-Trimethylcyclopentane	763.2
1,1,3-Trimethylcyclopentane	723.6
Methylcyclohexane	725.8
Ethylcyclopentane	733.8
1,1-Dimethylcyclohexane	787.0
Isopropylcyclopentane	812.1
n-Propylcyclopentane	830.3
Ethylcyclohexane	834.3
1,1,3-Trimethylcyclohexane	840.4
1-*cis*-3-Dimethylcyclopentane	682.7
1-*trans*-3-Dimethylcyclopentane	686.8
1-*cis*-2-Dimethylcyclopentane	720.9
1-*trans*-2-Dimethylcyclopentane	689.2
1-*trans*-2-Dimethylcyclopentane	801.8
1-*cis*-2-Dimethylcyclohexane	829.3
1-*trans*-3-Dimethylcyclohexane	805.6
1-*cis*-3-Dimethylcyclohexane	785.0
2-Methyl-2-butanol	626.2 [28]
1-Butanol	646.5
3-Methyl-2-butanol	666.0
2-Pentanol	682.7
3-Methyl-2-pentanol	717.6
3-Methyl-1-butanol	719.3
4-Methyl-2-pentanol	744.1
1-Pentanol	750.4
2-Methyl-3-pentanol	758.0
2,4-Dimethyl-2-pentanol	775.9
3,3-Dimethyl-1-butanol	778.8
3-Hexanol	780.4
2-Methyl-2-hexanol	817.3
2-Methyl-1-pentanol	818.4
2,4-Dimethyl-3-pentanol	821.2
4-Methyl-1-pentanol	821.2
2,3-Dimethyl-3-pentanol	823.7
2-Ethyl-1-butanol	825.9
3-Methyl-1-pentanol	828.8
5-Methyl-3-hexanol	838.2
3-Ethyl-3-pentanol	843.1
1-Hexanol	853.0
4-Heptanol	875.4
2,2,4-Trimethyl-3-pentanol	881.5
3,5-Dimethyl-3-hexanol	883.1
2-Methyl-2-heptanol	916.4
6-Methyl-2-heptanol	951.1
4-Ethyl-3-hexanol	953.3
4-Octanol	975.5
3-Octanol	982.0
3,6-Dimethyl-3-heptanol	986.6

TABLE 1 (continued)

Compound	*I* (Lit.) [28]
3-Methyl-2-butanone	640.9
2-Pentanone	666.3
3-Pentanone	676.4
3,3-Dimethyl-2-butanone	693.1
4-Methyl-2-pentanone	721.2
2-Methyl-3-pentanone	733.0
4-Methyl-3-pentanone	733.0
3-Methyl-2-pentanone	734.8
3-Hexanone	764.8
2-Hexanone	767.9
2,4-Dimethyl-3-pentanone	779.0
5-Methyl-3-hexanone	816.7
2-Methyl-3-hexanone	820.0
5-Methyl-2-hexanone	836.5
4-Heptanone	853.4
3-Heptanone	865.8
2-Heptanone	868.7
2,2,4,4-Tetramethyl-3-pentanone	900.0
2,6-Dimethyl-4-heptanone	954.7
2,2-Dimethyl-3-heptanone	964.7
3-Octanone	966.0
2-Octanone	968.8
Acetic acid, ethyl ester	600.0
Propionic acid, methyl ester	615.2
Isobutyric acid, methyl ester	671.0
Propionic acid, ethyl ester	694.2
Acetic acid, propyl ester	696.3
Butyric acid, methyl ester	705.6
Isobutyric acid, ethyl ester	744.6
Acetic acid, *sec*-butyl ester	743.8
Acetic acid, isobutyl ester	757.7
Isopentanoic acid, methyl ester	761.3
Butyric acid, ethyl ester	784.0
Propionic acid, propyl ester	792.6
Acetic acid, butyl ester	796.2
Butyric acid, isopropyl ester	827.6
Isopentanoic acid, ethyl ester	838.4
Propionic acid, isobutylester	852.8
Butyric acid, propylester	881.5
Acetic acid, 1,3-dimethylbutyl ester	885.1
Propionic acid, butyl ester	891.4
Acetic acid, pentyl ester	896.4
Isobutyric acid, isobutyl ester	900.0
Hexanoic acid, methyl ester	907.0
Butyric acid, isobutyl ester	940.3
Acetic acid, 2-ethylbutyl ester	957.0
Butyric acid, butylester	979.4
Hexanoic acid, ethyl ester	982.9
Propionic acid, pentyl ester	990.5
Acetic acid, hexyl ester	996.5
Propyl ether	681.6
Butylethyl ether	688.5
Butyl ether	876.3

TABLE 1 (continued)

Compound	*I* (Lit.) [27]
Octene-1	781.2
2-Methyl-3-ethyl-pentene-2	778.4
2,3,4-Trimethyl-pentene-2	765.9
2,5-Dimethyl-hexene-2	749.9
2,3-Dimethyl-hexene-1	739.3
2-Methyl-3-ethyl-pentene-1	735.0
2,2-Dimethyl-*cis*-hexene-3	716.8
2,2-Dimethyl-*trans*-hexene-3	692.8
2,4,4-Trimethyl-pentene-2	715.4
2,4,4-Trimethyl-pentene-1	704.3
2,3-Dimethyl-pentene-2	703.4
3-Ethyl-pentene-2	697.2
2-Methyl-hexene-2	691.2
cis-Heptene-3	690.4
trans-Heptene-3	687.5
3-Methyl-*trans*-hexene-3	691.2
3-Methyl-*cis*-hexene-3	684.6
Heptene-1	681.8
2-Ethyl-pentene-1	681.8
2-Methyl-hexene-1	678.1
3,4-Dimethyl-*trans*-pentene-2	678.3
3,4-Dimethyl-*cis*-pentene-2	670.6
3-Methyl-2-ethyl-butene-1	659.1
4-Methyl-hexene-1	657.9
4-Methyl-*trans*-hexene-2	656.7
2-Methyl-*cis*-hexene-2	654.9
2,3-Dimethyl-pentene-1	650.4
5-Methyl-hexene-1	650.0
3-Ethyl-pentene-1	646.9
3-Methyl-1-hexene	644.7
2,4-Dimethyl-pentene-2	640.6
2,4-Dimethyl-pentene-1	637.7
3,4-Dimethyl-pentene-1	636.9
4,4-Dimethyl-*cis*-pentene-2	635.5
4,4-Dimethyl-*trans*-pentene-2	614.7
3,3-Dimethyl-pentene-1	626.1
2,3-Dimethyl-butene-2	625.1
4,4-Dimethyl-pentene-1	604.6
cis-Hexene-2	603.6
trans-Hexene-2	596.9
3-Methyl-*trans*-pentene-2	612.7
3-Methyl-*cis*-pentene-2	602.8
2-Methyl-pentene-2	597.8
cis-Hexene-3	592.6
trans-Hexene-3	592.1
2-Ethyl-butene-1	592.0
Hexene-1	582.3
2-Methyl-pentene-1	580.1
2,3-Dimethyl-butene-1	558.8
4-Methyl-*trans*-pentene-2	561.9
2-Methyl-*cis*-pentene-2	556.2
3-Methyl-pentene-1	551.4
4-Methyl-pentene-1	549.4

TABLE 1 (continued)

Compound	*I* (Lit.) [27]
2-Methyl-butene-2	514.3
3,3-Dimethyl-butene-1	506.8
trans-Pentene-2	500.0
cis-Pentene-2	504.9
2-Methyl-butene-1	488.0
Pentene-1	481.8
3-Methyl-butene-1	450.3
trans-Butene-2	406.6
cis-Butene-2	416.9

works, was first described by Rumelhart and McClelland [26].

Data

A collection of 216 monofunctional compounds containing acyclic and cyclic alkanes, alkenes, alcohols, esters, ketones and ethers served as training data (Table 1). The alkane retention index data was taken from Rijks and Cramers [27]. These compounds were measured at 50°C on squalane as a stationary phase. The other data was taken from the Sadtler catalogue [28] and was generated at 60°C on OV1 as the stationary phase.

The prediction data set consisted of acyclic and cyclic terpenes (Table 2). This data was acquired from several papers denoted in [25]. Nonpolar phases, such as SE30, SF96, OV1 and OV101, were used at temperatures ranging from 80 to 130°C. The circumstances under which the retention index values were determined seem to be quite heterogeneous, but nevertheless we believe them to be comparable. Attention must be paid to the fact that bond types occurring in the prediction data set must also occur in the training data set.

Regression model and prediction

Multilinear regression was used to fit a model to the retention index data. This model will serve as a comparison to the results achieved when applying a neural network. Some remarks must therefore be made about the regression model (1)

$$I = B_0 + \sum_{j=1}^{n} B_j \beta_j \qquad (1)$$

TABLE 2

Terpene compounds used for prediction and corresponding experimental retention index data I

Compound	I (Lit.) [25]
Carvylpropionate	1440
2,6-Dimethyloctane	938
3,7-Dimethyl-1,6-octadiene	946
2,6-Dimethyl-2-octane	966
trans-p-Menthane	981
cis-p-Menthane	995
Limonene	1030
γ-Terpinene	1057
6,10-Dihydromyrcenol	1063
Terpinolene	1081
Tetrahydrolinalool	1087
Tetrahydromyrcenol	1090
Linalool	1092
1,2-Dihydrolinalool	1122
β-Terpineol	1137
Menthone	1143
Isopulegol	1145
Lavandulol	1154
Isomenthone	1156
Neomenthol	1159
δ-Terpineol	1160
Menthol	1171
Terpinen-4-ol	1175
Neoisomenthol	1180
Carvomenthone	1181
Isomenthol	1182
α-Terpineol	1185
Tetrahydrogeraniol	1185
β-Citronellol	1215
β-Nerol	1218
Geraniol	1243
Isopulegyl acetate	1258
Lavandulol	1274
Isomenthyl acetate	1283
Neoisomenthyl acetate	1297
Citronellyl acetate	1335
β-Neryl acetate	1345
Citronellyl propionate	1427
β-Neryl propionate	1436
Citronellyl isobutyrate	1469
β-Neryl isobutyrate	1474
Geranyl isobutyrate	1493
Citronellyl butyrate	1511
cis-Nerolidol	1524
Geranyl butyrate	1532
trans-Nerolidole	1553
β-Neryl isopentanoate	1574
Geranyl isopentanoate	1593
Citronellyl pentanoate	1608
Geranyl pentanoate	1632

$$\beta_j = \sum_i (S^l + S^r)_{ij} \quad (2)$$

The retention index I is given by Eqn. 1 with the regression coefficients B_0, B_j and the regression parameter β_j given by Eqn. 2. The bond index of a bond type j is given by the sum of the electrotopological index values S of the "left" and "right" atoms bonded together. The electrotopological index was introduced by Hall et al. [29] and described the topological environment and the electronic character of each skeletal atom in a molecule. The electrotopological index values are added together to form the regression parameter β_j. The β_j values served as a basis for the regression analysis carried out to find the corresponding regression coefficient B_j. These coefficients were then used to predict the terpene retention index data. Details of these investigations have been published in [24,25]. In order to describe the training and test data sufficiently, 29 bond types, respectively regression parameters B_j proved to be necessary. These bond types are all chemical bonds, e.g. CH_3–CH_2–, –CH_2–CH_2–, –CH=CH–, –CH_2–OH, etc. incorporated in the complete set of the investigated compounds.

Neural network model and prediction

The above-mentioned regression model was substituted by a neural network, with its topology reflecting the number of input value (29 neurons for the different bond types) and the number of output values (one neuron for the predicted retention index). One hidden layer was used and the number of neurons in it was altered to optimize the results achievable with this type of network. Network topologies will be denoted as 29-2-1 in the following; 29 input neurons fully interconnected to 2 hidden layer neurons fully interconnected to 1 output neuron.

An interval spanning from the minimum to the maximum of all of the electrotopological input data was transformed to an interval between 0.0 and 1.0. using a linear transformation. The interval spanning from a minimal to a maximal value of the retention index values in both the training and the prediction set was transformed to an interval between 0.1 and 0.9 (Table 4).

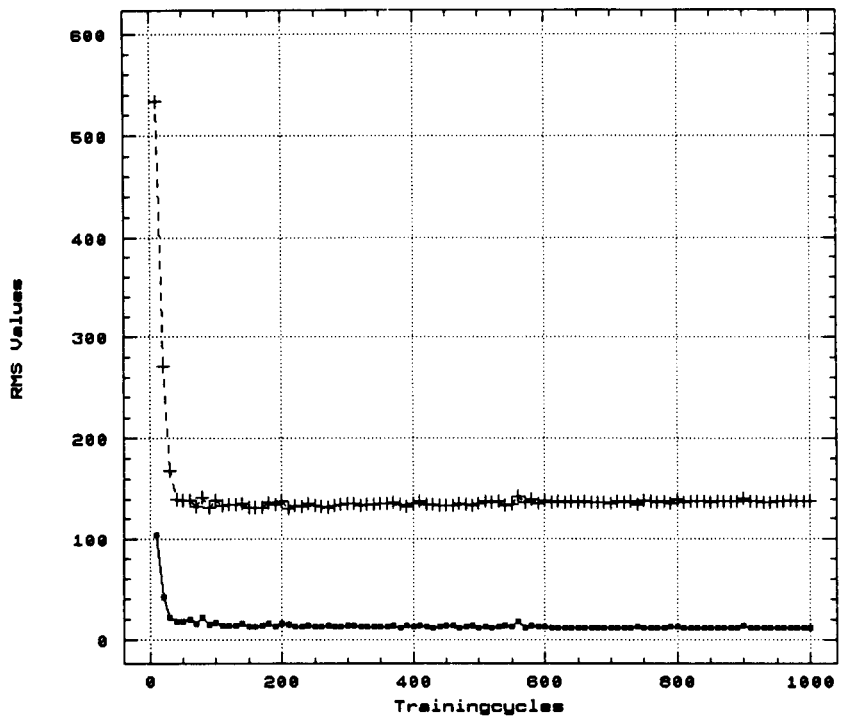

Fig. 1. Estimation and prediction RMS of retention index values during training of a neural network (29-2-1). Segregated training and prediction data: (■ ■ ■) estimation RMS (216 monofunctional compounds); (+ + +) prediction RMS (50 monoterpenes).

The sigmoidal transfer function, sometimes called "squashing function" has the characteristic of transforming all incoming values to an interval between 0.0 and 1.0. Only these values in this range are presented on the output side of the network. Scaling the desired values to a smaller interval facilitates faster learning. This is due to the sigmoidal function's asymptotic approach towards 0.0 and 1.0, in other words, these values could be reached, but only after infinite training times. Values ranging in a smaller interval are therefor easier and quicker to reach.

Every network was initialized before training; the weight values of the connections from neuron to neuron were randomly set to values between −0.1 and 0.1. Care was taken to ensure that each instance in the training set was presented 1000 times at random intervals to the network during supervised training. For training, a derivative of the standard backpropagation, fast backpropagation [30] was used. Learning coefficients decreased upon increasing the training time (no. of iterations) (Table 3).

At intervals of 10 presentations of the complete training data set the network's prediction of terpene retention index values was tested. A root-mean-square value was calculated and served as a measure for the network's prediction quality.

The development of this error, observable for both training and prediction, with proceeding network training can be seen in Figs. 1 and 2. The effect of different initial sets of weights on the network's error development during training

TABLE 3

Selection of learning rate and momentum term values, decreasing with increasing training time

Training cycles	Learning rate	Momentum term
0–50	0.9	0.6
50–100	0.6	0.4
100–200	0.5	0.3
200–500	0.4	0.3
500–1000	0.2	0.1

was investigated. Four networks were trained with identical sets of learning parameters, but were individually initialized before training. The development of the four error loggings showed minor differences, but the resulting prediction error was identical in all four cases.

Hardware and software environment

The neural networks were constructed and trained using NeuralWorks Professional II Plus (NeuralWare, Pittsburgh, IL) on an IBM PS2/50. The general settings of the training parameters and the value ranges for the networks are given in Tables 3 and 4. The input data for the networks was obtained by using a list processing system described in [3,4] on a VAX station 3100 (Digital Equipment, Maynard, MA) under LUCID Common LISP (LUCID, Menlo Park, CA). DECNET/PCSA software supported the connection between both computers via ethernet.

RESULTS AND DISCUSSION

In order to predict gas chromatographic retention indexes different topologies of backpropagation networks were investigated and the results were compared to those obtained by using multilinear regression.

Prediction of retention index data using neural networks

A first network with two hidden layer neurons was trained with a data set comprising acyclic and cyclic alkanes, alkenes, alcohols, esters, ketones and ethers (Table 1). The development of the root-mean-square (RMS) values for the training data and for the predicted data during training can be seen in Fig. 1. These RMS values level out after about 50 training cycles. A big difference between training data RMS value and prediction data RMS value can be observed. This becomes

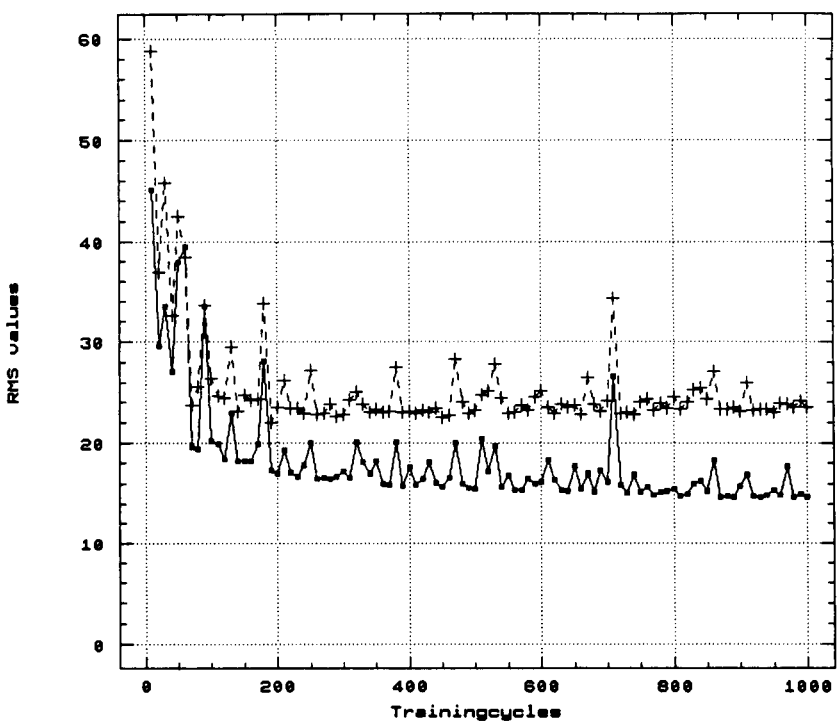

Fig. 2. Estimation and prediction RMS of retention index values during training of a neural network (29-2-1). Mixed training and prediction data: (■ ■ ■) estimation RMS (183 compounds); (+ + +) prediction RMS (83 compounds).

TABLE 4

General settings of backpropagation specific parameters during network training and retention index prediction

Gain for sigmoid transfer function	1.5
K-factor of fast backpropagation algorithm	2.0
Limits for weight randomization	−0.1; +0.1
Scaling limits for input data	0; 1
Scaling limits for output data	0.1; 0.9

even more evident when comparing the prediction results to the values in the literature as seen in Fig. 3. A significant difference between these values can be seen. In opposition hereto, a good agreement between the estimation of retention index data of monofunctional compounds by this neural network and the literature data can be seen in Fig. 2. Predicting terpene retention index values with a network trained with other compounds having comparable bonds obviously fails. A generalization in this form cannot be made.

One important fact may be responsible for this. The network input and output values may not come from the same region in the interval for the input and output data. Then input and output values for the terpene retention index prediction lie in a higher region of the scaled interval than these values for the other compounds do. The value space of prediction is not evenly covered by the training data.

To overcome these inhomogeneities both data sets were combined to form a new data set. This data set was devided into a training set of 183 compounds and a prediction set of 83 compounds. The training set now had instances more or less covering the value space needed for the prediction of terpene retention index values. The development of the RMS values for the training data and for the prediction data during training can be seen in Fig. 4. Denote a longer training time needed for the RMS values to level off now.

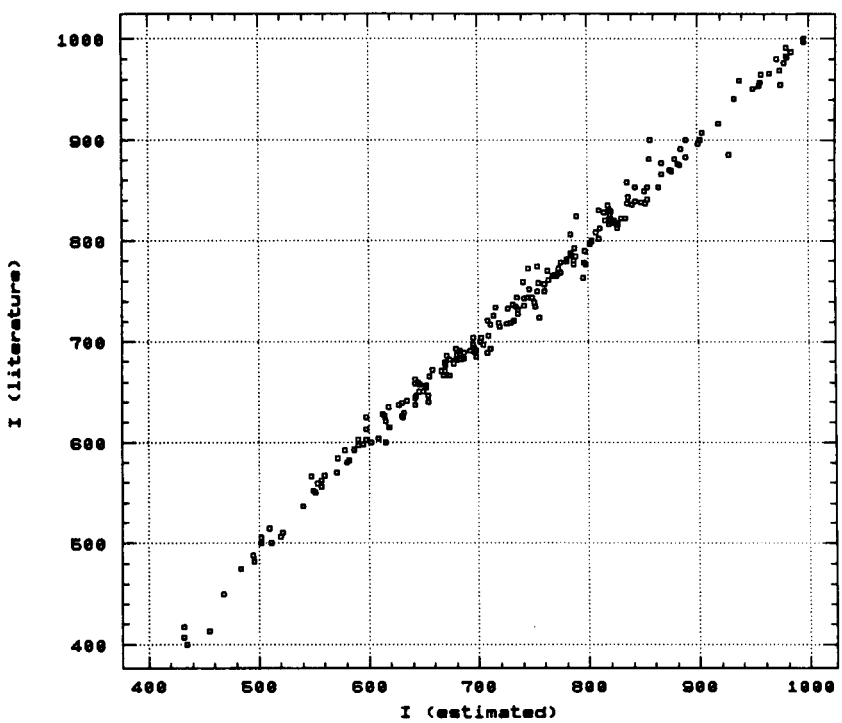

Fig. 3. Comparison of the retention index estimation of 216 monofunctional compounds (training data) with data from the literature.

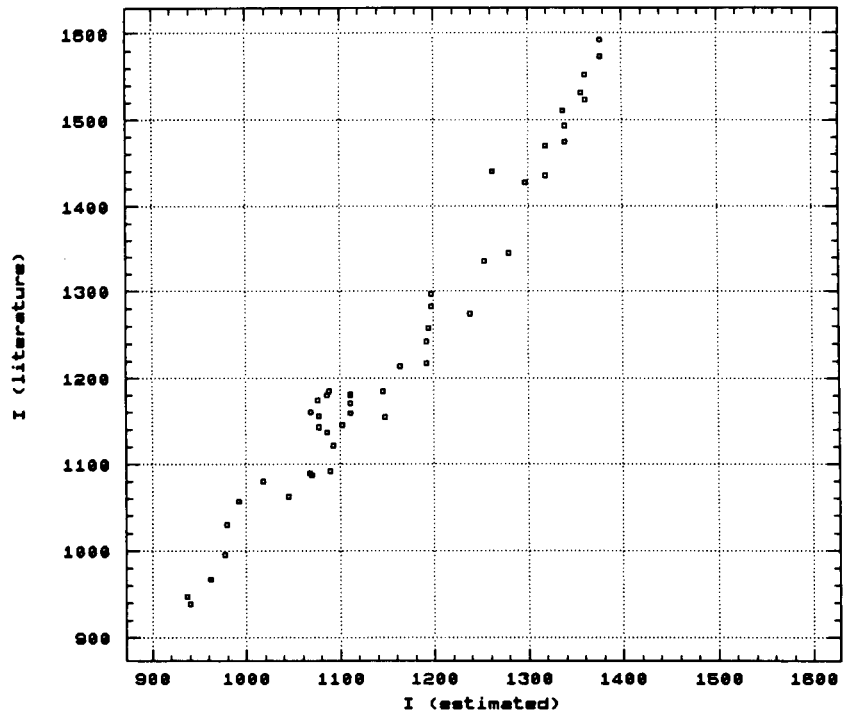

Fig. 4. Comparison of the retention index prediction of 50 monoterpenes (prediction data) with data from the literature.

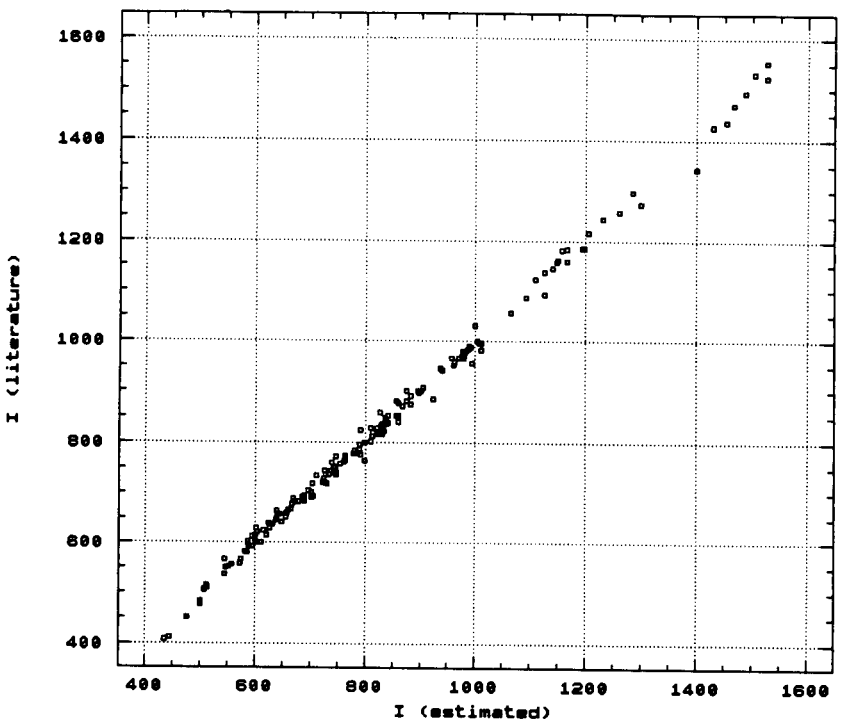

Fig. 5. Comparison of the retention index estimation of 183 compounds (training data) with data from the literature.

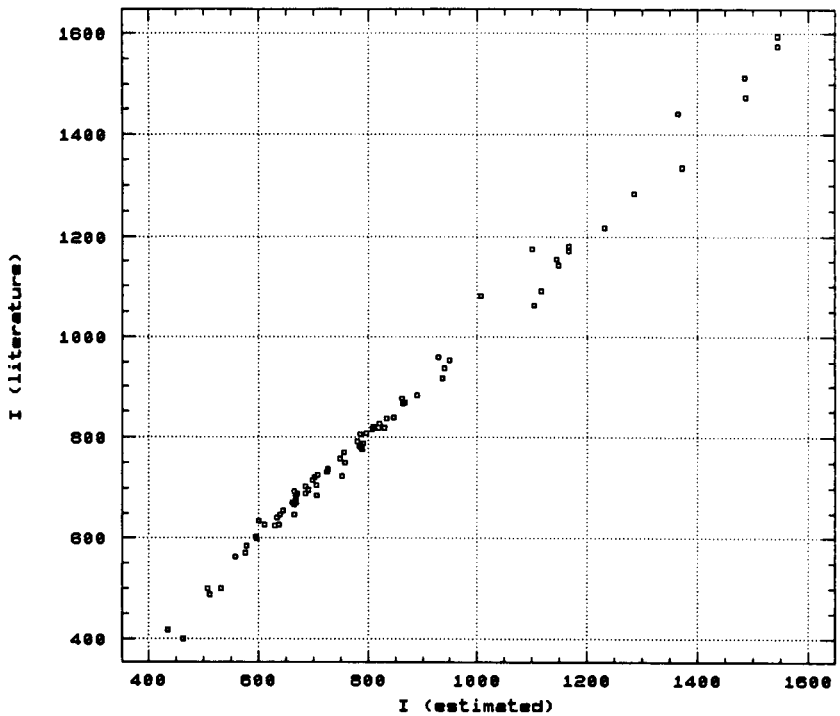

Fig. 6. Comparison of the retention index prediction of 83 compounds (prediction data) with data from the literature.

The difference between the final RMS values for training and prediction is much smaller.

The estimation of the retention index values of the compounds in the mixed training data set (Fig. 5) has a quality comparable to the retention index value estimation in the case of segregated training and prediction data (Fig. 3). A comparison of the network's prediction with values found in the literature shows a much better agreement now (Fig. 6). It can also be stated from Fig. 2, that the errors found at predicting indexes from unknown compounds and estimating the indexes from the training data in the case of mixed training and prediction data are now of the same order of magnitude, as opposite to the case of training data solely consisting of monofunctional compounds and the prediction data solely consisting of monoterpene compounds.

To investigate the influence of the number of neurons in the hidden layer on a prediction result, networks with neuron numbers ranging from 1 to 8 in the hidden layer were trained. This training was carried out for the cases of segragated training and prediction data and mixed training and prediction data. Figure 7 shows that two neurons in the hidden layer are sufficient enough for the prediction of retention index values in the case of a mixed training data set.

TABLE 5

Comparison of the retention index estimation and prediction accuracy achievable by neural network techniques and multilinear regression

Data	RMS	
	Network	Regression
Monofunctional compounds (training data)	11.6	11.1
Terpene compounds (prediction data)	138.0	43.0
Mixed compounds (training data)	14.7	17.2
Mixed compounds (prediction data)	23.6	23.4

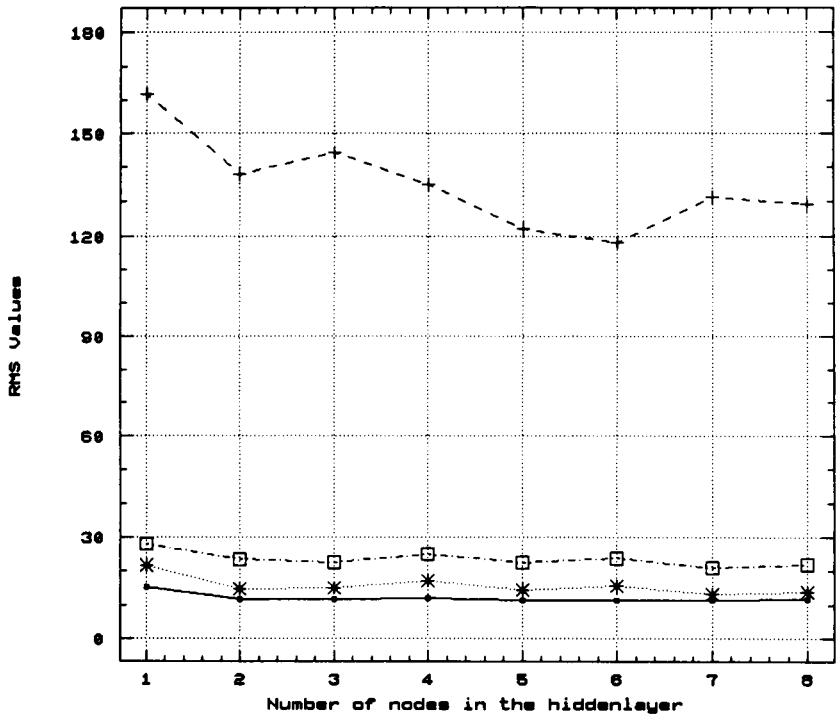

Fig. 7. Influence of the number of hidden layer neurons in a neural network on the estimation and prediction RMS of retention index values. Segregated training and prediction data: (+ + +) prediction RMS (50 monoterpenes); (■ ■ ■) estimation RMS (216 monofunctional compounds). Mixed training and prediction data: (□ □ □) prediction RMS (83 compounds); (* * *) estimation RMS (183 compounds).

Comparison of prediction results obtained by neural networks and multilinear regression techniques

An estimation of retention index data using multilinear regression techniques is presented in [24,25]. To facilitate a comparison between neural network techniques and regression techniques identical data was used. A summary of results obtained with both techniques is given in Table 5. With respect to the training data sets, the estimation errors are in the same range for both methods. Prediction of terpene retention index values with multilinear regression techniques is significantly superior to prediction with neural network techniques in the case of segregated training and prediction data. Combining terpene and monofunctional compounds to form mixed training and prediction sets again shows equivalent results for neural network and multilinear regression techniques. The characteristic of this regression is obviously more stiff than that of the neural network predicting data which is out of the training data range. As a result of the comparison it must be stated that in the discussed and similar problems multilinear regression methods are more efficient for data extrapolation than backpropagation neural networks.

Conclusions

Investigations in the field of retention index prediction show that linear models are sufficiently capable of predicting retention index values. The introduction of neural networks to this field is of no improvement of prediction quality. This seems to be in contradiction with the fact that more adjustable parameters (weighted connections from neuron to neuron) are present in a neural network than there are in multilinear regression equations. Even the ability of generalizing the relationship between structure and retention index is smaller in neural networks compared to linear regression. In order to obtain

reliable prediction results with neural networks it is necessary that the training data adequately covers the range spanned by the prediction data. In other words prediction results are only reliable when they do not exceed the range spanned by the training data.

On the other hand in the field of investigating non-linear structure–retention relationships neural networks may be advantageous. The present results were obtained using retention indexes measured in non-polar gas chromatographic columns. With respect to measurements carried out on polar columns, we expect non-linear effect. Studying the applicability of neural network techniques to these cases will be the subject of further work.

REFERENCES

1 D.T. Stanton, P.C. Jurs and M.G. Hicks, J. Chem. Inf. Comput. Sci., 31 (1991) 301.
2 A.J. Stuper, W.E. Brügger and P.C. Jurs, Computer Assisted Studies of Chemical Structure and Biological Function, Wiley, New York, 1979.
3 R. Gautzsch and P. Zinn, J. Chem. Inf. Comput. Sci., 32 (1992) 541.
4 R. Gautzsch and P. Zinn, J. Chem. Inf. Comput. Sci., 32 (1992) 551.
5 D.T. Stanton and P.C. Jurs, J. Chem. Inf. Comput. Sci., 32 (1992) 109.
6 M. Garbalena and W.C. Herndon, J. Chem. Inf. Comput. Sci., 32 (1992) 37.
7 Z. Mihalić, S. Nikolić and N. Trinajstić, J. Chem. Inf. Comput. Sci., 32 (1992) 28.
8 A.T. Balaban, N. Joshi, L.B. Kier and L.H. Hall, J. Chem. Inf. Comput. Sci., 32 (1992) 233.
9 A.T. Balaban, L.B. Kier and N. Joshi, J. Chem. Inf. Comput. Sci., 32 (1992) 237.
10 G.P. Stutton, L.S. Anker and P.C. Jurs, Anal. Chem., 63 (1991) 443.
11 K. Hasegawa, Y. Miyashita and S.-I. Sasaki, Chem. Intell. Lab. Sys., 16 (1992) 69.
12 P.H. Weiner, E.R. Malinowski and A.R. Levinstone, J. Phys. Chem., 74 (1970) 4537.
13 G. Bergmann, H.-J. Götze, A. Hermann and P. Zinn, Chromatographia, 32 (1991) 259.
14 S. Wold and W.J. Dunn, J. Chem. Inf. Comput. Sci., 23 (1983) 6.
15 L.S. Anker and P.C. Jurs, Anal. Chem., 64 (1992) 1157.
16 P.A. Janson, Anal. Chem., 63 (1991) 357A.
17 J. Zupan and J. Gasteiger, Anal. Chim. Acta, 248 (1991) 1.
18 N. Qian and T.J. Sejnowski, J. Mol. Biol., 202 (1988) 865.
19 V. Venkatasubramanian and K. Chang, AIChE J., 35 (1989) 1993.
20 M. Bos, A. Bos and W.E. van der Linden, Anal. Chim. Acta, 233 (1990) 31.
21 B.J. Wythoff, S.P. Levine and S.A. Tomellini, Anal. Chem., 62 (1990) 2702.
22 E.W. Robb and E. Munk, Microchim. Acta, 1 (1990) 131.
23 J.R. Long, V.G. Gregoriou and P.J. Gemperline, Anal. Chem., 62 (1990) 1791.
24 Chr. Duvenbeck and P. Zinn, J. Chem. Inf. Comput. Sci., 33 (1993) 211.
25 Chr. Duvenbeck and P. Zinn, J. Chem. Inf. Comput. Sci., 33 (1993) 220.
26 D.E. Rumelhart and J.L. McClelland, Paralell Distributed Processing, MIT Press, Cambridge, MA, 1986.
27 J.A. Rijks and C.A. Cramers, Chromatographia, 77 (1974) 99.
28 The Sadtler Standard Gas Chromatographic Retention Index Library, Sadtler Research Laboratories, Philadelphia, PA, 1985.
29 L.H. Hall, B. Mohney and L.B. Kier, J. Chem. Inf. Comput. Sci., 31 (1991) 76.
30 Neural Computing, Neural Ware Inc., Pittsburgh, 1991, p. 98.

Analytica Chimica Acta, 283 (1993) 881–886
Elsevier Science Publishers B.V., Amsterdam

Determination of ultratrace metals in biological standards by inductively coupled plasma atomic emission spectrometry with ultrasonic nebulisation

Tetsuo Uchida, Hirofumi Isoyama, Hideo Oda and Hiroko Wada

Department of Applied Chemistry, Nagoya Institute of Technology, Gokiso, Showa, Nagoya 466 (Japan)

Hideo Uenoyama

Nippon Jarrel-Ash, 2-63 Megawa, Makishima, Uji, Kyoto 611 (Japan)

(Received 31st March 1993; revised manuscript received 7th July 1993)

Abstract

Ultratrace cadmium, cobalt, copper, nickel and lead in biological standard samples were determined by inductively coupled plasma atomic emission spectrometry with ultrasonic nebulisation without removal of any matrix. The operating conditions of the ultrasonic system were examined in detail, together with the performance of the system. An internal standard method was essential to obtain accurate analytical results. The transport efficiencies of analyte (manganese) and solution to a plasma with the ultrasonic system were measured, and compared to those with a cross-flow nebuliser.

Keywords: Inductively coupled plasma spectrometry; Biological standards; Transport efficiency; Ultrasonic nebuliser; Ultratrace metals

Among the sample introduction systems for inductively coupled plasma atomic emission spectrometry (ICP-AES), the superiority of ultrasonic nebulisers has been established in sensitivity of many elements compared to pneumatic systems. Although a batch type ultrasonic nebuliser [1–5] was initially examined, a flow type [6–11] has been developed and used, for the latter is more convenient than the former in routine use. In flow types, as used for commercially available systems, a sample solution is supplied onto the vertically placed ultrasonic transducer through a pump, resulting in a high throughput with easy exchange and low consumption of sample solutions. However, these ultrasonic systems have been applied only to such samples of relatively low matrix concentration [12–16] as surface, drinking and waste waters. No application to samples of complicated matrix has so far been reported except for coastal sea water [17] after chelating resin separation and a spiked synthetic ocean water [18].

In the present study, one of commercially available ultrasonic nebulisation systems was successfully applied to the determination of ultratrace metals in some biological Certified Reference Materials (CRMs) after detailed investigations of operating conditions and some performance of the system. In particular, the transport efficiency of analyte or solution was examined

Correspondence to: T. Uchida, Department of Applied Chemistry, Nagoya Institute of Technology, Gokiso, Showa, Nagoya 466 (Japan).

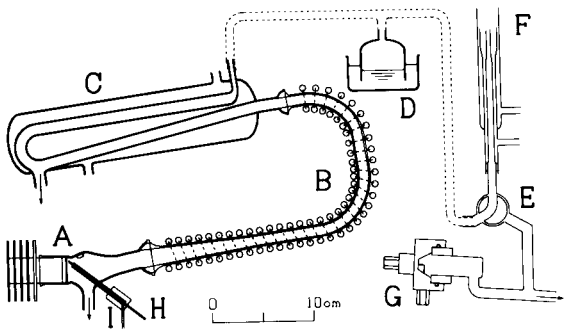

Fig. 1. Schematic diagram of the ultrasonic nebulisation system. A = ultrasonic nebuliser, B = heater, C = condenser, D = noise suppressor, E = 3-way valve, F = plasma torch, G = cross-flow nebuliser, H = inlet of sample solution, I = inlet of auxiliary rinse.

with difference measurement [7] and compared to that with a cross-flow nebuliser.

EXPERIMENTAL

A Nippon Jarrel-Ash Model ICAP-575 sequential ICP-AE spectrometer and Model U-5000 ultrasonic nebuliser were used under the operating conditions listed in Table 1. As shown in Fig. 1, the ultrasonic system was easily switched to an alternate system of cross-flow nebuliser with a small spray chamber (5.0 cm × 1.8 cm i.d.) via a 3-way glass valve without extinguishing a plasma [19]. This switching was quite convenient to compare the sensitivity under the same plasma conditions. The noise suppressor consisting of a bottomless bottle and beaker was attached on an aerosol transport tube to a torch.

Standard stock solutions were prepared from ultrapure metals, salts or oxides. Working solutions were prepared by mixing of the stock solutions after appropriate dilutions by mass. All reagents used were of analytical grade. Milli-Q water was used throughout.

The operating conditions listed in Table 1 were chosen, consulting those recommended by the manufacturer, with 0.1 $\mu g\ g^{-1}$ manganese or a mixture of 12 metals at 1 $\mu g\ g^{-1}$ each in 0.1 mol dm^{-3} nitric acid.

The sensitivity was defined as the net signal counts for 3-s integration. The signal stability was evaluated not only by the relative standard deviation (R.S.D.) for 10 sets of 3-s net counts regarded as long-term stability but also by the signal fluctuation within 3 s regarded as short-term stability. The latter was the averaged R.S.D. for 10 sets of 300 points sampled at 10-ms intervals [19], thus it corresponded to the signal chattering within 3 s. The memory was the time measured on a strip-chart recorder to obtain the signal less than 0.1% of that of the previous sample after replacing into a blank solution.

The transport efficiencies of analyte and solution were obtained from the differences in solution amounts and in analyte concentrations of an

TABLE 1

Operating conditions

ICAP-575 ICP-AE spectrometer						U-5000 ultrasonic system		
R.F. Power	1.2 kW					Frequency	1.4 MHz	
Ar flow-rate	16–0.6–0.8 $dm^3\ min^{-1}$					Current	4 A	
Sample flow-rate	2.5 $cm^3\ min^{-1}$					Heating temp.	140°C	
						Cooling Temp.	5°C	
High salt concn. torch of Fassel type								
Grating	1800 line mm^{-1}							
Focal length	75 cm					Cross-flow system		
Slit widths	25 μm					Spray chamber	1.8 cm i.d.	
Observation height	12.5 mm						5.0 cm long	
Wavelength (nm) and its order used								
Cr II	205.552	×3	Ni II	221.647	×3	Cu I	324.754	×1
Zn I	213.856	×3	Fe II	238.204	×3	Al I	396.153	×1
Cd II	214.438	×3	Co II	238.892	×3	Sr II	407.771	×1
Pb II	220.351	×3	Mn II	257.610	×2	Ba II	455.404	×1

aspirated sample and drain from chamber or condenser. The drain was successively collected at 30 min intervals after sufficient pre-nebulisation of the manganese solution. The sample flow-rate was kept constant at 2.3 cm^3 min^{-1} with a Gilson Minipulse II pump even for the cross-flow nebuliser having the above rate on free aspirating at the carrier flow of 0.8 dm^3 min^{-1}.

Standard samples analyzed were CRMs prepared from the National Institute for Environmental Study (NIES) in Japan; No. 1 Pepperbush, No. 3 Chlorella, No. 5 Human Hair, No. 6 Mussel and No. 7 Tea Leaves. After drying at 80°C for 2 h, 100 mg sample was decomposed with 2 cm^3 of nitric acid, 0.2 cm^3 of hydrochloric acid, 0.3 cm^3 of perchloric acid and 0.1 cm^3 of hydrofluoric acid in a doubly sealed PTFE vessel using a domestic microwave oven according to the previous work [20]. The mixture was then evaporated to complete dryness and dissolved in 10 g of 0.1 mol dm^{-3} perchloric acid containing 100 ng g^{-1} beryllium as an internal standard.

RESULTS AND DISCUSSION

Effects of operating conditions

With the higher input current to the ultrasonic transducer, the higher sensitivity was observed, however, the sensitivity was saturated above 3.5 A. The current ranging from 2.5 to 5.5 A gave little effect on either long- or short-term stability of signal.

The sample flow-rate onto the ultrasonic transducer had no effect on the sensitivity and stability at the flow-rate ranging from 2.0 to 4.0 cm^3 min^{-1}. The low sensitivity and insufficient stability (> 1% in R.S.D.) were observed at 1.0 cm^3 min^{-1} with some memory effect.

The plasma was extinguished at the heating temperature of the desolvator below 100°C. The sensitivity was increased remarkably below 140°C and gradually from 140 to 200°C with the increase of the heating temperature. The stability was good except for those below 120°C. Irrespective of the cooling temperature (0–20°C) of the condenser of the desolvator, the sensitivity and stability were maintained constant.

The free selection of carrier flow-rate without change in sample aspirating rate was one of the advantages of the ultrasonic system. Sensitivities and background intensities for 12 metals were measured at the carrier ranging from 0.6 to 1.1 dm^3 min^{-1}. Though the effect of carrier flow was not critical on the sensitivity from 0.7 to 1.0 dm^3 min^{-1}, the maximum sensitivity was observed at 0.8 dm^3 min^{-1} for the analysis line below 300 nm, and at 0.9 or 1.0 dm^3 min^{-1} for the lines

TABLE 2

Transport efficiency with ultrasonic and cross-flow nebulisation systems [a]

	Net signal counts s^{-1}	Solution mm^3 min^{-1} (%)	Analyte ng min^{-1} (%)
Ultrasonic	58140		
Aspirated		2343 ± 2 (100.0)	2343 ± 2 (100.0)
Chamber drain		1455 ± 17 (62.1)	1496 ± 17 (63.8)
Condenser drain		825 ± 16 (35.2)	396 ± 8 (16.9)
Torch		63 ± 29 (2.7)	451 ± 20 (19.3)
Cross-flow	3669		
Aspirated		2321 ± 4 (100.0)	2321 ± 2 (100.0)
Chamber drain		2274 ± 7 (98.0)	2293 ± 11 (98.8)
Torch		47 ± 3 (2.0)	28 ± 8 (1.2)
Ratios (ultrasonic/cross-flow)			
Aspirated		1.009	1.009
Chamber drain		0.64	0.65
Torch		1.32	15.9
Net signal			15.8

[a] Number of measurements: 6.

above 300 nm. The maximum signal-to-background ratio was observed at the carrier of 1.0 dm^3 min^{-1} for most metals, and a higher rate was recommended for the analysis lines above 300 nm. The carrier above 1.0 dm^3 min^{-1} sometimes caused a long-term instability of signals.

The noise suppressor was effective to smooth signals of high frequency components for distinguishing trace signals from the baseline, and it was independent of the sensitivity, response, memory and long-term stability of signals at all. The surface areas of water inside and outside the bottomless bottle were most important and the volume above the surface in the bottle was independent of the suppressor. The diameters of at least 5 and 7 cm were adequate for the bottle and beaker respectively, and resulting in a short-term stability of 1.2% which was fairly lower than that of 4.3% without the suppressor.

Comparisons of sensitivity and transport efficiency

Compared to the cross-flow system, the sensitivity was improved by a factor of 15.2 ± 0.8 with the ultrasonic system, irrespective of metals examined. Thus, the analyte as well as matrix elements in a sample were transported to a plasma and would cause background and/or spectral interferences as described later.

The transport efficiencies of analyte and solution were indirectly measured to examine the present system. As can be seen in Table 2, 19.3% of the aspirated analyte was transported to a plasma with the ultrasonic system used and only 1.2% was supplied with the cross-flow nebuliser, while a resembling transport efficiency of 2.0–2.7% was observed for solution with both nebulisation systems. The difference in the transport efficiency of analyte (1.2%) and solution (2.0%) was slightly larger than that expected with the cross-flow system. This phenomenon would be caused by dry argon used in the present measurements. The efficiency and amounts of analyte or solvent obtained here would be reasonable compared to those reported [9,21–24] with a similar system and sample flow-rate to the present one. The analyte transport ratio (15.9) in both systems agreed well to the improvement factor in sensitivity described above.

Effect of acids

The effect of hydrochloric, nitric and perchloric acids ranging from 0.01 to 1.0 mol dm^{-3} on sensitivity and background was conducted. For all metals examined, both hydrochloric and nitric acid of 0.3 and 1.0 mol dm^{-3} lowered the sensitivity to only 95 and 87% respectively, based on that at 0.1 mol dm^{-3} hydrochloric acid. Greater lowering was observed with perchloric acid, i.e., 93 and 56% at 0.1 and 1 mol dm^{-3}. The effect of the acid concentration on background was smaller than that on sensitivity. For practical analysis, therefore, the matrix matching and/or internal standard between sample and standard solutions would be recommended as shown later. On the contrary, these acid effects on sensitivity or background were almost negligible upto 1 mol dm^{-3} with the cross-flow system.

Memory and detection limits

The pre-nebulisation time required for a stable signal was ca. 50 s with the ultrasonic system. It was nearly twice that of the cross-flow system used here, and similar to that with a commercial spray chamber of large volume [19,25]. The memory examined with 10 μg g^{-1} manganese solution was at least 3 min without an auxiliary rinse. The rinse (additional washing) was carried out by the forced feed of another blank onto the transducer through the glass tube supporting the center PTFE tube for sample delivery. Some spontaneous peaks were also overlapped on a decreasing signal without the rinse. Such peaks were presumably caused by the renebulisation of sample drops attached near the transducer. On the other hand, the memory of less than 50 s was achieved by the rinse accompanying no peak. This memory was similar to that with pneumatic systems and no problem could be encountered in practice.

Although the same improvement factor in sensitivity was obtained for 12 metals, the improvement in the detection limit was depended on elements by a factor of 6–20 with the average of 12.

Application to the ultratrace metal determination in CRMs

The present system was applied to the determination of cadmium, lead, nickel, cobalt and copper in the CRMs. The background correction was taken at the lower wavelength from the peak of each analysis line. Analytical results with and without internal standard were listed in Table 3, together with the certified values and the previous results using the same ICP-AES system coupled with electrothermal vaporization (ETV-ICP) [26]. As the internal standard, beryllium was used, because of its absence in the samples and relatively high sensitivity in ICP-AES.

Most of the metals in the CRMs were difficult to be measured with the ETV-ICP system, though its detection limit was better than that with conventional pneumatic nebulisers. The present system enabled to measure the metals even in the presence of complicated matrix. As shown in Table 3, the analytical values obtained with the internal standard were agreed well with the certified values and those previously measured by ETV-ICP, except for lead in Mussel and Tea Leaves. The reason for the low lead level of the above CRMs is unknown yet. High values for cobalt in Chlorella and Human Hair were due to the failure in resolving the Co 238.892 nm line from Fe 238.863 nm in spite of the use of the third order lines. The iron content is as high as 1850 and 225 $\mu g\ g^{-1}$ in Chlorella and Human Hair, respectively.

In the present application, any matrix matching between sample and standard solutions was not performed, i.e., the standard solutions contained only ultratrace metals in 0.1 mol dm^{-3} perchloric acid. Consequently, lower values than the certified (see lines without I.S. in Table 3) were partly ascribed to the lack of internal standard. As described earlier, the ultrasonic system

TABLE 3

Analytical results ($\mu g\ g^{-1}$) of ultratrace elements in NIES CRMs [a]

Sample and method	Cd	Pb	Ni	Co	Cu
No. 1 Pepperbush					
Ultrasonic with I.S.	5.93 ± 0.05	4.8 ± 0.2	6.8 ± 0.1	19.1 ± 0.1	11.9 ± 0.1
Ultrasonic without I.S.	4.9 ± 0.2	3.94 ± 0.04	5.6 ± 0.3	15.8 ± 0.6	9.8 ± 0.4
ETV-ICP	6.4 ± 0.3	5.3 ± 0.5	–	22 ± 1	11.9 ± 0.5
Certified value	6.7 ± 0.5	5.5 ± 0.8	8.7 ± 0.6	23 ± 3	12 ± 1
No. 3 Chlorella					
Ultrasonic with I.S.	0.029 ± 0.001	0.55 ± 0.06	0.46 ± 0.01	(1.8)	3.5 ± 0.1
Ultrasonic without I.S.	0.021 ± 0.001	0.45 ± 0.08	0.39 ± 0.01	(1.6)	3.1 ± 0.1
ETV- ICP	–	–	–	–	–
Certified value	(0.026)	(0.60)	0.8?	0.87 ± 0.05	3.5 ± 0.3
No. 5 Human Hair					
Ultrasonic with I.S.	0.194 ± 0.002	5.6 ± 0.1	1.7 ± 0.1	(0.19)	16.0 ± 0.2
Ultrasonic without I.S.	0.173 ± 0.005	5.0 ± 0.2	1.5 ± 0.2	(0.17)	14.4 ± 0.3
ETV-ICP	–	6.1 ± 0.5	–	–	16.9 ± 1.6
Certified value	0.20 ± 0.03	(6.0)	1.8 ± 0.5	(0.10)	16.3 ± 1.2
No. 6 Mussel					
Ultrasonic with I.S.	0.78 ± 0.02	0.74 ± 0.03	0.80 ± 0.04	0.40 ± 0.02	5.2 ± 0.2
Ultrasonic without I.S.	0.66 ± 0.04	0.62 ± 0.05	0.67 ± 0.02	0.34 ± 0.01	4.4 ± 0.3
ETV-ICP	0.64 ± 0.09	0.3 ± 0.1	–	–	4.8 ± 0.5
Certified value	0.82 ± 0.03	0.91 ± 0.04	0.93 ± 0.06	(0.37)	4.9 ± 0.3
No. 7 Tea Leaves					
Ultrasonic with I.S.	0.021 ± 0.001	0.49 ± 0.04	5.8 ± 0.1	0.16 ± 0.01	6.5 ± 0.2
Ultrasonic without I.S.	0.019 ± 0.001	0.43 ± 0.04	5.1 ± 0.1	0.14 ± 0.01	5.7 ± 0.1
ETV-ICP	–	–	–	–	–
Certified value	0.03 ± 0.003	0.80 ± 0.03	6.5 ± 0.3	(0.12)	7.0 ± 0.3

[a] Number of measurements = 3, internal standard = Be, –: not determined

transported larger amounts of analyte to a plasma than pneumatic systems with corresponding amounts of matrix in a sample solution, which cause interference. However, it is not clear in which step was dominant, the nebuliser, desolvation or plasma [7,8]. An internal standard method would be essential to apply an ultrasonic system to a variety of practical samples. Either the matrix matching at least for major constituents or the standard addition method was recommended.

In addition, large amounts of alkali and/or alkaline earth metals contained in the samples analyzed caused the slight devitrification of a transparent quartz torch.

REFERENCES

1 C.E. Taylor and T.L. Floyd, Appl. Spectrosc., 35 (1981) 408.
2 J.M. Mermet and C. Trassy, in R.M. Barnes (Ed.), Developments in Atomic Plasma Spectrochemical Analysis, Heyden, London, 1981, pp. 245.
3 P.D. Goulden and D.H. Anthony, Anal. Chem., 56 (1984) 2327.
4 Y.Q. Tang and C. Trassy, Spectrochim. Acta, 41B (1986) 143.
5 P.E. Walter and C.A. Barnardt, Spectrochim. Acta, 43B (1988) 325.
6 P.W.J.M. Boumans and F.J. De Boer, Spectrochim. Acta, 27B (1972) 391.
7 P.W.J.M. Boumans and F.J. De Boer, Spectrochim. Acta, 30B (1975) 309.
8 P.W.J.M. Boumans and F.J. De Boer, Spectrochim. Acta, 31B (1976) 355.
9 K.W. Olsen, W.J. Haas Jr., and V.A. Fassel, Anal. Chem., 49 (1977) 632.
10 M.A. Floyd, V.A. Fassel, T.W. Winge, J.M. Katzenberger and A.P. D'Silvia, Anal. Chem., 52 (1980) 431.
11 V.A. Fassel and B.R. Bear, Spectrochim. Acta, 41B (1986) 1089.
12 P.W.J.M. Boumans and F.J. De Boer, Proc. Anal. Div. Chem. Soc., 12 (1975) 140.
13 K.J. Fredeen, Am. Lab., 22 (1990) 22.
14 G.A. Petrucci and J.C. Van Loon, Spectrochim. Acta, 45B (1990) 959.
15 J. Anderson, At. Spectrosc., 13 (1992) 99.
16 I.B. Brenner, P. Bremier and A. Lemarchand, J. Anal. At. Spectrom., 7 (1992) 819.
17 S.S. Berman, J.M. McLaren and S.N. Willie, Anal. Chem., 52 (1980) 488.
18 T.M. Castillano, N.P. Vela, J.A. Caruso and W.C. Story, J. Anal. At. Spectrom., 7 (1992) 807.
19 H. Isoyama, T. Uchida, T. Niwa, C. Iida and G. Nakagawa, J. Anal. At. Spectrom., 4 (1989) 351.
20 H. Isoyama, T. Uchida, K. Oguchi, C. Iida and G. Nakagawa, Anal. Sci., 6 (1990) 385.
21 M.A. Tarr, G. Zhu and R.F. Browner, Appl. Spectrosc., 45 (1991) 1424.
22 A.P. Weber, R. Keil, L. Tobler and U. Baltensperger, Anal. Chem., 64 (1992) 672.
23 M.A. Tarr, G. Zhu and R.F. Browner, J. Anal. At. Spectrom., 7 (1992) 813.
24 R.H. Clifford, P. Sohal, H. Liu and A. Montaser, Spectrochim. Acta, 47B (1992) 1107.
25 H. Isoyama, T. Uchida, C. Iida and G. Nakagawa, J. Anal. At. Spectrom., 5 (1990) 307.
26 H. Isoyama, S. Okuyama, T. Uchida, M. Takeuchi, C. Iida and G. Nakagawa, Anal. Sci., 6 (1990) 555.

Analytica Chimica Acta, 283 (1993) 887–893
Elsevier Science Publishers B.V., Amsterdam

On-line microcolumn preconcentration with desolvation and determination of trace elements by flow-injection inductively coupled plasma atomic emission spectrometry

Xuejun Peng

Department of Chemistry, Xiamen University, Fujian 361005 (China)

Zucheng Jiang and Yun'e Zen

Department of Chemistry, Wuhan University, Wuhan 430072 (China)

(Received 27th April 1993; revised manuscript received 8th July 1993)

Abstract

A desolvation device was connected to a microcolumn (40 mm × 3.0 mm i.d.) in which 8-hydroxyquinoline-5-sulphonic acid was immobilized on the substrate of active carbon–silica gel. The analyte and 1.0 M sodium acetate–acetic acid buffer solution (pH 5.6) were mixed and pumped through the microcolumn. The analyte was then preconcentrated and eluted from the column with 2.0 M hydrochloric acid. The efficiency of desolvation, improvement in sensitivity and signal stability over the temperature range 70–120°C were studied in detail. It was found that aluminium, copper, cadmium, iron and manganese could be separated from various co-existing elements with a sample volume of 1.2 ml and a carrier flow-rate of 1.2 ml min^{-1}. The desolvation efficiency at a desolvation temperature of 120°C was 73%. The column could be used more than 100 times. The detection limits for the above metal ions were 0.34–5.1 ng ml^{-1} and the relative standard deviations ($n = 6$) were 2.6–4.3%. The reliability of the method was confirmed for the analysis of human serum, and the results were in good agreement with those given by graphite furnace atomic absorption spectrometry.

Keywords: Atomic emission spectrometry; Inductively coupled plasma spectrometry; Flow injection; Sample preparation; Desolvation; Preconcentration; Serum; Trace elements

The signal intensity of the analyte in inductively coupled plasma atomic emission spectrometry (ICP-AES) depends on several factors including the ICP operating conditions and the amounts of analyte, matrix and aerosol. It has been shown that solvent molecules apparently influence the ICP discharge characteristics because of the extra consumption of plasma energy, which makes the excitation temperature decrease in the evaporation and dissociation process. Various kinds of desolvation devices have been developed for ICP-AES to improve the detection limits [1,2].

An on-line flow-injection (FI) sample introduction system incorporated with a microcolumn preconcentration manifold for ICP-AES has been reported to be the most effective means for the determination of trace elements [3,4]. The system allows high enrichment factors with limited amounts of sample and improves the precision and the speed of analysis. In addition, the possibilities of contamination and losses are considerably decreased. After separating the analyte from

Correspondence to: Xuejun Peng, Department of Chemistry, Xiamen University, Fujian 361005 (China).

interfering matrix, the detection limit for most elements can be improved by one or two orders of magnitude.

Various solid–liquid extraction systems have been proposed for preconcentration purposes [5]. 8-Hydroxyquinoline (HQ) as a selective functionality chelating reagent has been widely employed for immobilization on many substrates such as silica [6], controlled-pore glass [7–10], resins [11,12], active carbon [13], cellulose [14] and C_{18} material [15–17] for the determination of trace elements, neutral organic compounds and inorganic anions. Its derivative 8-hydroxyquinoline-5-sulphonic acid (HQSH) has been used in liquid chromatography and capillary zone electrophoresis [18,19], but there have been few reports of its use in the ICP-AES detection of trace elements with an on-line preconcentration system [20].

In this work, HQSH immobilized on an active carbon–silica gel substrate was developed for FI microcolumn on-line preconcentration and ICP-AES determination of trace elements. A desolvation system was used to improve the sensitivity for the determination of trace elements; at a desolvation temperature of 120°C, analyte concentrations as low as the ng ml^{-1} level could be simultaneously determined by the proposed method. The results obtained for copper, manganese, iron, aluminium and cadmium in human serum were in good agreement with those given by graphite furnace atomic absorption spectrometry (GFAAS)

EXPERIMENTAL

Apparatus

A schematic diagram of the desolvation and on-line preconcentration FI–ICP-AES system is shown in Fig. 1. A 2-kW, 27 ± 3 MHz ICP spectrometer (Beijing Broadcast Instrument Fact.) equipped a conventional plasma torch and pneumatic nebulization with a two-layer glass spray chamber were used. Other equipment included an HFS-2 peristaltic pump (Hitachi), furnished with three-way rotatory valve, a PC-1500 microcomputer (Sharp), a UV-3000 dual-wavelength–dual-recording spectrophotometer (Shimadzu) and a pH meter (Shanghai Reichi Fact.). A microcolumn (40 mm × 3.0 mm i.d.) and a desolvation device with a heater and a condenser were made in the laboratory [21]. PTFE tubes of 0.5 mm i.d. were used. The operating parameters are given in Table 1.

TABLE 1

Operating parameters

Incident power	1.6 kW
Plasma Ar flow-rate	15 l min^{-1}
Nebulizer Ar flow-rate	1.2 l min^{-1}
Auxiliary Ar flow-rate	0.8 l min^{-1}
Observation height	12 mm
Entrance slit width	14 μm
Exit slit width	14 μm
Sample flow-rate	1.2 ml min^{-1}
Eluent flow-rate	1.2 ml min^{-1}
Eluent acidity	2.0 M HCl
Buffer solution	1.0 M NaOAc–HOAc (pH 5.6)
Desolvation temperature	120°C
Analytical lines	Cu 324.7, Mn 257.6, Al 309.2, Fe 259.9, Cd 326.1 nm

Reagents

Stock standard solutions of 1.0 mg ml^{-1} copper, manganese, nickel, iron, cadmium and aluminium were prepared by dissolving the pure metal or oxide in hydrochloric or nitric acid.

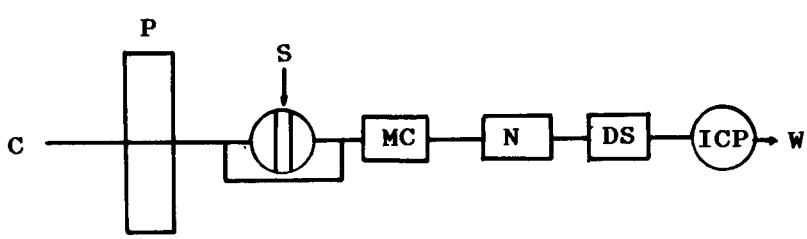

Fig. 1. Schematic diagram of desolvation and on-line FI–ICP-AES system. P = Peristaltic pump; C = carrier; MC = microcolumn; DS = desolvation device; W = waste; S = sample.

Working standard solutions at the $\mu g\ ml^{-1}$ level were prepared by dilution.

Buffer solutions of 1.0 M sodium acetate–acetic acid (NaOAc–HOAc) (pH 3.19–6.22) were prepared. HQSH (0.5%) was obtained from Sigma. The active carbon–silica gel (AG) substrate was prepared in the laboratory by a recommended method [22]. Human serum freshly stored in a polyethylene bottle below 0°C was provided by the Medical Academy of Hubei. Analytical-reagent grade reagents and doubly distilled water were used throughout.

Preparation of column packing material

Organic reagents are usually immobilized on substrates in a chemical or physical manner. In this work, the substrate was immersed in the organic reagent solution to prepare the packing material on which the reagent was loaded by adsorption. A 1.0-g amount of AG was added to 0.5% HQSH solution, the mixture was maintained at 40°C for 24 h, then filtered and washed with water and the residue was transferred to a dryer at 160°C for 8 h. After cooling to room temperature, a black powder with HQSH immobilized on AG was obtained.

A 0.1000-g amount of this packing material was weighed and mixed with water, then the slurry was filled into the microcolumn and equilibrated with water. A Glass-fibre plug was used to prevent leakage of the packing material from the microcolumn.

Recommended procedure

A test solution containing 1.0 $\mu g\ ml^{-1}$ of each analyte was pumped through the microcolumn at a suitable flow-rate; the metal ions reacted with HQSH and were retained on the microcolumn. The column was washed with buffer solution (pH 5.6) and then eluted with 2.0 M hydrochloric acid. The eluate was led directly to the desolvation device where the aerosol molecules of water were partly desolvated, and the dry aerosol was introduced into the ICP with argon gas and the spectral signal of the analyte was simultaneously recorded.

RESULTS AND DISCUSSION

Characteristics of reaction of HQSH with metal ions

Reactions of HQSH with some metal ions in NaOAc–HOAc buffer solution of pH 3.19–6.22 were studied in detail. It was found that Al^{3+}, Co^{2+}, Cd^{2+}, Cu^{2+}, Mn^{2+}, Fe^{3+} and Ni^{2+} could react rapidly with HQSH and formed stable complexes. The order of stability was $Fe^{3+} > Al^{3+} > Ni^{2+} > Mn^{2+} \approx Cd^{2+} \approx Cu^{2+}$. However, alkali metal and alkaline earth metal ions did not react with HQSH under these conditions.

Determination of adsorption capacity

A 0.1-g amount of packing material of HQSH immobilized on AG was added to 1.0 M NaOAc–HOAc buffer solution (pH 5.6), then the solution containing 20 mg the analyte was added and the mixture was stirred for 24 h, the metal ions becoming adsorbed. After filtration and washing, the amounts of metal ions in the filtrate were determined and the static adsorption capacity of each metal ion was calculated (Table 2).

A mixed solution (pH 5.6) containing 50 $\mu g\ ml^{-1}$ of each metal ion was pumped through the microcolumn until the signal intensity reached a stable value; after washing out the unreacted metal ions with buffer solution (pH 5.6), 2.0 M HCl was used to elute the analyte from the microcolumn. The dynamic adsorption capacity of each metal ions was calculated (Table 2).

It was found that the static and dynamic adsorption capacities were approximately the same. This also demonstrated that HQSH immobilized

TABLE 2

Adsorption capacities ($mg\ g^{-1}$) [a]

Element	Static [b]	Dynamic
Cu	4.65	4.09
Mn	4.02	3.53
Fe	6.13	5.38
Cd	8.22	7.22
Al	2.96	2.60
Ni	4.99	3.77

[a] Means of triplicate determinations. [b] With conventional ICP-AES method.

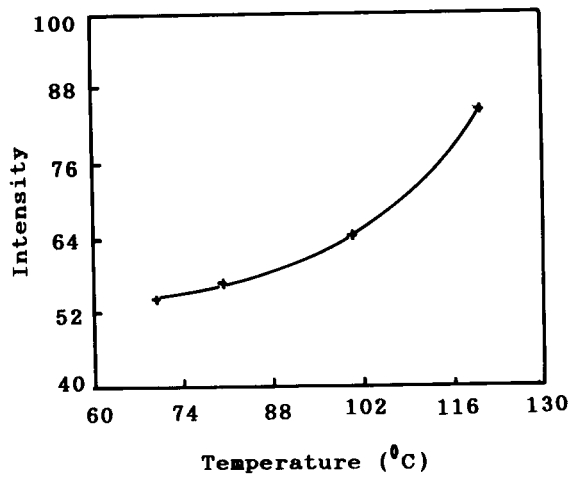

Fig. 2. Effect of desolvation temperature. Conditions: Cu^{2+} 1.0 μg ml^{-1}, flow-rate 1.2 ml min^{-1}, sample volume 1.2 ml, pH 5.6 buffer solution, 2.0 M HCl eluent.

on AG can react rapidly with the above metal ions.

Effect of desolvation temperature

It is obvious from Fig. 2 that the signal intensity increased with increasing desolvation temperature between 70 and 120°C. Therefore, a desolvation temperature of 120°C was chosen. At this temperature a desolvation efficiency of 34% was obtained and a sample introduction efficiency of 73% was determined [21].

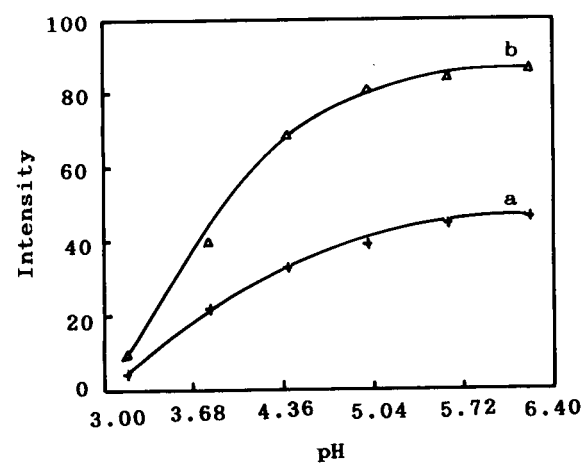

Fig. 3. Effect of pH. Sample volume: (a) 1.2 and (b) 0.6 ml. Conditions: F_c 1.2 ml min^{-1}, Cu^{2+} 1.0 μg ml^{-1}, 2.0 M HCl eluent, 120°C.

TABLE 3

Effect of pH on retention efficiencies and enrichment times [a]

pH	Enrichment times		Retention efficiency (%)	
	1.2 ml [b]	0.6 ml [b]	1.2 ml [b]	0.6 ml [b]
3.19	2.40	1.15	13.4	12.0
3.80	8.30	4.17	46.5	44.4
4.40	14.4	6.77	80.2	78.3
5.00	16.7	8.33	93.0	87.0
5.60	17.5	9.17	97.7	95.7
6.22	17.9	9.58	100	100

[a] Conditions: Cu^{2+} 1.0 μg ml^{-1}, F_c = 1.2 ml min^{-1}, 120°C, 2.0 M HCl. [b] Sample volume.

Effect of pH

The preconcentration behaviour of the analyte using buffers of different pH was studied (Fig. 3). It was found that the signal intensity increased with the increase in pH. At pH 5.0, the signal reached a stable value, indicating that the chelating reaction had gone to completion. In this work, 1.0 M NaOAc–HOAc buffer solution of pH 5.6 was chosen as the medium for preconcentration, with which optimum enrichment factors and retention efficiency were obtained (Table 3).

Effect of sample volume

Figure 4 shows that the signal intensity increased with increase in sample volume, owing to

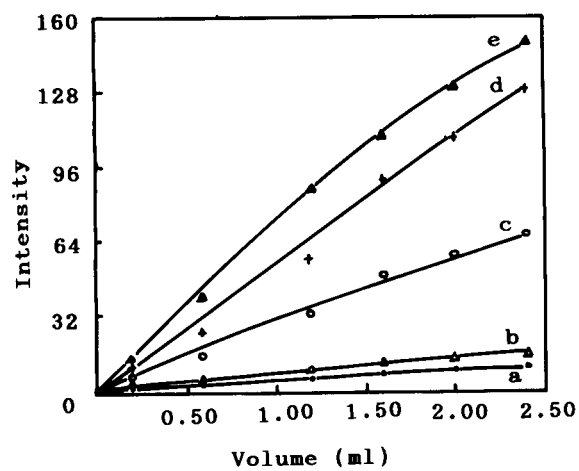

Fig. 4. Effect of sample volume. (a) Cu 1.0 μg ml^{-1}; (b) Mn 1.0 μg ml^{-1}; (c) Al 2.0 μg ml^{-1}; (d) Fe 1.0 μg ml^{-1}; (e) Cd 1.0 μg ml^{-1} Conditions: F_c 1.2 ml min^{-1}, pH 5.6 buffer solution, 2.0 M HCl eluent, 120°C.

TABLE 4

Effect of sample volume on retention efficiencies (RE) and enrichment times (k) [a]

Sample volume (ml)	Parameter	Cu	Mn	Al	Fe	Cd
0.4	k	2.92	5.41	4.14	7.16	15.67
	RE (%)	95.3	96.2	97.3	96.8	94.2
0.6	k	9.07	12.9	8.08	12.2	21.2
	RE (%)	95.7	95.1	97.8	95.7	93.2
1.2	k	18.0	29.9	17.2	25.7	32.9
	RE (%)	97.7	94.6	97.0	96.2	94.1
1.6	k	22.9	47.4	25.8	36.5	49.6
	RE (%)	97.2	94.8	96.5	94.7	94.3
2.4	k	31.3	66.0	35.5	37.2	59.1
	RE (%)	95.4	93.7	95.8	93.6	92.8

[a] Conditions: Cu^{2+} 1.0 μg ml^{-1}, flow-rate 1.2 ml min^{-1}, 120°C, pH 5.6, 2.0 M HCl.

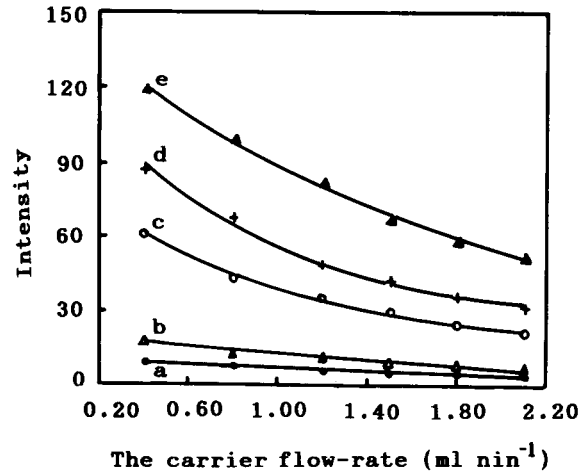

Fig. 5. Effect of carrier flow-rate. (a) Cu 1.0 μg ml^{-1}; (b) Mn 1.0 μg ml^{-1}; (c) Al 2.0 μg ml^{-1}; (d) Fe 1.0 μg ml^{-1}; (e) Cd 1.0 μg ml^{-1} Conditions: sample volume 1.2 ml, pH 5.6 buffer solution, 2.0 M HCl eluent, 120°C.

the increased amounts of metal ions in the column; however, a large sample volume leads to a long analysis time and breakthrough may also occur. A sample volume of 1.2 ml was chosen, which gave a sample frequency of 12 h^{-1} was achieved.

The enrichment factors also increased with increase in sample volume (Table 4), but there was no influence on the retention efficiency over the range of the dynamic adsorption capacity of the analyte.

Effect of the carrier flow-rate (F_c)

The signal intensities and enrichment factors decreased with increase in F_c (Fig. 5, Table 5). This was due to the incomplete preconcentration and serious dispersion at high F_c. An F_c of 1.2 ml min^{-1} was adopted in subsequent experiments.

Effect of eluent acidity

Acidity of the eluent over the range 0.01–4.0 M HCl was tested. As can be seen from Fig. 6, 2.0 M HCl completely eluted the analyte from the column. Under this condition, the column could be used more than 100 times.

Precision and detection limits

A solution containing 1.0 μg ml^{-1} each of Cu^{2+}, Mn^{2+}, Fe^{3+}, Cd^{2+} and 2.0 μg ml^{-1} of Al^{3+} was pumped through the microcolumn for six replicate analyses. The relative standard deviations (R.S.D.s) for the above metal ions were 4.3, 2.7, 2.6, 2.8 and 2.8%, respectively, at the 95% confidence level and the detection limits were 0.34, 0.52, 3.1, 5.1 and 1.8 ng ml^{-1}, respectively.

Interference studies

The ICP interferences from 1.0 mg ml^{-1} Na^+, Ca^{2+} and Mg^{2+} and 0.5 mg ml^{-1} NH_4^+, Cr^{3+} and Ni^{2+} passed through the column with which the analytes were tested. These ions had no influence on the signal intensity.

TABLE 5

Relationship between retention efficiency (%) and F_c [a]

Element	F_c (ml min^{-1})					
	0.4	0.8	1.2	1.5	1.8	2.1
Cu	24.8	20.5	17.4	14.1	11.6	11.0
Mn	45.3	30.1	29.7	23.0	18.3	15.7
Al	31.0	20.2	17.3	15.4	13.7	10.4
Fe	43.6	31.2	25.7	23.7	23.5	22.8
Cd	52.7	33.9	32.9	30.6	33.6	26.67

[a] Means of triplicate determinations. Conditions: sample volume 1.2 ml, pH 5.6, 2.0 M HCl, 120°C.

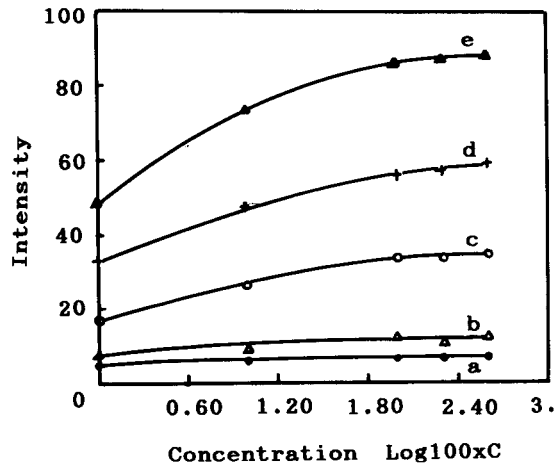

Fig. 6. Effect of eluent acidity. (a) Cu μg ml^{-1}; (b) Mn 1.0 μg ml^{-1}; (c) Al 2.0 μg ml^{-1}; (d) Fe 1.0 μg ml^{-1}; (e) CD 1.0 μg ml^{-1}. Conditions: pH 5.6 buffer solution, sample volume 1.2 ml, F_c 1.2 ml min^{-1}, 120°C.

Analysis of human serum

A 5.0-ml volume of human serum was dissolved in small volume of perchloric acid–nitric acid (1 + 4, v/v). After immersing 2 h, the sample solution was heated gently and further portions of the acid mixture were added until the sample solution became clear. The mixture was evaporated to a small volume (about 0.5 ml) and transferred into a 25-ml volumetric flask, diluted to volume with water and analysed according to the proposed procedure. The analytical results for 5 ml human serum are given in Table 6. The results were in good agreement with those obtained by a GFAAS method [23,24]. The regression equations for cadmium, iron, aluminium, manganese and copper over the concentration range 0–100 ng ml^{-1} were as $I_{Cd} = 0.0567[Cd^{2+}] + 0.023$, $I_{Fe} = 0.095[Fe^{3+}] + 0.088$, $I_{Al} = 0.3458[Al^{3+}] + 0.026$, $I_{Mn} = 0.5029[Mn^{2+}] - 0.054$ and $I_{Cu} = 0.8000[Cu^{2+}] - 0.086$; the regression coefficients were 0.9973, 0.9988, 0.9997, 0.9999 and 0.9997, respectively.

TABLE 6

Determination of trace elements (μg ml^{-1}) in human serum

Element	This method [a]	GFAAS [b]
Cu	1.12 ±0.05	1.18
Mn	0.27 ±0.01	0.31
Al	0.017±0.001	0.016
Fe	1.25 ±0.03	1.24
Cd	0.016±0.001	0.020

[a] Mean ± S.D. of six determinations at the 95% confidence level. [b] According to [23,24].

Conclusions

The sensitivity and selectivity could be effectively improved by desolvation and on-line microcolumn preconcentration of the analyte prior to ICP-AES determination. An organic solvent could probably be used as the eluent in this system of on-line column preconcentration with desolvation in trace element determinations by ICP-AES.

REFERENCES

1 A. Canals, J. Wagner, R.F. Browner and V. Hernandis, Spectrochim. Acta, Part B, 43 (1988) 1321.
2 D.R. Wiederin and R.S. Houk, Anal. Chem., 62 (1990) 1155.
3 S. Hirata, Y. Umezaki and M. Ikeda, Anal. Chem., 58 (1986) 2602.
4 S.D. Hartenstein, J. Ruzicka and G.D. Christian, Anal. Chem., 57 (1985) 21.
5 V. Kuban and F. Ingman, CRC Crit. Rev. Anal. Chem., 22 (1991) 491.
6 R.E. Sturgeon, S.S. Willie and J.A.H. Desanlines, Anal. Chem., 53 (1981) 2337.
7 R.E. Santelli, M. Gallego and M. Valcarecel, J. Anal. At. Spectrom., 4 (1989) 547.
8 M.A. Marshall and H.A. Mottola, Anal. Chem., 57 (1985) 729.
9 Z. Fang, J. Ruzicka and E.H. Hansen, Anal. Chim. Acta, 164 (1984) 23.
10 Z. Fang, Z. Zhu, S. Zhang, S. Xu, L. Guo and L. Sun, Anal. Chim. Acta, 214 (1988) 41.
11 R. Purohit and S. Devi, Talanta, 38 (1991) 753.
12 W.M. Landing, C. Heraldson and N. Paxews, Anal. Chem., 58 (1986) 3031.
13 Y. Okamoto, A. Murata and T. Kumamura, Anal. Sci., 7 (1991) 879.
14 E. Beinrohr, M. Cakrt, J. Garaj and M. Rapta, Anal. Chim. Acta, 230 (1990) 163.
15 J. Ruzicka and A. Krndal, Anal. Chim. Acta, 216 (1989) 243.
16 H.W. Thompson and J.R. Jezorek, Anal. Chem., 63 (1991) 75.
17 H. Watanabe, K. Goto, S. Taguchi, T.W. McLaren, S.S. Berman and D.S. Russel, Anal. Chem., 53 (1981) 738.

18 A.E. Mentasti, A. Nicolotti, V. Porta and C. Sarzanini, Analyst, 114 (1989) 1113.
19 D.F. Sweile and M.J. Sepanick, Anal. Chem., 63 (1991) 179.
20 S. Devi, K.A.J. Habib and A. Townshend, Quim. Anal., 8 (1989) 159.
21 X.-J. Peng, Z.-C. Jiang and Y. Zeng, Guangpuxue Yu Guangpu Fenxi, in press.
22 Z. Yu, L. Li and J. Cheng, Pure Chemical Reagents: Part 1, Higher Education Press, Beijing, 1955, p. 315.
23 X.-H.Wu, G.-C. Cui and Y. Peng, Fenxi Huaxue, 19 (1991) 1352.
24 Y.-Q. Jiang, J.-Y. Yao and B.-L. Huang, Fenxi Huaxue, 17 (1989) 692.

Analytica Chimica Acta, 283 (1993) 895–901
Elsevier Science Publishers B.V., Amsterdam

Simultaneous atomic fluorescence spectrometric determination of traces of iron, cobalt and nickel after conversion to their carbonyls and gas-phase atomization by microwave-induced plasma

Vladimir Rigin

Research and Design Institute for Problems of Development of the Kansk–Achinsk Coal Basin, Kirensky-street 87, Krasnoyarsk 660041 (Russian Federation)

(Received 17th March 1992; revised manuscript received 26th April 1993)

Abstract

In sample solution iron-group metals are converted into volatile carbonyls by means of reductive carbonylation by simultaneous treatment with carbon monoxide and $NaBH_4$. The carbonyls released are collected in a cold trap packed with pyrolytic carbon filaments that have been treated preliminarily with a low-pressure oxygen plasma. This packing serves for gas chromatographic concentration and separation of carbonyl, with wide bandwidth atomic fluorescence spectrometric monitoring. To eliminate problems arising from the relatively slow formation of carbonyls of iron and cobalt, sub-quantitative isolation of these carbonyls was used. For atomic fluorescence measurements a laboratory-made fibre-optic spectrometer with atomization by means of a microwave-induced plasma was used. The detection limits were 5 pg for Fe, 3 pg for Ni and 20 pg for Co. The proposed method was used for the analysis of pure water and some other materials. Solid samples were dissolved with XeF_4 in an autoclave.

Keywords: Atomic fluorescence spectrometry; Cobalt; Iron; Nickel

Spectrometric control of microelements in natural and industrial materials is a routine analytical task in many branches of industry and science. For this purpose one uses very powerful and expensive apparatus such as high-resolution spectrometers and gas chromatographs–mass spectrometers. These devices allow the simultaneous determination of many microelements. However, the real need for such simultaneous determinations of large numbers of microelements occurs only in the analytical control of materials that must be analysed only very rarely. Usually an industrial laboratory deals with the same product, samples of which have roughly the same chemical composition and are manufactured with constant technology. In that event one needs to determine only a few of the most important microelements that characterize the technology used and the purity of the materials. The determination of such a restricted list of microelement indicators can often be achieved with simple and cheap apparatus.

Iron-group metals are highly attractive as such indicator microelements owing to their widespread occurrence in nature and industry. The contents of these metals in pure materials often indicates both the quality of the material and the

Correspondence to: V. Rigin, Research and Design Institute for Problems of Development of the Kansk–Achinsk Coal Basin, Kirensky-street 87, Krasnoyarsk 660041 (Russian Federation)

effectiveness of the processes used for manufacture and purification [1]. For instance, the appearance and accumulation of microamounts of Fe, Co, Ni in primary circuit coolant water of nuclear power plants serves as indicators of the beginning of corrosion of the steam supply system, tanks, pumps and pipe lines, i.e., units in contact with coolant water [2]. Hence their determination is an important task in the analytical control of water-handling facilities of nuclear power plants [3]. Iron-group metals are also the most important impurities in semiconductor materials [4].

Frequently the presence of adverse contents of iron-group metals lies much lower than detection limits of the most routine spectrometric methods. Most of the usual preconcentration techniques are connected with both uncontrollable losses of microelements to be determined and unpredictable contamination of sample [5]. Moreover, in most reagents used in preconcentration procedures the certified contents of iron-group metals exceeds their contents in the analyte materials, occasionally by several orders of magnitude. Because of this, the search for an efficient preconcentration technique is a crucial part of the elaboration of an acceptable spectrometric method of analysis.

In some instances the microelements of interest may be converted into gaseous (volatile) compounds and then isolated as a gas-phase analytical concentrate [6]. Such an approach allows these elements to be concentrated and separated by gas chromatography, during which the concentrate must be kept free from contamination.

Iron-group metals form reasonably stable, volatile carbonyls that may serve for obtaining a gas-phase concentrate for analysis. The most effective procedure for the conversion of these metals into carbonyls consists in reductive carbonylation of their solution, i.e., simultaneous treatment of a sample solution with carbon monoxide and a strong reducing agent such as $NaBH_4$. Nickel reacts very rapidly and is completely converted into a gas-phase concentrate in a very short time. This technique has been used for nickel determination in marine water [7–9]. Iron and cobalt react relatively slowly, so that complete conversion of these metals into a gas-phase concentrate is not achieved in a reasonable time. In this event one can apply the sub-quantitative (or rather sub-stoichiometric) isolation of the elements to be determined, as described elsewhere [10].

In this paper a selective method for the determination of microamounts of Fe, Co and Ni in pure materials, is described based on the use of gas-phase concentrates and final monitoring by atomic fluorescence spectrometry.

EXPERIMENTAL

Apparatus

For reductive carbonylation carbon monoxide free from the slightest traces of iron-group metals is required. Commercially available pure carbon monoxide is always contaminated with considerable amounts of volatile compounds of iron-group metals, because the gas is packed in steel cylinders. Carbon monoxide of the required purity was obtained by the high-temperature reaction of calcium carbonate with zinc dust. This reaction proceeds at temperature above 700°C. The rate of carbon monoxide production can be regulated by varying the temperature in the reaction zone. Figure 1 shows the apparatus used. The reactor is a quartz tube (550 mm × 38 mm i.d. × 44 mm o.d.), sealed at one end, that is loaded to two thirds of its full length with a fine mixture of $CaCO_3$ and zinc dust, the latter present in twice the amount required for the stoichiometric relationship. The reactor is equipped with an external heating coil that is supplied with a continuous thermocouple controller for monitoring the temperature of the reaction zone.

The system for purification of the gas obtained includes a water cooler for condensation of zinc vapour, a Drechsel bottle containing 2-propanol for gas scrubbling, a Fresenius column filled with granulated lithium oxide, a PTOM-type fine gas filter made of sintered titanium sponge, and a rheometer for control of the gas flow-rate. When Z-50 zinc dust (Russia) and $CaCO_3$ of "chromatographic purity" grade were used no traces of iron-group metals were detected in the gas ob-

tained using methods such as chromatography–mass spectrometry and neutron activation analysis.

The carbonylator for sample solution treatment is a Drechsel bottle with a thermostated water-jacket; the temperature of the solution can be adjusted in diapasone from 20 to 60°C with an accuracy of ±0.5°C. The trap for recovery of the carbonyl from the carbonylator gases consists of a dryer filled with granulated anhydrous magnesium perchlorate and a cold trap made of coiled quartz tubing (1220 mm × 6 mm i.d. ×8 mm o.d.) packed with pyrolytic carbon filaments that had been treated with a low-pressure oxygen plasma. This packing serves both for trapping metal carbonyls and for their gas chromatographic separation and isolation. The cold trap temperature was maintained at −60 ± 1°C by means of dry-ice–acetone.

A schematic diagram of the laboratory-made atomic fluorescence spectrometer is shown in Fig. 2. The spectrometer is mounted from preassembled modules: (A) source of excitation radiance, (B) atomization unit and (C) registration unit. The modules are connected with each other by quartz fibre-optic conduits.

A gas-phase analytical concentrate requires much less thermal energy for atomization than solid or liquid samples. The case considered provides an excellent possibility of using a low-power microwave-induced plasma for atomization. The atomization unit module includes an EHR 541/N Beenakker-type microwave resonator (Electromedical Supplies, UK) that is powered by a Radarmed microwave generator (Bosch Elektronik, Germany) with frequency 2450 MHz at an incident power of 50 W and a reflected power of less than 1 W. Atomization of the gas-phase concentrate takes place in a zirconia ceramic capillary (60 mm × 1.45 mm i.d. ×1.95 mm o.d.) that is installed in the active zone of the resonator. The atomic fluorescence measurements

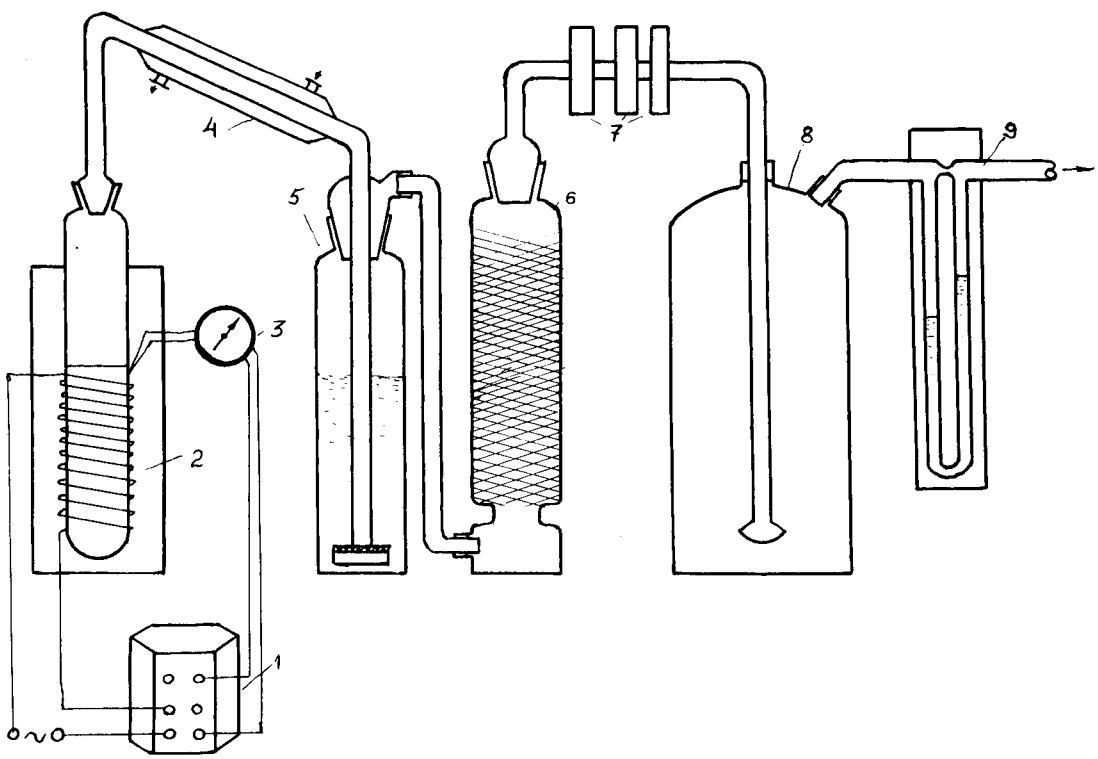

Fig. 1. System for obtaining pure carbon monoxide. 1 = Current regulator for heating coil; 2 = reaction quartz tube containing a mixture of Zn and $CaCO_3$; 3 = thermocouple monitor; 4 = quartz water cooler; 5 = Drechsel bottle containing 2-propanol; 6 = Fresenius column containing lithium oxide; 7 = PTOM fine gas filter; 8 = compensating manostat bottle; 9 = rheometer.

were carried out using a plasma torch above the outlet of the capillary.

The source of excitation radiance module contains an L 5212 miniature xenon flash-lamp (Perkin-Elmer), power 8.3 W, working in the impulse mode. The duration of an impulse is 50 μs and the impulse frequency is 230 Hz. The lamp radiation is focused on the face of a fibre-optic light conduit by means of a plano-concave quartz lens of focal length 110 mm and diameter 20 mm, and then transmitted to the atomization module. The transmitted radiation flux is focused on the plasma torch by means of a quartz lens of focal length 120 mm and diameter 16 mm.

The fluorescent radiation is registered at right-angles to the exciting radiation beam. The fluorescence radiation flux is collected by a quartz lens of focal length 150 mm and diameter 30 mm and focused on the face of a fibre-optic cable that transfers this radiation to the registration module.

Atomic fluorescence radiation is detected with an FEU-101 photomultiplier (Russia) equipped with an interference light filter and installed in a cold housing that is thermostated at −60°C by means of dry-ice–acetone. The anodic current of the photomultiplier is monitored by using a linear narrow-band amplifier with sharp tuning on the frequency of impulses of exciting radiation. The amplifier is interfaced with an elektronika-60 microprocessor (Russia) that is connected with an I-5 current integrator (Russia).

The analytical signal used was the integral of the atomic fluorescence intensity I_f, calculated by integration of the anodic current of the photomultiplier for a period from the moment of the appearance of the current signal to the moment when the anodic current returned to the "dark" value (conditional zero value).

Measurements of radioactivity were made with an MST-17 end-window counter interfaced with a B-2 digital integrator (Russia).

Procedures

In order to ascertain the optimum conditions for determination, the influences of temperature and duration of the carbonylation process on the completeness of transfer of the analyte elements from the sample solution into the final gas-phase concentrate that enters to atomizer capillary were

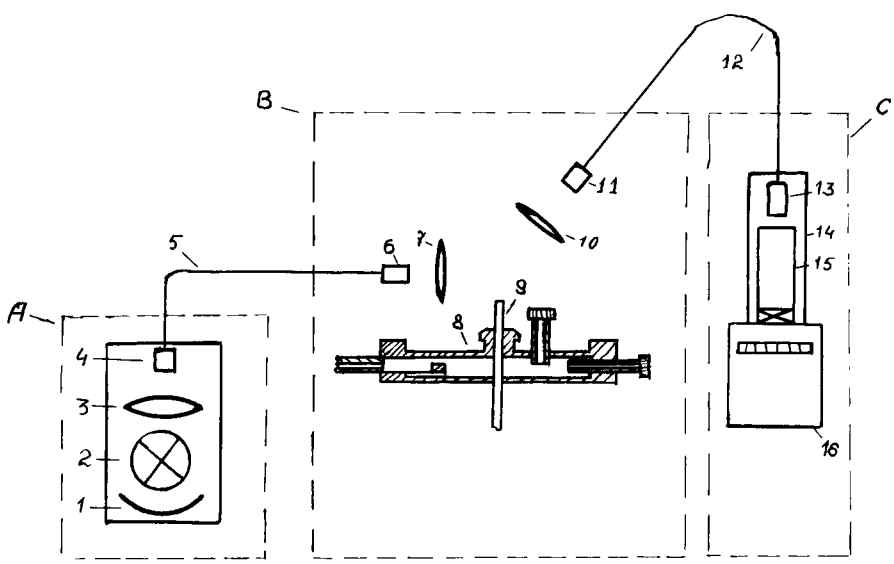

Fig. 2. Schematic diagram of atomic fluorescence spectrometer. A = source of excitation radiance; module; B = atomization module; C = registration module. 1 = Parabolic mirror; 2 = xenon arc lamp; 3, 7, 10 = focusing quartz lenses; 4, 6, 11, 13 = faces of fibre-optic cables; 5, 12 = fibre-optic cables; 8 = microwave resonator; 9 = zirconia capillary atomizer; 14 = photomultiplier housing; 15 = photomultiplier; 16 = integrator of anodic current.

investigated. The method of radioisotope tracers was used. For this purpose a few series of aqueous solutions of pure salts of Fe, Co, Ni (preferably nitrates), were prepared and labelled with ^{59}Fe, ^{60}Co, ^{65}Ni radionuclides.

The working analytical procedure is as follows. The test solution is filtered through a Vladipor membrane filter (Russia) with a pore size of 0.1 μm. An aliquot of filtrate (20–200 ml, depending on the expected contents of the analyte elements) is introduced into the carbonylator, then 1 ml of a 10% solution of thiourea and 2 ml of a 1 M solution of tris(hydroxymethyl)aminomethane are added and mixed thoroughly. After adjusting the temperature of the carbonylator, the flow of CO through the carbonylator and cold trap is regulated at a mean flow-rate of 180 ml min^{-1}. With a peristaltic metering pump (Model 314, PZM, Poznan, Poland) 10 ml of a 5% solution of $NaBH_4$ that is 0.01 M in NaOH are fed into the carbonylator at a flow-rate of 2.5 ml min^{-1}. The duration of sample treatment in the carbonylator must be set in diapasone from 5 to no more than 30 min, taking into account a reasonable total time for the whole analysis.

The gas flow from the carbonylator passes through a dryer packed with NaA and CaA zeolites, then enters a cold trap. After completion of carbonylation the cooling system of the cold trap is replaced with a heating block with programmable control of temperature. To the inlet of the cold trap is fitted a tube for feeding a mixture of pure argon and carbon monoxide (5 + 1), at a flow-rate of 120 ml min^{-1}. The outlet of the cold trap is connected with a suitable measuring system: a flow cell for the measurement of the radioactivity of the eluted gases or the atomizer capillary of the spectrometer for the measurement of atomic fluorescence. Then the temperature of the heating block is increased from −60 to 50°C at 15°C min^{-1}, and held at 50°C for 10 min. The signal obtained is monitored continuously.

The atomic fluorescence spectrometer was calibrated using pure standard solutions of iron-group metals. The starting solutions (Merck, Darmstadt) were diluted to the required concentrations with 0.05% nitric acid. Each solution was treated as described above. The effective analytical signal used was the difference between the atomic fluorescence intensity for a standard solution, $(I_f)_s$, and the background atomic fluorescence intensity, obtained by the working procedure on replacing the sample solution with an equivalent volume of pure water, $(I_f)_b$. The mean values of the effective analytical signal, estimated

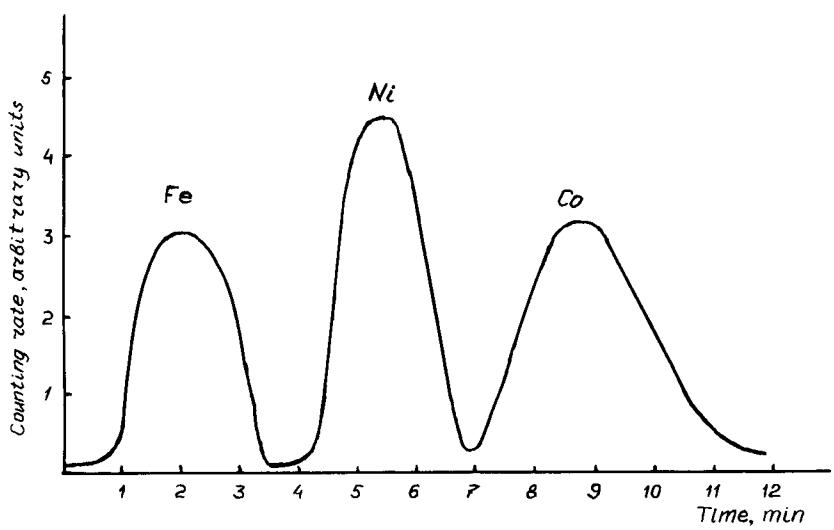

Fig. 3. Example of elution of labelled carbonyls from cold trap into gaseous phase. The content of each metal carrier is 15 ng. Total radioactivity: $^{59}Fe = 1.5 \times 10^6$; $^{60}Co = 2.4 \times 10^6$; $^{65}Ni = 2.1 \times 10^6$ counts min^{-1}.

at a temperature of the carbonylator of 50°C and a duration of sample treatment of 20 min, were used for the construction of calibration graphs for the corresponding metals.

Water-soluble (miscible) samples were analysed after dissolution in pure water; solid samples/(biological and technical) were decomposed with XeF_4 as described elsewhere [11] and then dissolved in pure water.

To establish the reliability and correctness of the proposed method, atomic emission spectrometry with a Jobin-Yvon JY-48 spectrometer was used as an independent method for comparison.

All instruments were installed in plastic gloveboxes filled with pure nitrogen at an excess pressure of ca. 100 Pa. Analytical-reagent grade reagents were used.

RESULTS AND DISCUSSION

Figure 3 shows a plot of counting rate versus time for the elution of a mixture of labelled carbonyls from the cold trap on heating. This diagram represents a chromatogram of the studied carbonyls, the observed peaks corresponding to the order of their gas chromatographic separation. It is interesting that the less volatile iron carbonyl elutes before the more volatile nickel carbonyl. This effect may be due to the peculiarities of the interaction between carbonyl molecules and the surface of the packing material.

The relatively slow formation of iron and cobalt carbonyl does not allow complete conversion of these metals to be achieved in an acceptable time for analytical purposes. To avoid this problem sub-quantitative isolation of iron and cobalt carbonyls from the sample solution was used. This technique is based on the corollary of the standard equation for chemical reaction rate: under constant conditions within equal timespans from the beginning of reaction, chemical transformations of equal parts of the initial concentrations of given components occur, whatever the absolute values of the concentrations in the reaction medium. Analytical applications of some variations of this technique have been described elsewhere [10]. It is necessary for the extent of transfer of an analyte metal into the final gas-phase concentrate to be relatively constant and to ensure large enough values of the analytical signal over the whole range of concentrations to be determined. It was established that at a temperature of carbonylation of 50 ± 1°C and a duration of sample treatment in the carbonylator of 20 ± 1 min the extent of transfer of iron is 0.83 ± 0.04 and that of cobalt is 0.69 ± 0.04. These are sufficient to ensure the reliability of proposed method.

It should be mentioned that at temperatures of carbonylation above 55°C the results for cobalt becomes unreliable, probably owing to the beginning of thermal decomposition of cobalt carbonyl.

The small volume of the final gas-phase concentrate allows low-power atomizers to be used. As the most suitable atomization method a microwave-induced plasma was used. The short path of the atomized concentrate through the hot zone of the atomizer prevents losses of atomization products on the wall of the atomizer capillary and ensures of absence of memory effects.

To confirm the reliability of proposed technique the standard reference material SRM 1643a Trace Elements in Water (NIST, Gaithersburg, MD) was analysed. Iron and cobalt were deter-

TABLE 1

Analysis of NIST SRM 1643a Trace Elements in Water

Element	Found (ng g^{-1}) [a]	Certificate value (ng g^{-1})
Fe	79 ± 6	88 ± 4
Co	17 ± 3	19 ± 2
Ni	61 ± 5	55 ± 3

[a] Mean ± 95% confidence limits, $n = 5$.

TABLE 2

Figures of merit of proposed technique

Characteristic	Element		
	Fe	Ni	Co
Instrumental detection limit (pg)	5	3	20
Lower determination range (%)	5×10^{-8}	5×10^{-9}	1×10^{-7}
Upper determination range (%)	1×10^{-3}	7×10^{-3}	3×10^{-3}

TABLE 3

Analysis of various pure materials

Material	Found by proposed technique (%) [a]			Found by independent method [b] (%)		
	Fe	Ni	Co	Fe	Ni	Co
Silicon KSD, monocrystal	$(6.7 \pm 0.8) \times 10^{-7}$	$(4.1 \pm 0.3) \times 10^{-7}$	$(9.8 \pm 1.7) \times 10^{-8}$	5×10^{-7}	3×10^{-7}	1×10^{-7}
Alumina, Suprapur	$(1.8 \pm 0.4) \times 10^{-5}$	$(4.5 \pm 0.9) \times 10^{-6}$	$(4.2 \pm 0.8) \times 10^{-6}$	3×10^{-5}	6×10^{-6}	8×10^{-6}
Sodium nitrate, Suprapur	$(2.6 \pm 0.7) \times 10^{-6}$	$(3.5 \pm 0.6) \times 10^{-7}$	$(2.1 \pm 0.6) \times 10^{-7}$	5×10^{-6}	8×10^{-7}	1×10^{-7}
Ethanol, suprapur	$(5.7 \pm 0.6) \times 10^{-7}$	$(1.5 \pm 0.4) \times 10^{-7}$	$(4.0 \pm 0.5) \times 10^{-7}$	3×10^{-7}	5×10^{-7}	5×10^{-7}
Rain water (in mountains)	$(4.4 \pm 0.3) \times 10^{-3}$	$(1.4 \pm 0.2) \times 10^{-4}$	$(3.6 \pm 0.6) \times 10^{-5}$	6×10^{-3}	1×10^{-4}	8×10^{-5}
Neve ice (East Sayan)	$(6.1 \pm 0.4) \times 10^{-3}$	$(5.0 \pm 0.3) \times 10^{-5}$	$(2.5 \pm 0.5) \times 10^{-5}$	9×10^{-3}	8×10^{-5}	6×10^{-5}

[a] Mean ± 95% confidence limits, $n = 5$. [b] Atomic emission spectrometry.

mined in the sub-quantitative mode. The results obtained were well within the limits of acceptability that may be considered as evidence of the analytical applicability of the proposed method (Table 1).

Table 2 gives some figures of merit for the proposed method. The instrumental limit of detection (ILD) is defined as the minimum amount of metal that gives an analytical signal exceeding by 3σ the mean value of the fluctuation of the conditional zero signal, i.e., the "dark" value of the anodic current of the photomultiplier. The lower determination range (LDR) corresponds to the minimum concentration of metal in a sample aliquot determined with a relative standard deviation of not more than 0.33 in triplicate analyses. The upper determination range is limited by non-compliance with the Lambert–Beer law.

The analytical possibilities of the proposed method are demonstrated by analysis of some pure materials that were analysed preliminarily by an independent method. The results obtained are given in Table 3. The good agreement of the data indicates a sufficient reliability of the proposed method.

Conclusion

A method for the simultaneous atomic fluorescence determination of picogram amounts of iron-group metals based on their conversion into volatile carbonyls with subsequent isolation in the form of a gas-phase concentrate has been developed. For iron and cobalt the sub-quantitative mode of isolation is used. For atomic fluorescence measurement a fibre-optic spectrometer with microwave gas-phase atomization and single-detector monitoring is used.

REFERENCES

1 A.I. Belyaev, E.A. Zhemchuzhina and L.A. Firsanova, Metallurgiya Chistyh Metallov i Elementarnyh Poluprovodnikov, Metallurgiya, Moscow, 1969.
2 P. Jones, K. Barron and L. Ebdon, J. Chromatogr., 354 (1986) 411.
3 O.I. Martynova, L.M. Zhivilova and H.L. Subbotina, Khimicheskij Kontrol's Vodnogo Rezhima Atomnyh Elektrostancij, Atomizdat, Moscow, 1980.
4 F.W. Voltmer and F.A. Padovani, Semiconductor Silicon, Academic Press, New York, 1973.
5 Yu. A. Zolotov and N.M. Kuz'min, Koncentrirovanie Mikroelementov, Khimiya, Moscow, 1982.
6 V.I. Rigin, Fesenius' Z. Anal. Chem., 335 (1989) 15.
7 D.C. Lee, Anal. Chem., 54 (1982) 1182.
8 J. Alary, J. Vandele and R. Harran, Talanta, 33 (1986) 748.
9 R.E. Sturgeon, S.N. Willie and S.S. Berman, J. Anal. At. Spectrom. 4 (1989) 443.
10 V.I. Rigin, J. Anal. At. Spectrom. 5 (1990) 407.
11 V.I. Rigin, Zh. Anal. Khim., 39 (1984) 648.

Analytica Chimica Acta, 283 (1993) 903–907
Elsevier Science Publishers B.V., Amsterdam

Raman scattering interference in constant-wavelength synchronous spectrofluorimetry

Yao Qun Li, Xian Zhi Huang and Jin Gou Xu

Department of Chemistry, Xiamen University, Xiamen 361005 (China)

(Received 28th April 1993; revised manuscript received 29th June 1993)

Abstract

Various aspects of the influence of Raman scattering on constant-wavelength synchronous spectra and means of decreasing the interference are discussed theoretically. General rules for dealing with the problem are described. The observations could provide guidelines for experimental design.

Keywords: Fluorimetry; Raman scattering

Raman scattering commonly occurs in solvents used in spectrofluorimetry and is a serious interfering factor in fluorescence analysis. A decrease in its contribution to the fluorescence spectra of analytes is beneficial to the identification of the fluorescence characteristics of weakly fluorescent compounds and the measurement of solvent impurities. For quantitative work, a decrease in Raman scattering is also advantageous for increasing sensitivity in fluorimetry and the optimization of detection limits. Therefore, the effect of Raman scattering has became a major problem that has attracted much attention.

Synchronous spectrofluorimetry involves generating a synchronous fluorescence spectrum by scanning the excitation and emission wavelengths simultaneously [1]. This technique has the advantages of narrowing of the spectral bands, spectral simplification and contraction of the spectral range. It has greater selectivity and gives lower detection limits than conventional spectrofluorimetry. There are three variants of synchronous spectrofluorimetry: constant-wavelength [2–5], constant-energy [6–9] and variable-angle techniques [10–12], depending on the scanning mode of the spectra. The constant-energy mode has the advantage of decreasing Raman scattering effectively [13,14], but this method has limited application. In contrast, constant-wavelength synchronous spectrofluorimetry is widely employed owing to its simplicity. A suggestion has been proposed to decrease the effect of Raman scattering [15]. In this paper, various aspects of the influence of Raman scattering on constant-wavelength synchronous spectra and means of decreasing the interference are discussed theoretically. General rules for dealing with the problem are described using simple illustrations.

Correspondence to: Y.Q. Li, Department of Chemistry, Xiamen University, Xiamen 361005, China.

THEORY

Common solvents used in fluorimetry exhibit Raman scattering. Although the wavelength of Raman scattering is not constant, there is a fixed difference, $\Delta\bar{\nu}_R$, i.e., the Raman transition energy, between the emission frequency and excitation frequency in a given solvent, which corresponds to a vibrational quantum of the solvent molecule.

If λ_{em} and λ_{ex} (nm) are the wavelengths of the emission monochromator and excitation monochromator, respectively, then for constant-wavelength synchronous spectrofluorimetry a constant interval between λ_{em} and λ_{ex} ($\Delta\lambda = \lambda_{em} - \lambda_{ex}$) is maintained during spectral scanning. Consequently, the energy difference, $\Delta\bar{\nu}_\lambda$, between the excitation and emission monochromators can be expressed as

$$\Delta\bar{\nu}_\lambda = 10^7(1/\lambda_{ex} - 1/\lambda_{em})$$

or

$$\Delta\bar{\nu}_\lambda = 10^7\Delta\lambda/[\lambda_{ex}(\lambda_{ex} + \Delta\lambda)] \quad (1)$$

where $\Delta\bar{\nu}_\lambda$ is in cm^{-1}. It can be seen that $\Delta\bar{\nu}_\lambda$ is not constant and varies with λ_{ex}. When the value of $\Delta\bar{\nu}_\lambda$ coincides with that of $\Delta\bar{\nu}_R$ (which is constant) of the solvent during spectral scanning, Raman scattering radiation would appear. Thus,

$$\Delta\bar{\nu}_R = 10^7\Delta\lambda/[\lambda^R_{ex}(\lambda^R_{ex} + \Delta\lambda)] \quad (2)$$

where λ^R_{ex} represents the wavelength position of the Raman scattering peak on the synchronous spectrum, which can be called the synchronous Raman peak, in terms of excitation wavelength. λ^R_{ex} can be deduced from the Eqn. 2 as

$$\lambda^R_{ex} = -\Delta\lambda/2 \pm \sqrt{\Delta\lambda^2/4 + 10^7\Delta\lambda/\Delta\bar{\nu}_R} \quad (3)$$

Because λ^R_{ex} is positive,

$$\lambda^R_{ex} = \sqrt{\Delta\lambda^2/4 + 10^7\Delta\lambda/\Delta\bar{\nu}_R} - \Delta\lambda/2 \quad (4)$$

EXPERIMENTAL

Apparatus

Fluorescence measurements on *m*-dihydroxybenzene and vitamins were made with a Hitachi Model 650-10S spectrofluorimeter and those of pheophytins with a Hitachi Model 850 spectrofluorimeter. Both spectrofluorimeters were equipped with a 150-W xenon lamp. The excitation and emission slits were both set at a 5-nm bandpass.

Reagents

Doubly deionized water was used throughout. Vitamins B_2 and B_6 were biochemical reagents (99% purity). Chlorophyll *a* and *b* were purchased from Shanghai Inst. of Plant Physiol. All other chemicals were of analytical-reagent grade and used as received.

m-Dihydroxybenzene. A stock standard solution of *m*-dihydroxybenzene was prepared in water. A working standard solution was obtained by diluting the stock standard solution with disodium citrate–hydrochloric acid buffer (pH 3.0).

Vitamins. Stock standard solutions of vitamins B_2 and B_6 were prepared in water. Working standard solutions were obtained by diluting the stock standard solutions with disodium hydrogenphosphate–citric acid buffer (pH 7.0).

Pheophytins. Chlorophyll *a* and *b* solutions were prepared in acetone–water (90 + 10). The purity of each chlorophyll solution was checked by UV–visible spectrophotometry with a Beckman DU-8Bc spectrophotometer. Stock standard solutions of pheophytin *a* and *b* were prepared by the addition of one or two drops of 0.1 M hydrochloric acid to the chlorophyll solutions [16]. Working standard solutions of pheophytin *a* and *b* were prepared by diluting the stock standard solutions with acetone–water (90 + 10).

RESULTS AND DISCUSSION

The λ^R_{ex} values of a specific solvent, corresponding to various $\Delta\lambda$ values, can be calculated from Eqn. 4 and the Raman transition frequency, $\Delta\bar{\nu}_R$, is a known constant value for the solvent. The relationships between the wavelength positions of synchronous Raman peaks and $\Delta\lambda$ are illustrated in Fig. 1 for three kinds of solvents. The $\Delta\bar{\nu}_R$ values are 3380 cm^{-1} for water, 2920 cm^{-1} for ethanol and 740 cm^{-1} for tetrachloromethane. Because the second Raman scatter from ethanol with a $\Delta\bar{\nu}_R$ value of 1400 cm^{-1} is weak, it is not included in Fig. 1. The $\Delta\bar{\nu}_R$ value of cyclohexane is approximately equal to that of ethanol, hence the synchronous Raman peaks for both would appear in similar positions.

Several observations can be made from Fig. 1 and Eqn. 4.

If the chosen $\Delta\lambda$ value is very small, the synchronous Raman peak for a solvent is located at

a short wavelength where the synchronous fluorescence for most fluorescent systems rarely appears. Therefore, the interference of solvent Raman scattering with the synchronous fluorescence spectra is negligible. However, too small a $\Delta\lambda$ value would increase the interference from other kinds of scattered light such as Rayleigh scattering, Tyndall scattering and light reflected off the cell faces. To solve this problem, the placement of polarizers in the light path can suppress these kinds of scattered light, as shown in Fig. 2.

When the $\Delta\lambda$ value is relatively large, the synchronous Raman peak for a solvent is present in the long-wavelength region. Because the intensity of Raman light is proportional to $1/\lambda^4$, the synchronous Raman signal is weak in the long-wavelength region and then the interference of Raman radiation is of no importance. Further, when the selected $\Delta\lambda$ value for a system is very large, the synchronous Raman peak would shift to a region of such long wavelength that it is beyond the fluorescence-emitting range and hence has no influence on analyte measurements.

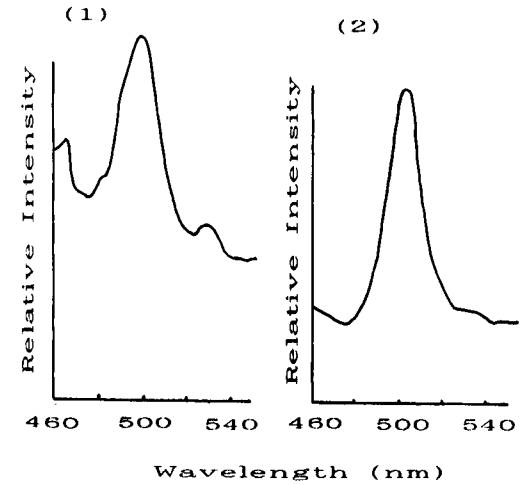

Fig. 2. Synchronous fluorescence spectra of 6 ng ml^{-1} fluorescein. $\Delta\lambda = 5$ nm. (1) Normal; (2) with polarizers inserted with EM polarizer perpendicular to EX polarizer.

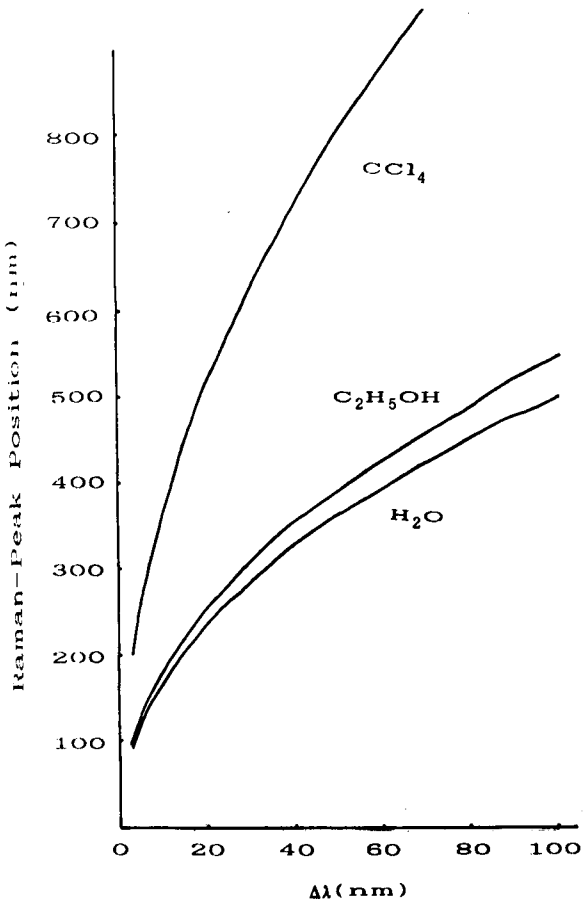

Fig. 1. Raman peak positions of solvents in synchronous fluorescence spectra in terms of excitation wavelength vs. $\Delta\lambda$.

It should be mentioned that the influence of Raman scattering varies with the solvent in a synchronous fluorescence spectrum. The smaller is $\Delta\bar{\nu}_R$, the lower is the possibility of Raman scattering interfering with constant-wavelength synchronous fluorescence spectra. For example, for tetrachloromethane with a small value of $\Delta\bar{\nu}_R$, Raman scattering interference occurs in a narrow $\Delta\lambda$ range, which leads to a flexible selection of $\Delta\lambda$ in synchronous spectrofluorimetry. For solvents with a larger value of $\Delta\bar{\nu}_R$ such as water, ethanol and cyclohexane, the effect of Raman scattering exists in a broader range of $\Delta\lambda$ values and should receive more attention.

The synchronous Raman peak can diverge from the synchronous fluorescence peak by changing the $\Delta\lambda$ value and thus the influence of Raman radiation on the analyte system is decreased, as can be seen in Fig. 3. The analyte fluorescence band is usually located in a small part of the overall spectral range and its shift is different

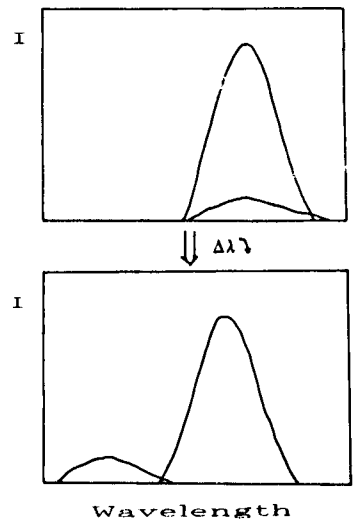

Fig. 3. Schematic diagram for the separation of Raman scattering from fluorescence signals by changing $\Delta\lambda$ values with synchronous scanning.

from that of Raman radiation, although the location of the synchronous fluorescence peak would also change with the $\Delta\lambda$ value. The synchronous fluorescence spectrum is derived from the interaction of the excitation spectrum and emission spectrum of a fluorophore, which are limited to a certain wavelength range. Therefore, in comparison with a synchronous Raman peak, the position of a synchronous fluorescence peak, which is restricted by excitation and emission spectra, is located in a limited region. Hence it is possible to decrease the influence of the solvent Raman peak on the synchronous fluorescence peak by changing the $\Delta\lambda$ value. However, this may have the adverse effect of weakening the fluorescence signal and decreasing selectivity in some instances.

A small change in $\Delta\lambda$ would cause a large shift in the location of the synchronous Raman peak when $\Delta\lambda$ is relatively small. With increasing $\Delta\lambda$ value, the extent of the shift will decline. As a result, it is more effective to avoid Raman scattering interference by changing the $\Delta\lambda$ value in cases when the latter is relatively small.

The above observations are useful to understanding the interference of Raman scattering and could provide guidelines for the experimental design of constant-wavelength synchronous spectrofluorimetry. Equation 4 and Fig. 1 can be consulted for reference in practical applications.

m-Dihydroxybenzene

The excitation and emission peaks of *m*-dihydroxybenzene are located at 280 and 310 nm, respectively. When the selected $\Delta\lambda$ value is 30 nm, the synchronous fluorescence peak occurs at 280 nm in terms of the excitation wavelength, on the other hand, the location of the synchronous Raman peak for water solvent is at 283 nm (as seen from Fig. 1 or calculated from Eqn. 4), which coincides with the location of the synchronous fluorescence peak of *m*-dihydroxybenzene. Therefore, the determination of *m*-dihydroxybenzene would be influenced by Raman scattering in this instance. If the selected $\Delta\lambda$ value is 20 nm, the synchronous Raman peak of water would occur at 233 nm (obtained in the same way as for $\Delta\lambda = 30$ nm), which is far beyond the fluorescence-exciting region of *m*-hydroxybenzene and will have not any effect on its synchronous fluorescence peak. Consequently, the interference of Raman scattering with the determination of *m*-dihydroxybenzene could be avoided by using $\Delta\lambda = 20$ nm. The prediction is consistent with the experimental results [17].

Vitamins

Synchronous fluorescence spectrometry has been proposed for the simultaneous determination of vitamins B_2 and B_6 [5]. The fluorescence emission peaks of vitamins B_2 and B_6 are located at 523 and 393 nm, respectively, and the major fluorescence excitation peaks are at 472 and 328 nm, respectively. The wavelength interval between the excitation and emission peaks for vitamins B_2 and B_6 are 51 and 65 nm, respectively, hence values of ca. 51–65 nm can be tested for $\Delta\lambda$ in synchronous scanning. The synchronous Raman peak of water is located between 360 and 407 nm, as seen from Fig. 1 or calculated from Eqn. 4, and the synchronous fluorescence peaks of vitamins B_2 and B_6 occur at ca. 472 and 328 nm, respectively. Therefore, the synchronous Raman peak will appear between two synchronous fluorescence peaks which are distant from each other and thus have no effect on the simultane-

ous determination of vitamins. Hence the investigation of the effect of Raman scattering becomes an unnecessary step when choosing a suitable $\Delta\lambda$ value for spectral scanning because the influence from Raman radiation can be omitted.

Pheophytins

The peaks in the fluorescence emission spectra of pheophytins *a* and *b* are at 672 and 657 nm, respectively. Two excitation peaks of pheophytin *a* were obtained at 412 and 667 nm and of pheophytin *b* at 437 and 656 nm. Therefore, the possible chosen value of $\Delta\lambda$ would be so large or small that no Raman scattering interference can be observed. Hence it is also unnecessary to investigate the influence of Raman scattering when choosing a suitable $\Delta\lambda$ value. The experimental results supported the prediction [18].

Conclusions

The influence of Raman scattering on constant-wavelength synchronous fluorescence spectra varies with $\Delta\lambda$ for constant-wavelength synchronous scanning and $\Delta\bar{\nu}_R$ of the solvent. In this paper, various aspects of the influence of Raman scattering and means of decreasing the interference have been discussed. The applications presented here have demonstrated the utility of the general rules for dealing with the problem. This work facilitates the design of suitable experimental procedures and decreases the number of trial tests needed for constant-wavelength synchronous spectrofluorimetry.

This project was supported by the National Natural Science Foundation of China. The authors express their gratitude to Professor G.Z. Chen for helpful discussions and encouragement.

REFERENCES

1 S. Rubio, A. Gomez-Hens and M. Valcarcel, Talanta, 33 (1986) 633.
2 T. Vo-Dinh, Anal. Chem., 50 (1978) 396.
3 F.G. Sanchez, A.L. Ramos Rubio and C.C. Blanco, Talanta, 37 (1990) 579.
4 T. Vo-Dinh, Appl. Spectrosc., 36 (1982) 576.
5 Y.Q. Li, X.Z. Huang, J.G. Xu and G.Z. Chen, Acta Pharm. Sin., 27 (1992) 52.
6 E.L. Inman and J.D. Winefordner, Anal. Chem., 54 (1982) 2018.
7 E.L. Inman, L.A. Files and J.D. Winefordner, Anal. Chem., 58 (1986) 2156.
8 L.A. Files, M. Moore, M.J. Kerkhoff and J.D. Winefordner, Microchem. J., 35 (1987) 305.
9 Y.Q. Li, X.Z. Huang, J.G. Xu and G.Z. Chen, Anal. Chim. Acta, 256 (1992) 285.
10 J.N. Miller, Analyst, 109 (1984) 191.
11 F.G. Sanchez and A.L.R. Rubio, Anal. Chim. Acta, 228 (1990) 293.
12 Y.Q. Li, X.Z. Huang, J.G. Xu and G.Z. Chen, Chin. Chem. Lett., 2 (1991) 23.
13 E.L. Inman and J.D. Winefordner, Anal. Chim. Acta, 138 (1982) 245.
14 Y.Q. Li, X.Z. Huang and G.Z. Chen, Chin. Sci. Bull., 36 (1991) 1312.
15 J.C. Andre, M. Bouchy and M.L. Viriot, Anal. Chim. Acta, 105 (1979) 297.
16 K.G. Boto and J.S. Bunt, Anal. Chem., 50 (1978) 392.
17 R.T. Xu and J.G. Xu, J. Xiamen Univ., 31 (1992) 518.
18 Y.Q. Li, S. Ding, X.Z. Huang and G.Z. Chen, Chin. Spectrosc. Spectral Anal., 12 (1992) 43.

Analytica Chimica Acta, 283 (1993) 909–915
Elsevier Science Publishers B.V., Amsterdam

Off-line and on-line preconcentration of trace levels of beryllium using complexing agents with atomic spectrometric and fluorimetric detection

D.B. Do Nascimento [1] and G. Schwedt

Institut für Anorganische und Analytische Chemie, Technische Universität Clausthal, Paul-Ernst-Str. 4, 38678 Clausthal-Zellerfeld (Germany)

(Received 12th May 1993; revised manuscript received 15th July 1993)

Abstract

Two methods were investigated for the determination of traces of beryllium. One was developed using polyethylene powder as an adsorbent for preconcentration of the stable complex formed between beryllium and Chrome Azurol S. After elution, the preconcentrated metal was determined by graphite furnace atomic absorption spectrometry. With the analytical procedure developed for water analysis, detection limits of 0.8 $\mu g\ l^{-1}$, relative standard deviations of 2.5–4.1% and recoveries of 92–104% can be achieved for beryllium in tap water. In the other method, ion exchange was incorporated in a flow-injection system by using an ion-exchange microcolumn in the sample loop of a six-port valve. The effects of sampling time, eluent composition and concentration and sample acidity were investigated to develop a preconcentration procedure for the determination of beryllium in tap water using fluorimetric detection with morin reagent. The proposed method was characterized by a precision of about 1.5%, a detection limit of 0.2 $\mu g\ l^{-1}$ and recoveries of 95–105%.

Keywords: Atomic absorption spectrometry; Fluorimetry; Beryllium; Preconcentration; Waters

Separation and preconcentration are important problems in the determination of traces of metals. In addition to commercial chelating resins and ion exchangers used for these purposes [1,2], other sorbents have become increasingly popular [3–5], and especially interesting are silica gels modified with various reagents [6–8].

In this work, polyethylene powder was used as an adsorbent for the beryllium–Chrome Azurol S complex. Polyethylene has recently been used for the preconcentration of some metal ions as their complexes by using its property as an adsorbent [9]; it has the advantages that both adsorption and desorption (elution) of the complexes are rapid and elution can be completed with a very small volume of eluent. After elution, beryllium was determined by graphite furnace atomic absorption spectrometry.

Flow-injection analysis has been used in conjunction with several techniques, such as atomic absorption spectrometry [10], potentiometry with ion-selective electrodes [11] and amperometry [12]. Good sensitivity, high sample throughputs and high reproducibility are considered to be the main advantages. An additional combination of flow-injection systems with ion exchangers has been employed in recent years mainly for on-line preconcentration [13–18]. Concentration by ion exchange can be attained in flow systems by plac-

Correspondence to: G. Schwedt, Institut für Anorganische und Analytische Chemie, Technische Universität Clausthal, Paul-Ernst-Str. 4, 38678 Clausthal-Zellerfeld (Germany).

[1] Present address: Departamento de Química, Universidade Federal de Santa Maria, 97119 911 Santa Maria (Brazil).

ing a resin column in the sample loop of an injector and elution can be achieved by replacing the sample carrier stream with the eluent stream. In a second method, the optimization of the conditions for the selective determination of traces of beryllium by flow-injection analysis using fluorimetric detection with morin reagent is described, following preconcentration and separation of beryllium ions on a cation-exchange microcolumn.

Both methods were applied to the determination of traces of beryllium in tap water.

EXPERIMENTAL

Preconcentration on a polyethylene column

Apparatus. A Gilson Minipuls-3 peristaltic pump and a Perkin-Elmer Model 1100B atomic absorption spectrometer equipped with a Model HGA-700 graphite furnace and an AS-70 autosampler were used.

Reagents. All chemicals were of analytical-reagent grade. Beryllium stock solution (1000 μg l^{-1}) was prepared from a 1000 mg Be l^{-1} standard solution (Merck, Darmstadt). A 0.6% aqueous solution of Chrome Azurol S (CAS) and a 0.5 mol l^{-1} succinic acid buffer solution with the pH adjusted to 4.5 with 1 mol l^{-1} NaOH were prepared. The eluent was ethanol.

Column preparation. A 1000-μl Eppendorf pipette tip was filled with polyethylene (PE) of spectroscopic grade (Merck) (ca. 300 mg) and used as a column. Glass-wool was attached to the outlet of the tip and packed with PE. A second pipette tip, completely filled with glass-wool, was used to close the open side of the tip packed with PE. The solutions were aspirated into the column by means of a peristaltic pump with silicone-rubber tubes (1.0 mm i.d.).

The PE and pipette tips were previously washed with nitric acid–ethanol (1 + 9) for 48 h, then with ethanol and deionized water and dried.

Procedures. Working solutions of beryllium with concentrations from 1 to 25 μg l^{-1} were prepared by diluting the stock beryllium solution with water. To various volumes of these solutions (to produce different preconcentration factors), 2.0 ml of succinate buffer and 2.0 ml of CAS solution were added.

The preconcentration on the PE column was carried out at a flow-rate of 0.5 ml min^{-1}. Next, the excess CAS was eliminated from the column with 10 ml of water. After drying of the column with an air flow for 5 min to improve the contact between the eluent and PE, the Be–CAS complex was eluted with 4.0 ml of ethanol at a flow-rate of 0.4 ml min^{-1}. To avoid contact of the eluate with other parts of the system, the elution procedure was carried out with an inverse flow with respect to the preconcentration procedure.

The eluate solutions were then injected into the graphitefurnace and the beryllium recovery was determined by interpolation on a calibration graph.

Determination of beryllium by electrothermal atomic absorption spectrometry. Calibration and standard solutions were prepared from 1000 mg l^{-1} Be standard solution (Merck) diluted with ethanol. The solutions were measured with deuterium background correction. The measurements were carried out at the instrumental settings given in Table 1, without a chemical modifier.

Analysis of tap water samples. Water samples were adjusted to pH 3 with HCl, filtered through

TABLE 1

Spectrometer and furnace conditions

Monochromator	
Wavelength	239.4 nm
Lamp current	5 mA
Spectral slit width	0.7 nm
Furnace conditions	
Tubes	Pyrolytic graphite-coated graphite with L'vov platform
Purge gas	Argon
Sample injection	20 μl
Temperature programme:	

Step	Temperature (°C)	Ramp time (s)	Hold time (s)	Gas flow-rate (ml min^{-1})
1	100	20	5	300
2	850	55	5	300
3	1500	2	5	200
4	2500	0	4	50
5	2650	1	1	300

a 0.45-μm membrane filter and stored in pre-cleaned [nitric acid–ethanol (1 + 9)] PE bottles. The preconcentration procedure was carried out as described above.

Portions of 20.0, 50.0 and 100.0 ml of this sample were buffered (pH 4.5) with succinate buffer, 2.0 ml of the CAS solution were added and after 15 min these solutions were passed through the PE column (flow-rate 0.5 ml min^{-1}) and elution was carried out with 4.0 ml of ethanol after elimination of the excess CAS and the drying procedure.

The samples were also analysed by the standard additions method. For this purpose, the samples were spiked with 0.04 μg of Be and subsequent treatments were the same as those described above. The recoveries are presented in Table 2.

Preconcentration in flow-injection system

Apparatus. A Gilson Minipuls-3, a peristaltic pump Perkin-Elmer LS 30 luminescence spectrometer, a Knauer *X–Y* recorder and a six-port high-pressure switching valve to provide the connections for the eluent, concentration column and sample were used.

Reagents. Beryllium solutions were prepared as described above. A 0.012% morin solution was prepared in 0.5, 1.0 and 2.0 mol l^{-1} NaOH. The eluents were 0.6 mol l^{-1} HCl and 0.2 mol l^{-1} sodium citrate solution.

Column preparation. A guard column (4 × 4 mm i.d.) (Hewlett-Packard) was filled with 40 mg of Dowex 50-X12–400 cation exchanger (Sigma) in the H^+ or Na^+ form.

Flow diagram. The flow diagrams used for the preconcentration and elution of beryllium ions are shown in Fig. 1. In Fig. 1a the sample (S) was aspirated through the column while the morin solution (M) and the eluent (E) were mixed to form a solution with suitable pH for the formation of the morin–beryllium complex. After aspiration of the desired sample volume, defined by the flow-rate and time of aspiration, the column was washed with 0.05 mol l^{-1} NaCl solution or 0.01 mol l^{-1} HCl (three-port valve, 3p). After sampling and washing the microcolumn was introduced into the eluent stream (Fig. 1b). The beryllium ions were eluted and at point Y the sample zone met the morin reagent and in the following coil (2.2 m) mixing and chemical reactions occurred. The fluorescent compound produced was measured in the flow-through fluorescence detector, the recorded signal being proportional to the beryllium content in the sample.

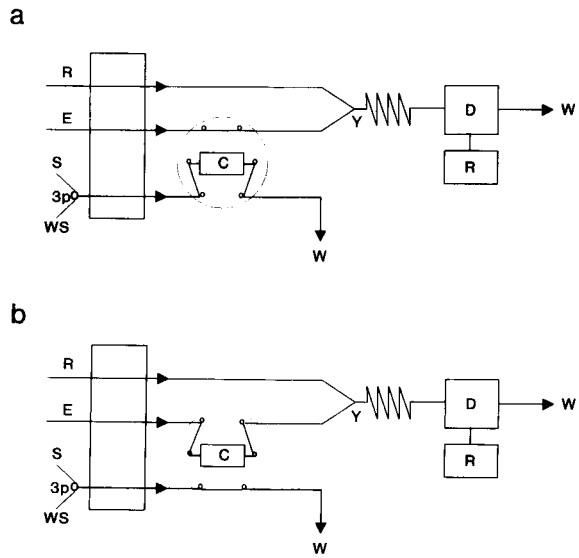

Fig. 1. Flow diagram of the system used, showing the (a) sampling and (b) elution positions. For details, see text.

TABLE 2

Analysis of tap water samples

Preconcentration on PE			Preconcentration in flow system		
Sample No.	Volume (ml)	Recovery (%) [a]	Sample No. [b]	Volume (ml)	Recovery (%) [c]
1	20	104.2 ± 4.2	1	2.5	105.3 ± 1.7
2	50	95.8 ± 5.1	2	5.0	94.8 ± 1.6
3	100	92.7 ± 5.4	3	10.0	97.2 ± 1.1
			4	2.5	103.7 ± 1.8
			5	5.0	105.3 ± 1.9
			6	10.0	102.8 ± 1.3

[a] Recoveries were assessed by adding 0.04 μg of Be to the sample volume. Results are means ± standard deviations (n = 5). [b] Samples 1–3 eluted with HCl and samples 4–6 with sodium citrate solution. [c] Recoveries from 4 μg l^{-1} spiked samples. Results are means ± standard deviations (n = 5).

After elution, the microcolumn was washed with the wash solution (WS).

Procedure. The fluorescence detector was calibrated with 1.0 mol l^{-1} chinin sulphate solution in 0.1 mol l^{-1} H_2SO_4 with absorption at 355 nm and emission at 455 nm.

The optimum flow-rates of the sample, eluent and morin solution were 1.0, 1.0 and 0.7 ml min^{-1}, respectively. The effects of eluent, eluent concentration and sample acidity were investigated.

Hydrochloric acid and sodium citrate were employed successfully as eluents. The effect of eluent concentration was tested for HCl concentrations from 0.4 to 1.0 mol l^{-1} and for 0.2 mol l^{-1} citrate. When HCl with concentration up to 0.7 mol l^{-1} was used as the eluent the morin reagent was dissolved in 1.0 mol l^{-1} NaOH; for HCl concentrations higher than 0.7 mol l^{-1} the reagent was dissolved in 2.0 mol l^{-1} NaOH and citrate was used as the eluent in 0.5 mol l^{-1} NaOH. By this means a pH between 12 and 13, suitable for development of the complex [19], was reached.

The sample acidity was studied with respect to two factors: hydrolysis of the beryllium ions and the effect of ethylenediaminetetraacetic acid (EDTA) as masking agent towards interfering ions. Because hydrolysis is a pH-dependent process, the fluorescence signals of the samples were measured within the pH range 0–10. Samples with pH between 0 and 10 were also tested in the simultaneous presence of Ca^{2+}, Mg^{2+}, Ba^{2+}, Zn^{2+}, Fe^{3+} and Al^{3+} ions and EDTA. The ion concentrations were varied from 1 to 10 mg l^{-1} for EDTA concentrations up to 1%. A calibration graph was obtained for each situation with beryllium standards ranging from 0.0 to 10.0 μg Be l^{-1} and all measurements were performed in triplicate. The standard solutions were aspirated for 2–10 min.

The stability of the system was checked by repeating the analysis of a 10 μg Be l^{-1} standard for 2.5 min twenty times (2 h).

Analysis of tap water samples. Tap water samples were prepared as described above. EDTA was added to the samples (1% final concentration) and the solutions were adjusted to pH 4.0. Samples were aspirated for 2.5, 5.0 and 10.0 min and eluted with 0.6 mol l^{-1} HCl or 0.2 mol l^{-1} sodium citrate solution. The sample were also spiked with beryllium ions (4.0 μg l^{-1} final concentration) and the entire procedure was carried out. The recoveries are presented in Table 2.

TABLE 3

Recoveries from different beryllium solutions after preconcentration on a PE column with graphite furnace atomic absorption spectrometric determination

Concentration before enrichment (μg l^{-1})	Volume (ml)	Enrichment factor	Recovery (%) [a]
1.0	20	5	99.0±4.1
2.0	20	5	103.5±3.5
3.0	20	5	99.5±2.5
4.0	20	5	97.3±2.6
0.5	100	25	94.7±5.3
1.0	50	12.5	97.2±4.8

[a] Means ± standard deviations ($n = 3$).

RESULTS

Preconcentration on a polyethylene column

As PE powder shows a good adsorbent features towards some complexing agents and complexes, mainly in acidic solutions [9], and as the Be–CAS complex is stable in acidic solutions [20] and shows good adsorbability on PE, this process can be successfully used for the preconcentration of traces of beryllium. The main parameters are given in Table 3.

The precision was characterized by relative standard deviations of 2.5–4.1%, depending on the beryllium concentration in the samples, and the mean recoveries ranged from 94.7 to 103.5%.

To determine the detection limit of graphite furnace atomic absorption measurements, the preconcentration process was applied to 20 ml of a blank solution. From the mean ($n = 5$) of the measured absorptions a detection limit of 0.8 μg Be l^{-1} (9×10^{-8} mol l^{-1}) was calculated.

A chemical modifier was not used because no background absorption or chemical interferences were detected when the preconcentrated solutions were inserted alone in the graphite furnace.

Preconcentration in flow-injection system

Low HCl concentrations (0.4 mol l^{-1}) caused a delay in elution, which was virtually constant when the concentration was in the range 0.5–0.7 mol l^{-1}. For HCl concentrations higher than 0.7 mol l^{-1} the elution was so fast that characteristic and reproducible peaks were not obtained. The analyte signals obtained with 0.2 mol l^{-1} sodium citrate solution were analogous to those obtained with 0.6 mol l^{-1} HCl, in addition to the calibration graph (Fig. 2).

The influence of sample acidity is shown in Fig. 3. The differences in peak height were probably caused by hydrolysis of the beryllium ions, which form a series of hydroxo complexes whose structures are pH dependent [19]. Between pH 3 and 6 the influence of the sample acidity on the peak height was small, and therefore the sample acidity was kept at pH 4.

The interfering effect of foreign ions was studied in the presence of EDTA as masking agent. The low stability of the Be–EDTA complex [21] and the build-up of anionic complexes or neutral molecules (not retained on the column) between EDTA and metallic cations allowed the addition of EDTA to the samples and to the morin solution at a concentration of up to 1% in the presence of 10 mg l^{-1} of each foreign ion studied.

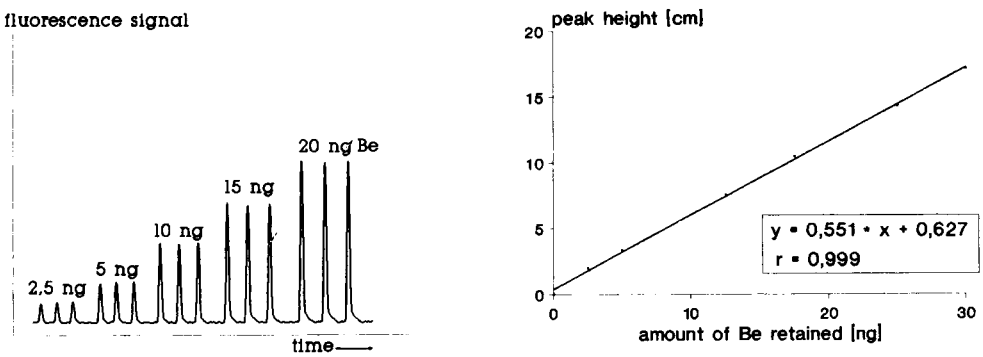

Fig. 2. Analyte signals and calibration graphs with different eluents for beryllium determination.

TABLE 4

Recovery of beryllium (10 $\mu g\ l^{-1}$) in the presence of foreign ions

Ion	Concentration ($mg\ l^{-1}$)	EDTA concentration ($mg\ l^{-1}$)		Recovery (%)
		In sample	In morin solution	
Ca^{2+}	0.1	0.2	–	97.5 ± 1.5
	1	0.2	–	94.3 ± 1.1
Mg^{2+}	0.1	0.2	–	93.4 ± 0.6
	1	0.2	–	101.6 ± 0.5
Ba^{2+}	0.1	0.2	–	102.5 ± 0.7
	1	0.2	–	101.1 ± 1.4
Zn^{2+}	0.1	0.2	–	98.6 ± 0.4
	1	0.2	–	95.7 ± 0.3
Fe^{3+}	0.1	0.2	–	101.7 ± 0.1
	1	0.2	–	103.6 ± 1.7
Al^{3+}	0.1	0.2	–	98.5 ± 1.2
	1	0.2	–	100.1 ± 1.3
In simultaneous presence of Ca^{2+}, Mg^{2+}, Ba^{2+}, Zn^{2+}, Fe^{3+} and Al^{3+} ions				
0.1		0.2	–	100.2 ± 1.4
1		0.2	–	97.8 ± 1.1
5		0.2	–	94.3 ± 1.5
5		0.2	0.1	96.0 ± 1.2
10		1.0	0.1	93.5 ± 1.4

[a] Means ± standard deviations ($n = 5$).

Table 4 shows the influence of each ion individually and of all ions simultaneously on the recovery of beryllium ions.

The reproducibility of the method was studied on ten samples containing 10 μg Be l^{-1}. The relative standard deviations obtained were 1.1% (HCl as eluent) and 1.8% (citrate as eluent). The recoveries of beryllium ions in the presence of Ca^{2+}, Mg^{2+}, Ba^{2+}, Zn^{2+}, Fe^{3+} and Al^{3+} ions at various concentrations ranged between 93.4 and 103.6%, and recoveries from 94.8 to 105.3% were achieved for beryllium in tap water samples. From the mean ($n = 10$) of the blanks measured detection limits of 0.2 μg Be l^{-1} (20×10^{-8} mol l^{-1}) and 0.9 μg Be l^{-1} (1×10^{-7} mol l^{-1}) with HCl and citrate eluents, respectively, were calculated.

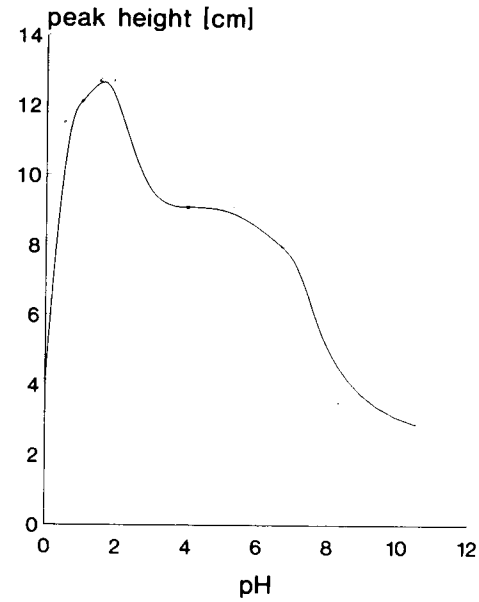

Fig. 3. Influence of sample acidity on peak height (for a 20 $\mu g\ l^{-1}$ beryllium solution).

DISCUSSION

The results show that both methods are satisfactory for the determination of beryllium in tap water samples. With preconcentration on the PE column sample volumes of 100 ml could be analysed and an enrichment factor of 20 could be achieved. The measurement of the ethanolic eluent in the graphite furnace showed no interferences.

In on-line preconcentration, the combination of the preconcentration process with fluorescence detection of beryllium as the morin complex readily allows the determination of 1 μg Be l^{-1}. With addition of EDTA no interferences were detected in the determination of 10 μg Be l^{-1} together with 1000 times more concentrated solutions of Ca^{2+}, Mg^{2+}, Ba^{2+}, Zn^{2+}, Fe^{3+} and Al^{3+} ions. For selection of the sample acidity, the hydrolysis of beryllium ions and the presence of EDTA were considered. Low pH values probably

hinder the hydrolysis process of beryllium ions but simultaneously decrease the masking action of EDTA, which has its maximum complexing strength at higher pH.

The two methods show good sensitivity with a detection limits of 0.8 $\mu g\ l^{-1}$ with preconcentration on the PE column and 0.2 $\mu g\ l^{-1}$ (HCl as eluent) in the flow-injection system, and the precisions of both methods were satisfactory, 5% for the off-line and 1.5% for the on-line procedure.

The results obtained for tap water samples by both methods are given in Table 2. Although beryllium was not found in the tap water samples (the concentration is below the detection limit), the methods can be regarded as satisfactory owing to the good recoveries of 95–105% from spiked samples.

REFERENCES

1 K.L. Lieser, Analytikertaschenbuch, Band 6, Springer, Berlin, 1. Aufl., 1987, p. 125.
2 K. Isshiki, F. Tsuji and T. Kuwamoto, Anal. Chem., 59 (1987) 2491.
3 X.G. Yang and E. Jackwerth, Fresenius' Z. Anal. Chem., 327 (1987) 179.
4 P. Burba and P.G. Willmer, Fresenius' Z. Anal. Chem., 321 (1985) 109.
5 G. Schwedt, Methoden der Spurenanreicherung Anorganischer und Organischer Stoffe aus Wässern, Vogel, Würzburg, 2. Aufl., 1988.
6 G. Schwedt, LaborPraxis, (1983) 816.
7 O.S. Wolfbeis and H. Offenbacher, Fresenius' Z. Anal. Chem., 319 (1984) 282.
8 C. Samara and Th.A. Kouimtzis, Anal. Chim. Acta, 174 (1985) 305.
9 D.B. Nascimento, PhD Thesis, Technische Universität Clausthal, Clausthal-Zellerfeld, 1991.
10 V. Kubán, J. Komárek and Z. Zdráhal, Collect. Czech. Chem. Commun., 54 (1989) 1785.
11 W. Frenzel and P. Brätter, Anal. Chim. Acta, 185 (1986) 127.
12 C.E. Lunte, S. Wong, T.H. Ridgway, W.R. Heineman and K.W. Chan, Anal. Chim. Acta, 188 (1986) 165.
13 H. Bergamin F°, B.F. Reis, A.O. Jacintho and A.G. Zagatto, Anal. Chim. Acta, 117 (1980) 81.
14 Z. Fang, S. Xu and S. Zhang, Anal. Chim. Acta, 164 (1984) 41.
15 S.D. Hartenstein, J. Ruzicka and G.D. Christian, Anal. Chem., 57 (1985) 21.
16 M. de la Torre, F. Fernández-Gámez, F. Lázaro, M.D. Luque de Castro and M. Valcárcel, Analyst, 116 (1991) 81.
17 V. Kubán, J. Havel and B. Patocková, Collect. Czech. Chem. Commum., 54 (1989) 1777.
18 Z. Fang, Flow Injection Separation and Preconcentration, Verlag Chemie, Weinheim, 1993.
19 N.N. Greenwood und A. Earnshaw, Chemie der Elemente, Verlag Chemie, Weinheim, 1. Aufl., 1988.
20 F.D. Snell, Photometric and Fluorimetric Methods of Analysis—Metals, Wiley, New York, 1978.
21 A.A. Amsheva and E.M. Yakimets, Zh. Anal. Khim., 29 (1974) 1526.

Analytica Chimica Acta, 283 (1993) 917–921
Elsevier Science Publishers B.V., Amsterdam

Utilization of polyethylene glycol for the separation of chlorophenols by capillary isotachophoresis

Petr Praus

Chemical Laboratory of Povodí Odry, Varenská 49, 701 26 Ostrava (Czech Republic)

Václav Dombek

Underground Exploration and Mine Safety, Inc., Laboratory for Waste Analysis, 739 21 Paskov (Czech Republic)

(Received 5th July 1993)

Abstract

The separation of some chlorophenols (CPs) by capillary isotachophoresis using polyethylene glycol (PEG) as a polar additive dissolved in the leading electrolyte was studied. The distribution process of CPs between the PEG polymer network, considered to be the pseudo-stationary phase not bonded on the capillary walls, and the aqueous mobile phase is described. The optimum concentration of PEG for the complete separation of pentachlorophenol, 2,4,5-trichlorophenol, 2,4,6-trichlorophenol and 2,4-dichlorophenol was found to be 4% (w/v).

Keywords: Electrophoresis; Chlorophenols; Isotachophoresis

Various stationary phases for application in capillary electrophoretic (CE) techniques have been developed in recent years. A variety of methods of coating capillaries for CE have been reviewed [1]. Another approach is the use of so-called pseudo-stationary phases in micellar electrokinetic capillary chromatography (MECC) [2,3] and ion-exchange electrokinetic capillary chromatography (IEECC) [4]. Neutral additives for CE, such as cyclodextrins [5], which improve the separation of various compounds, act as stationary phases.

Isotachophoretic (ITP) applications of non-ionic additives to the electrolyte systems, acting as stationary phases, have also been reported. Separations based on interactions with, e.g., cyclodextrins [6,7] and polyvinylpyrrolidone [8] were tested recently.

Correspondence to: P. Praus, Chemical Laboratory of Povodí Odry, Varenská 49, 701 26 Ostrava (Czech Republic).

Chlorinated phenols (CPs) belong to the category of priority environmental pollutants [9]. In previous studies attempts were made to separate some chlorophenols by using capillary ITP. It was shown that separation is possible according to their pK values in various operational systems with different pH values [10] or in one system by adding β-cyclodextrin to the leading electrolyte [11]. The aim of this paper is to demonstrate the influence of polyethylene glycol PEG as a polar, non-ionic polymer additive on the ITP separation of CPs.

THEORETICAL

In order to describe the ITP separation process in a modified operational system with a pseudo-stationary phase, a general equation for the effective mobility of an ion interacting with a stationary phase should be derived.

From conventional chromatographic theory, the retardation factor R_F can be defined as

$$R_F = u/u_0 \quad (1)$$

where u and u_0 are the effective mobilities of separands in the system with and without a stationary phase, respectively. The retardation factor depends on the capacity factor k according to

$$R_F = 1/(1+k) \quad (2)$$

The capacity factor is also related to the distribution coefficient, K_D, of a solute between the stationary and mobile phases as suggested Scott and Kucera [12]:

$$k = K_D\phi \quad (3)$$

where $\phi = V_s/V_m$ and V_s and V_m are volumes of the stationary and mobile phase, respectively. Combination of Eqns. 1–3 gives

$$u = u_0/(1+K_D\phi) \quad (4)$$

The effective mobility of a migrating ion is usually defined by its molecular weight M and the effective charge Z [13,14]. Taking into account only migration in an electric field without electroosmotic flow, one can write

$$u_0 = |Z|a/M^n + b \quad (5)$$

where $0 < n \leq 1$ and a and b are empirical coefficients determined for the system without a stationary phase. By substitution of Eqn. 5 into Eqn. 4, the following holds:

$$u = (a|Z|/M^n + b)/(1+K_D\phi) \quad (6)$$

This relationship generally describes the migration behaviour of ions interacting with a stationary phase. Non-ionic PEG does not migrate electrophoretically and its polymer network is dispersed in the whole separation compartment. Under these conditions, PEG can be considered as a pseudo-stationary phase. An attempt to verify the validity of Eqn. 6 for the ITP separation of CPs in the presence of PEG was made in the experimental part of this work.

EXPERIMENTAL

Chemicals

All chemicals were of analytical-reagent grade. Hydrochloric acid, methanol, sodium hydroxide and barium hydroxide were obtained from Lachema (Brno, Czech Republic), L-asparagine monohydrate from Merck (Darmstadt, Germany), trishydroxymethyl)aminomethane (Tris) from Serva (Heidelberg, Germany), polyvinyl alcohol 62 800 (PVA) from Riedel-de Haën (Seelze, Germany) and chlorophenols from Supelco (Bellefonte, PA, USA). Polyethylene glycol (PEG) with a molecular weight of 1000 was supplied by Janssen Chimica (Beerse, Belgium).

Tris was purified by recrystallization from methanol. PVA was purified on a mixed-bed ion exchanger. A standard mixture of chlorophenols (100 mg l^{-1}) was prepared by dissolution of pentachlorophenol (PCP), 2,4,5-trichlorophenol (2,4,5-TCP), 2,4,6-trichlorophenol (2,4,6-TCP) and 2,4-dichlorophenol (2,4-DCP) in 0.01 M sodium hydroxide solution.

Instrumentation

A CS isotachophoretic analyser (VVZ PJT, Spišská Nová Ves, Slovak Republic) in a one-column configuration (150 × 0.3 mm i.d.) provided with a conductivity detector was used for all measurements. The current was kept constant at 75 μA and after about 600 s was switched to 30 μA. Isotachopherograms were recorded on a TZ 4200 two-channel recorder (Laboratorní přístroje, Prague, Czech Republic) at a chart drive speed of 1 mm s^{-1}. The pH values of the operational systems were measured with a digital pH meter from Radelkis (Budapest, Hungary). Sampling was performed with Hamilton microsyringes (maximum volume 10 μl).

Statistical treatment of the experimental data was performed by the statistics program ADSTAT version 1.25 from TriloByte Statistical Software (Prague, Czech Republic).

RESULTS AND DISCUSSION

The influence of PEG on the effective mobilities of CPs was tested on the standard mixture (see *Chemicals*). Separated zones were defined by $h^{(rel)}$ values calculated according to the equation

$$h^{(rel)} = (h_i - h_L)/(h_T - h_L) \quad (7)$$

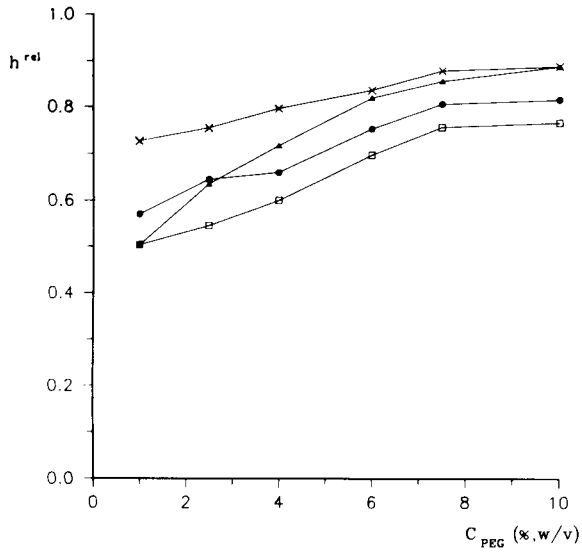

Fig. 1. Effect of the amount of polyethylene glycol added to the leading electrolyte on the $h^{(rel)}$ values of (▲) PCP, (□) 2,4,6-TCP, (●) 2,4,5-TCP and (×) 2,4-DCP. Each point was calculated from three measurements.

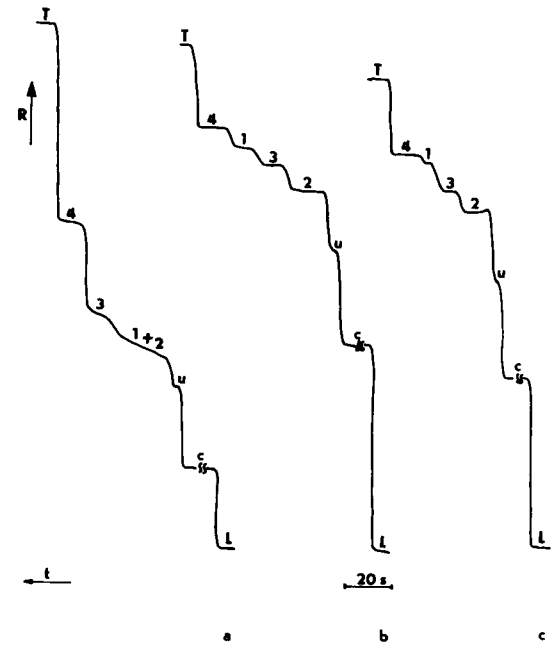

Fig. 2. Isotachopherograms of the separation of chlorophenols. Volume injected, 3 μl of standard mixture; detection current, 30 μA. (a) Without PEG; (b) with 4% PEG; (c) with 6% PEG. 1 = PCP; 2 = 2,4,6-TCP; 3 = 2,4,5-TCP; 4 = 2,4-DCP, c = HCO_3^-; u = unidentified impurity originating from operational system; L = Cl^-; T = asparagine. t = Time; R = resistance.

where h_i, h_L and h_T are the step heights obtained from the conductivity detector response of the examined, leading and terminating ions, respectively.

The pH value of the leading electrolyte (pH_L) was taken from [10]. The migration order in the non-modified electrolyte system is 2,4,6-TCP, PCP, 2,4,5-TCP and 2,4-DCP. The resolution of the first two separands is poor but the others are well separated. At lower concentrations of PEG (0.001–1.0%), no influence on separation was observed. The effective mobilities of CPs were significantly influenced in the concentration range 1–10% (Fig. 1). Figure 2 shows the separation of CPs in the unmodified and in the modified system containing 4 and 6% of PEG. At higher concentrations (above 10%) the resistance of the electrolyte system is too high and the ITP separation process is unsatisfactory.

In order to provide immobility of the PEG non-ionic polymer network in the whole separation compartment, the electroosmotic flow was eliminated by adding PVA to the unmodified and modified leading electrolytes [15] (Table 1).

The definition of ϕ in Eqn. 6 was given above. Here, V_m can be determined from the molar concentration c_{PEG} and the partial molar volume v_{PEG} of PEG. V_m can be calculated as the differ-

TABLE 1

Operational system used in the separation of chlorophenols

Parameter	Leading electrolyte	Terminating electrolyte
Anion	Cl^-	Asparagine
Concentration (mM)	10	5
Counter ion	Tris	Ba^{2+}
pH	7.80	9.5–10.0
Additive	PVA	–
Concentration (%, w/v)	0.05	–
Pseudo-stationary phase	PEG	–
Concentration range (%, w/v)	0.001–10	–
Solvent	Water	Water

ence between total internal volume of the capillary, V_c, and V_s. This leads to

$$\phi = \frac{V_s}{V_m} = \frac{v_{PEG} c_{PEG}}{1 - v_{PEG} c_{PEG}} \quad (8)$$

The partial molar volumes of PEG in aqueous solution were determined as [16]

$$v_{PEG} = \frac{M_{PEG}}{d_{Sol}} - \frac{(1 + w_{PEG} M_{PEG})}{d_{sol}^2} \left(\frac{\partial d_{Sol}}{\partial w_{PEG}} \right)_{T,P} \quad (9)$$

where M_{PEG} is the molar weight of PEG, d_{Sol} is the density of the PEG solution and w_{PEG} is the molal concentration of PEG. The values of the partial molar volumes were determined in the range 0.835–0.811 l mol^{-1} for 1–10% PEG at 20°C. The effective mobilities can be expressed via the $h^{(rel)}$ values [17], i.e.,

$$u = \frac{u_L}{\left[1 + h^{(rel)} \left(\frac{u_L}{u_T} - 1 \right) \right]} \quad (10)$$

where u_L and u_T are the effective mobilities of the leading and terminating ions, respectively. The absolute mobilities of the ions used in this work and their pK_a values (Cl^-, $u_L = u_L^0 = -79.1 \times 10^{-5}$ m^2 V^{-1} s^{-1}; asparagine, $u_T^0 = -31.6 \times 10^{-5}$ m^2 V^{-1} s^{-1}, pK_a = 8.72; Tris, $u_c^0 = 29.5 \times 10^{-5}$ m^2 V^{-1} s^{-1}, pK_c = 8.076) were taken from the literature [15]. The pH value of the terminating zone, needed for the determination of u_T, was calculated according to the simple relationship derived by Mosset et al. [18].

Under the given experimental conditions, the effective mobilities depend only on K_D and ϕ (Eqn. 6). Figure 3 shows plots of $1/u$ vs. ϕ. The plots for 2,4,6-TCP, 2,4,5-TCP and 2,4-DCP show good linearity (the regression coefficients are given in Table 2). The assumption of linearity for the "triangular" dependence of PCP was statistically confirmed at the $\alpha = 0.05$ significance level by regression tests [19]. The outlying points corresponding to 10% PEG ($\phi = 0.088$) were excluded from the linear regression. As was mentioned before, with larger amounts of PEG the resistance of the electrolyte system increases. This effect leads to a temperature rise by Joule heating in the capillary and thus to a decrease in K_D values according to the Van't Hoff equation.

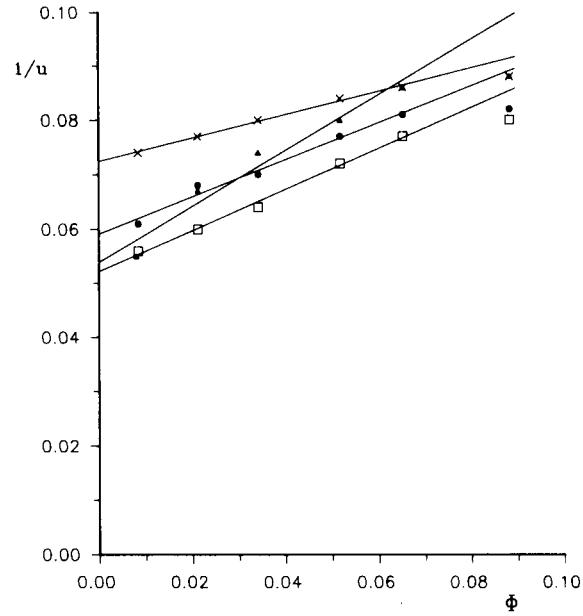

Fig. 3. Dependence of the reciprocal of effective mobility, $1/u$, on ϕ. Each point was calculated from three measurements. ▲ = PCP; □ = 2,4,6-TCP; ● = 2,4,5-TCP; × = 2,4-DCP.

The distribution coefficients K_D evaluated by dividing the slopes by the intercepts of these lines are given in Table 2. These values must be taken only as a first approximation because the ϕ values were calculated from the partial molar volumes determined at 20°C and do not correspond exactly to the real temperature in the capillary during the separation process.

TABLE 2

Distribution coefficients evaluated from the linear dependences of $1/u$ vs. ϕ and the pK_a values of chlorophenols

Compound	K_D [a]	r [b]	pK_a [c]
PCP	9.93 ± 0.37	0.9880	4.93 ± 0.03
2,4,6-TCP	7.61 ± 0.10	0.9981	6.51 ± 0.07
2,4,5-TCP	5.95 ± 0.12	0.9943	7.20 ± 0.07
2,4-DCP	3.15 ± 0.06	0.9949	8.51 ± 0.05

[a] The confidence interval was calculated at the $\alpha = 0.05$ significance level. [b] r = correlation coefficient of the relationship $1/u$ vs. ϕ. [c] From [20].

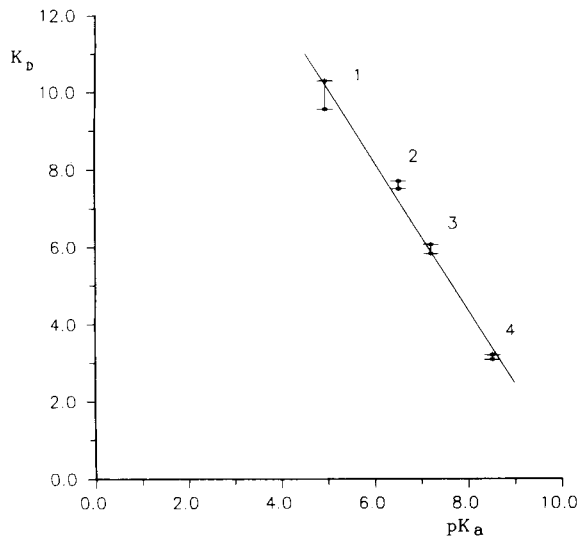

Fig. 4. Dependence of the evaluated distribution coefficients, K_D, on the pK_a values of chlorophenols. 1 = PCP; 2 = 2,4,6-TCP; 3 = 2,4,5-TCP; 4 = 2,4-DCP.

The distribution coefficients K_D were correlated with the pK_a values of CPs (Fig. 4, Table 2) and a good correlation ($r = 0.9932$) was found. At constant pH_L, the pK_a values characterize the polarity of CPs and the K_D values describe the degree of interaction of CPs with the pseudo-stationary phase. From Fig. 4 it is evident that the more polar phenols are more influenced than the less polar derivatives by PEG. The correlation dependence obtained agrees with the suggestion that the polymer network of PEG interacts with CPs as the polar pseudo-stationary phase.

The optimum condition for the separation of CPs was found to be 4% PEG. All separands are well resolved from each other (Fig. 2b). The correctness of the separation was verified by the construction of calibration lines that were linear for PCP ($r = 0.9929$), 2,4,5-TCP ($r = 0.9979$), 2,4,6-TCP ($r = 0.9976$) and 2,4-DCP ($r = 0.9965$) in the range 50–500 ng μl^{-1}.

Conclusion

The use of PEG as a polar pseudo-stationary phase for the ITP separation of chlorophenols was tested. The migration behaviour of these compounds was described by the equation derived for the effective mobilities of ions interacting with a stationary phase. Using these relationships, the distribution coefficients between polyethylene glycol and aqueous phases were evaluated. The chlorophenol derivatives can all be sufficiently resolved from each other with 4% PEG in the leading electrolyte.

REFERENCES

1 T. Wehr, LC·GC Int., 6 (1993) 70.
2 S. Terabe, K. Otsuka and T. Ando, Anal. Chem., 57 (1985) 834.
3 S. Terabe, K. Otsuka and T. Ando, Anal. Chem., 61 (1989) 251.
4 S. Terabe and T. Isemura, Anal. Chem., 62 (1990) 650.
5 J. Snopek, I. Jelínek and E. Smolková-Keulemansová, J. Chromatogr., 452 (1988) 571.
6 I. Jelínek, J. Snopek, J. Dian and E. Smolková-Keulemansová, J. Chromatogr., 470 (1989) 113.
7 J. Snopek, H. Soini, M. Novotný and E. Smolková-Keulemansová, J. Chromatogr., 559 (1991) 215.
8 V. Madajová, E. Turcelová and D. Kaniansky, J. Chromatogr., 589 (1992) 329.
9 O.V. Thomas, J.R. Stork and S.L. Lammert, J. Chromatogr. Sci., 18 (1980) 583.
10 P. Praus and V. Dombek, Anal. Chim. Acta, 277 (1993) 97.
11 P. Praus and V. Dombek, Anal. Chim. Acta, 281 (1993) 397.
12 R.P.W. Scott and P. Kucera, J. Chromatogr., 142 (1977) 213.
13 V. Jokl, J. Chromatogr., 13 (1964) 451.
14 O. Fujishita, S. Higuchi, M. Yoshikawa, T. Aoyama and M. Horioka, Chem. Parm. Bull., 31 (1983) 2134.
15 P. Boček, M. Deml, P. Gebauer and V. Dolník, Analytická Kapilární Izotachoforéza, Academia, Prague, 1987.
16 O. Fisher, V. Vetterl and J. Kypr, Fyzikální Chemie Makromolekul a Koloidních Soustav, SPN, Prague, 1984, p. 108.
17 E. Kendler and P. Jenner, J. Chromatogr., 390 (1987) 185.
18 D. Mosset, P. Gareil and R. Rosset, J. Chromatogr., 390 (1987) 241.
19 M. Meloun and J. Militký, Statistické Zpracování Experimentálních dat na Osobních Počítačích, Vol. II/A, Finish, Pardubice, 1992, p. 57.
20 S. Li, M. Paleologou and W.C. Purdy, J. Chromatogr. Sci., 29 (1991) 66.

Analytica Chimica Acta, 283 (1993) 923–926
Elsevier Science Publishers B.V., Amsterdam

Cerimetric determination of oxygen balance in oxide superconductors

Josef Novák, Zuzana Málková, Zdena Pokorná and Věra Hamplová

Institute of Physics, Academy of Sciences of the Czech Republic, Na Slovance 2, 18040 Prague 8 (Czech Republic)

(Received 22nd April 1993)

Abstract

This method is based on the oxidation of a known amount of iron(II) ions with oxide superconductors YBaCuO and BiSrCaCuO in a 2–5 mol l^{-1} solution of hydrobromic acid. The unreacted iron(II) ions were determined by cerimetric titration with ferroin as the indicator. This procedure allows the dissolution of samples even at elevated temperature. The reliability interval is 5%.

Keywords: Titrimetry; Cerimetric determination of oxygen balance; Iron; Oxygen; Superconductors

The determination of the oxygen balance in oxide superconductor materials becomes important when studying and interpreting physical characteristics of these materials. Harris and Hewston [1] suggested a differential visual iodometric titration and Dousek [2] used a coulometric method for the determination. However, a dissolution of compact samples in hydrochloric acid (7 mol l^{-1}) in the presence of potassium iodide at a low temperature [1] does not lead to satisfactory results, especially in the case of BiSrCaCuO samples.

If BiSrCaCuO and YBaCuO are dissolved in hydrochloric acid [3] or nitric acid [4] in the presence of iron(II) salt, the values of the determination of the active oxygen content are lower than the correct ones because of the loss of molecular oxygen. The amount of gaseous oxygen released depends on the concentration of acids and iron(II) salt [5] used for the determination. Oku et al. [6] used in this case the Fe^{2+}/Fe^{3+} system in a mixture of phosphoric acid and perchloric acid. The determination of small deviation from the oxygen stoichiometry in YBaCuO superconductors using the Fe^{2+}/Fe^{3+} system has also been studied by Goguel [7].

The present method makes it possible to determine the oxygen balance in very fine-powdered samples as well as in compact samples after dissolution in hydrobromic acid in the presence of a known quantity of iron(II) salt at elevated temperature. The release of gaseous oxygen under these conditions is eliminated. The unreacted iron(II) ions are determined by visual cerimetric titration. We also paid attention to the homogeneity of the analyzed samples.

Correspondence to: Z. Málková, Institute of Physics, Academy of Sciences of the Czech Republic, Na Slovance 2, 18040 Prague 8 (Czech Republic).

EXPERIMENTAL

Reagents

Reagents used were, hydrobromic acid, 35% (w/w); hydrochloric acid, 18% (w/w); iron(II) bromide, solution containing 9×10^{-3} mol l^{-1} in 10% (w/w) solution of hydrobromic acid; cerium(IV) sulfate, 0.01 mol l^{-1} in 0.5 mol l^{-1}

sulfuric acid; ferroin, 0.005 mol l^{-1} solution in H_2O; and nitrogen gas.

Procedure

Into a flask equipped with a reflux condenser [3] 3 ml of hydrobromic acid and 5 ml of iron(II) salt are placed and air is removed from the flask by a stream of nitrogen. Under this inert atmosphere a microscope slide bearing 30–80 mg of the sample is put into the flask and the sample is dissolved by boiling for 2 min. The solution was cooled down to room temperature and transferred into an Erlenmeyer flask which contained 50 ml of water, 5 ml of hydrochloric acid and 3 drops of ferroin (titrated beforehand by a Ce^{4+} solution). The solution was titrated by cerium(IV) sulphate until the red colour disappeared. The blank titration with the same content of iron(II) bromide was carried out in the same way and the difference in the amounts of cerium(IV) sulphate solution indicates the quantity of the active oxygen in the sample.

RESULTS AND DISCUSSION

The suggested method is suitable for the determination of the active oxygen content in oxide superconductor materials after their dissolution in hydrobromic acid in the presence of a known amount of Fe^{2+} ions under inert nitrogen atmosphere. The excess of iron(II) ions is determined by a cerium(IV) sulphate titration in the presence of ferroin as indicator.

The main advantage of this method is a fast and complete dissolution of even crude samples and a sharp colour change of the indicator at the equivalence point.

Even for superconductors with a high content of bismuth the solutions are not coloured by the redish-orange BiI_4^- complex which is formed during iodometric titration [1].

The influence of concentration of hydrobromic acid on the reactivity of solid samples with iron(II) salt is shown in Fig. 1. It is evident that the formal potential of Fe^{2+}/Fe^{3+} in the concentration range 2–5 mol l^{-1} of hydrobromic acid is reduced to such an extent that gaseous oxygen is not released as in hydrochloric acid. On the other hand the potential is so high that the iron(III) ions do not oxidize bromide ions to elementary bromine. At a concentration of hydrobromic acid higher than 6 mol l^{-1}, oxygen may be released and hence the obtained results are too low.

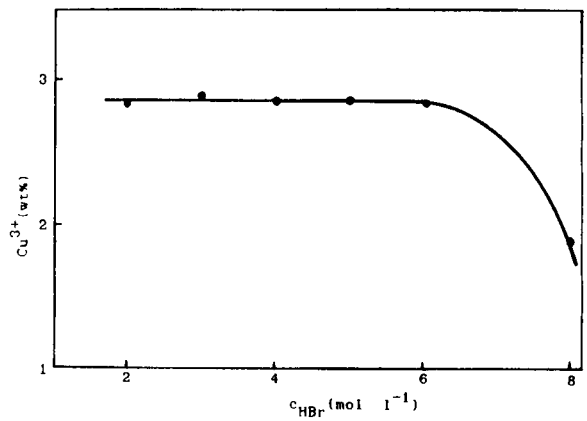

Fig. 1. Effect of concentration of hydrobromic acid on the oxidation of Fe^{2+} ions by the same amount of powdered and homogenized superconductor expressed as wt.% Cu^{3+} (starting volume of mixture for dissolution is 10 ml, $c_{Fe^{2+}} = 54 \times 10^{-4}$ mol l^{-1}, 50 mg $Bi_{2.4}Sr_{1.4}Ca_{0.2}CuO_{6.2+x}$, N_2 atmosphere, dissolved by boiling for 2 min).

Table 1 shows the stability of iron(II) salt on air in 7 mol l^{-1}, 3.5 mol l^{-1} and 1.75 mol l^{-1} hydrobromic acid solutions. We can see that the oxidation rate of a solution of iron(II) salt decreases with a decreasing concentration of hydrobromic acid. Solutions of hydrobromic acid are subject to oxidation too. Therefore free bromine is removed by metallic aluminium.

TABLE 1

Stability of Fe^{2+} ions in hydrobromic acid solutions ($c_{Fe} = 9 \times 10^{-3}$ mol l^{-1})

Time (h)	Content of Fe^{2+} (%) in HBr		
	7.00 mol l^{-1}	3.50 mol l^{-1}	1.75 mol l^{-1}
0	100.0	100.0	100.0
1	99.4	100.0	100.0
2	97.1	99.7	100.1
3	93.6	99.4	100.0
4	90.2	98.6	99.8
5	85.5	98.0	99.9

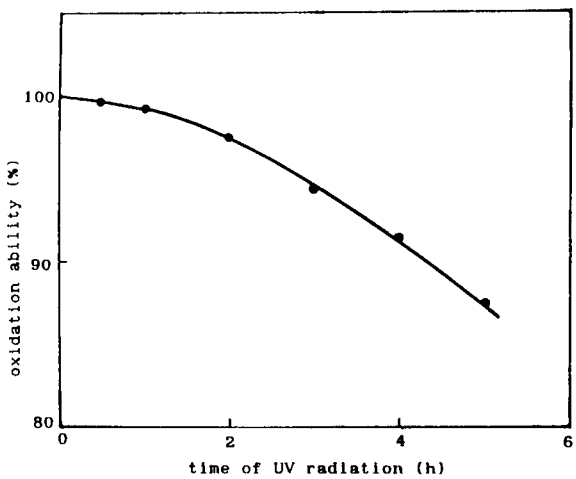

Fig. 2. Plot of the oxidation power of BiSrCaCuO sample against time of UV radiation (the UV radiation source: a 500-W high-pressure mercury discharge tube, radiation power 1.34 mW cm^{-2}, was placed at a distance of 18 cm from the exposed sample [9]).

The method suggested is used for the determination of the oxidation power for small fragments or thoroughly homogenized samples of YBaCuO, BiSrCaCuO and BiSrCuO superconductors. The results of the cerimetric titration after dissolution in hydrobromic acid, in hydrochloric acid, or in their mixture are given in Table 2. In cases of samples with a good solubility in hydrochloric acid at room temperature, the oxidation power by the iodometric titration [1] was determined as well. It can be seen in Table 2 that the results obtained with hydrochloric acid are ca. 30–40% lower compared with hydrobromic acid; the mixture of 2.5 mol l^{-1} hydrobromic acid and 3 mol l^{-1} hydrochloric acid gives results lower by about 7–10%. The results obtained by the cerimetric method are in good agreement with those obtained by the iodometric method. For the cerimetric method with hydrobromic acid the reliabil-

TABLE 2

Oxidation ability of superconductors expressed as the content of Cu^{3+} determined by cerimetry and iodometry

Number of sample	Compound	Preparation of sample [a]	Cu^{3+} (wt.%) found					
			Cerimetry in HBr		Cerimetry in HCl		Iodometry	
1	YBaCuO	– [a]	3.74	3.71	2.24	2.23	3.68	3.71
			3.75		2.23		3.70	
2	YBaCuO	– [a]	3.40	3.42	2.32	2.27	3.39	3.42
			3.39					
		– [b]	3.36	3.38	2.47	2.32	3.35	3.39
			3.33					
3	BiSrCaCuO	– [a]	2.26	2.62	1.67	1.59	2.67	2.63
			2.67					
		– [b]	2.69	2.67	1.64	1.35	–	
			2.66					
4	BiSrCaCuO	– [a]	2.22	2.26	1.49	1.46	2.31	2.27
			2.25		1.44		2.25	
		– [b]	2.24	2.21	1.28	1.21	–	
			2.21		1.29			
5	BiSrCuO	– [a]	1.88	1.91	–		1.73	1.76
			1.86				1.80	1.85
		– [b]	0.63	1.46	–		–	
			3.58	1.86				
6	BiSrCaCuO	– [a]	2.56	2.58	2.44	2.39	–	
			2.60		2.41	– [c]		
7	BiSrCaCuO	– [b]	1.77	1.81	1.63	1.65	–	
			1.75		1.55	– [c]		

[a] Homogenized sample. [b] Nonhomogenized fragments of sample. [c] In HBr + HCl.

ity interval is 5% for $\alpha = 0.05$ in the case of homogenized samples. The reliability intervals for nonhomogenized samples are higher; they were not comprised in the statistical evaluation. A statistical evaluation was made by the Dean and Dixon method [8].

The sensitivity of samples to ultraviolet radiation can be one of the reasons for inhomogeneities in the active oxygen content in samples. For example, a BiSrCaCuO powder sample which was irradiated by UV for 4.5 h showed a lowering of its oxidation ability by about 10% (Fig. 2).

The effects concerning this inhomogeneity and its distribution throughout the samples will be studied later.

REFERENCES

1 D.C. Harris and T.A. Hewston, J. Solid State Chem., 69 (1987) 182.
2 J. Dousek, personal communication.
3 J. Novák, P. Vyhlídka, D. Zemanová, E. Pollert and A. Tříska, Phys. C, 157 (1989) 346.
4 Y. Idemoto and K. Fueki, Phys. C, 168 (1990) 167.
5 D. Zemanová, personal communication.
6 M. Oku, J. Kímura, M. Hosoya, K. Takada and K. Hirokawa, Fresenius' Z. Anal. Chem., 332 (1988) 237.
7 R. Goguel, Fresenius' Z. Anal. Chem., 336 (1990) 311.
8 K. Eckschlager, Errors, Measurement and Results in Chemical Analysis, Van Nostrand Reinhold, London, 1969, p. 89.
9 F. Karel and J. Novák, Chem. Listy, 73 (1979) 1276.

Chromatography of Mycotoxins

Techniques and Applications

edited by **V. Betina**

Journal of Chromatography Library Volume 54

This work comprises two parts, Part A: Techniques and Part B: Applications. In Part A the most important principles of sample preparation, extraction, clean-up, and of established and prospective chromatographic techniques are discussed in relation to mycotoxins. In Part B the most important data, scattered in the literature, on thin-layer, liquid, and gas chromatography of mycotoxins have been compiled. Mycotoxins are mostly arranged according to families, such as aflatoxins, trichothecenes, lactones etc. Chromatography of individual important mycotoxins and multi-mycotoxin chromatographic analyses are also included. Applications are presented in three chapters devoted to thin-layer, liquid, and gas chromatography of mycotoxins.

Contents:

1993 xiv + 440 pages
Price: US $ 180.00 / Dfl. 315.00
ISBN 0-444-81521-X

ORDER INFORMATION

For USA and Canada
ELSEVIER SCIENCE PUBLISHERS
Judy Weislogel,
P.O. Box 945
Madison Square Station,
New York, NY 10160-0757
Fax: (212) 633 3880

In all other countries
ELSEVIER SCIENCE PUBLISHERS
P.O. Box 211,
1000 AE Amsterdam
The Netherlands
Fax: (+31-20) 5803 705

US$ prices are valid only for the USA & Canada and are subject to exchange rate fluctuations; in all other countries the Dutch guilder price (Dfl.) is definitive. Customers in the European Community should add the appropriate VAT rate applicable in their country to the price(s). Books are sent postfree if prepaid.

ELSEVIER
SCIENCE PUBLISHERS

Capillary Electrophoresis

NOW ALSO IN PAPERBACK

Principles, Practice and Applications

by **S.F.Y. Li**, *National University of Singapore, Singapore*

Journal of Chromatography Library Volume 52

Capillary Electrophoresis (CE) has had a very significant impact on the field of analytical chemistry in recent years as the technique is capable of very high resolution separations, requiring only small amounts of samples and reagents. Furthermore, it can be readily adapted to automatic sample handling and real time data processing. Many new methodologies based on CE have been reported. Rapid, reproducible separations of extremely small amounts of chemicals and biochemicals, including peptides, proteins, nucleotides, DNA, enantiomers, carbohydrates, vitamins, inorganic ions, pharmaceuticals and environmental pollutants have been demonstrated. A wide range of applications have been developed in greatly diverse fields, such as chemical, biotechnological, environmental and pharmaceutical analysis.

This book covers all aspects of CE, from the principles and technical aspects to the most important applications. It is intended to meet the growing need for a thorough and balanced treatment of CE. The book will serve as a comprehensive reference work and can also be used as a textbook for advanced undergraduate and graduate courses. Both the experienced analyst and the newcomer will find the text useful.

Contents:

1. Introduction. Historical Background. Overview of High Performance CE. Principles of Separations. Comparison with Other Separation Techniques. **2. Sample Injection Methods.** Introduction. Electrokinetic Injection. Hydrodynamic Injection. Electric Sample Splitter. Split Flow Syringe Injection System. Rotary Type Injector. Freeze Plug Injection. Sampling Device with Feeder. Microinjectors. Optical Gating. **3. Detection Techniques.** Introduction. UV-Visible Absorbance Detectors. Photodiode Array Detectors. Fluorescence Detectors. Laser-based Thermooptical and Refractive Index Detectors. Indirect Detection. Conductivity Detection. Electrochemical Detection. Mass Spectrometric Detection. **4. Column Technology.** Uncoated Capillary Columns. Coated Columns. Gel-filled Columns. Packed Columns. Combining Packed and Open-Tubular Column. **5. Electrophoretic Media.** Electrophoretic Buffer Systems. Micellar Electrokinetic Capillary Chromatography. Inclusion Pseudophases. Metal-complexing Pseudophases. Other Types of Electrophoretic Media. **6. Special Systems and Methods.** Buffer Programming. Fraction Collection. Hyphenated Techniques. Field Effect Electroosmosis. Systematic Optimization of Separation. **7. Applications of CE.** Biomolecules. Pharmaceutical and Clinical Analysis. Inorganic Ions. Hydrocarbons. Foods and Drinks. Environmental Pollutants. Carbohydrates. Toxins. Polymers and Particles. Natural Products. Fuel. Metal Chelates. Industrial Waste Water. Explosives. Miscellaneous Applications. **8. Recent Advances and Prospect for Growth.** Recent Reviews in CE. Advances in Injection Techniques. Novel Detection Techniques. Advances in Column Technology. Progress on Electrolyte Systems. New Systems and Methods. Additional Applications Based on CE. Future Trends. **References. Index.**

1992 608 pages Hardbound
US$ 225.75 / Dfl. 395.00
ISBN 0-444-89433-0
1993 608 pages Paperback
Price: US$ 114.25 / Dfl. 200.00
ISBN 0-444-81590-2

"Everything seems to be there, any detection system you have ever dreamed of, any capillary coating, enough electrolyte systems to saturate your wits, and more..."

"...by far the most thorough and comprehensive book in the field yet to appear."

P.G. Righetti, Milan

ORDER INFORMATION

For USA and Canada
ELSEVIER SCIENCE PUBLISHERS
Judy Weislogel,
P.O. Box 945
Madison Square Station,
New York, NY 10160-0757
Fax: (212) 633 3880

In all other countries
ELSEVIER SCIENCE PUBLISHERS
P.O. Box 211,
1000 AE Amsterdam
The Netherlands
Fax: (+31-20) 5803 705

US$ prices are valid only for the USA & Canada and are subject to exchange rate fluctuations; in all other countries the Dutch guilder price (Dfl.) is definitive. Customers in the European Community should add the appropriate VAT rate applicable in their country to the price(s). Books are sent postfree if prepaid.

ELSEVIER
SCIENCE PUBLISHERS

PUBLICATION SCHEDULE FOR 1994

	S'93	O'93	N'93	D'93	J	F						
Analytica Chimica Acta	281/1 281/2 281/3	282/1 282/2 282/3	283/1 283/2	283/3 284/1 284/2	284/3 285/1 285/2	285/3 286/1 286/2						
Vibrational Spectroscopy		6/1			6/2							

INFORMATION FOR AUTHORS

Detailed "Instructions to Authors" for *Analytica Chimica Acta* was published in Volume 256, No. 2, pp. 373–376. Free reprints of the "Instructions to Authors" of *Analytica Chimica Acta* and *Vibrational Spectroscopy* are available from the Editors or from: Elsevier Science Publishers B.V., P.O. Box 330, 1000 AH Amsterdam, The Netherlands. Telefax: (+31-20) 5862845.

Manuscripts. The language of the journal is English. English linguistic improvement is provided as part of the normal editorial processing. Authors should submit three copies of the manuscript in clear double-spaced typing on one side of the paper only. *Vibrational Spectroscopy* also accepts papers in English only.

Abstract. All papers and reviews begin with an Abstract (50–250 words) which should comprise a factual account of the contents of the paper, with emphasis on new information.

Figures. Figures should be prepared in black waterproof drawing ink on drawing or tracing paper of the same size as that on which the manuscript is typed. One original (or sharp glossy print) and two photostat (or other) copies are required. Attention should be given to line thickness, lettering (which should be kept to a minimum) and spacing on axes of graphs, to ensure suitability for reduction in size on printing. Axes of a graph should be clearly labelled, along the axes, outside the graph itself. All figures should be numbered with Arabic numerals, and require descriptive legends which should be typed on a separate sheet of paper. Simple straight-line graphs are not acceptable, because they can readily be described in the text by means of an equation or a sentence. Claims of linearity should be supported by regression data that include slope, intercept, standard deviations of the slope and intercept, standard error and the number of data points; correlation coefficients are optional.

Photographs should be glossy prints and be as rich in contrast as possible; colour photographs cannot be accepted. Line diagrams are generally preferred to photographs of equipment.

Computer outputs for reproduction as figures must be good quality on blank paper, and should preferably be submitted as glossy prints.

Nomenclature, abbreviations and symbols. In general, the recommendations of the International Union of Pure and Applied Chemistry (IUPAC) should be followed, and attention should be given to the recommendations of the Analytical Chemistry Division in the journal *Pure and Applied Chemistry* (see also *IUPAC Compendium of Analytical Nomenclature, Definitive Rules*, 1987).

References. The references should be collected at the end of the paper, numbered in the order of their appearance in the text (*not* alphabetically) and typed on a separate sheet.

Reprints. Fifty reprints will be supplied free of charge. Additional reprints (minimum 100) can be ordered. An order form containing price quotations will be sent to the authors together with the proofs of their article.

Papers dealing with vibrational spectroscopy should be sent to: Dr J.G. Grasselli, 150 Greentree Road, Chagrin Falls, OH 44022, U.S.A. Telefax: (+1-216) 2473360 (Americas, Canada, Australia and New Zealand) or Dr J.H. van der Maas, Department of Analytical Molecule Spectrometry, Faculty of Chemistry, University of Utrecht, P.O. Box 80083, 3508 TB Utrecht, The Netherlands. Telefax: (+31-30) 518219 (all other countries).

0003-2670/93/$06.00

This issue is printed on acid-free paper.

PRINTED IN THE NETHERLANDS

Electrochemical and Electrocatalytic Reactions of Carbon Dioxide

edited by **B.P. Sullivan**, University of Wyoming, Laramie, WY, USA, **K. Krist**, Gas Research Institute, Chicago, IL, USA and **H.E. Guard**, Office of Naval Research, Department of the Navy, Arlington, VA, USA

The recycling of atmospheric molecules for use as fuels and chemicals is a goal which can only be achieved through a deeper understanding of catalytic processes, particularly electrocatalysis whereby redox transformations can be interfaced with solar or nuclear energy input. Carbon dioxide is a prototypical small molecule in many regards since it is chemically inert. In addition, because of the likely role of carbon dioxide in global temperature cycles, it will be imperative in the future to regulate the output from industrial processes. The purpose of this book is to present a unified discussion of the carbon dioxide chemistry which is necessary for the understanding and design of electrochemically-driven processes for the reduction of carbon dioxide and to provide an impetus for the further development of electrocatalytic carbon dioxide chemistry.

Contents:

1993 xiv + 300 pages
Price: US $ 212.50 / Dfl. 340.00
ISBN 0-444-88316-9

ELSEVIER
SCIENCE PUBLISHERS

ORDER INFORMATION

For USA and Canada
ELSEVIER SCIENCE PUBLISHERS
Judy Weislogel
P.O. Box 945
Madison Square Station,
New York, NY 10160-0757
Tel: (212) 989 5800
Fax: (212) 633 3880

In all other countries
ELSEVIER SCIENCE PUBLISHERS
P.O. Box 211
1000 AE Amsterdam
The Netherlands
Tel: (+31-20) 5803 753
Fax: (+31-20) 5803 705

US$ prices are valid only for the USA & Canada and are subject to exchange rate fluctuations; in all other countries the Dutch guilder price (Dfl.) is definitive. Books are sent postfree if prepaid.

711/414\140\0001-00

0003-2670(19931126)283:2;1-7